Advances in Quantum Chemistry

Theory of Heavy Ion Collision Physics in Hadron Therapy

Volume 65

Volume Editor
Dževad Belkić

Series Editors
John R. Sabin
and Erkki Brändas

VOLUME SIXTY FIVE

ADVANCES IN QUANTUM CHEMISTRY

Theory of Heavy Ion Collision Physics in Hadron Therapy

EDITORIAL BOARD

VOLUME SIXTY FIVE

ADVANCES IN QUANTUM CHEMISTRY

Theory of Heavy Ion Collision Physics in Hadron Therapy

Edited by

DŽEVAD BELKIĆ
Professor of Mathematical Radiation Physics
Nobel Medical Institute, Karolinska Institute
Stockholm
Sweden

Series Editors
John R. Sabin
and Erkki Brändas

ELSEVIER

Amsterdam • Boston • Heidelberg • London
New York • Oxford • Paris • San Diego
San Francisco • Singapore • Sydney • Tokyo
Academic Press is an imprint of Elsevier

Academic Press is an imprint of Elsevier
The Boulevard, Langford Lane, Kidlington, Oxford, OX51GB, UK
32, Jamestown Road, London NW1 7BY, UK
Radarweg 29, PO Box 211, 1000 AE Amsterdam, The Netherlands
225 Wyman Street, Waltham, MA 02451, USA
525 B Street, Suite 1900, San Diego, CA 92101-4495, USA

First edition 2013

ISBN: 978-0-12-396455-7
ISSN: 0065-3276

For information on all Academic Press publications
visit our web site at *store.elsevier.com*

Printed and bound in USA
13 14 15   10 9 8 7 6 5 4 3 2 1

CONTENTS

Preface

This Special Issue is within a wider realm of physical and biological effects of irradiation of tissue and tissue-like targets by energetic heavy ions of high relevance to hadron therapy. The main goal is to review the leading theories describing fast collisions of ions with atoms and molecules by emphasizing the possibilities for improving the existing data bases for energy losses of heavy charged particles during their passage through matter. Ion-atom collisions are included in this topic by presenting those theoretical formalisms that are universally applicable to general targets, including molecules from tissue. Although the main focus is on energy losses due to electromagnetic interactions, also reviewed are the pertinent cross sections and stopping powers for nuclear reactions. Data bases of electronic and nuclear stopping powers coupled with the associated modeling of biological responses of cells to irradiation are essential to hadron therapy.

When determining a treatment plan for a patient with cancer, the radiation oncologist must make a key assumption on the actual amount of dose needed to eradicate all the tumor cells. It is here that the biophysical input is required, accounting for the precise extent of the deposited physical doses, as well as for their biological counterparts that modify the initial impact of radiation by the cell repair processes. The overall success of radiotherapy is contingent upon the dose planning, dose delivery and dose verification systems. To meet with success, radiotherapy must include the most adequate descriptions of energy losses of particle beams in tissue and the cell recovery. Deep-seated tumors are usually treated with energetic hadrons because of the optimal conformity of heavy ions to the targets by way of a very precise local deposition of doses in the vicinity of the Bragg peak.

Versatile biophysical aspects of the topics of this Special Issue are expounded through 14 chapters with the following specific themes:

Chapter 1 (H. Bichsel) examines the stochastic variations of energy losses and biological effects of protons and carbon nuclei in their high-energy collisions with water.

Chapter 2 (H. Paul) performs a comparative analysis of the accuracy of different methods and simulation codes for stopping powers and ion ranges.

Chapter 3 (J.R. Sabin, J. Oddershede and S.P.A. Saue) reviews the theoretical and experimental aspects of determination of the mean excitation energy of water.

Chapter 4 (F. Ziad) studies the molecular scale Monte Carlo simulations of ion tracks using the GEANT4-DNA code with the inclusion of the effects of secondary electrons.

Chapter 5 (J. Beebe-Wang, P. Vaska, F.A. Dilmanian, S.G. Peggs and D.J. Schlyer) investigates the radiation treatment verifications in proton therapy using positron-emission tomographic imaging and Monte Carlo simulations.

Chapter 6 (I. Abril, R. Garcia-Molina, P. de Vera, I. Kyriakou and D. Emfietzoglou) reports on inelastic collisions of energetic protons in tissue-like media using a combination of molecular dynamics and Monte Carlo simulations.

Chapter 7 (C.C. Montanari and J.E. Miraglia) presents a combination of the dielectric formalism with the shell-wise local plasma approximation for inelastic processes in high-energy ion-matter collisions.

Chapter 8 (M.A. Bernal-Rodriguez and J.A. Liendo) assesses the usefulness of the available empirical cross sections relative to the continuum distorted wave theories and experimental data for single ionization of liquid water by protons, alpha particles and carbon nuclei.

Chapter 9 (R.D. Rivarola, M.E. Galassi, P.D. Fainstein and C. Champion) reviews distorted wave methods for electron capture, ionization and excitation processes in high-energy inelastic collisions of ions with water.

Chapter 10 (C. Champion, J. Hanssen and R.D. Rivarola) presents the results of the first Born approximation for ionization and electron transfer in energetic collisions between multiply-charged ions and water.

Chapter 11 (T. Kirchner, M. Murakami, M. Horbatsch and H.J. Lüdde) reports on cross sections for single- and multiple-electron processes in ion-water collisions using the time-dependent density functional theory in the independent electron model.

Chapter 12 (Dž. Belkić, I. Mančev and N. Milojević) deals with the four-body formalism of distorted wave second-order perturbation methods for double electron transitions through simultaneous electron transfer and ionization processes in ion-atom collisions at high impact energies.

Chapter 13 (V.Yu. Lazur and M.V. Khoma) reviews the theoretical concept of the Dodd-Greider integral equations with Coulomb interactions for one- and two-electron capture processes in fast ion-atom collisions.

Chapter 14 (Dž. Belkić and K. Belkić) contributes to a further improvement of the effectiveness of the current radiation treatments of cancer through the amended dose planning systems based on an adequate description of cell survival valid at all doses as predicted by the new mechanistic repair-based Padé linear-quadratic biophysical model.

Dževad Belkić, Guest Editor
Professor of Mathematical Radiation Physics
Nobel Medical Institute, Karolinska Institute
Stockholm
Sweden

ACKNOWLEDGMENT

The Guest Editor is highly appreciative of the support from the Swedish Cancer Fund, Karolinska University Hospital's Radiumhemmet and the Karolinska Institute Research Fund.

Contributors

Isabel Abril
Departament de Física Aplicada, Universitat d'Alacant, E-03080 Alacant, Spain

Joanne Beebe-Wang
Brookhaven National Laboratory, P.O. Box 5000, Upton, NY 11973, USA

Dževad Belkić
Nobel Medical Institute, Karolinska Institute, P.O. Box 260, S-171 76 Stockholm, Sweden

Karen Belkić
Nobel Medical Institute, Karolinska Institute, P.O. Box 260, S-171 76 Stockholm, Sweden

Mario A. Bernal-Rodríguez
Instituto de Física Gleb Wataghin, Universidade Estadual de Campinas, Brazil

Hans Bichsel
CENPA, University of Washington, Seattle, WA 98195-4290, USA

Christophe Champion
Université Bordeaux 1, CNRS/IN2P3, Centre d' Etudes Nucléaires de Bordeaux-Gradignan, CENBG, Gradignan, France

Pablo de Vera
Departament de Física Aplicada, Universitat d'Alacant, E-03080 Alacant, Spain

F. Avraham Dilmanian
Brookhaven National Laboratory, P.O. Box 5000, Upton, NY 11973, USA

Dimitris Emfietzoglou
Medical Physics Laboratory, University of Ioannina Medical School, GR-45110 Ioannina, Greece

Pablo D. Fainstein
Centro Atómico Bariloche, Comisión Nacional de Energía Atómica, Avda E. Bustillo 9500, 8400 Bariloche, Argentina

Ziad Francis
Saint Joseph University, Faculty of Sciences, Department of Physics, Mkalles, Beirut, Lebanon

Mariel E. Galassi
Instituto de Física Rosario (CONICET-UNR) and Facultad de Ciencias Exactas, Ingeniería y Agrimensura, Universidad Nacional de Rosario, Avenida Pellegrini 250, 2000 Rosario, Argentina

Rafael Garcia-Molina
Departamento de Física, Centro de Investigación en Óptica y Nanofísica, Universidad de Murcia, E-30100 Murcia, Spain

Jocelyn Hanssen
Laboratoire de Physique Moléculaire et des Collisions, UMR CNRS 7565, Université de Lorraine, Metz, France

Marko Horbatsch
Department of Physics and Astronomy, York University, Toronto, Ontario, Canada M3J 1P3

Mykhaylo V. Khoma
Theoretical Physics, Uzhgorod National University, Uzhgorod, Ukraine

Tom Kirchner
Department of Physics and Astronomy, York University, Toronto, Ontario, Canada M3J 1P3

Ioanna Kyriakou
Medical Physics Laboratory, University of Ioannina Medical School, GR-45110 Ioannina, Greece

Volodymyr Yu. Lazur
Theoretical Physics, Uzhgorod National University, Uzhgorod, Ukraine

Jacinto A. Liendo
Departmento de Física, Universidad Simón Bolívar, Caracas, Venezuela

Hans Jürgen Lüdde
Institut für Theoretische Physik, Goethe-Universität, D-60438 Frankfurt, Germany

Ivan Mančev
Department of Physics, Faculty of Sciences and Mathematics, University of Niš, Niš, Serbia

Nenad Milojević
Department of Physics, Faculty of Sciences and Mathematics, University of Niš, Niš, Serbia

Jorge E. Miraglia
Instituto de Astronomía y Física del Espacio, CONICET and Universidad de Buenos Aires, casilla de correo 67, sucursal 28, C1428EGA, Buenos Aires, Argentina

Claudia C. Montanari
Instituto de Astronomía y Física del Espacio, CONICET and Universidad de Buenos Aires, casilla de correo 67, sucursal 28, C1428EGA, Buenos Aires, Argentina

Mitsuko Murakami
Department of Physics and Astronomy, York University, Toronto, Ontario, Canada M3J 1P3

Jens Oddershede
Institute for Physics, Chemistry, and Pharmacology, University of Southern Denmark, 5230 Odense M, Denmark

Helmut Paul
Atomic Physics and Surface Science, Institute for Experimental Physics, Johannes Kepler University, Altenbergerstrasse 69, A-4040, Linz, Austria

Stephen G. Peggs
Brookhaven National Laboratory, P.O. Box 5000, Upton, NY 11973, USA

Roberto D. Rivarola
Instituto de Física Rosario (CONICET-UNR) and Facultad de Ciencias Exactas, Ingeniería y Agrimensura, Universidad Nacional de Rosario, Avenida Pellegrini 250, 2000 Rosario, Argentina

John R. Sabin
Departments of Physics and Chemistry, University of Florida, Gainesville, Florida 32611, USA

Stephan P.A. Sauer
Department of Chemistry, University of Copenhagen, Copenhagen, Denmark

David J. Schlyer
Brookhaven National Laboratory, P.O. Box 5000, Upton, NY 11973, USA

Paul Vaska
Brookhaven National Laboratory, P.O. Box 5000, Upton, NY 11973, USA

CHAPTER ONE

Stochastics of Energy Loss and Biological Effects of Heavy Ions in Radiation Therapy

Hans Bichsel
CENPA, University of Washington, Seattle, WA 98195-4290, USA

Contents

Advances in Quantum Chemistry, Volume 65
ISSN 0065-3276, http://dx.doi.org/10.1016/B978-0-12-396455-7.00001-7

Abstract

Energy loss functions for protons and Carbon ions (not including fragmentation) are calculated with convolutions. For C-ions a treatment dose $D = 2$ Gy at the Bragg peak needs only ten ions traversing a cell of area 100 μm^2. Therefore the use of a *mean particle fluence per cell* N_D rather than D is used to assess the *primary* source of stochastic effects. The stochastics of specific energy z are calculated. It shows large variations because the particle fluence per cell as well as the energy spectrum of the ions have large variations. A new interpretation of the relation between energy deposition and cell survival must be found.

1. INTRODUCTION

This review is a supplemental study of the theory of energetic collisions of heavy ions with matter, including tissue, by using stochastic as well as analytic methods. The theory in this field offers a wealth of important data bases of immediate usefulness in many research areas including health sciences.[1] The most frequently used data from this branch of collision physics are differential and total cross sections, electronic stopping power, ranges, and mean excitation energies. They constitute critical input data for modeling energy losses of heavy ions passing through matter. The accuracy of these data is of direct relevance to biological effects of ions, especially near the position of the Bragg peak.[2, 3] The theory used here for the calculations is based on the Bethe–Fano method. It is outlined in the Appendix and the text. It gives agreement of 1% or better with existing experimental and calculated data for particle energies above 2–5 MeV/u for ions from protons to Carbon ions.

In radiation therapy a major problem is the determination of the effect of the radiation dose on the irradiated tissues. It has been found that dose-effect functions are steep: to achieve tumor control[4] between 25% and 75% the difference in dose is about 20%. It thus is reasonable to aim for uncertainties of ±2% in *physical* quantities in dosimetry.[5]

The biological effects of radiation therapy occur in cells. Therefore we must study energy losses and energy deposition in microscopic volumes. In medical radiation therapy the cells of interest usually are located deep inside the body. For heavy charged particles (protons, $M_0c^2 = 938\,\mathrm{MeV}$, Carbon ions, $M_0c^2 = 11178\,\mathrm{MeV}$) beams of ions are used to penetrate to these volumes. One method used for therapy is the scanning of the tumor volume with pencil beams.[6, 7]

This method is studied here. Since the calculations described are made with computers, they can readily be extended for other beam geometries as well as cell geometries.

The study consists of several parts:

- Calculation of Bragg functions with major emphasis of generating the energy spectra of the particles for each layer of absorber along the trajectories of the particles, Sections 2 and 3.
- Calculation of detailed *energy deposition spectra* for therapy doses at the Bragg peak, Sections 4–6.
- For the biological effects a major problem is the stochastics of particle fluence per cell, Section 5.2.
- Conclusions.

In order to explicitly evaluate the *stochastic nature* of the energy deposition in cells the interaction of particles with matter cannot be explored on the basis of the Bethe mean energy loss $\mathrm{d}E/\mathrm{d}x$. Instead the detailed nature of the individual collisions of the particles with the absorber must be studied, using "collision cross sections" CCS. Cross sections are described in Appendices A and B.

The CCS are needed for the convolution method which is used here,[8–12] Sections 2.2 and 2.3 as well as for Monte Carlo calculations, Section 2.4.[13–15]

It must be understood that in general energy *loss* and energy *deposition* must be clearly distinguished, Section 4.2. For many of the particle interactions the particle speed $\upsilon = \beta c$ is the relevant parameter rather than the energy. The parameter $\gamma = \sqrt{1/(1-\beta^2)}$ is also used, where $M_0c^2(\gamma - 1)$ is the kinetic energy of the ion with mass l MeV.

To study the limitations of calculations and measurements of the physical processes in biological cells we explore the spectra of specific energy z imparted[16, 17] to cubic volumes

$$V_\mathrm{c} = 10 \times 10 \times 10\ \mu\mathrm{m}^3 \tag{1}$$

by particles incident perpendicularly on one of the surfaces. For volumes with different shapes the data derived here will have larger spreads. Methods to determine energy loss and energy deposition are described in Sections 2–5. *Bio-effects* are explored briefly in Section 6.

In this paper it is assumed that all calculations are made numerically on computers because none of the functions can easily be written in analytic form. It is an advantage of numerical results (i.e., tables) that it is trivial to *invert* a function such as given in Eq. (3) and Figures B.3 and B.4.[†] Calculations made with continuous functions will be called "analytic" here in contrast to Monte Carlo calculations. A *mean particle fluence* N_D *per cell* is used to quantify radiation.

[†] One inverts the columns of numbers of the data, then uses cubic spline interpolation to get a convenient scale for the inverted primary variable.

2. ENERGY LOSS AT MACROSCOPIC LEVEL

The "classical" approach based on Bohr, Bethe and Fano theories of continuous energy losses, i.e., stopping power, is discussed in Section 2.1. The more detailed study using *straggling functions* is described in Sections 2.2, 2.3, and Appendices A and B. The method of following individual particles along their tracks with Monte Carlo simulations is discussed in Section 2.4. *Multiple elastic scattering* is relegated to Appendix C, and *nuclear interactions* to Section 3.1 and Appendix D. The macroscopic properties of the energy deposition field are described by Bragg functions, Section 3. *Microscopic* energy loss and energy deposition are described in Section 4 and stochastic variations in Section 5. Consequences for biological effects are outlined in Section 6.

Calculations are made for $T = 200\,\text{MeV}$ protons ($\beta\gamma = 0.687$) and $T = 3600\,\text{MeV}$ C-ions ($\beta\gamma = 0.865$) traversing water (see Appendix B about organic matter). For simplicity a cubic cell of water is used to approximate the microscopic volume V_c for which energy deposition is calculated, see Section 5. The ion beam is incident perpendicularly on the cube.

Since pencil beams are used for the scanning treatment of tumors[6, 7] they are used here for the calculations.

The most important interaction of the ions with matter is the collision with molecular electrons, see Appendix B for details. The elastic interaction with atoms produces multiple scattering, Appendix C. It broadens a pencil beam and is of some importance for protons, but can be neglected for C-ions. Nuclear reactions are infrequent and not correlated with the above interactions and can be dealt with independently for the continuous transport and convolution methods, Section 3.1 and Appendix D.

2.1 Continuous transport of particles through matter: Classical approach

In classic theory the Bethe stopping power S(T), frequently written[18] as dT/dx, or $M_1(\beta)$ in Eq. (B.6), is used to calculate the *mean energy loss* $\langle\Delta\rangle$ of particles with energy T traversing absorbers of thickness ξ (units: length). If the mean energy of the ions is reduced by less than $\sim$ 5% we can use the approximation

$$\langle\Delta\rangle = \xi \cdot S(T). \tag{2}$$

For larger energy losses, the analytic *range calculation* can be used to follow the ions through the absorber with

$$y = \int_{T_0-\langle\Delta\rangle}^{T_0} \frac{\mathrm{d}T}{S(T)} \quad \text{and} \quad R(T) = \int_0^T \frac{\mathrm{d}T}{S(T)}, \tag{3}$$

where y is the distance traversed in the absorber and $R(T)$ is the "mean CSDA range" of the particles. It is practical to calculate a range table $R(T)$ as a function of T (Refs. 19,20).

Range approximations have been used extensively for the calculation of "radiation doses".[21–24]

In the nonrelativistic Bohr approximation[25] the spectrum of energies T of the particles emerging from the absorber of thickness y is assumed to be a *Gaussian* of width σ related to the second moment M_2 of the collision cross section,[26, 27] Eq. (B.6).[‡]

$$M_2' = 0.1569 z^2 \frac{Z}{A}\ (\mathrm{MeVcm})^2/\mathrm{g}, \quad \sigma = \sqrt{yM_2'}\ \mathrm{MeV}, \tag{4}$$

where ze is the electric charge of the particle, Z the atomic number of the absorber, A its number of nucleons per molecule. Note that M_2' does not depend on particle speed. A more sophisticated method was derived by Tschalär.[28§]

The energy loss spectra ("straggling") implicit in Eq. (2) actually are not symmetric.[9, 10, 29–31] This can be taken into account by the use of convolutions for Eq. (3).

2.2 Convolutions for range straggling

For the transport through thick absorbers a *convolution calculation* can be used.[8, 10–12, 29, 32] Assume that we know the energy spectrum $\Phi(y, T)$ $(T_2 < T < T_1)$ at a plane surface at y, see Figure 1.1. To calculate the spectrum $\Phi(y + \xi, T)$ after the traversal of a thin layer ξ, we use straggling functions $V(\xi, \Delta, T)$ to determine the energy loss for ions with energy between T and $T + \delta T$ (where $\delta T \ll (T_1 - T_2)$), for each energy bin δT between T_1 and T_2. These energy losses are then added together to produce the spectrum at $y + \xi$ at $T - \Delta$. The process is shown in Figure 1.1. The straggling spectra $V(\xi, \Delta, T)$ for thin absorbers are calculated with the methods described in Section 2.3.

For one track segment ξ, Figure 1.1, a convolution integral for *each* energy interval $T, T + \delta T$ between T_1 and T_2 is calculated (s is the range in Δ of $V(\xi, \Delta, T + \Delta)$, Figure 1.1)

[‡] The density of water is approximated by 1.00. Both g and cm^3 are used as units interchangeably, as convenient. We also assume that LET is the same as $\mathrm{d}T/\mathrm{d}x$.

[§] Measurements for 70 MeV protons at NIRS[11] were analyzed with this method and that of Section 2.2 for $T < 20$ MeV. The reproducibility of the measurements was better than 1%. The I-value for water was derived as 79.7 ± 0.5 eV.

$$\Phi(y+\xi;T) = \int_0^s \Phi(y, T+\Delta) \times V(\xi, \Delta, T+\Delta)\mathrm{d}\Delta \quad \text{or} \tag{5}$$

$$\Phi(y+\xi;T-\Delta) = \int \Phi(y, T) \times V(\xi, \Delta, T)\mathrm{d}\Delta. \tag{6}$$

The reader is invited to select the equation which looks more plausible. This integral then is calculated for each energy between T_1 and T_2.

For present purposes (e.g., total range of 200 MeV protons[11, 33] or 3600 MeV C-ions[12] in water) Vavilov–Fano straggling functions V are used. The results of the calculations are given in Section 3. This method is of the order of 50 times faster than corresponding MC calculations.

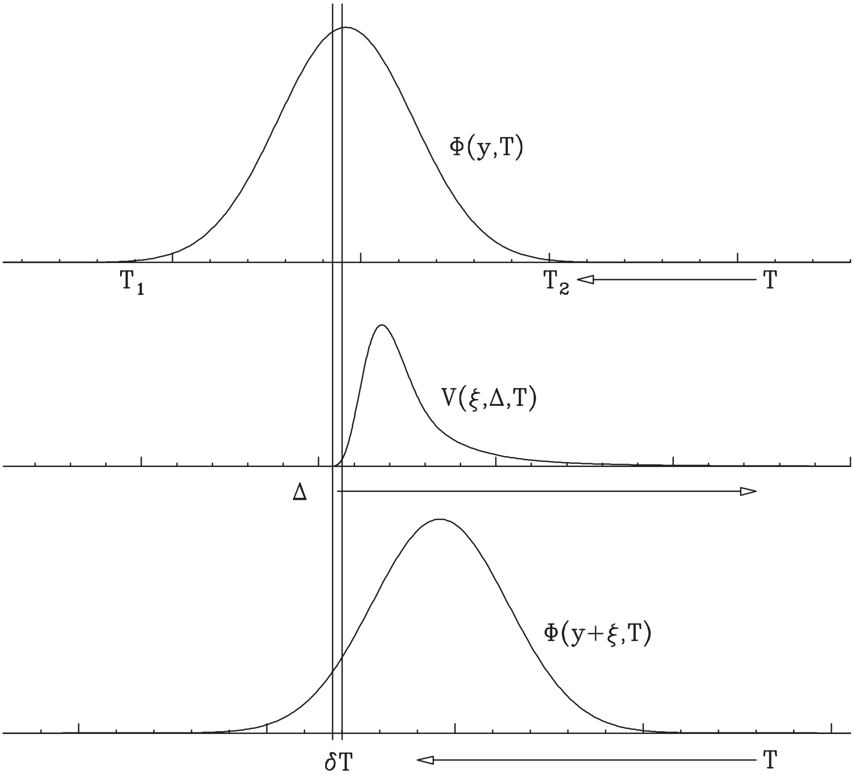

Figure 1.1 Illustration of the convolution method. The initial energy spectrum $\Phi(y;T)$ is shown at the top. For each narrow band of energies δT (shown by the vertical parallel lines) the straggling spectrum $V(\xi, \Delta, T+\Delta)$ is added successively to the spectrum $\Phi(y+\xi;T)$ shown at the bottom.

2.3 Straggling in thin segments

Analytic methods to calculate straggling for thin absorbers have been developed for over 80 years.[29–31, 34–37] One of the most comprehensive calculations and comparison with experimental data for Si detectors is in Ref. 9. Here the convolution method for straggling[9, 30, 31] has been used. The agreement between measurements and calculations is good. The reader is invited to assess the data.

2.4 Monte Carlo methods

Many computer programs use Monte Carlo (MC) methods to calculate particle spectra.[13, 14, 38–42] Time consuming computations are needed to obtain accurate data for the functions describing the depth dose functions.[33] An outline of the method is given here, details are given in Section 4. In one system the interactions occurring during the passage of the particles through matter are simulated one at a time, collision by collision,[43, 44] and include secondary collisions by the δ-rays produced. For the calculations shown in Figure 1.7, the following procedure was used: A particle j travels random distances x_i between successive collisions, calculated by selecting a random number r_r and determining the distance x_i to the next collision from the mean free path between collisions $\lambda(\upsilon) = 1/\mathrm{M}_\mathrm{o}(\upsilon)$ (particle speed v is used here rather than T)

$$x_\mathrm{i} = -\lambda(\upsilon)\ \ln r_\mathrm{r}. \tag{7}$$

The energy loss E_i is selected with a second random number from the cumulative collision spectrum, Eq. (B.6), shown in Figures B.3 and B.4. This process is repeated until $\sum x_\mathrm{i}$ exceeds the segment length x. The total energy loss Δ_j of the particle is $\Delta_\mathrm{j} = \sum_\mathrm{i} E_\mathrm{i}$. To get E_i practically, the inverse function $E(\Phi;\, \beta\gamma)$ of $\Phi(E;\, \beta\gamma)$ is calculated with e.g., cubic spline interpolation[44] (see footnote †). By binning the Δ_j the straggling function $f(\Delta)$ is obtained.[44, 45]

The Monte Carlo method can be used for all absorber thicknesses, but with decreasing particle speed[44] it is necessary to change $\lambda(\upsilon)$ (Fig. B.4) and $\Phi(E;\, v)$ (Figs. 1.3 and 1.6) at appropriate values of υ. It may not be very practical for very thick absorbers, e.g., for the full range of one 200 MeV proton in water ($R \sim 25$ cm) the number of collisions is of the order of 3 million. In order to get reasonable straggling functions, tracks for 2 million protons may be needed.[33**]

[**] A study of the equivalence of the convolution and MC methods is being prepared.

In several systems of MC calculations a "condensed history" approach is used.[13, 15, 40, 46] It consists of using energy loss straggling functions for the determination of successive random *electronic* energy losses in short track segments. Since the convolution method also uses such functions, any problems[††] found in their use will also appear in MC calculations, but will be more difficult to evaluate in the MC.

3. BRAGG FUNCTIONS

A Bragg function describes the properties of the energy spectrum $\Phi(y, T)$ of the ions in the absorber as a function of penetration y in the absorber. The methods described in Section 2 have been used to calculate $\Phi(y, T)$ and its properties at y (Eqs. (8)–(11) and B.7):

- particle fluence $N(y)$;
- particle mean energy $\langle T \rangle(y)$;
- mean energy loss $D(y)$ in a thin layer ξ;
- standard deviation $\sigma(y)$ of $\Phi(y, T)$;
- the specific energy imparted z to cells at y;
- number of particle $s(y)$ stopping in ξ.

The Bragg functions shown here have been calculated with the convolution method. In most publications about Bragg functions the only function shown is $D(y)$ (Figs. 1.2 and 1.5). If Bragg functions are evaluated with the "classical" methods of Section 2.1, there will be differences from the data given in Table 1.1.

Since the major features of the Bragg peak result from the interactions of particles with atomic electrons, I have excluded nuclear interactions and multiple scattering to show the features of the electron interactions clearly,[12] also see Section 3.1 and Appendices C and D.

Table 1.1 Properties (Eqs. (8)–(12)) of the fluence functions $\Phi(y, T)$ shown in Figure 1.3 for protons. Five functions are shown from a total of 1400 functions calculated. The skewness of $\Phi(y, T)$ is given by γ_3, for γ see Sect. 3.2

N_0	y cm	$\langle T \rangle$	σ	γ_3	N (y)	D (y)	r%
0	24.52	42.68	3.822	0.299	1.00	14.0	0
2	25.532	25.68	5.827	0.576	0.9945	21.9	0.04
3	26.046	15.35	6.214	0.030	0.7598	28.7	0.55
4	26.27	12.06	5.616	−0.212	0.4624	26.6	0.95
7	26.58	9.03	4.643	−0.464	0.1058	6.2	1.6

[††] Such as problems related to effective particle energy at the center of segments etc.

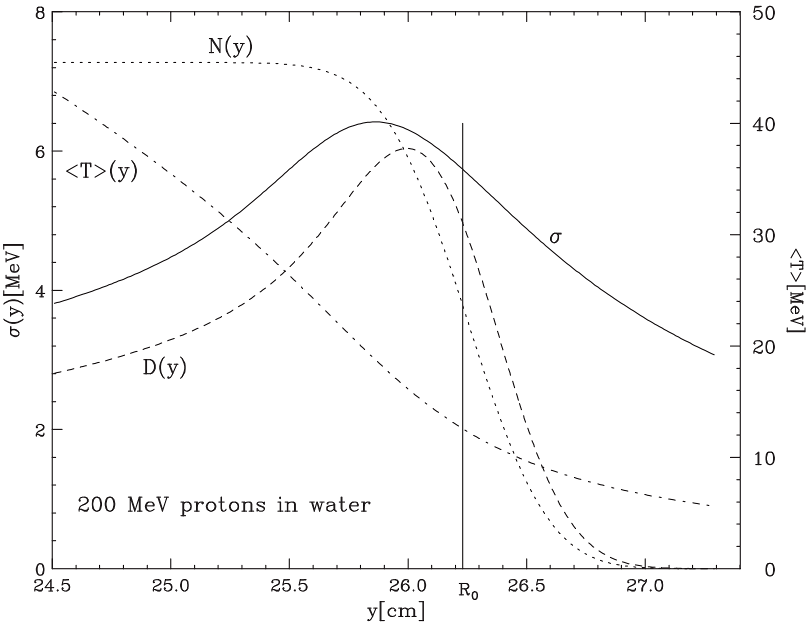

Figure 1.2 Bragg functions for 200 MeV protons traversing water. The thickness of water traversed is y, the dose is $D(y)$, the number of residual protons is $N(y)$, the mean energy of the spectrum $\Phi(y;T)$ is $\langle T\rangle$, and the standard deviation of $\Phi(y;T)$ is $\sigma(y)$.

The quantities defined above are calculated as follows using the method shown in Figure 1.1

$$N(y) = \int \Phi(y;\, T)\mathrm{d}T. \tag{8}$$

In each track interval ξ the number $N(y)$ is reduced by the number of ions reaching $T = 0$, as given by $s(y)$ in Figure 1.4. The specific dose $D_s(y)$ at y is given in terms of an average stopping power

$$D_s(y) = \int \Phi(y;\, T)S(T)\mathrm{d}T, \tag{9}$$

where $S(T)$ is the stopping power for ion energy T. The mean ion energy at y is given by

$$\langle T\rangle(y) = \int \Phi(y;\, T)T\,\mathrm{d}T. \tag{10}$$

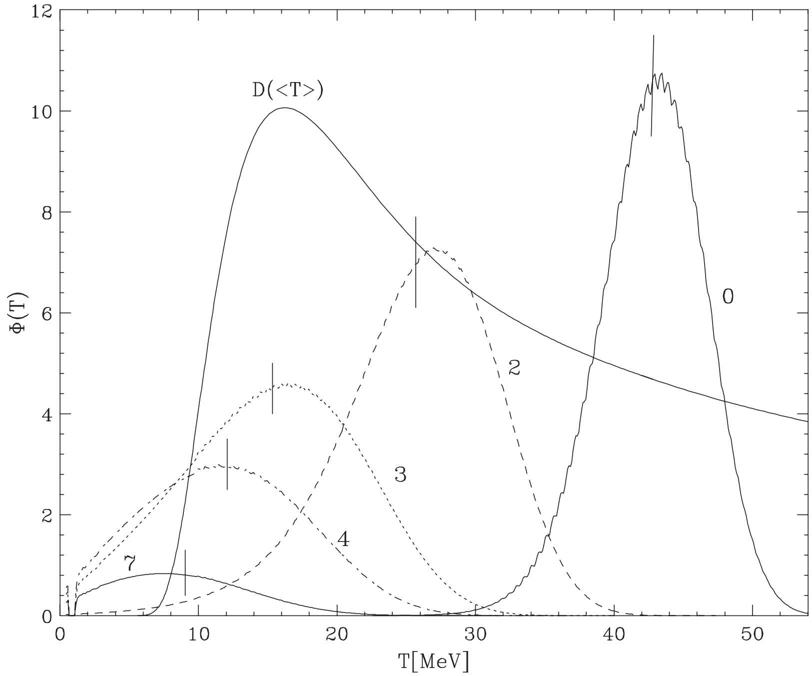

Figure 1.3 Proton spectra $\Phi(T;y)$ (straggling functions for energy loss of $T_0 = 200$ MeV protons) at different depths y in water. Data are given in Table 1.1: $\langle T\rangle$ is the mean energy of $\Phi(T;y)$, σ its standard deviation, γ_3 its skewness and $N(y)$ the residual number of protons in the beam. For each function $\langle T\rangle$ is indicated by a vertical line near the peak.

There will be a small difference between $D_s(y)$ and $S(\langle T\rangle(y))$, Figure 1.4. The variance σ^2 of the energy loss distribution at y is calculated with

$$\sigma^2(y) = \int \Phi(y;\,T)(T - \langle T\rangle)^2 \mathrm{d}T. \tag{11}$$

The above functions are shown in Figures 1.2–1.6.

3.1 Nuclear interactions

Three aspects of nuclear interactions can be distinguished:

- reduction of fluence $\Phi(y;\,T)$ of primary particles. This can be taken into account in Eqs. (5) and (6) by reducing $\Phi(y;\,T)$ by $\delta\Phi = N\xi\sigma_n(T)$ where N is the number of nuclei per unit volume and $\sigma_n(T)$ is the cross section for nuclear interactions. For protons it can be approximated by Bichsel[47]

$$\sigma_n(T) = 5.3 \cdot 10^{-26} A^{2/3}\ \mathrm{cm}^2. \tag{12}$$

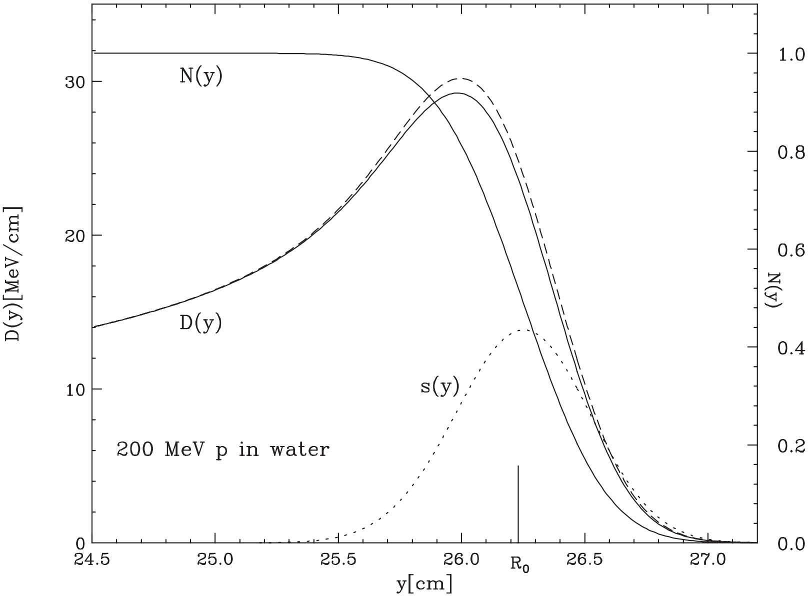

Figure 1.4 Additional Bragg functions for 200 MeV protons traversing water. The thickness of water traversed is y, the number of residual protons is $N(y)$, and the *range straggling* function is $s(y)$. Its FWHM is $w = 6.4$ mm. Two dose functions are given: the dashed line is $D(y)$ given by Eq. (9), the solid line gives the energy deposited $D_d(y)$, in each segment ξ. The number of ions stopping inside ξ at R_0 is ~ 0.2 %.

For water, $N\sigma_n(T) \sim 0.012/\text{cm}$, for a mean free path $\Lambda = 82\,\text{cm}$, for C-ions in water $\Lambda \sim 25\,\text{cm}$ (Ref. 48), in PMMA $\Lambda \sim 20\,\text{cm}$ (Ref. 49).

- electronic energy losses by secondary particles from the nuclear interactions. It will be necessary to make *a supplemental MC simulation* for this process. See Appendix D for other details.
- multiple scattering of the particles. Since this process produces negligible energy losses it will not change the spectrum $\Phi(y;\, T)$ of primary particles. For broad beams of particles, the lateral displacement of the particles will only affect the edges of the beam.[11] There is a shortening of the projected track length which can be calculated analytically with the Bichsel–Uehling method.[50] For 200 MeV protons in water the range shortening is given as 0.12% or 0.3 mm in.[19] For pencil beams the analytic form of the Moliere theory can be used[51] to calculate lateral scattering, see Appendix C. For 3600 MeV C-ions it is negligible.[12]

3.2 Practical details for protons

Calculations were made for protons with kinetic energy $T = 200\,\mathrm{MeV}$. Their csda range is $R_o(T) \sim 26.2\,\mathrm{cm}$, Figure 1.2. The use of Vavilov straggling functions $V(\xi;\, T + \Delta, \Delta)$ requires a choice of ξ for which $\Delta \ll T$. This means that ξ must be reduced with decreasing T. For the calculations described here, for $y < 24.5$ cm (at a mean energy of 42.2 MeV, with a spread from 28 to 68 MeV) $\xi = 1$ mm was used, for $y > 24.5$ cm $\xi = 20$ μm was used. The functions $\Phi(y;\, T)$ given here must be considered preliminary because even with $\xi = 20$ μm some problems with accuracy remain. Results for the Bragg peak are given in Figures 1.2 and 1.4. Some approximations are used in the program to simplify it. They cause errors of the order of 0.2% in the mean range R_0. Also they contribute the irregularity in the spectra in Figure 1.3. For present purposes they are insignificant. Good agreement between calculations and measurements for 70 MeV protons was found,[11] also with MC calculations for 200 MeV.[‡‡] For $y > 25.3$ cm the energy $D_d(y)$ deposited in each segment consists of the energy lost by particles traversing ξ and the residual energy lost by particles stopping inside ξ, see $s(y)$ (the range straggling function) in Figure 1.4. Energy deposited[§§] is recorded in two parts: D_h for protons with initial energy $T \rangle 1.5\,\mathrm{MeV}$ and D_l for $T \langle 1.5\,\mathrm{MeV}$, $D_d(y) = D_h + D_l$.

The ratio $r = D_l/D_d$ is given in Table 1.1. The largest number of protons stopping inside of $\xi = 20$ μm at the peak of $s(y)$ is 0.3% and their contribution D_l to dose is less than 1%. Thus they are unlikely to contribute to an increase in RBE.

3.3 Practical details for C-ions

Calculations were made for C-ions with kinetic energy $T = 3600\,\mathrm{MeV}$. Their csda range is $R_o(T) \sim 17.31\,\mathrm{cm}$. For the calculations described here, for $y < 15.26$ cm (at a mean energy of 1057 MeV, with a spread from 970 to 1175 MeV) $\xi = 0.5$ mm was used, for $y > 15.26$ cm $\xi = 100$ μm. Results for the Bragg peak are given in Table 1.2 and in Figure 1.5. The spectra in selected layers $\xi = 100$ μm are shown in Figure 1.6. The functions given must be considered preliminary because ξ is too large and the Vavilov functions were calculated with a spacing of 3 MeV in T. This causes the structures seen for functions 3–5.

[‡‡] In a comparison in 2008 with Monte Carlo functions calculated at Karolinska Institute with SHIELD-HIT[52] differences of less than 0.5 mm were seen for the functions.

[§§] This is an arbitrary choice: S(1.5MeV)~20 keV/μm =LET (∞) corresponds to the calculations in Ref. 53.

Table 1.2 Properties (Eqs (8)–(12)) of the fluence functions of C-ions with initial $T_0 = 3600$ MeV shown in Figure 1.6. Data are given for six from a total of 220 functions calculated. Depth in water is *y*. *T* and σ in MeV, *D*(*y*) in MeV/cm. For *r* see Sect. 3.2.

#	y cm	$\langle T \rangle$	σ	γ_3	N (y)	D (y)	r%
1	16.05	809	17.27	−1.06	0.99	346	0
2	16.55	617	21.30	−1.06	0.984	425	0.04
3	16.95	419	28.52	−0.75	0.975	575	0.55
4	17.15	285	39.24	−0.15	0.972	792	0.95
5	17.31	136	50.39	−1.19	0.794	1350	1.6
6	17.35	106	44.4	−2.0	0.526	1113	1.6

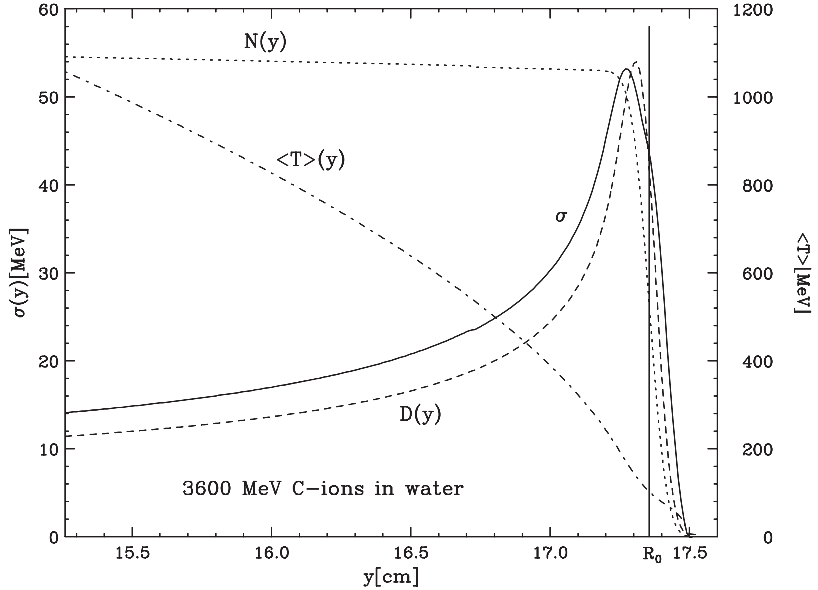

Figure 1.5 Bragg functions for 3600 MeV C-ions traversing water. The thickness of water traversed is *y*, the number of residual ions is $N(y)$. The *mean energy* of the ions at *y* is $\langle T(y) \rangle$, the dose is $D(y)$, Eq. (9), dashed line, σ is the standard deviation of the functions shown in Figure 1.6. Nuclear fragments are not included in order to show the nature of electronic collisions more clearly, see Section 3.1.

The range of C-ions with $T = 10$ MeV is ~10 μm (Refs. 20, 54). Because they will deposit all their energy in one or two cells, details about their interactions (e.g., charge state of ion) are not important, see Sections 4.3 and 5. The number of ions stopping in *one cell* at the Bragg peak is ~0. 8%.

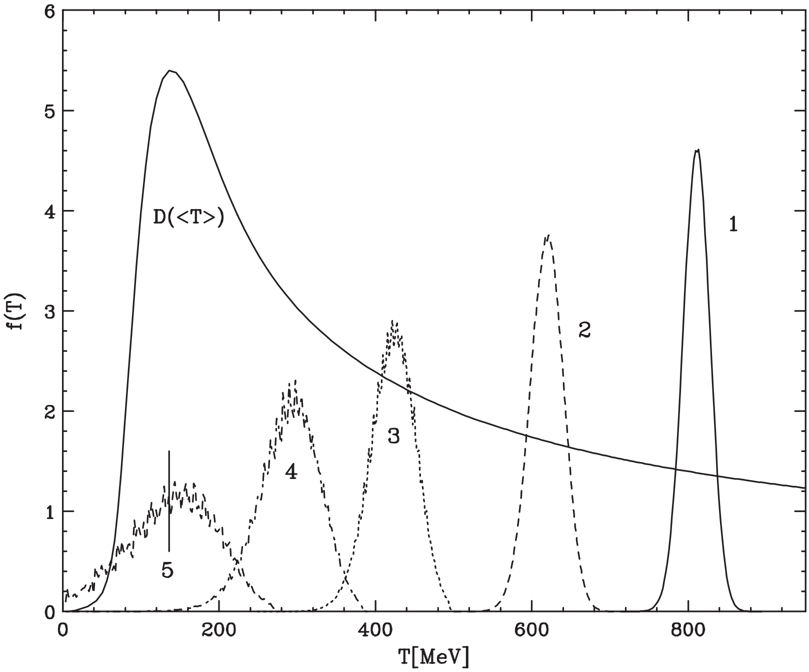

Figure 1.6 C-ion spectra $\Phi(T; y) = f(T)$ (straggling functions for energy loss) at different depths y in water. Data are given in Table 1.2: $\langle T\rangle$ is the mean energy of $\Phi(T; y)$, σ its standard deviation, γ_3 its skewness and $N(T)$ the residual number of ions in the beam. For function 5 the value $\langle T\rangle$ is indicated by a vertical line near the peak. The narrow peaks in functions 3-5 are due to a coarse table of $V(xi, \Delta, t)$ of Figure 1.1.

The mean range is R_0, it is given at $N(y) = N(0)/2$ and corresponds to the csda range. Numerical values of $\langle T\rangle$ are given in Table 1.1.

Good agreement between calculations and measurements for 3600 MeV C-ions was found.[12]

4. ENERGY LOSS AND DEPOSITION AT MICROSCOPIC LEVELS

4.1 Energy loss

In order to assess the limitations of calculations and measurements we explore the spectra of specific energy z imparted[16, 17] to cubic volumes $V_c = 10 \times 10 \times 10\ \mu\mathrm{m}^3$. Here, z is a stochastic quantity and the determination of its local values and variations is a major purpose of this study. Since the stochastic variation of the particle fluence is largest for C-ions we consider primarily C-ion beams with kinetic energy $T = 3600\,\mathrm{MeV}$ (or $300\,\mathrm{MeV/u}$). In addition we restrict the absorber to be water for most of the study (see Appendix B). Three kinds of interactions of the ions are considered:

- inelastic collisions with atomic electrons ("electronic"), Appendices A, B;
- elastic collisions with atoms, Appendix C;
- nuclear interactions, Section 3.1 and Appendix D.

Interactions are described as *collisions* and the effect on the particle is an *energy loss*, Figure 1.7.

The cross sections are described in Appendices A and B. A schematic description of the electronic collisions is given in Figure 1.7. Further details are given in Appendices B, C, and D.

For particles heavier than electrons, elastic collisions cause small energy losses (of order of eV) and angular deflections of the particles leading to multiple scattering, described in Appendix C.

4.2 Energy deposition

For large volumes (>1 ml in solids, >1 l in gases) energy loss approximates energy deposition closely. For smaller volumes *wall effects* must be taken into account. In particular, delta rays and secondary photons can be shared by neighboring volumes. For cells the conversion of the primary energy into heating and chemical effects is complex (radicals, diffusion etc.[55, 56]) and is of minor relevance for the present study. The collisions of particles traversing matter occur at random. This is shown in Figure 1.7 for protons. For C-ions with $T = 150\,\mathrm{MeV}$ (at Bragg peak) the mean free path between collisions is $\lambda \sim 0.4\,\mathrm{nm}$ (Table A.1), but, presumably, the pattern is still similar. Note that for protons λ is much larger than the diameter of DNA ($\sim 2.5\,\mathrm{nm}$), but for C-ions with $T < 1000\,\mathrm{MeV}$ it is less.

4.3 Energy deposition in microscopic volumes

For fast C-ions the energy deposition is in-homogeneous in space. As an example $T = 150\,\mathrm{MeV}$ ions are described. Their LET is $136\,\mathrm{keV/\mu m}$, and the mean free path between collisions is 0.4 nm, Table A.1. The procedure of Figure 1.7 is used, for one ion, with data from Figure B.4. It is assumed that for energy losses $E > 30\,\mathrm{eV}$ a secondary electron ("delta ray") is produced. The delta rays in turn will lose their energies in multiple collisions. Frequently "radial dose distributions" are used to describe the energy deposition and to assess radiation effects.[57] Here a different method is used which demonstrates the *stochastics of energy deposition*. Consider water layers of thickness $\xi = 1\ \mu\mathrm{m}$. Numbers are listed in Table 1.3: four cylindrical

Table 1.3 Data for energy deposition around the track of one C-ion ($T = 150$ MeV) traversing $\xi = 1$ µm of water, based on Figure B.4. E_u(eV), r(nm), V(nm^3), Φ_0 number of ion collisions per µm, Φ_1 (keV/µm) energy lost per ion per cylinder, z (Gy) specific energy inside each sylinder

cyl.	Eu	r	Vu	Φ_0	Φ_1	z
A	152	3	$3\ 10^4$	2160	68.5	365000
B	1012	35	$4\ 10^6$	78	28.6	1100
C	8371	1000	$4\ 10^9$	11	26.6	1
D	28000	15000	$7\ 10^{11}$	1	14.0	0.003

volumes V_u around the center of the track are studied. They are based on the regions of energy loss shown in Figure B.4. The radii of the volumes are defined by the mean radial range $r(E_u)$ in nm (Ref. 58) of the delta ray associated with the highest energy loss E_u(eV) in each region.[***] The outer volumes are exclusive of the inner[†††] ones as are the values of Φ_0 and Φ_1, Figure B.4. The total energy loss of the ion to the delta rays stopping in a cylinder is $\Phi_1$keV. The energy deposition by one C-ion is given. The sums are $\Phi_0 = 2250$ *primary collisions*/µm, $\Phi_1 = 137.3$ keV/µm total energy loss. The average energy loss per collision is $\langle E \rangle = 61$ eV.

Note: On the average, *a single delta ray* carries away 10% of the energy loss into volume D.[‡‡‡]

The average energy deposition per ion collision in volume A is 32 eV.

One primary collective excitation fills a volume of $\sim 14\text{nm}^3$ (Ref.60) for a total volume in cylinder A of $2160 \cdot 14 = 30240$ nm^3, i.e., volume A is a solid tube of collective excitation with specific energy $z \sim 365$ kGy, Table 1.3. This does not include the contributions from the collisions by delta rays going into the outer volumes.

A reader wishing to know this contribution is invited to calculate it.[§§§]

In cylinder B, $\Phi_0 = 78$ electrons deposit energy into individual volumes from 5 to 40 nm^3, i.e., at most ~ 1000 nm^3 of the total volume $V_B = 4$ million nm^3.

[***] No correction is made for the reduction of the energy of the delta ray due to the binding of the electrons (*K*-shell and collective excitations). Thus for the outer three volumes the energy deposition is equal to the energy loss by delta rays. For cylinder A the energy density is so high that this is irrelevant.

[†††] "Annular space between cylinders."

[‡‡‡] Delta rays lose energy at the rate of 30 to 50 eV/collision, with mean free paths from 50 nm to 1 nm along their track.[59] The volume of a collective excitation along the electron tracks is estimated to be from 15 to 1 nm^3 (Ref.60). Some energy may be carried into neighboring layers, "wall effect."

[§§§] For electrons with $E < 0.8$ keV S~25 eV/nm, for $E < 0.8$ keV $S \sim 13.5/E^{0.767}$ eV/nm. For details see Refs. 59, 61, 62.

In cylinder C the energy deposition is by 11 electrons filling volumes between 40 and 1000 nm^3, inside the total volume $V_C = 4$ billion nm^3.

In cylinder D one electron (with an energy between 8 and 28 keV) on the average fills volumes between 1000 and 100000 nm^3. This electron will usually deposit its energy in more than one layer of water. Its contribution to z on the track is between 0 and 20%.

This suggests that the LEM model[57, 63] will have large stochastic variations outside of cylinder A and will not be applicable outside of cylinder C. Similar descriptions have been given in chapter 9 of IAEA-TECDOC-799,[64] but without the concept of localized collective excitations.

Readers are encouraged to explore patterns of collective excitations in volumes B, C, and D and explore their effects on DNA.

This energy deposition pattern by heavy ions differs greatly from that expected for X-rays.

5. STOCHASTICS OF ENERGY LOSS IN CELLS

5.1 General features

We calculate the details of energy loss of C-ions in the "cell volume" $V_c = 1000\ \mu\text{m}^3$, Eq. (1), the surface area of $A_c = 100\ \mu\text{m}^2$ and the thickness $\xi = 10\ \mu\text{m}$ with the method shown in Figure 1.7. Let us consider segment 5 of Table 1.2, $y = 17.31$ cm with mean energy $\langle T \rangle = 136$ MeV. The mean energy loss is $\langle \Delta \rangle = \xi \cdot M_1 = 1443$ keV (Table A.1), the mean number of collisions is $n \sim 25000$. The uncertainty of this number is less than 1% and thus we can disregard *straggling* (but see Section 4.3). The average energy loss per collision is $\langle E \rangle = M_1/M_0 \sim 60$ eV.

To explore the *stochastics of the physical processes* we must use the specific energy deposited per ion in the cells rather than the dose. As a reference concept for z, for *one* C-ion with kinetic energy T to a cell with volume V_c, we use the approximation

$$z_1 = S(T)/6250\ \text{Gy}, \tag{13}$$

where $S(T)$ has units MeV/cm.[****] If we assume a mean fluence $N_D = 20$ ions cell the irradiation dose is $D = 4$ Gy. Next we calculate the actual

---

[****] One ion per A_c corresponds to $\Phi = 10^6$ ions/cm^2, Eq. (9). As an example, assume $<T> = 136$ MeV and S(T) = 1443 MeV/cm (near the mean energy at the Bragg peak). The dose D then is $D = \Phi(T)S(T) = 144 \times 10^{15}$ eV/g$=1.44 \times 10^{18}$ eV/kg$=$ 0.231 Gy. With $S(T) = 1443$ in Eq. (13), $z = 0.231$ Gy.

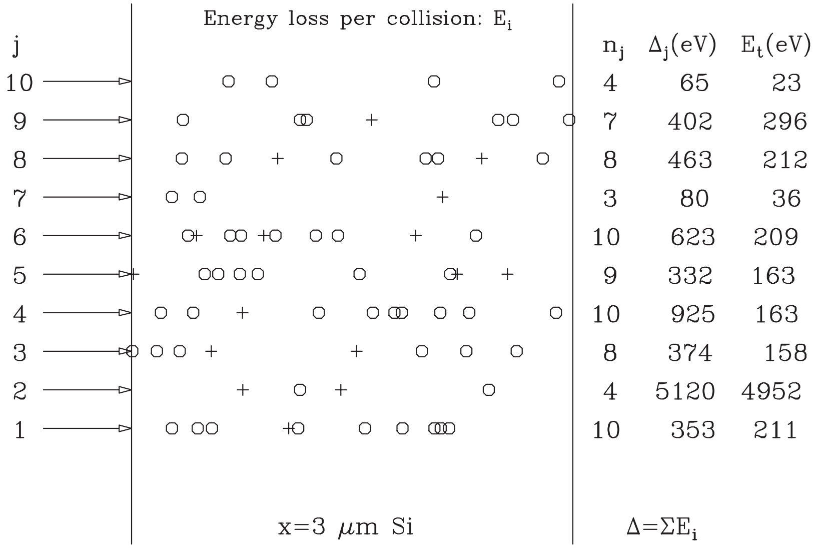

Figure 1.7 Monte Carlo simulation, Section 2.3, of the passage of $T = 16$ MeV ($\beta^2 = 0.033$ at Bragg peak) protons (index j), through one layer of water of thickness $\xi = 6\lambda$, where $\lambda = 20$ nm, Table A.2, is the mean free path between collisions. The direction of travel is given by the arrows. Inside the absorber, the tracks are straight lines defined by the symbols showing the location of collisions (total number $\Sigma n_j = 56$). At each collision point a random energy loss E_i is selected from the distribution function $\Phi(E; T)$, similar to Figure 1.13. Two symbols are used to represent energy losses: o for $E_i < 33$eV, × for $E_i > 33$eV. Segment statistics are shown to the right: the number of collisions for each track is given by n_j, with a nominal mean value $\langle n \rangle = x/\lambda = 6$. The total energy loss is $\Delta_j = \sum E_i$, with the nominal mean value $\langle \Delta \rangle = x\mathrm{d}T/\mathrm{d}x = 370$ eV, where $\mathrm{d}T/\mathrm{d}x$ is the stopping power, M_1, in Table A.2. The largest energy loss E_t on each track is also given. The mean value of the Δ_j is 325 ± 314 eV and is 15% less than $\langle \Delta \rangle$. Note that the largest possible energy loss in a single collision is $E_M = 33000$eV, Eq. (A.1).

process in cells at the Bragg peak for a therapy irradiation. There are many stochastic variations which occur during the irradiation:

- From Figure 1.8 we see that T has values between 10 and 280 MeV, with LET between 700 and 80 keV/ μm.[††††] Within these limits we have no control over T or z for any ion in any cell.
- The ions intercept a flat layer of cells at random locations and the number of ions traversing a cell is given by a Poisson distribution $P_n(N_D)$, Eq. (6.1) in Ref 9. We assume the mean value $\langle T \rangle = 136$ MeV (Table A.1)

[††††] We are not interested in details for energies below 10 MeV, see Section 3.3.

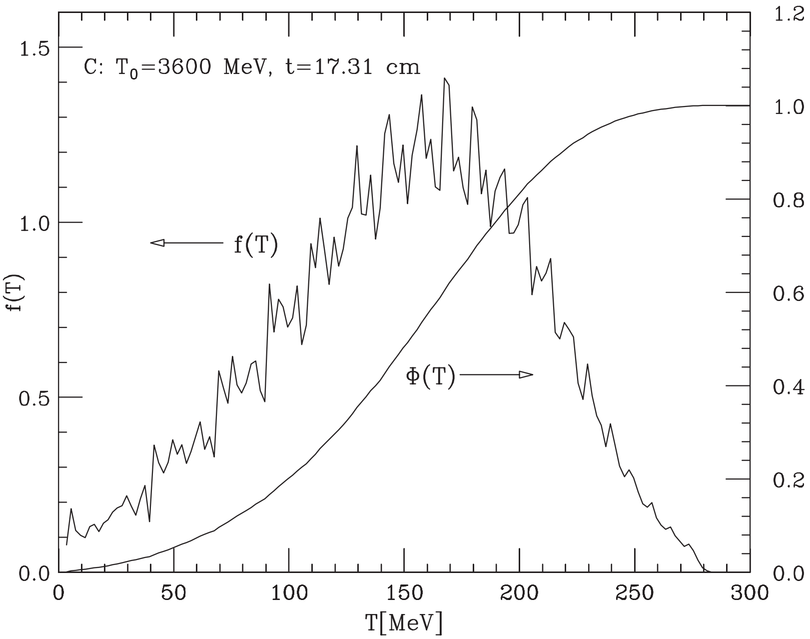

Figure 1.8 Enlarged energy spectrum $f(T)$ of C-ions traversing water at Bragg peak (function 5 in Figure 1.6). The mean value of the energy of the ions is $\langle T \rangle \sim 136$ MeV. The structure of $f(T)$ is due to an approximation of using a limited number of Vavilov functions ($V(\xi, \Delta, T)$ in Fig. 1.1) for the convolutions, Eq. (6). The cumulative function $\Phi(T)$, Eq. (B.7), normalized to 1, is also given. It is used for the MC calculations in Section 5.2.2, also see footnote §§. The jagged structure of $f(T)$ is due to the coarseness of the energy loss grid.

($S(T) = 1443$ MeV/cm) and make a calculation for $N_D = 20$ ions.[‡‡‡‡] The “mean dose” then is

$$D = N_D \cdot z_1 = 4.6\ Gy. \tag{14}$$

The results of the MC simulation in Figure 1.9 will show us whether this use of $\langle T \rangle$ is appropriate.

- In *experiments* to determine survival functions S_v, the effects on a *limited number of cells* are measured.
- The ions traverse cells at random time intervals.

[‡‡‡‡] The practice of defining a *mean S(T)* at the mean energy <*T*> of the spectrum of the ions to calculate the *dose* in cell irradiations is frequently used.

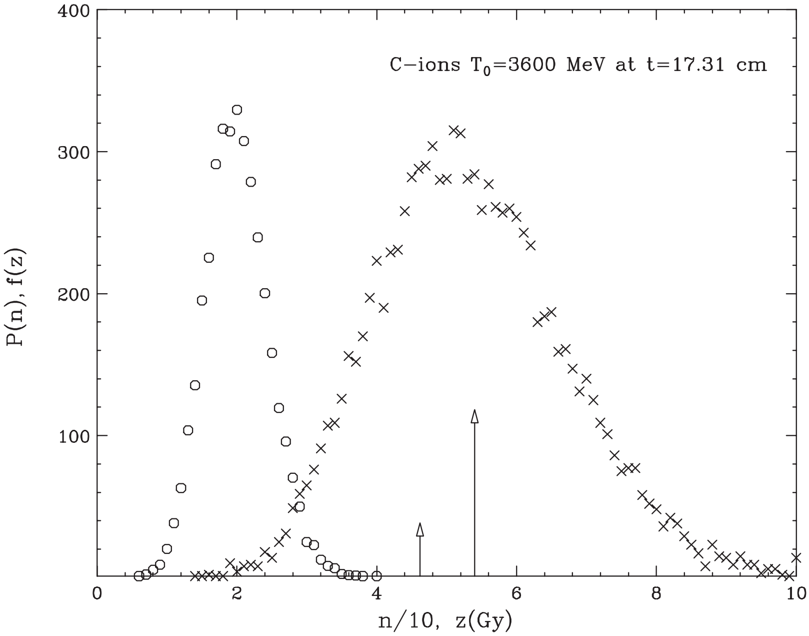

Figure 1.9 MC calculation of the spectrum of the number n of ions traversing cells is given by o. It approximates a Poisson distribution with mean value $N_D = 20$. The spectrum of z per cell, Eq. (15), is given by $\times$, values of z are $(n/10)$Gy. The mean value is $\langle z\rangle = \langle D\rangle \sim 5.4$ Gy, shown by the arrow. The value $D(\langle T\rangle)$ is $\langle z\rangle \sim 4.6$ Gy, Eq. (14), shown by the short arrow.

- Nuclear interactions in the cell layer are infrequent, Appendix D, and fragments from earlier layers traverse the cell and contribute to the dose, but they are disregarded.[§§§§]
- Delta rays with large energies E and K-shell X-rays occur infrequently.
- Several other stochastic variations are mentioned in Appendix D.

For the calculation of energy deposition we shall simulate the stochastics of the first two items only. Variations thus obtained will be smaller than the total which would include all the above effects. Programs and results are described in the next sub sections.

5.2 MC simulation of stochastics at the Bragg peak

A Monte Carlo calculation simulates two primary effects given above.

[§§§§] Fragments have smaller LET and only one or two will traverse the cell[65] at $N_D = 10$. The effect will increase the variance.

5.2.1 Simulation of random number n_j of ions traversing cell j

The following simple minded algorithm is used: Place a square A_c the size of the cell (i.e., $10 \times 10\,\mu\text{m}$) into the middle of a square with side length $s = 100\ \mu\text{m}$. Select two random numbers for two sides (at 90° of the large square). If the point given by these coordinates is inside the cell use it as the location of an incident ion. Repeat this for $N_D \cdot 100$ ions, Eq. (14), which results in n_j ions randomly distributed over A_c. For many cells it can be represented analytically by a Poisson distribution, as shown in Figure 1.9. The average value of n_j is N_D.

5.2.2 Energy deposition z in cells

With a second random number an energy T_i from $\Phi(T)$, Figure 1.8, is selected for *each ion*. Its energy deposition z_1 in the cell is approximated using Eq. (13) $S(T)$, from Table A.1)[*****] and the corresponding total energy z_j imparted to cell j is given by

$$z_j = \sum_{1}^{n_j} z_1 \tag{15}$$

The distribution ("spectrum") of z for $K = 10000$ cells at the Bragg peak is given in Figure 1.9. The simulated Poisson distribution from Section 5.1 is also given. The average value of z for all cells is the dose D of the irradiation.

6. BIO-EFFECTS

A detailed study of biological effects on cells (e.g., cell survival) is beyond the scope of this paper. We conclude though that the broadness of the energy spectra of the ions seen in Figures 1.8 and 1.9 requires a more detailed study than that with the assumption of *mean values* shown in Figure 1.9, used e.g., in Ref. 66. For C-ion therapy the small number of ions passing through individual cells will cause a further spread in the radiation dose per cell.

Studies of these effects by the author are in progress.[67] A difficulty which must be assessed is the wide spread in particle energies (and the associated LET[66]) at the Bragg peak, Figure 1.8.

[*****] The contribution from straggling[9] is small and is not included. Also see Table 1.3.

7. CONCLUSIONS

I. A remarkable result of this study is the wide spread of cell doses due to the random nature of the two independent functions in Figure 1.9.[†††††]

II. A major problem in determining the biological effects of irradiations with C-ions at the Bragg peak is in the large values and the wide variation of the specific energy z per cell V_c: the variation for T is from 20 to 250 MeV, giving z_1 from 1.1 to 0.14 Gy. For the most probable ion energy at the Bragg peak, Figure 1.8, $T \sim 160$ MeV, it is $z_1 = 0.2$ Gy, footnote.[†††]

III. The second problem is the random number of ions traversing the cells given by the Poisson distribution P_n. A *mean dose*$D = 2$ Gy thus requires only $N_D = 10$ ions traversing a cell. As a consequence the large spread in dose in Figure 1.9 would be even larger. Note that $\langle D \rangle$ and $D(\langle T \rangle)$ differ by close to 20%, Figure 1.9. If $\langle T \rangle$ is derived from the range energy function by using the thickness t at which the measured Bragg peak is located D may differ even more.

IV. For heavy charged particles the *primary description of the beam should be made with the fluence* N_D *per cell* V_c. This will remind the user of the importance to consider the Poisson distribution. The dose D is a derived quantity which is spread out as seen in Figure 1.9.[‡‡‡‡‡] In particular, D from Eq. (14) cannot readily be used in the derivation of survival values.

V. The physical processes described in Figures 1.1–1.9 and the Appendices are well understood and have been found to be accurate to about to 2% (Refs. 9, 10, 12, 18, 44, 45).

The stochastic nature for the biological effects become evident when we study small volumes and small doses: Figure 1.9. Further variations occur due to the nature of cell survival which is expressed by the exponential form of the relation between cell survival S_v and physical dose D (Ref. 66).

VI. At this time I have not considered the consequences for radiation therapy with C-ions. I suggest that a more detailed analysis of the physical parameters (or quantities) than just the "dose" should be made for cell survival experiments to establish survival functions. In particular the randomness due to the particle fluence, Eq. (14) should be studied. *For Ne-ions the particle fluence would be half as much as that for C-ions.*

VII. It is evident that for the doses currently considered for radiation therapy with C-ions (2–6 Gy) the randomness of the number of ions

---

[†††††] It must be understood that all the data points of any one of the methods are represented by *one single value* on the survival curves of the biological measurements.[66]

[‡‡‡‡‡] The agreement between calculations and measurements was good in Ref. 12.

traversing cells will cause large variations in the survival of cells as well as on the local spectrum of the energies of the ions. These effects seem to have been taken into account in some methods of treatment planning[41, 53, 57, 68] but the procedures used are not evident to me.

VIII. To properly convert specific dose into bio-effect it may be necessary to *measure primary bio-effects for mono-energetic ions*.

IX. The absolute accuracy of the data for water has not been determined. In view of the wide spread of the specific energy found in Figure 1.9 it may not be very important, but a comparison with experiments similar to that for Si, Ref. 9, should be made.

X. Experimental data for 70 MeV protons and 3600 MeV C-ions agreed to better than 1% with calculations described in Sections 2 and 3, see Refs. 10, 11, 54.

APPENDIX A. COLLISION CROSS SECTIONS CCS

The most frequent interactions of heavy ions with matter occur between the electric charge ze of the ion and the electrons of matter, resulting in an energy transfer (or loss) E by the particle in *inelastic collisions*. The energy is transferred to excited states of atoms, to many electrons as a *collective excitation* or to single free electrons called delta rays. They can be considered as Secondary Radiations. Details about Auger electrons, fluorescence, Bremsstrahlung, Cherenkov radiation, etc. are less important for current purposes and are not discussed.

To describe the probabilities for collisions cross sections are defined.

A.1 Rutherford cross section

For the collision process with *free electrons* the Rutherford or Coulomb collision cross section[27, 69–71] $\sigma_R(E)$ is used. It serves as a *first approximation for cross sections*.[28, 30, 31, 35] For a heavy particle with charge ze and speed $\beta = v/c$ colliding with an electron with mass m at rest it can be written as[§§§§§]

$$\begin{aligned} \sigma_R(E,\beta) &= \frac{k}{\beta^2}\frac{(1-\beta^2 E/E_M)}{E^2}, \\ k &= \frac{2\pi e^4}{mc^2}\cdot z^2 = 2.54955\cdot 10^{-19} z^2 \text{ eVcm}^2, \end{aligned} \tag{A.1}$$

[§§§§§] Additional factors for electrons and positrons and for particles with spin $\frac{1}{2}$ and spin 1 at high speeds ($\beta \backsim 1$) are given e.g. in Uehling.[72] An extensive description can be found in Evans.[69]

Table A.1 Bethe functions of C-ions traversing water with kinetic energies *T* (MeV), calculated with the FVP method. M_1(keV/µm) is the "stopping power," also called dT/dx, the number of collisions is M_0/µm and λ(nm) is the *mean free path* between collisions. The accuracy of M_1 is the order of 2%, but the uncertainty of M_0 and λ may exceed 10%

T (MeV)	M_1	M_0	λ
50.12	329.173	5723.27	.1747
63.10	274.492	4708.34	.2124
79.43	228.745	3870.74	.2583
100.00	190.147	3180.51	.3144
125.89	157.882	2612.56	.3828
158.49	131.100	2145.86	.4660
199.53	108.702	1762.86	.5673
251.19	90.190	1448.94	.6902
316.23	74.784	1191.94	.8390
398.11	62.101	981.81	1.0185
501.19	51.631	810.21	1.2343
630.96	42.977	670.25	1.4920
794.33	35.892	556.25	1.7978
1000.00	30.082	463.54	2.1573
1258.93	25.342	388.27	2.5755
1584.89	21.461	327.28	3.0554
1995.26	18.313	278.00	3.5971
2511.89	15.762	238.304	4.1964
3162.28	13.711	206.454	4.8439
3981.07	12.086	181.065	5.5230
5011.87	10.815	161.116	6.2070
6309.57	9.820	145.77	6.8603
7943.28	9.055	133.78	7.4752
10000.00	8.481	124.48	8.0331

where $E_M \sim 2mc^2\beta^2\gamma^2$ is the maximum energy loss of the particle in one collision. The mass of the particle does not appear in the equation.[69] This cross section has been used by Bohr,[25] Landau,[35] Vavilov,[30] and Tschalär[28] for the derivation of straggling functions. The approximation is quite good for large energy losses, Figures B.1 and B.2.

For gases and solid matter a more complex structure must be used for the cross sections. It is my opinion that at present the Bethe–Fano cross section is closest to reality for particles with energies above a few MeV/A. In a study of straggling in Si[9] the average difference between calculated and experimental data was less than ±0.2% for one set of more than 30 measurements, with average uncertainties of ±2% for single measurements. The reader is invited to look at the other nine data sets and to form her own opinion.

Table A.2 Bethe functions of protons traversing water with kinetic energies T (MeV), calculated with the FVP method and Dingfelder ε ($I = 81.8$ eV).[78] M_1 (keV/μm) is the "stopping power," also called dT/dx (or dE/dx), the number of collisions is M_0/μ m and λ(nm), Eq. (7), is the mean free path between collisions. The accuracy of M_1 is of the order of 2%, but the uncertainty of M_0 and λ may exceed 10%

T (MeV)	M_1	M_0	λ
1.000	26.6878	521.76	1.92
1.259	22.6437	432.76	2.31
1.585	19.1699	358.31	2.79
1.995	16.1517	296.18	3.38
2.512	13.5691	244.49	4.09
3.162	11.3836	201.57	4.96
3.981	9.5160	166.01	6.02
5.012	7.9388	136.60	7.32
6.310	6.6114	112.31	8.90
7.943	5.5032	92.29	10.83
10.000	4.5706	75.82	13.19
12.589	3.7959	62.27	16.06
15.849	3.1477	51.15	19.55
19.953	2.6095	42.04	23.79
25.119	2.1653	34.57	28.92
31.623	1.7977	28.47	35.13
39.811	1.4930	23.48	42.59
50.119	1.2430	19.41	51.51
63.096	1.0373	16.10	62.12
79.433	.8686	13.40	74.63
100.000	.7304	11.21	89.22
125.893	.6179	9.43	106.02
158.489	.5261	8.00	125.06
199.56	.4518	6.84	146.24
251.189	.3920	5.91	169.26
316.228	.3442	5.17	193.60
398.107	.3070	4.58	218.39
501.187	.2777	4.13	242.31
630.957	.2551	3.77	264.93

APPENDIX B. BETHE–FANO COLLISION CROSS SECTION

Bethe[73] derived an expression for a cross section as a function of energy loss E and momentum transfer K using the first Born approximation for inelastic scattering by electrons of the atomic shells. Fano[74] extended the method for solids. In its nonrelativistic form it can be written as the Rutherford cross section modified by the "inelastic form factor":[74–77]

$$\sigma(E, Q) = \sigma_R(E)|F(E, \mathbf{K})|^2 \frac{E^2}{Q^2}, \tag{B.1}$$

where $Q = q^2/2m$, with $\mathbf{q} = \hbar\mathbf{K}$ the momentum transferred from the incident particle to the absorber, and $F(E, K)$ is the transition matrix element for the atomic excitations or ionizations. For large momentum transfers, $Q \sim E$, Figure 1.2 in Ref. 74.

Usually, $F(E, \mathbf{K})$ is replaced by the generalized oscillator strength (GOS) $f(E, K)$ defined by

$$f(E, K) = \frac{E}{Q}|F(E, \mathbf{K})|^2, \tag{B.2}$$

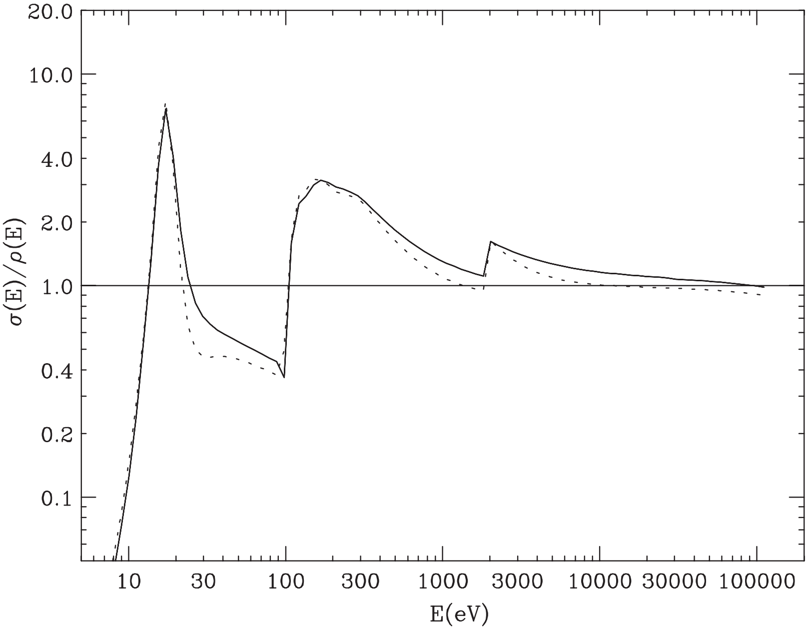

Figure B.1 Collision cross section for $T = 50$ MeV protons in Si, relative to the Rutherford cross section for 14 electrons. Solid line: calculated with B-F approximation, dashed line: w ith FVP approximation. The horizontal line represents the Rutherford cross section, Eq. (A.1). The differences between B-F and FVP balance to some extent. This indeed is the case for M_1, Eq. (B.6), but for the cumulative M_0 (equal to Φ_0 in Figure B.4, also Eq.(B.7)), the difference is 20% at E=20 eV, dropping to 8% at 10 keV.

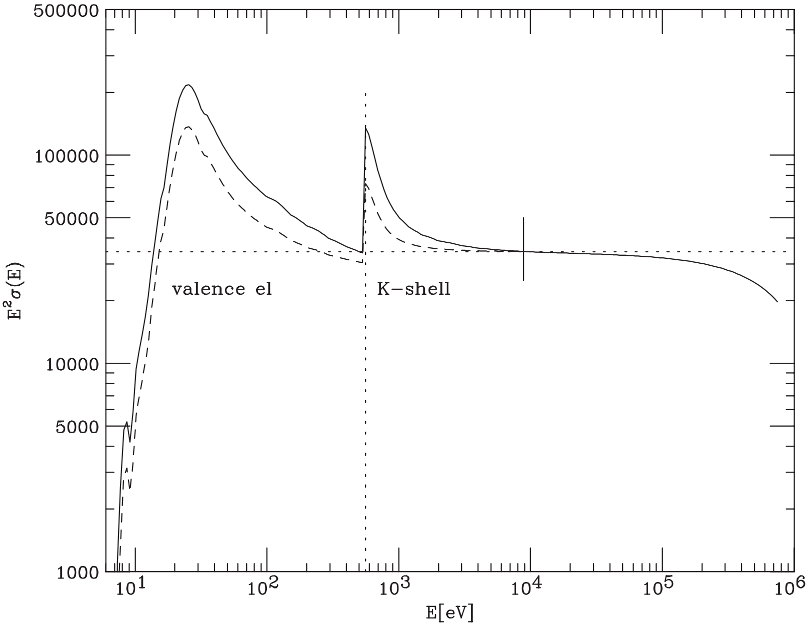

Figure B.2 Inelastic Collision cross sections for water, calculated with FVP approximation, relative to the Rutherford cross section for 18 electrons. Solid line: $T = 3600$ MeV C-ions, dashed line: $T = 50$ MeV C-ions. The horizontal line represents the Rutherford cross section, Section A.

and Eq. (B.1) then is written as

$$\sigma(E, Q) = \sigma_R(E)\frac{E}{Q}f(E, K). \tag{B.3}$$

The relativistic expression is given by Eq. (23) in Ref. 29 or Eq. (47) in Ref. 74.

In the limit $K \to 0$, $f(E, K)$ becomes the *optical dipole oscillator strength* (DOS) $f(E, 0)$ (Refs. 29, 45, 78).

The cross section as a function of energy loss E is obtained by integrating Eq. (B.3) over Q

$$\sigma(E; \beta) = \sigma_R(E; \beta)\int_{Q_{min}} Ef(E, K)\frac{\mathrm{d}Q}{Q}. \tag{B.4}$$

with $\mathrm{Q_{min}} \sim E^2/2mv^2$.The dependence on particle speed β enters via $\mathrm{Q_{min}}$. In our current understanding, this approach to the calculation of $\sigma(E)$ (solid line in Figure B.1) is closest to reality. Because of the factor $1/Q$ in Eqs. (B.2), (B.3), the accuracy of $f(E,0)$ enters significantly[78] into the calculations of cross sections and their moments, Eqs. (B.4–B.7).[******]

In condensed matter energy losses of the order of 20 eV are considered to cause *collective* excitations of the outer electrons of the atoms as well as Coulomb collisions with single electrons.[79] Energy losses greater than 40 to 100 eV will be mainly to single electrons, producing *delta rays*.[††††††]

We follow the suggestion of Chatterjee and Holley[60] by using a collective *core* (with a radius of 1.5 nm for $T = 150$ MeV C-ions) in which 50% of the energy loss is deposited by over 90% of the collisions, as described in Table 1.3 and Figure B.4.

The collective excitations have a similar nature for organic matter, especially DNA and proteins.[80–86] For present purposes a detailed study of the differences is not necessary.[‡‡‡‡‡‡]

B.1 Fermi-virtual-photon (FVP) cross section

The FVP calculation is an approximation based on the use of photo absorption cross sections $\sigma_\gamma(E)$ (where $E = \hbar\omega$ is the photon energy) and of the dielectric function $\varepsilon(\omega) = \varepsilon_1(\omega) + i\varepsilon_2(\omega)$ (Refs. 29, 74, 87). [§§§§§§] The collision cross section in the nonrelativistic form is given by Allison and Cobb[88]

$$\sigma(E,\beta) = \sigma_R(E,\beta)\left[Ef(E,0)2\,ln(2mc^2\beta^2/E) + \int_0^E f(E',0)\mathrm{d}E'\right], \tag{B.5}$$

where the integral over Q in Eq. (B.4) is approximated by the square bracket.

This model has the advantage that the generalized oscillator strength (GOS)[29, 45] for the absorber is not needed. Data for $f(E,0)$ can be extracted from a variety of optical measurements or from electron energy

---

[††††††] Details of the ionization of the inner shells of the atoms may have to be taken into account for specific biological effects.

[‡‡‡‡‡‡] The collective excitations will form a *full tube* of energy deposition as long as the mean free path between collisions is small: $\lambda < 1$ nm, i.e. $T < 400$ MeV for C-ions, Table 1.3.

[******] A description of the approximations in the Bethe derivation of "stopping power" can be found in Ref. 18.

[§§§§§§] The approach is also known under the names Photo-Absorption-Ionization model (PAI) and Weizsäcker–Williams approximation.

loss measurements.[89] A detailed description of the relativistic PAI model is found e.g., in Refs. 29, 45, 88, 90. For $E > E_M, \sigma(E) = 0$.

Examples of $\sigma(E)$ for Si and water are given by the lines in Figures B.1 and B.2.[******] The FVP approximation has been used extensively for the calculation of straggling functions and Monte Carlo calculations.

For convolutions and MC calculations the only parameter needed is M_0 and therefore the difference seen in Figure B.1 is of importance.

B.2 Collision cross sections for Si, water, and DNA

Cross section data for water and Si are given because both[†††††††] have been used for the dosimetry of heavy ion beams. For inelastic collisions of heavy ions the electronic structure of the atoms in the absorber (especially binding energies of the electrons) is important because probabilities for energy transfers E depend strongly on these structures, Figures B.1 and B.2. The collisions are also called the inelastic scattering of the particles. For a quantitative description the Bethe–Fano (B–F) method[9, 18, 29, 31, 73, 74, 77, 91] is closest to reality. For water a detailed study was made by Dingfelder, Inokuti and Paretzke,[78, 92] and should be used for accurate calculations. The Fermi-Virtual-Photon (FVP) method[34, 87, 88, 92, 93] requires less detailed input. Since the B–F method is accurate to about 1% (Ref. 9,18) it should be used for energy calibration of dosimeters and detectors. For current purposes electrons appear only as delta rays. Usually most or all of their energy is deposited inside the cell volumes V_c, Table 1.3, therefore details of their interactions are not important. The interactions with the organic molecules (DNA) in cells show a structure quite similar to that of water.[80] Delta rays with ranges larger than cell dimensions are infrequent: Table 1.3 and their contribution to z is small.[‡‡‡‡‡‡‡]

B.3 Integrals: cumulative functions and moments for water

The cumulative functions Φ_ν and the moments M_ν of the collision cross sections[45] are defined by

$$\Phi_\nu(E, \upsilon) = N \int_{E_m}^{E} E_s^\nu \sigma(E_s; \upsilon) \mathrm{d}E_s \qquad M_\nu(\upsilon) = N \int_{E_m}^{E_M} E_s^\nu \sigma(E_s; \upsilon) \mathrm{d}E_s, \tag{B.6}$$

[*******] Calculations have also been made for several gases.[45]

[†††††††] For simplicity it is assumed that DNA and other constituents of cells have the same dipole oscillator strength as water.[80]

[‡‡‡‡‡‡‡] The reader is encouraged to consider the geometry and stochastics in greater detail and compare it to the description in Refs. 13, 57.

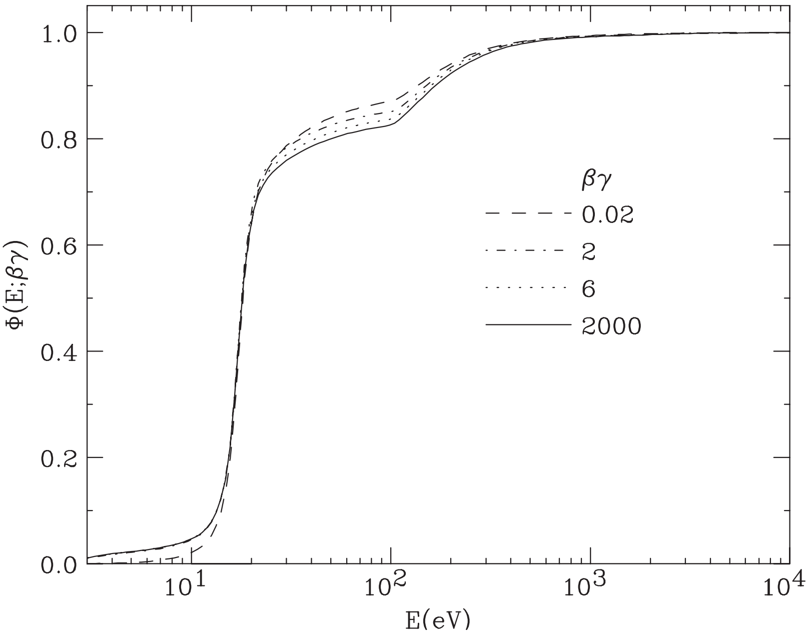

Figure B.3 Cumulative energy loss functions $\Phi(E)$, Eq. (B.7), for single collisions in Si are shown for several values of $\beta\gamma$. The excitation energy for L_2 electrons is 100 eV, for K electrons it is 1840 eV.[43] A table of the functions is given in Ref. 44.

where N is the number of electrons per unit volume, and $\nu = 0, 1, 2, 3 \ldots$ They are calculated numerically with Eq. (B.5). Examples are given in Figures B.3 and B.4.

For water moments for C-ions are given in Table A.1, for protons in Table A.2.[§§§§§§§] The moment $M_0(v)$, which is also written as $\Sigma_t(v)$, is the mean number of collisions per unit track length. It is an important quantity for the calculation of straggling functions[9, 31] $f(\Delta; x, v)$ because it is used to calculate $m_c = \xi \cdot M_0$, the mean number of collisions in a track segment ξ, Figure 1.7. From Figures B.1 and B.2 it is evident that the exact shape of $\sigma(E)$ for small E will greatly influence values of M_0 because of the factor $\frac{1}{E}$ in Eq. (B.4).

A calculation of M_0 with the Rutherford spectrum, Eq. (A.1) cannot be made because the lower limit in Eq. (B.4) is not defined.

[§§§§§§§] For Si and some gases moments M_0 and M_1 are given in Ref. 29, 45.

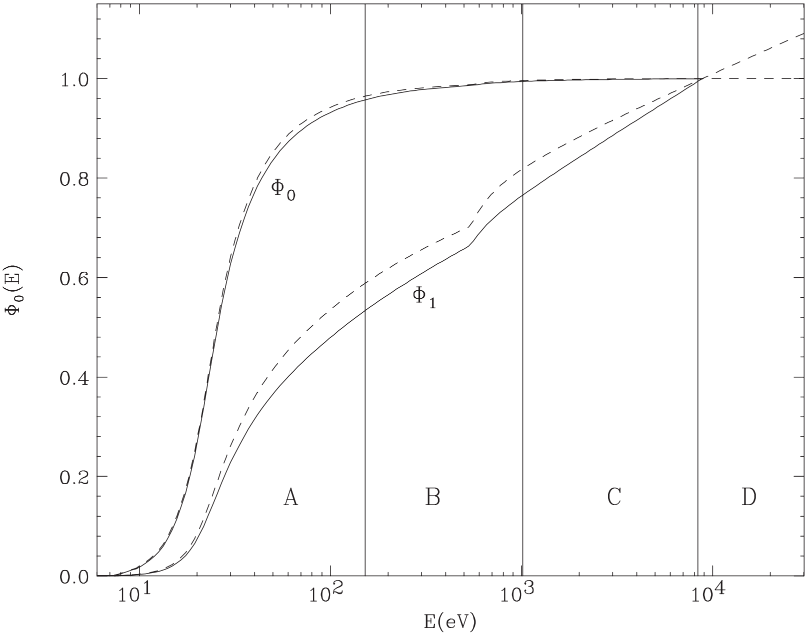

Figure B.4 The cumulative collision cross sections $\Phi(E; v)$ of Eq. (B.7) calculated with FVP for C-ions in water for two values of *T*. The functions are normalized to 1.0. The solid line is for $T = 50$ MeV, the dashed line for $T = 3600$ MeV. The difference between the two functions is less than 1%. Also shown are functions for the cumulative stopping power M_1, normalized to coincide at the largest energy loss for 50 MeV ions, $E_M = 9$ keV.

The moment $M_1(v)$ is usually known as the Bethe–Fano stopping power dT/dx, i.e., the mean energy loss per unit track length.[********]

For Si it was found that B–F and FVP calculations differ in M_1 by less than 1%, but for M_0 the differences may exceed 10% (Refs. 29, 45). M_2 is the Bohr straggling parameter.

In many publications it is customary to write the particle kinetic energy as *E*, then the stopping power is d*E*/d*x*. Here the names Barkas and Bloch are not included in the name for the stopping power because the expression for $\sigma(E; v)$ does not contain these corrections. On the other hand, Fano[74] formulated the expression for solids given in Ref. 78.

The higher moments can be used to calculate the *shape* of straggling functions for large energy losses.[26, 28, 71] For thin absorbers $M_1(v)$ will result in misleading information.[9] For the studies in his paper, the moments are calculated numerically with Eq. (B.6). Only M_0 and M_1 are used.

[********] A detailed study was made for Al and Si.[9, 18]

The dependence of $M_0(\beta\gamma)$ and $M_1(\beta\gamma)$ on particle speed is given in Tables A.1 and A.2. The normalized zeroth cumulative moment

$$\Phi(E, \upsilon) = \int_0^E \sigma(E'; \upsilon)\mathrm{d}E' / \int_0^\infty \sigma(E'; \upsilon)\mathrm{d}E' \tag{B.7}$$

is used extensively for the MC calculations. Examples are shown in Figures 1.8, B.3, and B.4.

A quantity which is of great importance for dealing with stochastic processes is the number of collisions per unit track length M_0 of Eq. (B.6)(Refs. 78, 94, 95). It is the inverse of the *mean free path* λ between collisions.

APPENDIX C. MULTIPLE SCATTERING

For this study the effects of multiple scattering are small and have been neglected. For a detailed study use the papers by Molière.[96–98] Experimental measurements give good agreement with the Molière theory.[51] For the determination of lateral displacement in ion trajectories, calculations have been made using[98] with results given in Ref. 99. For broad beams of protons and C-ions the effect was discussed in Refs. 11, 12. For a 1 mm pencil beam of 200 MeV protons after a distance of 26.2 cm in water (residual mean energy 6 MeV) the lateral spread has a FWHM ~ 8 mm. For C-ion beams a description is given in Ref. 7.

For measurements with a broad beam (several cm in diameter), multiple scattering will influence the dose distribution only at the edges of the beam. In the central part of the beam the range of the particles is reduced.[11, 12, 32, 50] Since the number of elastic collisions is of the same order of magnitude as that of electronic collisions, the effect can be calculated analytically with Moliere theory.[96–98]

For 3600 MeV C-ions the influence of multiple scattering on the CSDA range was less than 0.1% (Ref. 12).

APPENDIX D. NUCLEAR REACTIONS

The mean free paths Λ, Eq. (12), for nuclear interactions are large, so that only a fraction of the ions will interact. The net effect for the convolution method in Section 2.2 is to reduce the fluence $\Phi(\gamma, T)$ at each layer by $\delta\Phi = \xi/\Lambda$, Eq. (6). With $\xi = 0.01$cm for the C-ion calculations, the reduction would be $-dE/\rho d$ per layer, for a total reduction of about 30% at the Bragg peak. Further details for these estimates are given in Ref. 12, in particular it was found that the nuclear interactions in the passage across the peak will change the *shape* of the peak only slightly. For a study of effects of nuclear interactions a Monte Carlo calculation is needed. I am using results obtained with SHIELD-HIT[14, 15] to consider the influence of nuclear products for the radiation effects discussed in Section 6. The contribution to the dose at the Bragg peak estimated in Ref. 12 agree approximately with those shown in Ref. 14. The spectrum of fragments calculated in Ref. 65 shows mostly low LET particles which will have a small effect on the cell survival functions.

APPENDIX E. CELL SURVIVAL

Cell survival is a complex process, in particular the study of *sub-volumes* and *sub-lesions*[53,100–102] goes beyond the scope of this study.[67] The description of radial distribution of energy deposition, Section 4.3, Table 1.3, may be more suitable for this purpose than "radial dose distribution".[41] Some effects contributing[53] to stochastic or systematic variations in addition to those described in Section 5 are listed here:

a. The randomness of the energy deposition due to straggling.
b. The randomness in cell shape and size.
c. "Wall effects" due to multiple scattering, oblique traversals or delta rays.
d. The use of "linear-quadratic" survival assumptions.
e. Assumptions about the nature of cell survival, e.g., interactions of sub-lesions etc.[53]
f. The variety of responses for different cell types.[66]

ACKNOWLEDGMENTS

I am grateful for the help and advice by S. Hoedl, E. Swanson, J. Schwartz, R. Seymour, I. Gudowska, D.J. Brenner and M. Dingfelder.

REFERENCES

1. Belkić, Dž. Reviews of theories on ionization in fast ion-atom collisions with prospects for applications to hadron therapy. *J. Math. Chem.* **2010**, *47*, 1366.
2. Andreo, P. On the clinical spatial resolution achievable with protons and heavier charged particle radiotherapy beams. *Phys. Med. Biol.* **2009**, *54*, N205.
3. Paganetti, H. Range uncertainties in proton therapy and the role of Monte Carlo simulations. *Phys. Med. Biol.* **2012**, *57*, R99.

4. Battermann, J. J.; Hart, G. A. M.; Breur, K. Dose-effect relations for tumor control and complication rate after fast neutron therapy for pelvic tumors. *Br. J. Radiol.* **1981**, *54*, 899–904.
5. Wyatt, M.; Corredor, C.; Tamimi, M.; Miller, L. F. Comparison of treatment planning dose calculations with measurements and Monte Carlo calculations in a rando phantom. *Rad. Prot. Dosim.* **2005**, *116*, 461.
6. Pedroni, E.; Scheib, S.; Böhringer, T., et al. Experimental characteriztion and physical modelling of the dose distribution of scanned proton pencil beams. *Phys. Med. Biol.* **2005**, *50*, 541–561.
7. Krämer, M.; Jäkel, O.; Haberer, T.; Kraft, G.; Schardt, D.; Weber, U. Treatment planning for heavy-ion radiotherapy: physical beam model and dose optimization. *Phys. Med. Biol.* **2000**, *45*, 3299–3317.
8. Bichsel, H. Unpublished calculations of range straggling functions for pions by convolution of straggling functions for thin absorbers at Los Alamos, 1979.
9. Bichsel, H. Straggling in thin silicon detectors. *Rev. Mod. Phys.* **1988**, *60*, 663–699.
10. Bichsel, H. In *Energylosses of electrons below 10 keV*, Pfefferkorn Conference, Park City, May 1989.
11. Bichsel, H.; Hiraoka, T. Energy loss of 70 MeV protons in elements. *Nucl. Instrum. Methods B* **1992**, *66*, 345–351.
12. Bichsel, H.; Hiraoka, T.; Omata, K. Aspects of fast ion dosimetry. *Radiat. Res.* **2000**, *153*, 208–219.
13. Berger, M. J. Monte Carlo calculation of the penetration and diffusion of fast charged particles. *Methods Comput. Phys.* **1963**, *1*, 135–215.
14. Gudowska, I.; Sobolevsky, N.; Andreo, P.; Belkić, Dž.; Brahme, A. Ion beam transport using the Monte Carlo code SHIELD-HIT. *Phys. Med. Biol.* **2004**, *49*, 1933–1958.
15. Gudowska, I.; Sobolevsky, N. Calculations of particle and heavy ion interactions with space shielding materials using the SHIELD-HIT transport code. *Radiat. Meas.* **2006**, *41*, 1091.
16. ICRU Report 33, Radiation quantities and units, International Commission on Radiation Units, 7910 Woodmont Ave., Washington, DC, 1979.
17. ICRU Report 36, Microdosimetry, International Commission on Radiation Units, 7910 Woodmont Ave., Washington, DC, 1983.
18. Bichsel, H. Shell corrections in stopping powers. *Phys. Rev. A* **2002**, *65*, 052709.
19. ICRU Report 49, Stopping Powers and Ranges for Protons and Alpha Particles, International Commission on Radiation Units and Measurements, 7910 Woodmont Ave., Bethesda, MD, 1993.
20. ICRU Report 73, Stopping of ions heavier than Helium, International Commission on Radiation Units, 7910 Woodmont Ave., Washington, DC, 2005. Note that the tables for water are labelled incorrectly: the table for $-dE/\rho d\ell$ labelled "liquid water" is for water vapor and vice-versa, the range table is for water vapor rather than liquid water. Corrected Tables are at ICRU.org/images/pdf/errata-and-adenda.pdf.
21. Carlsson, A. K.; Andreo, P.; Brahme, A. Monte Carlo and analytical calculation of proton pencil beams for computerized treatment plan optimiztion. *Phys. Med. Biol.* **1997**, *42*, 1033–1053.
22. Hollmark, M.; Uhrdin, J.; Belkic, Dz.; Gudowska, I.; Brahme, A. Influence of multiple scattering and energy loss straggling on the absorbed dose distributions of therapeutic light ion beams: I. Analytical pencil beam model. *Phys. Med. Biol.* **2004**, *49*, 3247.
23. Kempe, J.; Gudowska, I.; Brahme, A. Depth absorbed dose and LET distributions of therapeutic ^{1}H, ^{4}He, ^{7}Li, and ^{12}C beams. *Med. Phys.* **2007**, *34*, 183–192.
24. Kempe, J.; Brahme, A. Energy-range relation and mean energy variation in therapeutic particle beams. *Med. Phys.* **2008**, *35*, 159.

25. Bohr, N. The penetration of atomic particles through matter*Dan. Mat. Fys. Medd* **1948**, *18.*
26. Bichsel, H. Straggling of heavy charged particles: Comparison of Born hydrogenic-wave-function approximation with free-electron approximation. *Phys. Rev. B* **1970**, *1*, 2854–2862.
27. Bichsel, H. Passage of Charged Particles Through Matter. In *American Institute of Physics Handbook*, 3rd ed.; Gray, D. E., Ed.; McGraw Hill, 1972; Chapter 8d.
28. Tschalär, Ch. Straggling distributions of large energy losses. *Nucl. Instrum. Methods* **1968**, *61*, 141.
29. Bichsel, H. Interaction of Radiation with Matter. In *Landolt-Boernstein, New Series, Group I*, Elementary Particles, Subvolume B, Detectors and Data Handling, Schopper, H. Ed., Springer, 2010; Vol. 21.
30. Vavilov, P. V. Ionization losses of high-energy heavy particles. *Sov. Phys. JETP* **1957**, *5*, 749–751.
31. Bichsel, H.; Saxon, R. P. Comparison of calculational methods for straggling in thin absorbers. *Phys. Rev. A* **1975**, *11*, 1286–1296.
32. Bichsel, H.; Hiraoka, T. Energy spectra and depth-dose curves for 70 MeV protons. *Int. J. Quantum Chemistry: Quantum Chem. Symp.* **1989**, *23*, 565–574.
33. Gudowska, I. Private Communication, 2009.
34. Williams, E. J. The straggling of β Particles. *Proc. Roy. Soc. A* **1929**, *125*, 420.
35. Landau, L. On the energy loss of fast particles by ionization. *J. Phys.* **1944**, *VIII*, 201–205.
36. Herring, J. R.; Merzbacher, E. Statistical problems in energy loss and ionization processes. *J. Elisha Mitchell Sci. Soc.* **1957**, *73*, 267.
37. Kellerer, A. M. G. S. F. Bericht B-1, Strahlenbiologisches Institut der Universität München, 1968.
38. Berger, M. J. Penetration of proton beams through water. I. Depth-dose distributions, spectra and LET distributions, Report NISTIR 5226, National Institute of Standards and Technology, Gaithersburg, MD, July 1993.
39. Nikjoo, H.; Uehara, S.; Emfietzoglou, D., et al. Track structure codes in radiation research. *Radiat. Meas.* **2006**, *41*, 1052–1074.
40. Niita, K.; Sato, T.; Iwase, H., et al. PHITS—a particle and heavy ion transport code system. *Radiat. Meas.* **2006**, *41*, 1080–1090.
41. Elsässer, T.; Cunrath, R.; Krämer, M.; Scholz, M. Impact of track structure calculations on biological treatment planning in ion radiotherapy. *New J. Phys.* **2008**, *10*, 075005.
42. Agostinelli, S.; Allison, J.; Amako, K., et al. Geant4—a simulation toolkit. *Nucl. Instrum. Methods A* **2003**, *506*, 250–303.
43. Bichsel, H. Inelastic electronic collision cross sections for Monte Carlo calculations. *Nucl. Instrum. Methods B* **1990**, *52*, 136.
44. Bichsel, H. <http://faculty.washington.edu/hbichsel>.
45. Bichsel, H. A method to improve tracking and particle identification in TPCs and silicon detectors. *Nucl. Instrum. Methods A* **2006**, *562*, 154–197.
46. Berger, M. J.; Seltzer, S. M. Multiple Scattering Corrections for Proton Range Measurements. p. 69–98 in Studies in Penetration of Charged Particles in Matter; Nat. Acad. Sci.-Nat. Res. Council, Publication 1133, 1964.
47. Bichsel, H. Charged Particle Interactions. In *Radiation Dosimetry*, 2nd ed.; Attix, F. H., Roesch, Wm. C., Eds.; Academic Press, 1968; pp. 157–228.
48. Schall, I.; Schardt, D.; Geissel, H., et al. Charge changing nuclear reactions of relativistic light-ion beams (5 < Z < 10) passaging through thick absobers. *Nucl. Instrum. Methods B* **1996**, *117*, 221–234.

49. Matsufuji, N.; Fukumura, A.; Komori, M.; Kanai, T.; Kohno, T. Influence of fragment reaction of relativistic heavy charged particles on heavy-ion radiotherapy. *Phys. Med. Biol.* **2003**, *48*, 1605–1623.
50. Bichsel, H.; Uehling, E. A. Multiple scattering correction for proton ranges and the evaluation of the L-shell correction and I-value for Al. *Phys. Rev.* **1960**, *119*, 1670–1680.
51. Bichsel, H. The multiple scattering of protons. *Phys. Rev.* **1958**, *112*, 182.
52. Gudowska, I. Private communication, July 2008.
53. Brenner, D. J. Track structure, lesion development and cell survival. *Radiat. Res.* **1990**, *124*, S29–S37.
54. Hiraoka, T.; Bichsel, H. Stopping power and range tables for C, N, Ne, Si and Ar ions in various dosimetric materials. *Medical Standard Dose* **2000**, *5*(Supplement 1), 1–145.
55. Cobut, V.; Frongillo, Y.; Patau, J. P.; Goulet, T.; Fraser, M.-J.; Jay-Gerin, J.-P. Monte Carlo simulation of fast electron and proton tracks in liquid water-I. physical and physicochemical aspects. *Radiat. Phys. Chem.* **1998**, *51*, 229–243.
56. Dingfelder, M. Track structure: time evolution from physics to chemistry. *Radiat. Prot. Dosimet.* **2006**, *122*, 16–21.
57. Elsässer, T.; Scholz, M. Cluster effects within the local effect model. *Radiat. Res.* **2007**, *167*, 319.
58. LaVerne, J. A.; Mozumder, A. Penetration of low-energy electrons in water. *Radiat. Res.* **1983**, *96*, 219–234.
59. Dingfelder, M.; Ritchie, R. H.; Turner, J. E.; Friedland, W.; Paretzke, H. G.; Hamm, R. N. Comparisons of calculations with PARTRAC and NOREC: transport of electrons in liquid water. *Radiat. Res.* **2008**, *169*, 584–594.
60. Chatterjee, A.; Holley, W. R. Computer simulation of initial events in the biochemical mechanisms of DNA damage. *Adv. Radiat. Biol.* **1993**, *17*, 181.
61. Dingfelder, M.; Hantke, D.; Inokuti, M.; Paretzke, H. G. Electron inelastic-scattering cross sections in liquid water. *Radiat. Phys. Chem.* **1998**, *53*, 1–18.
62. Turner, J. E.; Paretzke, H. G.; Hamm, R. N.; Wright, H. A.; Ritchie, R. H. Comparative study of electron energy deposition and yields in water in the liquid and vapor phases. *Radiat. Res.* **1982**, *92*, 47–60.
63. Beuve, M. Formalization and theoretical analysis of the local effect model. *Radiat. Res.* **2009**, *172*, 394–402.
64. Atomic and Molecular Data for Radiotherapy and Radiation Research, IAEA-TECDOC-799, May 1995.
65. Gudowska, I.; Kempe, J.; Sobolevsky, N. Low and high LET dose components in Carbon beam. *Radiat. Prot. Dosimet.* **2006**, *122*, 483.
66. Furusawa, Y.; Fukutsu, K.; Aoki, M.; Itsukaichi, H.; Eguchi-Kasai, K.; Ohara, H.; Yatagai, F.; Kanai, T.; Ando, K. Inactivation of aerobic and Hypoxic cells from three different cell lines by accelerated He-, C- and Ne-Ion beams. *Radiat. Res.* **2000**, *154*, 485–496.
67. Bichsel, H. *Cell survival*, Presentation at Annual Meeting of Rad. Res. Soc., September 2010, Maui.
68. Scholz, M.; Kellerer, A. M.; Kraft-Weyrather, W.; Kraft, G. Computation of cell survival in heavy ion beams for therapy. *Radiat. Environ. Biophys.* **1997**, *36*, 59.
69. Evans, R. D. *The Atomic Nucleus*; McGraw Hill.
70. Leroy, C.; Rancoita, P.-G. Principles of radiation interaction in matter and detection, World Scientific, 2004.
71. Sigmund, P. *Particle Penetration and Radiation Effects*; Springer.
72. Uehling, E. A. Penetration of heavy charged particles in matter. *Ann. Rev. Nucl. Sci.* **1954**, *4*, 315.
73. Bethe, H. Zur Theorie des Durchgangs schneller Korpuskularstrahlen durch Materie. *Ann. Phys.* **1930**, *5*, 325.

74. Fano, U. Penetration of protons, alpha particles, and mesons. *Ann. Rev. Nucl. Sci.* **1963**, *13*, 1.
75. Manson, S. T. Inelastic collisions of fast charged particles with atoms: ionization of the Al L shell. *Phys. Rev. A* **1972**, *6*, 1013.
76. Inokuti, M. Inelastic collisions of fast charged particles with atoms and molecules—the Bethe theory revisited. *Rev. Mod. Phys.* **1971**, *43*, 297.
77. Bote, D.; Salvat, F. Calculations of inner-shell ionization by electron impact with the distorted-wave and plane-wave Born approximation. *Phys. Rev. A* **2008**, 77, 042701.
78. Dingfelder, M.; Inokuti, M.; Paretzke, H. Inelastic-collision cross sections of liquid water for interactions of energetic protons. *Radiat. Phys. Chem.* **2000**, *59*, 255–275.
79. Ritchie, R. H.; Hamm, R. N.; Turner, J. E.; Wright, H. A.; Ashley, J. J.; Basbas, G. J. Physical aspects of charged particle track structure. *Int. J. Radiat. Appl. Instrum. Part D* **1989**, *16*, 141–155.
80. Wilson, W. E.; Nikjoo, H. A Monte Carlo code for positive ion track simulation. *Radiat. Environ. Biophys.* **1999**, *38*, 97–104.
81. Isaacson, M. Interaction of 25 keV electrons with the nucleic acid bases, adenine, thymine, and Uracil, I. outer shells, II. inner shells, *J. Chem. Phys.* **1972**, *56*, 1803 and 1813.
82. Johnson, D. E. The interaction of 25 keV electrons with Guanine and Cytosine. *Radiat. Res.* **1972**, *49*, 63.
83. Inagaki, T.; Hamm, R. N.; Arakawa, E. T.; Painter, L. R. Optical and dielectric properties of DNA in the extreme ultraviolet. *J. Chem. Phys.* **1974**, *61*, 4246.
84. Killat, U. Optical properties of C_6H_{12} ,..., C_5H_5N in the solid and gaseous state derived from electron energy losses. *J. Phys. C: Solid State Phys.* **1974**, 7, 2396.
85. Killat, U. Electron energy-loss measurements on 1,3-cyclohexadiene and 1,4-cyclohexadiene. *Z. Physik* **1974**, *270*, 169.
86. *Handbook of optical constants of solids: three volumes*; Academic Press: New York, 1985, 1991 and 1998.
87. Fermi, E. Ueber die Theorie des Stosses zwischen Atomen und elektrisch geladenen Teilchen. *Z. Phys.* **1924**, *29*, 315–327.Fermi, E. Sulla teoria dell'urto tra atomi e corpuscoli elettrici. *Nuovo Cimento* **1925**, *2*, 143–158.
88. Allison, W. W. M.; Cobb, J. H. Relativistic charged particle identification by energy loss. *Ann. Rev. Nucl. Part. Sci.* **1980**, *30*, 253.
89. Raether, H. *Excitation of plasmons and interband transitions by electrons*; Springer Verlag: New York, 1980.
90. Blum, W.; Rolandi, L. *Particle Detection with Drift Chambers*; Springer-Verlag
91. Fermi, E. The ionization loss of energy in gases and condensed materials. *Phys. Rev.* **1940**, *57*, 485.
92. Fernandez-Varea, J. M.; Salvat, F.; Dingfelder, M.; Liljequist, D. A relativistic optical-data model for inelastic scattering of electrons and positrons in condensed matter. *Nucl. Instrum. Methods B* **2005**, *229*, 187–217.
93. Liljequist, D. A simple calculation of inelastic mean free path and stopping power for 50 ev—50 keV electrons in solids. *J. Phys. D* **1983**, *16*, 1567.
94. Saxon, R. P. Total cross section for inelastic scattering of charged particles by atoms and Molecules. VII. The Neon atom. *Phys. Rev. A* **1973**, *8*, 839–849.
95. Inokuti, M.; Saxon, R. P.; Dehmer, J. L. Total cross-sections for inelastic scattering of charged particles by atoms and molecules-VIII. Systematics for atoms in the first and second row. *Int. J. Radiat. Phys. Chem.* **1975**, 7, 109.
96. Molière, G. Theorie der Streuung schneller geladener Teilchen I, Einzelstreuung am abgeschirmten Coulomb-Feld. *Z. Natf.* **1947**, *2A*, 133.
97. Molière, G. Theorie der Streuung schneller geladener Teilchen II, Mehrfach- und Vielfachstreuung. *Z. Natf.* **1948**, *3A*, 78.

98. Molière, G. Theorie der Streuung schneller geladener Teilchen III, Die Vielfachstreuung von Bahnspuren unter Berücksichtigung der statistischen Koppling. *Z. Natf.* **1955**, *10A*, 177.
99. Bichsel, H.; Hanson, K. M.; Schillaci, M. E. Lateral displacement in small angle multiple scattering. *Phys. Med. Biol.* **1982**, *27*, 959–961.
100. Rossi, H. H.; Zaider, M. Compound dual radiation action. *Radiat. Res.* **1997**, *132*, 178–183.
101. Sachs, R. K.; Hahnfeld, P.; Brenner, D. J. The link between low-LET dose-response relations and the underlying kinetics of damage production/repair/misrepair. *Int. J. Radiat. Biol.* **1997**, *72*, 351–374.
102. Carlson, D. J.; Stewart, R. D.; Semenenko, V. A.; Sandison, G. A. Combined use of Monte Carlo DNA damage simulations and deterministic repair models to examine putative mechanisms of cell killing. *Radiat. Res.* **2008**, *169*, 447–459.

CHAPTER TWO

On the Accuracy of Stopping Power Codes and Ion Ranges Used for Hadron Therapy

Helmut Paul
Atomic Physics and Surface Science, Institute for Experimental Physics, Johannes Kepler University, Altenbergerstrasse 69, A-4040, Linz, Austria

Contents

Abstract

Various stopping power theories and codes are compared statistically to available experimental data, in view of judging their reliability for hadron therapy. Both stopping powers and ranges are taken into consideration. The mean ionization energy of water is discussed in detail.

1. INTRODUCTION

One of the main characteristics of therapeutical hadron beams is the range which is mainly determined by the mean ionization potential *I* of the material. According to the relativistic Bethe formula (without corrections),[1, 2] the mass stopping power is given by

$$S/\rho = (0.307075\ \mathrm{MeVcm^2g^{-1}})\frac{Z_1^2}{\beta^2}\frac{Z_2}{A_2}L(\beta), \tag{1}$$

Advances in Quantum Chemistry, Volume 65
ISSN 0065-3276, http://dx.doi.org/10.1016/B978-0-12-396455-7.00002-9

where $S = -\mathrm{d}E/\mathrm{d}x$ is the linear stopping power (or linear energy transfer, LET), x is the distance, ρ is the density of the material; Z_1, E, and υ are charge number, energy and velocity of the ion; Z_2 and A_2 are charge number and mass number of the target; $\beta = \upsilon/c$, c is the speed of light; and the stopping number L is given by

$$L(\beta) = \ln \frac{2m\upsilon^2}{(1-\beta^2)} - \ln I - \beta^2, \tag{2}$$

where m is the mass of the electron. Eq. (2) is reliable at energies high enough (but not so high that the density correction becomes appreciable[2]). To extend the validity to lower energy, one customarily adds shell, Barkas–Andersen and Bloch corrections[2] to Eq. (2) if necessary.

In place of the mass stopping power, one also uses the stopping cross section S/n (where n is the atomic density), usually expressed in units of 10^{-15} eVcm^2/atom. For a solid absorber, this corresponds roughly to the energy loss per atomic layer.

For a compound, following the custom of Ziegler,[18] we express the stopping cross section in terms of 10^{-15} eVcm^2/atom, dividing the molecular cross section by the number of atoms in the molecule. This has the advantage that stopping cross sections are nearly the same for substances of similar composition but different A_2 (e.g., for polymers).

Since stopping power depends essentially on velocity rather than energy, one usually lists or plots it as a function of specific energy, i.e., energy per nucleon, or of velocity squared[†] (e.g., in MeV/u).

For a mixture or, assuming Bragg's additivity rule,[3] for a compound, the mass stopping power is obtained by a linear combination of the constituent stopping powers:[2]

$$\frac{S}{\rho} = \sum_j w_j \left(\frac{S}{\rho}\right)_j, \tag{3}$$

where w_j is the fraction by weight, and $(S/\rho)_j$ is the mass stopping power of the jth constituent.

Deviations from Bragg's additivity have been investigated for many years (see, e.g., Ref. 49). In Ziegler's SRIM program,[18] a correction is built in that can be used for many compounds (see Section 4.1). The SRIM program also provides a correction for the *negative* solid-gas difference that exists between the mass stopping powers of substances in different phases,

---

[†] Velocity squared in MeV/u is often incorrectly called "energy."

at low energy.[4] The *positive* solid-gas difference at high energy is, however, only described[31] by CasP,[8] not by SRIM.

The relation for the mean ionization energy corresponding to Eq. (3) is

$$\ln I = \left(\sum w_j \frac{Z_{2j}}{A_{2j}} \ln I_j\right) / \left\langle \frac{Z_2}{A_2} \right\rangle, \tag{4}$$

where

$$\left\langle \frac{Z_2}{A_2} \right\rangle = \sum w_j \frac{Z_{2j}}{A_{2j}}, \tag{5}$$

where $Z_{2\mathrm{j}}$ and $A_{2\mathrm{j}}$ define the *j*th constituent.

Lists of mean ionization energies can be found in ICRU Report 49.[2] Some of these values are probably outdated, and a Report Committee of the ICRU is working to improve the values for water and graphite.

To find the simplest approximation to the range *R*, it suffices to integrate the reciprocal of the linear stopping power over energy:

$$R_{\mathrm{CSDA}} = \int_0^R \mathrm{d}x = \int_{E_0}^0 \frac{\mathrm{d}E}{\mathrm{d}E/\mathrm{d}x} = \int_0^{E_0} \frac{\mathrm{d}E}{S}, \tag{6}$$

where E_0 is the initial energy. This is called the continuous-slowing-down (CSDA) approximation.[2] Due to scattering, actual ranges are somewhat smaller; this fact can be described by the "detour factor".[2] Projected ranges, i.e., the projection of the range onto the axis of the original direction of travel, are calculated by program SRIM.[18]

The therapeutic value of hadron beams lies in the fact that the mean ionization per unit length has its maximum (the "Bragg peak") close to the end of path.

2. TABLES AND PROGRAMS

The stopping power tables and computer programs discussed here are listed in Table 2.1. Program PASS (on which the tables in ICRU Report 73 and in the Erratum are based) and the program by Lindhard and Sørensen[5] (LS) are based on first principles only. The same is true for CasP, except that empirical values are used here for the ionic charge. The tables by Janni, by Hubert et al. and by Ziegler, and the program MSTAR are semi-empirical. Program LET is not further considered here since it is not independent, but based on Ziegler's programs. Program BEST has been used to produce the high energy parts of the tables in ICRU Report 49;[2] it is useful in that

Table 2.1 Tables and computer programs for the stopping power of matter for positive ions. “u” is the unified atomic mass unit, also called dalton

Name, reference	Z_1	Z_2	(Specific) energy range	Remarks
ATIMA[6]	1–92	1–92	≥10 MeV/u (as used here)	Based[a] on Lindhard–Sørensen above 30 MeV/u
BEST[7]	1–92	1–92; 180 compounds[b]	≥0.5 MeV/u	Bethe theory with corrections; bare ions
CasP v. 5.0[8]	1–92	1–92, any compound[c]	0.0001–200 MeV/u	Default settings used here for target ionization[d]
HISTOP[9]	many	6	0.01–30 MeV/u	HISTOP for the valence electrons, SCA for the K shell of carbon
Hubert et al.[10]	2–103	36 solid elements	2.5–500 MeV/u	
ICRU Report[e] 49[2]	1, 2	25 elements, 48 compounds or mixtures	0.001–10000 MeV (p); 0.001–1000 MeV (α)	Programs NIST PSTAR, NIST ASTAR
ICRU Report 73[11, 12]	3–18, 26	25 elements, 31 compounds	0.025–1000 MeV/u	Based on PASS
Janni[13]	1	1–92; 63 compounds	0.001–10000 MeV	
LET[14, 15]	1–92	19 materials	0.2–1000000 MeV/u	Based on Ziegler’s TRIM/SRIM programs (before 1999)
MSTAR[16]	3–18	31 elements, 48 compounds or mixtures	0.00025–250 MeV/u	Based on alpha stopping powers of ASTAR
PASS[17]	many	many	Above 0.025 MeV/u	Binary Theory, used for ICRU Rep. 73
SRIM[f] 2003[18]	1–92	1–92, many compounds	1.1 eV–10 GeV/u	SRIM stopping was not changed since 2003
Ziegler et al.[19]	1–92	1–92; many other targets	0.1–100000 keV/u	First program to treat all ions, all targets

[a] Below 10 MeV/u, the values are based on an old version of SRIM (Ziegler et al. 1985). Between 10 and 30 MeV/u, the values are interpolated between SRIM and LS.

[b] Additional compounds may be calculated by entering a chemical formula, assuming Bragg’s additivity.

[c] Compounds are calculated according to chemical formula, assuming Bragg’s additivity.

[d] Target and projectile ionization must be calculated separately, and added.

[e] At high energy, the ICRU table was calculated using BEST; the low energy part is based on experimental data.

[f] SRIM was called TRIM in earlier times.

the value of *I* can be changed, but it assumes a bare nucleus and is therefore not reliable below about 1 MeV/nucleon.

To represent stopping for heavy ions at the highest energies correctly, it is necessary to use the non-perturbative LS theory which is fully relativistic and, in addition, assumes projectile nuclei of finite size. For convenience, we have employed the program ATIMA instead which is based on the LS program above 30 MeV/u and which includes shell, Barkas and Fermi-density effect corrections and in addition, a correction for projectile mean charge. Results for ions heavier than Ar are shown in Ref. 31. But the use of the LS program will hardly be necessary for radiation therapy, since even for oxygen ions at 690 MeV/u, there is no difference between LS theory and Bethe theory [Eq. (1)].[20]

3. LIQUID WATER AS A TARGET

Because of the large water content of the human body, liquid water is one of the most important substances to be considered.

3.1 Stopping power of water for hydrogen ions

Figure 2.1, taken from our large collection of stopping graphs and data,[21] shows experimental values and theoretical or semi-theoretical descriptions of the stopping power of liquid and solid water for protons. In particular, it shows the recent measurements by the Kyoto group[26, 27] who used a liquid water jet in vacuum, and by the Jyväskylä group[28] who used a thin water sheet (enclosed between two thin copper sheets) in transmission. Figure 2.2 shows some of the same data again, but divided by the data from the proton table of ICRU Report 49,[2] to make small differences visible.

For the curves in Figure 2.2, the *I* value is given where known. On the average, above 10000 keV, the BEST (Bethe) curve ($I = 78$ eV) is 0.52% below the ICRU 49 curve at unity ($I = 75$ eV), as one expects comparing $L(\beta)$ for the two different *I*-values; for the PASS curve, the difference with respect to unity is slightly larger.

Inspection of Figure 2.2 shows a problem:[30, 31] the Bethe equation (i.e., BEST) is generally reliable[32] and depends essentially only on *I* and on the shell correction in the region above 10000 keV, and the latter correction is quite small here. The GarM09 curve and the PASS curve are very close to BEST, about 1% below ICRU 49 (i.e., unity), and they therefore all seem reliable. Hence it appears that the Kyoto measurements (and the Emf09

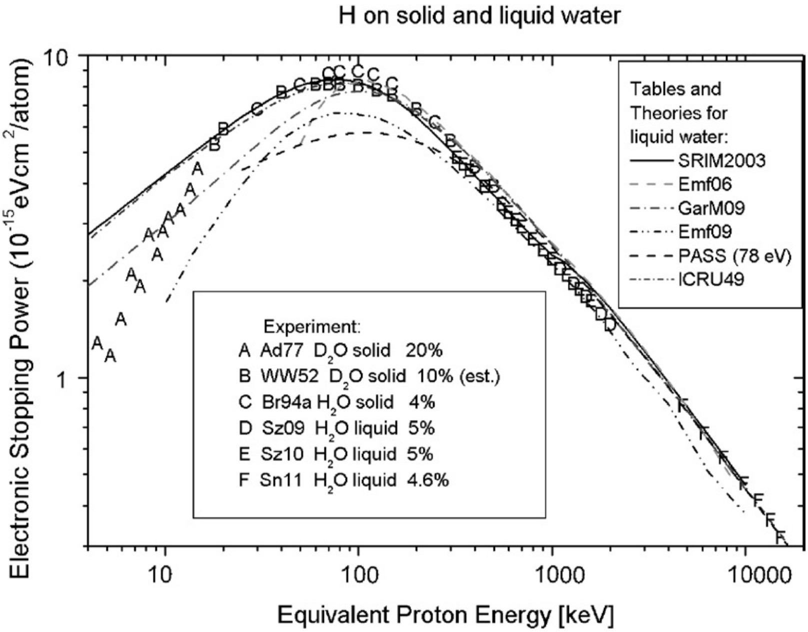

Figure 2.1 Electronic stopping power of solid and liquid water (we assume that the *I*-values for solid and liquid water are equal[46]) for protons, versus energy. The letters show experimental data; the corresponding data references can be found in Ref. 21. Some of the general tables and theories are listed in Table 1. In addition, there are the following theoretical curves: Emf06,[22] Emf09,[23] GarM09,[24] and PASS.[25]

theory)[‡] might be too low by about 10%. But Shimizu et al.[33] checked the accuracy of their stopping data by using He ions on their water jet target, and by measuring proton energy loss and scattering from an Al wire; in both cases, the results agreed with the data from ICRU 49. This discrepancy is not yet understood.

As seen in Figure 2.2, the Jyväskylä measurement (Sn11) is in good agreement with the GarM09, PASS, and BEST curves. The average value of the normalized Sn11 points is 0.986, i.e., 0.6% below the BEST curve. This corresponds to an experimental *I* value of 81.7 eV, but with a rather large error of 28 eV, due to the systematic error of 4.6% stated by Siiskonen et al.[28] for the stopping power values.

[‡] The low value is due to an unusually large shell correction in the Emf09 theory (priv. communication from D. Emfietzoglou to H. Paul, 2012).

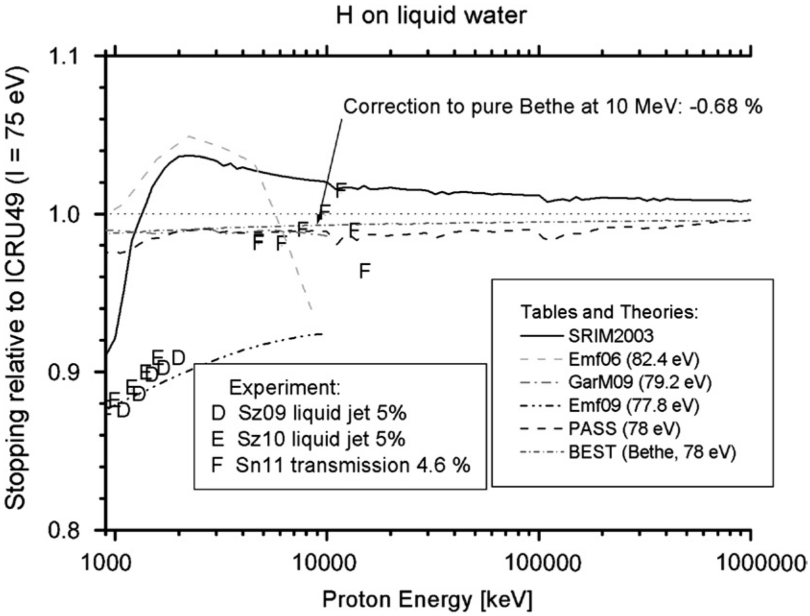

Figure 2.2 Electronic stopping power of liquid water for protons, normalized by the data from the proton table of ICRU Report 49.[2] The designations for tables and for experimental points are as in Figure 2.1. *I* values are shown in parentheses. The correction to Eq. (2) is −0.68% at 10 MeV, and even smaller beyond.

For He ions in liquid water, there are four data sets in the literature spanning the range from 300 to 7500 keV (see Ref. 21). The data points agree with the curve of ICRU 49 within 3%, on the average; this corresponds roughly to the experimental accuracies stated.

For heavier ions, there is only one data set: the stopping power for Li ions of 0.025–0.1 MeV/nucleon, measured by the inverted Doppler shift attenuation method.[34]

3.2 Range measurements for water, and mean ionization energy

Evidently, stopping power measurements are not yet sufficiently accurate for a precise determination of the *I* value of water, but one might hope that range measurements are better suited. Table 2.2 gives an overview of calculated and measured values of the mean ionization energy of liquid water,[31] based mostly on range and ionization measurements, and on theory (using optical data). On the basis of the data available in 1984, the value $I = 75.0$ eV was

Table 2.2 *I* values of liquid water. The missing references can be found in Ref. 31

I (eV)	Reference	Method or remark
75.4 ± 1.9	Thompson, 1952	Range, 340–200 MeV p, assuming. $I_{Cu} = 322$ eV
74.6 ± 2.7	Nordin et al. 1979	Stopping power, 60 MeV pions
75	Ritchie et al. 1978	Dielectric response function
75.4	Ashley, 1982	Dielectric response function
81.77	Janni, 1982	Averaging data for H and O
79.7 ± 2	Bichsel et al. 1992	Ionization curves, 70 MeV p
81.8	Dingfelder et al. 1998	Dielectric response function
80.0 ± 1.3	Bichsel[a] et al. 2000[37]	Ionization curves, C ions, 290 MeV/u
77	Kramer et al. 2000	Depth dose curves for C ions
78.4 ± 1	Kumazaki et al. 2007[29]	Depth dose curves for protons
77.8 ± 1	Emfietzoglou et al. 2009[23]	Dielectric response function
79.4	Garcia-Molina et al. 2009[24]	Dielectric response, MELF-GOS model
75.0 ± 3	Chosen in ICRU 37 and 49	
78.0	Chosen in Sigmund et al.[12]	Erratum; replaces the value 67.2 eV implicit in ICRU Report 73

[a] The error is quite small due to the high precision of measurements (±0.05 mm).

chosen in ICRU Report 37[35] and again in ICRU Report 49.[2] But evidently, all the more recent determinations indicate a larger *I* value.

Using a precision water column, Schardt et al.[36] have recently measured Bragg peak positions for ^{1}H, ^{7}Li, ^{12}C, and ^{16}O beams at altogether 22 different energies, see Tables 2.3 and 2.4. To deduce mean ranges from Bragg peak positions, they used Bichsel's[37] empirical rule that the mean range is the depth at which the Bragg curve has dropped to $p = 82\%$ of its maximum value. Bichsel et al.[37] deduced this rule for high energy carbon ions. The value $p = 80\%$ was originally derived by Berger[38] for protons, and it has been confirmed by Bortfeld.[39] Figure 2.3 shows a comparison of an analytical calculation by Bichsel[40] with a Monte Carlo calculation by Gudowska[41] for 200 MeV protons in water.[§] The values found ($p = 82\%$ and $p = 80\%$) are in fair agreement with Berger's value. Schardt et al.,[42]

[§] All attempts to determine *p* by means of SRIM Monte Carlo calculations gave lower values: $p = 76\%$ for 200 MeV protons, and even lower values for carbon ions. This probably points to some error in the scattering cross sections used in SRIM.

Table 2.3 Bragg peak (BP) positions of Li, C and O ion beams in water measured by Schardt et al.[36] at a density of 0.997 g/cm³ (error 0.20 mm), deduced mean ranges, and comparison to the ICRU 73 range table[a](based on $I=78$ eV)[12]

Ion	v^2	Spec. energy	BP pos.	Mean range		ICRU[12]	Ratio
	(MeV/u)	(MeV/A_1)	(mm)	(mm)	(g/cm²)	(g/cm²)	
^{7}Li	100	100.201	60.65	60.89	6.0707	6.031	0.9935
	200	200.410	203.7	204.5	20.389	20.206	0.9910
^{12}C	100	100	26.16	26.26	2.6181	2.601	0.9935
	150	150	53.16	53.32	5.316	5.296	0.9962
	200	200	87.22	87.49	8.7228	8.705	0.9980
	250	250	127.32	127.7	12.732	12.72	0.9991
	300	300	172.50	172.9	17.238	17.24	1.0001
	400	400	275.36	276.1	27.527	27.51	0.9994
^{16}O	200	199.881	65.44	65.6	6.5403	6.514	0.9960
	250	249.852	95.43	95.67	9.5383	9.513	0.9973
	300	299.822	129.27	129.6	12.921	12.888	0.9974
	400	399.763	206.24	206.7	20.608	20.572	0.9983
Average							0.9966 ± 0.0028

[a] Only those measured values are shown that are close to calculated range values in the ICRU table.

Table 2.4 Bragg peak (BP) positions (error 0.2 mm) and deduced ranges for protons in water measured by Schardt et al.[36] at a density of 0.997 g/cm³, compared to a combination of the ICRU 49 table with BEST ($I=78$ eV)

Ion	v^2	Spec. energy	BP pos.	Mean range		ICRU49&	Ratio
	(MeV/u)	(MeV/A_1)	(mm)	(mm)	(g/cm²)	BEST(78)	
p	125	125.91	115.8	117	11.665	11.664	0.9999
	150	151.092	159.4	161	16.052	16.056	1.0002
	175	176.274	208.4	210.3	20.967	20.986	1.0009
	200	201.456	262.1	264.6	26.381	26.410	1.0011
Average							1.00054 ± 0.00055

using CR39 sheets to count particles, obtained $p=85\%$ for ^{3}He ions in water at 170 MeV/u; they state that this agrees within uncertainties with Bichsel's $p=82\%$. It seems appropriate therefore to assume an average value $p=(82\pm3)\%$ for this conversion. Using the shape of the Bragg peak (see Fig. 2.3), this leads to an (additional) error of 0.08% or 0.2 mm, to be added to the error of the Bragg peak position. Assuming that both error

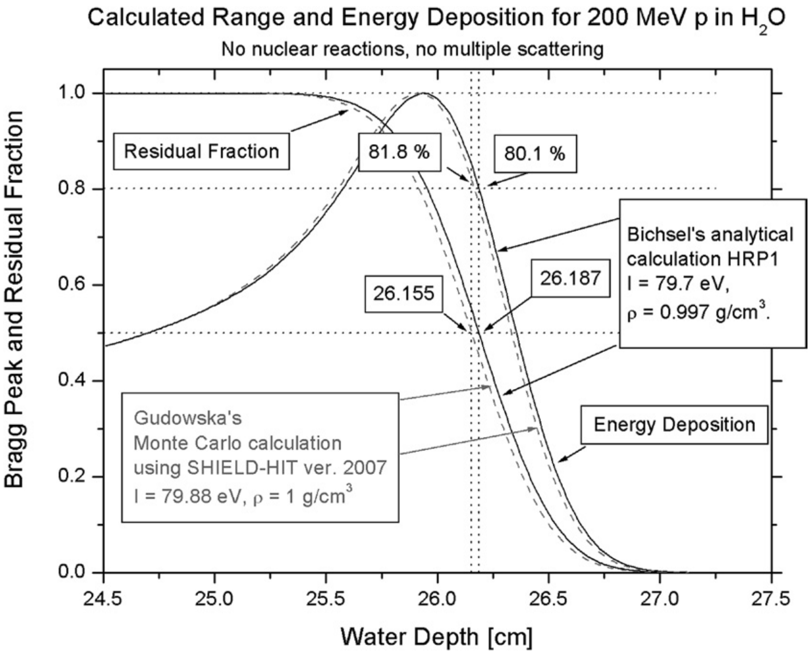

Figure 2.3 Bragg curve (ionization per unit distance) and integral range distribution for protons of 200 MeV in water, as calculated by Gudowska[41] (dashed) and by Bichsel[40] (full lines), respectively.

contributions are systematic, we arrive, conservatively, at a total range error of 0.4 mm.

Table 2.3 also lists the calculated ranges from the ICRU Erratum[12] and compares them to the measured ranges. Evidently, the calculated ranges (for $I = 78$ eV) are $(0.34 \pm 0.28)\%$ below measured ranges, on the average.[**]

To do a proper comparison between measured ranges and theoretical stopping power it would seem necessary to use a theory that has been tested against experiment. But unfortunately, there are no stopping power measurements for C and O ions, and almost none for Li ions, so a comparison is presently impossible. It seems better therefore, to resort to Schardt's proton measurements (Table 2.4), since here, comparisons with stopping power measurements are possible (see Figs. 2.1 and 2.2). For this purpose, we use the table from ICRU Report 49, merge it with the BEST curve for 78 eV at about 500 keV and integrate the reciprocal.[††]

[**] The standard deviations given here are always based on Eq. (9).

[††] Actually, the part of ICRU 49 makes an insignificant contribution to the integral.

Table 2.5 Like Table 2.4, but comparing to range values obtained from PASS ($I = 78$ eV) by integration

Ion	v^2 (MeV/u)	Spec. energy (MeV/A_1)	Bragg peak pos. (mm)	Mean range (mm)	(g/cm^2)	PASS ($I = 78$ eV)	Ratio
p	125	125.91	115.8	117	11.665	11.722	1.0049
	150	151.092	159.4	161	16.052	16.134	1.0051
	175	176.274	208.4	210.3	20.967	21.086	1.0057
	200	201.456	262.1	264.6	26.381	26.532	1.0057
Average							1.0053 ± 0.0004

The resulting ratio (1.00054 ± 0.00055) shows complete agreement with BEST.

Note that irrespective of the value of *I*, the range of the ions, with an accuracy of 0.4 mm, may be taken from Tables 2.3 and 2.4.

An additional comparison using PASS is shown in Table 2.5, which leads to a slightly larger ratio. A simple average of the ratios 0.9966, 1.0005, and 1.0053 from Tables 2.3–2.5 leads to an average ratio 1.0008 between calculated and measured ranges, with an estimated error of 0.008 (including the error of the range measurements), and hence,[‡‡] to a value $I = (78.5 \pm 5)$ eV, in agreement with the unweighted average $I = (79.2 \pm 1.6)$ eV of the values[§§] from the period 1992 to 2007 listed in Table 2.2.

4. OTHER TARGET SUBSTANCES AND STATISTICAL COMPARISONS

Many other substances are of interest in hadron therapy. A list of compositions of many non-elemental substances can be found in connection to the ESTAR program at NIST.[43] For some of these, stopping powers are given in ICRU Reports 49 and 73. Bragg functions and ranges have been measured for several substances by Bichsel et al. [37] Average *I* values for

---

[‡‡] The conversion from range error to error of *I* is conveniently done using program BEST in which *I* can be changed. This comparison shows that the relative error of *I* is 8 times larger than the relative error of range.

[§§] The Report Committee of the ICRU is probably arriving at a value around I = 78 eV (pers. comm. from Dr. Fernandez-Varea to H. Paul, February. 2012.

various “soft tissues” have been presented in Ref. 44, showing considerable variation.

Moyers et al.[45] have recently measured the linear stopping powers for protons at 135, 175, and 225 MeV in many compounds of interest to particle therapy, relative to a water target. They compared their results to the Janni[13] or LET[15] tables, finding agreement within 1 to 3%. As examples, Figure 2.4 shows a few results by Moyers et al., compared to the Janni, BEST, and SRIM tables. The BEST calculation uses the *I*-values of ICRU Report 49, except that $I = 78$ eV was taken for water.

Inspection of Figure 2.4 shows that the curves are essentially determined by the *I* values. In particular, the Janni curves are always above the BEST curves because of Janni’s rather high *I* value for water and his low *I* values for the other substances. Evidently, BEST agrees best with the Al measurements. For the compounds, BEST appears slightly low; this might point to slight errors of the *I* values used. Even so, if such high energy stopping powers are required and if *I* values are known or calculable using Eq. (4), a calculation using BEST should be useful.

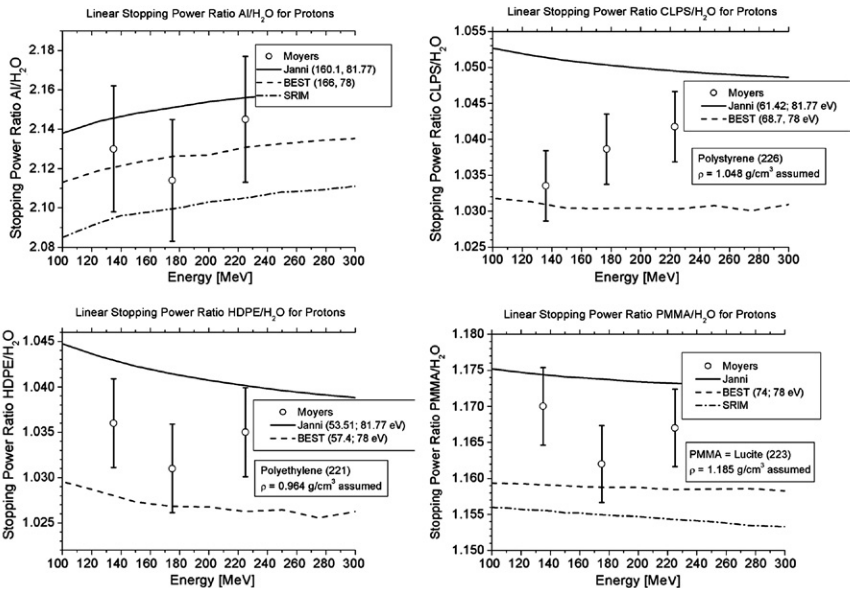

Figure 2.4 The linear stopping power of Al, clear polystyrene (CLPS), high density polyethylene (HDPE), and polymethyl methacrylate (PMMA), for protons relative to that of water, compared to the tables Janni, BEST, and SRIM. The 3-digit ID numbers from ICRU 49 are shown in parentheses. For the curves, the *I* values for both substances are shown in parentheses, where available. Experimental data are from Moyers et al.[45, 47]

A fairly complete collection of experimental stopping powers and many graphical presentations can be found in Ref. 21. Additional information is given in Ref. 31.

To determine the accuracy of various stopping tables and programs by statistics, we use our program "Judge".[46] This program calculates the normalized differences

$$\delta = (S_{\text{exp}} - S_{\text{tab}})/S_{\text{exp}} \tag{7}$$

for every data point. Here, S_{exp} is the experimental value, and S_{tab} the corresponding table value for the same ion, same target, and same energy. In every range of specific energy, i.e., energy per nucleon, it then determines the average normalized difference:

$$\Delta = \langle \delta \rangle \tag{8}$$

and its standard deviation

$$\sigma = \sqrt{\langle \delta^2 \rangle - \langle \delta \rangle^2}. \tag{9}$$

The averages are unweighted, except that obviously discrepant data are rejected (see "Statistical analysis" in Ref. 21). A small Δ usually signifies good agreement between table and experimental data; in such a case, σ is related to the mean experimental accuracy, and σ may be taken as a measure of the accuracy of the table, as determined from experiment.

In the following, "condensed" or "gaseous" means a substance condensed or gaseous at normal temperature and pressure.

Note that all the experimental data analyzed in the following chapter can be downloaded from our collection.[21]

4.1 Statistical comparisons for H and He ions

In Tables 2.6 and 2.7, the reliability of various stopping power tables for H and He ions in solid elements is given in terms of $\Delta \pm \sigma$. Here, E is the energy and A_1 is the mass number of the ion. These tables were originally published by Paul and Schinner,[32] but many new data have since been added.[31] This has not changed the results much, but it adds to the reliability.

One can see that σ always decreases with increasing energy, due to the higher accuracy of measurements at high energy. The numbers of experimental points averaged are also shown, to give an idea of the accuracy.

Table 2.6 Mean normalized deviations $\Delta \pm \sigma$ (in %) for H ions in 17 solid elements (Ag, Al, Au, Be, C, Cu, Fe, Gd, Ge, Mo, Pb, Pt, Si, Sn, Ti, U, W) covered by the ICRU Table, compared to various tables

***E/A*$_1$ (MeV)** *No. of points*	**0.01–0.1** *1357*	**0.1–1** *2492*	**1–10** *1212*	**10–100** *225*	**0.01–100** *5286*
Janni, 1982[13]	2.1 ± 11	−1.1 ± 7.1	−0.9 ± 3.6	−0.3 ± 0.5	−0.2 ± 7.7
Ziegler et al., 1985[19]	−1.3 ± 11	−3.1 ± 7.8	−0.4 ± 4.2	0.4 ± 2.2	−1.9 ± 8.2
ICRU, 1993[2]	0.8 ± 11	−0.7 ± 7.0	−0.3 ± 4.0	−0.1 ± 0.5	−0.2 ± 7.5
SRIM, 2003[18]	0.6 ± 10.3	−0.9 ± 6.7	−0.6 ± 3.7	−0.2 ± 0.6	−0.4 ± 7.2

Table 2.7 Mean normalized deviations $\Delta \pm \sigma$ (in %) for He ions in the same solid elements as in Table 2.6 covered by the ICRU Table (except for U), compared to various tables

***E/A*$_1$ (MeV)** *No. of points*	**0.01–0.1** *1036*	**0.1–1** *1913*	**1–10** *400*	**10–100** *11*	**0.01–100** *3360*
Ziegler et al., 1985[19]	3.2 ± 8.7	0.6 ± 5.6	−0.8 ± 3.3	0.8 ± 2.4	1.2 ± 6.7
ICRU, 1993[2]	2.6 ± 8.3	0.2 ± 5.6	0.1 ± 3.3	0.9 ± 0.9	0.9 ± 6.4
SRIM, 2003[18]	3.5 ± 8.2	0.6 ± 5.2	−0.3 ± 3.1	0.2 ± 0.9	1.4 ± 6.3

To provide a fair comparison with the smaller number of targets in the ICRU table, we compare only with the targets of that table, even though we have many more targets in our files.[21] We see that generally, σ has decreased and hence, the overall agreement between the experimental data and the tables has improved in time, with the exception of the TRIM program by Ziegler et al. (1985); but this was the first method capable of treating all ions and all targets.

Table 2.8 gives results for H ions in elemental gases. Here, we exclude measurements for low energy H ions in helium (see Ref. 31). Due to the threshold effect[48] these data would produce a very large Δ and thus obscure any other discrepancy. Except for the tables by Ziegler et al. (1985) (due to large discrepancies for H and He targets), the gas measurements appear here more reliable than those on solids.

Table 2.9 shows results for He ions in elemental gases. Again, the agreement with the data is much better than for solids, and we can observe a gradual improvement in time.

Table 2.8 Mean normalized difference $\Delta \pm \sigma$ (in %) for H ions in all elemental gases except F, Cl, Rn

E/A_1 (MeV)	**0.001–0.01**	**0.01–0.1**	**0.1–1.0**	**1–10**	**10–100**	**0.001–100**
No. of points	*124*	*335*	*535*	*303*	*11*	*1308*
Janni, 1982[13]	−0.9 ± 9.2	−0.0 ± 4.6	0.5 ± 3.9	0.9 ± 3.2	3.2 ± 0.6	0.4 ± 4.7
Ziegler et al., 1985[19]	22 ± 14	22 ± 11	0.4 ± 6.8	−1.1 ± 1.7	−1.0 ± 0.5	7.7 ± 14
ICRU, 1993[2]	−0.6 ± 6.7	−1.2 ± 5.0	−1.2 ± 3.7	−0.8 ± 1.6	−0.2 ± 0.5	−1.0 ± 4.1
SRIM, 2003[18]	2.1 ± 5.2	−0.1 ± 4.7	−0.4 ± 3.6	−0.2 ± 1.6	0.2 ± 0.3	−0.1 ± 3.9

Table 2.9 Mean normalized difference $\Delta \pm \sigma$ (in %) for He ions in all elemental gases except F, Cl, Rn

E/A_1 (MeV)	**0.001–0.01**	**0.01–0.1**	**0.1–1.0**	**1–10**	**0–10**
No. of points	*5*	*267*	*863*	*238*	*1373*
Ziegler et al. 1985[19]	7.2 ± 13	2.5 ± 5.9	3.0 ± 4.9	−0.5 ± 2.5	2.3 ± 5.0
ICRU, 1993	0.5 ± 6.8	−1.0 ± 4.2	0.1 ± 4.2	0.7 ± 2.3	0.0 ± 4.0
SRIM, 2003	−5.4 ± 6.1	0.3 ± 3.9	0.1 ± 3.8	−0.2 ± 2.2	0.1 ± 3.7

Data for compounds have been treated in Ref. 49. In our data base,[21] we have data for 150 different compounds. Table 2.10 shows results for hydrogen and helium ions in some of these compounds, compared to SRIM. Some of the normally liquid substances have been measured also in gaseous form at reduced pressure. Because of the different low energy limit chosen,[***] some of the results appear somewhat better than for elements. Again, the errors σ tend to be smaller for gases than for solids.

For the SRIM calculations in Table 2.10, Ziegler's built-in corrections for dependence on the target phase, and his corrections for deviations from the Bragg additivity rule Eq. (3) have been applied. These corrections amount to a few percent and exist only below 1 MeV/nucleon.[49]

Table 2.11 shows a comparison between SRIM 2003 and ICRU Report 49, for the smaller number of compounds covered by the latter

[***] This is to avoid large deviations due to the threshold effect in LiF.[54]

Table 2.10 Mean normalized deviations $\Delta \pm \sigma$ (in %) for H and He ions in condensed or gaseous compounds, as compared to SRIM (2003)

Ions	**Targets**	***E*/*A*$_1$ (MeV)**	**0.025–0.25**	**0.25–2.5**	**2.5–30**	**0.025–30**
H	cond.[a]	*No. of pts*	441	947	251	1639
		$\Delta \pm \sigma$	−1.1 ± 8.8	1.4 ± 6.3	−0.1 ± 3.9	0.5 ± 6.9
	gas[b]	*No. of pts*	508	378	24	910
		$\Delta \pm \sigma$	−0.9 ± 4.3	0.1 ± 3.3	−0.9 ± 2.1	−0.5 ± 3.9
He	cond.[c]	*No. of pts*	479	1471	14	1964
		$\Delta \pm \sigma$	0.4 ± 6.7	−0.5 ± 4.3	−2.0 ± 3.1	−0.3 ± 5.0
	gas[d]	*No. of pts*	997	1742	0	2739
		$\Delta \pm \sigma$	−2.6 ± 7.2	1.1 ± 2.9		−0.3 ± 5.2

[a] A150 tissue equiv. plastic, Al_2O_3, Anthracene, CaF_2, CdTe, CR39 nuclear track material, D_2O, Er_2O_3, Formvar, GaAs, GaN, GaP, Graphite, H_2O, Havar, In_2O_3, InP, KCl, LR115 cellulose nitrate, LiF, $LiNbO_3$, MuMetal, Mylar, Permalloy, Pliolite S-5A, Polyvinyltoluene, Polycarbonate, Polyethylene, Polyimide, Polypropylene, Polystyrene, Polysulfone, Sc_2O_3, SiO_2, Styrene, Terphenyl, TiO_2, Vyns, ZnSe, $ZnSiP_2$, ZnTe.

[b] Air, Butane, Butadiene, Butene, C_2H_2, C_2H_6, C_3H_8, C_6H_6, CCl_4, CH_4, CO_2, Cyclopropane, Decane, Ethylene, H_2O vapor, H_2S, Heptane, Hexane, Heptyne, Hexyne, N_2O, NH_3, NO, Nonane, Octane, Pentane, Pentyne, Propelene, Tissue equivalent gas.

[c] Al_2O_3, $BaCl_2$, BaF_2, C_2BrF, CCl_4, CdTe, CH_5Br, CH_5I, Chloroform, CO_2 solid, CR39, Cyclohexane, Dichloromethane, Ethyl alcohol, Er_2O_3, Ethyl cellulose, Formvar, GaAs, Graphite, H_2O, Havar, Heptane, Hexane, InP, LR-115, LiF, Methyl alcohol, MuMetal, Mylar, NE-111 scintillator, Octane, Propyl alcohol, Pentane, Pliolite S-5A, Polyvinyltoluene, Polycarbonate, Polyethylene, Polyimide, Polypropylene, Polystyrene, Polysulfone, SiC, SiO_2, Ta_2O_5, Teflon, $TiN_{1.1}O_{0.27}$, UO_2, Vyns, WO_3, ZnSe. ZnTe.

[d] Acetaldehyde, Acetone, Air, Allene, Benzene, Butyraldehyde, Butane, Butadiene, Butene, 2-Butanone, Butyne, C_2F_6, C_2H_2, $C_2H_2F_2$, $C_2H_4F_2$, C_2H_6, C_3F_8, C_3H_8, C_4F_8, $CBrF_3$, CCl_2F_2, CCl_4, $CClF_3$, CF_4, CH_3Br, CH_4, $CHCl_2F$, Chloroform, CO_2, CS_2, Cyclohexane, Cyclooctane, Cyclopropane, Cyclopentane, Cyclohexadiene, Cyclohexene, Cyclohexanone, Cyclopentene, Dichloromethane, Diethyl ether, Dioxane, Dimethylamine, Dimethyldisulfide, Dimethyl ether, Dimethyl sulfide, Ethyl alcohol, Ethylamine, Ethynylbenzene, Ethylene oxide, Ethylene sulfide, Ethylene, H_2O, H_2S, Heptane, Hexane, Hexene, Heptyne, Hexyne, Methyl alcohol, Methylamine, N_2O, NH_3, NO, Octane, Propyl alcohol, Pentane, Pentene, Pentanone, Pentyne, Propelene, Propyne, Propylene oxide, Propylene sulfide, SF_6, SO_2, Tissue eq. gas, Thiophene, Trimethylamine, Trimethylene sulfide, Toluene, Vinylmethyl ether.

Table 2.11 Mean normalized deviations $\Delta \pm \sigma$ (in %) for H and He ions in 23 (solid or gaseous) compounds covered by ICRU Report 49

***E*/*A*$_1$ (MeV)**	**0–0.03**	**0.03–0.3**	**0.3–3.0**	**3–30**	**0–30**
No. of points	*116*	*1036*	*1237*	*135*	*2524*
ICRU, 1993	0.2 ± 8.9	1.4 ± 5.9	1.3 ± 5.2	1.0 ± 4.4	1.3 ± 5.7
SRIM, 2003	−7.8 ± 12	−1.0 ± 6.4	0.4 ± 5.6	−0.6 ± 4.0	−0.6 ± 6.6

table, for H and He ions together.[49] For this restricted number of targets, ICRU Report 49 is clearly better than SRIM.

4.2 Application to therapy using H ions

Inspection of Tables 2.6 and 2.8 shows that, for protons in elements, in the range 10–100 MeV, the value of Δ is negligible for the ICRU and SRIM tables, and σ is 0.5%, on the average. Hence, in this energy range important for therapy, the ICRU and SRIM tables can be expected to be accurate to 0.5%. And the same accuracy may be expected up to 1000 MeV, if the ICRU or SRIM tables are extended[†††] using the pure Bethe theory Eq. (2), since the corrections to Bethe are minimal (cf. Fig. 2.2).

For protons in compounds, the highest energy range (Table 2.10) goes only up to 30 MeV, and σ is larger (2–4%). Hence, the predictive quality of SRIM appears worse for compounds. On the other hand, since Bragg's additivity holds at high energy, the stopping power of compounds at high energy may be calculated using Eq. (3), and in this way, the accuracy could be improved.

In therapy applications, the particle range is of greatest importance. The range for therapeutically relevant energies depends essentially on the I value, as has been discussed in Section 3.2 above. Range uncertainties have recently been considered by Andreo[44] and by Paganetti.[50] Unfortunately, Andreo's paper is based on an unrealistic variation of possible I values for water (67, 75, and 80 eV), due to the fact that his paper was published before the ICRU value $I = 67$ eV was officially declared as erroneous.[12] In the discussion by Paganetti,[50] the low value $I = 67$ eV has already been discarded.

Using our numbers from Section 3.2 ($I = 79.2$ eV with an error of 2.0%, and a conversion factor of 8), we arrive at a range error in water (due to the uncertainty of I) of 0.25%. Paganetti[50] arrives at the much larger estimate of 1.5% (for 1.5 standard deviations) for tissues because of the much larger variability of I values for tissues (see, e.g., Figs. 2.3 and 2.4 by Andreo).[44]

Concerning the conversion from dose distribution to range (see Section. 3.2), Paganetti states that ideally, $p = 80\%$ should be taken for proton therapy, but that, for historic reasons, $p = 90\%$ is used in most proton therapy facilities.

Monte Carlo programs like SHIELD-HIT[51] are an important tool to describe the passage of ions in all cases relevant to hadron therapy.

[†††] In the case of ICRU, this simply means using the ICRU table up to 1000 MeV.

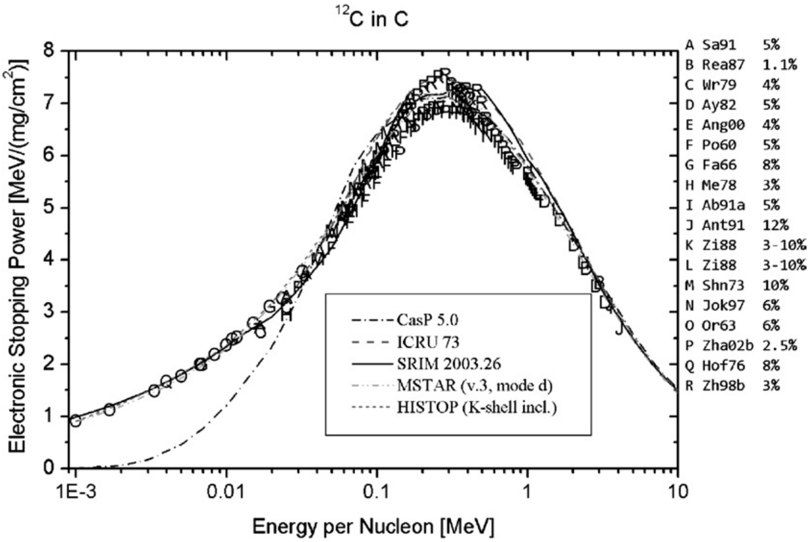

Figure 2.5 Electronic stopping power as a function of specific energy for C-ions in C, compared to various tables (cf. Table 2.1). Experimental points are marked by letters; the references corresponding to the reference codes given in the margin can be found in Ref. 21.

Such programs require a description of the stopping power over a large range of energies: the lowest energies are important for a proper description of the Bragg peak. But as we have seen above (Figs. 2.1 and 2.2), there is no reliable theory or table for the entire range of energy required. Hopefully, the Continuum Distorted Wave Method[52] will help to bridge this gap.

4.3 Statistical comparisons for carbon ions

Because of the importance of carbon ions for therapy, we treat these separately. As an example, Figure 2.5 shows stopping powers for carbon ions in carbon. Here, there is good agreement between the experimental data and the MSTAR, SRIM, HISTOP, and ICRU 73 tables in most energy regions, while CasP is too low at low energy.[‡‡‡]

Table 2.12 shows statistical results for carbon ions in solid elements covered by MSTAR. Since ICRU Report 73 does not treat Gd and Ta targets, the number of points is somewhat smaller for that table. The results

---

[‡‡‡] This discrepancy has not changed much from CasP v. 3.1 to v. 5.0.

are similar to those shown in Ref. 53, except that there, ions from $_3$Li to $_{18}$Ar were treated together. We find again that MSTAR and SRIM describe the data about equally well, but that the values from ICRU Report 73 are too high,[§§§] on the average, especially at low energies.

Similarly, Table 2.13 shows results for carbon ions in condensed compounds.

Table 2.14 shows results for carbon ions in gases. This table is of limited usefulness because of the small number of measured data points available for carbon ions that leads to rather erratic results. Possibly, if better results

Table 2.12 Mean normalized deviations $\Delta \pm \sigma$ (in %) for carbon ions in Ag, Al, Au, Be, C, Cu, (Gd), Ge, Mo, Ni, Pb, Si, Sn, (Ta), and Ti

E/A_1 (MeV) *No. of points*	**0.025–0.1** *202*	**0.1–1.0** *632*	**1–10** *229*	**10–100** *8*	**0.025–100** *1071*
MSTAR	−1.6 ± 9.6	0.6 ± 5.8	0.9 ± 5.1	0.0 ± 2.8	0.2 ± 6.6
SRIM, 2003	0.4 ± 8.3	−0.5 ± 5.3	−0.6 ± 5.2	1.0 ± 3.0	−0.3 ± 6.0
ICRU Rep. 73	−13 ± 12	−9.2 ± 10.9	−2.6 ± 5.8	−0.6 ± 3.8	−8.5 ± 10.8

Table 2.13 Mean normalized deviations $\Delta \pm \sigma$ (in %) for carbon ions in condensed compounds (Al_2O_3, Kapton, Mylar, Polycarbonate, Polyethylene, Polypropylene (not covered by ICRU 73), PVC, SiO_2)

E/A_1 (MeV) *No. of points*	**0.025–0.1** *27*	**0.1–1** *95*	**1–10** *98*	**10–100** *0*	**0.025–100** *220*
MSTAR	4.2 ± 8.8	−1.9 ± 5.3	3.8 ± 2.9		1.4 ± 5.8
SRIM, 2003	0.5 ± 5.4	−2.9 ± 4.4	−1.8 ± 3.4		−2.0 ± 4.3
ICRU Rep. 73	−6.9 ± 8.3	−8.1 ± 4.9	−2.6 ± 3.3		−5.8 ± 5.6

Table 2.14 Mean normalized deviations $\Delta \pm \sigma$ (in %) for carbon ions in gases (Air, Ar, H_2, He, N_2, Ne, O_2)

E/A_1 (MeV) *No. of points*	**0.025–0.1** *13*	**0.1–1** *2*	**1–10** *38*	**10–100** *4*	**0.025–100** *57*
MSTAR	−3.2 ± 8.9	0.6 ± 2.4	−1.1 ± 3.4	0.1 ± 4.2	−1.4 ± 5.3
SRIM, 2003	9.7 ± 7.1	−22 ± 2.3	−1.4 ± 7.2	−1.2 ± 8.3	0.4 ± 9.5
ICRU Rep. 73	−42 ± 21	−16 ± 0.7	−2.6 ± 5.0	0.4 ± 4.2	−12 ± 20

[§§§] Note that a negative Δ means that the table value is too high, according to the definition Eq. (7).

are required, the use of Table 2.3 from Ref. 53 (for ions from ${}_{3}$Li to ${}_{18}$Ar) may be preferable.

5. CONCLUSIONS

An overview of available tables and computer programs describing the stopping power of matter for positive ions is given. Experimental and table values for the stopping power of water for hydrogen ions are discussed in detail. An overview of measured and calculated values for the mean ionization energy of water is given; the average of recent values is found to be $I = (79.2 \pm 1.6)$ eV. The recent measurements of Bragg peak positions for light ions in water by Schardt et al. are discussed in detail; due to the uncertainty of converting these positions to range values, the I value 78.5 eV deduced from these is found to have the rather large error of 5 eV. Statistical comparisons of measured stopping powers with various tables for H, He, and C ions for many targets are given. The SRIM, ICRU 49, and MSTAR tables are found to describe the data best, on the average, but SRIM describes many more cases than the other tables. For protons of 10–100 MeV in elements, it is found that the ICRU 49 and SRIM tables may be expected to be accurate to 0.5%.

6. LIST OF ACRONYMS

ASTAR	NIST program for alpha stopping powers
ATIMA	Atomic Interactions in MAtter (a program)
BEST	BEthe Stopping program
BP	Bragg Peak
CasP	Convolution approximation for swift Particles
CR39	Nuclear track detector material
CSDA	Continuous slowing down approximation
ESTAR	NIST program for electron stopping powers
HISTOP	Heavy Ion Stopping program
ICRU	International Commission on Radiation Units and Measurements
ICRU 49	ICRU Report 49 for protons and alphas
ICRU 73	ICRU Report 73 for ions from ${}_{3}$Li to ${}_{18}$Ar
Judge	Statistical analysis program by Paul & Schinner

LET	Linear energy transfer
LS	Lindhard-Sørensen
MSTAR	MoreSTAR (going beyond PSTAR and ASTAR)
NIST	US National Institute of Standards and Technology
PASS	Peter-Andreas-Sigmund-Schinner
PSTAR	NIST program for proton stopping powers
SHIELD	Code for the simulation of the interaction of hadrons and arbitrary atomic nuclei with complex extended targets
SHIELD-HIT	Medical version of the code SHIELD
SRIM	The Stopping and Range of Ions in Matter

REFERENCES

1. Bethe, H. Bremsformel für Elektronen relativistischer Geschwindigkeit. *Z. Phys.* **1932**, *76*, 293.
2. ICRU Report 49, Stopping powers and ranges for protons and alpha particles, International Commission on Radiation Units and Measurements, Bethesda, MD, USA, 1993.
3. Bragg, W. H.; Kleeman, R. Range of ALPHA-particles of radium. *Phil. Mag.* **1905**, *10*, 318.
4. Paul, H. Some new results on stopping power for fast ions. *AIP Conf. Proc.* **2009**, *1099*, 251.10.1063/1.3120025
5. Lindhard, J.; Sørensen, A. H. Relativistic theory of stopping for heavy ions. *Phys. Rev. A* **1996**, *53*, 2443.
6. Geissel, H.; Scheidenberger, Ch.; Malzacher, P.; Kunzendorf, J; Weick, H. ATIMA. <http://www-linux.gsi.de/~weick/atima/>.
7. Berger, M. J.; Bichsel, H. BEST, BEthe Stopping power program, unpublished program recieved from M.J.Berger 1993.
8. Grande, P. L.; Schiwietz, G. CasP. In *Advances in Quantum Chemistry*, Cabrera-Trujillo, R., Sabin, J. R., Eds.;Vol. 45 p. 7, Elsevier, 2004. Program. <http://www.helmholtz-berlin.de/people/gregor-schiwietz/casp_en.html>.
9. Arista, N. R.; Lifschitz, A. F. Non-Linear Approach to the Energy Loss of Ions in Solids. In *Advances in Quantum Chemistry*, Sabin, J., Ed., 45 (2004), 47, Elsevier Inc.
10. Hubert, F.; Bimbot, R.; Gauvin, H. Range and stopping-power tables for 2.5–500 MeV/nucleon heavy ions in solids. *At. Data Nucl. Data Tables* **1990**, *46*, 1.
11. ICRU Report 73, Stopping of ions heavier than Helium, *J. ICRU* **2005**, *5*, 1.
12. Sigmund, P.; Schinner, A.; Paul, H. Errata and Addenda for ICRU Report 73, *J. ICRU* **2009**, *5*,1.
13. Janni, J. F. Proton range-energy tables. *Atomic Data Nucl. Data Tables* **1982**, *27*, 147.
14. Zajic, V.; Thieberger, P. Heavy ion linear energy transfer measurements during single event upset testing of electronic devices. *IEEE Trans. Nucl. Sci.* **1999**, *46*, 59.
15. Zajic, V. LET: Energy-LET-Range calculator v. 1.24. New York: Brookhaven National Laboratory, 2001. <http://tvdg10.phy.bnl.gov/let.html>.
16. Paul, H. MSTAR version 3, 2003. <http://www.exphys.uni-linz.ac.at/stopping/MSTARWWW/MSTAR312.zip>.
17. Sigmund, P.; Schinner, A. Binary theory of electronic stopping. *Nucl. Instrum. Methods Phys. Res., Sect. B* **2002**, *195*, 64.
18. Ziegler, J. F. SRIM 2003–SRIM 2012. <http://www.srim.org>.

19. Ziegler, J. F.; Biersack, J. P.; Littmark, U. The stopping and range of ions in matter Vol.1; Pergamon: New York, 1985.0-08-021603-X
20. Scheidenberger, C., et al. Direct observation of systematic deviations from the Bethe stopping theory for relativistic heavy ions. *Phys. Rev. Lett.* **1994**, *73*, 50.
21. Paul, H, Stopping power for light ions. <http://www.exphys.uni-linz.ac.at/stopping/>.
22. Emfietzoglou, D.; Nikjoo, H.; Pathak, A. Electronic cross sections for proton transport in liquid water based on optical-data models. *Nucl. Instrum. Methods Phys. Res., Sect. B* **2006**, *249*, 26.
23. Emfietzoglou, D.; Garcia-Molina, R.; Kyriakou, I.; Abril, I.; Nikjoo, H. A dielectric response study of the electronic stopping power of liquid water for energetic protons and a new I value for water. *Phys. Med. Biol.* **2009**, *54*, 3451.
24. Garcia-Molina, R.; Abril, I.; Denton, C. D.; Heredia-Avalos, S.; Kyriakou, I.; Emfietzoglou, D. Calculated depth-dose distributions for H^+ and He^+ beams in liquid water. *Nucl. Instrum. Methods Phys. Res., Sect. B* **2009**, *267*, 2647.
25. Sigmund, P. Personal communication to H. Paul, 2011.
26. Shimizu, M.; Kaneda, M.; Hayakawa, T.; Tsuchida, H.; Itoh, A. Stopping cross sections of liquid water for MeV energy protons. *Nucl. Instrum. Methods Phys. Res., Sect. B* **2009**, *267*, 2667.
27. Shimizu, M.; Hayakawa, T.; Kaneda, M.; Tsuchida, H.; Itoh, A. Stopping cross sections of liquid water. *Vacuum* **2010**, *84*, 1002.
28. Siiskonen, T., et al. Energy loss measurement of protons in liquid water. *Phys. Med. Biol.* **2011**, *56*, 2367.
29. Kumazaki, Y.; Akagi, T.; Yanou, T.; Suga, D.; Hishikawa, Y.; Teshima, T. Determination of the mean excitation energy of water from proton beam ranges. *Radiat. Meas.* **2007**, *42*, 1683.
30. Paul, H. Recent results in stopping power for positive ions, and some critical comments. *Nucl. Instrum. Methods Phys. Res., Sect. B* **2010**, *268*, 3421.
31. Paul, H. The stopping Power of Matter for Positive Ions, in Modern Practices in Radiation Therapy, Natanasabapathi G., Ed., InTech, ISBN 978-953-51-0427-8, 2012, Chapter 7. <http://www.intechopen.com/books/modern-practices-in-radiation-therapy>.
32. Paul, H.; Schinner, A. Judging the reliability of stopping power tables and programs for protons and alpha particles using statistical methods. *Nucl. Instrum. Methods Phys. Res., Sect. B* **2005**, *227*, 461.
33. Shimizu, M. Email to H. Paul, February, 2012.
34. Neuwirth, W.; Pietsch, W.; Richter, K.; Hauser, U. Electronic stopping cross sections of elements and compounds for swift Li ions. *Zeit. Physik A* **1975**, *275*, 209.
35. ICRU Report 37, Stopping powers for electrons and positrons, International Commission on Radiation Units and Measurements, Bethesda, MD, USA, 1984.
36. Schardt, D.; Steidl, P.; Krämer, M.; Weber, U.; Parodi, K.; Brons, S. Precision Bragg-Curve measurements for light-ion beams in water, GSI Scientific Report 2007 (2008–1) 373, and private communication from D. Schardt.
37. Bichsel, H.; Hiraoka, T.; Omata, K. Aspects of fast-ion dosimetry. *Radiat. Res.* **2000**, *153*, 208.
38. Berger, M. J. Penetration of proton beams through water. I. Depth-dose distribution, spectra and LET distribution, Report NISTIR 5226, National Institute of standards and technology, Gaithersburg, MD, 1993.
39. Bortfeld, T. An analytical approximation of the Bragg curve for therapeutic proton beams. *Med. Phys.* **1997**, *24*, 2024.
40. Bichsel, H. Personal communication to H. Paul, 2008.
41. Gudowska, I. Personal communication to H. Paul, 2008.
42. Schardt, D. et al. unpublished (2004) (See Ref. 36).
43. <http://physics.nist.gov/PhysRefData/Star/Text/table1con.html>.

44. Andreo, P. On the clinical spatial resolution achievable with protons and heavier charged particle radiotherapy beams. *Phys. Med. Biol.* **2009**, *54*, N205.
45. Moyers, M. F., et al. Ion stopping powers and CT numbers. *Med. Dosimet.* **2010**, *35*, 179.
46. Paul, H.; Schinner, A. An empirical approach to the stopping power of solids and gases for ions from Li to Ar. *Nucl. Instrum. Methods Phys. Res., Sect. B* **2001**, *179*, 299.
47. Moyers, M. F. Personal communication to H. Paul, 2011.
48. Fermi, E.; Teller, E. The capture of negative mesotrons in matter. *Phys. Rev.* **1947**, *72*, 399.
49. Paul, H.; Schinner, A. Statistical analysis of stopping data for protons and alphas in compounds. *Nucl. Instrum. Methods Phys. Res., Sect. B* **2006**, *249*, 1.
50. Paganetti, H. Range uncertainties in proton therapy and the role of Monte Carlo simulations. *Phys. Med. Biol.* **2012**, *57*, R99.
51. Hansen, D. C.; Lühr, A.; Herrmann, R.; Sobolevsky, N.; Bassler, N. Recent improvements in the SHIELD-HIT code. *Int. J. Radiat. Biol.* **2012**, *88*, 195.
52. Belkić, Dž. Review of theories on ionization in fast ion-atom collisions with prospects for applications to hadron therapy. *J. Math. Chem.* **2010**, *47*, 1366.
53. Paul, H. A comparison of recent stopping power tables for light and medium-heavy ions with experimental data, and applications to radiotherapy dosimetry. *Nucl. Instrum. Methods Phys. Res., Sect. B* **2006**, *247*, 166.
54. Markin, S. N. et al., *Phys. Rev. Lett.* **2009**, *103*, 113201.

This page is intentionally left blank

CHAPTER THREE

On the Determination of the Mean Excitation Energy of Water

John R. Sabin[a,b], **Jens Oddershede**[a,b] **and Stephan P.A. Sauer**[c]
[a]Departments of Physics and Chemistry, University of Florida, Gainesville, Florida 32611, USA
[b]Institute for Physics, Chemistry, and Pharmacology, University of Southern Denmark, 5230 Odense M, Denmark
[c]Department of Chemistry, University of Copenhagen, Copenhagen, Denmark

Contents

Abstract

Water is a ubiquitous substance in nature, and thus the mean excitation energy of water is an important quantity for understanding and prediction of the details of many fast ion/molecule collision processes such as those involved in external beam radiotherapy of tumors. There are several methods for determining numerical values for a mean excitation energy for water, both theoretical and experimental. Here the factors affecting the determination of the value of the mean excitation energy of water, especially from experiment, are discussed.

1. INTRODUCTION

"The mean excitation energy of water is 75.0 eV." What is the meaning of such a statement?

As the use of fast ions for medical purposes, especially tumor therapy, becomes more usual, the understanding of the basic physics of the interaction of swift ions with biomaterial in combination with water at clinically relevant energies (≈3–300 MeV/u) becomes more crucial. For example, the end result of ion radiation should be destruction of tumors without,

Advances in Quantum Chemistry, Volume 65
ISSN 0065-3276, http://dx.doi.org/10.1016/B978-0-12-396455-7.00003-0

or with only minimal, damage to surrounding tissue. Thus, understanding of the dosimetry for the interaction of fast ions with tissue becomes of primary importance for prediction of dose-depth curves and the spatial resolution of such radiotherapy beams.[1] However there are uncertainties[2] which also must be addressed.

As biological tissue is predominantly water, and as radiation damage to cells is predominantly due to reaction of secondary water fragments with cellular biomolecules,[3, 4] it is of primary importance to understand the interaction of fast ions with water, in particular the details of the energy transfer from the fast ion to water. In this process, the kinetic energy of the fast ion is transferred to water, resulting in electronic and vibrational excitation, ionization, and/or fragmentation. In this regard, an accurate determination of the ratio of ion beam energy deposition per unit path-length in water to that in air [the stopping power ratio—STPR] is the most important quantity for external beam radiotherapy dosimetry according to the Code of Practice of the International Atomic Energy Agency.[5] This ratio thus becomes critically important for accurate clinical dosimetry,[6] as it is this ratio that determines the mean projected range and thus the dose-depth curves. The ratio of the mass stopping power for an ion in water and in air, $s^0_{\text{water, air}}$, is conventionally written:[6, 7]

$$s^0_{\text{water, air}} = \frac{(S_e(E)/\rho)_{\text{water}}}{(S_e(E)/\rho)_{\text{air}}} = \frac{(Z_2/A_2)_{\text{water}}}{(Z_2/A_2)_{\text{air}}} \frac{\ln(2mv^2/I_0^{\text{water}})}{\ln(2mv^2/I_0^{\text{air}})}, \tag{1}$$

where Z_2 and A_2 are the electron number and relative mass of the target, ρ is the scatterer density of the medium, $S_e(E)$ is the stopping power at projectile energy E, and m and v are the projectile mass and velocity. Thus, the quantity I_0 becomes the critical quantity. I_0 measures the ease with which energy can be deposited by the ion in the target material; in other words, I_0 is a measure of the ability of a target system to absorb kinetic energy from a projectile, and is called the mean excitation energy of the target (sometimes referred to as the average ionization potential). I_0 is thus central to the determination of the stopping power of the target. The mean excitation energy, which is specific to each target, may be obtained either theoretically or experimentally, and "Thereby hangs a tale".[8] Although the mean excitation energy is a well-defined quantity (*vide infra*), values of the mean excitation energy of water obtained by experimental and theoretical means are found to vary by as much as 20% (*vide infra*), with those values deduced from experiment generally being higher. Such a large uncertainty is unacceptable for many applications, including external beam radiotherapy dosimetry. To quote Gottschalk:[9] "Unfortunately, I_0 is particularly problematic for water."

In this report we explore one aspect of that problem; namely the determination of the mean excitation energy of water, a quantity necessary to the understanding of the physics of the characteristics of ion energy deposition in water. Which values should be used for understanding and predicting external beam radiotherapy dosimetry and dose/depth curves? The theoretical or the experimental? We maintain that the value of the mean excitation energy obtained from theory and the value extracted from stopping experiments can be quite different, and that their usage should not be confused. Although there is only one mean excitation energy for any target substance such as water in a particular phase, we will refer to the values extracted from theory as I_0^{theo} and the values extracted from experiment as ${I_0}^{\text{exp}}$ in order to be clear as to the origin of the value of the mean excitation energy under discussion.

2. SOME BASIC THEORY

The energy loss per unit pathlength in a material, or stopping power of the material, for a fast ion is generally written as a function of projectile velocity (ν):

$$-\frac{\mathrm{d}E}{\mathrm{d}x} = n\,S\,(v) = \frac{4\,\pi\,n\,e^4\,Z_1^2\,Z_2}{m_\mathrm{e}\,v^2}L\,(v)\,, \tag{2}$$

where $S(v)$ is referred to as the stopping cross section, n is the target scatterer density, Z_1 and Z_2 are the projectile charge and target electron number, respectively, and m_e is the electron rest mass. $L(\,v)$, known as the target stopping number, is frequently expanded in a Born series in the projectile charge, which, for fixed projectile charge, can be written as:

$$L(v) = \sum_{i=0} Z_1^i L_i(v). \tag{3}$$

Each term can then be expanded, suppressing ν, as:

$$L_i = \sum_{j=0} L_{ij}. \tag{4}$$

In the following, we ignore relativistic $-\ln(1-\beta^2)-\beta^2$ and density $(\delta/2)$ corrections which are small in the energy range of interest here.[10] Although there are several ways to express L, L_i, and L_{ij}, for the purposes here, the most convenient and most commonly employed are the Bethe term L_0:[11]

$$L_0 = \ln\frac{2m_e\, v^2}{I_0} - \frac{C(v)}{Z_2}, \tag{5}$$

the Lindhard[12] version of the Barkas correction:[13]

$$L_1 = L_{10} = \frac{3\pi\, e^2 I_0}{2\,\hbar\, m_e\, v^3}\ln\frac{2\,m_e\, v^2}{I_0}, \tag{6}$$

and the Bloch correction:[14]

$$L_2 = L_{20} = -\sum_{l=0}^{\infty}(l+1)^{-3}\frac{v_0^2}{v^2} \cong -1.202\frac{v_0^2}{v^2}. \tag{7}$$

Here, v_0 is the Bohr velocity ($2.187691\times10^6\,\mathrm{m/s}$).

The quantity of interest for describing energy deposition, the mean excitation energy, was first introduced in this context by Bethe.[11] His original derivation considered that the projectile velocity was much larger than that of the target electrons with which it collided and exchanged energy. As this assumption is not applicable to slow ions nor to collisions with core electrons in atoms or molecules, the shell corrections, $C(v)/Z_2$, were added to correct for this. However, the mean excitation energy is a well-defined quantity, namely the first energy weighted moment of the dipole oscillator strength distribution (DOSD) of the target system in whatever overall state the system finds itself:

$$\ln I_0 = \frac{\int \frac{\mathrm{d}f}{\mathrm{d}E}\ln E\,\mathrm{d}E}{\int \frac{\mathrm{d}f}{\mathrm{d}E}\,\mathrm{d}E}. \tag{8}$$

Thus, were the entire set of excitation energies and oscillator strengths of the system (molecule, liquid, or mixture, and gas, liquid, or solid) known, the unique mean excitation energy of the system would be obtainable, either theoretically or experimentally. It should be noted that, in principle, the mean excitation energy is not a parameter. It is a well-defined function of the electronic excitation properties of the target and only of the target. It is not a function of projectile velocity, and, in principle, does not depend in any way on the properties of the projectile.

3. THEORETICAL DETERMINATION OF I_0

The mean excitation energy was originally defined by Bethe[11] in his derivation of the stopping cross section, and is defined in Eq. (8). The definition is unique, and given the exact quantum mechanical solution of the target electronic structure, that is, the DOSD, or the complete set of all electronic transitions and their dipole oscillator strengths, the integrals could be carried out. In practice, this is not possible, as various theoretical approximations must be made in order to carry out the calculation of the DOSD: level of theory, molecular geometry, basis set size, target orientation with respect to the beam, isolated molecule or condensed system, and others. However, at least for most atoms, one can approximate[13] $I_0 \approx 10 Z_2\,\text{eV}$ and then one can obtain an approximation for the value of I_0 for a single molecule by application of the Bragg rule.[15]

We, on the other hand, have carried out a number of calculations on the DOSD of an isolated water molecule,[16–21] using the polarization propagator scheme[22] in the dipole length formulation at the random phase approximation (RPA) level of theory. Calculations were carried out using various extended basis sets[23–25] at the water equilibrium geometry. The calculations yielded values of the mean excitation energy of water with an average value of 73.0 ± 0.6 eV for the various bases employed. Calculations of the DOSD in the length, velocity, and mixed formulations gave only slightly different results: 73.2 ± 0.1 eV, while density functional theory calculations[26] with the B3LYP exchange-correlation functional in the length formulation and a somewhat larger basis set[27] gave with 72.2 eV a slightly smaller result.

These results are in reasonable agreement with the semiempirical result of Zeiss and Meath[28] (ZM) of 71.62 eV. However, we note that although theoretical, the ZM method does not directly evaluate Eq. (8).

In a theoretical determination of the mean excitation energy of a molecule, there are other considerations as well.

As the electronic structure of a molecule changes with its geometry, so does the DOSD and thus the mean excitation energy. Calculation gives a ground state mean excitation energy of 72.92 eV[16] for H_2O while vibrational averaging, using the Morse-oscillator-rigid-bender scheme of Jensen,[29] yields a value of 71.61 eV, nearly 2% smaller. Although isotopic composition will not change the DOSD of the target molecule, it will influence the vibrationally averaged values of the mean excitation energy through the vibrational wavefunction.

Although the target mean excitation energy does not depend at all on the projectile, it does depend on the orientation of a non-spherically symmetric target molecule such as water with respect to the beam, as only molecular electronic states with the correct polarization with respect to the beam direction can be excited.[30] Calculations on water in its equilibrium geometry, fixed in the x–z plane with the z axis as the C_2 symmetry axis,[18] give a rotationally averaged mean excitation energy of 72.91 eV, having directional components in the x, y, and z directions of 69.21, 76.76, and 72.87 eV, respectively.

Finally, as water seldom exists as a single molecule, the effect of hydrogen bonding on the mean excitation energy of water is of interest. Calculations of the mean excitation energy of H_2O and of $(H_2O)_2$ give mean excitation energies[20] of 73.56 and 73.18 eV, respectively, a difference of less than 1%.

Consideration of the effect of a few hydrogen bonds on the mean excitation energy of a water molecule is not sufficient to determine the mean excitation energy of bulk (liquid) water. However, the mean excitation energy for a bulk system can also be determined from a study of the dielectric response of the bulk system.[31] In this approach, the mean excitation energy can be obtained from:

$$\ln I_0 = \frac{\int_0^\infty E \ln E \, \mathrm{Im}\,[-1/\varepsilon(E,0)]\, \mathrm{d}E}{\int_0^\infty E \, \mathrm{Im}\,[-1/\varepsilon(E,0)]\, \mathrm{d}E}. \tag{9}$$

Using a Drude-like dielectric function of the form

$$\varepsilon(E,q) = 1 + \sum_j f_j\left(q\right) E_p^2 \left\{E_j^2(q) - E^2 - iE\gamma_j(q)\right\}^{-1}, \tag{10}$$

where $E_p = 2\sqrt{n\pi a_0}$ is the nominal plasmon energy of the medium and n is the electronic density (for water, $E_p = 21.4$ eV). Here, the quantities $[E_j, \gamma_j, f_j]$ refer to the energy, lifetime, and oscillator strength of each of the j electronic transitions. Using this dielectric function in Eq. (9), the mean excitation energy for liquid water obtained from the dielectric response model is 77.8 eV.[31] We note that a detailed description of the dielectric response of the system is given in Ref. 31.

Thus, using theory, one can investigate the properties of the DODS and thus the behavior of the mean excitation energy under various conditions without reference to experiment.

4. EXPERIMENTAL DETERMINATION OF I_0

On the other hand, clinical application of swift ion radiation in terms of tumor therapy is concerned with energy deposition to a specific place, and thus with dosimetry: prediction of dose/depth properties of ion radiation. In order to determine the relevant quantities for proper dosimetry determinations, the ratio of stopping powers for air (a) and water (w) $s^0_{\text{water, air}}$, for the ion beam is needed.[32–34] A good approximation to the water/air mass stopping ratio for a particular projectile species at a particular energy (velocity), or with a delta function fluence differential in energy, can be written[35] as Eq. (1). Thus, the mean excitation energy is of primary importance. Although practitioners, due to the difficulties discussed in this contribution, may simply measure dose/depth curves directly rather than attempting to calibrate beam energies closely and then construct $s^0_{\text{water, air}}$ from experimentally determined mean excitation energies, I_0 is still reported in the literature. The question arises as to how the appropriate mean excitation energies should be obtained.

As it is not feasible to evaluate Eq. (8) directly from experiment, the value of the mean excitation energy is frequently deduced from experiment. There are several ways to obtain I_0^{exp}.

Perhaps the most reasonable way to extract the mean excitation energy from experiment while invoking the least number of assumptions is to use an experimental dielectric response function in Eq. (9).[36] This procedure gives an experimental value of the mean excitation energy of water of 81.8 eV.

Another, and in the radiological community more usual, way to obtain the mean excitation energy of a bulk substance is to fit stopping power data from energy deposition experiments. In principle, one chooses an ansatz for the stopping power or range of an ion as a function of projectile kinetic energy[†] and then treats the mean excitation energy as a fitting parameter determined by adjusting it to get the best fit of the ansatz function to the experimental stopping or range data. Programs such as the Monte Carlo based SHIELD-HIT[37, 38] or FLUKA[39] are frequently used for this purpose.[1]

[†] In fact, projectile velocity is the relevant quantity (see Eqs. (2)–(7)). However, velocities are generally expressed in terms of the corresponding kinetic energy per nucleon: eV/u, keV/u, or MeV/u. Energy/u has units of projectile velocity squared, but must be scaled by the one half the projectile mass in appropriate units to give projectile velocity squared [see articles in volumes 45 and 46 (1994), *Theory of the Interaction of Swift Ions with Matter*, for details].

The problem then arises as to how the relevant quantities such as shell corrections and the Barkas and Bloch corrections are to be chosen, as the choice of the ansatz fitting function will affect the resulting value of I_0. To extract the mean excitation energy of water from experiment, one might choose values of the shell corrections and the Barkas correction, and then, using the mean excitation energy as a fitting parameter to Eqs. (2–6), determine the "experimental" value of I_0 yielding the best fit to the experimental data over a range of projectile velocities. The result is then reported as the experimentally determined value of the mean excitation energy, namely I_0^{exp}.

However, problems and uncertainties arise. Previous work has shown that shell corrections may vary considerably according to the method of calculation.[40] In addition, shell corrections are generally not available for molecules, so the approximate Bragg additivity rule:[41]

$$\frac{C(v)}{Z_2} = \sum_{i=\mathrm{atoms}} \left(\frac{C(v)}{Z_2}\right)_i, \tag{11}$$

or

$$\frac{C(v)}{Z_2} = \sum_{i=\mathrm{fragments}} \left(\frac{C(v)}{Z_2}\right)_i, \tag{12}$$

is frequently employed,[42] introducing further uncertainty into the experimental value of the mean excitation energy.

To illustrate the effect of variation in the shell corrections on the mean excitation energy extracted from experiment, we consider the simplest, or Bethe, case where the stopping cross section is written

$$S(v) = \frac{4\pi\, e^4\, Z_1^2\, Z_2}{m_\mathrm{e}\, v^2} L_0\,(v) = \frac{4\pi\, e^4\, Z_1^2\, Z_2}{m_\mathrm{e}\, v^2}\left(\ln\frac{2\, m_\mathrm{e}\, v^2}{I_0} - \frac{C(v)}{Z_2}\right). \tag{13}$$

A formula for extraction of a value of the mean excitation energy, I_0^{exp}, from experimental values of the stopping cross section can be written

$$I_0^{\mathrm{exp}} = \frac{2\, m_\mathrm{e}\, v^2}{\exp\left[\frac{m_\mathrm{e}\, v^2 S(v)}{4\pi\, e^4\, Z_1^2\, Z_2} + \frac{C(v)}{Z_2}\right]}. \tag{14}$$

Consider the effect of differing shell corrections when used in extracting an experimental mean excitation energy for protons with $v = 6\,v_0$, and thus a kinetic energy of 900 keV, impinging on water. We choose a proton energy which is low from the radiological standpoint as the corrections to the Bethe term are largest for lower ion velocities, and thus the deviations and variations will represent maximum encountered values. Shell corrections for such a situation run from 0.15[43] up to 0.50,[44] with various values in between also reported.[45] Table 3.1 illustrates the variation in I_0 from Eq. (14) for 900 keV protons on water using a typical value of the stopping cross section [$S(6) = 11.52$ a.u.] and various values of the shell corrections.

Similarly, the Barkas correction, L_1, can be determined in several ways, the most usual being the numerical scheme of Ashley et al.[46] or the analytical form of Lindhard.[12] Again, uncertainties are introduced which will affect the value of the mean excitation energy obtained from experimental data.[47, 48] In Table 3.2 we present some values of Lindhard's L_1 as calculated from Eq. (6).

Over this range of mean excitation energies, the Barkas correction does not vary much, consistent with observation.[49–51] Thus, the choice of Barkas correction is less critical to the extraction of a mean excitation energy from experiment than is the choice of shell corrections.

Table 3.1 Mean excitation energies from equation 14 for 900 keV protons on water for various values of the shell corrections

C/Z_2	I_0 (eV)
0.00	72.3
0.10	65.4
0.15	62.2
0.25	56.3
0.32	52.5
0.40	48.5
0.50	43.9

Table 3.2 Barkas correction using the Lindhard form for 900 keV protons on water using various values of the mean excitation energy

I_0 (eV)	L_1 (a.u.)
72.30	0.191
62.23	0.172
56.31	0.160

If one measures the oscillator strength distribution for water in its different phases, it is seen that the distribution is different, especially near the maximum, depending on the target phase.[52] Target phase thus affects the value of the measured mean excitation energy. As water readily exists in all three phases, the mean excitation energy of water depends somewhat on the sample phase, with the liquid phase having a value of I_0^{exp} that is some few percent greater than the gas.[10, 53] Although there is no direct evaluation of Eq. (8) for liquid water, comparison of direct calculation of I_0 for an isolated water molecule and for its hydrogen bonded dimer shows the isolated molecule to have a larger value of the mean excitation energy by a fraction of a percent.[20]

The mean excitation energy is a property of the target only, by definition. It thus does not depend on any property of the projectile, in particular the projectile speed. Thus, in the simplest, or Bethe, case where the stopping cross section is written as in Eq. (13), the formula for extraction of I_0 from experimental values of the stopping cross section is written as Eq. (14). This presents another problem, as values of the experimental mean excitation energy extracted from $S(v)$ measured at different projectile velocities[54] using calculated, Bragg rule based, shell corrections,[41] yield quite different experimental values of I_0, depending on to which velocity the stopping cross section corresponds. This is clearly incorrect behavior for a quantity that should be independent of the projectile.

The addition of Barkas and Bloch corrections leads to the expression:

$$\left[1+\frac{3\pi e^2}{2\hbar m_e}\frac{I_0}{v^3}\right]\ln\frac{2m_e v^2}{I_0}=\left[\frac{v^2 m_e S(v)}{4\pi e^4 Z_1^2 Z_2}+\frac{C(v)}{Z_2}+1.202\frac{v_0^2}{v^2}\right] \quad (15)$$

This equation must be solved iteratively to determine a value for a I_0^{exp}. However, there is still no independence of the experimental value of the mean excitation energy extracted in this manner on projectile velocity.

Another problem which must be confronted when extracting a value of I_0 from measured data is that of projectile charge exchange. As a projectile travels through a target sample, charge exchanging collisions are expected.[55, 56] Thus, a measured depth-dose curve or stopping power curve for a projectile in a condensed phase target will, in fact, contain contributions for the various charge states available to the projectile under the circumstances. For example, one would expect contributions from both H^+ and H in measuring the stopping of a beam of protons in water. The description of the energy loss under these circumstances using Eqs. (2), (3), (5), (6), (7) will thus involve a value of I_0 which, rather than being determined directly as mean excitation energy, will again be an effective fitting parameter which includes charge exchange and gives a best fit to the measured depth/dose or stopping curve.

The range of an ion in a condensed phase target is of greatest interest in radiological terms, as it is at the end of the projectile trajectory that the greatest amount of projectile energy is deposited in the target.[57] Were one to calculate the range in the continuous slowing down approximation, one would integrate the stopping cross section from the initial energy, E_0 to when the ion stops.

$$R(E_0) = -\int_{E_0}^{0} \frac{1}{nS(E)}\,\mathrm{d}E. \tag{16}$$

This would return the length of the pathway, in a straight line, from the entrance of the ion into the medium to the point where it stopped. However, in an experimental situation, the projectile ion undergoes many collisions, with concomitant changes in velocity, along its pathway, and thus the actual penetration depth, d, could differ significantly from the pathlength.[58] A mean excitation energy extracted from experiment using Eq. (2), if depth data is used, will then have this ambiguity included.

Mean excitation energies for water varying from 68 eV[59] to 81.1 eV[36] have been reported resulting from both theoretical evaluations of Eq. (8) and from fitting of experimental data. This corresponds to an uncertainty of some 18.5%, which is certainly significant, and is unacceptable when I_0 is being used to determine details of hadron therapy.

5. CONCLUSION

The conclusion is that while the mean excitation energy is well-defined and can consistently be determined theoretically, values of the mean excitation energy extracted from experiment are not well-defined. Rather, they depend significantly on the assumptions made concerning the method of extraction of the mean excitation energy from, typically, a stopping power or range measurement. Thus, if high accuracy $s^0_{\text{water, air}}$ are needed for calculation of dose-depth curves for radiation therapy as opposed to direct measurement, both the ansatz equation and parameters used to obtain the experimental mean excitation energy by fitting to experimental data need to be specified when reporting the experimental mean excitation energy. Values of I_0 obtained from theory and experiment are in principle identical, and, from a practical standpoint, would be expected to be of the same order. However they are not the same, as the theoretical values come from the definition of the quantity [Eq. (8)] and the experimental values come from using the mean excitation energy as a free fitting parameter to experimental data. Their differences can lead to clinically unacceptable uncertainties in dosimetry prediction. The experimental values of the mean excitation energy should thus be reported only with reference to the details of its determination. Thus, using I_0 in Monte Carlo or other simulations for energy deposition in hadrontherapy should only be done with care and attention to the method by which I_0 was determined.

For reasons cited, we would recommend that values of the mean excitation energy derived from experiment be referred to as an *effective* value of the mean excitation energy rather than as an *experimental* mean excitation energy.

"The mean excitation energy of water is 75.0 eV." What is the meaning of such a statement? Clearly the statement itself is not meaningful without qualification of exactly how the reported mean excitation energy was determined.

ACKNOWLEDGMENTS

S.P.A.S. acknowledges support by grants from the Danish Center for Scientific Computing, the Danish Natural Science Research Council/Danish Councils for Independent Research (Grant No. 272-08-0486) and the Carlsberg foundation.

REFERENCES

1. Andreo, P. On the clinical special resolution achievable with protons and heavier charged particle radiotherapy beams. *Phys. Med. Biol.* **2009**, *54*, N205.
2. Paganetti, H. Range uncertainties in proton therapy and the role of Monte Carlo simulations. *Phys. Med. Biol.* **2012**, *57*, R99.
3. von Sonntag, C. *The chemical basis for radiation biology*; Taylor and Francis: London, 1987.
4. von Sonntag, C. *Free-radical DNA damage and its repair—a chemical perspective*; Springer Verlag: Heidelberg, 2005.
5. Andreo, P.; Burns, D.T.; Hohlfeld, K.; Huq, M. S.; Kanai, T.; Laitano, F.; Smythe, V. G.; Vynckier, S. Absorbed dose determination in external beam radiography: an international code of practice for dosimetry based on standards of absorbed dose to water, Technical Report Series No. 398, International Atomic Energy Agency, Vienna, 2000.
6. Lühr, A.; Hansen, D. C.; Jäkel, O.; Sobolevsky, N.; Bassler, N. Analytical expressions for water-to-air stopping-power ratios relevant for stopping power dosimetry in particle therapy. *Phys. Med. Biol.* **2011**, *56*, 2515.
7. Paul, H. A comparison of recent stopping tables for light and medium-heavy ions with experimental data, and applications to radiotherapy dosimetry. *Nucl. Inst. Meth B* **2006**, *247*, 166.

8. Shakespeare, W. The taming of the shrew, Grumio (1593) Act 4, Scene 1.
9. Gottschalk, B. Comments on 'calculation of water equivalent thickness of materials of arbitrary density, elemental composition and thickness in proton beam irradiation'. *Phys. Med. Biol.* **2010**, *55*, L29.
10. Berger, M. J.; Seltzer, S. M. Stopping powers and ranges of electrons and positrons, ICRU Report #37, Bethesda, 1984.
11. Bethe, H. Zur Theorie des Durchgangs schneller Korpuskularstrahlen durch Materie. *Ann. Phys. (Leipzig)* **1930**, *5*, 325.
12. Lindhard, J. Barkas effect—or Z_1^3, Z_1^4—corrections to stopping of swift charged particles. *Nucl. Instrum. Methods* **1976**, *132*, 1.
13. Barkas, W. H.; Dyer, J. N.; Heckman, H. H. Resolution of the Σ–mass anomaly. *Phys. Rev. Lett.* **1963**, *11*, 26.
14. Bloch, F. Zur Bremsing rasch bewegter Teilchen beim Durchgang durch Materie. *Ann. Phys. (Leipzig)* **1933**, *16*, 285.
15. Bragg, W. H.; Kleeman, R. On the alpha particles of radium and their loss of range in passing through various atoms and molecules. *Philos. Mag.* **1905**, *10*, 318.
16. Geertsen, J.; Oddershede, J.; Sabin, J. R. Calculation of molecular mean excitation energies via the polarization propagator formalism: H_2 and H_2O. *Phys. Rev. A* **1986**, *34*, 1104.
17. Jensen, P.; Oddershede, J.; Sabin, J. R. Geometric dependence of the mean excitation energy and spectral moments of water. *Phys. Rev. A* **1991**, *43*, 4040.
18. Sauer, S. P. A.; Sabin, J. R.; Oddershede, J. Directional characteristics of the moments of the dipole-oscillator-strength distribution of molecules: H_2 and H_2O. *Phys. Rev. A* **1993**, *47*, 1123.
19. Sauer, S. P. A.; Sabin, J. R.; Oddershede, J. Calculated molecular mean excitation energies for some small molecules. *Nucl. Instrum. and Methods B* **1995**, *100*, 458.
20. Sauer, S. P. A.; Oddershede, J.; Sabin, J. R. Mean excitation energies and their directional characteristics for energy deposition by swift ions on the DNA and RNA nucleobases. *J. Phys. Chem. C* **2010**, *114*, 20335.
21. Sauer, S. P. A.; Oddershede, J.; Sabin, J. R. Mean excitation energies for biomolecules: Glycine to DNA. *Adv. Quantum Chem.* **2011**, *62*, 215.
22. Oddershede, J.; Jørgensen, P.; Yeager, D. L. Polarization propagator methods in atomic and molecular calculations. *Compt. Phys. Rep.* **1984**, *2*, 33.Oddershede, J. *Adv. Chem. Phys.* **1987**, *69*, 201.Sauer, S. P. A. *Molecular Electromagnetism: A Computational Chemistry Approach*; Oxford University Press
23. Lazzeretti, P.; Zanasi, R. Quantum mechanical approach to IR intensities via nuclear electric shielding tensors. I. Water. *J. Chem. Phys* **1985**, *83*, 1218.
24. Sauer, S. P. A.; Paidarová, I.; Oddershede, J.; Correlated and gauge origin independent calculation of magnetic properties. 2. Shielding constants of simple singly bonded molecules., *Theoret. Chim. Acta* **1994**, *88*, 351.
25. Sauer, S. P. A.; Oddershede, J.; Sabin, J. R. Directional dependence of the mean excitation energy and spectral moments of the dipole oscillator strength distribution of Glycine and its zwitterion. *J. Phys. Chem. A* **2006**, *110*, 8811.
26. Bruun-Ghalbia, S.; Sauer, S. P. A.; Oddershede, J.; Sabin, J. R. Comparison of the directional characteristics of swift ion excitation for two small biomolecules: Glycine and Alanine. *J. Phys. Chem. B* **2010**, *144*, 633.
27. Ligabue, A.; Sauer, S. P. A.; Lazzeretti, P. Correlated and gauge invariant calculations of nuclear magnetic shielding constants using the continuous transformation of the origin of the current density approach. *J. Chem. Phys.* **2003**, *118*, 6830.
28. Zeiss, G. D.; Meath, W. J. Additivity of atomic and molecular dipole properties and dispersion energies using H, N, O, H_2, N_2, O_2, NO, N_2O, NH_3 and H_2O as models. *Mol. Phys.* **1980**, *39*, 1055.

29. Jensen, P. A new Morse oscillator-rigid bender internal dynamics (morbid) hamiltonian for triatomic-molecules. *J. Mol. Spectrosc.* **1988**, *128*, 478. Hamiltonians for the internal dynamics of triatomic molecules. *J. Chem. Soc. Faraday Trans. II* **1988**, *84*, 1315.
30. Mikkelsen, H. H.; Oddershede, J.; Sabin, J. R.; Bonderup, E. A Bethe theory for the directional dependence of stopping by molecules. *Nucl. Instrum. Methods Phys. Res., Sect. B* **1995**, *100*, 451.
31. Emfietzoglou, D.; Garcia-Molina, R.; Kyriakou, I.; Abril, I.; Nikjoo, H. A dielectric response study of the electronic stopping power of liquid water for energetic protons and a new I-value for water. *Phys. Med. Biol.* **2009**, *54*, 3451.
32. International Atomic Energy Agency (IAEA), Absorbed dose determination in external beam radiography: an international code of practice for dosimetry based on standards of absorbed dose to water, Report TRS-398, Vienna, 2000.
33. Paul, H.; Geithner, O.; Jäkel, O. The influence of stopping powers upon dosimetry for radiation therapy with energetic ions. *Adv. Quantum Chem.* **2007**, *52*, 289.
34. See also the discussion in Section 2 of Ref. 3.
35. Henkner, K.; Bassler, N.; Sobolevsky, N.; Jäkel, O. Monte Carlo simulations on the water-to-air stopping power ratio for carbon ion dosimetry. *Med. Phys.* **2009**, *36*, 1230.
36. Dingfelder, M.; Hantke, D.; Inokuti, M.; Paretzke, H. G. Electron inelastic-scattering cross sections in liquid water. *Rad. Phys. Chem.* **1998**, *53*, 1.
37. Dementyev, A.V.; Sobolevsky, N. M. SHIELD—universal Monte Carlo hadron transport code: scope and applications. *Radiat. Meas.* **1999**, *30*, 553.
38. Gudowska, I.; Sobolevsky, N.; Andreo, P.; Belkić, Dž.; Brahme, A. Ion transport in tissue-like media using the Monte Carlo code SHIELD-HIT. *Phys. Med. Biol.* **2004**, *49*, 1933.
39. FLUKA site. <http://www.FLUKA.org/FLUKA.php>.
40. Bichsel, H. Shell corrections in stopping powers. *Phys. Rev. A.* **2002**, *65*, 052709.
41. Bragg, W. H.; Elder, M. A. On the alpha particles of radium, and their loss of range in passing through various atoms and molecules. *Phil. Mag.* **1905**, *10*, 318.
42. Zeiss, G. D.; Meath, W. J. Accurate evaluation of stopping and straggling mean excitation-energies for N, O, H_2, N_2, O_2, NO, NH_3, H_2O, and N_2O using dipole oscillator strength distributions - test of validity of Braggs rule. *Radiat. Res.* **1977**, *70*, 284.
43. International Commission on Radiation Units and Measurements, ICRU Report 49, Bethesda, MD: ICRU, 1993.
44. Emfietzoglou, D.; Pathak, A.; Nikjoo, H. Electronic stopping power of liquid water for protons down to the Bragg peak. *Rad. Protect. Dosim.* **2007**, *126*, 97.
45. Oddershede, J.; Sabin, J. R. Orbital and whole-atom proton stopping power and shell corrections for atoms with Z ≤ 36. *At. Data Nuc. Data Tables* **1984**, *31*, 275.
46. Ashley, J. C.; Ritchie, R. H.; Brandt, W. Z_1^3 effect in stopping power of matter for charged-particles. *Phys. Rev. B* **1972**, *5*, 2393. Z_1^3-dependent stopping power and range contributions. *Phys. Rev. A* **1973**, *8*, 2402. Z_1^3-dependent range contributions. *Phys. Rev A* **1974**, *10*, 737.
47. Sabin, J. R.; Oddershede, J. A comment on the abstraction of mean excitation-energies from experimental reduced stopping powers. *Nucl. Instrum. Methods Phys. Res., Sect. B* **1990**, *44*, 253.
48. Soltani-Nabipour, J.; Sardari, D.; Cata-Danil, Gh. Sensitivity of the Bragg peak curve to the average ionization potential of the stopping medium. *Rom. J. Phys.* **2009**, *54*, 321.
49. Andersen, H. H.; Bak, J. F.; Knudsen, H.; Nielsen, B. R. Stopping power of Al, Cu, Ag, and Au for MeV hydrogen, helium, and lithium ions—Z_1^3 and Z_1^4 proportional deviations from Bethe formula. *Phys. Rev. A* **1977**, *16*, 1929.
50. Basbas, G. Inner-shell ionization and the Z_1^3 and Barkas effects in stopping power. *Nucl. Instrum. Methods Phys. Res., Sect. B* **1984**, *4*, 227.
51. Reiter, G.; Kniest, N.; Pfaff, E.; Clausnitzer, G. Proton and helium stopping cross-sections in H_2, He, N_2, O_2, Ne, Ar, Kr, Xe, CH_4, and CO_2. *Nucl. Instrum. Methods Phys. Res., Sect. B* **1990**, *44*, 399.

52. Hayashi, H.; Watanabe, N.; Udagawa, Y.; Kao, C.-C. The complete optical spectrum of water measured by inelastic X-ray scattering. *Proc. Nat. Acad. Sci.* **2000**, *97*, 6264.
53. Thwaites, D. I.; Watt, D. E. Similarity treatment of phase effects in stopping power for low-energy heavy charged-particles. *Phys. Med. Biol.* **1978**, *23*, 426.
54. Paul, H. Phase effect for H ions in water. <http://www.exphys.jku.at/stopping/>.
55. Cabrera-Trujillo, R.; Sabin, J. R.; Deumens, E.; Öhrn, Y. Orientational effects in energy deposition by protons in water. *Adv. Quantum Chem.* **2005**, *48*, 47.
56. Schiwietz, G.; Grande, P. L. Stopping of protons—improved accuracy of the UCA model. *Nucl. Instrum. Methods Phys. Res., Sect. A* **2012**, *273*, 1.
57. Inokuti, M. Inelastic collisions of fast charged particles with atoms and molecules—the Bethe theory revisited. *Rev. Mod. Phys.* **1971**, *43*, 297.
58. Lindhard, J.; Scharff, M.; Schiøtt, H. E. Range concepts and heavy ion ranges. *Mat. Phys. Medd. Dan. Vid. Selsk* **1963**, *33/10*, 1.
59. Porter, L. E.; Thwaites, D. I. Physical state effects on the mean excitation energy of water as determined from alpha-particle stopping power measurements. *Phys. Rev. A* **1982**, *25*, 3407.

This page is intentionally left blank

CHAPTER FOUR

Molecular Scale Simulation of Ionizing Particles Tracks for Radiobiology and Hadrontherapy Studies

Ziad Francis
Saint Joseph University, Faculty of Sciences, Department of Physics, Mkalles, Beirut, Lebanon

Contents

Abstract

This study looks into Monte-Carlo simulation methods that are used for radiotherapy and radiobiology studies. Although simulation methodologies for the two mentioned fields are quite different since one deals with macroscopic effects rather than the cellular scale effects in the case of the other, the results obtained by both fields are complementary for understanding radiation effects on cellular substructures and the resulting reactions of irradiated biological tissues. It has been concluded through the literature that the deoxyribonucleic acid (DNA) damage is the most important result to look at among other radio-induced lesions in the cell. Thus, most of the research projects on radiation damage including Monte-Carlo studies are now concentrated on radio-induced DNA breaks and cell repair activities. Among the simulation programs

Advances in Quantum Chemistry, Volume 65
ISSN 0065-3276, http://dx.doi.org/10.1016/B978-0-12-396455-7.00004-2

we can distinguish the general purpose codes that are mostly used for macroscopic calculations and the step by step track structure codes that are dedicated for subcellular scale simulations mostly dealing with particles interactions with the DNA structure. However, none of the proposed toolkits can completely cover all the simulation cases since we are usually limited by the lack of cross sections for a certain particle type and in a certain energy domain depending on the code content. This obstacle can be overridden by some approximations on the macroscopic scale but when it comes to submicron calculations the energy deposit patterns should be as precise as possible for radiobiological analysis. On the DNA scale, chemical reactions and free radicals diffusion through target media were taken into account in some studies considering also the DNA structure geometry in the simulation. Although this type of approaches is aiming to be as realistic as possible, it can be a complex task to reproduce and also very time consuming requiring an important computing power. So in an effort to simplify and accelerate the calculations, several alternative methods were developed by different authors giving an acceptable estimation of radio-induced DNA damage quantification and making this issue more accessible for quick studies. The work described in this chapter reviews some of the numerical calculations of basic microdosimetric quantities for particles that are generally used in hadrontherapy, mainly protons and carbon ions, taking into account the secondary electrons tracks that are generated in tissue-like media (water). Using the Geant4-DNA package of the Geant4 Monte-Carlo simulation toolkit it is possible to track particles in a step by step mode taking also advantage of the available geometry modules and the standard physics processes of the standard Geant4 toolkit. Simulations are then described and the DNA damage quantification algorithms are studied with an effort to show the link between ionizing track structure and the resulting damage yields. The results obtained by different numerical methods are compared together then a discussion describes the advantages of each of the mentioned calculations.

1. INTRODUCTION

Generally and for a long period of time treatment planning in radiotherapy was mostly based on observations obtained from experimental data of cell survival rates after irradiations. The linear quadratic model of cell population survival is still in use by the medical community especially for X-ray irradiations. The safety of this model was studied and confirmed by Brenner et al.[1] concluding that no noticeable improvement can be added by using more sophisticated models. However, in the case of ions the energy deposit pattern is denser than for X-rays and ions proved to be more effective for deep seated tumors taking advantage from the so called "Bragg peak" of the energy deposition profile. Recently the number of protons and ions treatment facilities was increasing through the world. Protons are used in the United States, e.g., Massachusetts, Boston, and Loma Linda, California, while heavier ions therapy is still missing. In Japan we may cite the Heavy Ion Medical Accelerator in Chiba (HIMAC), another accelerator in Hyogo and recently the Gunma University facility. In Germany the Heidelberg Ion-Beam Therapy (HIT) center started ion treatments in 2009, with parallel research activities focusing on ions interactions in tissue and improving treatment protocols for a better tumor control probability. Other countries in Europe are also using proton beams for therapy or therapeutic research we can cite among many the National Institute of Nuclear Physics (INFN) accelerator in Italy (Catania), the Uppsala Svedberg laboratory in Sweden and one treatment facility in the United Kingdom. In France protons are used at the Proton Therapy Center of the Curie Institute at Orsay (ICPO) and the Lacassagne Center Biomedical Cyclotron (CLCB) in Nice along with new projects that are in progress for heavy ions therapy and research installations, e.g., Hadrontherapy project opening in Lyon (France) in 2016 and the Advanced Resource Center for Hadrontherapy in Europe (ARCHADE) mainly dedicated for research activities. As a general observation, developed countries are now tending to invest in heavy ions irradiation facilities with several emerging projects especially after the success of the Heidelberg treatment center. With the spread of ions accelerators, research emphasis was put on new treatment protocols and new cell survival models development, since these two latter are major database sets that are needed in the medical medium. One of the ions specific models that are presently in use in the medical medium is the Local Effect Model (LEM). The idea was developed by Kramer and Scholz[2] where the carbon ions Relative Biological Effectiveness (RBE) could be calculated using numerical computation and based on X-rays RBE database. The main advantage of the LEM is that it proved its reliability in RBE prediction for several tissue types and over a wide range of atomic numbers and particle energies without the need to perform cell irradiation experiments. Treatment planning programs were further developed by Kramer et al.[3] and reviewed by Jakel et al.[4] in order to provide the essential data base for ion treatment. In comparison with X-rays, ions have a high linear energy transfer (LET) in tissue and consequently a high biological effectiveness, and in this case the dose delivered to the tumor should be as accurate as possible in order to avoid normal tissue damage around the tumor. Also, the difference between the treatment planning and the treatment delivery is of high importance in the case of ions. Since this difference can have a non-negligible impact on the surroundings of the irradiated tumor, the range accuracy in carbon ion treatment planning was investigated by Rietzel et al.[5] concluding that carbon ranges can be controlled within $\sim 1\,\text{mm}$ in soft tissue for typical treatments of head and neck tumors.

Although at this stage studies are able to define the basics for ions treatment planning they do not provide any precise information about processes occurring on the single cell level, and the damage yields within the subcellular structures. In fact, the cell survival probability depends on many factors like the type of the irradiated cell, the severity of the damage that is induced to the DNA molecule, the replication phase of the cell being irradiated, the repair activities within the cell and also on the irradiation properties like the beam type and energy. Understanding the cell reaction to different types of radiation requires a tight collaborative work involving biologists and physicists studying single cell irradiation experiments. Measurements of DNA damages including strand breaks and base lesions were carried out by some studies using different analysis techniques like gel electrophoresis, e.g., Stypczynska et al.,[6] X-ray photoelectron spectroscopy, e.g., Ptasinska et al.[7] and the Enzyme-Linked Immunosorbent Assay (ELISA) experiment, e.g., Smialek et al.[8] Moreover, the effect of the DNA surrounding conditions were also investigated like the presence of amino acids combined to DNA during irradiation by Stypczynska et al.,[6] the presence of scavengers and repair enzymes in the medium by Milligan,[9] and Gulston et al.[10] and the influence of the chromatin organization on damage yields by Magnander et al.[11]

In parallel, microdosimetry studies were carried out on different particle beams using micrometric Tissue Equivalent Proportional Counters (TEPC), e.g., Borak et al.[12] With microdosimetry techniques it is possible to measure the lineal energy distribution of a particle type revealing the energy deposit characteristics on the micrometric and the nanometric scale (see Refs. 13–15). However, the literature does not cover all typical radiation cases that are encountered in the radiotherapy field. Monte-Carlo method simulations can be a theoretical alternative providing a good estimation of such measurements.

During the last 20 years numerical modeling became the most accessible method to study interactions of particles crossing biological targets and other materials enabling users to obtain the energy deposit distributions in the target volumes. General purpose Monte-Carlo codes like Fluka (Fluctuating Kaskade, see Ref. 16), Geant4 (Geometry and Tracking, see Ref. 17), MCNP (Monte-Carlo N-Particle transport code, see Ref. 18) and the SHIELD-HIT code (Heavy Ion Therapy code, see Refs. 19, 20) are able to simulate photons and ions interactions with different materials taking into account the secondary particles that are created in the medium. However, these codes are practical and adapted for macroscopic simulations and cannot be used for submicron scale calculations. In fact, simulations can be very lengthy in many cases and in order to save computing time, using an energy cut-off is a common solution for most of these codes. This means that when a particle's energy drops below the chosen cut-off the particle is killed and its energy is deposed locally at that point. Other techniques are also used, an energy production threshold is chosen by the user for each particle, in this way only secondary particles with energies above this threshold are created and simulated, this approach is adopted in the Geant4 toolkit. In this way one can avoid generating a big number of low energy secondary particles losing all their energy within few nanometers from the primary particle's track and cannot be distinguished from this latter from a macroscopic point of view. On the sub-cellular level, simulations should include all the secondary particles that are created in the target as low as their kinetic energy can be and these particles should be followed nearly until complete energy loss. In other words the energy cut-off should be set to the minimum and physics processes should take into account all the possible occurring interactions. This type of detailed simulation is also called the "step by step" particle tracking and its use is restricted to simulations confined within volumes of few micrometers, due to the lengthy required computing time. However, for this method the results precision is reasonable for molecular scale analysis. Many studies are based on track structure modeling of DNA damage after irradiation.

In general, in the simulations we can distinguish among the different levels of the complexity of the DNA damage since the repair activities are strongly dependent on the type of the damage and the damage yields in the cell. Some of the detailed history Monte-Carlo codes are able to track chemical species and free radicals creation and diffusion to estimate the indirect radiation effect on DNA. For the sake of completeness the DNA structure is also modeled in some studies (Ref. 21–23, and others) showing the effect of the geometrical shape and distribution of the DNA on the resulting damages. On another hand, more approximate approaches were developed enabling DNA damage estimation after irradiations, like the work of Semenenko et al.[24] where cell repair activities are also taken into account, and Francis et al.[25, 26] where the energy deposit spatial distribution is directly linked to DNA damage using clustering algorithms on track structures of different particles.

In the following sections, we will briefly summarize the cross sections that are of use for submicron simulations and review the microdosimetry basics citing some experiments that can be interesting for the radiobiology community and also for Monte-Carlo codes validation. Then the emphasis is put on the discussion of DNA damage estimation following different methodologies from the detailed event by event modeling to the fast approximate statistical procedures that can be found in the literature.

2. DETAILED STEP BY STEP TRACK STRUCTURE CODES

2.1 Monte-Carlo codes

General purpose Monte-Carlo codes are now available for public use providing also users support mostly through manuals and forums available on the Web. Among these codes that are specific for radiation interactions we can mention MCNPX,[18] FLUKA,[16] GEANT4,[17] Penelope (A Code System for Monte-Carlo Simulation of Electron and Photon Transport, see Ref. 27), and the SHIELD-HIT code that was tested for tissue-like media by Gudowska et al.[19] These codes are well adapted for large scale simulations and they offer good results precision for a reasonable amount of computing time, and some benefit from integrated variance reduction techniques (e.g., MCNPX) in order to further improve the results statistics. Generally, in these codes the tracking is done in a condensed history steps, interactions with energy loss values less than the fixed energy cut-off and occurring between two major energy transfers are skipped and the total energy loss is accounted for in one point situated at the end of the mentioned step of interaction. In this case, the total cross section is obtained by integrating the single differential cross section between the energy cut-off E_{cut} and the maximum energy that can be transferred to the medium in one single interaction noted as E_{max}. It follows the expression:

$$\sigma = \int_{E_{\text{cut}}}^{E_{\text{max}}} \frac{d\sigma}{\mathrm{d}E} \mathrm{d}E, \tag{1}$$

where E represents the energy transfer per single interaction.

And the energy loss per distance unit taking into account only the skipped interactions with energy transfers below the energy cut-off value is obtained by:

$$\frac{\mathrm{d}E}{\mathrm{d}x} = \int_{0}^{E_{\text{cut}}} \frac{\mathrm{d}\sigma}{\mathrm{d}E} E \cdot \mathrm{d}E. \tag{2}$$

Depending on the step size the energy loss dE is calculated using the previous expression and it is added on the energy deposit value at the end of the step.

This method is used by several codes (e.g., MCNP and Geant4) as it avoids loosing time on small energy transfers and generating a big number of secondary particles (mostly electrons) that are not important on the whole simulation scale from the macroscopic point of view. The energies of the skipped secondary electrons in this case do not exceed the energy cut-off values, usually set between 250 eV and 1 keV noting that their ranges in water and tissue remains within 1 μm from the primary particle's track.[28] One may generally conclude that the adopted spatial resolution in these simulations is about 0.5–1 μm. We should note here that the dimensions of a biological cell can vary depending on its type, and its nucleus dimensions are around 10–20 μm as a rough approximation. As for a chromatin fiber the typical dimension scale is of the order of few nanometers depending on the number of the considered nucleosomes. DNA double strand breaks can be formed by two single strand breaks separated by less than 10 base pairs which is equivalent to a maximum distance of ~3.2 nm. So for DNA damage calculations, simulations should have a nanometer scale precision and this is not provided by the general purpose MC codes. For this reason detailed interactions track structure codes were developed with physics processes and cross sections that are especially dedicated for precise molecular scale calculations, e.g., code of Gervais et al.,[29] PARTRAC (Particle Tracks, see Ref. [21, 30, 31]), PITS (Positive Ion Track Simulation[32]), NOREC (National Oak Ridge Electron Transport Code, see Ref. 33), Geant4-DNA which is an extension to the previously introduced Geant4 code enabling simulations on the DNA scale,[34] and others. Here it is important to note that most of the cross sections are calculated for water as we consider that the stopping powers of water and tissue are almost equivalent.

2.2 Collision processes: cross sections

Cross sections for protons inelastic collisions (excitation and ionization) can be calculated using different methods like the First Born Approximation (FBA) and the Rudd semi-empirical formula as it is the case in Geant4-DNA[35] and PARTRAC[36] codes. The dielectric response function of water is fitted to experimental data of Heller et al.[37] and Hayashi et al.[38] using Drude equations and the double differential cross section is obtained and integrated to calculate the single differential and the total cross sections. This approach works well for high incident energies and fails when the incident particle speed becomes comparable to the speed of the target orbiting electrons. So for low energy protons (below 500 keV) the FBA should be replaced by an alternative model. The Rudd semi-empirical formula gives the energy differential cross section down to incident energies as low as 1 keV. A relativistic approach of the Rudd model was also presented by Plante and Cucinotta[43] for protons and heavier ions enabling calculations of ionization cross sections for energies between ~1 MeV/amu and $\sim 10^5$ MeV/amu using no additional alternative models. The mentioned relativistic Rudd formula was also implemented in Geant4-DNA allowing Geant4 users to simulate relativistic ions in water taking into account ionization processes.[26] Theories of ionization collisions for fast incident ions were thoroughly reviewed and discussed by Belkić[39] where ionization cross sections are calculated according to different theoretical assumptions including the continuum distorted waves approximations and the results were compared to experimental data. It was shown that while the FBA diverges from the experimental results for intermediate and slow ion velocities, the Modified Coulomb Born (MCB) method, which is related to Continuum Distorted Wave-Eikonal Initial State (CDW-EIS) method gives better cross sections in a wider energy region. Track codes usually do not use the second-order theories, such as the MCB, Continuum Distorted Wave (CDW)[39] or CDW-EIS approaches. One of such codes described by Gervais et al.[29] employs the CDW-EIS method for ion interaction with water and the Rudd semi-empirical formula is used to track the generated secondary electrons. This code also takes into account the chemical reactions that take place after the physical interactions in the target medium. However, since it is configured in a way that the projectile energy is held constant over the whole simulation length, so that the simulation corresponds to a well-defined energy and a constant particle LET, it is not possible to simulate a complete ion range and to retrieve the Bragg peak position in this case.

Charge change contribution to energy loss cannot be neglected especially in the Bragg peak area where it reaches 30% of the total energy loss in the case of protons. Charge transfer cross sections for protons and alpha particles are well described by Dingfelder et al.[36, 40] For heavier ions when the cross sections for each of the charge change channels are not available the common procedure that is followed is to consider an effective charge that takes into account all the possible charge states of the ion depending on its stripped charge number and also on its velocity. High energy ions tend to be stripped and charge change contribution increases when the ion energy decreases. Modeling the effective charge of an ion can be achieved by using semi-empirical formulas that were fitted so that the calculated stopping power agrees with the corresponding experimental values. We may cite the model of Barkas et al.,[41] Booth and Grant model[42] that is used in the simulation code described by Plante and Cucinotta[43] and also in Geant4-DNA for ions heavier than protons by Francis et al.[26] A detailed study on the effect of the Barkas correction to the Bethe-Bloch stopping power can be found in Porter.[44]

For inelastic collisions of electrons, the FBA can be used for sufficiently high energies in water as described by Dingfelder et al.[45] and Emfietzoglou and Nikjoo.[46] For relativistic energies above ~35 keV an adapted formalism is applied to the FBA by Bousis et al.[47] And for low kinetic energies, corrections can be applied to the cross sections as described by Emfietzoglou and Nikjoo.[46] The mentioned corrections may vary from a simple fitting factor bringing the calculated cross section closer to the experimental values to more theoretical models taking into account higher order perturbations. In Dingfelder et al.[45] the differential cross section was multiplied by an empirical factor and the final values agree with the experimental data of electrons collisions in vapor water. Alternative corrections have been studied like the classic coulomb field correction by Vriens[48] and the second order perturbation term described by Emfietzoglou and Nikjoo.[46] The latter correction considers a second order perturbation term based on the work of Ashley et al.[49] Also Kim and Rudd[50] proposed a binary dipole semi-empirical model providing reasonable values of ionization cross sections.

Although no energy loss is induced by elastic collisions of electrons, the effect of this process on the particle diffusion and consequently on the track pattern is non-negligible. Elastic scattering cross sections were fitted by Brenner and Zaider[51] mainly based on values obtained by experiments for electrons below 200 eV. For higher energies the screened Rutherford model is applied. A recent model was published by Champion et al.[52] and implemented into Geant4-DNA. Michaud et al.[53] have also published elastic scattering cross sections for electrons collisions with ice, however, these values are not expected to be the same as for liquid water. In fact, cross sections of electron collisions have been abundantly studied in the literature; for the sake of simplicity it is not possible to state all the proposed models in this work. The main challenge for Monte-Carlo studies today remains in simulating the so called sub-excitation electrons. When the electron energy drops below about 12–8 eV its wave length size approaches the target molecule dimensions and reaches ~1 nm for energies around 1.5 eV. For these energies the dominating processes are elastic scattering, vibrational and rotational excitations. Experiments on sub-excitation electrons and on electrons thermalization processes in water are technically very difficult to realize so the data published in the literature is very scarce and the few available sources are not in full agreement. Since there are no theoretical models that are able to reproduce or predict the inelastic cross section shape for such low energy electrons in water a commonly adopted procedure is to take the data presented by Michaud et al.[53] for ice and scale its values to liquid water. The scaling is usually done by enhancing the cross section values by a factor of 2.[29] This procedure is very approximate but it can be used as an extrapolation of electron tracks till complete energy loss, considering that the cross sections for energies below 2 eV are obtained by a simple extrapolation of the lowest energy cross section. One way to verify the reliability of the so obtained simulations is to compare the ranges of sub-excitation electrons with the ranges published by the mentioned work of Michaud et al.

2.3 Sub excitation electrons and the chemical phase

Moreover, investigations of the effect of electrons with energies below 20 eV on DNA molecules are still in progress by many authors, e.g., Boudaiffa et al.,[54] Huels et al.,[55] Sanche.[56] It has been proven that for specific energies of electrons (around 8–10 eV) there is a certain resonance leading to a peak in the yields of DNA strand breaks. An example of low energy electrons calculations showed that ranges of such electrons can reach values as high as ~30 nm which is relatively high in comparison with DNA nucleosome size according to Uehara and Nikjoo,[57] Meesungnoen et al.,[58] and Munoz et al.[59] Thus, numerical simulations for such electrons should be reviewed and improved through accurate cross-sections calculations or measurements.

The interest in these low energy electrons comes not only from the fact that they can induce direct damage in the DNA but also at the end of its track an electron becomes aqueous and can interact with water molecules, oxygen or hydrogen in the medium leading to a free radical creation. Free radicals are very reactive species and can interact with the DNA causing strand breaks. Also the local energy depositions can lead to chemical reactions in the medium creating new interactive species that can modify the DNA structure and cause strand breaks. Creation of chemical elements depends on the initial preceding physical process at the interaction point.

For numerical simulations chemical species creation may be summarized as following; an ionized water molecule (H_2O^+) decays into H_3O^+ and OH, and an excited water molecule ($H_2O^\star$) decays into one of seven channels depending on the excitation state leading to H, OH, H_2O_2, H_3O^+, or aqueous electrons production. The branching ratios for the different channels may vary slightly in the literature from one source to another. Differences can be due to the adjustments that are made by authors in order to agree with the data obtained by experiments. In fact, using different cross section models in the physical phase leads to differences in the initial energy deposit distributions that can be corrected when handling chemistry. Then the created species are diffused in the medium during the chemical phase which happens between 10^{-12} and 10^{-6} s after the passage of the ionizing particle. Diffusion follows a Brownian dynamics and the simulation at this phase is processed using time steps that are usually of the order of 10^{-12} of a second. The reason behind using time steps is that the different species can interact with each other's and for every time step new positions are assigned for each element and a test runs over the different radicals in the simulation to check their separating distances. Each radical type has an interaction radius and the interaction of neighboring radicals can lead to new chemical elements creation. The reaction radius depends on both neighboring free radicals and can vary from 2.5×10^{-5} nm to 0.94 nm according to calculations of Uehara and Nikjoo.[57] This simulation approach was also adopted by Frongillo et al.[60] and the yields of H_2 and aqueous electrons from 10^{-12} to 10^{-6} s after 5 MeV and 300 MeV protons irradiations were compared to experimental measurements showing good agreement. The chemical phase simulation is also taken into account by other codes that we will not detail in this chapter for the sake of brevity. However, most of the mentioned codes are very specific and somehow difficult to access since they were built for single type of local applications in their development laboratories. For this reason chemistry processes were included in the Geant4-DNA toolkit and will be released in the future public versions of Geant4 after going through the required validation phase.

3. RADIATION MICRODOSIMETRY ANALYSIS

3.1 Theoretical and experimental microdosimetry

Radiation can be characterized using concepts introduced by the microdosimetry formalism and that can be obtained numerically and experimentally. Microdosimetry was first introduced by Rossi in the sixties in an effort to improve the classic dosimetry through more accurate concepts. A global review about Rossi and his work with the historical development of microdosimetry can be found in Kellerer et al.[61] Numerical methods for microdosimetry quantities calculations were reviewed and thoroughly explained by Kellerer and Chmelevsky.[62, 63] Then the mentioned formalism found its most important applications in measurement techniques for radiation protection purposes and in radiation therapy.

In order to show the separating edge between dosimetry and microdosimetry, a simple simulation of 400 MeV/amu carbon ions crossing a spherical volume of water was realized using Geant4.9.5 standard processes. The energy deposit points were scored in the target and the total energy per mass unit was calculated for different target dimensions. The results were reported in Figure 4.1 showing the variation of the energy deposit with the different mass values. We can notice that for targets

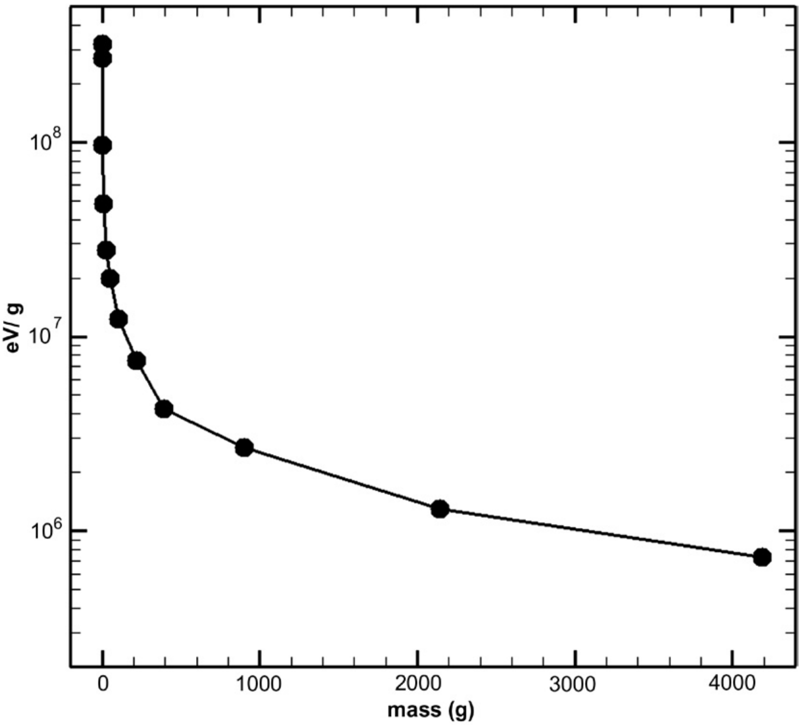

Figure 4.1 Energy deposit per mass unit for spherical targets of different dimensions irradiated with 400 MeV/amu carbon ions. The results are presented versus the mass of the irradiated target and were obtained using Geant4.9.5 Monte-Carlo simulation. The lines on the plot are kept to guide the eye.

below ~500 g the energy deposit varies quickly with the target mass while showing a more stable behavior for targets above this mass threshold. Note that this threshold depends on the mean free path of the particle in the medium that will strongly affect the energy deposition distribution inside of the target. In fact, in large volumes the total energy deposited by a particle is not a stochastic value and remains almost the same using different calculation methods but for relatively small volumes, e.g., in the presented example volumes with less than 500 g of water, the particle energy loss within the target varies from one event to another so it is considered a stochastic variable that we call the "imparted energy" in the microdosimetry formalism. The specific energy is the imparted energy per mass unit and is generally noted by the letter "z," it is the analog of the deposited dose in classic dosimetry. The lineal energy transfer is obtained by dividing the imparted energy in a target over the mean cord length of the tracks crossing the target volume, and it is the analog of the linear energy transfer in classic dosimetry. The specific energy and the lineal energy transfer are stochastic quantities and their distributions can be of importance for radiation quality assessment. Lindborg and Nikjoo[64] studied the radiation quality factors for radiotherapy applications using X-ray, protons, neutrons, and carbon ions irradiations and Nikjoo et al.[65] presented a database of microdosimetry quantities calculated for electrons, protons, alpha particles and carbon ions. At the HIMAC facility, experiments published by Tsuda et al.[66] were carried out measuring the lineal energy distributions for carbon ions and also for five ion fragments (proton, helium, lithium, beryllium, and boron) in the lineal-energy range of 0.1–1000 keV/μm at eight different depths between 7.9 and 147.9 mm in an acrylic phantom.[67] These kinds of measurements are mostly done using adapted tissue proportional equivalent counters (TEPC). Tissue-equivalent gas volumes are used to simulate the presence of a tissue volume with micrometric or nanometric dimensions. This assumption considers that the energy loss of an energetic particle would be the same through both targets. This is achieved by considering that the energy loss in tissue and gas is obtained respectively by:

$$\Delta E_{\mathrm{t}} = \left(\frac{\mathrm{d}E}{\rho \mathrm{d}x}\right)_{\mathrm{t}} \rho_{\mathrm{t}} l_{\mathrm{t}} \quad \text{and} \quad \Delta E_{\mathrm{g}} = \left(\frac{\mathrm{d}E}{\rho \mathrm{d}x}\right)_{\mathrm{g}} \rho_{\mathrm{g}} l_{\mathrm{g}}, \tag{3}$$

where ρ represents the density of the tissue and l the mean chord length of the target volume.

As detailed in the International Commission on Radiation Units and Measurements (ICRU) report 16 on Microdosimetry,[68] the volume of a biological tissue can be simulated by a gas volume when the atomic compositions of the tissue and the gas are identical and the mass stopping power is independent of the density. In spite of the technical difficulties, e.g., detector's wall effect and others, the challenge using this type of dosimeters was always to reach the finest resolution of energy deposit measurements on the nanometric level. This inspired new techniques that are able to reach this scale for different radiation types, some related details can be found in De Nardo et al.[69] and Grosswendt et al.[70]

These measurements are now frequently used to characterize radiation fields and are also of interest for Monte-Carlo codes validation. Using the code described by Bigildeev and Michalik,[71] Palajova et al.[72] calculated the lineal energy distributions for protons with energies 47, 62, 76, 93, 115, 139, and 172 MeV crossing a spherical volume of water with 3 μm diameter. The dimensions of the target are chosen to match with the TEPC detector that is used in the experiments of Borak et al.[12] The distributions and the mean values of the calculated lineal energies were compared to the results obtained by the experiment. Two experimental sets of data were presented; one was obtained using the mentioned TEPC and the other set using a position-sensitive silicon spectrometer. A better agreement was obtained with simulations involving only ionization processes. For the sake of validation, the Geant4-DNA package was also used to generate frequency distributions and mean lineal energies for the same target geometry. The results of mean lineal energies are reported in Table 4.1 showing data of Borak et al. and calculations of Palajova et al. compared with Geant4-DNA

Table 4.1 Frequency mean lineal energy obtained by the experiments of Borak et al.[12] using TEPC counter and a silicon detector, by the calculations of Palajova et al.[79] and calculations of Francis et al.[80] using the Geant4-DNA processes of the Geant4 toolkit

Protons energy (MeV)	TEPC[12]	Silicon detector[12]	Palajova et al.[79] calculations	Geant4-DNA calculations[80]
47	1.03	1.5	–	1.36
62	0.94	1.06	0.84	1.06
76	0.81	0.86	–	0.88
93	0.69	0.73	0.63	0.725
115	0.58	0.63	–	–
139	0.5	0.55	0.5	–
172	0.43	0.51	0.42	–

calculations and a good agreement was obtained for protons with the previously mentioned energies.[35]

Another comparison between Geant4-DNA and the code by Bigildeev and Michalik[71] consisted on shooting 1 MeV protons through separate spherical water targets of 30 nm and 2 nm of diameter. Then the total energy deposit is computed taking into account the build-up effect by placing the source at a certain distance from the target achieving electronic equilibrium. The results consisted on showing the total energy deposit per mean track length in the target versus the eccentricity of the incident beam which is the distance between the beam and a parallel segment going through the target center. The two codes are in agreement for both target sizes and the results are reported in Tables 4.2 and 4.3.

Table 4.2 Energy deposition per track length unit of 1 MeV protons crossing spherical water target with 30 nm diameter versus the incident beam eccentricity. The comparison between the 2 codes calculations shows a good agreement

Eccentricity (nm)	Code by Bigildeev and Michalik[71] (eV/nm)	Geant4-DNA (eV/nm)
0	21.65	22.6
5	20.34	21.35
10	15.77	16.6
12	12.47	12.4
15	3.29	3.46
18	0.98	0.9
20	0.63	0.7

Table 4.3 Energy deposition per track length unit of 1 MeV protons crossing spherical water target with 2 nm diameter versus the incident beam eccentricity

Eccentricity (nm)	Code by Bigildeev and Michalik[71] (eV/nm)	Geant4-DNA (eV/nm)
0	9.6	9.7
0.2	9.34	9.6
0.4	8.73	9.25
0.6	7.68	8.09
0.8	6.04	6.2
1	1.71	2.28
1.2	1.32	1.15
1.4	1.07	0.916
1.8	0.69	0.799
2.5	0.35	0.33

3.2 Ions RBE estimation

Most of the numerical studies on energy deposition in small nanometric volumes were influenced by the scale of the DNA fragments size. The outcome of these studies started to be put in practice for radioprotection and radiobiology as summarized by Lindborg and Nikjoo.[64] Gerlach et al.[73] have already used a derivate formalism to calculate radiation RBE for radiotherapy use. Experiments in microdosimetry started mostly using X-rays and gamma radiation due to the accessibility of such sources and the data is somehow abundantly available for this type of particles. However, with the new needs in the ion therapy domain, studies had to be made on a wider range of particles covering configurations that are in use today in the medical medium. Moreover, for carbon ions, due to the fragmentation effects the radiation field becomes very complex including more than seven secondary particles that can contribute significantly to the total energy delivered in the irradiated medium, e.g., protons, alpha particles, lithium ions, tritons, deuterons, beryllium, and boron ions including also the different elements isotopes. A simulation of carbon ions crossing a water volume was carried out using Geant4 version 9.5. The energy of the beam was 400 MeV/amu since this is the highest energy that is used for medical accelerators and this would show the upper limit of secondary contributions in radiotherapy irradiations. For more precision, the quantum molecular dynamics model was used instead of the binary ion cascade. The obtained results showed that 64.1% of the global dose is deposited by carbon ions and up to 35.9% by the produced fragments including all their isotopes. Protons contribution was about 14% against 13% for alpha particles. Other fragments contributions include lithium 1.7%, boron 4.2%, beryllium 1.3%, deuteron 1.3%, and triton 0.4%, approximately. Neutrons are produced abundantly in the fragmentation processes and most of their interactions in water are with hydrogen atoms producing recoil protons so their contribution is indirectly accounted for with protons contribution.

It is to mention here that the Geant4 fragmentation models were investigated and benchmarked with the Fluka code[74] in comparison with some experimental values. The comparison included total nuclear cross sections for carbon interaction with hydrogen and oxygen between 10 MeV/amu and 500 MeV/amu, total and partial charge change cross sections in water and polycarbonate as well as other results obtained from simulations like angular yields of H, He, Li, and B and yields of fragments with respect to the depth of the track in water. Although an agreement can be seen for the general trend of the obtained results, in the case of single differential values discrepancies of 10% are noticed between the two codes. However, since data is still scarce for this kind of validations, and here we are only presenting a general approximate idea about fragmentation yields and energy deposition, we will assume that the present state of fragmentation processes in Geant4 is reliable for our study.

The energy deposition by 400 MeV/amu carbon ions versus the beam depth in water is shown in Figure 4.2 revealing a Bragg peak around 27.5 cm. The total fragments contribution and individual contributions of protons, alphas, and boron ions are also illustrated. We can notice that the energy deposition by fragments can reach distances over 40 cm from the target entry point mainly due to protons and alpha particles especially beyond

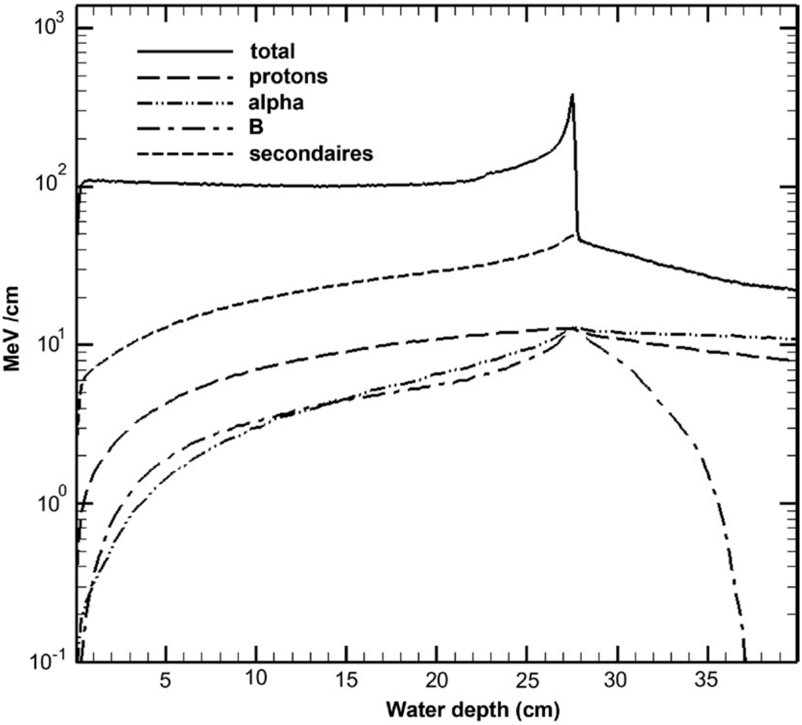

Figure 4.2 Energy deposition by 400 MeV/amu carbon ions at different depths crossing a water volume. Simulations were done using Geant4 (version 9.5) and the quantum molecular dynamics for fragmentation processes. The results include total contribution of fragments to the energy deposition and individual contributions for protons, alpha particles, and boron ions.

~37 cm. As a rough approximation we can conclude from the plot that the energy deposition per distance unit at 40 cm depth is about 20 MeV/cm which correspond to 10 eV of deposition per 5 nm of particle distance mainly due to protons and alphas. Theoretically, assuming that we need at least ~8.2 eV of energy deposition to ionize a DNA base, it is obvious that the fragments energy deposition tail at this depth can still induce DNA strand breaks and have an effect on biological cells. Thus, this part of the energy profile cannot be neglected.

On another side the kinetic energy profiles of protons and He nuclei at 30 cm depth are shown in Figure 4.3. The mean kinetic energy for protons at this point is around ~100 MeV and for He nuclei it is ~212 MeV/amu. The range of particles at these energies easily exceeds 5 cm and may reach 28 cm in the case of He nuclei which leads to an overall depth of 58 cm in the mentioned water volume. Thus, the risk of mutation and radio-induced cancer probability should be further investigated for such type of ions.

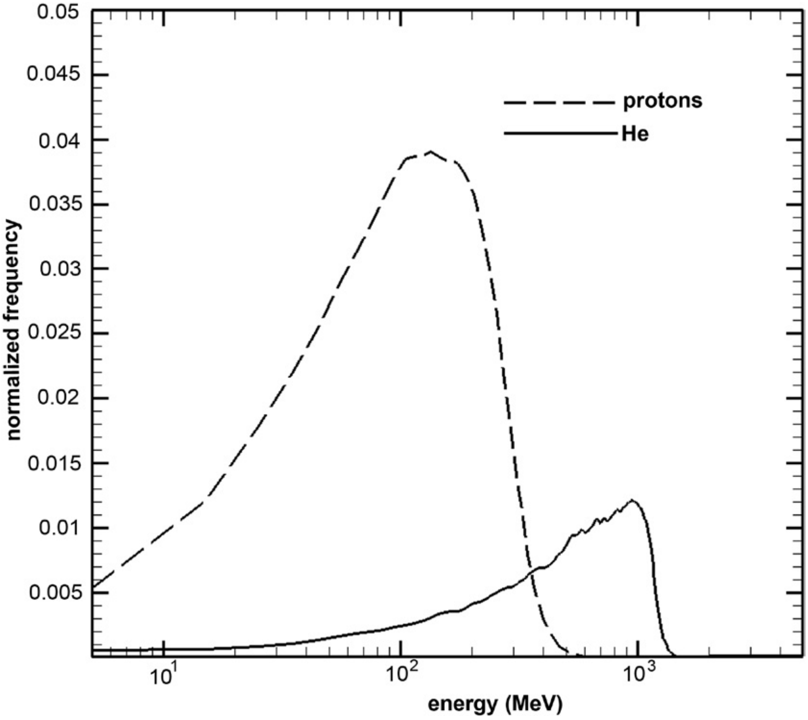

Figure 4.3 Energy distribution of protons and alphas at 30 cm depth in water target. Particles are issued form 400 MeV/amu carbon ions fragmentation in the medium.

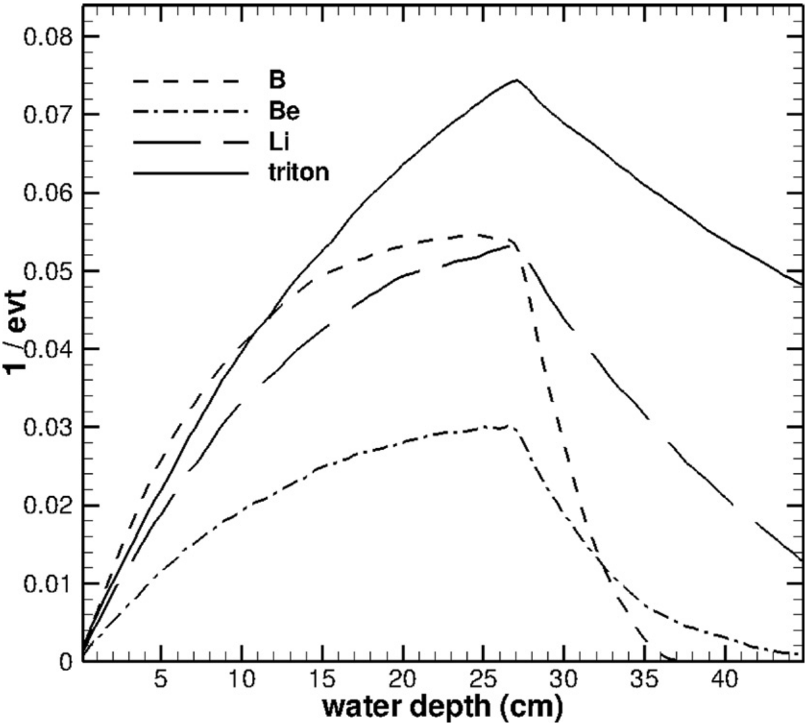

Figure 4.4 Build-up of B, Be, Li, and triton ions issued from the fragmentation of carbon ions of 400 MeV/amu crossing a water volume.

Figures 4.4 and 4.5 show the fragments build-up through the target in number of ions per primary event for B, Be, Li, triton, He, protons, and neutrons. Gamma photons were also abundantly produced in the medium but are not represented on our plots. Here also it is easy to notice that protons and He yields are the highest among other charged ions in the target. This is also reflected in the fragments energy deposition curves presented in Figure 4.2 where most of this energy is carried by He and protons.

The previously mentioned study of Gerlach et al.[73] was mainly focused on the analysis of the carbon complex radiation field and the related RBE calculations for medical applications. Using a TEPC detector, measurements of microdosimetric spectra were performed near a perspex phantom surface for carbon ion beam with energies between 89 MeV/amu and 430 MeV/amu and at different depths including the neighborhood of the Bragg peak area. The advantage of such an experiment is that measurements are done for the whole field including the fragments

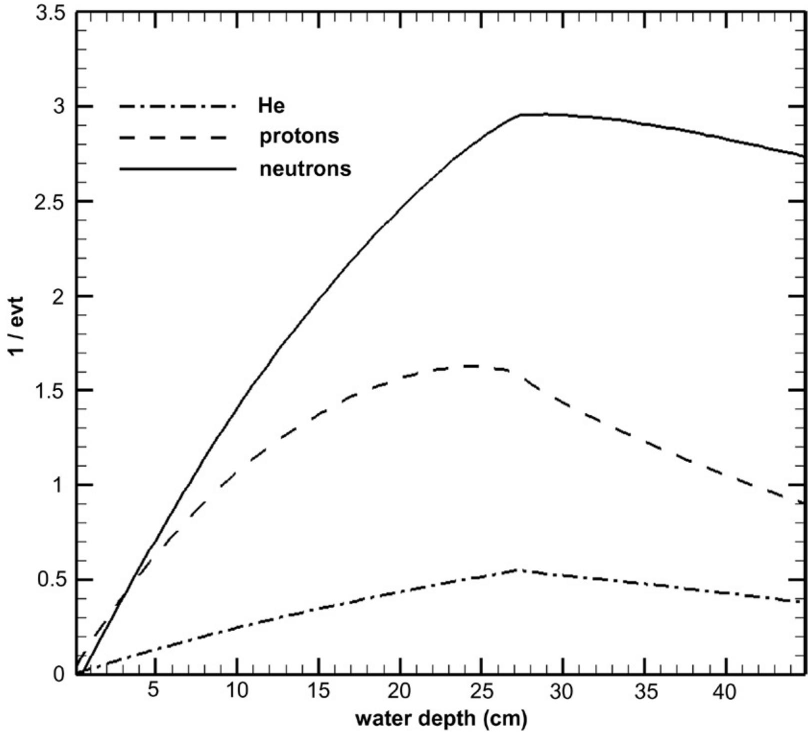

Figure 4.5 Build-up of He, protons, and neutrons issued from the fragmentation of carbon ions of 400 MeV/amu crossing a water volume.

cascade effects and their contribution to the dose deposition. Then the total RBE including contributions of all the secondary particles can be calculated by weighting the measured lineal energies spectra $d(y)$ with the so called biological weighting function $r(y)$ as described by the following expression:

$$RBE = \int r(y)d(y)\mathrm{d}y. \tag{4}$$

The biological weighting function depends on the cell type and on the irradiation conditions; it can be obtained only after experimental trials. In the study of Gerlach et al.[73] the RBE of neutrons were measured at nine different neutron irradiation facilities for mice crypt cells. The absorbed dose was the same for the nine irradiations (8 Gy) given in one single fraction. Also the lineal energies of the irradiation facilities were measured for the same conditions using a special TEPC detector developed for therapy radiation simulating a tissue volume of 1 μm of diameter. The biological function was then calculated for the mentioned cell types as a solution function for the nine irradiation cases. In an attempt to calculate the carbon ions RBE the same algorithm was used taking into account the biological function that was obtained after neutron irradiations. Although this method is an interesting step toward ions RBE calculation using microdosimetry, the effect of radiation type on the biological function is not clearly known yet, so the obtained RBE can only be considered as an approximation that should be validated by experimental RBE measurements in carbon ion fields and for the same cell type. So far, numerical RBE estimation often lacks of experimental data in the case of heavy ions irradiation. Although recent data is being published (e.g., Ref. 66), experiments and RBE measurements regarding therapy ion beams are still scarce in the literature. In fact, due to the restricted access to the few available carbon irradiation facilities, data sets that are usually needed to further develop and validate the related numerical algorithms for microdosimetry properties or RBE calculations, are somehow hard to obtain and most of the studies are still based on the results coming from X-rays or other available sources.

4. DNA DAMAGE ESTIMATION

4.1 Track structure detailed approach

Understanding the cell reaction to radiation and the resulting RBE of different radiation types requires a detailed knowledge of the molecular characteristics of the damage that is created within the cell. Calculations of DNA damage might generally be differentiated according to the complexity of the adopted approach and the details that are taken into account in the DNA modeling phase. In fact the first set of simulations started by taking particle tracks crossing small cylinders of water with nanometric dimensions and randomly placed in a water volume. The cylinders presented an approximation of the chromatin fiber fragments and energy deposits within such small volumes were studied mainly for X-rays and ions like protons and alpha particles of different energies. This kind of simulation played an important role in understanding the differences between low versus high LET radiation effects.[75] Then progress was carried out toward more detailed methods like the complete atomistic DNA modeling, e.g., Friedland et al.[30] where the PARTRAC code was used to generate tracks of particles through the target geometries taking into account the chemical effects in the medium. Simulations included different chromosome shapes (lymphocytes and fibroblasts) and different DNA arrangements. The yields of single and double strand breaks and the frequency distributions of DNA fragments with different lengths after irradiations were calculated. Further details about similar procedures can be found in the literature and by other references that are not mentioned here for the sake of brevity; in fact having a geometrical model for the DNA was a principal point for many projects trying to pre-estimate DNA damage effects using Monte-Carlo track structure codes. In spite of the many differences between the different adopted models, the DNA configurations might have a common standard that was followed by almost all the authors where the DNA double helix is surrounding the histone volume of few nanometers (6–7 nm of diameter) forming the nucleosomes. These latter are then placed together in different configurations to form the chromatin fibers. It is more frequent that at this level, differences will arise from one author to another since configurations of nucleosomes and even of chromatin fragments that constitute the whole chromosome can be completely random or can follow some imposed criteria to reach a certain DNA density or a desired base pair number in a fixed volume of the target. Having the DNA geometry at hand one can distinguish between the contributions of direct versus indirect effects of radiation and have access to data like DNA damage complexity and resulting DNA fragments lengths. As advanced as this procedure can be, having the complete perfect model of the DNA geometry is a very complex task not to mention the required computing power that is needed in this case due to the big number of elements one has to introduce in the simulation.

4.2 Stewart and Semenenko MCDS method

In parallel to the mentioned studies, other methods were found with simpler requirements and leading to a fair approximation of DNA damage calculations. An interestingly fast approach is the one adopted by Semenenko et al.,[24,76] where the initial damage is generated randomly on the DNA array taking into account the initial particle energy and LET. So the number of damages is directly related to the particle's properties but their spatial distribution is sampled randomly. This approximation avoids the particle tracks simulation phase and also the chemical species diffusion phase thus accelerating the simulation by a considerable amount of time. Then the emphasis is put on the damage analysis, damages on opposite strands separated by less than 10 base pairs of distance can form a double strand break and if more than two damages are present in such a limited area they are considered as a complex damage. This latter type is considered lethal for the cell since it cannot be handled by the repair mechanisms, also its presence might stop the cell reproduction cycle and lead to the cell death. In fact, in the work of Nikjoo et al.[77] damages were classified into categories; single strand breaks representing only one strand damage and are referred to as SSB, complex single strand breaks when more than one damage occur on the same strand within a distance of 10 base pairs and are noted as SSB+, double strand breaks (DSB) represent two damages on opposite strands located within the 10 base pairs distance, damages noted by DSB+ are formed by a SSB and a SSB+ located on opposite strands and DSB++ are the most complex damages as they can be formed by a combination of DSB damages within a limited base pairs distance. This classification was then adopted by many other studies and other authors since it summarizes somehow most of the occurring configurations of DNA damage types.

The work of Semenenko and Stewart included also cell repair activities through Base excision repair and Nucleotide excision repair pathways, however, this subject is not to be discussed here since it is out of the scope of this paragraph. The results obtained by Semenenko and Stewart showed good agreement with the detailed calculation methods discussed previously and with the experimental values on DNA mutation frequency after irradiation. Hereafter when referring to Semenenko and Stewart approach we mean the Monte-Carlo Damage Simulation (MCDS) that does not take into account any repair activities in the calculations. This is seen as an appropriate choice for a comparison with other algorithms where the repair activities are also neglected.

4.3 Garty statistical approach

Another study that is more based on microdosimetry is the one published by Garty et al.[78] Garty and co-workers assumed that there is a one-to-one correspondence between the ionizations formed within a considered sensitive volume and those formed within a DNA segment of equivalent size. Distributions of ionizations occurring in the sensitive volume can be obtained experimentally using a gas tissue equivalent counter or by numerical simulations using a track structure code. The size of the sensitive volume is chosen to be equivalent to the size of a DNA segment of one or two helical turns. Thus the sensitive volume is represented by a cylinder of about ~6 nm of length and ~4 nm of diameter. These dimensions are based on the assumption that damages occurring within such a distance can interact together to form double strand breaks or more complex lesions. Assuming also that every single ionization has a fixed probability to be converted into a

DNA lesion and an equal chance to fall on one of the two strands, yields of single and double strand breaks can be obtained by the following expressions:

$$G_{\mathrm{SSB}} = C \times \frac{\rho \cdot V_{\mathrm{SV}}}{W} \times \sum_{n_{\mathrm{ion}}} \left\{ f(n_{\mathrm{ion}}) \times 2\left[\left(1 - \frac{p_{\mathrm{SB}}}{2}\right)^{n_{\mathrm{ion}}} - (1 - p_{\mathrm{SB}})^{n_{ion}}\right]\right\}, \tag{5}$$

$$G_{\mathrm{DSB}} = C \times \frac{\rho \cdot V_{\mathrm{SV}}}{W} \times \sum_{n_{\mathrm{ion}}} \left\{ f(n_{\mathrm{ion}}) \times \left(1 - 2\left(1 - \frac{p_{\mathrm{SB}}}{2}\right)^{n_{\mathrm{ion}}} + (1 - p_{\mathrm{SB}})^{n_{\mathrm{ion}}}\right)\right\}, \tag{6}$$

where C is a conversion factor, and for $C = 9.6 \times 10^{-10}$ the yield G is obtained in ($\mathrm{Gy}^{-1}\mathrm{Da}^{-1}$). The sensitive volume V_{SV} is in (nm^3), p_{SB} is the probability that an ionization is transformed into a strand break (usually taken between ~9% and ~12%) and W is the mean energy deposited (in eV) by a single event in the sensitive volume. $f(n_{\mathrm{ion}})$ is the frequency probability of ionization number n_{ion} induced within the sensitive volume for one event, it can be obtained experimentally by taking a tissue equivalent detector volume of the same size of the studied target or also by simulating tracks crossing a similar sensitive volume. Note that this procedure is purely statistical and its main advantage is that it requires only one input parameter to be fixed by the user, which is the strand break induction probability. For $p_{\mathrm{SB}} = 11.7\%$ this approach leads to good agreement with experimental results of gel electrophoresis analysis on plasmid DNA irradiated with electrons and X-rays.

4.4 DBSCAN clustering estimation

Another study based on clustering algorithms is described in Francis et al.[26] In this case the DNA distribution inside of the cell nucleus is considered to be overall homogenous. So the radiation track structure simulations are carried out in a water volume with the same size as the nucleus of the studied cell type. The energy deposition locations and values are scored in a separate file that is treated by the algorithm after the simulation phase is completed. Chemical reactions are not modeled directly only the physical track structure is calculated, however, in our calculation we take into account that an energy deposition that is sufficiently close to DNA can induce indirect damage to this latter. So we consider that there is a certain sensitive area surrounding the DNA geometry which might also be explained as a geometrical cross section defining the percentage of the volume where an energy deposition may lead to DNA damage. The damage sampling follows also a linear distribution function having 0 probability of damage induction for energy deposition below 5 eV and a probability of 1 above 35 eV depositions. At the final stage a Density Based Clustering Algorithm with Noise (DBSCAN) runs over all the sampled damage points and according to their separating distances clusters of several damages are formed. The calculated damages here follow also the classification of Nikjoo et al.[77] for single strand breaks and double strand breaks. The obtained results for protons with energies between 0.5 MeV and 50 MeV were compared with the calculations of the PARTRAC code and with experimental data of plasmid damage after irradiation showing a good agreement. This model takes three main input parameters, the already introduced geometrical cross section (~16%), the maximum distance within which damages belong to the same cluster and its value should remain close to a 10 base pairs distance (~3.2 nm) and the damage probability function equation.

Figure 4.6 shows a comparison of the predicted DSB/SSB ratio induced by protons irradiations with energies between 0.5 MeV and 50 MeV.

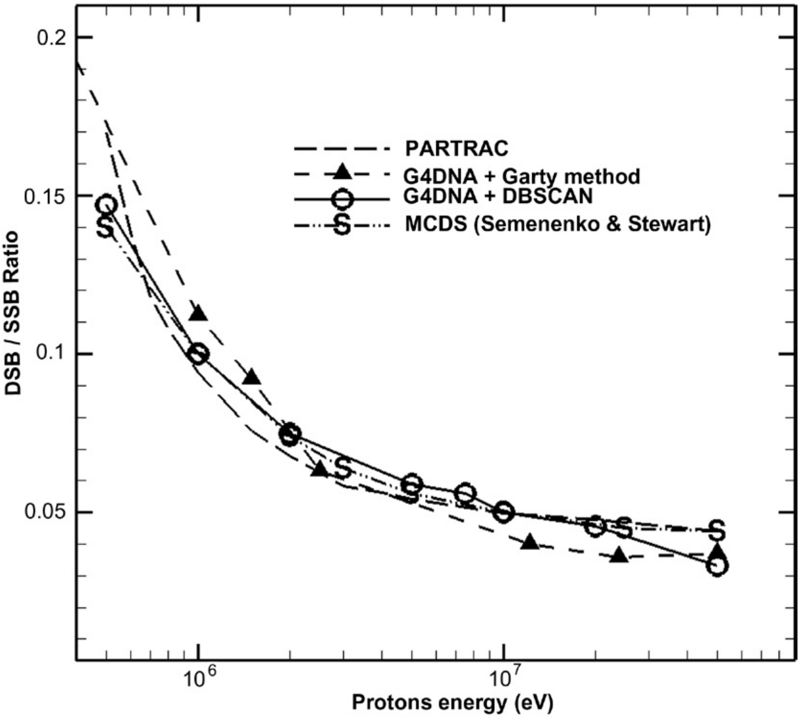

Figure 4.6 Comparison of double strand breaks over single strand breaks ratio obtained with the PARTRAC code,[21] the approach described by Garty et al.,[78] the clustering method of Francis et al.,[25] and the MCDS model described by Semenenko and Stewart.[76]

The comparison includes values from PARTRAC code simulations compared to the results obtained by using the approach of Garty combined with ionization distributions simulated using the Geant4-DNA processes. Also the results obtained by the DBSCAN clustering algorithm and tracks generated with Geant4-DNA are shown with the predictions of the MCDS of Semenenko and Stewart[76] A general agreement can be noticed between the different approaches although differences start to grow for low energies meaning with higher LET. In fact in the PARTRAC calculations the chemical phase was completely modeled including the scavenging effect that is enhanced at high LET due to the high density of chemical species created in the medium. Since the chemical species diffusion was not taken into account in the other calculations, differences may increase with increasing radiation LET.

In general, these models agree with each other's and with some experiments on plasmid DNA, although track structures are generated in liquid water without taking into account the DNA interaction cross sections. It has been shown in the literature that the differences between water and DNA bases cross sections cannot be neglected and DNA cross sections should be used instead of water for DNA simulations. Moreover experiments with sub-excitation electrons showed that these latter can cause DNA damage even at very low kinetic energies that are not considered to induce direct ionizations. In fact, studies of Boudaiffa et al.[54] showed that there is a resonant formation of DNA strand breaks irradiated with electrons of energies between 3 and 20 eV and surprisingly double strand breaks can still be induced by electrons with energies as low as 5 eV. In most of the track structure codes that are in use today these low energy electrons are either killed assuming that their energy is not high enough to induce direct DNA ionizations or simply transported with one single step of condensed history until their end of track location. Few specific codes studying only sub-excitation electrons can model detailed and precise tracking in this case. It is clear that in their present state, the approximation algorithms that were mentioned here before cannot reproduce the results of Boudaiffa et al. where most of the damages are induced by vibrational and rotational excitations and by electron attachment processes.

5. CONCLUSION

Here in this chapter a brief summary was presented reviewing the different basic approaches that can be used for modeling ionizing particles tracks with molecular scale resolution. An emphasis on the importance of such studies for the radiobiology and the hadrontherapy fields was built up during the whole text showing some of the examples that were published in the literature and presenting a clear idea of the different methodologies that can be used to study DNA radiation damage.

In the second paragraph describing track structure codes, most of the mentioned physics models are based on the processes that were included in the Geant4-DNA package. Although, other existing codes are well developed in the field, the main difficulty remains mostly in the accessibility of these "homemade" programs that are often built for one single or a restricted application type. The Geant4-DNA project aims to present a detailed track structure code that enables all Geant4 users to simulate particles interactions in biological tissue following a detailed step by step tracking with nanometric scale precision. The presented particles and their physical processes are already available to download with the public version of Geant4 and a typical example of a microdosimetry application is also provided in the Geant4 examples folder. The particles that can be modeled with the present version are electrons, protons, alphas and some heavier ions like carbon, only for a restricted energy range according to the available cross sections. On another hand, cross sections of particles interactions in DNA material are under development and the molecules diffusion processes that are needed for the chemical phase simulation are going through validation tests and will be published in the upcoming releases. Also a typical atomistic model of DNA is under construction and will be included in one of the examples in the future Geant4 releases. These efforts aim to present a publicly available library that can be used by any researcher interested in the mentioned applications taking benefit from a user support forum and a publicly available manual that is under continuous development.

In spite of the multiple efforts that are put by the different communities, improvements are still required to take care of some of the commonly adopted approximations. Here, tracking sub-excitation electrons in water and modeling their interactions with DNA material is still an open field. So far, the angular inelastic diffusion of sub-excitation electrons is considered isotropic which was never precisely confirmed by theoretical studies nor by adequate experiments. It is important here to mention the need of a reliable set of double differential cross sections taking into account both energy and angular diffusions of electrons. The importance of these latter particles is underlined in the previously mentioned study of Boudaiffa et al.[54] showing an unexpected sensitivity of DNA toward low incident energies.

Another point worth to mention is the DNA geometry models that are used in detailed simulations. These models often represent one single specific chromosome structure while a big variety of configurations are encountered in reality which limits the applicability of the simulations to very specific cases of cell irradiations. In fact the genome geometry depends on the cell type and on the cell replication phase so simulations should include several geometrical models to extend the applicability of their results to a wider range of irradiation configurations. As far as the author is aware, such advanced investigations were started by Friedland et al.[30] but no other efforts were published regarding calculations with chromosomes irradiated in different cell replication phases.

For hadrontherapy, carbon ions fragmentation is now under the scope of several investigations. The fragmentation gives arise to secondary ions that are responsible for the tail of energy deposition after the "Bragg peak." In order to make a numerical estimation of the RBE of these ions and their effect on the treatment area, important information can be found through nanometric scale track structure simulations. In the Geant4-DNA framework, using a speed scaling procedure with the previously calculated protons ionization cross sections and an effective charge model, it is possible to derive ionization cross sections for most of the fragmentation products. This process is already included in Geant4-DNA and a step by step model is used to track ions heavier than alpha particles for energies above 1 MeV/amu taking into account ionization interactions. At the end of its track when the ion energy drops below the mentioned threshold inaccuracies arise since nuclear collisions are not taken into account. An adapted model of ions elastic scattering is being studied in an effort to fill the gap of the lacking cross sections, the final goal would be to follow all the fragmentation products in a step by step mode until complete ion stop. Also here improvements are needed regarding the interactions cross sections since most of the discrepancies between nucleus collisions models arise in the low energy parts.

For validation purposes, experiments using microdosimetry techniques for carbon ion beams analysis are of extreme importance for numerical codes control and should be supported in order to provide a wider data base. The required data may include lineal energies spectra in nanometric targets of different sizes and for different beam energies. Also DNA damage experiments using typical DNA samples like plasmid are of importance for the validation of the different damage estimation algorithms. Most of the presented approaches that were developed for damage prediction are validated with the results of experiments using different radiation sources sometimes of different types. However, DNA damage yields depend strongly on the particle type even for different particles of the same LET as demonstrated in Francis et al.[26] So for hadrontherapy applications, a precise validation of DNA damage prediction methods should mainly rely on values issued from experiments that are done using, to an extent, the same real conditions and parameters as in the treatment cases. Finally, we can mention that a comparison between the RBE calculations obtained using the multiple different studies would be of importance for the medical purposes.

ACKNOWLEDGMENTS

The author would like to thank the Geant4 collaboration, the low energy electromagnetic working group and the Geant4-DNA project. The support of Professor N. Mason, Dr. A. Stypczynska and the Open University in Milton Keynes is highly appreciated.

REFERENCES

1. Brenner, D. J.; Hlatky, L. R.; Hahnfeldt, P. J., et al. The linear-quadratic model and most other common radiobiological models result in similar predictions of time–dose relationships. *Rad. Res.* **1998**, *150*, 83.
2. Kramer, M.; Scholz, M. Treatment planning for heavy-ion radiotherapy: calculation and optimization of biologically effective dose. *Phys. Med. Biol.* **2000**, *45*, 3319.
3. Kramer, M.; Jakel, O.; Haberer, T., et al. Treatment planning for heavy-ion radiotherapy: physical beam model and dose optimization. *Phys. Med. Biol.* **2000**, *45*, 3299.
4. Jakel, O.; Kramer, M.; Schulz-Ertner, D., et al. Treatment planning for carbon ion radiotherapy in Germany: review of clinical trials and treatment planning studies. *Radiother. Oncol.* **2004**, *73*, 86.
5. Rietzel, E.; Schardt, D.; Haberer, T. Range accuracy in carbon ion treatment planning based on CT-calibration with real tissue samples. *Radiat. Oncol.* **2007**, *2*, 14.
6. Stypczynska, A.; Ptasinska, S.; Bahnev, B., et al. The influence of amino acids on DNA damage induced by cold plasma radiation. *Chem. Phys. Lett.* **2010**, *500*, 313.
7. Ptasinska, S.; Stypczynska, A.; Nixon, T., et al. X-ray induced damage in DNA monitored by X-ray photoelectron spectroscopy. *J. Chem. Phys.* **2008**, *129*, 065102.
8. Smialek, M. A.; Moore, S. A.; Mason, N. J., et al. Quantification of radiation-induced single-strand breaks in plasmid DNA using a TUNEL/ELISA-based assay. *Radiat. Res.* **2009**, *172*, 529.
9. Milligan, J. R.; Aguilera, J. A.; Nguyen, T. T., et al. DNA strand-break yields after post-irradiation incubation with base excision repair endonucleases implicate hydroxyl radical pairs in double-strand break formation. *Int. J. Radiat. Biol.* **2000**, *76*, 1475.
10. Gulston, M.; Fulford, J.; Jenner, T., et al. Clustered DNA damage induced by gamma radiation in human fibroblasts (HF19), hamster (V79–4) cells and plasmid DNA is revealed as Fpg and Nth sensitive sites. *Nucleic Acids Res.* **2002**, *30*, 3464.
11. Magnander, K.; Hultborn, R.; Claesson, K., et al. Clustered DNA damage in irradiated human diploid fibroblasts: influence of chromatin organization. *Radiat. Res.* **2010**, *173*, 272.
12. Borak, T. B.; Doke, T.; Fuse, T., et al. Comparisons of LET distributions for protons with energies between 50 and 200 MeV determined using a spherical tissue-equivalent proportional counter (TEPC) and a position-sensitive silicon spectrometer (RRMD-III). *Radiat. Res.* **2004**, *162*, 687.
13. De Nardo, L.; Colautti, P.; Baek, W. Y., et al. Track nanodosimetry of an alpha particle. *Radiat. Prot. Dosimetry* **2002**, *99*, 355.

14. Grosswendt, B.; Pszona, S. The track structure of alpha-particles from the point of view of ionization-cluster formation in "nanometric" volumes of nitrogen. *Radiat. Environ. Biophys.* **2002**, *41*, 91.
15. Bantsar, A.; Grosswendt, B.; Pszona, S., et al. Radiation oncology Single track nanodosimetry of low energy electrons Nuc. *Instum. Methods Phys. Res., Sect. A* **2009**, *599*, 270.
16. Fasso, A.; Ferrari, A.; Ranft, J., et al. In *New developments in FLUKA modeling hadronic and EM interactions, SARE 3*. Proceedings of the Third Workshop on Simulating Accelerator Radiation Environments, Japan, KEK Proceedings 97–5, June, H/R/D; Hirayama, H, Ed., 1997; p 32.
17. Agostinelli, S.; Allison, J.; Amako, K., et al. Geant4-a simulation toolkit. *Nucl. Instrum. Methods Phys. Res., Sect. A* **2003**, *506*, 250.
18. Hughes, G.; Adams, K. J.; Chadwick, M. B., et al. In *MCNPX – the LAHET/MCNP code merger SARE 3*. Proceedings of the Third Workshop on Simulating Accelerator Radiation Environments, Japan, KEK Proceedings 97–5, June, H/R/D; Hirayama, H., Ed., 1997; p 44.
19. Gudowska, I.; Sobolevsky, N.; Andreo, P., et al. Ion beam transport in tissue-like media using the Monte Carlo code SHIELD-HIT. *Phys. Med. Biol.* **2004**, *49*, 1933.
20. Henkner, K.; Sobolevsky, N.; Jakel, O., et al. Test of the nuclear interaction model in SHIELD-HIT and comparison to energy distributions from GEANT4. *Phys. Med. Biol.* **2009**, *54*, 509.
21. Friedland, W.; Jacob, P.; Bernhardt, P., et al. Simulation of DNA damage after proton irradiation. *Radiat. Res.* **2003**, *159*, 401.
22. Ballarini, F.; Alloni, D.; Facoetti, A., et al. Heavy-ion effects: from track structure to DNA and chromosome damage. *New J. Phys.* **2008**, *10*, 075008.
23. Ponomarev, A. L.; Sachs, R. K. Polymer chromosome models and Monte Carlo simulations of radiation breaking DNA. *Bioinformatics* **1999**, *15*, 957.
24. Semenenko, V. A.; Stewart, R. D.; Ackerman, E. J. Monte Carlo simulation of base and nucleotide excision repair of clustered DNA damage sites. I. Model properties and predicted trends. *Radiat. Res.* **2005**, *164*, 180.
25. Francis, Z.; Villagrasa, C.; Clairand, I. Simulation of DNA damage clustering after proton irradiation using an adapted DBSCAN algorithm. *Comput. Methods Programs Biomed.* **2011**, *101*, 265.
26. Francis, Z.; Incerti, S.; Ivanchenko, V., et al. Monte Carlo simulation of energy-deposit clustering for ions of the same LET in liquid water. *Phys. Med. Biol.* **2012**, *57*, 209.
27. Stewart, R. D.; Wilson, W. E.; McDonald, J. C., et al. Microdosimetric properties of ionizing electrons in water: a test of the PENELOPE code system. *Phys. Med. Biol.* **2002**, *47*, 79.
28. Francis, Z.; Incerti, S.; Karamitros, M., et al. Stopping power and ranges of electrons, protons and alpha particles in liquid water using the Geant4-DNA package. *Nucl. Instrum. Methods Phys. Res., Sect. B* **2011**, *269*, 2307.
29. Gervais, B.; Beuve, M.; Olivera, G. H., et al. Numerical simulation of multiple ionization and high LET effects in liquid water radiolysis. *Radiat. Phys. Chem.* **2006**, *75*, 493.
30. Friedland, W.; Paretzke, H. G.; Ballarini, F., et al. First steps towards systems radiation biology studies concerned with DNA and chromosome structure within living cells. *Radiat. Environ. Biophys.* **2008**, *47*, 49.
31. Friedland, W.; Dingfelder, M.; Kundrat, P., et al. Track structures, DNA targets and radiation effects in the biophysical Monte Carlo simulation code PARTRAC. *Mutat. Res.* **2011**, *711*, 28.
32. Wilson, W. E.; Nikjoo, H. A Monte Carlo code for positive ion track simulation. *Radiat. Environ. Biophys.* **1999**, *38*, 97.
33. Semenenko, V. A.; Turner, J. E.; Borak, T. B. NOREC, a Monte Carlo code for simulating electron tracks in liquid water. *Radiat. Environ. Biophys.* **2003**, *42*, 213.
34. Incerti, S.; Ivanchenko, A.; Karamitros, M., et al. Comparison of GEANT4 very low energy cross section models with experimental data in water. *Med. Phys.* **2010**, *37*, 4692.

35. Francis, Z.; Incerti, S.; Capra, R., et al. Molecular scale track structure simulations in liquid water using the Geant4-DNA Monte-Carlo processes. *Appl. Radiat. Isot.* **2011**, *69*, 220.
36. Dingfelder, M.; Inokuti, M.; Paretzke, H. G. Inelastic-collision cross-section of liquid water for interactions of energetic protons. *Radiat. Phys. Chem.* **2000**, *59*, 255.
37. Heller, J. M.; Hamm, R. N.; Birkhoff, R. D., et al. Collective oscillation in liquid water. *J. Chem. Phys.* **1974**, *60*, 3483.
38. Hayashi, H.; Watanabe, N.; Udagawa, Y. Optical spectra of liquid water in vacuum UV region by means of inelastic X-ray scattering spectroscopy. *J. Chem. Phys.* **1998**, *108*, 823.
39. Belkić, Dž. Review of theories on ionization in fast ion-atom collisions with prospects for applications to hadron therapy. *J. Math. Chem.* **2010**, *47*, 1366.
40. Dingfelder, M.; Toburen, L.H.; Paretzke; H.G. An effective charge scaling model for ionization of partially dressed helium ions with liquid water. In *The Monte Carlo Method: Versatility Unbounded in a Dynamic Computing World, April 17–21, 2005*; LaGrange Park, Tennessee: American Nuclear Society, 2005.
41. Barkas, W. H.; Birnbaum, W.; Smith, F. M. Mass-ratio method applied to the measurement of L-Meson masses and the energy balance in pion decay. *Phys. Rev.* **1956**, *101*, 778.
42. Booth, W.; Grant, I. S. Energy loss of oxygen and chlorine ions in solid. *Nucl. Phys.* **1965**, *63*, 481.
43. Plante, I.; Cucinotta, F. Ionization and excitation cross sections for the interaction of HZE particles in liquid water and application to Monte Carlo simulation of radiation tracks. *New J. Phys.* **2008**, *10*, 125020.
44. Porter, L. E.; Cabrera-Trujillo, R.; Sabin, J. R. *The Barkas-Effect Correction to Bethe–Bloch Stopping Power. Advances in Quantum Chemistry*; Academic Press
45. Dingfelder, M.; Hantke, D.; Inokuti, M., et al. Electron inelastic scattering cross sections in liquid water. *Radiat. Phys. Chem.* **1998**, *53*, 1.
46. Emfietzoglou, D.; Nikjoo, H. The effect of model approximations on single-collision distributions of low-energy electrons in liquid water. *Radiat. Res.* **2005**, *163*, 98.
47. Bousis, C.; Emfietzoglou, D.; Hadjidoukas, P., et al. Electron ionization cross-section calculations for liquid water at high impact energies. *Nucl. Instrum. Methods Phys. Res., Sect. B* **2008**, *266*, 1185.
48. Vriens, L. Binary-Encounter Electron-Atom Collision Theory. *Phys. Rev. Lett.* **1966**, *141*, 88.
49. Ashley, J. C.; Ritchie, R. H.; Brandt, W. Z3 effect in the stopping power of matter for charged particles. *Phys. Rev. B* **1972**, *5*, 2393.
50. Kim, Y. K.; Rudd, M. E. Binary-encounter-dipole model for electron-impact ionization. *Phys. Rev. A* **1994**, *50*, 3954.
51. Brenner, D. J.; Zaider, M. A computationally convenient parameterization of experimental angular distributions of low energy electrons elastically scattered off water vapor. *Phys. Med. Biol.* **1983**, *29*, 443.
52. Champion, C.; Incerti, S.; Aouchiche, H., et al. A free-parameter theoretical model for describing the electron elastic scattering in water in the Geant4 toolkit. *Radiat. Phys. Chem.* **2009**, *78*, 745.
53. Michaud, M.; Wen, A.; Sanche, L. Cross sections for low-energy (1–100 eV) electron elastic and inelastic scattering in amorphous ice. *Radiat. Res.* **2003**, *159*, 3.
54. Boudaiffa, B.; Cloutier, P.; Hunting, D., et al. Resonant formation of DNA strand breaks by low-energy (3 to 20 eV) electrons. *Science* **2000**, *287*, 1658.
55. Huels, M. A.; Boudaiffa, B.; Cloutier, P., et al. Single, double, and multiple double strand breaks induced in DNA by 3–100 eV electrons. *J. Am. Chem. Soc.* **2003**, *125*, 4467.
56. Sanche, L. Low energy electron-driven damage in biomolecules. *Eur. Phys. J. D* **2005**, *35*, 367.
57. Uehara, S.; Nikjoo, H. Monte Carlo simulation of water radiolysis for low-energy charged particles. *J. Radiat. Res.* **2006**, *47*, 69.
58. Meesungnoen, J.; Jay-Gerin, J. P.; Filali-Mouhim, A., et al. Low-energy electron penetration range in liquid water. *Radiat. Res.* **2002**, *158*, 657.

59. Munoz, A.; Blanco, F.; Garcia, G., et al. Single electron tracks in water vapor for energies below 100 eV. *Int. J. Mass Spectrom.* **2008**, *277*, 175.
60. Frongillo, Y.; Goulet, T.; Fraser, M. J., et al. Monte Carlo simulation of fast electron and proton tracks in liquid water – II. Nonhomogeneous chemistry. *Radiat. Phys. Chem.* **1998**, *51*, 245.
61. Kellerer, A. M. Microdosimetry: reflections on Harald Rossi. *Radiat. Prot. Dosimetry* **2002**, *99*, 17.
62. Kellerer, A. M.; Chmelevsky, D. Concepts of Microdosimetry. I. Quantities. *Radiat. Environ. Biophys.* **1975**, *12*, 61.
63. Kellerer, A. M.; Chmelevsky, D. Concepts of Microdosimetry. II. Probability distributions of the microdosimetric variables. *Radiat. Environ. Biophys.* **1975**, *12*, 205.
64. Lindborg, L.; Nikjoo, H. Microdosimetry and radiation quality determinations in radiation protection and radiation therapy. *Radiat. Prot. Dosimetry* **2011**, *143*, 402.
65. Nikjoo, H.; Uehara, S.; Emfietzoglou, D., et al. A database of frequency distributions of energy depositions in small size targets by electrons and ions. *Radiat. Prot. Dosimetry* **2011**, *143*, 145.
66. Tsuda, S.; Sato, T.; Takahashi, F., et al. Measurement of microdosimetric spectra with a wall-less tissue-equivalent proportional counter for a 290 MeV/u 12C beam. *Phys. Med. Biol.* **2010**, *55*, 5089.
67. Endo, S.; Takada, M.; Onizuka, Y., et al. Microdosimetric evaluation of secondary particles in a phantom produced by carbon 290 MeV/nucleon ions at HIMAC. *J. Radiat. Res.* **2007**, *48*, 397.
68. ICRU. Microdosimetry Report 36: ICRU, International Commission on Radiation Units and Measurements, Bethesda, MD, 1983.
69. De Nardo, L.; Colautti, P.; Conte, V., et al. Ionization-cluster distributions of alpha-particles in nanometric volumes of propane: measurement and calculation. *Radiat. Environ. Biophys.* **2002**, *41*, 235.
70. Grosswendt, B.; De Nardo, L.; Colautti, P., et al. Experimental equivalent cluster size distributions in nanometric volumes of liquid water. *Radiat. Prot. Dosimetry* **2004**, *110*, 851.
71. Bigildeev, E. A.; Michalik, V. Charged particle tracks in water of different phases, Monte Carlo simulation of electron tracks. *Radiat. Phys. Chem.* **1996**, *47*, 197.
72. Palajova, Z.; Spurny, F.; Davidkova, M. Microdosimetry distributions for 40–200 MeV protons. *Radiat. Prot. Dosimetry* **2006**, *121*, 376.
73. Gerlach, R.; Roos, H.; Kellerer, A. M. Heavy ion RBE and microdosimetric spectra. *Radiat. Prot. Dosimetry* **2002**, *99*, 413.
74. Bohlen, T. T.; Cerutti, F.; Dosanjh, M., et al. Benchmarking nuclear models of FLUKA and GEANT4 for carbon ion therapy. *Phys. Med. Biol.* **2010**, *55*, 5833.
75. Goodhead, D. T.; Nikjoo, H. Track structure analysis of ultrasoft X-rays compared to high- and low-LET radiations. *Int. J. Radiat. Biol.* **1989**, *55*, 513.
76. Semenenko, V. A.; Stewart, R. D. A fast Monte Carlo algorithm to simulate the spectrum of DNA damages formed by ionizing radiation. *Radiat. Res.* **2004**, *161*, 451.
77. Nikjoo, H.; O'Neill, P.; Wilson, W. E., et al. Computational Approach for Determining the Spectrum of DNA Damage Induced by Ionizing Radiation. *Radiat. Res.* **2001**, *156*, 577.
78. Garty, G.; Schulte, R.; Shchemelinin, S., et al. A nanodosimetric model of radiation-induced clustered DNA damage yields. *Phys. Med. Biol.* **2010**, *55*, 761.
79. Palajova, Z.; Spurny, F.; Davıdkova, M. Microdosimetry distributions for 40–200 MeV protons. *Radiat. Prot. Dosimetry* **2006**, *121*, 376.
80. Francis, Z.; Incerti, S.; Capra, R., et al. Molecular scale track structure simulations in liquid water using the Geant4-DNA Monte-Carlo processes. *Appl. Radiat. Isot.* **2011**, *69*, 220.

CHAPTER FIVE

Verifying Radiation Treatment in Proton Therapy via PET Imaging of the Induced Positron-Emitters

Joanne Beebe-Wang, Paul Vaska, F. Avraham Dilmanian, Stephen G. Peggs and David J. Schlyer
Brookhaven National Laboratory, P.O. Box 5000, Upton, NY 11973, USA

Contents

Abstract

Positron Emission Topography (PET) is a promising technique to verify the dose distribution from proton therapy, a precise treatment modality increasingly used in radiation oncology because its radiation pattern conforms more closely to the configuration of a tumor than does that from X-ray radiation, thereby sparing normal healthy tissue. Proton therapy produces positron-emitting isotopes along the beam's path, allowing PET to image the distribution of therapeutic energy, viz., a form of quality assurance of the treatment. This ability is especially important when treating heterogeneous organs, such as the lungs or the head-and-neck, where calculating the expected dose distribution for treatment is complex. Here, we present the findings from our Monte Carlo simulations of the yield of positron emitters produced by proton beams of up to 250 MeV, followed by our statistically realistic Monte Carlo simulation of the images expected from a clinical PET scanner. Our emphases lay in predicting accurately the distribution of positron emitters, and in determining the quality of the PET signal near the Bragg peak that is critical to the success of PET imaging for verifying the proton beam's location and dosimetry. We also demonstrate that the results depend strongly on the accuracy of the available nuclear reaction cross section data. Accordingly, we quantify the differences in the calculated positron-emitter yields from four different sets of such data, comparing them to the simulated distributions of positron-emitter production and absorbed proton energies.

Advances in Quantum Chemistry, Volume 65
ISSN 0065-3276, http://dx.doi.org/10.1016/B978-0-12-396455-7.00005-4

1. INTRODUCTION

The subject of the present study relates to the main topic of this book, namely high-energy collisions of heavy ions with matter, if we extend the subject to cover (a) biological tissues and (b) hadron therapy of cancer.[1, 2] The goal is to use Monte Carlo simulations for evaluating the applicability of positron emission tomography (PET)[3] for monitoring dose distributions produced in biological subjects in proton therapy. This chapter presents such a simulation using a voxel-based Monte Carlo algorithm. Application of PET to proton therapy dose monitoring rests upon detecting positron annihilation γ rays following the decay of the small amounts of positron emitters (typically ^{11}C, ^{13}N, and ^{15}O) produced via the non-elastic nuclear reaction of protons with the target nuclei of the irradiated tissue. The input data for such simulations are mainly electronic and nuclear stopping powers of protons in matter, and the attenuation of the resulting 511 keV gamma rays in their way out of the subject towards the detector.[4, 5] To arrive at realistic estimates, we employ several data sets from a comprehensive database of the available cross sections and stopping powers.

The present work clearly shows that PET is potentially a very useful tool for monitoring the distribution of the dose deposited in a patient during proton therapy. The adequacy of the implementation of the therapy can be verified by comparing PET images revealing the distribution of positron activity with the predicted target dose-distribution used in planning treatment. The most important feature of this technique is that the resulting PET images are the inverse of the deposited energy distribution in the subject because the bulk of the positron-emitting isotopes are produced in the tissues proximal to the target and in fact such isotope production is diminished at the target itself. This is because the non-elastic nuclear reaction cross sections, where the largest amount of protons' energies are deposited, are the largest at the protons' entrance to the subject and gradually diminish towards reaching the Bragg peak. However, effective dose verification still can be made by focusing at the tissue volume at target's edges and by comparing the radioisotope distribution produced in that region as measured by PET with the yield of the positron emitters predicted from the treatment planning code.

Various researchers explored the possibility of monitoring proton therapy with PET through experimental measurements[6–10] and by computer simulations.[11–14] So far, most of the simulations studies were performed with general particle transport codes originally developed for high-energy physics, such as FLUKA,[15] GEANT4,[16] and SHIELD-HIT.[17] Some efforts have been made to improve and evaluate the underlying physics in the low energy range incorporated in the general codes, as well as to implement them into clinical applications.[18–22] However, there is a need to benchmark them against one or more dedicated proton transport codes. In addition, the reliability of nuclear reaction cross section data is essential to predicting positron-emitter production. However, such data are very limited currently, either incomplete or not compiled, because there are very few experimental measurements of these reactions, especially in the energy range below 50 MeV. Therefore, an investigation of the impact of cross section data on the predicted positron-emitter production is also needed.

In this study, we examine the positron-emitter production through nuclear interactions of a proton beam in a full range of proton energy (0.1–250 MeV) with a dedicated simulation code SRNA-BNL,[13] and assess the quality of the PET signal in the region near the Bragg peak that is critical to the success of PET imaging in verifying the location and dosimetry of the proton beam. In addition, the results are calculated with four sets of nuclear reaction cross section data to demonstrate dependence of the result on the reliability of nuclear reaction cross section data.

2. POSITRON EMITTER PRODUCTION

Although many isotopes are produced through different nuclear interactions during proton therapy, only six major channels produce the positron emitters ^{11}C, ^{13}N, and ^{15}O in human tissue (Table 5.1).

Table 5.1 Major channels of nuclear interactions leading to the production of positron-emitters in human tissue during proton therapy

Nuclear reactions	**Threshold energy (MeV)**	**Half-life (min)**	**Positron max. energy (MeV)**
^{16}O(p, pn)^{15}O	16.79	2.037	1.72
^{16}O(p, 2p2n)^{13}N[a]	5.66[c]	9.965	1.19
^{14}N(p, pn)^{13}N	11.44	9.965	1.19
^{12}C(p, pn)^{11}C	20.61	20.39	0.96
^{14}N(p, 2p2n)^{11}C[a]	3.22[c]	20.39	0.96
^{16}O(p, 3p3n)^{11}C[b]	27.50[c]	20.39	0.96

[a] (p, 2p2n) includes (p, α).
[b] (p, 3p3n) includes (p, α pn).
[c] The thresholds refer to (p, α) and (p, α pn).

Table 5.2 Low-probability reactions that produce positron-emitting nuclei

Nuclear reactions	Threshold energy (MeV)	Half-life (min)	Positron max. energy (MeV)
$^{12}C(p, p2n)^{10}C$	34.5	0.32	1.87
$^{12}C(p, \gamma)^{13}N$	0	9.97	1.19
$^{13}C(p, p2n)^{11}C$	25.5	20.3	0.96
$^{13}C(p, n)^{13}N$	3.2	9.97	1.19
$^{14}N(p, n\alpha)^{10}C$	17.2	0.32	1.87
$^{14}N(p, \gamma)^{15}O$	0	2.04	1.72
$^{14}N(p, n)^{14}O$	6.6	1.18	1.81
$^{15}N(p, n\alpha)^{11}C$	14.7	20.3	0.96
$^{15}N(p, nd)^{13}N$	20.4	9.97	1.19
$^{15}N(p, t)^{13}N$	13.8	9.97	1.19
$^{15}N(p, n)^{15}O$	3.8	2.04	1.72
$^{16}O(p, \gamma)^{17}F$	0	1.07	1.74
$^{16}O(p, 3p4n)^{10}C$	39.1	0.32	1.87
$^{16}O(p, p2n)^{14}O$	30.7	1.18	1.81
$^{18}O(p, n)^{18}F$	2.6	109.8	0.64

Table 5.2 summarizes the other 15 more exotic nuclear reactions that generate positron emitters. Since ^{13}C, ^{15}N, and ^{18}O have very low abundances in the human body, the reactions induced by protons with them are negligible. The cross sections of the radioactive capture reactions, (p, γ), typically are in the order of microbarns; they are three orders-of-magnitude smaller than the six main channels listed in Table 5.1. Also, due to the very small quantities of the ^{10}C and ^{14}O isotopes generated, the uncertainties in their cross sectional data render calculations meaningless. Therefore, we excluded from our study the reactions listed in Table 5.2.

3. NUCLEAR REACTION CROSS SECTIONS

Three factors govern the expected number of positron-emitters: nuclear reaction cross sections; the number of incoming particles limited by target dose; and the number of target particles. If the flux of the incoming proton beam and the target's particle-density are fixed, the production of positron emitters is determined by the cross section data used in the simulations. Therefore, the reliability of such data is essential to predicting positron-emitter production. However, the available data are very limited because there are very few experimental measurements of these reactions, especially in the energy range below 50 MeV. To demonstrate the differences in the results, in this study, we used four sets of nuclear reaction cross section data for comparison:

1. Data extracted from the emission spectra of recoils in the ENDF electronic file of the ICRU Report 63[23] (2000) used by Beebe-Wang et al.[13]
2. Data from "Experimental Nuclear Reaction Data File (EXFOR)"[24] maintained by the National Nuclear Data Center (BNL) used by Parodi et al.[8]
3. Data from TERA 95/19 TRA15[25] (1995) used by Del Guerra et al.[26]
4. Data from eight different resources published during 1962–1996, and collected by Litzenberg for his Ph.D. dissertation.[18]

The cross section data on the six main production channels amongst these four sources are compared in Figures 5.1–5.6. In the higher energy range, where some data were lacking, extrapolation was used to extend the data to 250 MeV.

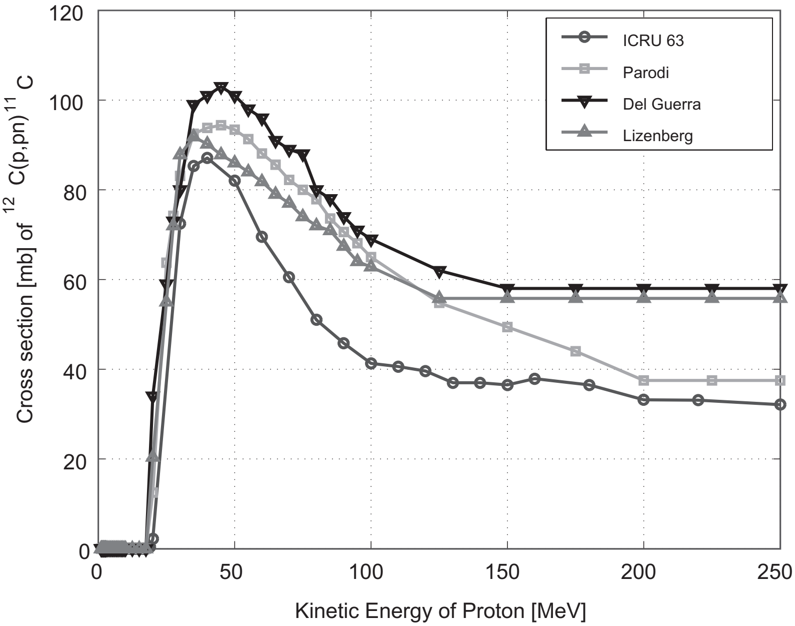

Figure 5.1 Nuclear reaction cross sections of ^{12}C(p, pn)^{11}C. The data from four different resources are compared.

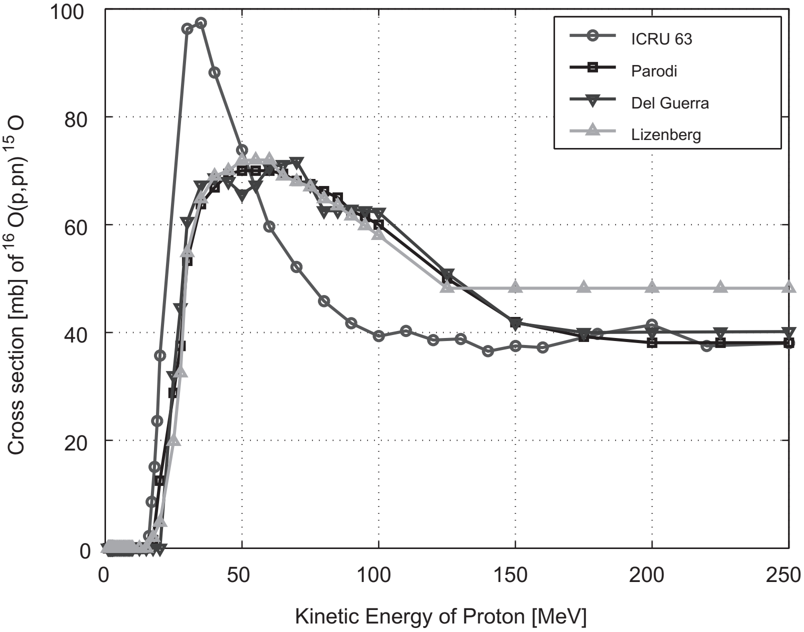

Figure 5.2 Nuclear reaction cross sections of ^{16}O(p, pn)^{15}O. The data from four different resources are compared.

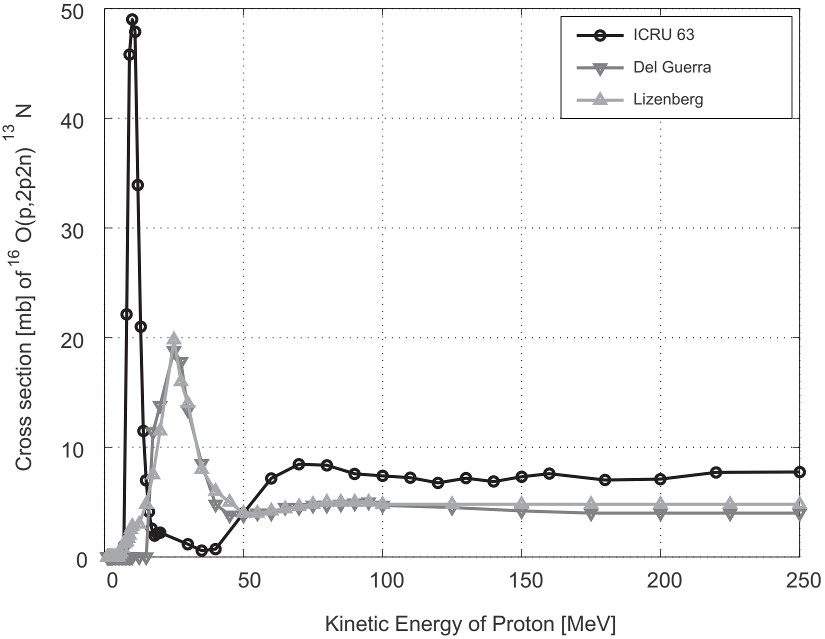

Figure 5.3 Nuclear reaction cross section of ^{16}O(p, 2p2n)^{13}N. The data from three different resources are compared.

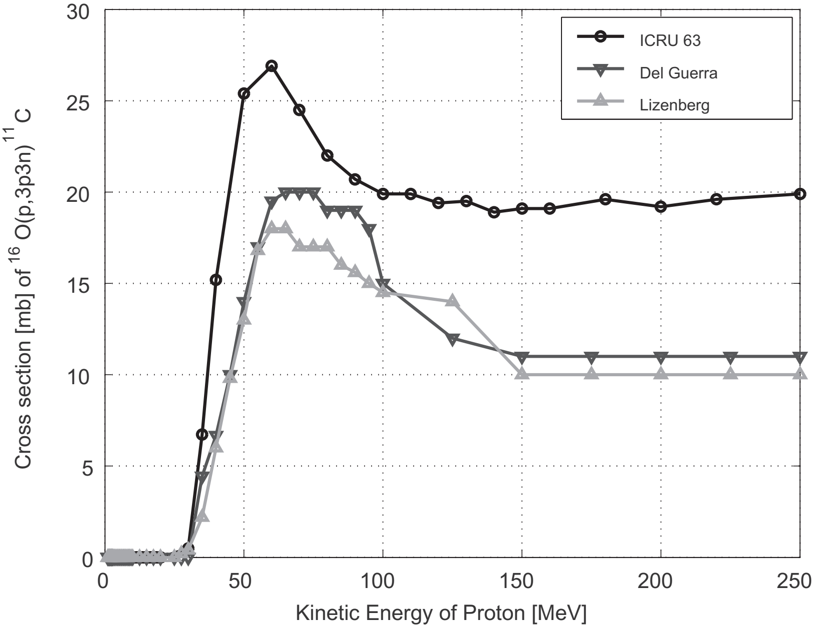

Figure 5.4 Nuclear reaction cross section of ^{16}O(p, 3p3n)^{11}C. The data from three different resources are compared.

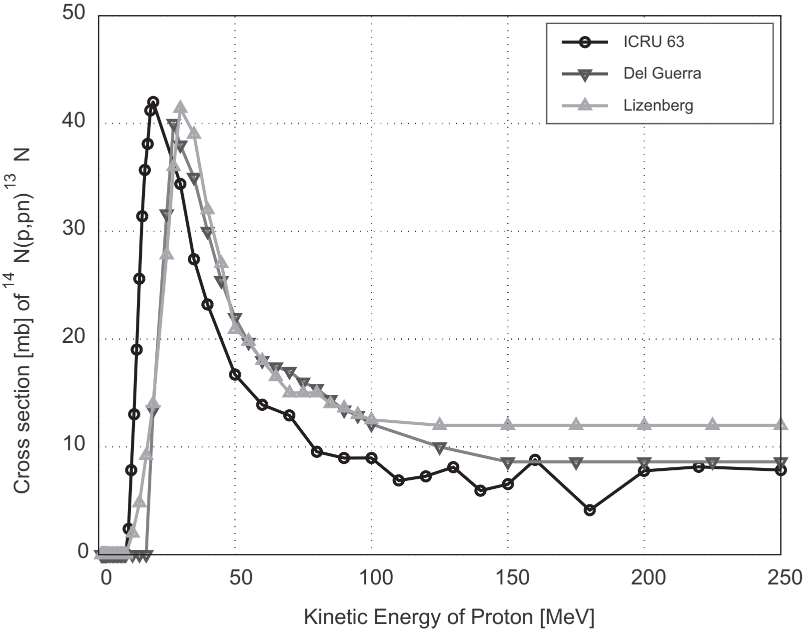

Figure 5.5 Nuclear reaction cross section of ^{14}N(p, pn)^{13}N. The data from three different resources are compared.

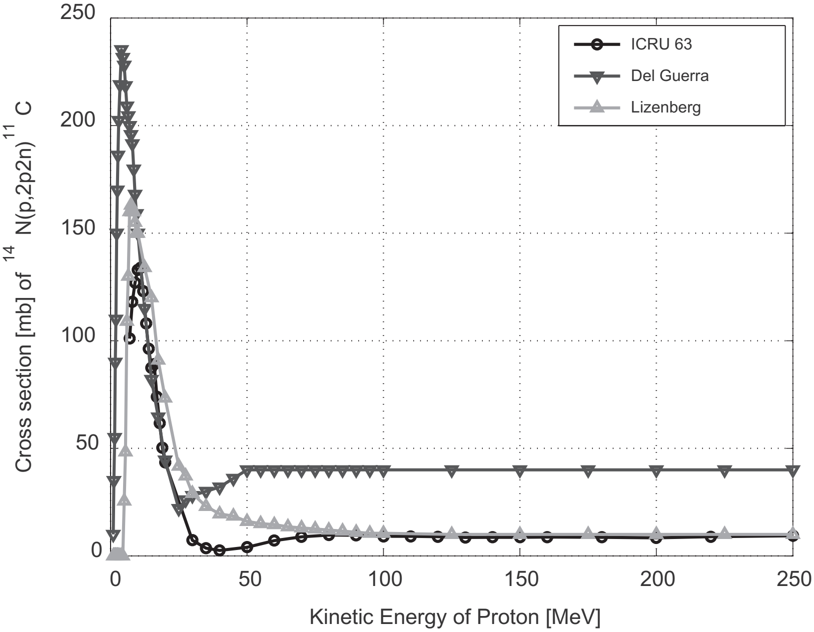

Figure 5.6 Nuclear reaction cross section of ^{14}N(p, 2p2n)^{11}C. The data from three different resources are compared.

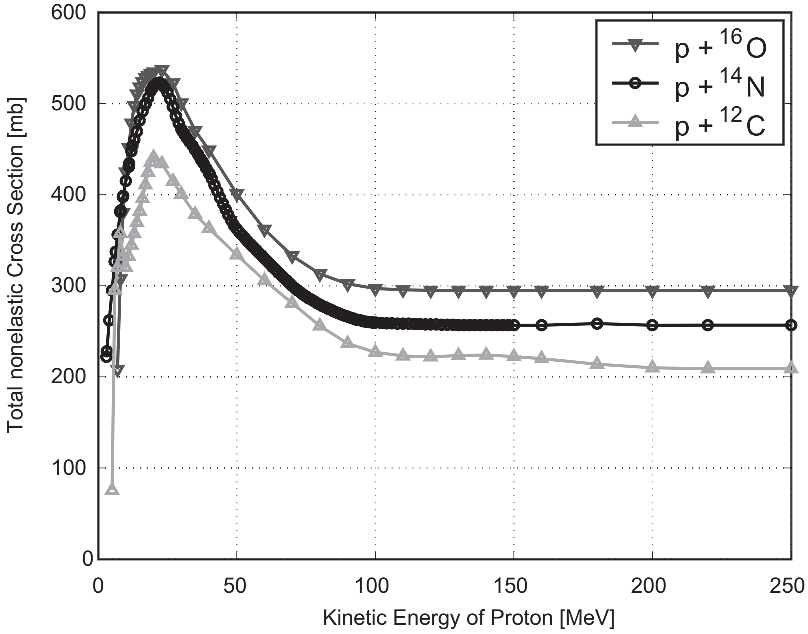

Figure 5.7 Total non-elastic nuclear reaction cross sections of protons incident on ^{16}O, ^{14}N, and ^{12}C as functions of kinetic energy.[23]

The number of particles, protons, and produced particles through nuclear interactions deposited at the end of the proton beam's track is governed by the initial flux of the proton beam and the probabilities of proton interactions with nuclei. The total non-elastic nuclear cross sections of protons incident on ^{16}O, ^{14}N, and ^{12}C are important to this study, as well as to treatment planning, since the accuracy of predicting the dose in the target volume (tumor) is limited by their exactness. Figure 5.7 shows the total non-elastic cross section of protons incident on ^{16}O, ^{14}O, and ^{12}C as functions of the proton's kinetic energy used in our simulation.[23]

4. MONTE CARLO SIMULATIONS

We used the SRNA-BNL software package originally developed as SRNA-2KG by Ilić et al.;[27–29] we modified the simulation code for this work to include the production of positron-emitter nuclei. SRNA-2KG is a Monte Carlo code employed for assessing proton transport, radiotherapy, and dosimetry. It transports protons, within an energy range of 100 keV–250 MeV, with pre-specified spectra in a 3D geometry through material zones confined by planes and second-order surfaces. SRNA-2KG can treat proton transport in 279 different materials, including elements from $Z=1$ to $Z=98$, and in 181 compounds and mixtures.

The simulation of proton transport is based on the multiple-scattering theory of charged particles, and on a model for compound-nucleus decay after proton absorption in non-elastic nuclear interactions. For each part of the range, the code calculates an average loss of energy[30] with a fluctuation from Vavilov's distribution and with Schulek's correction, and then samples the deflection angle of the protons from Moliere's distribution.[27–29] Benchmarking SRNA-2KG against the well-known programs GEANT,[17] and PETRA[31] demonstrated very good agreement under the same conditions.

The positron emitters ^{11}C, ^{13}N, and ^{15}O are created through the decay processes of compound nuclei that include the emission of protons, deuterons, tritons, alpha particles, or photons. The decay products are sampled using Poisson's distribution, with the appropriate average multiplication factors for each particle. The energy and angle of particle emissions, and the multiplication factors, are obtained from comparing the direct cross sections available for reaching the daughter nuclei with that from integrating the differential cross sections for non-elastic nuclear interactions (see Figs. 5.1–5.6). Sampling of the emission spectra yields the energy and angle of secondary neutron emission. The transport of secondary protons follows that of primary protons of that particular energy. The spatial location and the angle of the neutron and the photon are recorded, but are not treated further. The emitted deuterons, tritons, and alpha particles are assumed to be absorbed where they were created.

The study was for a typical absorbed dose (2 Gy) in a typical target volume (5 cm diameter), achieved by modulating the kinetic energies of five beam pulses so that the depths of the Bragg peaks are located 1 cm apart. The relative beam intensities were 1.0, 0.39, 0.31, 0.24, and 0.22 from the highest to the lowest energy pulse. Proton beams of 2 mm diameter, with kinetic energies up to 250 MeV and a zero divergence angle were transported in a human tissue using the SRNA-BNL simulation code. The soft tissue in the simulation had a 0.55 ratio of the averaged atomic number to atomic mass (Z/A), and a density of 1.0 g/cm.[3] Its elemental composition was 10.11% hydrogen, 11.11% carbon, 2.60% nitrogen, and 76.18% oxygen (ICRU 4-component). The estimated number of protons producing an absorbed dose of 2 Gy at the Bragg peak of a single pulse was 2×10^7.

The positron emitter spatial distributions were simulated with the cross section data from ICRU Report 63 (see Ref. 23) shown by the curves with the circle markers in Figures 5.1–5.6; these data are more recent and more complete in the low-energy range than those from other sources. To reduce random noise, the values are obtained from averaging 45 sets of simulation data.

To obtain a realistic PET image from the resulting distribution of positron emitters, we simulated PET data using the SimSET Monte Carlo PET scanner simulation package.[32] SimSET handles the most important aspects of the image formation process, including photon attenuation and scatter, the geometry and photon acceptance of the tomograph, and binning of the coincidence data. For this study, we introduced modifications at BNL to accommodate a block detector layout, and standard 3D sinogram binning. We simulated a clinical whole-body HR+ tomograph (Siemens, Knoxville, TN) with the proton beam direction aligned with the scanner's axis. The attenuation map of a typical human head (ellipse with axes of 15 cm and 18 cm in the transaxial planes) provided more realistic statistics. We reconstructed the output sinograms into volumetric images using the standard filtered backprojection technique.

In order to estimate the mean and variance of the PET signal, we produced 100 statistically independent PET data sets with SimSET using the same input positron distribution. Each PET image was processed by summing the activity over each transaxial plane, resulting in a 1D depth profile of the PET image. From all 100 profiles, an average and standard deviation were calculated for each depth position. Furthermore in order to reduce statistical fluctuations, each profile was also fit to a polynomial and the mean and standard deviation vs. depth similarly calculated.

5. RESULTS

The results of linear production densities of ^{15}O, ^{13}N, and ^{11}C are presented, respectively, in Figures 5.8–5.10. On the right-hand side of these figures, we added a vertical scale of the energy absorbed by the tissue to allow comparisons at depth. These positron emitter distributions were

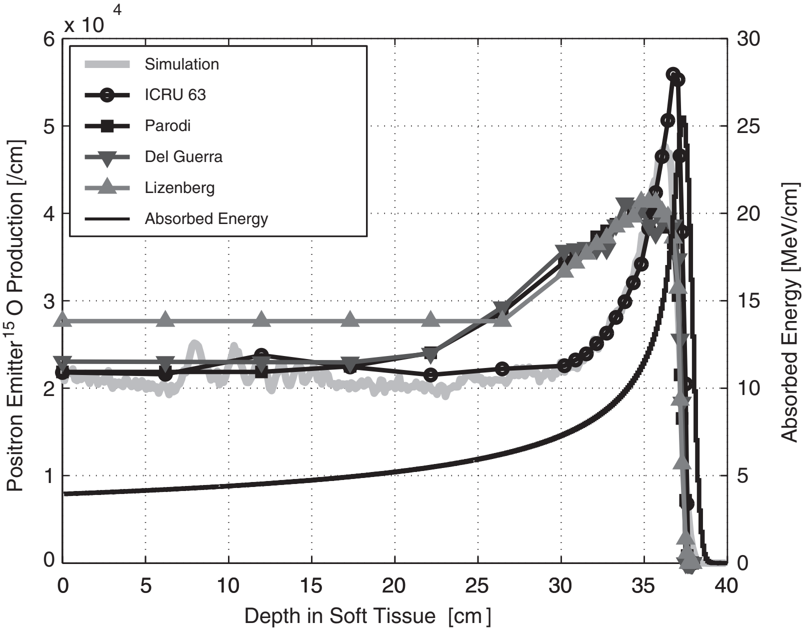

Figure 5.8 The estimated production of ^{15}O israpy session. The distributions are shown from the simulation and the calculations with four different cross section data resources.

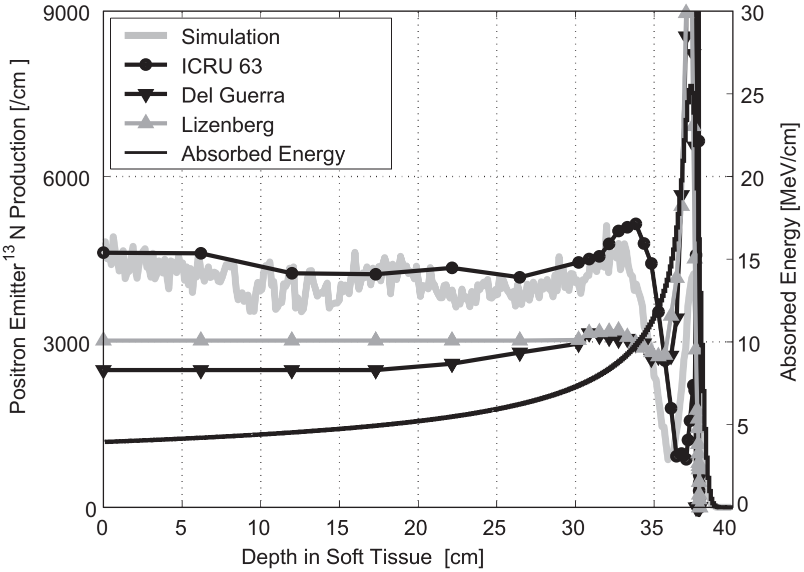

Figure 5.9 The estimated production of ^{13}N isotopes during a single pulse-proton-therapy session. The distributions are shown from the simulation and the calculations with four different cross section data resources.

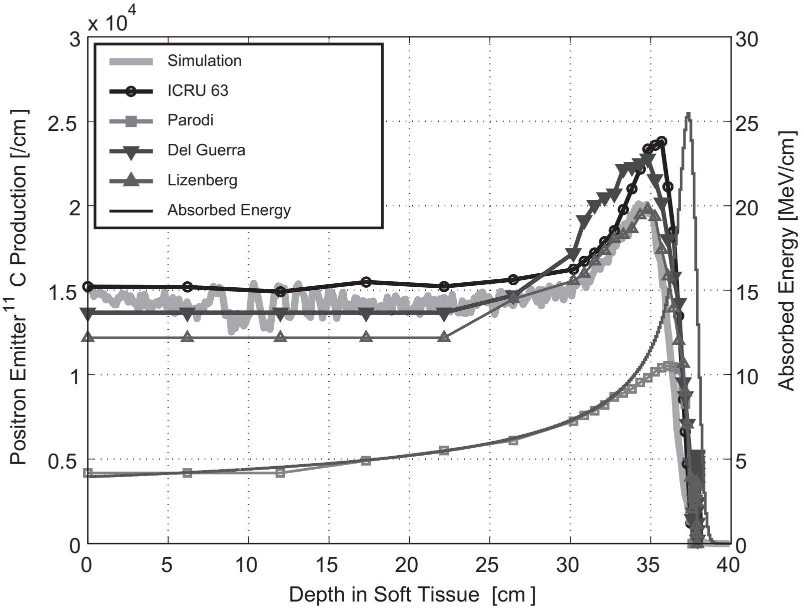

Figure 5.10 The estimated production of ^{11}C isotopes during a single pulse-proton-therapy session. The distributions are shown from the simulation and the calculations with four different cross section data resources.

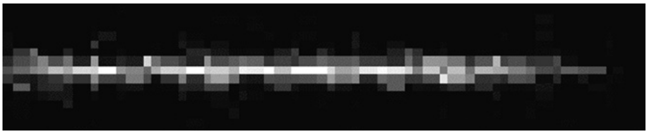

Figure 5.11 A 1.7 mm thick coronal slice through the activity distribution of the 3D PET image. The beam entered from the left. The horizontal (axial) dimension is 15.5 cm (full scanner FOV). Pixel size is 2.4 mm horizontal by 1.7 mm vertical.

used as inputs to obtain the PET images using the SimSET Monte Carlo tomograph simulation.

Figure 5.11 is a coronal slice from a reconstructed PET image. Despite only about 14,000 coincidence counts in the entire image, the narrow trans-axial distribution and lack of background activity afford sufficient contrast to define the distribution. Figure 5.12 depicts the expected PET image's activity

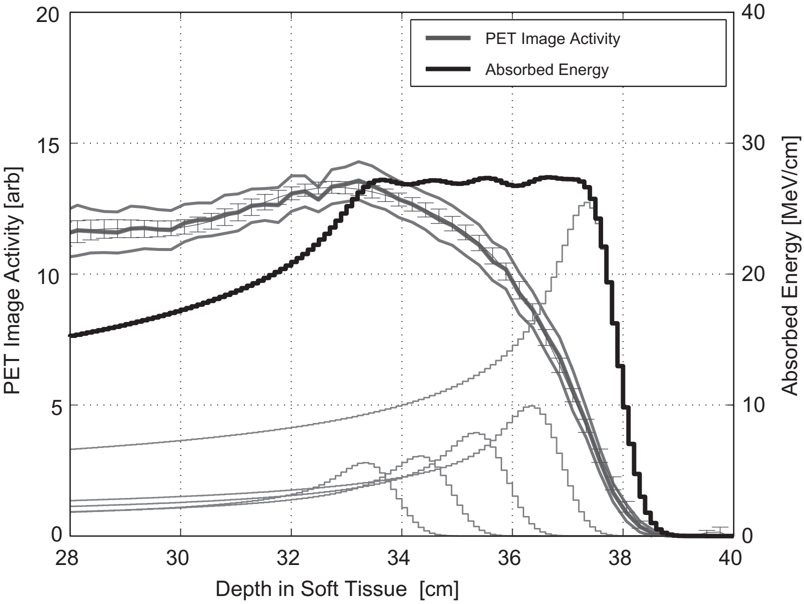

Figure 5.12 Average PET activity (dark gray curves) and its standard deviation (light gray curves), determined from 100 statistically independent PET images. The "spread-out Bragg peak" (thick black curve), created by five proton beam pulses (thin black curves), is superimposed with a right-side vertical scale for depth comparison. The PET results were also processed with a simple algorithm of polynomial curve fit. The average value of the processed data (the thin curve through the middle of the error bars) is coincident with the expected PET image activity (dark gray curve) with a much smaller standard deviation (error bars) compared to unprocessed data (light gray curves).

signal (dark gray curve) and its standard deviation (light gray curves), determined by the data extracted from the 100 sets of PET images. The "spread-out Bragg peak" (thick black curve), created by five proton beam pulses (thin black curves), is superimposed with a right-side vertical scale in Figure 5.12 for depth comparison. Figure 5.12 reveals that, with the help of a simple polynomial fit, the fitted data (the thin curve through the middle of the error bars) retains its fidelity to the raw data (dark gray curve) but has a much smaller standard deviation (error bars) compared to unprocessed data (light gray curves). We assessed that the depth at half maximum of the distribution of the PET-image activity was 6.3 mm from the end of the "spread-out Bragg peak" in the soft tissue. Based on the projection of the error bars onto the depth axis at that point, we estimate an error of about 1 mm.

6. DISCUSSION AND CONCLUSIONS

Our study has demonstrated that for a typical absorbed dose (2 Gy) in a typical target volume (5 cm diameter) during a proton therapy session, the PET image subsequently acquired has a sufficiently good signal-to-noise ratio to determine the depth of the Bragg peak to approximately 1 mm accuracy. Note that this accuracy reflects the error due only to the PET imaging process, as the error analysis was carried out with multiple statistical realizations of a fixed input positron distribution. The accuracy of this method in a clinical setting is expected to be lower for a variety of practical reasons, including cross section estimates as discussed below. We also demonstrated, using our simple algorithm of polynomial curve fit, that simple PET image analysis software could increase the prediction accuracy on the depth of the Bragg peak. Future clinical applications require the development of a more advanced and robust algorithm for fitting the PET data in the presence of noise. The ultimate goal of such work is comparing the radioisotope distribution measured by PET with the yield of positron emitters predicted from the treatment planning code. Matching these two implies that the treatment conformed to the plan. For treatment involving multiple ports, including some with opposing angles, the centroid of the target dose can be also computed with that of the PET image.

We also demonstrated the differences in the predicted distributions of the positron emitters produced by employing cross section data from different resources. In depths less than 30 cm, the linear density of the isotopes is almost without structure, reflecting the fact that the cross sections remain almost unchanged in the energy range above 100 MeV. Within this range, the yields calculated with cross section data from four different resources agree fairly well with each other. The exception is the level of ^{11}C isotope production obtained with data used in Ref. 8. Its production is only about 30% of that obtained using other data sources. Apparently, this is mainly because the cross section data used in Ref. 8 accounts for only one of the three major channels producing the ^{11}C isotope.[26] In the depth range between 30 cm and 38 cm where the Bragg peak is located, the calculated productions for all three isotopes are significantly different (Figs. 5.8–5.10). The high yield of ^{13}N and ^{15}O calculated with information from ICRU 63 report[23] is credited to the cross section data on reactions ^{16}O(p, 2p2n)^{13}N and ^{16}O(p, pn)^{15}O in the low-energy range that became available only during year 2000.

As we mentioned in Section 3 the total non-elastic nuclear-reaction cross sections for protons incident on ^{16}O, ^{14}N, and ^{12}C are also important to this study and to the treatment planning, since their accuracy limits the precision of dose prediction in the target volume (tumor).

This investigation points to the on-going need to develop a library of accurate cross section data for proton- and neutron-induced reactions on the elements in human tissue. A reliable simulation or calculation depends upon the accuracy of such data, especially for investigations in the region near the Bragg peak where accurate cross section information in the low energy range (below 50 MeV) is needed. This is critical to the success of PET imaging for verifying the location of the Bragg peak of the proton beam, and for dosimetry.

ACKNOWLEDGMENTS

The authors would like to thank Dr. R.D. Ilić and the Imaging Research Lab at the University of Washington for providing the SRNA-2KG and SimSET software packages.

REFERENCES

1. Amaldi, U.; Kraft, G. Radiotherapy with beams of carbon ions. *Rep. Prog. Phys.* **2005**, *68*, 1861.
2. Belkić, Dž. Reviews of theories on ionization in fast ion-atom collision with prospects for applications to hadron therapy. *J. Math. Chem.* **2010**, *47*, 1366.
3. Enghardt, W.; Parodi, K.; Crespo, P., et al. Dose quantification from in-beam positron emission tomography. *Radiother. Oncol.* **2004**, *73*, S96.
4. Andreo, P. On the clinical spatial resolution achievable with protons and heavier charged particle radiotherapy beams. *Phys. Med. Biol.* **2009**, *54*, N205.
5. Paganatti, H. Range uncertainties in proton therapy and the role of Monte Carlo simulations. *Phys. Med. Biol.* **2012**, *57*, R99.
6. Paans, A. M. J.; Schippers, J. M. Proton Therapy in combination with PET as monitor: a feasibility study. *IEEE Trans. Nucl. Sci.* **1993**, *40*, 1041.
7. Oelfke, U.; Lam, G. K.; Atkins, M. S. Proton dose monitoring with PET: quantitative studies in Lucite. *Phys. Med. Biol.* **1996**, *41*, 177.

8. Parodi, K.; Enghardt, W.; Haberer, T. In-beam PET measurements of β+ radioactivity induced by proton beams. *Phys. Med. Biol.* **2002**, *47*, 21.
9. Knopf, A.; Parodi, K.; Paganetti, H., et al. Quantitative assessment of the physical potential of proton beam range verification with PET/CT. *Phys. Med. Biol.* **2008**, *53*, 4137.
10. Knopf, A.; Parodi, K.; Bortfeld, T., et al. Systematic analysis of biological and physical limitations of proton beam range verification with offline PET/CT scans. *Phys. Med. Biol.* **2009**, *54*, 4477.
11. Ferrero, M. I.; Ragona, R.; Rolando, V., et al. Monte Carlo simulation of a Protontherapy system for the calculation of the dose distribution in a patient, TERA 94/5 TRA 14, 1995.
12. Parodi, K.; Enghardt, W. Potential application of PET in quality assurance of proton therapy. *Phys. Med. Biol.* **2000**, *45*, N151.
13. Beebe-Wang, J.; Dilmanian, F. A.; Peggs, S., et al. PET Imaging of dose distribution in proton-beam cancer therapy. *Nucl. Tech. Radiat. Protect.* **2005**, *XX*, 23.
14. Pshenichnov, I.; Mishustin, I.; Greiner, W. Distributions of positron-emitting nuclei in proton and carbon-ion therapy studied with GEANT4. *Phys. Med. Biol.* **2006**, *51*, 6099.
15. Fasso, A.; Ferrari, A.; Ranft, J., et al. FLUKA: a Multi-particle Transport Code, CERN-2005-10, INFN/TC_5/11, SLAC-R-773, 2005.
16. Agostinelli, S.; Allison, J.; Amako, K., et al. GEANT4—a simulation toolkit. *Nucl. Instrum. Methods Phys. Res. A* **2003**, *506*, 250.
17. Gudowska, I.; Sobolevsky, N.; Andreo, P., et al. Ion beam transport in tissue-like media using the Monte Carlo code SHIELD-HIT. *Phys. Med. Biol.* **2004**, *49*, 1933.
18. Litzenberg, D. W. On-line monitoring and PET imaging of the positron-emitting activity created in tissue by proton radiotherapy beams. Ph.D. Thesis, University of Michigan, 1997.
19. Sommerer, F.; Parodi, K.; Ferrari, A., et al. Investigating the accuracy of the FLUKA code for transport of therapeutic ion beams in matter. *Phys. Med. Biol.* **2006**, *51*, 4385.
20. Parodi, K.; Ferrari, A.; Sommerer, F., et al. A MC tool for CT-based calculations of dose delivery and activation in proton therapy. *J. Phys.: Conf. Ser.* **2007**, *74*, 021013.
21. Parodi, K.; Ferrari, A.; Sommerer, F., et al. Clinical CT-based calculations of dose and positron emitter distributions in proton therapy using the FLUKA Monte Carlo code. *Phys. Med. Biol.* **2007**, *52*, 3369.
22. Paganetti, H.; Jiang, H.; Parodi, K., et al. Clinical implementation of full Monte Carlo dose calculation in proton beam therapy. *Phys. Med. Biol.* **2008**, *53*, 4825.
23. ICRU 63, Nuclear data for neutron and proton radiotherapy and for radiation, ICRU Report 63, 2000.
24. Experimental Nuclear Reaction Data File, Energy Sciences and Technology Department, BNL. <http://www.nndc.bnl.gov/nndc/exfor/>.
25. Mukhopadhyay, D.; Del Guerra, A.; Di Domenico, O. For PET- monitored hadron therapy, TERA 95/19 TRA15, 1995.
26. Del Guerra, A.; Di Domenico, O. Positron Emission Tomography as an aid to in "vivo" dosimetry for proton radiotherapy: a Monte Carlo simulation, TERA 93/10 TRA 9, 1993.
27. Ilić, R. D. *SRNA-2KG—Proton Transport Simulation by Monte Carlo Techniques*. Institute of Nuclear Sciences Vinca, Phys. Lab. (010), Beograd, Yugoslavia, 2002.
28. Ilić, R. D.; Spasić-Jokić, V.; Belićev, P., et al. The Monte Carlo SRNA code as the engine in ISTAR proton dose planning software for the TESLA accelerator installation. *Nucl. Tech. Radiat. Protect.* **2004**, *XIX*, 30.
29. Ilić, R. D.; Spasić-Jokić, V.; Belićev, P., et al. The Monte Carlo SRNA-VOX code for 3D proton dose distribution in voxelized geometry using CT data. *Phys. Med. Biol.* **2005**, *50*, 1011.

30. Stopping power and ranges for protons and alpha particles, ICRU Report 49, 1993.
31. Medin, J. Studies of clinical proton dosimetry using Monte Carlo simulation and experimental techniques. Ph.D. Thesis, Stockholm University, 1997.
32. Harrison, R. L.; Vannoy, S. D.; Kaplan, M. S., et al. Slat collimation and cylindrical detectors for PET simulations using simSET. *In IEEE Nuclear Science Symposium Conference. Record* 3, 2005, 20/89.

CHAPTER SIX

Inelastic Collisions of Energetic Protons in Biological Media

Isabel Abril[a], Rafael Garcia-Molina[b*], Pablo de Vera[a], Ioanna Kyriakou[c] and Dimitris Emfietzoglou[c]

[a]Departament de Física Aplicada, Universitat d'Alacant, E-03080 Alacant, Spain
[b]Departamento de Física, Centro de Investigación en Óptica y Nanofísica, Universidad de Murcia, E-30100 Murcia, Spain
[c]Medical Physics Laboratory, University of Ioannina Medical School, GR-45110 Ioannina, Greece

Contents

Abstract

We study the energy deposited by swift proton beams on materials of biological interest, such as liquid water, DNA, and PMMA. An appropriate description of the target energy-loss function, which provides its electronic excitation spectrum, is obtained from available experimental optical data properly extended to non-vanishing momentum transfers. The main magnitudes characterizing the energy-loss distribution of the beam particles in the target are calculated analytically (in the dielectric framework) and compared with available experimental data. The depth–dose distribution of the energy delivered by the proton beam on the biological targets is simulated by the SEICS (Simulation of Energetic Ions and Clusters through Solids) code, which includes the main interaction phenomena between the projectile and the target constituents by means of Molecular Dynamics and Monte Carlo techniques. Also, the proton-beam energy distribution at several depths in the target for liquid water and PMMA are simulated, and finally, the properties of PMMA as a water-equivalent material are discussed.

---

[*] *E-mail address:* rgm@um.es

Advances in Quantum Chemistry, Volume 65
ISSN 0065-3276, http://dx.doi.org/10.1016/B978-0-12-396455-7.00006-6

1. INTRODUCTION

The destruction of malignant tumor cells by using energetic proton beams was suggested in 1946 by Wilson.[1] In less than a decade after this pioneering proposal, animal studies were performed,[2] and later ion therapy was applied to human patients.[3] Presently, there are over 30 ion therapy facilities worldwide, most of which use proton beams either exclusively or in addition to other light ions, and the number is expected to double within the next 5–10 years.[4] The energy delivered by swift ions as a function of the target depth has a nearly flat shape at the entrance of the target and gradually grows up to having a notorious peak almost at the end of their trajectories; this is the so-called Bragg curve. The position and intensity of the Bragg peak depend on the projectile energy and type, as well as on the target nature. The success of using ion, instead of photon or electron, beams for cancer treatment lies in the high energy they can deposit in a delimited region of the tumor volume with a sparing effect to the surrounding healthy tissue. Another important advantage of ion therapy is that the beam particles have larger biological effectiveness than other ionizing radiations,[5] and lower lateral scattering.

The primary beam energies used in ion therapy are typically hundreds of MeV/u for deep-seated tumors; see Ref. 6 for a recent state-of-the-art-review. The energy range below a few MeV/u (for light ions) becomes relevant around the Bragg peak, where the particles exhibit their highest RBE.[7] At the energy range of interest to ion therapy, the dominant slowing down mechanism of the swift projectiles is the electronic energy loss due to ionization and excitation of target atoms.

For a long time the standard input data to Monte Carlo simulation for energy losses due to ionization came from the Bethe–Bloch stopping power formula,[8] which provides energy-loss values for light ions over a wide variety of materials.[9, 10] However, this formula is only sufficiently accurate at high energies. The usefulness of the Bethe–Bloch formula within the Monte Carlo users' community is due to the lack of a general awareness on the existence of better theoretical predictions derived from purely quantum-mechanical methodologies, such as the continuum distorted wave (CDW) method[11] or its simplified version, the continuum distorted wave-eikonal initial state (CDW-EIS) approximation.[12] The interested reader is referred to Ref. 6 for a detailed discussion of the computational advances of these methodologies to obtain cross sections for energetic ion collisions aimed at hadrontherapy applications.

A fundamental problem in extending the Bethe–Bloch theory down to the Bragg peak region is that its two main assumptions, namely, the Born and dipole (or optical) approximations, turn gradually invalid.[13] Specifically, as the projectile velocity decreases, the minimum momentum transfer increases and non-dipole collisions practically dominate over dipole collisions, rendering the dipole approximation invalid. The effect is more pronounced for inner shells associated with large binding energies, the contribution of which to the energy-loss process gradually vanishes at low projectile energy. The so-called shell-corrections to Bethe's theory are meant to account (to first order) for the above effect,[14] but their formal evaluation proceeds through the, generally unknown, generalized-oscillator strength (GOS) or, for condensed targets, the dielectric response function.[15] A common approach is to employ hydrogen-like GOSs for the inner shells and scaling laws for the outer shells ignoring any aggregation and phase effects.[14, 16]

An alternative approach, which becomes particularly suitable for condensed-phase targets, is to use a dynamic and non-local dielectric response function.[17] This is the so-called dielectric approach, having the advantage that shell-corrections are automatically included (as a matter of fact, they are build into the model to all orders); in this manner, the electronic energy loss in the Born approximation can be calculated without resorting to Bethe's dipole approximation. The Lindhard dielectric function of the homogeneous electron gas within the random-phase-approximation (RPA) is most represented in the literature due to its analytic properties which extend over the whole energy–momentum plane.[18]

An analytic dielectric function from first-principles (similar to the one derived by Lindhard) is not available for realistic materials and alternative approaches must be sought for. The extended-optical-data models (or, simply, optical-data models) currently represent the state of the art for constructing an analytic description of the dielectric response function of condensed phase targets regardless of their nature (insulators, semiconductors, or conductors). Powell[19] was perhaps the first to suggest that experimental optical data can be used in inelastic scattering calculations within the dielectric framework. Soon after, Ritchie and Howie[20] put forward a semi-empirical scheme whereby experimental optical data were used to obtain the dependence of the dielectric function on the energy transfer, with physically motivated *extension* algorithms providing the dependence of the dielectric function on momentum transfer. Besides its simplicity, the main advantage of this scheme was that the use of optical data specific to the material being studied automatically accounts for electronic-structure effects in a realistic manner not always possible within the *electron gas* models. The first application of the Ritchie–Howie recipe to ion stopping in solids was made by Ashley[21] using a very simple extension scheme based on the (undamped) plasmon-pole approximation with a quadratic dispersion relation for the dependence of the plasmon energy on momentum transfer.

Several modifications over the original work of Ritchie and Howie[20] have been published (see Ref. 22 for more details). One of the most fruitful is based on the use of the Mermin dielectric function[23] instead of the Drude dielectric function, because the former automatically provides the extension to nonzero momentum transfers. This scheme will be the basis of the target description that enters in the dielectric formalism, to be presented in Section 2. The charge-exchange processes affecting the charge-state of the projectile will be discussed in Section 3, whereas in Section 4 we obtain the main inelastic energy-loss magnitudes for targets of biological interest (liquid water, DNA, and PMMA). These magnitudes are used as input to simulate the depth–dose distribution and the energy delivery of the proton beam through the target, which is discussed in detail in Section 5. Finally, the main conclusions are summarized in Section 6.

2. DIELECTRIC FORMALISM FOR INELASTIC SCATTERING

Based on the plane-wave Born approximation, the dielectric formalism[24, 25] gives simple expressions for the differential inelastic scattering cross section in condensed media, where the charged particle interacts simultaneously with a large number of electrons belonging to different atoms or molecules of the target, which is suitably described by its dielectric function $\epsilon(k,\omega)$, where $\hbar k$ and $\hbar\omega$ are, respectively, the transferred momentum and energy from the projectile to the target electrons. When a swift projectile (with mass M_1, atomic number Z_1, kinetic energy T, and charge q) moves through a target, it induces electronic excitations and ionizations in the material, losing energy in the process. Thus, the double-differential (in energy and momentum transfer) inverse inelastic mean free path (IIMFP) Λ_q of the projectile, is given by

$$\frac{\mathrm{d}^2\Lambda_q(T,\omega)}{\mathrm{d}\omega\,\mathrm{d}k} = \frac{e^2}{\hbar^2\pi}\frac{M_1[Z_1-\rho_q(k)]^2}{T}\frac{1}{k}\mathrm{Im}\left[\frac{-1}{\epsilon(k,\omega)}\right], \tag{1}$$

where e is the absolute value of the electron charge and $\rho_q(k)$ is the Fourier transform of the projectile electronic charge density. It can clearly be observed the contribution of two factors: one of them only depends on the projectile, $M_1[Z_1 - \rho_q(k)]^2/T$, and the other only depending on the target properties through the energy-loss function (ELF), $\mathrm{Im}\,[-1/\epsilon(k,\omega)]$. The latter accounts in an effective and compact way for the target electronic spectrum corresponding to excitations or ionizations of individual electrons or even excitations of collective modes in the condensed medium. The macroscopic inelastic scattering cross section σ is related to the IIMFP by the relation $\Lambda = \mathcal{N}\sigma$, where $\mathcal{N}$ is the atomic (or molecular) density of the target.

The dielectric formalism avoids the difficulty of multi-electron transitions by considering either individual ionizations or collective excitations, but the interested reader should be aware of recent advances in treating two-electron transitions in atomic targets.[26]

Within the dielectric formalism the relevant magnitudes describing the projectile energy-loss distribution can be obtained from the double-differential inelastic cross section (Eq. (1)) by suitable integrations over the energy $\hbar\omega$ and momentum $\hbar k$ transfers. The single-differential (in energy transfer) inverse inelastic mean free path is found by integrating Eq. (1) over the momentum transfer $\hbar k$, which represents the probability per unit path length $P_q(T,\omega)$ that a projectile with charge-state q and energy T produces in the target an inelastic process of energy $\hbar\omega$ (i.e., individual and collective electronic excitations as well as ionizations), irrespective of the momentum transferred. This probability is

$$P_q(T,\omega) = \frac{\mathrm{d}\Lambda_q(T,\omega)}{\mathrm{d}\omega} = \frac{M_1 e^2}{\pi\hbar^2 T}\int_{k_{\min}}^{k_{\max}} \frac{\mathrm{d}k}{k}[Z_1 - \rho_q(k)]^2 \mathrm{Im}\left[\frac{-1}{\epsilon(k,\omega)}\right]; \tag{2}$$

for heavy projectiles, when $M_1 \gg m_e$ (where m_e is the electron mass), the integration limits can be approximated by $k_{\max} \approx \infty$ and $k_{\min} = \omega/\sqrt{2T/M_1}$.

Hence, the moments of the electronic energy-loss distribution can be found by integrating Eq. (2) over the transferred energy $\hbar\omega$. In consequence the total inverse inelastic mean free path, will be obtained by

$$\Lambda_q(T) = \int_0^\infty \mathrm{d}(\hbar\omega) P_q(T,\omega). \tag{3}$$

The stopping power (or stopping force) represents the mean electronic energy lost by the projectile per unit path length, and is given by

$$S_q(T) = \int_0^\infty \mathrm{d}(\hbar\omega)\hbar\omega P_q(T,\omega). \tag{4}$$

Analogously, the energy-loss straggling, which represents the mean square deviation per unit path length of the energy-loss distribution, can be obtained through

$$\Omega_q^2(T) = \int_0^\infty \mathrm{d}(\hbar\omega)(\hbar\omega)^2 P_q(T,\omega). \tag{5}$$

In order to obtain these stopping magnitudes, Eqs. 3–5, the description of the projectile charge density and the target excitation spectrum by means of its energy-loss function (ELF) are needed. In particular in this work we will restrict to the study of energetic protons beams incident in media of biological, such as liquid water, DNA, or PMMA.

2.1 Projectile description: electronic charge density

The charge density of the projectile is described by the statistical model proposed by Brandt and Kitagawa (BK),[27] where the effective charge of energetic ions is calculated in the dielectric response approximation. The projectile, with atomic number Z_1 has N bound electrons and moves with velocity v with respect to the target electrons. The BK model presupposes that the cloud of bound electrons is screening the projectile nucleus over a radius Υ that depends on the projectile velocity. Therefore, target electrons that approach the projectile with impact parameters larger than Υ (that is, distant collisions) perceive the projectile as a point charge with charge $q = (Z_1 - N)e$, irrespective of its internal structure. However, when the impact parameter is smaller than Υ (i.e., close collisions) the target electrons penetrate the screening cloud of the bound electrons of the projectile, sensing a partially screened potential corresponding to a projectile charge larger than q. An average over all the impact parameters will give the charge of the projectile, that determines their energy loss.

The Brandt and Kitagawa model[27] characterizes the bound electrons of the projectile by a generic orbital, where the screening radius Υ is treated as a variational parameter. In order to derive analytical results, the electronic charge density of the projectile is described by the simple expression:

$$\rho_q(r) = \frac{N}{4\pi\Upsilon^3}\frac{\Upsilon}{r}e^{-r/\Upsilon}, \tag{6}$$

where r is the distance to the projectile nucleus. The internal energy of the projectile can be written as:

$$E = E_{\mathrm{en}} + \lambda E_{\mathrm{ee}} + E_{\mathrm{kin}}, \tag{7}$$

where E_{en} is the potential energy from electron–nucleus interaction, E_{ee} is the potential energy from the electron–electron interaction weighted by the variational parameter λ, and E_{kin} is the electron kinetic energy. After applying the following conditions to the energy:

$$\frac{\mathrm{d}E}{\mathrm{d}\Upsilon} = 0, \tag{8}$$

$$\left.\frac{\mathrm{d}E}{\mathrm{d}N}\right|_{N=Z_1} = 0, \tag{9}$$

the following value for the screening radius Υ is obtained:

$$\Upsilon = \frac{0.48N^{2/3}}{Z_1 - \lambda N/4} a_0, \tag{10}$$

with $\lambda = 4/7$, and a_0 is the Bohr radius ($a_0 = 0.529 \times 10^{-10}$ m).

A modification of the parameter Υ was introduced when there are $N=1$ or 2 bound electrons:[28]

$$\Upsilon = \frac{3}{2[Z_1 - 0.3(N-1)]} a_0. \tag{11}$$

From Eq. (6) we obtain the Fourier transform of the electronic charge density of the projectile

$$\rho_q(k) = \frac{N}{1 + (k\Upsilon)^2}, \tag{12}$$

with Υ given by Eq. (10) (or Eq. (11) when the projectile has only 1 or 2 bound electrons).

2.2 Target description: Electronic excitation spectrum

The ELF of the material as a function of the momentum and energy transfer is known as the Bethe surface, and it contains all the information about the electronic excitations that the target can sustain.

Experimental information of the ELF of a medium can be obtained from the analysis of the spectra of photon or electron beams interacting with the material. For many materials there are available optical data of the ELF (i.e., at zero momentum transfer, $k = 0$) over the valence excitation range up to ~100 eV. To obtain information of the ELF at $k \neq 0$, electron-energy-loss spectroscopy (EELS) is typically used, where the spectra of the electrons at different scattering angles correspond to different momentum transfers. However, due to multiple scattering effects it is almost impracticable to obtain information of the ELF at high momentum transfers. Therefore to avoid this experimental difficulty it is necessary to have theoretical models that provide the Bethe surface in a broad range of energy and momentum transfers. Theoretical calculations from first-principles are very hard for condensed media, then semi-empirical calculations using optical-data models are generally employed.[19,20] They utilize the ELF at the optical limit, $k = 0$, from the experimental data together with a theoretical model to make the proper extension at $k \neq 0$. These models can be applied to study the inelastic scattering of swift projectiles in any material (metal, semiconductor, or insulator), and their major advantage consists in the incorporation of the (individual and collective) excitations of the target, taking into account the aggregation and chemical effects inherent to condensed matter, since they are based on experimental ELF.[29]

In this work we use the MELF–GOS model (Mermin-Energy-Loss-Function–Generalized-Oscillator Strength) to describe the energy-loss spectrum of the target.[30,31] Here the target electron excitations are split into two parts, one related to excitations of the inner-shell electrons, and the other resulting from excitations of the outer (weakly bound) electrons, namely

$$\mathrm{Im}\left[\frac{-1}{\epsilon(k,\omega)}\right] = \mathrm{Im}\left[\frac{-1}{\epsilon(k,\omega)}\right]_{\text{inner}} + \mathrm{Im}\left[\frac{-1}{\epsilon(k,\omega)}\right]_{\text{outer}}. \qquad (13)$$

The inner-shell electrons keep their atomic character due to their large binding energies, where the excitation spectrum is insensitive to the target phase. So a suitable and useful approximation is to describe those electrons by their generalized oscillator strengths in the hydrogenic approach, as if they were bound to isolated atoms. The connection between the ELF and the GOS model for a compound $\mathrm{A}_{\alpha_1}\mathrm{B}_{\alpha_2}\ldots$ is given by[15]

$$\mathrm{Im}\left[\frac{-1}{\epsilon(k,\omega)}\right]_{\text{inner}} = \frac{2\pi^2\mathcal{N}}{\omega}\sum_j \alpha_j \sum_{nl} \frac{\mathrm{d}f_{nl}^{(j)}(k,\omega)}{\mathrm{d}\omega}\Theta\left(\omega - \omega_{\text{ioniz},nl}^{(j)}\right), \qquad (14)$$

where $\mathcal{N}$ is the molecular density of the target, α_j is the stoichiometric contribution of the different elements in the compound, $\mathrm{d}f_{nl}^{(j)}(k,\omega)/\mathrm{d}\omega$ and $\omega_{\text{ioniz},nl}^{(j)}$ are, respectively, the GOS and the ionization energy of the (n,l) sub-shell of the j-element of the target, finally, Θ is the step function. The summation in Eq. (14) must be extended over all the inner shells of all the atoms in the compound.

The collective and single-particle excitations of the outer electrons of the target are described by fitting the experimental optical ELF ($k = 0$) to a linear combination of Mermin-type ELFs,[23]

$$\begin{aligned}\operatorname{Im}\left[\frac{-1}{\epsilon(k=0,\omega)}\right]_{\text{outer}} &= \operatorname{Im}\left[\frac{-1}{\epsilon(k\approx 0,\omega)}\right]_{\text{exp}} \\ &= \sum_i \frac{A_i}{\omega_i^2}\operatorname{Im}\left[\frac{-1}{\epsilon_{\mathrm{M}}(\omega_i,\gamma_i;k=0,\omega)}\right]\Theta(\omega-\omega_{\text{th},i}),\end{aligned} \tag{15}$$

where ϵ_{M} is the Mermin dielectric function,[23] which can be expressed in terms of the Lindhard dielectric function ϵ_{L} of complex energy as

$$\epsilon_{\mathrm{M}}(k,\omega) = 1 + \frac{(1+i\gamma/\omega)[\epsilon_{\mathrm{L}}(k,\omega+i\gamma)-1]}{1+(i\gamma/\omega)[\epsilon_{\mathrm{L}}(k,\omega+i\gamma)-1]/[\epsilon_{\mathrm{L}}(k,0)-1]}. \tag{16}$$

The Mermin dielectric function goes beyond the Lindhard dielectric function, since it includes plasmons with a finite lifetime (i.e., damped) at any momentum transfer, as it happens in real materials. In the above expression γ is a phenomenological damping constant that represents phonon-assisted electronic transitions via electron–ion collisions. At the limit of zero damping, the Mermin dielectric function recovers the Lindhard dielectric function.

The parameters ω_i, γ_i, and A_i in Eq. (15) are related, respectively, to the position, width, and intensity of the ith peak in the target experimental-ELF, which are determined by a fitting to experimental optical data; $\hbar\omega_{\text{th},i}$ is a threshold energy. At the optical limit ($k = 0$), the Mermin-ELF is identical to the Drude-ELF, therefore the following expression can be used to obtain the fitting parameters ω_i, γ_i, and A_i:

$$\operatorname{Im}\left[\frac{-1}{\epsilon_{\mathrm{M}}(\omega_i,\gamma_i;k=0,\omega)}\right] = \frac{\omega_i^2\omega\gamma_i}{(\omega_i^2-\omega^2)^2+(\omega\gamma_i)^2}. \tag{17}$$

One of the main benefits of the MELF–GOS method is that once the fitting of the ELF in the optical limit is made, the ELF is analytically and automatically extended to $k \neq 0$ through the properties of the Mermin dielectric function and the GOS model.[31,32] So, dispersion relations schemes, as in other optical-data models, are not necessary (see Refs. 22, 33 for a detailed discussion of different dispersion relation schemes). Thus, from the experimental optical-ELF the MELF–GOS model provides the whole Bethe surface of the target.

The ELF constructed in this manner must be consistent with physically motivated constrains. Then, the ELF must satisfy the f-sum rule at any k (Ref. 22)

$$N_{\mathrm{eff}}(\omega) = \frac{m_{\mathrm{e}}}{2\pi^2 e^2 \mathcal{N}} \int_0^{\omega} \mathrm{d}\omega' \, \omega' \, \mathrm{Im}\left[\frac{-1}{\epsilon(k,\omega')}\right], \tag{18}$$

which gives the effective number of target electrons per molecule that participate in inelastic collisions with energy transfer up to a maximum value $\hbar\omega$. When the transferred energy $\hbar\omega$ goes to infinity, then $N_{\mathrm{eff}}(\omega \to \infty)$ tends to the target atomic number. As the f-sum rule of Eq. (18) is more sensible to high-energy transfers (corresponding to inner-shell electrons), the ELF must also fulfill further sum rules, such as the Kramers–Kronig (KK) (or perfect screening) sum-rule, which is more sensitive to the low-part of the excitation spectrum. The KK sum rule is given by[22]

$$\mathrm{KK}(\omega) = \frac{2}{\pi} \int_0^{\omega} \mathrm{d}\omega' \frac{1}{\omega'} \mathrm{Im}\left[\frac{-1}{\epsilon(k=0,\omega')}\right] + n^{-2}(0), \tag{19}$$

where $n(0)$ is the refractive index at low-energy transfer. When the energy transfer goes to infinity the KK-sum rule tends to unity.

2.2.1 Optical energy-loss function of biological materials

As we did mention previously, the key parameter to obtain reliable results for the inelastic energy-loss magnitudes is the ELF of the material, $\mathrm{Im}\,[-1/\epsilon(k,\omega)]$, for the whole k–ω plane. Fortunately, experimental information about the ELF in the optical limit, $k = 0$, exists for important biological materials, such as liquid water, DNA, or PMMA. We show in Table 6.1 some characteristic data of these materials, such as their chemical composition, atomic number, molecular mass, and mass density.

In Figure 6.1 we show by symbols the available experimental optical-ELF for liquid water (circles),[36] dry DNA (squares)[37], and PMMA (triangles),[38] as a function of the energy transfer $\hbar\omega$ corresponding to the excitation of outer-shell electrons. All these optical-ELFs look rather similar, since they show only a single peak at ~21 eV, but there are sizeable

Table 6.1 Properties of the biological targets studied in this work: liquid water, DNA, and PMMA. We show their chemical composition, atomic number (Z_2), molecular mass (M_2), and mass density.

Target	**Liquid water**	**DNA**[34]	**PMMA**[35]
Chemical formula	H_2O	$(C_{20}H_{27}N_7O_{13}P_2)_n$	$(C_5H_8O_2)_n$
Z_2	10	330	54
M_2	18.0152	635.42	100.117
Density (g/cm^3)	1.000	1.350	1.188

differences in the values of their ELF magnitude. The curves in Figure 6.1 represent the results of fitting the experimental data by the MELF–GOS model using a linear combination of Mermin-type ELFs.

At high energy excitations usually there are not measurements of the ELF, in particular for the biological materials here analyzed. So, in this energy range, the optical-ELF of a compound target $A_{\alpha_1}B_{\alpha_2}\ldots$ will be

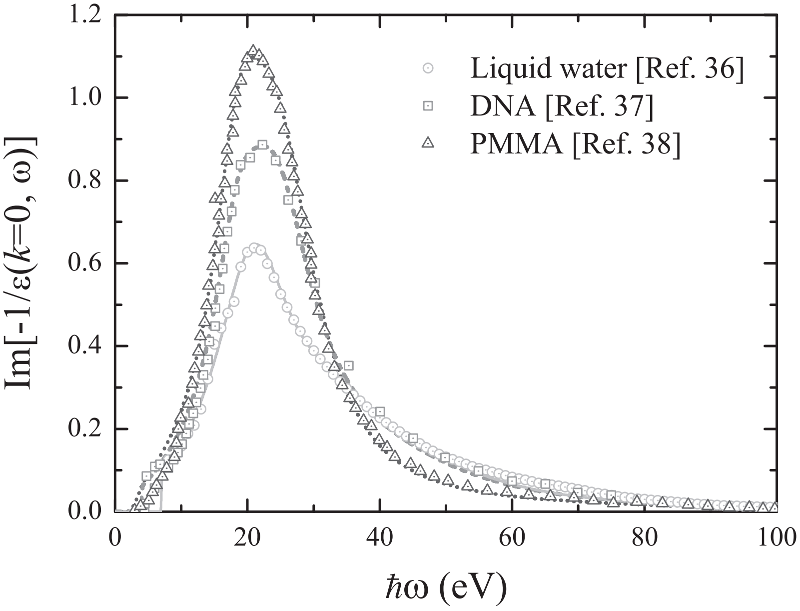

Figure 6.1 Energy-loss function, or ELF, for liquid water, DNA, and PMMA in the optical limit ($k = 0$), as a function of the energy transfer, $\hbar\omega$. Circles represent experimental data of liquid water,[36] squares correspond to DNA,[37] and triangles are data for PMMA.[38] The curves are the result of fitting those data by using the MELF–GOS model.

derived from the optical-ELFs of its elemental constituents applying the weighted additivity rule:[31, 39]

$$\mathrm{Im}\left[\frac{-1}{\epsilon(k=0,\omega)}\right] = \mathcal{N}\sum_j \frac{\alpha_j}{n_j}\mathrm{Im}\left[\frac{-1}{\epsilon(k=0,\omega)}\right]_j, \tag{20}$$

where n_j and $\mathrm{Im}\,[-1/\epsilon(k=0,\omega)]_j$ are the atomic density and the ELF, respectively, of the *j*th element of the target. The ELF of each elemental constituent of the target can be obtained from the X-ray measurements of the atomic scattering factors, which are available up to very high energies.[40]

In Figure 6.2 we depict the optical-ELF of liquid water, dry DNA, and PMMA at high-energy transfer as obtained with the MELF–GOS model (solid lines). For comparison purposes we also show by dotted lines the corresponding ELF obtained from experimental X-ray scattering factors[40] for the inner-shell electrons of the elements in each compound target, according to Eq. (20). In the case of liquid water we have added the results (triangles) from the FFAST database of NIST for the water molecule.[41] Notice that the optical ELF in Figure 6.2 contains the contribution from the outer (Eq. (15)) as well as from the inner-shell electron excitations (Eq. (14)). Sharp edges can be observed in the figure, corresponding to the threshold energy of each inner shell. In our model we treated as inner shell

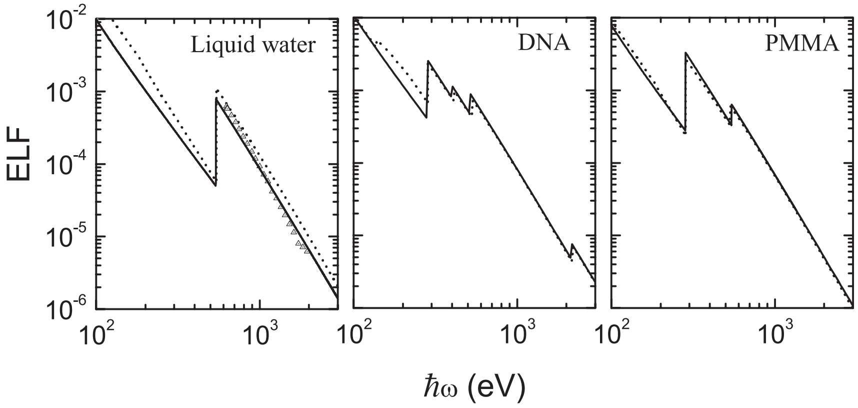

Figure 6.2 Energy-loss function, or ELF, in the optical limit ($k = 0$) of liquid water, dry DNA, and PMMA at high-energy transfer. Solid lines correspond to the ELF resulting from the MELF–GOS model. Dotted lines represent the results derived from X-ray atomic scattering factors.[40] Triangles correspond to calculations from the FFAST database of NIST for the water molecule.[41]

(using hydrogenic GOS) the *K*-shell of O for liquid water, the *K*-shell of C, N, O, and P for dry DNA, and the *K*-shell of C and O for PMMA.

In summary, the optical-ELF is constructed in such a wide region of energy transfer by using the optical-ELF experimental data (in the low-energy region) and the GOS for the elemental atoms forming the target (in the high-energy region). These two regions are connected by a reasonable matching by imposing the fulfillment of the sum rules, Eqs. (18) and (19), which are satisfied to better than 99%. Proceeding in this manner, we obtain analytical expressions for the optical-ELF that properly reproduce the energy-loss spectra of the different targets to be discussed in this work.

2.2.2 Bethe surface of biological materials

Once we build, from the MELF–GOS methodology, the optical ELF ($k = 0$) as a function of the energy transfer, the analytical properties of the Mermin-ELF and the GOS will extend automatically the ELF to finite values of the momentum transfer, $k \neq 0$, without *ad hoc* dispersion relations,[22] which allow to obtain the Bethe surface, i.e., the target electronic excitations in the whole k–ω plane. It is worth to emphasize that chemical bonding, and aggregation effects, as well as the characteristic collective excitations of condensed phase are included in the MELF–GOS description of the target excitation spectrum.

In order to check the reliability of the MELF–GOS model at finite momentum transfers it is desirable to compare the calculated Bethe surface with existing experimental data,[32, 42] although experimental information of the ELF at $k \neq 0$ is scarce. Luckily for liquid water there are experimental data of ELF at several finite momentum transfers ($k \approx 0$–3.6 a.u.) obtained from inelastic X-ray scattering spectroscopy measurements (IXSS).[43, 44] The experimental ELF of liquid water at $k = 0.85$, 1.34, and 2.79 a.u... are compared with the results obtained from the MELF–GOS model (solid lines) in Figure 6.3. We observe a good agreement between the experimental ELF of liquid water at $k \neq 0$ and our model, which reproduces the experimental broadening and shifting toward high-energy transfers as the momentum transfer increases, and it is consistent with the theoretical expectation that single-particle excitations should gradually prevail over collective excitations at large momentum transfer. A detailed discussion of different optical-data models applied to liquid water can be found in Ref. 22.

The calculated Bethe surface from the MELF–GOS model are presented for (a) liquid water, (b) dry DNA, and (c) PMMA in Figure 6.4.

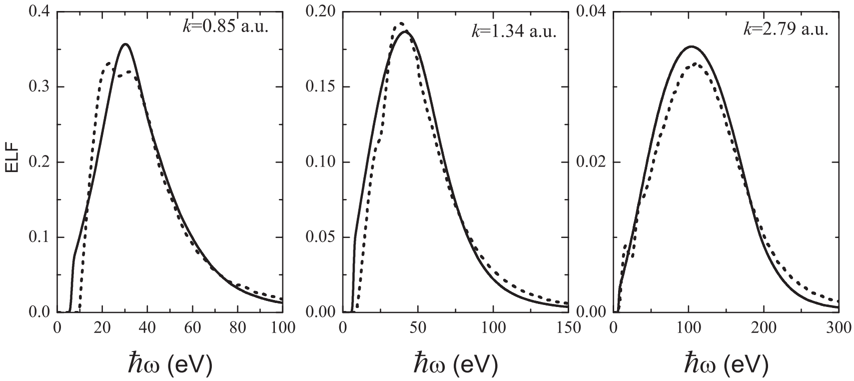

Figure 6.3 Energy-loss function, or ELF, of liquid water at the finite momentum transfers $k = 0.85$, 1.34, and 2.79 a.u. Dotted lines are experimental data[43, 44] and solid lines represent the results of the MELF–GOS model.

As we did mention before the Bethe surface is required in the dielectric formalism to evaluate the inelastic scattering cross section as a function of the particle energy. In all the biological targets analyzed here we observe that an increase in the momentum transfer k shifts the maximum of the ELF to higher energies and decreases its amplitude. Thus, the Bethe ridge is broadened due to chemical and/or phase effects, and its behavior is not a delta function as it happens for two-body collision where the struck electron is free and stationary, which implies a quadratic relation between energy and momentum transfer and a sharply peaked Bethe ridge of zero width. So, with the present description of the Bethe surface we have considered the many-body effects that take place in real condensed media, which cause a smearing on the otherwise delta-like profile of the ELF over the energy–momentum plane.

2.3 Mean excitation energy

At high projectile energies it is appropriate to use the relativistic Bethe formula for the stopping power,[8] namely:

$$S_{\mathrm{Bethe}}(v) = \frac{4\pi e^4 Z_1^2 Z_2 \mathcal{N}}{v^2}\left[\ln\left(\frac{2m_e v^2}{I(1-(v/c)^2)}\right) - (v/c)^2\right], \quad (21)$$

where v and c are, respectively, the projectile and the light velocities. Here I denotes the so-called mean excitation energy of the material, which only

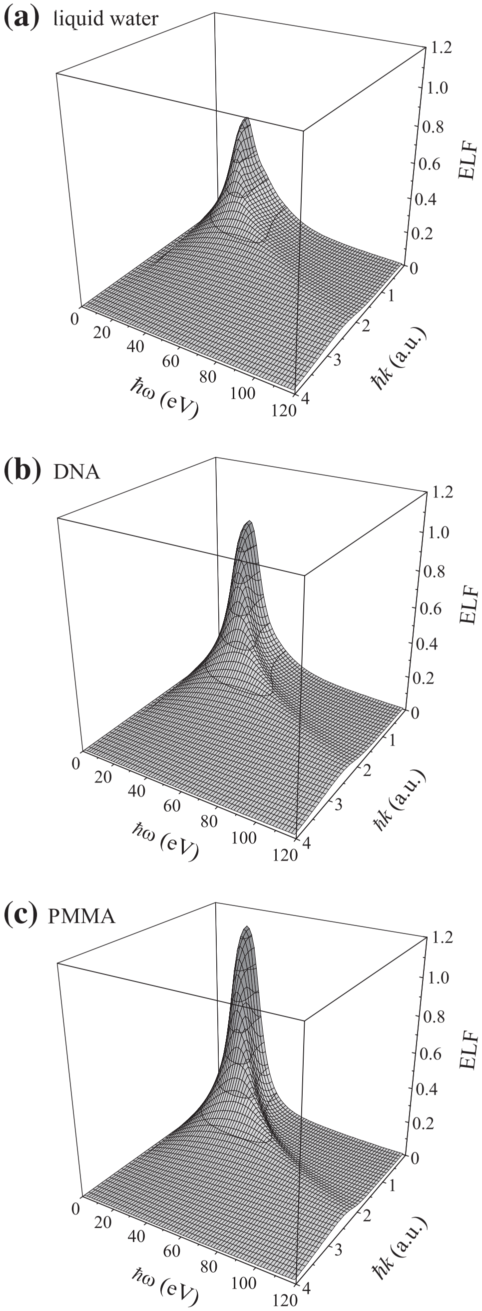

Figure 6.4 Bethe surface obtained from the MELF–GOS model for (a) liquid water, (b) DNA, and (c) PMMA.

depends on the electronic structure of the target, and is defined in terms of the target ELF by the relation:

$$\ln I = \frac{\int_0^\infty d\omega'\, \omega' \,\ln \omega' \,\mathrm{Im}[-1/\epsilon(k=0,\omega')]}{\int_0^\infty d\omega'\, \omega' \,\mathrm{Im}[-1/\epsilon(k=0,\omega')]}. \tag{22}$$

Note that in the high-energy limit, the Bethe stopping formula depends on the material through the mean excitation energy *I*. Therefore accurate values of *I* are desirable, in particular for biological materials, where a few percent in the uncertainty of the *I* values might cause sizeable changes in the range and stopping maximum (i.e., the Bragg peak) of therapeutic ion beams,[45, 46] which have energies of the order of several hundred of MeV/u.

The mean excitation energy *I* of a biological material can be evaluated through Eq. (22), with the optical-ELF $\mathrm{Im}[-1/\epsilon(k=0,\omega)]$ provided by the MELF–GOS method. We show in Table 6.2 the *I* values obtained from the MELF–GOS model corresponding to liquid water, DNA, and PMMA targets. Our calculations predict that the outer and inner-shell electron excitations contribute in almost the same proportion to the mean excitation energy.

It is worth to notice that the *I* value of PMMA (70.3 eV) is considerably smaller than the ones corresponding to liquid water (79.4 eV) or DNA (81.5 eV), which implies a larger stopping of projectiles in PMMA. In Table 6.2 a comparison with other *I*-values from the literature is presented; for a detailed analysis see Ref. 50. For liquid water a *I*-value ≃80 eV prevails in most of sources, while for DNA there is more dispersion between the *I*-values obtained from different sources.

Table 6.2 Mean excitation energy *I* (eV) obtained from the MELF–GOS model for liquid water, DNA, and PMMA. A comparison with other values is also presented.

	Liquid water	**DNA**	**PMMA**
MELF–GOS model	79.4[47]	81.5[34]	70.3[35]
Bragg rule (ICRU49)[14]	75 ± 3	85	74.0 ± 1.5
Tan et al.	72.5[48]	86.64[49]	68.37[48]
Paul[50]	80.8 ± 2.0		
Kumazaki et al.[51]	78.4 ± 1.0		
Emfietzoglou et al.[52]	77.8		
LaVerne and Pimblott[53]		77.9	
Akkerman and Akkerman[54]			68.5

3. CHARGE-EXCHANGE PROCESSES

The charge-state q of a projectile, with atomic number Z_1, moving through a condensed medium can vary due to electron-capture and -loss processes. Thus at low and intermediate projectile energies, these processes give a continuous dynamic charge-exchange of the projectile in its path through the target, therefore affecting its energy loss.

When charge equilibrium is reached, usually a few femtoseconds after the projectile penetrates into the target, the energy-loss magnitudes (Eqs. (2)–(5)) can be obtained from a weighted sum of the corresponding energy-loss magnitudes for each charge-state q of the projectile,[31] namely

$$P(T,\omega) = \sum_{q=0}^{Z_1} \phi_q(T) P_q(T,\omega), \tag{23}$$

$$\Lambda(T) = \sum_{q=0}^{Z_1} \phi_q(T) \Lambda_q(T), \tag{24}$$

$$S(T) = \sum_{q=0}^{Z_1} \phi_q(T) S_q(T), \tag{25}$$

$$\Omega^2(T) = \sum_{q=0}^{Z_1} \phi_q(T) \Omega_q^2(T), \tag{26}$$

where $\phi_q(T)$ is the probability of finding the projectile in a given charge-state q at the energy T. The sums in Eqs. (23)–(26) extend over all possible charge-states q of the projectile. We assume the charge-state fractions at equilibrium, which depend on the target nature, the projectile and its energy. The values of ϕ_q are obtained from a parameterization to experimental data,[55] which uses Bragg's additivity rule for compound targets. In Figure 6.5 we show the charge-state fractions of a proton beam incident in water, DNA, and PMMA as a function of the beam energy. No differences appear in the charge-state fractions for these three biological targets, due to their similar composition by light elements. It is worth to notice that the fraction of neutral hydrogen is zero at energies $\gtrsim 200\,\text{keV}$.

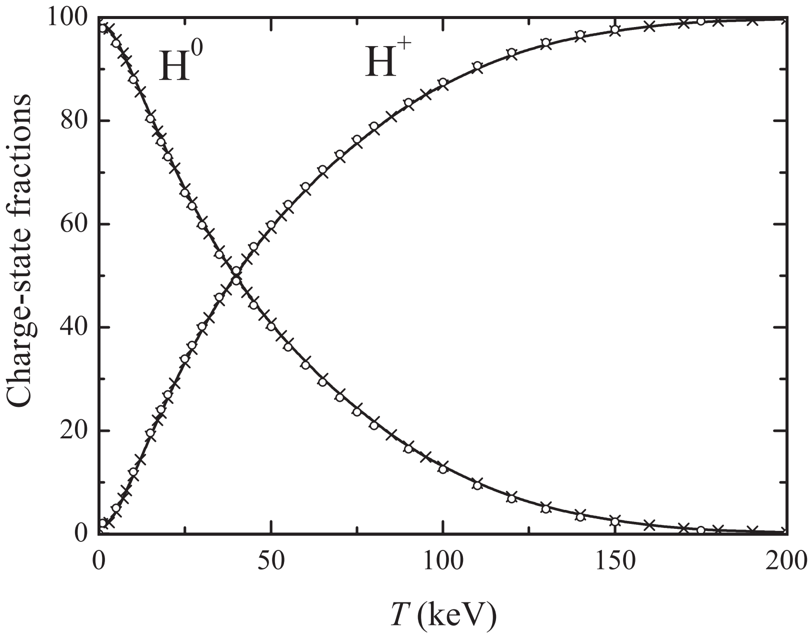

Figure 6.5 Charge-state fractions of H^0 and H^+ in water (solid line), DNA (crosses), and PMMA (circles) as a function of the projectile energy.

4. INELASTIC ENERGY-LOSS MAGNITUDES

The inelastic collisions that a projectile experiences in its travel through a target can be characterized by several energy-loss magnitudes, as we discussed previously in Section 2. Now we present results of these magnitudes for proton beams impinging in liquid water, dry DNA, and PMMA. All the calculations are based in the dielectric formalism, with a realistic description of the electronic properties of the target by the MELF–GOS model, and taking into account charge-exchange processes of the projectile.

Figure 6.6 shows the electronic excitation probability $P(T,\omega)$, as given by Eqs. (2) and (23), which represents the probability to produce electronic excitations of energy $\hbar\omega$ per unit path length in liquid water (solid line), dry DNA (dashed line), and PMMA (dotted line) by a proton with incident energy $T = 0.5$, 1, 5, and 10 MeV.

We find that independently of the projectile energy T these three biomaterials present the maximum of the electronic excitations at the same values of the transferred energy $\hbar\omega$, although the absolute value and shape

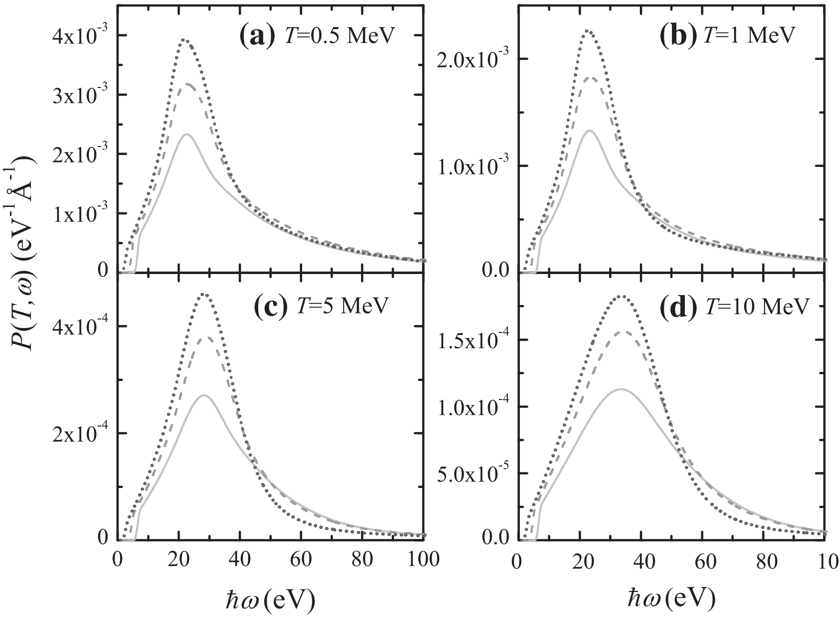

Figure 6.6 Probability per unit path length $P(T, \omega)$ that a proton beam induces electronic excitations of energy $\hbar\omega$ in liquid water (solid line), dry DNA (dashed line), and PMMA (dotted line). Results for several projectile energies are displayed: (a) $T = 0.5$ MeV, (b) $T = 1$ MeV, (c) $T = 5$ MeV, and (d) $T = 10$ MeV.

of $P(T, \omega)$ is different in each case. As the projectile energy increases the energy for the maximum of the electronic excitations slightly shifts to higher incident energies, going from ~22 eV at $T = 0.5$ MeV up to ~33 eV at $T = 10$ MeV. Also the intensity of the maximum probability P to produce electronic excitations decreases as the proton energy increases, indicating that a larger number of electronic excitations are created when the projectile has lower energies, a circumstance that takes place at the Bragg peak. It is remarkable to mention that the most probable electronic excitations have energies in the range ~10 − 50 eV for the analyzed targets. This result is significant because although the damage in DNA can be produced by direct ionization of inner shells of the target constituents, recent works point to electrons with sub-ionizing energies as the ones responsible for producing lethal damage in DNA.[56, 57]

Due to the stochastic nature of the inelastic collisions of charged particles moving through condensed media, their electronic energy-loss distribution can be evaluated by integrating the different moments of the electronic excitation probability $P(T, \omega)$ over the energy transfer, $\hbar\omega$. In what follows we present our calculations for the main stopping magnitudes: the inverse inelastic mean free path, the stopping power, and the energy-loss straggling for proton beams traveling through liquid water, dry DNA, and PMMA.

Figure 6.7 shows the inverse inelastic mean free path, or IIMFP, for protons in liquid water (solid line), dry DNA (dashed line), and PMMA (dotted line) calculated from the dielectric formalism and the MELF–GOS model (Eqs. (3) and (24)). At proton energies lower than ~1 MeV, sizeable differences between the IIMFP corresponding to the three materials are obtained, which can be ascribed to their different energy-loss function. At the maximum value of the IIMFP, corresponding to a proton energy ~75 keV for the three biological materials, the IIMFP in DNA is 35% larger than in liquid water, whereas the IIMFP in PMMA is more than 50% greater than in liquid water.

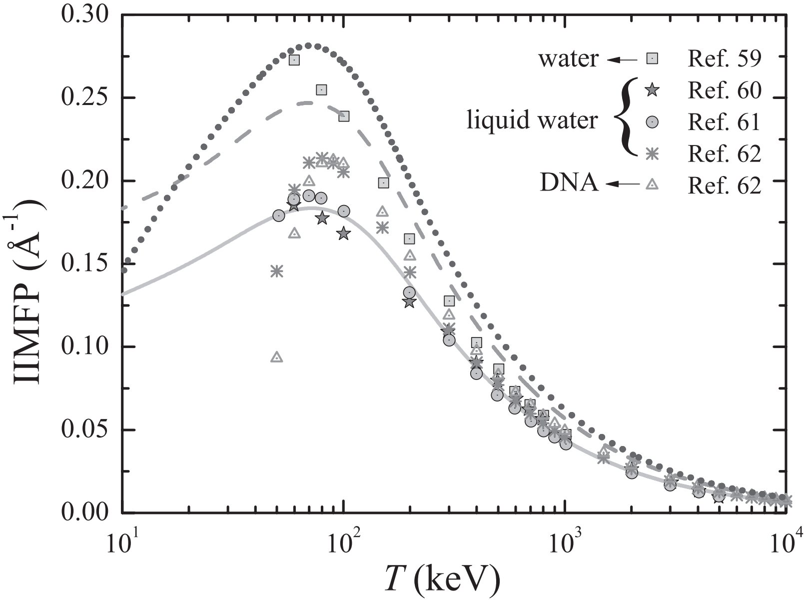

Figure 6.7 Inverse inelastic mean free path, or IIMFP, of a proton beam in liquid water (solid line), in DNA (dashed line), and PMMA (dotted line) calculated with the dielectric formalism and the MELF–GOS model. Squares correspond to the IIMFP in water from Uehara et al.[59] stars are the calculations in liquid water from Dingfelder et al.[60] circles correspond to the IIMFP in liquid water obtained by Emfietzoglou et al.[61] and asterisks and triangles are, respectively, theoretical calculations in liquid water and DNA from Tan et al.[62]

Usually the IIMFP is required as basic input data in Monte Carlo simulations, to account for electronic interactions and evaluate the damage on biological tissue by the irradiation with energetic charged particles. Although in this work we will use the IIMFP, and related magnitudes, derived from the dielectric formalism, cross sections obtained from first principles, like the continuum distorted wave-eikonal initial state approximation, have recently been implemented in Monte Carlo studies of the interaction of swift ions with liquid water.[58]

It is important to know that all the biomaterials have not similar IIMFP, but there are sizeable variations in their value. In Figure 6.7 we also compare our calculated IIMFP with results from other models. For protons in water we present results from Uehara et al.[59] (squares), who obtain high IIMFP values since in their model they use water vapor cross sections, calculations from Dingfelder et al.[60] (starts) and from Emfietzoglou et al.[61] (circles); the latter two sets of results agree rather well with our calculations. Results from Tan et al.[62] give similar IIMFP for liquid water (asterisks) and DNA (triangles) contrary to our findings; this coincidence of IIMFP for liquid water and DNA may have its origin in that these calculations[62] are based in the optical data model of Ashley[21] and on an evaluation approach for the optical energy-loss function.

The calculated stopping power S (Eqs. (4) and (25)) of liquid water (solid line), dry DNA (dashed line), and PMMA (dotted line) for proton beams is shown as a function of the projectile energy in Figure 6.8. Our model predicts that these biomaterials present the maximum values of S at the same projectile energy, around 100 keV. However the stopping power values of liquid water are always lower than those of dry DNA and PMMA; at $T = 100\ \mathrm{keV}$ their differences are ~30%, but even at high proton energies there are substantial differences between the stopping power of liquid water and the other biomaterials. The stopping power of DNA and PMMA are rather similar at intermediate and high proton energies, which can be due to the balance between their ELF (larger for PMMA than for DNA) and their different electron densities (smaller for PMMA than for DNA: $\mathcal{N}^{\mathrm{e}}_{\mathrm{PMMA}} = 0.385\ \mathrm{electron}/\text{Å}^3, \mathcal{N}^{\mathrm{e}}_{\mathrm{DNA}} = 0.421\ \mathrm{electron}/\text{Å}^3$. However, when comparing the electronic properties of liquid water and DNA or PMMA, both the ELF and the electron density ($\mathcal{N}^{\mathrm{e}}_{\mathrm{liq.\ water}} = 0.334\ \mathrm{electron}/\text{Å}^3$) for liquid water are smaller than for DNA and PMMA, which explains the smaller stopping power of liquid water as compared to the other biomaterials. We also include in Figure 6.8, experimental data of the stopping power of liquid water[63, 64, 65] and ice.[66–68]

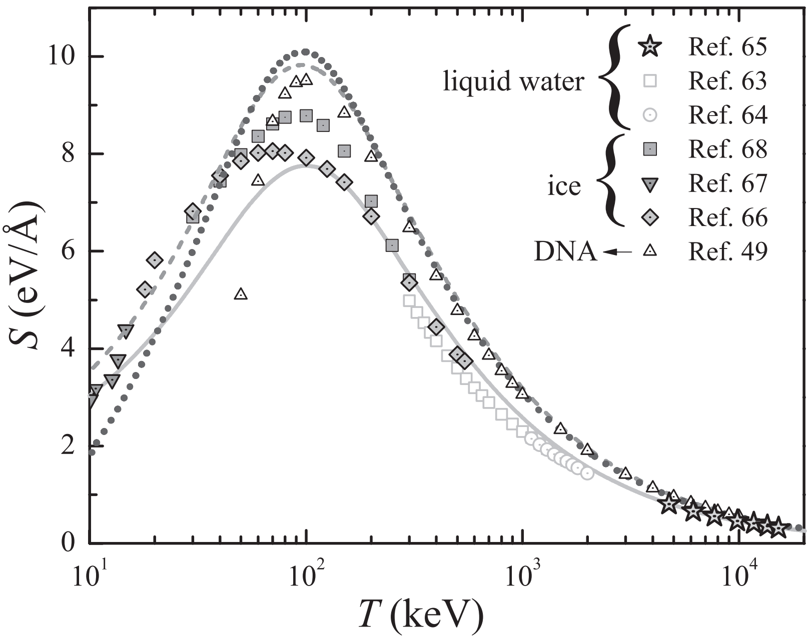

Figure 6.8 Stopping power of liquid water (solid line), dry DNA (dashed line), and PMMA (dotted line) for a proton beam, as a function of the incident energy, obtained with the dielectric formalism and the MELF–GOS method. Experimental data for protons in liquid water[63-65] and ice[66–68] are depicted by symbols. The stopping power of DNA calculated by Tan et al.[49] is shown by empty triangles.

We find an excellent agreement of our stopping calculations with the newest experimental data in liquid water at high proton energies,[65] which does mean that the mean excitation energy I of liquid water obtained from the MELF–GOS model, $I = 79.4$ eV,[47, 69] is in very good agreement with the features of the recent experimental results.[65] Note also that experimental results for liquid water from Refs. 63, 64, covering the range from 0.3 to 2 MeV, were obtained with a thin liquid jet in vacuum, whose diameter was treated as a fitting parameter.

The calculated stopping power by the dielectric formalism and by the MELF–GOS model at lower energies differs from the available experimental data of protons in ice. The close similarity[70, 71] between the excitation spectra of liquid water[36] and ice[72] implies that the corresponding mean excitation energies are comparable and, therefore, the stopping power at high projectile energies coincides for both liquid water and ice.

But, nevertheless there are small differences in the band structure of liquid water and ice, which lead to the observed differences in the stopping power at low projectile energies.

Finally, we also depict in Figure 6.8 by triangles the stopping power of DNA calculated by Tan et al.[49] which also were evaluated applying the dielectric formalism to the optical-ELF of DNA, but with a different extension algorithm to $k \neq 0$ values.

The second moment in the energy-loss distribution corresponds to the energy-loss straggling Ω^2, which is related to the variance in the distribution of the stochastic inelastic collision phenomena. We show in Figure 6.9 the energy-loss straggling Ω^2 of liquid water (solid line), dry DNA (dashed line), and PMMA (dotted line) for a proton beam as a function of its energy, calculated from Eqs. (5) and (26). The Ω^2 for liquid water is appreciably smaller than for DNA or PMMA in the whole proton energy range. The arguments to explain this behavior are the same that we discussed in relation to the stopping power. It is worth to notice that the contribution of the inner-shell electrons to the energy-loss straggling is larger than in the stopping power, representing a considerable percentage at high projectile energies. Therefore, an accurate description of electron inner-shell excitations is desirable, which

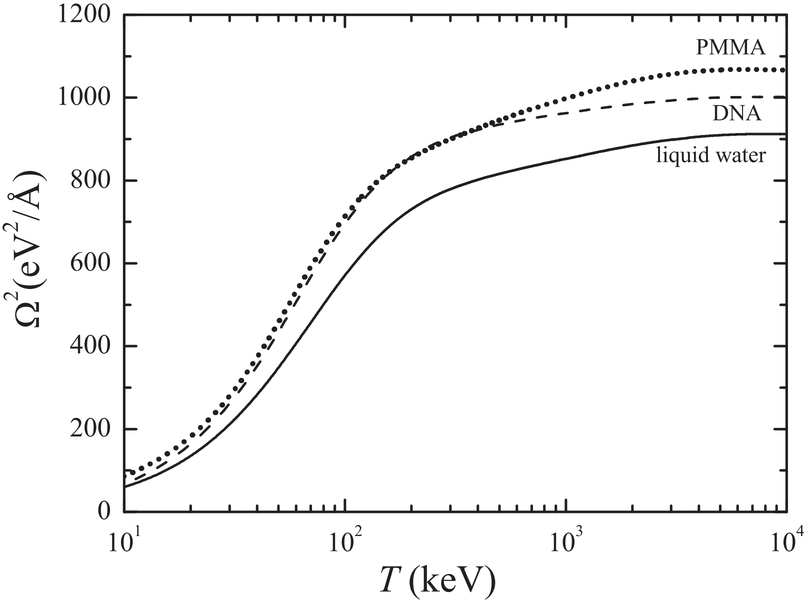

Figure 6.9 Energy-loss straggling, calculated with the dielectric formalism and the MELF–GOS method, of liquid water (solid line), dry DNA (dashed line), and PMMA (dotted line) for a proton beam as a function of the incident energy.

are accounted for in this work by the GOS (in the hydrogenic approach) of the elemental constituent of the compound target.

A proper description of the energy-loss straggling is important because recent detailed simulations of the spatial distribution of the energy deposition by proton beams in liquid water did show that the position of the Bragg peak is determined mainly by the stopping power, whereas its width can be attributed to the energy-loss straggling.[69]

In order to evaluate the possible damage induced in biological materials due to the irradiation with energetic particles, another interesting magnitude is the average energy $W_{\text{average}}(T)$ transferred by a projectile of energy T to the target producing electronic excitations and ionizations, which is defined by:

$$W_{\text{average}}(T) = \frac{\sum_{q=0}^{Z_1} \phi_q(T) \int_0^\infty \mathrm{d}\omega (\hbar\omega) P_q(T,\omega)}{\sum_{q=0}^{Z_1} \phi_q(T) \int_0^\infty \mathrm{d}\omega \, P_q(T,\omega)}. \tag{27}$$

Figure 6.10 shows $W_{\text{average}}(T)$ as a function of the energy of a proton beam in liquid water (solid line), DNA (dashed line), and PMMA (dotted line). We can observe that $W_{\text{average}}(T)$ is rather similar for liquid water and DNA, however the average energy is smaller for PMMA in all the range of proton energies analyzed here. This fact is related to the behavior of the probability to induce electronic excitations $P(T,\omega)$ in terms of the transferred energy $\hbar\omega$, which, as has been shown in Figure 6.6, is quite smaller for PMMA than for liquid water or DNA at high-energy transfers. $W_{\text{average}}(T)$ increases with proton energy T, being $\sim$20 eV at $T = 10$ keV for liquid water and DNA ($\sim$10 eV for PMMA) up to $\sim$70 eV for $T = 50$ MeV ($\sim$60 eV for PMMA). We also show by dots in Figure 6.10 the values reported by Pimblott and LaVerne[73] for the average energy of the secondary electrons generated by swift protons. These results derive from Monte Carlo simulations of the proton tracks based on experimental optical-ELF for liquid water, but using the quadratic extension to finite k. We can observe that the agreement with our calculations is quite good, the small discrepancies being due probably to the different extension algorithm used in each methodology, and because we also include electronic excitations.

As the probability of electronic excitations, characterized by $P(T,\omega)$, decreases with the projectile energy T (see Fig. 6.6), and the average energy of the excitations increases with T, hence a maximum in the stopping power is clearly expected, which is found around $T = 100$ keV for liquid water, DNA, and PMMA (see Fig. 6.8).

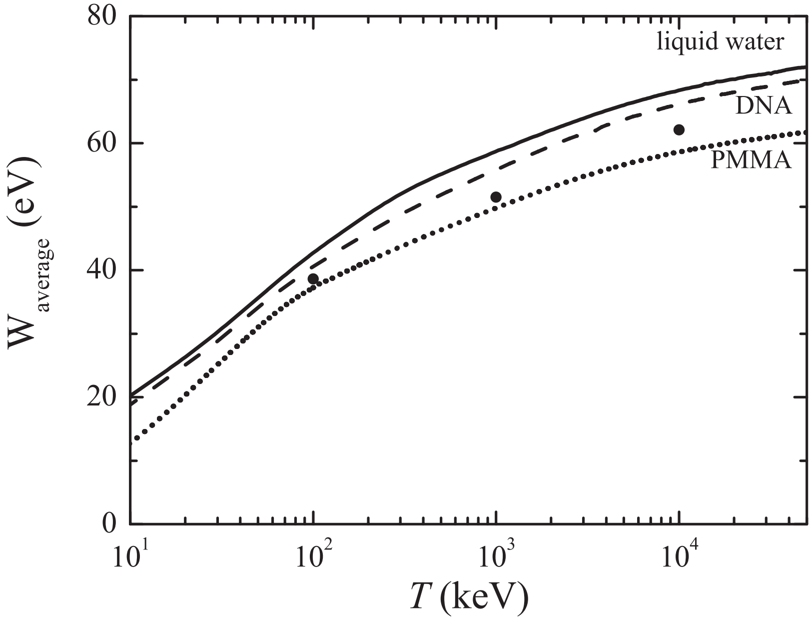

Figure 6.10 Average energy W_{average} transferred by the projectile producing electronic excitations and ionizations in liquid water (solid line), dry DNA (dashed line), and PMMA (dotted line) induced by a proton beam as a function of its energy. The calculations were obtained with the dielectric formalism and the MELF–GOS model. Circles correspond to results for ionization processes from a proton beam in liquid water from Pimblott and LaVerne.[73]

An estimation of the energy carried by the secondary electrons generated by energetic protons is obtained as $W_{\text{average}} - E_{\text{bind}}$, where E_{bind} is a representative value characterizing the binding energy of the target electrons, which is $E_{\text{bind}} \sim 10$ eV for biomaterials.[74] Therefore, the generated secondary electrons produced in liquid water, DNA, or PMMA could be very effective in producing DNA strand breaks, due to the low threshold energy for radiation damage in biomolecules,[75] with the average energy of the secondary electrons produced by proton beam being similar in liquid water and DNA, and a little bit smaller in PMMA.

5. SIMULATION OF THE DEPTH–DOSE DISTRIBUTIONS

The depth–dose profile of energetic protons in biological materials as well as the energy distribution of the beam as a function of the depth is simulated by the SEICS code (Simulation of Energetic Ions and Clusters through Solids). In brief, this code uses Molecular Dynamics to follow in detail the motion of the charged projectiles through the target, and a Monte Carlo procedure to treat the statistical nature of the elastic and inelastic scattering as well as the charge-exchange processes between the projectile and the target. In what follows we present the basic features of the simulation code; for more details the reader is referred to Refs. 69, 76.

The trajectory of an energetic particle through the target is obtained by numerically solving its equation of motion. Given the instantaneous position $\vec{r}(t)$, velocity $\vec{v}(t)$, and force $\vec{F}(t)$ acting on the projectile at a given time t, its new position $\vec{r}(t+\Delta t)$ and velocity $\vec{v}(t+\Delta t)$ after a time step Δt, are obtained by using the velocity variant of Verlet's algorithm[77]

$$\vec{r}(t+\Delta t) = \vec{r}(t) + \vec{v}(t)\Delta t + \frac{\vec{F}(t)}{2M_1}(\Delta t)^2 \left[1-(v(t)/c)^2\right]^{3/2}, \quad (28)$$

$$\vec{v}(t+\Delta t) = \vec{v}(t) + \frac{\vec{F}(t)+\vec{F}(t+\Delta t)}{2M_1}(\Delta t) \left[1-(v(t)/c)^2\right]^{3/2}, \quad (29)$$

where c is the speed of light and the term in brackets is an *ad hoc* modification of the original algorithm to account for the relativistic effects on the motion of the projectile, which must be considered when studying the interaction of high energetic beams in biomaterials, as in the case of hadrontherapy.

The force $F(t)$ that slows down an energetic particle travelling with charge-state q through the target is the electronic stopping force. But due to the stochastic nature of the inelastic energy-loss processes, the stopping force is obtained from a randomly sampled Gaussian distribution:

$$F = -\left[S_q + \Omega_q/\sqrt{\Delta s}\sqrt{-2\ln\xi_1}\cos(2\pi\xi_2)\right], \quad (30)$$

where the mean value of the distribution is the stopping power S_q and its variance σ is related to the energy-loss straggling Ω_q^2 through $\sigma = \sqrt{\Omega_q^2/\Delta s}$, with $\Delta s = v(t)\Delta t$ being the distance traveled in a time step Δt, and ξ_1 and ξ_2 are two random numbers uniformly distributed between 0 and 1.

We use in the SEICS code the stopping power and the energy-loss straggling for a projectile with charge q, calculated with the dielectric formalism together with the MELF–GOS model, see Eqs. (4) and (5). Nonetheless, at high projectile energies ($E \gtrsim 10$ MeV/u), analytical formulas from the relativistic Bethe stopping power[8] and the relativistic Bohr energy-loss straggling are used.

Although inelastic scattering is the main responsible of the energy loss of the projectile, the SEICS code also includes the elastic scattering between the projectile and the target constituent atoms. These mainly result in angular deflection of the projectile trajectory and also contributes to the energy loss at low energies. The code uses a Monte Carlo algorithm to treat multiple scattering based in Ref. 78.

As the electronic energy loss strongly depends on the charge state of the projectile, which varies during its travel through the target, then electronic capture and loss processes by the projectile are included in the SEICS code in order to know the charge state of the projectile at each time during its trajectory.

The simulated depth–dose distribution obtained by the SEICS code for a 100 MeV proton beam in liquid water and PMMA is shown in Figure 6.11. Solid lines are the results when all the interactions are included in the simulation, whereas dotted lines represent results obtained when energy-loss straggling

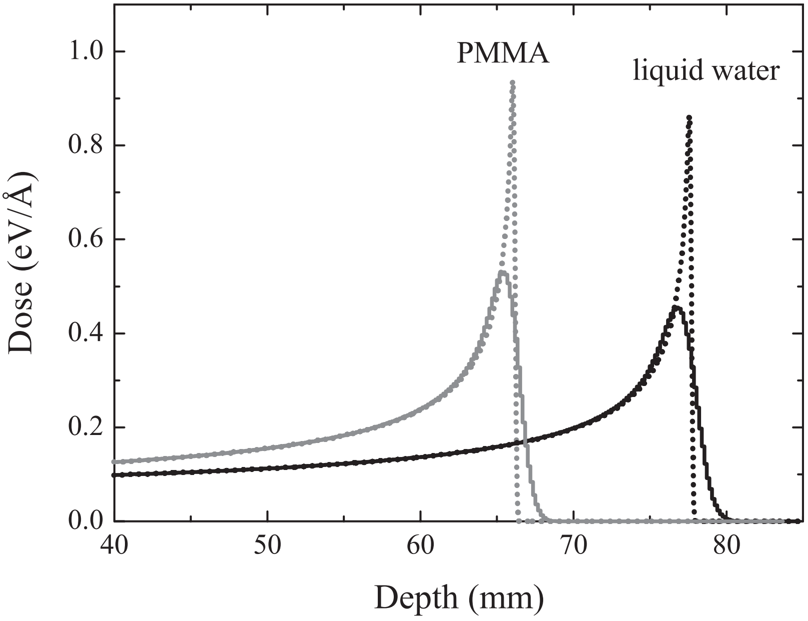

Figure 6.11 Simulated depth–dose distribution of a 100 MeV proton beam in liquid water (black curves) and in PMMA (grey curves). Solid lines are the results obtained from the SEICS code when all the interactions are taken into account, whereas dotted lines represent results of the same simulation without energy-loss straggling.

was not considered. Nuclear fragmentation processes are not included in the simulation since they do not affect significantly the depth–dose curves for protons below 100 MeV. The plateau and peak position of the Bragg curve are mostly determined by the electronic stopping force, but the shape of the Bragg peak strongly depends on the fluctuations of the projectile energy loss along its full path, accounted for by the energy-loss straggling. The Bragg peak for liquid water (black curves) is deeper than for PMMA (grey curves), because the PMMA stopping power (see Fig. 6.8) and its density is larger than for liquid water, so protons in PMMA slow down faster than in liquid water, reaching lower depths. Also, the differences in their stopping powers translate in a higher dose in PMMA than in liquid water at all depths.

In Figure 6.12 we show the results provided by the SEICS code for the average energy $\langle E \rangle$ (dashed lines) of 100 MeV protons incident on liquid water (black dashed curve) and on PMMA (grey dashed curve), as a function of the depth. The energy distributions of the protons at different depths in these biomaterials are depicted by solid lines, showing the broadening with depth of the initially monoenergetic beam. For comparison purposes the depth–dose distributions corresponding to each material are

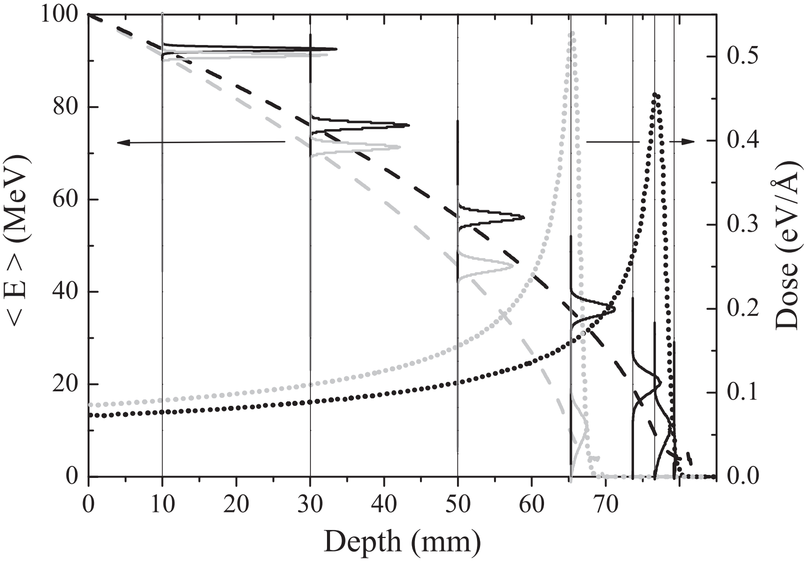

Figure 6.12 Left axis: Average energy $\langle E \rangle$ (dashed lines) of protons incident with 100 MeV in liquid water and in PMMA, as a function of the depth. The beam energy distribution at each depth is depicted by solid lines. Right axis: Depth–dose distribution for liquid water and PMMA (dotted lines). Black (or grey) lines correspond to liquid water (or PMMA).

shown by dotted lines (right axis). The average energy of protons in liquid water and in PMMA decreases with depth mostly due to inelastic collisions with target electrons, and the initially monoenergetic proton beam becomes broader as the depth inside the target increases.

It is interesting to notice that at the Bragg peak the projectile energy distribution is asymmetric since around that depth some projectiles start to stop, with the consequent increase in the lower energy tail of the energy distribution. From the previous discussion we emphasize the importance of taking into account the energy distribution of the protons around the Bragg peak because proton energy determines the spectrum of the generated secondary electrons, which are mainly responsible for the DNA damage.[75]

The SEICS code is also a useful tool to evaluate the water-equivalent properties of PMMA. This target is a plastic commonly used as a water-equivalent material in dosimetry measurements, since it has relatively similar properties and since it is easier to manipulate a solid target than a liquid one. The water-equivalence is based in the fact that a measured thickness in PMMA can be converted to an equivalent thickness in liquid water through[79, 80]

$$z_{\mathrm{water}} = z_{\mathrm{PMMA}} c_{\mathrm{PMMA}} = z_{\mathrm{PMMA}} \frac{\rho_{\mathrm{PMMA}}}{\rho_{\mathrm{water}}} \frac{\overline{S}_{\mathrm{PMMA}}}{\overline{S}_{\mathrm{water}}}, \tag{31}$$

where z_{water} and z_{PMMA} are the equivalent depths in water and PMMA, respectively, and c_{PMMA} is the depth-scaling factor (or water-equivalent ratio, WER), which depends on the density and mean mass stopping power ratios, $\rho_{\mathrm{PMMA}}/\rho_{\mathrm{water}}$ and $\overline{S}_{\mathrm{PMMA}}/\overline{S}_{\mathrm{water}}$, respectively.

The WER is usually calculated as the ratio of the continuous slowing down approximation (CSDA) ranges of protons in PMMA and water. An alternative is to use the Bragg curves calculated within the SEICS code, defining the range as the thickness in which the dose is 80% after the maximum. We have determined the WER of PMMA in this way for 75 MeV and 100 MeV proton beams, obtaining in both cases a value of 1.174. This value can be compared with the ones reported by other authors, which are summarized in Table 6.3. Note that the WER depends on the density, according to Eq. (31), and then we have corrected all the values to match the density $\rho_{\mathrm{PMMA}} = 1.188\ \mathrm{g/cm^3}$ used by us.

In Figure 6.13 we show the Bragg curves for a 100 MeV proton beam in water and PMMA, normalized to the entrance dose, and with the thickness in PMMA scaled according to Eq. (31), with WER = 1.174. As it can be seen, the two curves are totally superimposed, indicating excellent water-equivalent properties of PMMA when nuclear fragmentation processes are neglected.

Regarding the differences between the WERs shown in Table 6.3, the maximum difference is observed between our value of 1.174 and the one by ICRU49 CSDA ranges[14] of 1.157 (1.45%). Such a difference translates, for a 100 MeV proton beam, in an uncertainty of the order of 1.2 mm in the Bragg peak position. Therefore, it is important to count on the most reliable values of stopping magnitudes (and also with realistic radiation transport codes, which allow a precise calculation of WER) if a submillimetric accuracy is desired.

Other useful information the SEICS code can evaluate regarding the water equivalence of PMMA is the energy distribution of projectiles at the Bragg peak in both targets. Although the macroscopic dose is completely equivalent, as we have already shown, the knowledge of the equivalence of the energy distribution is also important from a microscopic point of

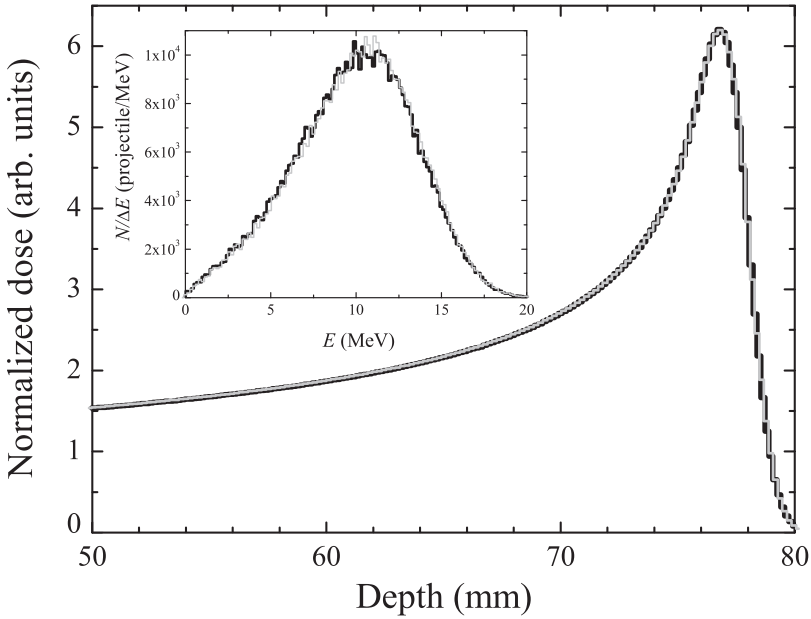

Figure 6.13 Normalized (at the entrance) depth–dose curves of a 100 MeV proton beam in liquid water (black solid line) and in PMMA at water-equivalent depth (grey solid line). The inset shows the energy distribution of the proton beam just at the Bragg peak in liquid water (black solid line) and PMMA (grey solid line); see the text for more details.

Table 6.3 Water-equivalent ratios, or WER, for protons in PMMA from different sources.

	ρ_{PMMA} (g/cm^3)	WER	WER ($\rho_{\mathrm{PMMA}} = \mathbf{1.188}$ g/cm^3)
This work (75 MeV, 100 MeV)	1.188	1.174	1.174
ICRU49 (CSDA)[14] (75 MeV)	1.195	1.164	1.157
Palmans et al.[79] (75 MeV)	1.186	1.159	1.161
Zhang et al.[80] (75–250 MeV)	1.185	1.157–1.167	1.160–1.170

view, since the energy of the particles will affect the emission of secondary electrons. This issue is relevant if further analysis of radiation damage will be carried out using PMMA as a water substitute. The inset of Figure 6.13 shows the energy distribution of particles, at the Bragg peak depth, for both liquid water (black line) and PMMA (grey line), i.e., the number of projectiles, N, which travel, at this depth, with a certain energy, E, divided by the bin width, ΔE. This division is performed in order to avoid differences in height due to different widths of the histogram bin. As it can be seen, the proton beam is also equivalent for water and PMMA from a microscopic point of view. This point remarks the water equivalence of PMMA when nuclear fragmentation reactions are neglected, and of course when the WER is accurately known.

6. CONCLUSIONS

We have presented in this paper an account of our recent work applied to the interaction of proton beams with materials of biological interest, such as liquid water (∼70% constituent of living beings), DNA (the biomaterial per excellence), and PMMA (a plastic widely used in dosimetry). This research is linked to the recent use of proton beams in cancer therapy, a promising and successful technique known as ion therapy (or hadrontherapy).

The main magnitudes useful for describing the energy deposited by a projectile moving through a biological target with charge-state q are the stopping power S_q and the energy-loss straggling Ω_q^2, which can conveniently be evaluated in the dielectric formalism. We use a suitable description of the target excitation spectrum, based in optical experimental data for the outer electronic excitations and hydrogenic generalized oscillator strengths for the inner-shell electrons of the target, properly extended to finite momentum transfers conveniently extended to finite momentum transfers; this procedure constitutes the fundamentals of the so-called Mermin Energy Loss Function–Generalized Oscillator Strength method, from which we can easily obtain, besides S_q and Ω_q^2, the target mean excitation energy, the projectile inverse inelastic mean free path, the average energy transferred to electronic excitations and ionizations, or the probability that the projectile induces electronic excitations of a given energy. The projectile electronic density is accounted for by the Brandt–Kitagawa model.

There are sizeable differences among the calculated stopping powers of liquid water and those of DNA and PMMA, which are rather similar. Our stopping power of liquid water for protons compares fairly well with the available experimental data explicitly measured for liquid water, with differences appearing for ice water stopping power (probably due to the different phase state of the target).

The average energy transferred by the beam to the targets lies in the ~10 and ~70 eV range, showing the same increasing trend as the projectile energy grows, although being slightly larger for liquid water, DNA, and PMMA (in this order). Our results are a little bit larger than previously published results[73] for liquid water, because we also consider electronic excitations.

By means of the Simulation of Energetic Ions and Clusters through Solids code, which is based in Molecular Dynamics and Monte Carlo to follow the trajectories of the projectiles through the target, we are able to obtain the depth–dose curves (Bragg curves), as well as the energy distribution of the proton beam as a function of the depth in liquid water and PMMA, both materials being widely studied for the propagation of proton beams. From these simulations we obtain the water-equivalent thickness of PMMA as well as other interesting magnitudes in dosimetry, such as the water-equivalent ratio, which is compared to values available in the literature, obtained by different methods. Comparing the extreme values (ours and ICRU49[14]) of the water-equivalent ratio for a 100 MeV proton beam, an uncertainty of ~1.2 mm in the Bragg peak appears.

Finally, we have shown that the energy distributions of a 100 MeV proton beam at the Bragg peak are practically identical in liquid water and PMMA (when nuclear fragmentation is not taken into account), which means that both materials are equivalent with respect to the energy distribution.

ACKNOWLEDGMENTS

This work has been financially supported by the Spanish Ministerio de Ciencia e Innovación (Project FIS2010-17225) and the European Union FP7 ANTICARB (HEALTH-F2-2008-201587). PdV thanks the Conselleria d'Educació, Formació i Ocupació de la Generalitat Valenciana for its support under the VALi+d program. This research is part of the COST Action MP 1002, Nanoscale Insights into Ion Beam Cancer Therapy.

REFERENCES

1. Wilson, R. Radiological use of fast protons. *Radiology* **1946**, *47*, 487.
2. Tobias, C. A.; Anger, O. H.; Lawrence, J. H. Radiological use of high-energy deuterons and alpha-particles. *Am. J. Roentgenol.* **1952**, *67*, 1.
3. Tobias, C. A.; Lawrence, J. H.; Born, J. L.; McCombs, R. K.; Roberts, J. E.; Anger, H. O.; Low-Beer, B.V. A.; Huggings, C. B. Pituitary irradiation with high-energy proton beams. A preliminary report. *Cancer Res.* **1958**, *18*, 121.
4. Amaldi, U.; Bonomi, R.; Braccini, S.; Crescenti, M.; Degiovanni, A.; Garlasché, M.; Garonna, A.; Magrin, G.; Mellace, C.; Pearce, P.; Pittà, G.; Puggioni, P.; Rosso, E.; Verdú Andrés, S.; Wegner, R.; Weiss, M.; Zennaro, R. Accelerators for hadrontherapy: From Lawrence cyclotrons to linacs. *Nucl. Instrum. Methods Phys. Res., Sect. A* **2010**, *620*, 563.
5. Nikjoo, H.; Uehara, S.; Emfietzoglou, D.; Brahme, A. Heavy charged particles in radiation biology and biophysics. *New J. Phys.* **2008**, *10*, 075006.
6. Belkić, Dž. Review of theories on ionization in fast ion-atom collisions with prospects for applications to hadron therapy. *J. Math. Chem.* **2010**, *47*, 1366.
7. Paganetti, H.; Niemerko, A.; Ancukiewicz, M.; Gerweck, L. E.; Goitein, M.; Loeffler, J. S.; Suit, H. D. Relative biological effectiveness (RBE) values for proton beam therapy. *Int. J. Radiat. Oncol. Biol. Phys.* **2002**, *53*, 407.
8. Inokuti, M. Inelastic collisions of fast charged particles with atoms and molecules – the Bethe theory revisited. *Rev. Mod. Phys.* **1971**, *43*, 297.
9. Sigmund, P. Stopping power in perspective. *Nucl. Instrum. Methods Phys. Res., Sect. B* **1998**, *135*, 1.
10. Sabin, J. R.; Oddershede, J. Stopping power-what next? *Adv. Quantum Chem.* **2005**, *49*, 299.
11. Belkić, Dž. A quantum theory of ionization in fast collisions between ions and atomic systems. *J. Phys. B: At. Mol. Phys.* **1978**, *11*, 3529.
12. Crothers, D. S. F.; McCann, J. F. Ionization of atoms by ion impact. *J. Phys. B: At. Mol. Phys.* **1983**, *16*, 3229.
13. Sigmund, P. Light-ion stopping near the maximum. *Nucl. Instrum. Methods Phys. Res., Sect. B* **1994**, *85*, 541.
14. ICRU, Stopping powers and ranges for protons and alpha particles, ICRU Report 49, Bethesda, MD, 1993.
15. Fano, U. Penetration of protons, alpha particles, and mesons. *Annu. Rev. Nucl. Sci.* **1963**, *13*, 1.
16. Bichsel, H. Shell corrections in stopping power. *Phys. Rev. A* **2002**, *65*, 052709.
17. Ritchie, R. H. Energy losses by swift charged particles in the bulk and at the surface of condensed matter. *Nucl. Instrum. Methods* **1982**, *198*, 81.
18. Echenique, P. M.; Flores, F.; Ritchie, R. H. Dynamic screening of ions in condensed matter. *Solid State Phys.* **1990**, *43*, 229.
19. Powell, C. J. Attenuation lengths of low-energy electrons in solids. *Surf. Sci.* **1974**, *44*, 29.

20. Ritchie, R. H.; Howie, A. Electron excitation and the optical potential in electron microscopy. *Philos. Mag.* **1977**, *36*, 463.
21. Ashley, J. C. Optical-data model for the stopping power of condensed matter to protons and antiprotons. *J. Phys.: Condens. Matter* **1991**, *3*, 2741.
22. Garcia-Molina, R.; Abril, I.; Kyriakou, I.; Emfietzoglou, D. Energy loss of swift protons in liquid water: role of optical data input and extension algorithms. In *Radiation Damage in Biomolecular Systems*; García Gómez-Tejedor, G., Fuss, M. C., Eds.; Springer: Dordrecht, 2012; Chapter 15.
23. Mermin, N. D. Lindhard dielectric function in the relaxation-time approximation. *Phys. Rev. B* **1970**, *1*, 2362.
24. Lindhard, J. On the properties of a gas of charged particles. *K. Dan. Vidensk. Selsk. Mat.-Fys. Medd.* **1954**, *28*(8).
25. Ritchie, R. H. Interaction of charged particles with a degenerate Fermi–Dirac electron gas. *Phys. Rev.* **1959**, *114*, 644.
26. Belkić, Dž.; Mančev, I.; Hanssen, J. Four-body methods for high-energy ion-atom collisions. *Rev. Mod. Phys.* **2008**, *80*, 249.
27. Brandt, W.; Kitagawa, M. Effective stopping-power charges of swift ions in condensed matter. *Phys. Rev. B* **1982**, *25*, 5631.
28. Brandt, W. Effective charges of ions and the stopping power of dense media. *Nucl. Instrum. Methods* **1982**, *194*, 13.
29. Powel, C. J.; Jablonski, A. Evaluation of calculated and measured electron inelastic mean free paths near solid surfaces. *J. Phys. Chem. Ref. Data* **1999**, *28*, 19.
30. Abril, I.; Garcia-Molina, R.; Denton, C. D.; Pérez-Pérez, F. J.; Arista, N. R. Dielectric description of wakes and stopping powers in solids. *Phys. Rev. A* **1998**, *58*, 357.
31. Heredia-Avalos, S.; Garcia-Molina, R.; Fernández-Varea, J. M.; Abril, I. Calculated energy loss of swift He, Li, B, and N ions in SiO_2, Al_2O_3, and ZrO_2. *Phys. Rev. A* **2005**, *72*, 052902.
32. Planes, D. J.; Garcia-Molina, R.; Abril, I.; Arista, N. R. Wavenumber dependence of the energy loss function of graphite and aluminium. *J. Electron Spectrosc. Relat. Phenom.* **1996**, *82*, 23.
33. Emfietzoglou, D.; Abril, I.; Garcia-Molina, R.; Petsalakis, I. D.; Nikjoo, H.; Kyriakou, I.; Pathak, A. Semi-empirical dielectric descriptions of the Bethe surface of the valence bands of condensed water. *Nucl. Instrum. Methods Phys. Res., Sect. B* **2008**, *266*, 1154.
34. Abril, I.; Garcia-Molina, R.; Denton, C. D.; Kyriakou, I.; Emfietzoglou, D. Energy loss of hydrogen- and helium-ion beams in DNA: calculations based on a realistic energy-loss function of the target. *Radiat. Res.* **2011**, *175*, 247.
35. de Vera, P.; Abril, I.; Garcia-Molina, R. Inelastic scattering of electron and light ion beams in organic polymers. *J. Appl. Phys.* **2011**, *109*, 094901.
36. Hayashi, H.; Watanabe, N.; Udagawa, Y.; Kao, C.-C. The complete optical spectrum of liquid water measured by inelastic x-ray scattering. *Proc. Natl. Acad. Sci. USA* **2000**, *97*, 6264.
37. Inagaki, T.; Hamm, R. N.; Arakawa, E. T.; Painter, L. R. Optical and dielectric properties of DNA in the extreme ultraviolet. *J. Chem. Phys.* **1974**, *61*, 4246.
38. Ritsko, J. J.; Brillson, L. J.; Bigelow, R. W.; Fabish, T. J. Electron energy loss spectroscopy and the optical properties of polymethylmethacrylate from 1 to 300 eV. *J. Chem. Phys.* **1978**, *69*, 3931.
39. Moreno-Marín, J. C.; Abril, I.; Garcia-Molina, R. Stopping power calculation of rubidium and strontium for protons. *Nucl. Instrum. Methods Phys. Res., Sect. B* **2002**, *193*, 30.
40. Henke, B. L.; Gullikson, E. M.; Davis, J. C. X-ray interactions: photoabsorption, scattering, transmission, and reflection at $E = 50$–$30{,}000$ eV, $Z = 1$–92. *At. Data Nucl. Data Tables* **1993**, *54*, 181.

41. The ASCII files for the f_1 and f_2 scattering factors of the different elements can be obtained from Chantler, C. T.; Olsen, K.; Dragoset, R. A.; Chang, J.; Kishore, A. R.; Kotochigova, S. A.; Zucker, D. S. X-ray form factor, attenuation and scattering tables (version 2.1). National Institute of Standards and Technology: Gaithersburg, MD, 2005. <http://www.nist.gov/pml/data/ffast/index.cfm>.
42. Denton, C. D.; Abril, I.; Garcia-Molina, R.; Moreno-Marín, J. C.; Heredia-Avalos, S. Influence of the description of the target energy-loss function on the energy loss of swift projectiles. *Surf. Interface Anal.* **2008**, *40*, 1481.
43. Watanabe, N.; Hayashi, H.; Udagawa, Y. Bethe surface of liquid water determined by inelastic X-ray scattering spectroscopy and electron correlation effects. *Bull. Chem. Soc. Jpn.* **1997**, *70*, 719.
44. Watanabe, N.; Hayashi, H.; Udagawa, Y. Inelastic X-ray scattering study on molecular liquids. *J. Phys. Chem. Solids* **2000**, *61*, 407.
45. Paul, H.; Geithner, O.; Jäkel, O. The influence of stopping powers upon dosimetry for radiation therapy with energetic ions. *Adv. Quantum Chem.* **2007**, *52*, 289.
46. Andreo, P. On the clinical spatial resolution achievable with protons and heavier charged particle radiotherapy beams. *Phys. Med. Biol.* **2009**, *54*, N205.
47. Garcia-Molina, R.; Abril, I.; Denton, C. D.; Heredia-Avalos, S.; Kyriakou, I.; Emfietzoglou, D. Calculated depth–dose distributions for H^+ and He^+ beams in liquid water. *Nucl. Instrum. Methods Phys. Res., Sect. B* **2009**, *267*, 2647.
48. Tan, Z.; Xia, Y.; Zhao, M.; Liu, X.; Li, F.; Huang, B.; Ji, Y. Electron stopping power and mean free path in organic compounds over the energy range of 20–10,000 eV. *Nucl. Instrum. Methods Phys. Res., Sect. B* **2004**, *222*, 27.
49. Tan, Z.; Xia, Y.; Zhao, M.; Liu, X. Proton stopping power in a group of bioorganic compounds over the energy range of 0.05–10 MeV. *Nucl. Instrum. Methods Phys. Res., Sect. B* **2006**, *248*, 1.
50. Paul, H. The stopping power of matter for positive ions. In *Modern Practices in Radiation Therapy*; Natanasabapathi, G., Ed.; InTech: Rijeka, 2012; Chapter 7.
51. Kumazaki, Y.; Akagi, T.; Yanou, T.; Suga, D.; Hishikawa, Y.; Teshima, T. Determination of the mean excitation energy of water from proton beam ranges. *Radiat. Meas.* **2007**, *42*, 1683.
52. Emfietzoglou, D.; Garcia-Molina, R.; Kyriakou, I.; Abril, I.; Nikjoo, H. A dielectric response study of the electronic stopping power of liquid water for energetic protons and a new *I*-value for water. *Phys. Med. Biol.* **2009**, *54*, 3451.
53. LaVerne, J. A.; Pimblott, S. M. Electron energy-loss distributions in solid, dry DNA. *Radiat. Res.* **1995**, *141*, 208.
54. Akkerman, A.; Akkerman, E. Characteristics of electron inelastic interactions in organic compounds and water over the energy range 20–10000 eV. *J. Appl. Phys.* **1999**, *86*, 5809.
55. Schiwietz, G.; Grande, P. L. Improved charge-state formulas. *Nucl. Instrum. Methods Phys. Res., Sect. B* **2001**, *175–177*, 125.
56. Boudaïffa, B.; Cloutier, P.; Hunting, D.; Huels, M. A.; Sanche, L. Resonant formation of DNA strand breaks by low-energy (3 to 20 eV) electrons. *Science* **2000**, *287*, 1658.
57. Huels, M. A.; Boudaïffa, B.; Cloutier, P.; Hunting, D.; Sanche, L. Single, double, and multiple double strand breaks induced in DNA by 3-100 eV electrons. *J. Am. Chem. Soc.* **2003**, *125*, 4467.
58. Gervais, B.; Beuve, M.; Olivera, G. H.; Galassi, M. E. Numerical simulation of multiple ionization and high LET effects in liquid water radiolysis. *Radiat. Phys. Chem.* **2006**, *75*, 493.
59. Uehara, S.; Toburen, L. H.; Wilson, W. E.; Goodhead, D. T.; Nikjoo, H. Calculations of electronic stopping cross sections for low-energy protons in water. *Radiat. Phys. Chem.* **2000**, *59*, 1.

60. Dingfelder, M.; Inokuti, M.; Paretzke, H. G. Inelastic-collision cross sections of liquid water for interactions of energetic protons. *Radiat. Phys. Chem.* **2000**, *59*, 255.
61. Emfietzoglou, D.; Pathak, A.; Papamichael, G.; Kostarelos, K.; Dhamodaran, S.; Sathish, N.; Moscovitch, M. A study on the electronic stopping of protons in soft biological matter. *Nucl. Instrum. Methods Phys. Res., Sect. B* **2006**, *242*, 55.
62. Tan, Z.; Xia, Y.; Zhao, M.; Liu, X. Proton inelastic mean free path in a group of bioorganic compounds and water in 0.05–10 MeV range – including higher-order corrections. *Nucl. Instrum. Methods Phys. Res., Sect. B* **2010**, *268*, 2337.
63. Shimizu, M.; Hayakawa, T.; Kaneda, M.; Tsuchida, H.; Itoh, A. Stopping cross-sections of liquid water for 0.3–2.0 MeV protons. *Vacuum* **2010**, *84*, 1002.
64. Shimizu, M.; Kaneda, M.; Hayakawa, T.; Tsuchida, H.; Itoh, A. Stopping cross sections of liquid water for MeV energy protons. *Nucl. Instrum. Methods Phys. Res., Sect. B* **2009**, *267*, 2667.
65. Siiskonen, T.; Kettunen, H.; Perajarvi, K.; Javanainen, A.; Rossi, M.; Trzaska, W. H.; Turunen, J.; Virtanen, A. Energy loss measurement of protons in liquid water. *Phys. Med. Biol.* **2011**, *56*, 2367.
66. Wenzel, W. A.; Whaling, W. The stopping cross section of D_2O ice. *Phys. Rev.* **1952**, *87*, 499.
67. Andrews, D. A.; Newton, G. The stopping power of heavy ice for low-energy (10–30 keV) deuterons. *J. Phys. D: Appl. Phys.* **1977**, *10*, 845.
68. Bauer, P.; Kaferbock, W.; Necas, V. Investigation of the electronic energy loss of hydrogen ions in H_2O: influence of the state of aggregation. *Nucl. Instrum. Methods Phys. Res., Sect. B* **1993**, *93*, 132.
69. Garcia-Molina, R.; Abril, I.; Heredia-Avalos, S.; Kyriakou, I.; Emfietzoglou, D. A combined molecular dynamics and Monte Carlo simulation of the spatial distribution of energy deposition by proton beams in liquid water. *Phys. Med. Biol.* **2011**, *56*, 6457.
70. Vinson, J.; Kas, J. J.; Vila, F. D.; Rehr, J. J.; Shirley, E. L. Theoretical optical and X-ray spectra of liquid and solid H_2O. *Phys. Rev. B* **2012**, *85*, 045101.
71. Michaud, M.; Wen, A.; Sanche, L. Cross sections for low-energy electron elastic and inelastic scattering in amorphous ice. *Radiat. Res.* **2003**, *159*, 3.
72. Kobayashi, K. Optical spectra and electronic structure of ice. *J. Phys. Chem.* **1983**, *87*, 4317.
73. Pimblott, S. M.; LaVerne, J. A. Production of low-energy electrons by ionizing radiation. *Radiat. Phys. Chem.* **2007**, *76*, 1244.
74. Mozejko, P.; Sanche, L. Cross sections for electron scattering from selected components of DNA and RNA. *Radiat. Phys. Chem.* **2005**, *73*, 77.
75. Sanche, L. Low energy electron-driven damage in biomolecules. *Eur. Phys. J. D* **2005**, *35*, 367.
76. Garcia-Molina, R.; Abril, I.; de Vera, P.; Kyriakou, I.; Emfietzoglou, D. In Proton beam irradiation of liquid water: a combined molecular dynamics and Monte Carlo simulation study of the Bragg peak profile; *Fast Ion-Atom and Ion-Molecule Collisions*, Belkić, Dž. Ed.; World Scientific Publishing Company: Singapore, 2012, Chapter 8, pp. 271–304.
77. Allen, M. P.; Tildesley, D. J. *Computer Simulation of Liquids*; Oxford University Press: Oxford, 1989.
78. Möller, W.; Pospiech, G.; Schrieder, G. Multiple scattering calculations on ions passing through thin amorphous foils. *Nucl. Instrum. Methods* **1975**, *130*, 265.
79. Palmans, H.; Symons, J. E.; Denis, J.-M.; de Kock, E. A.; Jones, D. T. L.; Vynckier, S. Fluence correction factors in plastic phantoms for clinical proton beams. *Phys. Med. Biol.* **2002**, *47*, 3055.
80. Zhang, R.; Taddei, P. J.; Fitzek, M. M.; Newhauser, W. D. Water equivalent thickness values of materials used in beams of protons, helium, carbon and iron ions. *Phys. Med. Biol.* **2010**, *55*, 2481.

CHAPTER SEVEN

The Dielectric Formalism for Inelastic Processes in High-Energy Ion–Matter Collisions

Claudia C. Montanari and Jorge E. Miraglia
Instituto de Astronomía y Física del Espacio, CONICET and Universidad de Buenos Aires, casilla de correo 67, sucursal 28, C1428EGA, Buenos Aires, Argentina

Contents

Abstract

In this chapter we analyze the possibilities and ranges of validity of the dielectric formalism to deal with correlated bound electrons in matter by using the shellwise local plasma approximation. This model describes the response of the electrons of the same binding energy as a whole (collectively), screening the interaction with the impinging ion. It considers separately each sub-shell of target electrons, with the corresponding dielectric response. The density of electrons and the energy gap are included explicitly by employing the Levine and Louie dielectric function. The goal of this chapter is to summarize and review the capability of this model to deal with fundamental magnitudes of the atomic collisions expressed as different moments of

Advances in Quantum Chemistry, Volume 65
ISSN 0065-3276, http://dx.doi.org/10.1016/B978-0-12-396455-7.00007-8

the energy loss: ionization cross sections (single or multiple, differential, and total), stopping power (and mean excitation energy), and energy loss straggling. This review covers a wide range of the collisions of ions with gases and solids, paying special attention to multi-electronic targets. The advantages and disadvantages of the model in comparison with independent electron ones, ranges of validity and future prospect will be considered.

1. INTRODUCTION

When a swift heavy particle travels through matter, different inelastic processes take place. The atomic electrons are excited or ionized, making the particle to lose energy. The probability of these events to happen, the mean energy loss during the ion passage, the effects on the target atoms (i.e., how deep are the ionized shells, what is the final charge state of the atom) are subjects of study for the different theories on heavy particle collisions.[1, 2] This research branch finds important applications in many fields, including medicine within hadron therapy (for recent reviews, see Refs. 3–6).

In this chapter we discuss the possibilities and ranges of validity of the shellwise local plasma approximation (SLPA) to deal with some of the fundamental inelastic collisions mentioned above. This is a many-electron model within the frame of the dielectric formalism, especially suitable for multi-electronic targets and high energy collisions in which target deep shells are involved.[7, 8] The SLPA describes the electronic response of each sub-shell of target electrons as a whole, including screening among electrons.[9] This is of particular interest when describing many-electron sub-shells such as $4f$ or $3d$, for example. The main characteristics of the SLPA are the independent-shell approximation (a dielectric function for each sub-shell of target electrons, meaning that only the electrons of the same binding energy respond collectively to the ion perturbation and screen among them) and the inclusion of the binding energy explicitly (not free-electron gas, but electron gas with an energy threshold).

It must be stressed that the SLPA is an *ab initio* calculation (no parameters included) whose only inputs are the atomic densities of the different sub-shells and the corresponding binding energies. It allows us to calculate the different moments of the energy loss: ionization cross sections (single or multiple, differential, and total), stopping power (and mean excitation energy), and energy loss straggling. The advantages and disadvantages of the model, as well as ranges of validity and future prospects will be discussed in the following pages.

2. THE SHELLWISE LOCAL PLASMA APPROXIMATION

2.1 Historical aspects

When a fast heavy ion moves in a medium, it polarizes the target electron cloud. This gives rise to an induced potential, which can be described as a trailing wake that follows the motion of the projectile (see Ref. 9 and references therein). The many-body consistent treatment for an ion traveling through an homogeneous free-electron gas was developed by Lindhard[10] and by Ritchie,[11] within the linear response approximation (LRA).

This dielectric formalism was extended to deal with atomic bound electrons as a free-electron gas of local density, known as the local plasma approximation (LPA). It was applied to stopping power (energy loss per unit length) of heavy ions in matter using the logarithmic high energy limit.[12,13] Later on developments of the LPA included the extension to isolated atoms by Rosseau et al.[14] and to intermediate energies by employing the fully dielectric formulation.[15–17] In the LPA by Lindhard and subsequent works, the response of bound electrons, even local, considers the electronic cloud as a whole by using the total density of electrons in the atom.

In the last years we have improved and extended the use of the dielectric formalism to deal with bound electrons of gaseous and solid targets (insulators and metals), not only for energy loss calculations, but also for ionization probabilities and energy loss straggling.[7, 8, 18–33] The full dielectric formalism was employed together with the theoretical description of bound electrons through the atomic wave functions and binding energies.

Our developments for the SLPA had two main steps. First the separate dielectric response for each shell, by considering the independent-shell approximation. Physically, this independent-shell approximation means that when an electron of the *nl* sub-shell is ionized only the other *nl*-electrons are included in the screening of the ion potential. This gave very good results for the energy loss even at intermediate energies,[18–25] as far as the perturbative approximation is valid. A previous proposal of the independent shells within the LPA, known as the orbital OLPA, is due to Meltzer et al.[34]

However, this approach uses the logarithmic high energy limit for the stopping power.

The second step was the inclusion of the ionization gap using the Levine and Louie dielectric function.[35] This is a very important point to advance in the calculation of ionization probabilities, not only for inner-shells of metals, but also for insulators[26] and gases.[27] In this sense, the SLPA provides an interesting alternative to the independent electron models, with very good results as compared with complex formulations such as the continuum distorted wave eikonal initial state (CDW-EIS) approximation,[28] and with great advantages in the computational effort and time.

The Levine and Louie dielectric function[35] keeps the characteristics of Lindhard's,[10] i.e., electron–electron correlation to all orders, collective response, and *f*-sum rule (particle number conservation). It must be noted that the SLPA is a first order approximation (as far as the dielectric functions are calculated in LRA, like Lindhard's [10] or variations, such as Mermin's[36] or Levin–Louie's[35]). It means that it is a perturbative description valid for $Z_P/v < Z_T$ and $v > v_e$ with v_e being the mean velocity of the electrons of the *nl*-shell. The SLPA with this dielectric function proved to give good results in stopping power calculations[7, 29–33] in an extended energy range that includes the maximum of the stopping, and for inner-shell ionization of very heavy targets at high enough impact velocities.[8]

2.2 Theoretical details: The Levine–Louie dielectric function and the independent-shell approximation

Consider a bare ion of charge Z_P moving at velocity v in a free-electron gas (FEG) of homogeneous density ρ, a Fermi momentum $k^F = [3\pi^2\rho]^{-1/3}$ and a Seitz radio $r_S = [(4/3)\pi\rho]^{1/3}$. Following the dielectric formalism, the stopping power per unit length is expressed as

$$S = \frac{2Z_P^2}{\pi v^2} \int_0^\infty \frac{\mathrm{d}k}{k} \int_0^{kv} \omega \,\mathrm{Im}\left[\frac{-1}{\varepsilon(k,\omega)}\right] \mathrm{d}\omega, \tag{1}$$

with $\varepsilon(k,\omega)$ being the quantum dielectric function of the medium.[9] Different approximations are employed for the dielectric function, with the Mermin–Lindhard dielectric function[36] being the most accurate one to account for the plasmon time decay. This dielectric function depends on the constant density of electrons ρ and the plasmon damping γ, both characteristics obtained from the optical properties of each material[37] and from tabulations.[38]

The SLPA formulation has a general expression for the different moments of the energy loss. It describes the inelastic collision considering the interaction with each nl sub-shell of target electrons separately, with $S_{nl}^{(t)}$ being its energy moment of order t ($t = 0$ the ionization cross section, $t = 1$ the stopping power, $t = 2$ the square energy loss straggling) given by

$$S_{nl}^{(t)} = \frac{2}{\pi v^2} \int_0^{\infty} \frac{Z_{\mathrm{P}}^2 \, \mathrm{d}k}{k} \int_0^{kv} \omega^t \, \mathrm{Im}\left[\frac{-1}{\varepsilon_{nl}(k,\omega)}\right] \mathrm{d}\omega. \tag{2}$$

The total moment will be the addition of the shell contributions $S^{(t)} = \sum_{nl} S_{nl}^{(t)}$.[29] In the case of metals, electrons are treated differently depending on whether they belong to the free-electron gas (FEG) or to the inner-shells (bound electrons).

The dielectric function $\varepsilon_{nl}(k,\omega)$ in Eq. (2) is a mean value of a local response that depends on the density of electrons of the shell $\rho_{nl}(r)$ and the ionization gap ϵ_{nl}

$$\mathrm{Im}\left[\frac{-1}{\varepsilon_{nl}(k,\omega)}\right] = \int \mathrm{Im}\left[\frac{-1}{\varepsilon^{\mathrm{LL}}(k,\omega,k_{nl}^{\mathrm{F}}(r),\epsilon_{nl})}\right] \mathrm{dr} \tag{3}$$

with $k_{nl}^{\mathrm{F}}(r) = [3\pi^2 \rho_{nl}(r)]^{1/3}$ the local Fermi velocity. The dielectric function employed $\varepsilon^{\mathrm{LL}}$, is the Levine–Louie one,[35] which includes explicitly the energy gap of each shell. It is defined as

$$\mathrm{Im}\left[\varepsilon^{\mathrm{LL}}(q,\omega,k_{nl}^{\mathrm{F}}(r))\right] = \begin{cases} \mathrm{Im}\left[\varepsilon^{\mathrm{L}}(q,\omega_g,k_{nl}^{\mathrm{F}}(r))\right], & \omega > |\epsilon_{nl}| \\ 0, & \omega < |\epsilon_{nl}| \end{cases} \tag{4}$$

with $\omega_g = \sqrt{\omega^2 + \epsilon_{nl}^2}$ and $\varepsilon^{\mathrm{L}}(q,\omega,k_{nl}^{\mathrm{F}}(r))$ being the usual Lindhard dielectric function.[10] Note that if we consider no binding energy, $\epsilon_{nl} = 0$, the usual expression for the probability in the dielectric formalism (Lindhard) is recovered. Once the imaginary part is defined, the real part, $\mathrm{Re}\left[\varepsilon^{\mathrm{LL}}(q,\omega,k_{nl}^{\mathrm{F}}(r))\right]$ is obtained in closed form through the Kramers–Kronig relation, as shown in Ref. 35. This model for the dielectric function, proposed originally for semiconductors and insulators,[35] satisfies the so-called f-sum rule, or particle number conservation, that is the desirable feature for a dielectric function. In fact, this modified version of the SLPA was first applied to calculation of stopping power in insulators.[26]

The density of electrons of the shell $\rho_{nl}(r)$ and the ionization gap ϵ_{nl} are the only inputs for the SLPA. For atoms they can be obtained from the Hartree–Fock wave functions tabulated by Clementi and Roetti[39] or by Bunge et al.[40] For very heavy atoms ($Z > 54$) they can be calculated using the relativistic solutions of the Schrödinger equation.[7, 8, 32]

In the case of an ion with N bound electrons and charge state $q = Z_P - N$, the interaction with target electrons can be expressed through a screened ion-charge $Z_P^{(q)}(r)$ that depends on the distance to the nucleus (with the ion electrons frozen, just screening the nucleus). It verifies $Z_P^{(q)}(r) \to q$ for long distance collisions and $Z_P^{(q)}(r) \to Z_P$ for close collisions.

In order to include this inhomogeneous screened ion-charge in Eq. (2), instead of Z_P, we need the Fourier transform of $Z_P^{(q)}(r)$ given by

$$Z_P^{(q)}(k) = Z_P - \sum_{j=1}^{N} \left\langle \varphi_j \left| e^{i\mathbf{k}.\mathbf{r}} \right| \varphi_j \right\rangle . \tag{5}$$

Using Flannery integrals[41] and the Slater-type expansion for the projectile wave functions (Clementi and Roetti tables[39] for neutral atoms and for positive ions), $Z_P^{(q)}(k)$ has an analytical closed form (see the Appendix in Ref. 8 for the details).

We calculated $Z_P^{(q)}(r)$ for different ions from He^{+q} ($q = 0, 1$) up to Ne^{+q} ($q = 0, \ldots, 9$). In order to express it in a simple way to be included in the programs of calculus we fitted the exact $Z_P^{(q)}(r)$ with two exponentials as follows:

$$Z_P^{(q)}(r) = q + \sum_{j=1}^{2} Z_j \exp(-a_j r). \tag{6}$$

In Tables 7.1 and 7.2 we include the parameters Z_j, a_j for the different ions and charge states.

The inclusion of $Z_P^{(q)}(k)$ in Eq. (2) is straightforward. The SLPA for the total energy moment of order t due to the interaction with an ion of nucleus charge Z_P and charge state q is

$$S_{(q)}^{(t)} = \sum_{n,l} \frac{2}{\pi v^2} \int_0^\infty \frac{[Z_P^{(q)}(k)]^2 \,\mathrm{d}k}{k} \int_0^{kv} \omega^t \,\mathrm{Im}\left[\frac{-1}{\varepsilon_{nl}(k,\omega)}\right] \mathrm{d}\omega. \tag{7}$$

In the following sections we present and discuss the current state of the SLPA to deal with energy loss (Section 3), its straggling (Section 4), and with ionization cross sections (Section 5). The order was chosen by

Table 7.1 Parameters to fit the screened ion-charge as function of the distance to the nucleus for He^{+q} to N^{+q}. These functions were obtained using Hartree–Fock wave functions by Clementi and Roetti.[39] for neutral atoms and for positive ions

Ion	q	Z_1	a_1	Z_2	a_2
He^{+}	1	−1.289	4.722	2.289	3.529
He^{0}	0	−0.288	7.784	2.288	2.359
Li^{2+}	2	−0.101	1.017	1.101	3.411
Li^{+}	1	−0.195	0.957	2.195	3.024
Li^{0}	0	1.123	0.531	1.877	3.347
Be^{3+}	3	−0.100	1.359	1.100	4.554
Be^{2+}	2	−0.334	16.900	2.334	5.298
Be^{+}	1	1.172	0.942	1.828	4.635
Be^{0}	0	2.412	0.824	1.588	5.161
B^{4+}	4	−0.106	1.730	1.106	5.674
B^{3+}	3	3.684	7.832	−1.684	11.561
B^{2+}	2	1.250	1.376	1.750	6.138
B^{+}	1	2.532	1.255	1.468	6.823
B^{0}	0	3.631	1.075	1.369	7.285
C^{5+}	5	−0.097	2.101	1.097	6.891
C^{4+}	4	−0.208	2.120	2.208	6.459
C^{3+}	3	1.783	7.227	1.217	1.731
C^{2+}	2	2.591	1.661	1.409	8.473
C^{+}	1	3.753	1.520	1.247	9.114
C^{0}	0	4.801	1.331	1.199	9.446
N^{6+}	6	−0.058	2.353	1.058	8.420
N^{5+}	5	−0.216	2.452	2.216	7.553
N^{4+}	4	1.805	8.357	1.195	2.086
N^{3+}	3	2.639	2.077	1.361	10.093
N^{2+}	2	3.846	1.965	1.154	11.027
N^{+}	1	4.953	1.792	1.047	11.776
N^{0}	0	5.973	1.596	1.027	12.094

Table 7.2 Similar to Table 7.1 for O^{+q} to Ne^{+q} ions

Ion	*q*	Z_1	a_1	Z_2	a_2
O^{7+}	7	−0.093	2.776	1.093	9.228
O^{6+}	6	−0.207	2.825	2.207	8.744
O^{5+}	5	1.766	9.774	1.234	2.514
O^{4+}	4	1.299	10.976	2.701	2.591
O^{3+}	3	3.899	2.395	1.101	12.836
O^{2+}	2	5.043	2.237	0.957	13.962
O^{+}	1	6.113	2.052	0.887	14.782
O^{0}	0	7.087	1.824	0.913	14.749
F^{8+}	8	−0.043	2.881	1.043	11.032
F^{7+}	7	−0.130	2.543	2.130	10.157
F^{6+}	6	1.754	11.088	1.246	2.912
F^{5+}	5	1.296	13.463	2.704	2.896
F^{4+}	4	3.958	2.834	1.042	15.007
F^{3+}	3	5.190	2.750	0.810	16.145
F^{2+}	2	6.277	2.554	0.723	17.556
F^{+}	1	7.245	2.286	0.755	18.684
F^{0}	0	8.213	2.064	0.787	18.438
Ne^{9+}	9	−0.095	3.316	1.095	11.422
Ne^{8+}	8	−0.166	3.366	2.166	11.214
Ne^{7+}	7	1.787	12.100	1.213	3.247
Ne^{6+}	6	1.309	14.616	2.691	3.279
Ne^{5+}	5	1.024	16.471	3.976	3.256
Ne^{4+}	4	5.181	3.129	0.819	19.045
Ne^{3+}	3	6.299	2.953	0.701	21.086
Ne^{2+}	2	7.350	2.738	0.650	22.470
Ne^{+}	1	8.360	2.524	0.640	23.075
Ne^{0}	0	9.326	2.306	0.674	22.586

historical reasons: the dielectric formalism, and more specifically, the local plasma approximation, was developed to describe the energy loss of heavy particles in solids. Instead, using a collective formalism to calculate ionization probabilities of solids and, even more of gaseous targets, is much more demanding and is new theoretical development due to the SLPA.

3. ENERGY LOSS IN PARTICLE PENETRATION OF MATTER

The mean value of the energy loss of particles in matter, also known as stopping power, is a necessary ingredient of many parts of basic science, of medical and technological applications.[42, 43] It is an average of the ion energy loss per unit path length. At intermediate to high impact velocities, this energy loss is related to ionization of target electrons. The higher the ion energy, the deeper the excited electrons. In the case of metals, it means that at intermediate and high impact energies, the description of the stopping power due to excitation of valence electrons (the FEG of metals) is not enough, and target inner-shells must be included.

Different experimental methods are used to determine stopping powers[44] and important collections of data, statistics, and semiempirical functions are available in the web.[45, 46] Many semiempirical and theoretical models have been developed (see Refs. 47–50 and references therein). However, the description of very heavy targets, i.e., those with the close 4*f* sub-shell with 14 electrons, remains a heavy task for first principle theoretical calculations. On the contrary, the SLPA, being a many-electron model, describes with the same degree of complexity Ne, Cu, or Au targets. Furthermore, the more electrons the shell has, the more suitable the method is. On the other hand, this model works within the dielectric formalism, so dynamical screening effects among electrons are included. This proved to be of particular interest for the case of the *f*-shells.[32]

The only inputs for the SLPA are the density of electrons around the nucleus for each sub-shell and the binding energy. As far as these inputs are known, the SLPA calculations reduce to rather simple numerical integrations, given by Eqs. (2) and (7). Moreover, the extension of this formalism to deal with complex targets (compounds, molecules of biological interest, water) is straightforward if these inputs are known.

3.1 The SLPA in stopping power of metals for protons

The SLPA gives good results for energy loss by protons in metal targets.[7, 31, 32] We consider and discuss here three cases of special interest , Cu ($Z=29$), W ($Z=74$), and Au ($Z=79$). This choice is founded on their experimental and technological interest, and on the availability of data. Cu and Au are the two targets with the largest amounts of stopping measurements. For W, new interest is related to its properties as inner-wall of fusion reactors.[51] For our theoretical interest, these are targets for which outer electrons can be described as FEG and we can deal separately with bound electrons using the SLPA. This separate description of the response of bound and valence electrons as inhomogeneous and homogeneous electron gases, respectively, is part of the good agreement obtained. On the other hand, the separate calculations allow using different models in each case (i.e., the SLPA for bound electrons and a non-perturbative formalism for the FEG).

For Cu, the densities and binding energies were obtained from the tabulated Hartree–Fock wave functions.[39, 40] For Au and W, the atomic wave functions are the solutions of the relativistic Dirac equation instead the nonrelativistic Schrödinger equation. We employed to this end the fully relativistic *ab initio* wave functions obtained by using the HULLAC[52] code (see Ref. 7 for the details). The binding energies were compared with tabulated experimental binding energies in solids by Williams.[53]

For H ions in solids we calculate the stopping cross section just considering H^+(Refs. 7, 32). At low velocities, the screening of the H^+ nucleus is strong enough to have very loose or directly no bound electron.[54, 55]

The total stopping of protons in Cu is displayed in Figure 7.1. This value was obtained by adding the bound electron and the FEG contributions. The former was calculated with the SLPA formalism (Eq. (2) with $t = 1$) and adding the contributions of the different sub-shells to get total stopping of bound electrons. The latter by employing the dielectric formalism (perturbative approximation) with the Mermin–Lindhard dielectric function.[36] The characteristic plasmon frequency and width employed here for Cu FEG are $\omega_p = 0.703$ a.u. and $\gamma = 0.950$ a.u., respectively. This yields a mean value of electrons in the FEG as $N_e = 3.14$, and a Seitz radius as $r_S = 1.82$ a.u. These values were obtained from the optical data of the energy loss function[37] by considering only the first important peak. These number of electrons in the FEG is similar to the experimental value recommended by Isaacson.[38] To keep the total number of electrons, we considered Cu as [Ar] $3d^{7.86}$ and the "3.14" electrons as FEG.

In Figure 7.1 we compare our total stopping cross sections of Cu for protons, with the experimental data available,[45] and with SRIM08 results.[46] The contribution from the FEG and the bound electrons are

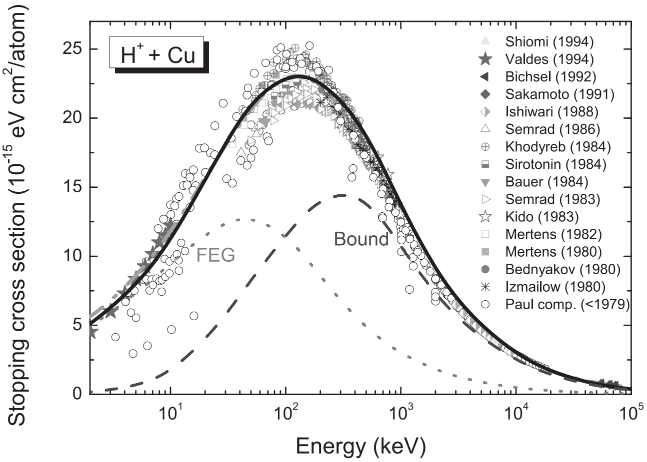

Figure 7.1 Stopping cross sections of Cu for protons. Curves: solid line, total stopping adding the contributions by bound electrons (blue dashed line, SLPA) and by the FEG (red dotted line, Mermin–Lindhard dielectric calculation); orange dash dotted line, SRIM08 results.[46] Symbols: experiments as reported by Paul;[45] different symbols marked within the figure, experimental data since 1980; black hollow circles, experimental data corresponding to (1935–1979).

displayed separately. About the experimental data, we indicate separately only the data since 1980, while earlier data is plotted together with a single type of symbol. The agreement with the experimental data and with the SRIM08 curve[46] is very good in the whole energy range. The stopping maximum is correctly described in energy and value. The differential description for the FEG and the bound electron contribution is the basis for this agreement.[56]

We display in Figures 7.2 and 7.3 the stopping cross sections of Au and W for protons.[7, 32] These are very interesting targets because the $4f$ sub-shell plays a major role. For solid Au, we describe the FEG with the Mermin–Lindhard dielectric function and the following parameters (in atomic units): Seitz radio $r_S = 1.17$ a.u. (17 electrons in the FEG), plasmon energy $\omega_P = 1.37$ a.u., and a damping $\gamma = 1.37$ a.u. These values were obtained as a first approximation to optical energy loss function tabulated in the Handbook of Optical Constants by Palik and Ghosh.[37] This means that the atomic $5p^6, 5d^{10}$ and $6s^1$ electrons are considered as the homogeneous FEG, and the first bound electrons are those of the $4f$ sub-shell. The bound electron contribution was calculated using the SLPA with the fully relativistic wave functions and binding energies.[7]

In Figure 7.2 we display our theoretical results for the stopping cross section together with the large amount of experimental data available,[45] and the SRIM 2008 values. The contributions of the FEG and the bound electrons are displayed separately. The FEG contribution in gold, even the main one, cannot explain the total results for energies above 100 keV. As observed in the figure, there is an important dispersion of experimental values, mainly around the stopping maximum, which makes any theoretical description not conclusive. In order to have a cleaner picture of the situation, we displayed separately the stopping measurements of the last 25 years. This arbitrary classification allowed us to note that, except for the results by Martinez-Tamayo et al.[57] the latest stopping measurements tend to be close to a single curve. The semiempirical SRIM08 code [46] gives a curve in accordance with these latest experimental data.

The total stopping cross section obtained using the SLPA for bound electrons describes well the experimental data in the whole energy range. It has a maximum at 130 keV, shifted and higher than SRIM08,[46] and in rather good agreement with theoretical predictions by Heredia-Avalos et al.[58] and

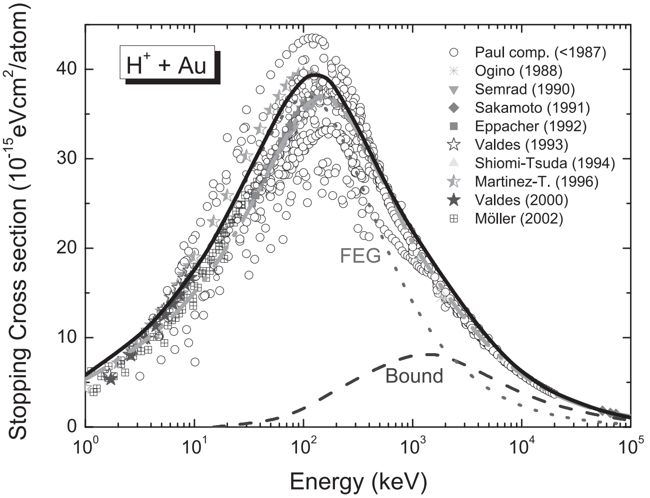

Figure 7.2 Stopping cross section of Au for protons. Curves: dashed line, present SLPA calculation for the bound electrons; dotted line, FEG contribution using the Mermin–Lindhard dielectric function;[36] solid line, total stopping as the addition of the previous two contributions; dashed dotted line, SRIM08.[46] Symbols: experiments as reported by Paul;[45] different symbols within the figure are data since 1987; hollow circles, previous measurements.

with the measurements by Martinez-Tamayo et al.[57] and to previous ones by Kreussler et al.[59] and Santry and Werner.[60]

It is worth mentioning that the relativistic results for the binding energies of Au show spin-orbit split in energy $E_{n,l,l\pm\frac{1}{2}}$ (see Fig. 1 in Ref. 7). It is an important point, because these are sub-shells that are very close in energy. As mentioned before, the SLPA describes collectively those electrons with *equal* binding energy, allowing screening among them. We use $E_i \pm \Delta E_i$ as criterion of *equal* binding energy, with ΔE_i being the quantum uncertainty

$$\Delta E_i \approx \frac{1}{\Delta t_i} = \frac{v}{\langle r \rangle_i}, \tag{8}$$

with E_i and $\langle r \rangle_i$ being the energies and mean radius of the sub-shell.

Using this criterion we have found that in the cases studied, the spin-orbit split is not resolved. Physically this implies that the 14 electrons of the $4f$ sub-shell respond together shielding the projectile, and not the 8 electrons $4f_{7/2}$ and the 6 electrons $4f_{5/2}$ separately. This separated or not-separated response of the sub-shells is very clear in the case of protons in W, as displayed in Figure 7.3. For W, not only cannot the $4f_{7/2}$ and $4f_{5/2}$ be resolved, but there is also inter-shell screening between $5p$ and $4f$ electrons. As displayed in Table 7.3, these sub-shells are very close in energy and respond collectively to the ion passage. The importance of this effect is clear

Table 7.3 Fully-relativistic binding energies of the N and O-shells of Au and W. These results have been calculated by Mitnik and collaborators[7, 32] with the HULLAC code[52] for isolated atom. Also included are the experimental values, E^{expt}, compiled by Williams.[53] The binding energies are in atomic units

	$E_{\text{Au}}^{\text{expt}}$	$E_{\text{Au}}^{\text{th}}$	$E_{\text{W}}^{\text{expt}}$	E_{W}^{th}
$4s$	28.0	26.0	21.8	20.8
$4p_{1/2}$	23.6	22.8	18.0	17.3
$4p_{3/2}$	20.1	19.2	15.6	14.8
$4d_{3/2}$	13.0	12.5	9.40	9.0
$4d_{5/2}$	12.3	11.9	8.95	8.5
$5s$	3.94	4.1	2.78	2.9
$4f_{5/2}$	3.22	3.2	1.23	1.3
$4f_{7/2}$	3.08	3.1	1.16	1.2
$5p_{1/2}$			1.66	1.9
$5p_{3/2}$			1.35	1.5

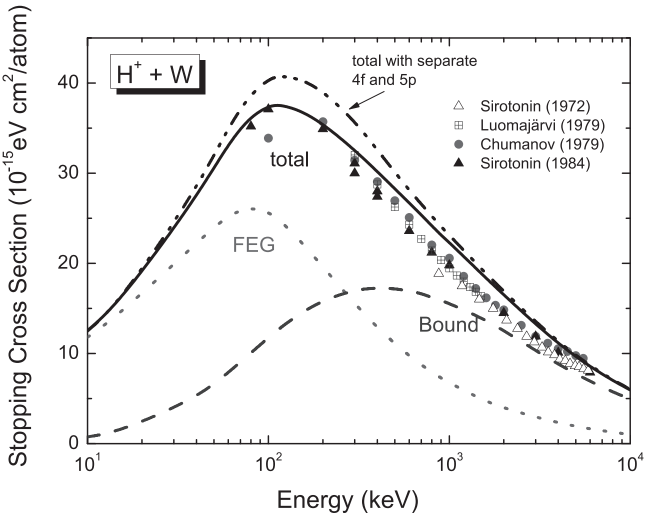

Figure 7.3 Stopping cross sections of W for protons. Curves: solid lines, present theoretical results for the contributions by bound electrons (SLPA) and the FEG, and total stopping as the addition of the previous two; dash lines, results obtained using the SLPA with independent *5p* and *4f* responses. Symbols: different symbols within the figure are the experimental data as reported by Paul.[45]

while comparing total theoretical and experimental stopping in Figure 7.3. Note that the screening among electrons reduces the stopping cross section in all the cases (in Au, too). This effect can only be taken into account with a many-electron model and a collective description of bound electrons. The results displayed in Figure 7.3 describe the stopping maximum quite well. However an overestimation of the experimental data around 2 MeV is found. We will return to this matter in the following section in relation to the Bethe high energy limit.[61]

3.2 Stopping number and Bethe limit

The SLPA provides an interesting alternative to describe the energy loss of different materials for energetic ions. At high energies the ion losses energy due to the interaction with deep bound electrons, so the behavior of the stopping power at high energies is a good test for the model.

The stopping power can be expressed in terms of the dimensionless stopping number $L(v)$ as

$$S(v) = \frac{4\pi Z_P^2 Z_T}{v^2} L(v). \tag{9}$$

In the high-but-nonrelativistic velocity regime, the stopping number is described by the Bethe asymptotic formulae[61]

$$\lim_{v\to\infty} L(v) = L^{\mathrm{Bethe}}(v) = \ln\left(\frac{2v^2}{I}\right), \tag{10}$$

with I being the mean excitation energy, characteristic of each target.[62] Our theoretical description of the energy loss should converge to the Bethe high (but nonrelativistic) energy limit.

In Figure 7.4 we display the stopping number comparing the SLPA, Bethe limit, and SRIM08 values,[46] the latter representing the behavior of the experimental data for each target. Using the Lindhard and Scharff scaling with v^2/Z_{T} (valid for elements of high atomic number[63]) we plot together the SLPA results for the stopping number of W and Au. The straight-line in the logarithmic scale of v^2 is the Bethe limit.

It is an interesting figure because different aspects can be observed: the Lindhard and Scharff scaling is valid for W and Au; the SLPA tends to the Bethe limit, as expected theoretically; the description of the experimental data with the SLPA is good at the lower energies displayed in this figure, but in the high energy region the SLPA is closer to Bethe than to the experiments. This is a 10% of theoretical-experimental difference in the energy region 1–4 MeV, the energy region observed in Figure 7.3.

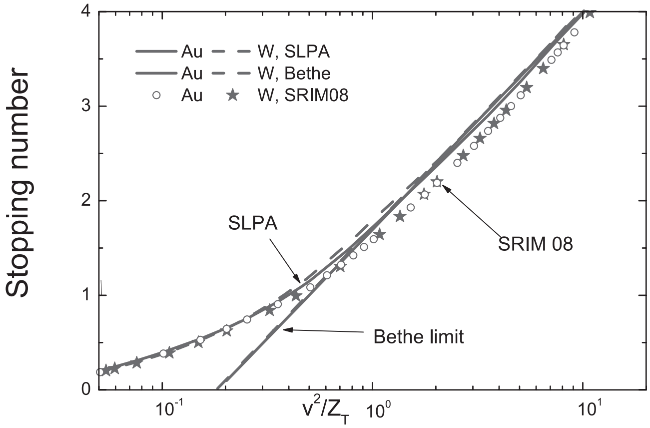

Figure 7.4 Lindhard scaling for the stopping number L. Curves: SLPA results for Au (solid line) and W (dashed line); Bethe high energy limit obtained using Eq. (10) and the mean excitation energies I suggested by the ICRU49 Report (Ref. 44) $I_W = 727 \pm 30$ eV, and $I_A u = 790 \pm 30$ eV. Symbols: SRIM08 values for Au (hollow circles) and W (stars).

This means a certain overestimation by the SLPA in the high energy region, which is related to the theoretical tie to the Bethe limit.

3.3 Stopping for dressed ions

By dressed ions we mean those ions with bound electrons, whether they be neutral or with a certain charge state. In this case, while the ion moves through a medium, loss and capture processes take place until reaching an equilibrium distribution of charge states q ($q = 0, \ldots, Z_P$) within the foil, depending on the ion velocity v. In the equilibrium regime, the mean energy loss will be the average of the stopping cross sections $S_{(q)}$ given by Eq. (7), with the calculated screened ion-charge (Tables 7.1 and 7.2), weighted with the data of fraction of ions with charge q at that velocity, $\phi_q(v)$. Namely

$$S = \sum_{q=0}^{Z_P} \phi_q(v) S_{(q)}. \tag{11}$$

The equilibrium charge fractions at each impact velocity, $\phi_q(v)$, are external inputs. A fitting of a large amount of experimental values of charge states exiting the solid, combining different ions and targets is due to Schiwietz and Grande.[64] It is available within the CasP5.0 code.[65]

On the other hand, for ions with nuclear charge $Z_P \geqslant 2$, the perturbative description for the FEG contribution is found to underestimate the experimental data for energies below that of the maximum of stopping power. For this reason for He and heavier ions we combine the SLPA for the bound electrons with a non-perturbative model for the FEG. As the energy loss by ionization of inner-shells contributes at high energies, the perturbative approximation used in the SLPA is still valid. In fact, for the stopping power of Zn for different ions we found the description of bound electrons ($1s$ up to $3d^9$) with the SLPA to be valid for He up to C projectiles, as displayed in Figure 7.5. For O ions in Zn the perturbative SLPA overestimates the total stopping cross section.[33]

Figure 7.5 summarizes previous results for the different ions[22, 29, 30, 33] in Zn. The non-perturbative model for the FEG employed in these calculations is the Transport Cross Section-Extended Friedel Sum Rule (TCS-EFSR) approach by Arista and coworkers.[66, 67]

To analyze in detail the stopping of dressed ions in matter, we consider the stopping of Cu and Au targets for He. In Figure 7.6 we display the

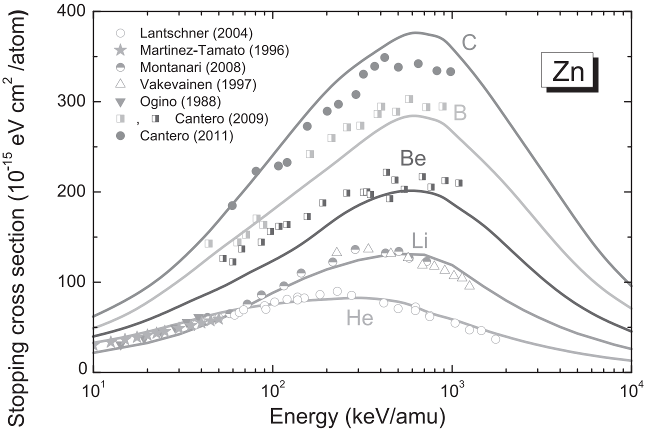

Figure 7.5 Total stopping cross sections of different ions in Zn. Curves: theoretical calculations adding SLPA for bound electrons and HISTOP (non-perturbative) for the FEG.[22, 29, 30, 33] Symbols: experimental data for He, Li, Be, and B ions as in Figure 6 of Cantero et al.;[30] for C ions, Cantero et al.[33]

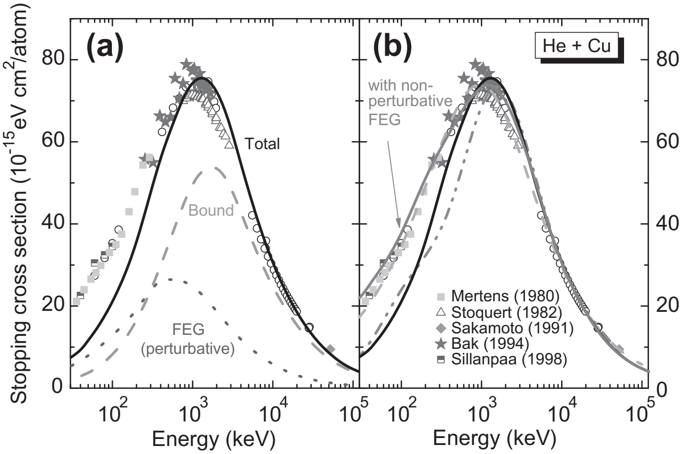

Figure 7.6 Stopping cross sections of Cu for He ions. Curves: (a) dashed line, the bound electron contribution obtained using the SLPA; dotted line, the FEG contribution with Mermin dielectric function (perturbative); solid line, total stopping adding both contributions (similar to Figure 7.1); (b) black solid line, total stopping adding the SLPA results for bound electrons and a perturbative description for the FEG with Mermin dielectric function as in (a); gray solid line, total stopping adding the SLPA results for bound electrons and a non-perturbative model for the FEG by Arista for He in Zn;[22] dashed dotted line, SRIM08;[46] dashed double-dotted line, Casp5.0.[65] Symbols: experiments as reported by Paul;[45] different symbols within the figure are data since 1980; hollow circles, previous measurements.

partial and total stopping cross section for He in Cu. In Figure 7.6a the contributions of bound electrons and FEG are displayed separately. The former calculated with the SLPA, the latter with the dielectric formalism (perturbative, LRA), using the Mermin–Lindhard dielectric function (similar to the case of protons in Cu). The behavior of the total stopping displayed in Figure 7.6a has already been found for Zn (Ref. 22), i.e., below 100 keV/amu ($v < 2$ a.u.) the perturbative model does not describe the experimental data. The replacement of the perturbative FEG-stopping by the non-perturbative one gives the total stopping displayed in Figure 7.6b. For the FEG we employed, as first approximation, the results for the FEG of Zn for He (with $r_s = 2.02$) by Arista using the TCS-EFSR in Ref. 22. The theoretical-experimental disagreement at low energies may be related to this. However, the tendency to correct the underestimation due to the perturbative calculation is clear. We also include in Figure 7.6b Schiwietz and Grande results with the unitary convolution approximation (UCA) for swift particles (available in the CasP5.0 code[65]), and the semiempirical values by the SRIM08 code.[46] Above the stopping maximum all the theoretical results agree quite well. For energies below this value the combination of different calculations, for bound electrons and FEG shows very good agreement if the non-perturbative FEG model is used.

For He in Au, in Figure 7.7 we display the theoretical results obtained in perturbative approximation, with the SLPA for bound electrons and Mermin–Lindhard dielectric function for valence electrons. As observed in the case of protons in Au, for He in Au the dispersion of the experimental data is important for impact energies below the stopping maximum. The theoretical description is quite good for impact energies above 400 keV. The maximum of the stopping is correctly described around 1 MeV. For energies below 400 keV we are outside the limit of validity of the perturbative approximation. The combination of SLPA with a non-perturbative description for stopping due to valence electrons of Au (as for Cu or Zn targets) is expected to improve these results.

4. ENERGY LOSS STRAGGLING

The theoretical square energy loss straggling, Ω^2, or the second moment of the energy loss ($t = 2$ in Eqs. (1) and (7)), describes the statistical dispersion of the energy loss. It represents the energy loss variance per unit path length of a Gaussian-type energy loss distribution.[68] The condition for obtaining a Gaussian distribution is that the energies transferred in

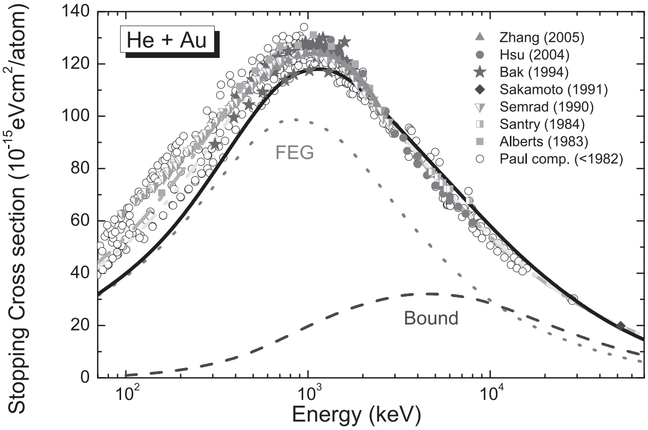

Figure 7.7 Stopping cross sections of Au for helium. Curves: dashed line, the bound electron contribution obtained using the SLPA; dotted line, the FEG contribution with Mermin dielectric function (perturbative); solid line, total stopping adding both contributions (similar to Figure 7.1); dashed double-dotted line, SRIM08 results;[46] dashed dotted line, ICRU49;[44] dashed double-dotted line, Casp5.0.[65] Symbols: experiments as reported by Paul;[45] different symbols within the figure are data since 1982; hollow circles, previous measurements.

the individual collisions should be small as compared to the width of the final distribution.[69]

The high energy limit for the energy loss straggling was calculated by Bohr[69] as

$$\Omega_B^2 = 4\pi Z_P^2 Z_T, \tag{12}$$

which is proportional to Z_T, the total number of target electrons active in the collision at sufficiently high energies.

The energy loss straggling is an interesting parameter to study theoretically and experimentally. It represents a sensitive input for many calculations (Ziegler[46] or Ma et al.[70]) and computer simulations, like SIMNRA by Mayer[71] for material analysis, or SEICS by Garcia-Molina and coworkers[72, 73] for elements of biological interest.

For the stopping power, there are important compilations of data available[45] and wellknown and tested semiempirical programs[46] and recommended values.[44] However, the situation is completely different for energy loss straggling. The most widely used electronic energy loss straggling is Yang empirical fitting[74] included in modern ion beam analysis codes such as SIMNRA, NDF, CORTEO, and MCERD.[75] However the accuracy of this formulae is questioned for different reasons.[25, 76] The source of the Yang expression is a compilation of data prior to 1990 which presents serious problems. Measurements of energy loss straggling set severe requirements to target preparation (well defined thin films, uniformity, and homogeneity).[77] Experimental methods, such as transmission or Rutherford back scattering, are very sensitive to roughness and inhomogeneity of the samples, which introduce important additional energy loss straggling, especially at low energies.[68, 77, 78] It produces overestimation in a region around the stopping maximum[68] and an important dispersion among data. The weight of this contribution in the experimental straggling is clear in some measurements previous to 1980 included in Yang''s compilation and fitting.[74] Fortunately, there is a great number of recent measurements from different laboratories and using different techniques that show less spread and tend to be close to a single band.[79–85]

In this section we present different theoretical results calculated with the SLPA. These results improve those by Chu[86] using the LPA with Hartree–Fock densities and considering the electronic cloud as a whole. The difference between our results and those by Chu is the shell to shell description of the dielectric response.

In Figure 7.8 we display the SLPA results for square energy loss straggling normalized to Bohr value[69] for H and He ions in Cu. The different

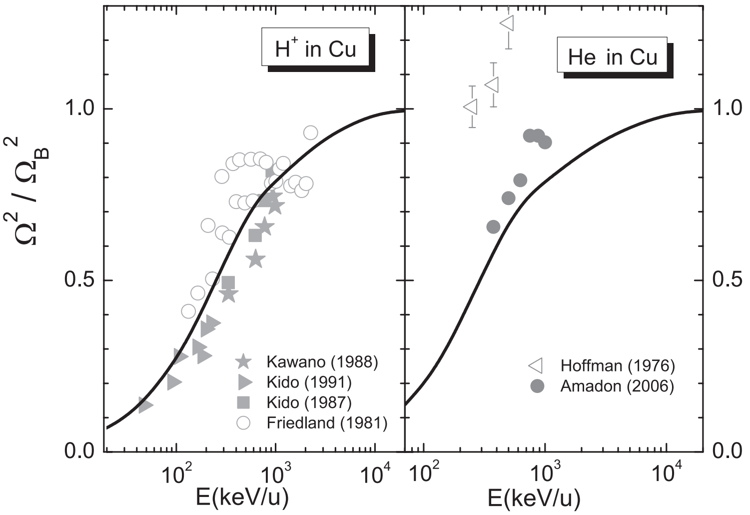

Figure 7.8 Squared straggling of Cu for H and He ions, normalized to Bohr high energy limit. Curves: solid lines, our SLPA results. Symbols: experimental data as indicated in the figure. For H^+ in Cu (Refs. 80–82, 88); for He in Cu (Refs. 83, 87).

charge states of He in Cu were considered to obtain these values, however no important differences with respect to He^{2+} were obtained for energies above 200 keV/amu. We include in Figure 7.8 the experimental data by Hoffman and Powers[87] and by Friedland and Kotze,[88] which are not corrected to exclude the inhomogeneity contribution. The overshooting of these values is clear, mainly in the data by Hoffman and Powers.[87]

The SLPA values for the energy loss straggling tend to the Bohr limit from below, and do not show the overshooting (Bethe–Livingston shoulder[89]) around the energy of maximum stopping power predicted by the binary collision formalisms.[89, 90] At high energies, the square energy loss straggling tends to a value proportional to the total number of target electrons, as predicted by Bohr.[69] If we calculate the square straggling as

$$\Omega^2/\Omega_B^2 = \sum_{nl} \Omega_{nl}^2/\Omega_B^2, \tag{13}$$

we can say that each term verifies that $\Omega_{nl}^2/\Omega_B^2 \to N_{nl}/Z_T$, with N_{nl} being the number of electrons in the *nl* sub-shell.[7, 25] This is an interesting point because it indicates the high energy limit expected for each shell. But it also represents a demanding requirement for the theoretical calculation, because all shells, even deep ones, contribute to the total straggling, i.e., the L-shell of Au with eight electrons is 10% of the Au energy loss straggling.

On the other hand, we found that the energy loss straggling normalized to Z_P^2 (Bohr limit) is almost independent of the ion atomic number Z_P, at least for low Z ions showing a perturbative dependence with the ion-charge.[25] In order to test this in Figure 7.9 we plotted together the experimental data for different ions in Au together with the SLPA values for the bare ions in Au. The experimental data included are those that explicitly take into account the roughness and inhomogeneity of the sample. In the case of the experimental data by Andersen et al.[91] they have been corrected in 10% due to the estimation of this contribution. The data by Møller et al. shows asymmetric error bars that correspond to Figure 5 in Ref. 92.

We can observe that the soft dependence with the ion-charge of the experimental data normalized to Bohr limit is valid at least for H, He, and Li ions. The data for B in Au by Hsu et al.[79] could indicate a deviation for higher Z ions. On the other hand, Figure 7.9 emphasizes the good description of the straggling obtained with the SLPA, even for unexpected low energies. Note that all target electrons have been considered in the calculation, even the very deep ones.

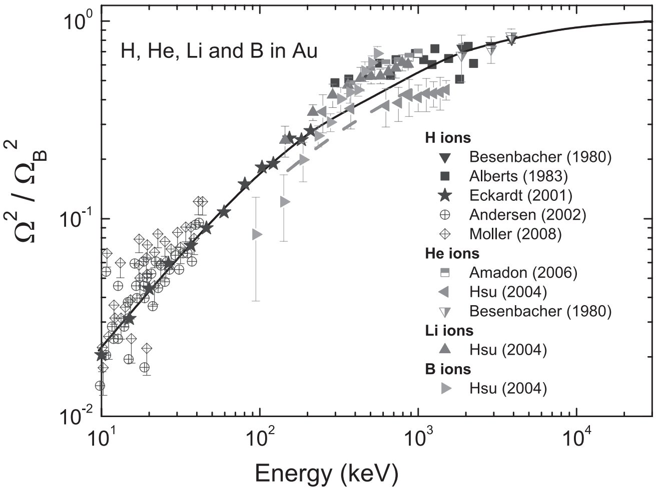

Figure 7.9 Squared straggling of Au for H, He, Li and B ions, normalized to Bohr high energy limit. Curves: solid line, SLPA straggling for bare ions; dashed line, Chu values.[86] Symbols: indicated in the figure; for H ions;[68, 84, 85, 91, 92] for He ions;[68, 79, 83] for Li and B ions.[79]

Based on the interest in new general expressions for the energy loss straggling, we used Lindhard's scaling, which proved to be valid for stopping by high Z-targets. In Figure 7.10 we plotted the square energy loss straggling normalized to Bohr, as function of v^2/Z_T, including experimental data for different ions (H to B) and targets (Cu, Au, Pb, and Bi). The theoretical SLPA results for Au to Bi are actually very close (they are hardly distinguishable in this figure). The SLPA results for Cu (dashed line) separates slightly from the others. This scaling for the energy loss straggling is an interesting proposal because it introduces the possibility of a simple universal function to describe it.

4.1 The SLPA for stopping and straggling of gases

The SLPA evolved from models developed to deal with solid targets. However there is no reason to restrict its use just to solid targets. The response of bound electrons employed is based on the atomic wave functions and binding energies, described in full Hartree–Fock or Hartree–Fock–Dirac methods (the latter for targets with $Z_T > 54$) .

In the previous sections we show the performance of the SLPA, with good results for the description of the energy loss of ions in solid matter, is

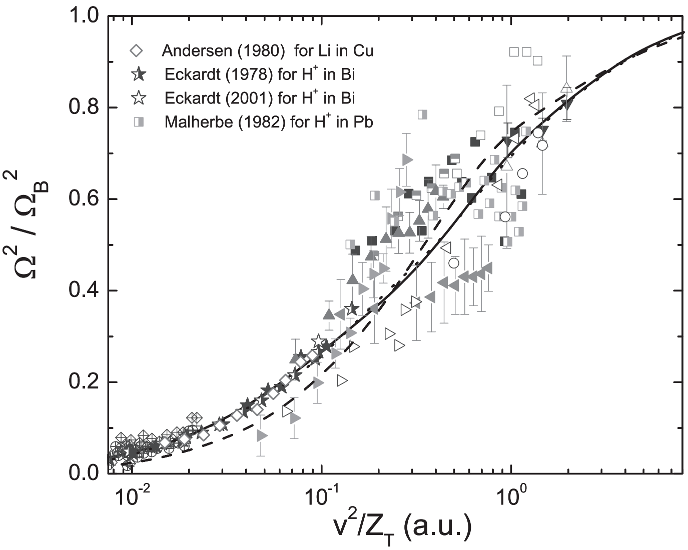

Figure 7.10 Scaling for the squared straggling normalized to Bohr as function of Lindhard parameter υ^2/Z_T. Curves: SLPA results for Au (solid line), Bi (dotted line) and Cu (dashed line). Symbols: similar to Figures 7.8 for H and He in Cu and to 7.9 for different ions in Au; additional data included[84, 93–95] as signed inside the figure.

the intermediate to high energy region. In Figures 7.11 and 7.12 we display the SLPA results for stopping and straggling of protons in four rare gases, and compare them with experimental data available.

Note that for gaseous targets we should include not only the ionization channel (as for solid Cu or Au, for which the valence electrons as FEG fills the outer bands). For gases, the excitation channel is allowed. For the rare gases we use the SLPA formulation given by Eq. (2) with energy gaps equal to that to the first excited state (i.e., in atomic units, we use for Ne, $E_{3s} = -0.1809$; for Ar, $E_{4s} = -0.1666$; for Kr, $E_{5s} = -0.1598$; for Xe, $E_{6s} = -0.1517$). The energy gap is a sensitive point in the SLPA. Different values for these excitation energies will change present results.

We display in Figures 7.11 and 7.12 the SLPA stopping and straggling of rare gases for protons. The stopping description in Figure 7.11 is good for proton impact above 300 keV in all the rare gases. Below this energy the theoretical values underestimate the data, especially for Ar. These results look quite different from those in metals. This is not surprising. In general stopping power in metals is better known and described than in gases. For example, for stopping of Ne, Ar, and Kr the very recent calculations by

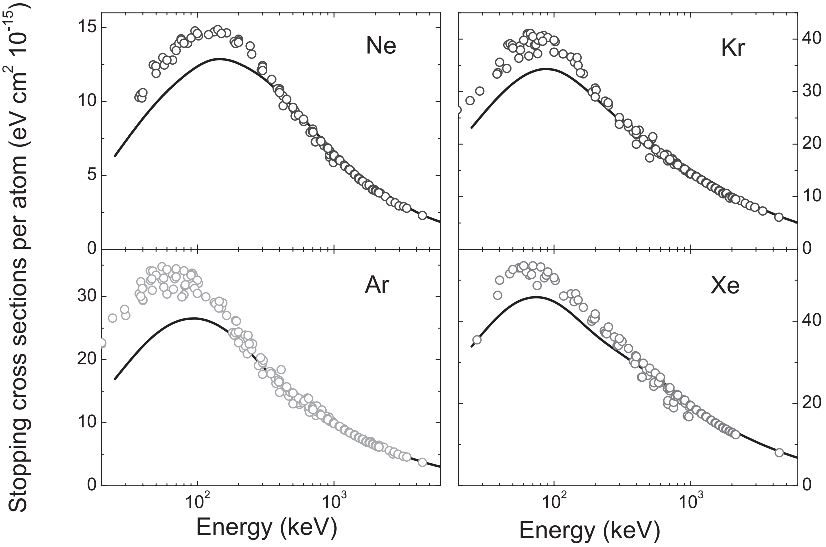

Figure 7.11 Stopping cross section of rare gases for H^+. The curves correspond to the SLPA results. The experimental data is available in Ref. 46.

Grande and Schiwietz [65] with the UCA consider that the underestimation is due to the contribution of projectile electron capture and loss. The SLPA results displayed in Figure 7.11 are quite similar to CasP5.0[65] without loss. To this stage and related only to the SLPA calculations, we consider as first step to review the values for the excitation energy. Changes in this value affects more to outer-than to inner-shells, so the effect will be noted in the low to intermediate energy region.

In Figure 7.12 we display the SLPA results and the corresponding measured values for energy loss straggling of the four rare gases for protons. The results are good, but for Xe they seem to underestimate the experimental data. The comparison of this collective electron model with the other independent electron formalisms, such as the UCA, the CDW-EIS,[96, 97] or the continuum distorted wave (CDW)[98] methods would be a good framework for future developments. Note that the CDW[98] and CDW-EIS[96, 97] methods use the same scattering wave function for the final state in the exit channel. They differ in entrance channel, where the CDW method employs the full Coulomb wave function for the electronic continuum state, which is in the CDW-EIS method approximated by the associated asymptotic form given by the eikonal logarithmic Coulomb phase. This difference yields the corresponding difference in the perturbation potentials in the CDW and CDW-EIS methods.

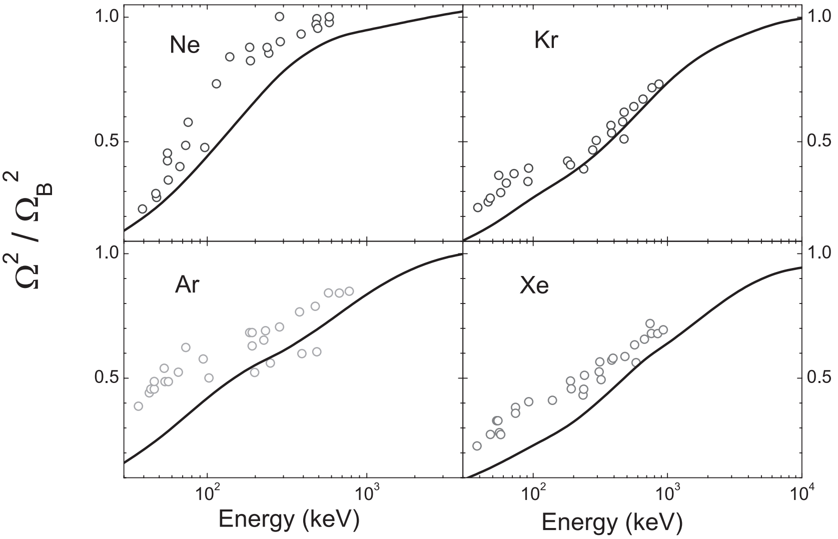

Figure 7.12 Straggling of rare gases for H^+. The curves correspond to the SLPA results. Experimental data by Besenbacher et al.[68]

The SLPA presents no specific problem to deal with the straggling and the stopping power, its calculation is straightforward. On the contrary, numerical difficulties are found to calculate the stopping power and straggling within the CDW-EIS approach. These magnitudes involve the elements, first and second moments of the energy, which depend on the behavior of very energetic electrons. The CDW-EIS approximation has serious numerical problems in two fronts. First, a good description of energetic electrons is required, which demands not only a calculation of a substantial grid of energies in this region (that would not contribute to the ionization cross section). Second, these states require a large amount of angular momenta l_{max} to describe the final continuum state.

To illustrate this point, Figure 7.13 shows the straggling and the stopping power of protons in Ne as a function of the proton velocity. Three sets of values are displayed: the results of CDW-EIS calculations with $l_{\text{max}} = 4, 8$, and the *exact* value ($l_{\text{max}} \approx 28$). This *exact* value agrees quite well with the SLPA, as can be observed in Figure 7.13. As the proton velocity increases, the straggling evidently requires a greater amount of angular momenta which makes the calculation more lengthy and harder. In addition, inner-shells become very important sources for the straggling. Although these inner-shells hardly contribute to the ionization cross sections, or even

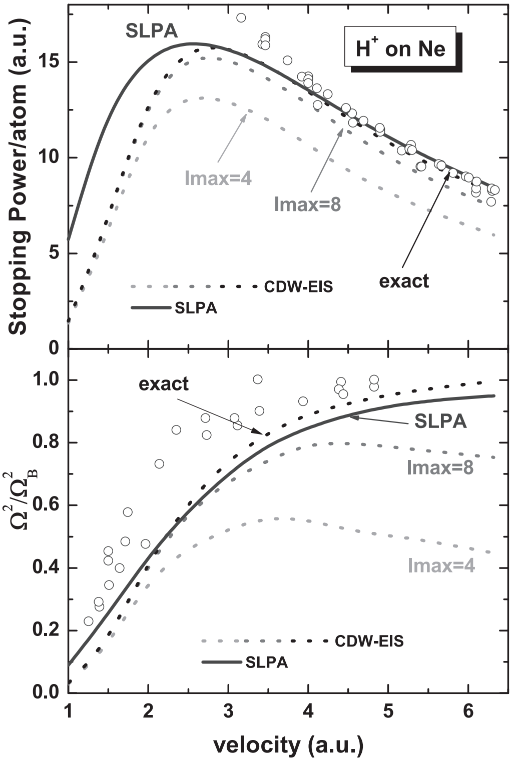

Figure 7.13 Stopping and straggling of H^+ in Ne. The curves correspond to the SLPA and CDW-EIS results, as marked in the figures. CDW-EIS values for different L_{max} are shown (see the text for details).

to the stopping power in our range of energy, they do contribute to the energy loss straggling. While the outer-shells are enough to calculate the cross section, for the straggling even deep shells are important. This makes the CDW-EIS calculation highly demanding in terms of computing time. This is a great advantage of the SLPA over distorted wave methods.

5. IONIZATION PROBABILITIES

As mentioned in the introduction, the energy moment of zero order, or cross section, is a much more sensitive parameter for the theoretical model than the stopping or straggling. In what follows we show the results of this dielectric model to deal with the description of a fundamental collisional process, the ionization.

5.1 Total ionization cross sections

The total ionization probabilities are calculated from Eq. (2) with $t = 0$. In Figure 7.14 we display the SLPA results for total ionization cross section of protons in four rare gases. We also include, as in the previous section, the comparison with the CDW-EIS values. The experimental total ionization cross sections include not only the direct ionization but also the post-collisional ionization also. As proved from multiple ionization calculations including Auger-type post-collisional contributions, the theoretical total cross section must include this contribution too.

The total cross sections displayed in Figure 7.14 are calculated adding the ionization of each sub-shell, and are afterwards corrected to include post-collisional ionization. To this end we used the ratios between total cross sections with and without post-collisional ionization in Ref. 99. In fact, this contribution is negligible for Ne and Ar targets, so the total cross sections are just the addition over the sub-shell contributions. But post-collisional influence increases with the target atomic number. For Kr it goes

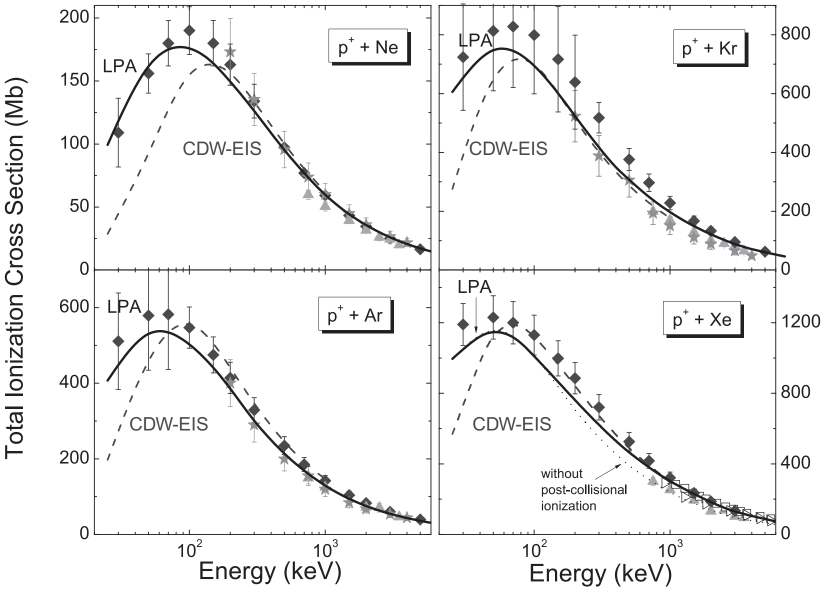

Figure 7.14 Total ionization cross sections of rare gases by proton impact. Curves: solid lines, present SLPA results; dashed lines, CDW-EIS calculations.[99] Symbols: experimental data by DuBois et al.[100] and Cavalcanti et al.[101] and recommended values by Rudd et al.[102] For Xe, we also included the electron impact data at high energies by Schram et al.[103] and by Nagy et al.[104]

from 5% at 300 keV to 24% at 5 MeV, and for Xe from 15% at 300 keV to 32% at 5 MeV (see Table 1 in Ref. 99). In Figure 7.14, for Xe target, we display both, direct ionization and total ionization including post-collisional ionization. We also include in Figure 7.14 the multiple-ionization data for electron in Xe in order to extend the description to high energies. The experimental values in Xe show the importance of post-collisional ionization in the total ionization.

The SLPA total ionization cross sections displayed in Figure 7.14 are amazing. The SLPA is good in the same energy region that the CDW-EIS. These values for ionization cross sections together with the stopping and straggling comparison in Figures 7.11 and 7.12 establish the SLPA as a good framework for further calculations.

These results consider the contribution of every shell of target electrons. We have also test the model for ionization of certain shells, such as K-shell of low Z elements[21] or, recent calculations for L- and M-shells of Au, Pb, and Bi,[8] with good agreement with the experimental data.

5.2 Multiple ionization

Multiple ionization is a quite demanding calculation for any theoretical model. It depends on the probabilities as function of the impact parameter. The SLPA implies a space-mean value of the dielectric response as given by Eq. (3). In principle the capability to describe total values may not be valid for the differential description. Moreover, the SLPA depends directly on the density of electrons of each sub-shell. It is tight to the zeros of the density distribution.

In Figure 7.15 we display the SLPA results for multiple ionization of Kr by high energy proton impact. In a many-electron description like this, the multiple ionization follows a Poisson distribution (instead of the multinomial distribution of the independent electron models).

The high energy region is governed by the post-collisional ionization.[27] The values displayed in Figure 7.15 take into account the post-collisional ionization following the method described in Ref. 27. This method includes the post-collisional electron emission in a semiempirical way by employing branching ratios of ionization distribution measured in sophisticated photo ionization experiments (see for example the values tabulated in Ref. 106).

We also display in Figure 7.15 the theoretical values for direct multiple ionization, in order to make the importance of the post-collisional

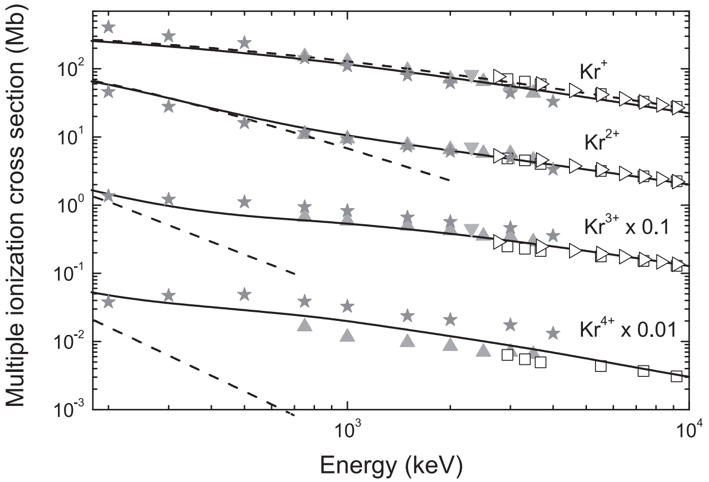

Figure 7.15 Multiple ionization of Kr by proton impact. Curves: SLPA results with (solid line) and without (dashed line) post-collisional ionization. Symbols: stars, DuBois et al.;[100] full up-triangles, Cavalcanti et al.;[101] full down-triangles, Haugen et al.;[105] open symbols for high energy electron impact data, open squares Schram et al.;[103] open triangles, Nagy et al.[104]

contribution clearer. The direct multiple ionization almost describes the single-ionization, but double-ionization cannot be explained only with direct ionization above 1 MeV. For higher orders of ionization, the importance of the post-collisional contribution increases at even lower energies than double-ionization, as can be noted for triple and quadruple ionization of Kr. As observed in Figure 7.15, the agreement of the SLPA with the experimental data is good. However some differences have been found for other targets (mainly for Ne) that require further research (analyzes of the branching ratios employed, other post-collisional contributions not considered, possibility of a semi-localized model, not so tied to the zeros of the density of electrons, etc.).

5.3 Differential cross sections

Another test for the SLPA is the differential cross section as function of the electron energy. In Figure 7.16 we display the SLPA results and compare them with experimental data by Rudd [107, 108] and by Toburen.[109] Two kinds of differential values are displayed: the differential cross sections $d\sigma/d\omega$, with ω the energy transferred to the emitted electron; and

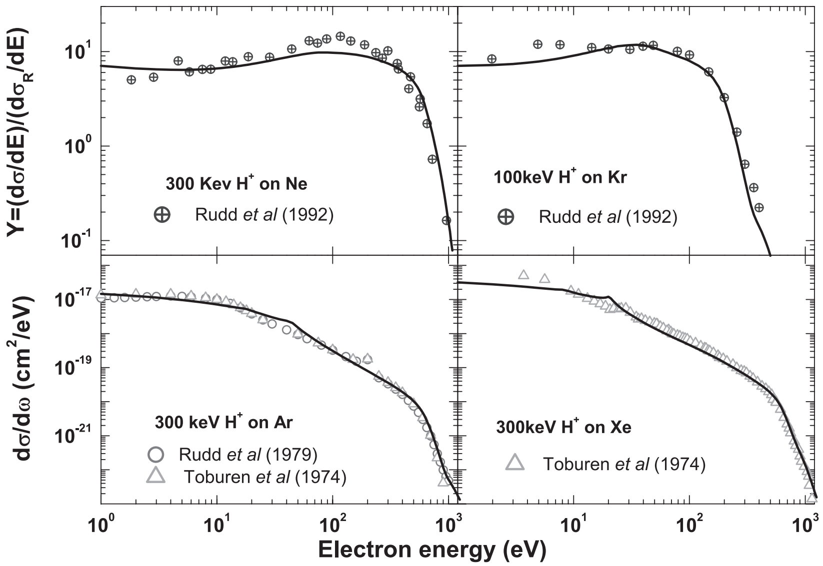

Figure 7.16 SLPA Differential ionization cross sections as function of the energy of the emitted electron for protons in Ar and Xe targets. Platzman plots for protons in Ne and Kr targets. Experimental data in Refs. 107–109.

the Platzman plots Y, which is a ratio between $\mathrm{d}\sigma/\mathrm{d}\omega$ and the modified Rutherford differential cross section $(\mathrm{d}\sigma/\mathrm{d}\omega)_{\mathrm{R}}$ by impact of one electron with the same energy,[110]

$$Y = \frac{\mathrm{d}\sigma/\mathrm{d}\omega}{(\mathrm{d}\sigma/\mathrm{d}\omega)_{\mathrm{R}}} = \frac{v^2(\omega + I)^2}{4\pi}\,\mathrm{d}\sigma/\mathrm{d}\omega, \tag{14}$$

where I is the binding energy of the outermost shell. The difference between the modified Rutherford expression and the "original" one is the presence of I. For the rare gases we used the values of Bunge et al.[40] ($I = 0.850$, 0.591, 0.524, and 0.457 a.u. for Ne, Ar, Kr, and Xe, respectively). The energy distributions present a scale involving several orders of magnitudes and so the finer details could go unnoticed. An alternative way to plot this is the Platzman plot, whose physical interpretation is the effective number of electrons. The magnitude Y is a powerful tool for analyzing and identifying the different features in the differential cross sections in fine detail.[110]

In Figure 7.16 we present the theoretical Platzman plots for Ne and Kr, while for Ar and Xe we display the differential cross sections $d\sigma/d\omega$. The SLPA results displayed in this figure are actually overwhelming. The distribution in electron energy describes the experimental data quite well. The comparison with a much more sophisticated and computer-time consuming calculation as the CDW-EIS confirms this evaluation (see this comparison in Ref. 110).

6. CONCLUSIONS AND FUTURE PROSPECTS

In this chapter the properties, possibilities, and ranges of validity of the SLPA have been presented, analyzed, and compared with other theoretical descriptions and with experimental data. This comparison for stopping power, energy loss straggling, and ionization cross sections, establishes this model as a trustworthy alternative to the independent electron model calculations. In addition, the SLPA is a simple-low-time calculation, and allows to correctly describe the inner-shells, which proved to be very important in energy loss straggling calculations

The possibilities for further developments may start in three different areas:

i. *The extension of the model to complex targets:* As far as the space dependent density of electrons in the shell and energies are available the SLPA calculation can be performed. This seems to be the next and most important step, with a wide spectrum of possibilities to deal with molecular, clusters, or even bio-structures.

ii. *A delocalized approximation for multiple ionization:* The SLPA describes the response of the bound electrons as function of their density. In this way the SLPA cancels where the density of electrons does. But the interaction with the ion should include a region around each point. This may be taken into account through a delocalized version that does not change the total values, which is currently under study.

iii. *Antiscreening:* Finally the description of the inelastic processes of the target with a dielectric function states a difference between projectile and target. Extending the SLPA to describe inelastic processes in the projectile should not be difficult, and would allow to extend the model to deal with antiscreening processes (inelastic processes in both centers[111]).

ACKNOWLEDGMENTS

This work was partially supported by the Consejo Nacional de Investigaciones Científicas y Técnicas, and the Agencia Nacional de Promoción Científica y Tecnológica of Argentina, as well as by the University of Buenos Aires.

REFERENCES

1. Belkić, Dž.; Mančev, I.; Hanssen, J. Four-body methods for high-energy ion-atom collisions. *Rev. Mod. Phys.* **2008**, *80*, 249.
2. Belkić, Dž. *Quantum Theory of High-Energy Ion-Atom Collisions*; Taylor and Francis: London, 2008.
3. Schardt, D.; Elsasser, T.; Schuls-Ertner, D. Heavy-ion tumor therapy: physical radiobiological benefits. *Rev. Mod. Phys.* **2010**, *82*, 383.
4. Belkić, Dž. Reviews of theories on ionization in fast ion-atom collisions with prospects for applications to hadron therapy. *J. Math. Chem.* **2010**, *47*, 1366.
5. Paganatti, H. Range uncertainties in proton therapy and the role of Monte Carlo simulations. *Phys. Med. Biol.* **2012**, *57*, R99.
6. Paul, H. The Stopping Power of Matter for Positive Ions. In *Modern Practices in Radiation Therapy*; Natanasabapathi, G., Ed.; InTech, 2012; p 113. <http://www.intechopen.com/books/modern-practices-in-radiation-therapy>.
7. Montanari, C. C.; Archubi, C. D.; Mitnik, D. M., et al. Energy loss of protons in Au, Pb, and Bi using relativistic wave functions. *Phys. Rev. A* **2009**, *79*, 032903.
8. Montanari, C. C.; Mitnik, D. M.; Miraglia, J. E. A collective model for inner shell ionization of very heavy targets. *Radiat. Eff. Defects Solids* **2011**, *166*, 338.
9. Echenique, P. M.; Flores, F.; Ritchie, R. H. Dynamic screening of ions in condensed matter. *Solid State Phys.* **1990**, *43*, 229.
10. Lindhard, J. On the properties of a gas of charged particles. *Mat. Fys. Medd. Dan. Vid. Selsk* **1954**, *28*, 1.
11. Ritchie, R. H. Interaction of charged particles with a degenerate fermi-dirac electron gas. *Phys. Rev.* **1959**, *114*, 644.
12. Lindhard, J.; Scharff, M. Energy loss in matter by fast particles of low charge. *Mat. Fys. Medd. Dan. Vid. Selsk* **1953**, *27*, 1.
13. Bonderup, E. Stopping of swift protons evaluated from statistical atomic model. *Mat. Fys. Medd. Dan. Vid. Selsk* **1967**, *35*, 1.
14. Rousseau, C. C.; Chu, W. K.; Powers, D. Calculations of stopping cross sections for 0.8- to 2.0-MeV alpha particles. *Phys. Rev. A* **1971**, *4*, 1066.
15. Chu, W. K.; Powers, D. Calculations of mean excitation energy for all elements. *Rev. Lett. A* **1972**, *40*, 23.
16. Wang, Y.-N.; Ma, T.-C. Stopping power for hydrogen molecular ions in solids: influence of the inner-shell electrons of target atoms. *Phys. Rev. A* **1994**, *50*, 3192.
17. Fuhr, J. D.; Ponce, V. H.; García de Abajo, F. J., et al. Dynamic screening of fast ions moving in solids. *Phys. Rev. B* **1998**, *57*, 9329.
18. Montanari, C. C.; Miraglia, J. E.; Arista, N. R. Dynamics of solid inner-shell electrons in collisions with bare and dressed swift ions. *Phys. Rev. A* **2002**, *66*, 042902.
19. Montanari, C. C.; Miraglia, J. E.; Arista, N. R. Antiscreening mode of projectile-electron loss. *Phys. Rev. A* **2003**, *67*, 062702.
20. Kadhane, U.; Montanari, C. C.; Tribedi, L. C. K-shell processes in heavy-ion collisions in solids and the local plasma approximation. *Phys. Rev. A* **2003**, *67*, 032703.

21. Kadhane, U.; Montanari, C. C.; Tribedi, L. C. Experimental study of K-shell ionization of low-Z solids in collisions with intermediate-velocity carbon ions and the local plasma approximation. *J. Phys. B* **2003**, *36*, 3043.
22. Lantschner, G. H.; Eckardt, J. C.; Lifschitz, A. F. Energy loss of helium ions in zinc. *Phys. Rev. A* **2004**, *69*, 062903.
23. Kadhane, U.; Kumar, A.; Montanari, C. C. K-shell ionization of low Z elements in ion–solid collisions and applicability of local plasma approximation. *Radiat. Phys. Chem.* **2006**, *75*, 1542.
24. Montanari, C. C.; Miraglia, J. E. Stopping power for swift dressed ions. *Phys. Rev. A* **2006**, *73*, 024901.
25. Montanari, C. C.; Miraglia, J. E.; Heredia-Avalos, S. Calculation of energy-loss straggling of C, Al, Si, and Cu for fast H, He, and Li ions. *Phys. Rev. A* **2007**, *75*, 022903.
26. Garcia, A. J.; Miraglia, J. E. Influence of surface channeling in the stopping of protons colliding with LiF surfaces. *Phys. Rev. A* **2006**, *74*, 012902.
27. Archubi, C. D.; Montanari, C. C.; Miraglia, J. E. Many-electron model for multiple ionization in atomic collisions. *J. Phys. B: At. Mol. Opt. Phys.* **2007**, *40*, 943.
28. Miraglia, J. E.; Gravielle, M. S. Ionization of the He, Ne, Ar, Kr, and Xe isoelectronic series by proton impact. *Phys. Rev. A* **2008**, *78*, 052705.
29. Montanari, C. C.; Miraglia, J. E.; Behar, M., et al. Theoretical and experimental study of energy loss of Li ions in Zn. *Phys. Rev. A* **2008**, *77*, 042901.
30. Cantero, E. D.; Fadanelli, R. C.; Montanari, C. C., et al. Experimental and theoretical study of the energy loss of Be and B ions in Zn. *Phys. Rev. A* **2009**, *79*, 042904.
31. Montanari, C. C.; Miraglia, J. E. *Theoretical Stopping Power of Copper for Protons Using the Shellwise Local Plasma Approximation*; Cornell University Library, 2009. Available from: <arXiv:0904.1386v1> [physics.atom-ph].
32. Montanari, C. C.; Mitnik, D. M.; Archubi, C. D., et al. Energy loss of protons in W using fully relativistic calculations and mean excitation energies of W, Au, Pb, and Bi. *Phys. Rev. A* **2009**, *80*, 012901.
33. Cantero, E. D.; Montanari, C. C.; Behar, M., et al. Experimental and theoretical study of the energy loss of C and O in Zn. *Phys. Rev. A* **2011**, *84*, 014902.
34. Meltzer, D. E.; Sabin, J. R.; Trickey, S. B. Calculation of mean excitation energy and stopping cross section in the orbital local plasma approximation. *Phys. Rev. A* **1990**, *41*, 220.
35. Levine, Z. H.; Louie, S. G. New model dielectric function and exchange-correlation potential for semiconductors and insulators. *Phys. Rev. B* **1982**, *25*, 6310.
36. Mermin, N. D. Lindhard dielectric function in the relaxation-time approximation. *Phys. Rev. B* **1970**, *1*, 2362.
37. Palik, E. D., Ghosh, G., editors *The Electronic Handbook of Optical Constants of Solids*; CA Academic: San Diego, 1999.
38. Isaacson, D. *Compilation of rs Values*; Radiation and Solid State Laboratory, New York University: New York, 1975; Doc. No. 02698.
39. Clementti, E.; Roetti, C. Roothaan–Hartree–Fock atomic wavefunctions: basis functions and their coefficients for ground and certain excited states of neutral and ionized atoms, Z = 54. *At. Data Nucl. Data Tables* **1974**, *14*, 177.
40. Bunge, C. F.; Barrientos, J. A.; Bunge, A. V., et al. Hartree–Fock and Roothaan–Hartree–Fock energies for the ground states of He through Xe. *Phys. Rev. A* **1992**, *46*, 3691.
41. Flannery, M. R.; Levi, H. Simple analytic expression for general two-center Coulomb integrals. *J. Chem. Phys.* **1969**, *50*, 2938.
42. Paul, H. New developments in stopping power for fast ions. *Nucl. Instrum. Methods Phys. Res. B* **2007**, *261*, 1176.

43. International Commission on Radiation Units and Measurements, ICRU Report 73, Oxford University Press, Oxford, 2005.
44. ICRU Report 49, International Commission on Radiation Units and Measurements, Bethesda, MD, 1993.
45. Paul, H. Stopping Power for Light Ions. *Graphs, Data, Comments and Programs*. <http://www.exphys.uni-linz.ac.at/stopping>.
46. Ziegler, J. F. The Stopping and Range of Ions in Matter. <http://www.srim.org>.
47. Sigmund, P. Particle Penetration and Radiation Effects Springer Series in Solid-State Physics; Springer: Berlin, 2006.
48. Arista, N. R. Energy loss of ions in solids: non-linear calculations for slow and swift ions. *Nucl. Instrum. Methods Phys. Res. B* **2002**, *195*, 91.
49. Grande, P. L.; Schiwietz, G. Ionization and Energy Loss Beyond Perturbation Theory. In , ; Cabrera-Trujillo, R., Sabin, J., Eds.; Advances in Quantum Chemistry; Elsevier: New York, 2004; 45, pp 7.
50. Abril, I.; Garcia-Molina, R.; Denton, CD., et al. Dielectric description of wakes and stopping powers in solids. *Phys Rev. A* **1998**, *58*, 357.
51. Balluc, N.; Abe, K.; Boutard, J. L., et al. Status of R&D activities on materials for fusion power reactors. *Nucl. Fusion* **2007**, *47*, S696.
52. Oreg, J.; Goldstein, W. H.; Klapisch, M., et al. Autoionization and radiationless electron capture in complex spectra. *Phys. Rev. A* **1991**, *44*, 1750.
53. Williams, G. P. *Electron Binding Energies of the Elements*; CRC Handbook of Chemistry and Physics, 66th ed.; Electron Binding Energies, X-Ray Data Booklet, Lawrence Berkeley Laboratory Pub-490 Rev., 1986; Vol. F170, Chapter 2.2. <http://www.jlab.org/gwyn/ebindene.html>
54. Arista, N. R. Charge States and Energy Loss of Ions in Solids. In *Ion Beam Science, Solved and Unsolved Problems*; Sigmund, P., Ed.; Mat. Fis. Medd. **2006**, *52*, 595.
55. Müller, J.; Bürgdorfer, J. Dynamical thresholds for the existence of excited electronic states of fast ions in solids. *Phys. Rev. A* **1991**, *43*, 6027.
56. Paul, H. Recent results in stopping power for positive ions, some critical comments. *Nucl. Instrum. Methods Phys. Res. B* **2010**, *268*, 3421.
57. Martinez-Tamayo, G.; Eckardt, J. C.; Lantschner, G. H. Energy loss of H^+ and He^+ in Al, Zn, and Au in the very low- to intermediate-energy range. *Phys. Rev. A* **1996**, *54*, 3131.
58. Heredia-Avalos, S.; Abril, I.; Denton, C. D. *J. Phys.: Condens. Matter.* **2007**, *19*, 466205.
59. Kreussler, S.; Varelas, C.; Sizmann, R. Electronic stopping power and effective charge of 50- to 230-keV D^+ and He^+ in carbon, aluminum, gold, and cesium. *Phys. Rev. B* **1982**, *26*, 6099.
60. Santry, D. C.; Werner, R. D. Stopping powers of C, Al, Si, Ti, Ni, Ag and Au for deuterons. *Nucl. Instrum. Methods Phys. Res. B* **1981**, *188*, 211.
61. Bethe, T. Zur theory des durchgangs schneller korpuskular-strahlen durch materie. *Ann. Phys.* **1930**, *5*, 325.
62. Kamakura, S.; Sakamoto, N.; Ogawa, H., et al. Mean excitation energies for the stopping power of atoms and molecules evaluated from oscillator-strength spectra. *J. Appl. Phys.* **2006**, *100*, 064905.
63. Lindhard, J.; Scharff, M. Stopping power of heavier substances. *Phys. Rev.* **1952**, *85*, 1058.
64. Schiwietz, G.; Grande, P. L. Improved charge-state formulas. *Nucl. Instrum. Methods Phys. Res. B* **2001**, *125*, 175–177.

65. Grande, P. L.; Schiwietz, G. Stopping of protons. Improved accuracy of the UCA model. *Nucl. Instrum. Methods Phys. Res. B* **2012**, *273*, 1.
66. Lifschitz, A. F.; Arista, N. R. Electronic energy loss of helium ions in aluminum using the extended-sum-rule method. *Phys. Rev. A* **1998**, *58*, 2168.
67. Arista, N. R.; Lifschitz, A. F. Non-Linear Approach to the Energy Loss of Ions in Solids. In , ; Cabrera-Trujillo, R., Sabin, J., Eds.; Advances in Quantum Chemistry; Elsevier Inc., pp 47.
68. Besenbacher, F.; Andersen, J. U.; Bonderup, E. Straggling in energy loss of energetic hydrogen and helium ions. *Nucl. Instrum. Methods Phys. Res. B* **1980**, *168*, 1.
69. Bohr, N. Penetration of atomic particles through matter. *K. Dan. Vidensk. Selsk. Mat. Fys, Medd.* **1948**, *24*, 19.
70. Ma, L.; Wang, Y.; Xue, J., et al. Energy loss and straggling of MeV ions through biological samples. *J. Appl. Phys.* **2007**, *102*, 084702.
71. Mayer, M. SIMNRA simulation program for the analysis of NRA, RBS and ERDA. *AIP Conf. Proc* **1999**, *475*, 541.
72. Heredia-Avalos, S.; Garcia-Molina, R. Energy-loss of swift $C_n^+(n = 2 - 60)$ clusters through thin foils. *Phys. Rev. A* **2007**, *76*, 012901.
73. Garcia-Molina, R.; Abril, I.; Heredia-Avalos, S., et al. A combined molecular dynamics and Monte Carlo simulation of the spatial distribution of energy deposition by proton beams in liquid water. *Phys. Med. Biol.* **2011**, *56*, 6475.
74. Yang, Q.; O'Connor, D. J.; Wang, Z. Empirical formulae for energy loss straggling of ions in matter. *Nucl. Instrum. Methods Phys. Res. B* **1991**, *61*, 49.
75. Barradas, N. P.; Rauhala, E. Data Analysis Software for Ion Beam Analysis. In *Handbook of Modern Ion Beam Materials Analysis*, ; Wang, Y., Nastasi, M., Eds.;; MRS: Warrendale, Pennsylvania, 2009., pp 307.
76. Msimanga, M.; Pineda-Vargas, C. A. .; Comrie, C. M. Heavy ion energy loss straggling data from time of flight stopping force measurements. *Nucl. Instrum. Methods Phys. Res. B* **2012**, *273*, 6.
77. Moon, D. W.; Le, H. I.; Kim, K. J., et al. Estimation of the electronic straggling using delta-doped multilayers. *Nucl. Instrum. Methods Phys. Res. B* **2001**, *183*, 10.
78. Eckardt, J. C.; Lantschner, G. H. Determination of thin foil thickness inhomogeneities by analysis of ion beam energy loss spectra. *Thin Solid Films* **1994**, *249*, 11.
79. Hsu, J. Y.; Yu, Y. C.; Liang, J. H. et al. Energy loss of He, Li and B isotopes with MeV energies in *Au. Nucl. Instrum. Methods Phys. Res. B* **2004**, *219–220,* 251.
80. Kido, Y. Energy straggling for fast proton beams passing through solid materials. *Nucl. Instrum. Methods Phys. Res. B* **1987**, *347*, 24–25.
81. Kido, Y.; Koshikawa, T. Energy straggling for medium-energy H+ beams penetrating Cu, Ag, and Pt. *Phys. Rev. A* **1991**, *44*, 1759.
82. Kawano, A.; Kido, Y. Effects of energy straggling on surface analysis with fast ion beams. *J. Appl. Phys.* **1988**, *63*, 75.
83. Amadon, S.; Lanford, W. A. He stopping power and straggle in Al, Ti, Co, Cu, Ag, Ta, and Au from 1.5 to 4 MeV. *Nucl. Instrum. Methods Phys. Res. B* **2006**, *249*, 34.
84. Eckardt, J. C.; Lantschner, G. H. Experimental energy straggling of protons in thin solid foils. *Nucl. Instrum. Methods Phys. Res. B* **2001**, *93*, 175–177.
85. Alberts, H. W.; Malherbe, J. B. Energy loss and straggling of p-, d- and a-particles in Au in the energy region 0.2 to 2.4 MeV. *Radiat. Eff.* **1983**, *69*, 231.
86. Chu, W. K. Calculation of energy straggling for protons and helium ions. *Phys. Rev. A* **1976**, *13*, 2057.
87. Hoffman, G. E.; Powers, D. Energy straggling of a particles in solid materials. *Phys. Rev. A* **1976**, *13*, 2042.

88. Friedland, E.; Kotze, C. P. Energy-loss straggling of protons, deuterons and a-particles in copper. *Nucl. Instrum. Methods Phys. Res.* **1981**, *191*, 490.
89. Livingston, M. S.; Bethe, H. A. Nuclear dynamics, experimental. *Rev. Mod. Phys.* **1937**, *9*, 245.
90. Sigmund, P.; Schinner, A. Barkas effect, shell correction, screening and correlation in collisional energy-loss straggling of an ion beam. *Eur. Phys. J. D* **2003**, *23*, 201.
91. Andersen, H. H.; Csete, A.; Ichioka, T., et al. An apparatus to measure stopping powers for low-energy antiprotons and protons. *Nucl. Instrum. Methods Phys. Res. B* **2002**, *194*, 217.
92. Møller, S. P.; Csete, A.; Ichioka, T., et al. Antiproton and proton energy loss straggling at keV energies. *Eur. Phys. J. D* **2008**, *46*, 89.
93. Andersen, H. H.; Besenbacher, F.; Goddiksen, P. Stopping power and straggling of 80–500 keV lithium ions in C, Al, Ni, Cu, Se, Ag, and Te. *Nucl. Instrum. Methods Phys. Res.* **1980**, *168*, 75.
94. Eckardt, J. C. Energy loss and straggling of protons and helium ions traversing some thin solid foils. *Phys. Rev. A* **1978**, *18*, 426.
95. Malherbe, J. B.; Alberts, H. W. Energy-loss straggling in lead of p, d and a-particles in the energy region 0.2–2.5 MeV. *Nucl. Instrum. Methods Phys. Res. B* **1982**, *196*, 499.
96. Crothers, D. S. F.; McCann, J. F. *J. Phys. B: At. Mol. Opt. Phys.* **1983**, *16*, 3229.
97. Fainstein, P. D.; Ponce, V. H.; Rivarola, R. D. A theoretical model for ionisation in ion-atom collisions. Application for the impact of multicharged projectiles on helium. *J. Phys. B: At. Mol. Opt. Phys.* **1988**, *21*, 287.
98. Belkić, Dž. A quantum theory of ionization in fast collisions between ions and atomic systems. *J. Phys. B* **1978**, *20*, 3529.
99. Montanari, C. C.; Miraglia, J. E. Antiproton, proton and electron impact multiple ionization of rare gases. *J. Phys. B: At. Mol. Opt. Phys.* **2012**, *45*, 105201.
100. DuBois, R. D.; Toburen, L. H.; Rudd, M. E. Multiple ionization of rare gases by H^+ and He^+ impact. *Phys. Rev. A* **1984**, *29*, 70.
101. Cavalcanti, E. G.; Sigaud, G. M.; Montenegro, E. C. Absolute cross sections for multiple ionization of noble gases by swift proton impact. *J. Phys. B: At. Mol. Opt. Phys.* **2003**, *36*, 3087.
102. Rudd, M. E.; Kim, Y-K.; Madison, D. H.; Gallagher, J. W. Electron production in proton collisions: total cross sections. *Rev. Mod. Phys.* **1985**, *57*, 965.
103. Schram, B. L.; Boerboom, A. J. H.; Kistermaker, J. Partial ionization cross sections of noble gases for electrons with energy 0.5–16 keV: I. Helium and neon. *Physica* **1966**, *32*, 185.Schram, B. L. Partial ionization cross sections of noble gases for electrons with energy 0.5–18 keV: II. Argon, Krypton and Xenon. *Physica* **1966**, *32*, 197.
104. Nagy, P.; Skutlartz, A.; Schmidt, V., et al. Absolute ionisation cross sections for electron impact in rare gases. *J. Phys. B: At. Mol. Opt. Phys.* **1980**, *13*, 1249.
105. Haugen, H. K.; Andersen, L. H.; Hvelplund, P., et al. Multiple ionization of noble gases by fully stripped ions. *Phys. Rev. A* **1982**, *26*, 1962.
106. Montanari, C. C.; Montenegro, E. C.; Miraglia, J. E. CDW-EIS calculations for multiple ionization of Ne, Ar, Kr and Xe by the impact of H^+ and He^+, including post-collisional electron emission. *J. Phys. B: At. Mol. Opt. Phys.* **2010**, *43*, 165201.
107. Rudd, M. E.; Kim, Y.-K.; Madison, D. H., et al. Electron production in proton collisions with atoms and molecules: energy distributions. *Rev. Mod. Phys.* **1992**, *64*, 441.
108. Rudd, M. E.; Toburen, L. H.; Stolterfoht, N. Differential cross sections for ejection of electrons from argon by protons. *At. Data Nucl. Data Tables* **1979**, *23*, 405.

109. Toburen, L. H. Distribution in energy and angle of electrons ejected from xenon by 0.3- to 2.0-MeV protons. *Phys. Rev. A* **1974**, *9*, 2505.
110. Miraglia, J. E. Ionization of He, Ne, Ar, Kr, and Xe by proton impact: single differential distributions in energy and angles. *Phys. Rev. A* **2009**, *79*, 022708.
111. Montenegro, E. C.; Meyerhof, W. E. Sum rules and electron–electron interaction in two-center scattering. *Phys. Rev. A* **1991**, *43*, 2289.

CHAPTER EIGHT

Single Ionization of Liquid Water by Protons, Alpha Particles, and Carbon Nuclei: Comparative Analysis of the Continuum Distorted Wave Methodologies and Empirical Models

Mario A. Bernal-Rodríguez[a] **and Jacinto A. Liendo**[b]
[a]Instituto de Física Gleb Wataghin, Universidade Estadual de Campinas, Brazil
[b]Departmento de Física, Universidad Simón Bolívar, Caracas, Venezuela

Contents

Abstract

Single ionization of liquid water by the impact of fast, but nonrelativistic heavy charged particles is reviewed. Special attention is focused on protons, alpha particles,

Advances in Quantum Chemistry, Volume 65
ISSN 0065-3276, http://dx.doi.org/10.1016/B978-0-12-396455-7.00008-X

and carbon ions. This phenomenon has been extensively studied by using theoretical methods during the last decades. Quantum-mechanical as well as semiclassical approaches have been developed. Nevertheless, experimental studies in this field are very scarce. Based upon both theoretical and experimental results, semiempirical formalisms have been reported. At the beginning, the first Born (B1) approximation emerged with some success in reproducing ionization cross sections corresponding to impact energies above a few hundreds of keV/u. The introduction of the distorted-wave formalism brought a remarkable improvement with respect to B1, mainly because of reproduction of the well-known two-center effects. The B1 approximation is treated here in order to be used as a reference model for all the subsequent comparisons. Also presented are the distorted-wave formalism and its variants. On the other hand, available experimental works for measuring ionization cross sections corresponding to water vapor targeted by hydrogen, helium, and carbon ions are summarized. In addition, the most relevant semiempirical approaches intended to calculate water ionization cross sections are addressed. Some of the experimental single ionization cross sections mentioned above are compared to those determined by the distorted-wave and semiempirical formalisms for liquid water. Finally, perspectives on the studies of the ionization problem are briefly commented.

1. INTRODUCTION

This chapter addresses the single ionization of water due to the impact of fast but not relativistic light ions ($Z \sim 1 - 6$). The main interest is focused on protons, alpha particles, and carbon ions with energies from a few tens of keV/u to about 10 MeV/u. The physical process under consideration has a great importance in areas such as medical radiation physics, space physics, plasma physics, material sciences, and others. Ionization cross sections (CS) are of critical importance in Monte Carlo codes used to simulate the passage of ionizing radiation through matter. In this work, the ionization problem is first explained from a phenomenological point of view. Later on, theoretical approaches to determine ionization CS are briefly reviewed: the first Born approximation and those based on the continuum-distorted wave approximation. Afterwards, a review of experimental works carried out to determine ionization CS in water vapor due to the impact of light ions is presented. In addition, a few semiempirical methods to calculate these CS are treated. Finally, the theoretical and semiempirical methods expounded here are compared with corresponding experimental results.

Atomic units are used throughout this chapter, except otherwise stated. In this system, the mass is expressed in units of the electron rest mass m; the length, in units of the Bohr radius $a_0 = \hbar^2/me^2$; the energy, in units of Hartrees ($1 \text{ Hartree} = me^4/\hbar^2 = 2 \text{ Ry} = 27.2 \text{ eV}$); the momentum, in units of $\hbar/a_0 = me^2/\hbar$; and the speed, in units of $e^2/\hbar$ ($e = m = \hbar = 1$).

1.1 The liquid water in radiation physics

It is well known that water is used as the main reference medium to study interactions of ionizing radiation with tissue, not only experimentally but also theoretically. Human body is composed of about 70% of water and, therefore, the procedure of considering water molecules as the approximate tissue-like targets seems to be reasonably well justified.

Ionizing radiations affect the genetic material when impacting on living beings. The DNA molecule can be damaged through direct and indirect processes. In the former, ionizing particles impact this macromolecule causing single, double, or multiple strand breaks. In the latter, chemical species created after the interaction of radiation with the medium will react with DNA structures. The nanodosimetry is the branch of physics that studies the energy distribution at nanometric scale, which is a very important matter in investigations where the radiation induced DNA damage is simulated numerically.

It is well known that light ions are more efficient to produce biological damage than electrons and photons, mainly because ions have higher linear energy transfer (LET). However, the LET does not determine the radiobiological effectiveness (RBE) of the radiation.[1] It is very important to accurately know the RBE corresponding to each ion beam, specially for those beams used in the radiation therapy of cancer.

Many secondary particles are produced during the passage of fast ions through matter, most of them are electrons released by ionization of targeted atoms or molecules. These very light charged particles are responsible for the deposition of the greatest fraction of incident energy no matter which the primary particles are. Consequently, electrons have to be taken into account in any application related to nanodosimetry and/or radiobiology. For these reasons, among others, the knowledge of ion-related ionization CS are extremely important.

The water molecule has 10 bound electrons. Its mass and molecular densities are about 1.0 g/cm^3 and $3.34 \times 10^{22} \text{ 1/cm}^3$, respectively, in the liquid phase. Table 8.1 shows electron binding energy and occupation number corresponding to the five molecular orbitals of liquid and gaseous water.

Table 8.1 Electron occupation numbers and binding energies for liquid and gaseous water subshells

Shells	*N*	I^{a}_{liquid} (eV)	I^{b}_{vapor} (eV)
$1b_1$	2	10.79	12.61
$3a_1$	2	13.39	14.73
$1b_2$	2	16.05	18.55
$2a_1$	2	32.30	32.2
$1a_1$	2	539.0	539.7

[a] Values from Dingfelder et al.[2]
[b] Values from Rudd et al.[3]

The four most outer shells have energies up to a few tens of eV and they contribute to the total ionization cross section much more than the inner shell, which corresponds to the oxygen *K*-shell.

Unfortunately, no experimental determination of ionization CS has been carried out in liquid water, mainly due to the difficulty of having an adequate liquid target and problems associated to the detection of very low energy electrons. In a forthcoming section, all experiments, to the best of our knowledge, carried out to determine ionization CS due to the impact of light ions on water vapor are summarized (see Section 3).

1.2 The ionization problem

1.2.1 Brief description

When a totally stripped ion impacts a molecular or atomic target, it interacts with bound electrons through the Coulomb field. The magnetic component of the interaction potential is negligible at the incident velocities considered here. In this situation, a bound electron can be released to the continuum through the so-called direct ionization phenomenon. Otherwise, the electron can be excited to a higher energy state or captured into a projectile bound state. These mechanisms are known as electronic excitation and electronic capture, respectively. It should be remarked that in the latter process, the target is also left ionized as in the direct ionization case. Hereafter, direct ionizations will be simply referred to as ionizations.

The main difficulty in the theoretical treatment of the ionization problem is the representation of the initial and final system states. Hydrogen-type wave functions have been a common choice used to describe the initial electron bound state,[4] even when the target is not hydrogen.[5–7] The hydrogen atom has the particularity that can be solved analytically by using quantum mechanics. In the exit channel, the electron moves under the influence of two Coulomb potentials (long range), due to its interaction with the projectile and the residual target. An exact solution for the final electron wave function in the ion–atom ionization problem has not been found yet, but the continuum distorted wave (CDW) function has been derived.[8] The CDW[8] and the CDW-type[4] approaches included in the present work satisfy asymptotic conditions both at the entrance and exit channels, but the first Born approximation (B1) does not.

Our efforts are focused on the single ionization mechanism described by reaction (1), although references will be made to the electron loss and electron capture processes. Double ionizations are relatively important at very low energies and for highly charged projectiles, but they are not treated in this work. Although the electron capture phenomenon is out of the scope of our work, it is marginally mentioned due to its relation with ionizations. In fact, these mechanisms are extremely competitive at impact energies below about 100 keV/u. More complex processes can take place when the incident ion carries one or more bound electrons:

$$\mathrm{P}^{Z_\mathrm{P}+} + \mathrm{T}^{(Z_\mathrm{T}-1)+} \rightarrow \mathrm{P}^{Z_\mathrm{P}+} + \mathrm{T}^{Z_\mathrm{T}+} + e^{-}. \tag{1}$$

Based on the fact that the projectile mass is much greater than that of the electron, the incident particle loses a small fraction of its original energy during a collision with the electron. When an impact between an ion and an electron, assumed initially at rest, is frontal, the energy transferred to the electron is maximum and equal to $2v^2$, and the maximum fractional energy loss is given by $\Delta E/E = 4/M$ where E, v, and M are the projectile incident energy, speed, and mass, respectively. In addition, the scattering of one nucleus by the other at impact energies above a few tens of keV/u is restricted to angles much lower than 1°. Furthermore, if the de Broglie wave length of the relative motion of the nuclei is much less than the target characteristic dimension, a trajectory can be assigned to the projectile. All said in this paragraph supports the idea that these energetic and relatively massive particles travel along a straight path. This argument is used by impact-parameter-based approximations (see Section 2). Under these conditions, a straight-line trajectory can be associated to the projectile, so that the transferred momentum during the collision q is minimum. Then, neglecting terms of order $(1/M)^2$ and higher,

$$q_{\min} = K_\mathrm{i} - K_\mathrm{f} = (2ME)^{1/2}[1 - (1 - \Delta E/E)^{1/2}] \approx \frac{\Delta E}{v}, \tag{2}$$

where $K_\mathrm{i}(K_\mathrm{f})$ and ΔE are the initial(final) projectile momentum and energy loss, respectively.

1.2.2 Liquid water phase effects

The water aggregation state influences the cross sections corresponding to the interaction of charged particles with this medium. One of the effects is the decrement of the electron binding energies in liquid water relative to water vapor due to the intermolecular interaction present in the liquid water phase (see Table 8.1). Note that outer orbitals are the most affected while the inner ones are practically independent of the aggregation state. Another important effect is that described by Enrico Fermi many decades ago. For a given traversed medium mass thickness, he explained the reduction of the expected energy loss of a primary particle in a condensed medium relative to a rarefied one. Let us briefly describe this phenomenon by a classical approach. The quantity q_min is related to the maximum impact parameter ρ_max ($\rho_\mathrm{max} \sim 1/q_\mathrm{min}$). In condensed media and for sufficiently high ion velocities, ρ_max is much greater than the mean inter-target distance (molecules or atoms), so that the projectile interacts with many targets simultaneously producing electric polarization in the medium. This polarization screens the electric field generated by the projectile on the target, the interaction potential weakens and the energy lost by the projectile per unit mass path length decreases. The Fermi density effect is important at high impact velocities, where ρ_max is large, and for low emitted electron energies, where ρ_max is also large. For energies (velocities) up to about 10 MeV/u and the projectile charges analyzed in this work, the Fermi-density correction can be safely disregarded. There are other phase effects such as the controversial collective excitations occurring in liquid water but they are not related to ionization cross sections so that they are not treated in the current work.

2. THEORETICAL APPROACHES

The purpose of this section is to give an overall description of the ionization process that will help the reader to better understand the experimental results shown below (see Section 3). Mathematical details on the approaches presented are not included in this work as they can be found in references given in this section.

Let us suppose the a totally stripped ion with charge, mass, velocity, and momentum along the z-axis Z_P, M_P, $\mathbf{v}$, and $\mathbf{K}$, respectively, impacts on a $1s$ hydrogen-like target with nuclear charge and mass Z_T and M_T, respectively.

In this case $M_{\mathrm{P}}, M_{\mathrm{T}} \gg 1$ so that the electronic states can be considered as independent of the relative motion of the involved nuclei (Born–Oppenheimer separation, see Chapters 1 and 4 of Ref. 9). The target recoil is neglected since the energy transferred to the electron is much greater than that imparted to the target nucleus, even in proton-hydrogen collisions. In addition, $Ka \gg 1$, where a is the characteristic target dimension, so that a straight-line trajectory defined by $\boldsymbol{\rho} \cdot \mathbf{v} = 0$ can be assigned to the projectile, where $\boldsymbol{\rho}$ is the 2D impact parameter vector. Under these conditions, the projectile position with respect to the target will always be $\mathbf{R} = \boldsymbol{\rho} + \mathbf{v}t$.

For the reasons given just above, the theoretical approaches treated here are based on the straight-line impact parameter model (IPM),[9] which is considered semiclassical due to the assigned projectile trajectory. The projectile–electron interaction is time-dependent and so is the perturbation theory used. Coupling with electron capture and excitation channels is not considered. The theoretical models addressed in this chapter describe the process shown in reaction (1). Consequently, we define

$$\mathbf{x} = \mathbf{r}_{\mathrm{e}} - \mathbf{r}_{\mathrm{T}}, \quad \mathbf{s} = \mathbf{r}_{\mathrm{e}} - \mathbf{r}_{\mathrm{P}},$$
$$\mathbf{R} = \mathbf{r}_{\mathrm{P}} - \mathbf{r}_{\mathrm{T}}, \quad \mathbf{r} = 1/2(\mathbf{x} + \mathbf{s}),$$

where $\mathbf{r}_{\mathrm{e}}$, $\mathbf{r}_{\mathrm{T}}$, and $\mathbf{r}_{\mathrm{P}}$ are the position vectors of the electron, target nucleus and projectile, respectively measured with respect to the laboratory frame of reference. Figure 8.1 depicts relevant vectors used for clarity purposes.

Schrödinger's equation for reaction (1) is

$$\left(H_{\mathrm{e}} - i\frac{\partial}{\partial t_{\mathbf{r}}} \right) \Psi = 0, \tag{3}$$

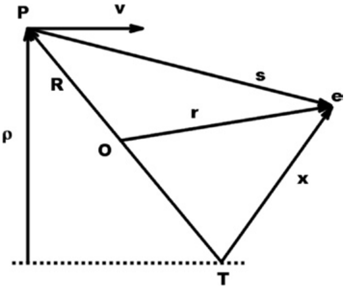

Figure 8.1 Relevant vectors used in theoretical models.

where

$$H_{\mathrm{e}} = -\frac{1}{2}\nabla_{\mathbf{r}}^{2} - \frac{Z_{\mathrm{T}}}{x} - \frac{Z_{\mathrm{P}}}{s} + \frac{Z_{\mathrm{T}} Z_{\mathrm{P}}}{R} \tag{4}$$

is the electronic Hamiltonian, and $(\mathbf{r}, t_r)$ are the independent variables. It is important to notice that ionization cross sections do not depend on the chosen origin O if this point belongs to the line joining the target and the projectile, and the resulting potential due to the projectile vanishes as $R \to \infty$ (Ref. 9).

2.1 The first Born approximation (B1)

In this approximation, the interaction potential between the projectile and the target electron is treated as a first-order perturbation. This is justified if this potential satisfies the condition $|U| \ll v/d$, where d is its action radius.[11] Taking $U \sim Z_{\mathrm{P}}/d$, this approximation can be written as $Z_{\mathrm{P}}/v \ll 1$. The inter-nuclear potential is discarded since it only introduces a phase factor in the transition amplitude, producing no change in the ionization differential cross section with respect to the electron parameters.[4, 8] In this approximation, the initial state is described by a stationary bound electron wave function modified by translational phases depending on $\mathbf{v}$ due to the coordinate transformation existing between frames of reference centered at the positions of the target and point O. In the exit channel, the movement of the electron with respect to the target is represented by a Coulomb distorted plane wave plus translational factors. According to the B1 approximation, the presence of the projectile causes no perturbation on the electronic wave functions corresponding to both the entrance and exit channels. Mathematical details on this approximation can be found elsewhere (see Chapter 7, Section 2 of Ref. 9). After the corresponding manipulations, for the ionization of a 1s hydrogen-like target, the B1 transition probability is given by[8]

$$\begin{aligned}\left|R_{\mathrm{if}}^{(\mathrm{B1})}(\boldsymbol{\eta})\right|^{2} = {} & \left(\frac{2^{7} Z_{\mathrm{T}}^{5} Z_{\mathrm{P}}^{2}}{\pi^{2} v^{2} q^{4}}\right) |N(\xi)|^{2} \\ & \times \exp\left[-2\xi \tan^{-1}\left(\frac{2 Z_{\mathrm{T}} k}{q^{2} + Z_{\mathrm{T}}^{2} - k^{2}}\right)\right] \\ & \times \frac{[(\mathbf{q}^{2} + \mathbf{q}\cdot\mathbf{k})^{2} + (\mathbf{q}\cdot\mathbf{k})^{2}\xi^{2}]}{[Z_{\mathrm{T}}^{2} + (q+k)^{2}][Z_{\mathrm{T}}^{2} + (q-k)^{2}][Z_{\mathrm{T}}^{2} + (\mathbf{q}+\mathbf{k})^{2}]^{4}},\end{aligned} \tag{5}$$

with

$$\mathbf{q} = -\boldsymbol{\eta} - \frac{\Delta E}{v}\hat{\mathbf{v}}, \tag{6}$$

where $\boldsymbol{\eta}$ is the transverse momentum transfer, $\mathbf{k}$ is the ejected electron momentum and $\xi = Z_{\mathrm{T}}/k$.

This transition probability shows a local maximum at high electron energies. The leading term, shown between brackets with exponent 4, has a minimum when $(\mathbf{q}+\mathbf{k}) \to 0$. Based on the fact that a large amount of moment is transferred during a head-on collision, the initial electron momentum can be safely neglected so that $\mathbf{q}+\mathbf{k}=0$. In this case, the final electron momentum is equal to the momentum transfer. Combining this equation with Eq. (6) and having into account that $\boldsymbol{\eta} \cdot \mathbf{v} = 0$, we have

$$\mathbf{k} \cdot \hat{\mathbf{v}} - \frac{\Delta E}{v} = 0. \tag{7}$$

This equation defines the binary sphere,[12] which describes the kinematics of a binary projectile–electron encounter. The double differential cross sections (DDCS) show a maximum at electron momenta satisfying Eq. (7), which represents the binary encounter (BE) peak. Furthermore, $\Delta E = \varepsilon_{\mathrm{f}} - \varepsilon_{\mathrm{i}} = \frac{1}{2}k^2 - \varepsilon_{\mathrm{i}}$, so that the solutions for the final electron momentum in this sphere, up to first order, are

$$k_{\mathrm{BE}}^{+} = v\cos(\theta)\left[1+\left(1+\frac{2\varepsilon_{\mathrm{i}}}{v^2\cos^2\theta}\right)^{1/2}\right] \approx 2v\cos\theta + \frac{\varepsilon_{\mathrm{i}}}{v\cos\theta}, \tag{8}$$

$$k_{\mathrm{BE}}^{-} = v\cos(\theta)\left[1-\left(1+\frac{2\varepsilon_{\mathrm{i}}}{v^2\cos^2\theta}\right)^{1/2}\right] \approx -\frac{\varepsilon_{\mathrm{i}}}{v\cos\theta}, \tag{9}$$

where θ is the electron ejection angle with respect to the incident particle direction.

Firstly, the BE peak is observed in experimental DDCS (e.g., see Ref. 16) for electron momenta close to k_{BE}^{+}. When the initial electron energy is disregarded, the result for k_{BE}^{+} is the one obtained for a binary encounter of a heavy particle ($M_{\mathrm{P}} \gg 1$) with an electron at rest ($k_{\mathrm{BE}} = 2v\cos\theta$). Secondly, it can be concluded, from the analysis of Eq. (5), that the maximum DDCS is obtained at $k \approx 0$, which conforms the "soft collision" (SC) region. The k_{BE}^{-} solution is usually close to zero and the corresponding peak is overlapped by the SC region, therefore it is commonly unspotted.

Summarizing, the B1 approximation treats the projectile–electron interaction as a first-order perturbation, condition that is not fulfilled in the following situations: (i) the projectile moves with velocities of the order of those of the bound electrons, (ii) the projectile is very close to the electron, for example when $\mathbf{k} \approx \mathbf{v}$, and (iii) the projectile charge is large. According to the transition amplitude (5), differential and total ionization cross sections scale as $(Z_\text{P}/v)^2$. Moreover, B1 cross sections depend on the projectile velocity, instead of its energy.

Hansen and Kocbach[5] used a variant of the B1 approximation to study electron emission after K-shell ionization due to protons. In fact, they followed an impact parameter plane-wave formulation of this approximation (IP-PWBA). Furthermore, they described the initial and final electron states through 1s hydrogen-type and plane wave functions, respectively. In this case, the transition amplitude is

$$a_\text{if}^\text{HK} = \frac{-i}{v} \int_{-\infty}^{+\infty} \mathrm{d}z \exp(iqz) \langle \Psi_\text{f}(\mathbf{x}) | V(s) | \Psi_\text{i}(\mathbf{x}) \rangle, \tag{10}$$

where q is the minimum momentum transfer (see Eq. (2)), $\Psi_\text{i}(\mathbf{x})$ and $\Psi_\text{f}(\mathbf{x})$ are the initial and final electron wave functions and $V(s)$ is the Coulomb projectile–electron potential. If the final wave function $\Psi_\text{f}(\mathbf{x}) = (2\pi)^{-3/2} \exp(-i\mathbf{k} \cdot \mathbf{x})$ is substituted in Eq. (10) and the initial wave function is represented by a 1s hydrogen-like wave function ($\Psi_\text{i}(\mathbf{x}) = \pi^{-1/2} p^{3/2} \exp(-px)$), then by using the Bethe integral, the peaking approximation and neglecting the initial electron momentum with respect to the final one, the integral shown in Eq. (10) can be solved. Thus, the Hansen–Kocbach (HK) transition amplitude is given by

$$a_\text{if}^\text{HK} = \frac{-i2^{3/2} Z_\text{P} p^{5/2} \exp(-i\boldsymbol{\rho} \cdot \mathbf{k}_\perp)}{\pi v k^2} \frac{\rho K_1(\rho[p^2 + (q - k_\parallel)^2]^{1/2})}{[p^2 + (q - k_\parallel)^2]^{1/2}}, \tag{11}$$

where $k_\parallel = \mathbf{k} \cdot \hat{\mathbf{v}}$, $\mathbf{k}_\perp$ is the electron momentum normal to $\mathbf{v}$ and K_1 is the first-order modified Bessel function of second kind.

Notice that this transition amplitude is maximum when $\mathbf{k} \cdot \hat{\mathbf{v}} - \Delta E/v = 0$, which reproduces the binary encounter sphere described above (see Eqs. (7) and (2)). Based on this theoretical approach, Stolterfoht developed a semiempirical method to determine ionization cross sections for the impact of light ions on matter.[13, 14] This is the so-called HKS model which is treated in Section 4.

2.2 The distorted wave formalism and its main variants

The CDW formalism was introduced by Cheshire[10] to study the resonant charge transfer in proton–hydrogen collisions. Subsequently, this methodology was extended by Belkić[8] to investigate the ionization problem when ions impact on atomic systems. Afterwards, working within the CDW theory,[8] Crothers and McCann[4] introduced a modification in the normalization of the initial electron state and replaced the perturbation in the entrance channel by an eikonal phase (CDW-EIS).

2.2.1 The continuum-distorted wave approximation (CDW)

In this approximation, the Hamiltonian shown in Eq. (4), for both entrance and exit channels, is separated as follows:[8]

$$H_{\mathrm{e}} = H_0 + U_{\mathrm{i}} + W_{\mathrm{i}} = H_0 + U_{\mathrm{f}} + W_{\mathrm{f}}. \tag{12}$$

The perturbation potentials W_{i} and W_{f} are chosen such that the Schrödinger equations

$$\left(H_0 + U_{\mathrm{i,f}} - i\frac{\partial}{\partial t_{\mathbf{r}}}\right)\chi_{\mathrm{i,f}}^{(\mathrm{CDW})\pm} = 0 \tag{13}$$

can be solved exactly. The unperturbed parts of the initial and final distorted wave functions $\chi_{\mathrm{i,f}}^{(\mathrm{CDW})\pm}$ are written in terms of the B1 wave functions in the entrance and exit channels, respectively. In the CDW approximation, the perturbation potentials are given by the scalar products of two gradient operators applied to the pertinent electronic wave functions of the bound and continuum states.

2.2.2 The continuum distorted wave eikonal initial state approximation (CDW-EIS)

In this case, the exit channel is treated as in the pure CDW approximation, but the wave function distortion in the entrance channel is accounted for through an eikonal phase.[4] In addition to the mentioned gradient operators in the perturbation potential from the transition amplitude, this phase for the eikonal initial state yields an extra term given by the electronic kinetic energy operator. In the CDW-EIS approximation, the final CDW states corresponding to different $\mathbf{k}$ are regarded as orthonormal and uncoupled, which is not an exact assumption because they are not the eigenfunctions of the total Hamiltonian. Moreover, the initial and final states are not orthogonal since their corresponding Hamiltonians are different. However, this is not an important problem for ionization as it is for charge transfer. Note that the distorted wave Born (DWB) approximation has also been obtained[8] as an alternative hybrid model when the B1 and the CDW wave functions are used in the entrance and exit channels, respectively.

The expression for the triple differential cross sections (TDCS) obtained by means of the CDW and CDW-EIS approximations can be found in Refs. 8 and 4, respectively. Some important results can be extracted from that expression: (a) the CDW-EIS cross sections depend directly on the transition amplitude obtained from the B1 approximation and the other terms represent the effect of the distortion produced by the projectile (which is neglected within the B1 approach). As the projectile speed increases, the TDCS in the CDW and CDW-EIS approximations tend to the one obtained in the B1 case, (b) the BE peak is reproduced once again, and (c) the factor

$$|N(\zeta)|^2 = \frac{2\pi\zeta}{1 - e^{-2\pi\zeta}} \tag{14}$$

with $\zeta = Z_P/p$, is maximized as $p \to 0$, where p is the electron momentum in the projectile reference system. This means that when the final electron momentum relative to that of the projectile is close to zero ($\mathbf{k} \approx \mathbf{v}$), a peak is produced in the TDCS as well as in the DDCS. This is the so-called electron capture into the continuum (ECC) peak, which is one of the two-center effects (see Section 5). This factor represents the density of electron continuum states around the projectile.

3. EXPERIMENTAL WORKS

Experiments for the determination of ionization cross sections due to the impact of ions on water are very scarce. All of them have been carried out by using water vapor as a target. Many research areas, such as nanodosimetry and radiobiology require of the knowledge of liquid water target cross sections but to setup experiments with this aggregation state has been very difficult. Table 8.2 summarizes these experiments for reference purposes.

Table 8.2 Summary of experiments for the determination of ion–water interaction cross sections. All experiments were carried out by using water vapor as a target

Reference	Projectile	Energy (MeV/u)	Cross sections	Uncertainties
Toburen et al.[15]	H^+, H^0	0.1–2.5	Single electron capture and loss	10–12%
Toburen and Wilson[16]	H^+	0.3, 0.5, 1.0, and 1.5	Single ionization	20%
Toburen et al.[17]	He^+	0.075, 0.2, 0.3, 0.4, and 0.5	Single ionization	20%

Table 8.2 (*Continued*)

Reference	Projectile	Energy (MeV/u)	Cross sections	Uncertainties
	He^{2+}	0.2, 0.3, 0.4, and 0.5	Single ionization	20%
Wilson et al.[18]	H^+	3.0 and 4.2	Single ionization	20%
Rudd et al.[19]	H^+	0.007–4.0	Single ionization and electron capture	8–20%
Rudd et al.[20]	He^+	0.005–0.45	Single ionization, electron capture and loss	5–12%
Bolorizadeh and Rudd[21]	H^+	0.015–0.15	Single ionization	20%
Werner et al.[22]	H^+	0.1–0.35	Water fragmentation	~10–50%
	He^{2+}	0.25	Water fragmentation	~10–50%
Gobet et al.[23]	H^+	0.02–0.15	Water fragmentation	N/A
Ohsawa et al.[24]	He^{2+}	6.0 and 10.0	Single ionization	~13%

4. SEMIEMPIRICAL METHODS

Various semiempirical models have been developed to reproduce ionization cross sections due to the impact of ions on water.[3, 2, 13, 25] In this section only three of them will be addressed.

4.1 The Rudd model

Rudd et al.[3, 26] built a semiempirical model to determine single ionization cross sections corresponding to proton impact on water as a function of secondary electron energy. It is based on pioneer works of E. Rutherford and J.J. Thomson on the impact of charged particles with matter (binary encounter approximation). The single differential cross sections (SDCS) depend only on the ejected and bound electron energies and the projectile velocity. The formulae to determine the ionization cross section differential in the secondary electron energy can be found in Ref. 3. This model can also be applied to multi-electronic targets by using the electron binding energy in each molecular or atomic shell.

Rudd and coworkers made a distinction between inner and outer subshells in multielectron targets. Those with binding energy higher and lower than twice that of the outermost subshell are regarded as inner and outer subshells, respectively. Dingfelder et al.[2] used this model to obtain liquid water stopping powers reported by ICRU[27] for proton energies below

0.5 MeV. In addition, they introduced a partition factor to weight the cross sections corresponding to each subshell in order to reproduce B1 approximation results at impact energies above 0.5 MeV. They determined a complete set of parameters and partition factors for liquid water. All parameters used in this model, corresponding to inner and outer subshells of liquid water (Dingfelder) and water vapor (Rudd) can be found in Table 3 of Ref. 2. Binding energies and partition factors for both water phases are displayed in Table 4 of the same reference.

4.2 The HKS method

Stolterfoht[13] used the transition amplitude (Eq. (11)) determined previously by Hansen and Kocbach[5] to develop a semiempirical method to calculate ionization cross sections for light ions. He found that these cross sections diverged as $k \to 0$ due to the neglect of the initial electron momentum. A semiempirical term was then included in the transition amplitude to remove that singularity. In addition, other modifications were incorporated in the original formalism to reproduce the results determined by using the B1 approximation formula published by Landau and Lifshitz.[11] This is the so-called HKS method. However, Bernal and Liendo[6] realized that previously published HKS expressions[13, 14] had some misprints so that they carried out all calculations analytically and corrected the HKS formulae. In addition, they compared the results obtained from the corrected HKS expressions for water ionization due to the impact of protons and alpha particles (see Section 5).

4.3 Formalism based on the dielectric response function

As pointed out by Fano,[28] macroscopic differential cross sections for energy and momentum transfer in a condense medium can be obtained within the B1 approximation from the expressions

$$\frac{\mathrm{d}\Sigma^2}{\mathrm{d}E\,\mathrm{d}q} = \frac{2Z_\mathrm{P}^2}{\pi v^2 q}\mathrm{Im}\left[\frac{-1}{\epsilon(E,K)}\right], \tag{15}$$

$$\frac{\mathrm{d}\Sigma}{\mathrm{d}E} = \frac{2Z_\mathrm{P}^2}{\pi v^2}\int_{q_\mathrm{min}}^{q_\mathrm{max}} \mathrm{Im}\left[\frac{-1}{\epsilon(E,K)}\right]\frac{\mathrm{d}q}{q}, \tag{16}$$

where $\epsilon(E,K)$ is the medium dielectric response function (DRF); E and q represent the energy and momentum transfer, respectively; q_min is given by Eq. (2), $q_{\max} = (2M_{\mathrm{P}})^{1/2}[\tau^{1/2} + (\tau - E)^{1/2}] \approx 2M_{\mathrm{P}}v$ is the maximum momentum transfer, and $\tau = M_{\mathrm{P}}v^2/2$ is the projectile kinetic energy.

This approach accounts for the polarization of the medium, collective excitations and many-body interactions in a consistent manner. The corresponding cross sections scale as $(Z_{\mathrm{P}}/v)^2$ because they are determined within the B1 approximation. An important advantage of this treatment is that available experimental data for liquid water (see Ref. 29, and references therein) can be used to fit the corresponding DRF. Dingfelder et al.[30] and Emfietzoglou et al.[25] based a series of works on this methodology to construct semiempirical formalisms for the determination of ionization and excitation cross sections due to the impact of electrons on liquid water. Later on, they extended these formalisms to protons impinging on this medium.[2, 25] These authors obtained the DRF from a linear superposition of Drude-type functions. In this case, bound electrons were supposed to move in a forced and damped oscillator. The group of Dingfelder used experimental optical reflectance data obtained by Heller et al.[31] while that of Emfietzoglou have used more recent inelastic X-ray scattering spectroscopy (IXSS) data reported by Hayashi et al.[29] The idea was to separate the discrete and continuum parts of the term Im [-1/ϵ (E, K)] in Eq. (15), also known as the energy-loss function (ELF). In addition, derivative Drude-type DRF were used for excitations, leading to more pronounce peaks. Experimental data were fitted to obtain the optical dielectric response function (ODRF), satisfying some physical constraints (see Ref. 32). For instance, as IXXS data were only reported for transferred energies in the range 6–160 eV, Emfietzoglou and Moscovitch[32] only included the four outermost subshells of the liquid water molecule. Parameters for the *K*-shell were determined by use of the NIST photoelectric database.[33]

In a more recent publication,[25] the oxygen *K*-shell was treated separately and a hydrogen-type generalized oscillator strength (GOS)[2] was employed to determine the ELF of this shell, using the same NIST database. It should be pointed out that several approximations have been used to extend transition energies to finite momentum transfers, many of them have been reviewed and compared in Ref. 25.

5. COMPARISON BETWEEN EXPERIMENTAL, THEORETICAL, AND SEMIEMPIRICAL RESULTS

Experimental cross sections for the ionization of water due to the impact of ions are very scarce, as mentioned previously (see Section 3). Moreover, these data have been only determined for water vapor which makes very difficult the validation of methods for the liquid water ionization cross section determination.

The B1 approximation has become a classical method to study ion–atom collisions. Most of the scientific publications generated in this field use this approach as a reference to compare their experimental and/or theoretical results. For this reason, the analysis of the B1 treatment is not carried out independently but together with CDW formalisms.

After the fundamental works of Cheshire,[10] Belkić,[8] and Crothers and McCann,[4] the CDW methodologies have been used by several investigators to study ion–atom collision problems (see, e.g., Refs. 34–36). Many of these variants have been employed to investigate processes such as transfer ionization, direct ionization, electron interference during direct ionization, target excitation, electron loss from negative ions due to proton impact, and more complex phenomena like multiple ionizations and the simultaneous projectile ionization and target excitation and/or ionization. The success of the CDW theories is mainly based on the reproduction of two-center effects,[34] which are due to the influence of both the projectile and residual target on the electron under consideration. Some of these effects are commented in the light of CDW methodologies in the following paragraphs. On the contrary, the B1 approximation is not capable to explain these effects. Only the most prominent effects are analyzed just below.

5.1 Ionization cross sections for water

As far as the authors know, Olivera et al.[35] published the first work on the use of the CDW-EIS formalism to determine single ionization cross sections for protons bombarding water. They employed the complete neglect of differential overlap (CNDO) method to obtain electron wave functions. However, their important work was aimed to the water vapor phase. Figure 8.2 shows total ionization cross sections reported by these authors in Ref. 37. Electron capture cross sections calculated using the Bragg's additivity rule instead of molecular wave functions are also displayed. Excellent agreement between theoretical and experimental results was obtained for projectile energies above approximately 30 keV.

Bernal and Liendo published a work on the determination of inelastic cross sections for the interaction of protons, alpha particles, and carbon ions with liquid water.[7] They calculated ionization cross sections by use of the CDW-EIS and HKS formalisms (see Section 2). In both methods hydrogen-like wave functions were used to represent the initial electron state. Occupation number and ionization energy values used in that research

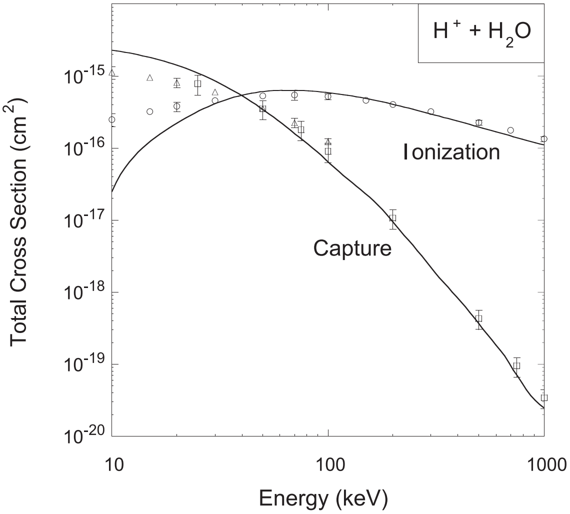

Figure 8.2 Total ionization and electron capture cross sections for the impact of protons on water vapor. Solid lines represent CDW-EIS calculations carried out by Olivera et al. squares are data obtained from experiments by Barnet et al. circles and triangles represent experimental results published in Ref. 19. Reprinted from Publication,[37] Copyright (1996), with permission from Elsevier.

are shown in Table 1 of Ref. 7. DDCS for 0.3 and 1.5 MeV protons, and 0.3 and 0.5 MeV alpha particles impacting on liquid water calculated by those authors are shown in Figures 8.3 and 8.4, respectively. Each curve is for a given secondary electron energy. Corresponding experimental values for water vapor[16, 17] are also displayed. The use of hydrogen-like wave functions to describe the electron initial state causes an underestimation of DDCS at backward angles.[13] Furthermore, CDW-EIS accounts for the projectile–electron interaction explicitly so that the attraction of the positively charged projectile on the atomic electron tends to reduce the electron ejection probability at large angles. This is one of the well-known two-center effects[34] and the reason why CDW-EIS underestimates the DDCS at backward angles more than HKS does. The attraction mentioned here also causes CDW-EIS to overestimate, for all projectile energies, the DDCS at forward angles with respect to the HKS values when the electron energy is close to the ECC peak energy W_{ECC}. This effect is more important for the strongest perturbation (Z_P/v), currently represented by the alpha particle case where DDCS corresponding to the entire electron energy range are affected. The shift of the CDW-EIS binary encounter

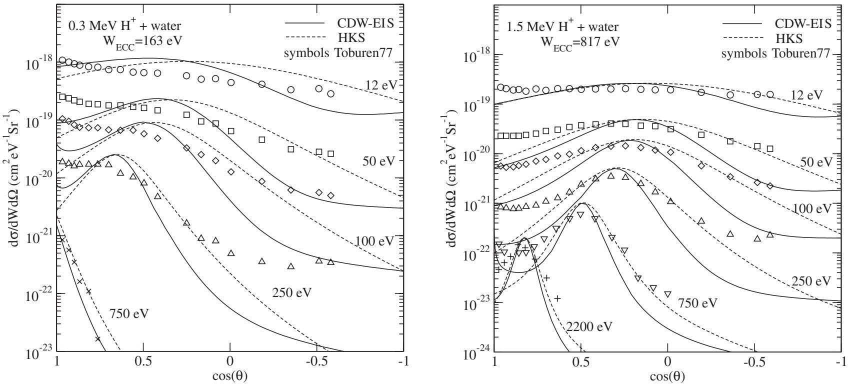

(a) **(b)**

Figure 8.3 DDCS determined by use of the HKS (dashed lines) and CDW-EIS (solid lines) methods for (a) 0.3 MeV and (b) 1.5 MeV protons. Corresponding experimental values for water vapor extracted from Ref. 16 (Toburen77). Reprinted from Publication,[7] Copyright (2007), with permission from Elsevier.

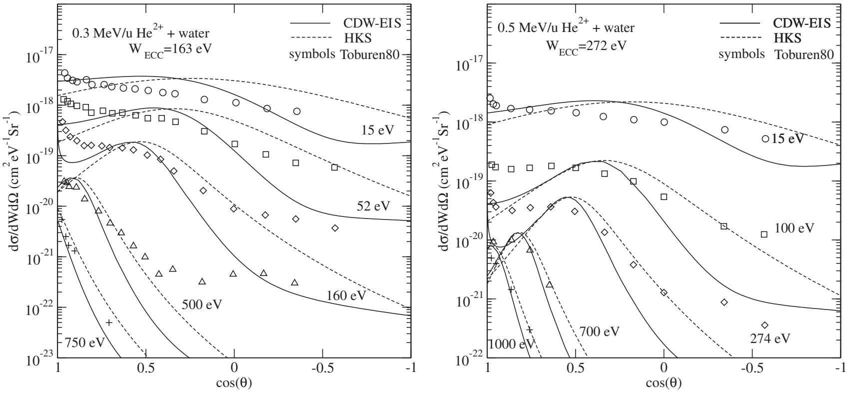

(a) **(b)**

Figure 8.4 DDCS determined by use of the HKS (dashed lines) and CDW-EIS (solid lines) methods for (a) 0.3 MeV/u and (b) 0.5 MeV/u alpha particles. Corresponding experimental values for water vapor extracted from Ref. 17 (Toburen80). Reprinted from Publication,[7] Copyright (2007), with permission from Elsevier.

peaks towards smaller angles with respect to those determined by the HKS method is another evidence of the presence of two-center effects. As expected, this fact is more conspicuous in the alpha particle case. Although the CDW-EIS approximation accounts for two-center effects, it was unable to reproduce experimental DDCS near 0°. This behavior could be caused by the use of hydrogen-like instead of realistic bound electron wave functions. Neither of the CDW-EIS and HKS formalisms provides a good agreement with experimental water vapor DDCS.

SDCS for protons and alpha particles impacting on liquid water computed by the CDW-EIS and HKS models[7] are displayed in Figure 8.5a and b, respectively. Corresponding experimental values previously published for water vapor are also included for comparison.[17, 18] In general, the HKS method provides a better agreement with the experimental results than the CDW-EIS formalism, for protons as well as for alpha particles. CDW-EIS cross sections are lower than those predicted by the HKS approach for all projectile energies, probably due to the significant underestimation of the DDCS at large ejection angles (see Figs. 8.3 and 8.4). At the same projectile speed (0.5 MeV/u), CDW-EIS and HKS SDCS are consistent with experimental data corresponding to *W* values above 10 eV and 30 eV for proton and alpha particle beams, respectively. This may be due to the fact that both CDW-EIS and HKS methods are first-order perturbative approaches. The greater the projectile charge, the worse the expected results for the same projectile velocity. Discrepancies below about 10 eV could be attributed to experimental difficulties, as commented in Ref. 18.

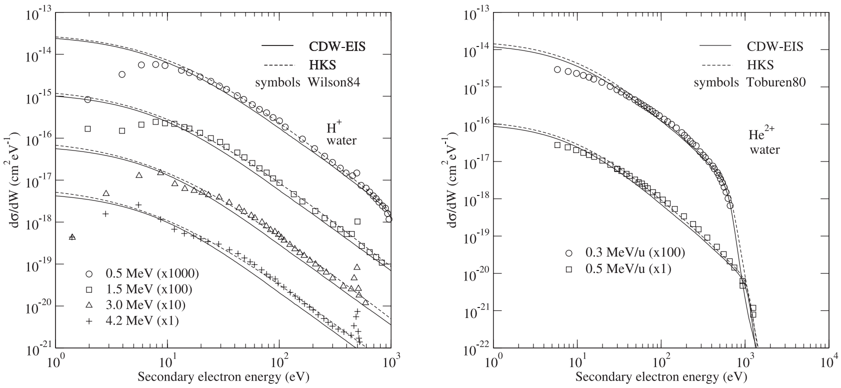

(a) (b)

Figure 8.5 SDCS for (a) 0.5, 1.5, 3.0, and 4.2 MeV protons and (b) 0.3 and 0.5 MeV/u alpha particles impacting on liquid water calculated by the CDW-EIS (solid lines) and HKS (dashed lines) formalisms. Experimental results corresponding to water vapor are shown (symbols).[18, 17] Reprinted from Publication,[7] Copyright (2007), with permission from Elsevier.

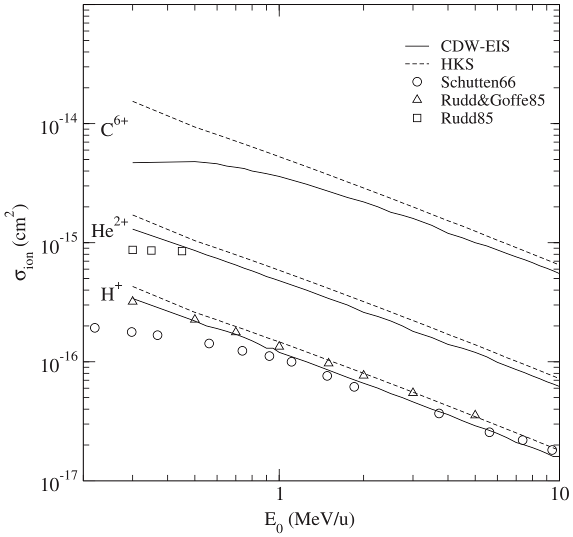

Figure 8.6 Total single ionization cross sections for H^+, He^{2+}, and C^{6+} ions impacting on liquid water calculated by the CDW-EIS (solid lines) and HKS (dashed lines) formalisms. Available experimental values are also shown (symbols).[38, 19, 20] Reprinted from Publication,[7] Copyright (2007), with permission from Elsevier.

Figure 8.6 shows the total single ionization cross sections for H^+, He^{2+}, and C^{6+} ions impacting on liquid water calculated by the CDW-EIS and HKS formalisms. Corresponding experimental data for the H^+ (Ref.19) and He^{2+} (Ref. 20) ions bombarding water vapor are also displayed for comparison purposes. In addition, analog values obtained by Schutten et al.[38] for electrons impinging on water vapor with the same speed as protons are also included in this figure. The agreement between the theoretical and experimental values for protons is better for E_0 below and above about 1 MeV/u for the CDW-EIS and HKS formalisms, respectively. The total cross section (TCS) obtained from experiments carried out with electrons as projectiles underestimate the theoretical values importantly for protons energies below about 1 MeV. Unfortunately, the experimental values for He^{2+} are not enough to make a good comparison but they show a good high-energy tendency.

Bernal and Liendo calculated corresponding excitation cross sections to determine inelastic electronic stopping cross sections (SCS) for protons, alpha particles, and carbon ions and compared their results with those

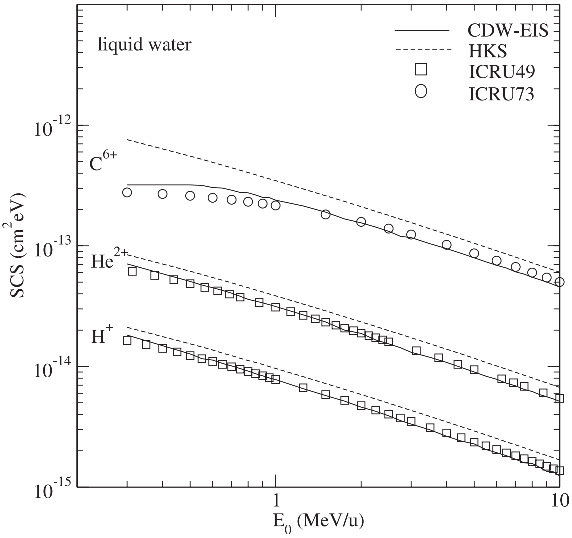

Figure 8.7 Electronic stopping cross sections for H^+, He^{2+}, and C^{6+} ions impacting on liquid water calculated by the CDW-EIS (solid lines) and HKS (dashed lines) formalisms. Corresponding reference values from ICRU reports are also shown (symbols).[27, 39] Reprinted from Publication,[7] Copyright (2007), with permission from Elsevier.

provided by ICRU.[27, 39] Figure 8.7 shows that the best SCS agreement with the reference values is obtained with the CDW-EIS formalism. It is important to remark that the CDW-EIS methodology is fully theoretical and only requires the knowledge of electron occupation numbers and binding energies of the target under study to be implemented.

Dal Cappello et al. published a work[40] in which double, single, and total ionization cross sections for water vapor bombarded by 6 MeV/u C^{6+} ions were determined by means of three variants of the HKS model: one obtained directly from the Hansen and Kocbach work[5](HKS_{orig}), another modified by Stolterfoht[13](HKS_{Stol}), and the corrected HKS expressions reported by Bernal and Liendo[7](HKS_{BL}). In addition, corresponding experimental and B1 approximation values, referred to as FBA-CW by Dal Cappello et al., were also reported. Moreover, the previously described model developed by Rudd (see Section 4.1) was included for SDCS comparison purposes. Figure 8.8 depicts SDCS reported in Ref. 40. In our opinion, the HKS_{BL} model is the most successful, in contrast to the conclusions of Dal Cappello et al. The reader should be aware that the

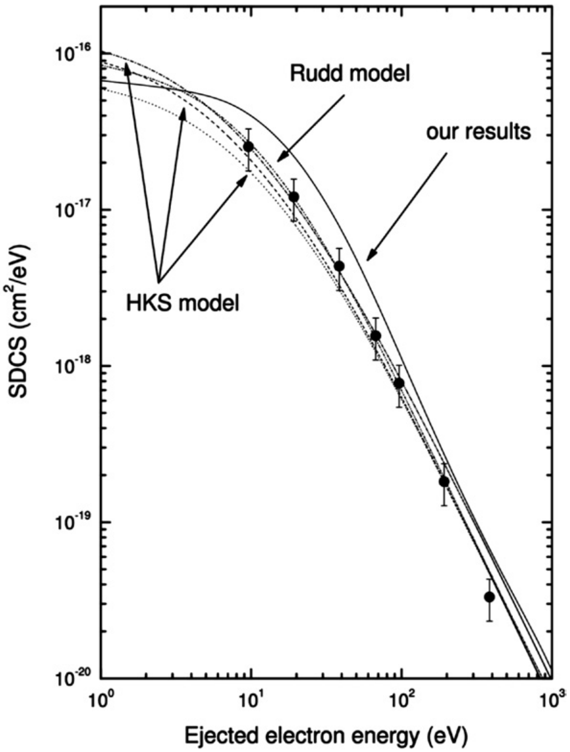

Figure 8.8 SDCS for the ionization of water vapor by the impact of 6 MeV/u C^{6+} ions. Solid circles show experimental values from the Ohsawa group (see Ref. 24). Results from the original HKS model[5] are represented by the dashed line; the HKS variant due to Stolterfoht et al.,[13] by the dotted line; the corrected HKS model due to Bernal and Liendo,[7] by the dashed-dotted line; and the Rudd model,[3] by the dashed-dotted-dotted line. Reprinted from Publication,[40] Copyright (2009), with permission from Elsevier.

greatest TCS components come from low energy SDCS corresponding to the interval $W < 100$ eV, where the $\mathrm{HKS_{BL}}$ variant provides better results than the other two HKS modifications. Among all the semiempirical models studied, the Rudd model produces the best agreement with the experiment. It is worth noting that the HKS expressions reported in Ref. 13,14 have some misprints. In other words, they cannot be obtained from the corresponding integration of the original transition probability reported by Hansen and Kocbach.[5]

Electronic stopping cross sections for protons on liquid water are shown in Figure 8.9. In this case, results from Emfietzoglou et al.[41] were

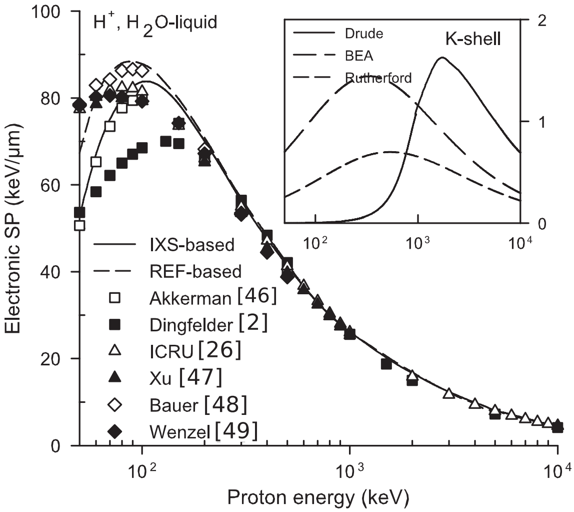

Figure 8.9 Electronic stopping power of liquid water for protons as reported by Emfietzoglou et al.[41] Solid and dotted lines show results obtained by those authors from the fit of inelastic X-ray scattering (IXS)[29] and optical reflectance data (REF),[31] respectively. The other results represent calculations and experimental determinations reported by the cited references. Printed from Publication,[41] Copyright (2006), with permission from Elsevier.

obtained by use of the semiempirical model based on the electronic response function of the medium (see Section 4.3). Other calculations as well as experimental determinations are shown. The reference numbers shown in this figure are according to Ref. 41 instead of the current work. In general, the agreement between all the methods shown is excellent for proton energies above 300 keV. Discrepancies arise near the Massey peak where the stopping cross section reaches a maximum. It should be remarked that the calculations carried out by Emfietzoglou et al.,[41] based on IXS data, represent the best fit of the ICRU reference values.

The semiempirical models developed by Rudd et al. (see Section 4.1) have been widely used to reproduce electron capture and single differential and total ionization cross sections for the impact of light ions on water vapor[19, 40] and liquid water.[2] They have also been used to fit cross sections corresponding to water vapor fragmentation due to proton bombardment.[22, 42] These models have the advantage of being easy to be implemented in Monte Carlo codes, providing a very high computing efficiency. The quality of the results obtained from them can be appreciated in Figure 8.8.

6. CONCLUSIONS AND PERSPECTIVES

The CDW methodologies have proven to be very successful to reproduce experimental single ionization cross sections for several projectile-target combinations in a very wide projectile energy range. Among them, the CDW-EIS approximation has thus far been the most successful. In general, these formalisms are capable to explain, unlike the B1 approximation, certain complex phenomena involved in ion–atom collisions, such as the well-known two-center effects. However, realistic bound electron wave functions must be used to obtain more accurate DDCS that are sensible to the initial electron state. In some physical situations, such as the double ionization of a multielectron target and the interaction between a partially ionized projectile and a hydrogen-like target, the four-body extended CDW formalisms arise as powerful tools to determine the corresponding cross sections. Efforts have been made in this sense by Belkić[36, 43] resulting in good agreement between theoretical and experimental cross sections for electron detachment from negative hydrogen ion by proton impact. This author and colleagues have recently reviewed four-body formalisms for various processes that take place in ion–atom collisions.[44]

To the best of our knowledge, all Monte Carlo codes developed to simulate energetic ion transport through matter use semiempirical methods to determine ion–atom interaction cross sections. Several of these methods lack a physical basis and are limited to fitting experimental cross sections. In our opinion, the CDW-EIS approximation can be used to calculate all the electronic cross sections required by these Monte Carlo codes, including the case of relativistic projectile energies of heavy ions.

The determination of experimental ionization cross sections for liquid water is a topic which still presents a considerable challenge to experimentalists. Although it is a very difficult task, we are optimistic in this respect. Recently, Kaneda et al.[45] have carried out the first experiment to measure the relative ion-fragment yields due to proton impact on liquid water. The availability of liquid water ionization cross sections will allow the needed tests of the corresponding theoretical models. This, in turn, would improve our understanding of the role of the liquid water phase effects that influence the ionization process.

ACKNOWLEDGMENTS

The authors are very grateful to professors R. Rivarola, C. Champion, and D. Emfietzoglou for kindly having provided experimental data and/or figures shown in this chapter. The authors also thanks Ms. Camilla Sampaio for having helped us during the construction of figures. M. Bernal wishes to thank the FAPERJ foundation in Brazil for the research Grant No. E-26/102.524/2009 and Prof. Carlos E. de Almeida for his support during the realization of this work.

REFERENCES

1. Friedland, W.; Jacob, P.; Paretzke, H., et al. Simulation of light ion induced DNA damage patterns. *Radiat. Prot. Dosim.* **2006**, *122*, 116.
2. Dingfelder, M.; Inokuti, M.; Paretzke, H. Inelastic-collision cross sections of liquid water for interactions of energetic protons. *Radiat. Phys. Chem.* **2000**, *59*, 255.
3. Rudd, M. E.; Kim, Y.; Madison, D. H., et al. Electron production in proton collisions with atoms and molecules: energy distributions. *Rev. Mod. Phys.* **1992**, *64*, 441.
4. Crothers, D.; McCann, J. Ionisations of atoms by ion impact. *J. Phys. B: At. Mol. Opt. Phys.* **1983**, *16*, 3229.
5. Hansen, J. P.; Kocbach, L. Ejection angles of fast delta electrons from K-shell ionisation induced by energetic ions. *J. Phys. B* **1989**, *22*, L71.
6. Bernal, M. A.; Liendo, J. A. The HKS model for electron production in liquid water by light ions. *Nucl. Instrum. Methods Phys. Res., Sect. B* **2006**, *251*, 171.
7. Bernal, M. A.; Liendo, J. A. Inelastic-collision cross sections for the interactions of totally stripped H, He and C ions with liquid water. *Nucl. Instrum. Methods Phys. Res., Sect. B* **2007**, *262*, 1.
8. Belkić, Dž. A quantum theory of ionisation in fast collisions between ions and atomic systems. *J. Phys. B: At. Mol. Phys.* **1978**, *11*, 3529.
9. McDowell, M.; Coleman, J. *Introduction to the Theory of Ion–Atoms Collisions*; North-Holland: Amsterdam, 1970.
10. Cheshire, I. M. Continuum distorted wave approximation; resonant charge transfer by fast protons in atomic hydrogen. *Proc. Phys. Soc.* **1964**, *84*, 89.
11. Landau, L. D.; Lifshitz, E. M. *Quantum Mechanics: Nonrelativistic Theory*; Pergamon Press: Barcelona, 1977.
12. Fainstein, P. D.; Ponce, V. H.; Rivarola, R. D. Electron emission from multielectronic atoms by ion impact at intermediate and high energies. *J. Phys. B: At. Mol. Opt. Phys.* **1989**, *22*, 1207.
13. Stolterfoht, N.; DuBois, R.; Rivarola, R. D. *Electron Emission in Heavy Ion–Atom Collisions*; Springer: Berlin, 1997.
14. Secondary electron spectra from charge particle interactions, Tech. Rep. 55, ICRU, Bethesda, MD, 1996.
15. Toburen, L. H.; Nakai, M. Y.; Langley, R. A. Measurement of high-energy charge-transfer cross sections for incident protons and atomic hydrogen in various gases. *Phys. Rev.* **1968**, *171*, 114.

16. Toburen, L. H.; Wilson, W. E. Energy and angular distributions of electrons ejected from water vapour by 0.3–1.5 MeV protons. *J. Chem. Phys.* **1977**, *66*, 5202.
17. Toburen, L. H.; Wilson, W. E.; Popovich, R. J. Secondary electron emission from ionization of water vapor by 0.3 to 2.0 MeV He^+ and He^{2+} ions. *Radiat. Res.* **1980**, *82*, 27.
18. Wilson, W. E.; Miller, J. H.; Toburen, L. H., et al. Differential cross sections for ionization of methane, ammonia and water vapour by high velocity ions. *J. Chem. Phys.* **1984**, *80*, 5601.
19. Rudd, M. E.; Goffe, T. V.; Dubois, R. D., et al. Cross sections for ionization of water vapor by 7–4000 keV protons. *Phys. Rev. A* **1985**, *31*, 492.
20. Rudd, M. E.; Itoh, A.; Goffe, T. V. Cross sections for ionization, capture, and loss for 5–450 keV He^+ on water vapor. *Phys. Rev. A* **1985**, *32*, 2499.
21. Bolorizadeh, M. A.; Rudd, M. E. Angular and energy dependence of cross sections for ejection of electrons from water vapor. II. 15–150 keV proton impact. *Phys. Rev. A* **1996**, *33*, 888.
22. Werner, U.; Beckord, K.; Becker, J., et al. 3D imaging of the collision-induced Coulomb fragmentation of water molecules. *Phys. Rev. Lett.* **1995**, *74*, 1962.
23. Gobet, F.; Eden, S.; Coupier, B., et al. Ionization of water by (20–150) keV protons: separation of direct-ionization and electron-capture processes. *Phys. Rev. A* **2004**, *70*, 062716.
24. Ohsawa, D.; Kawauchi, K.; Hirabayashi, M., et al. An apparatus for measuring the energy and angular distribution of secondary electrons emitted from water vapor by fast heavy-ion impact. *Nucl. Instrum. Methods Phys. Res., Sect. B* **2005**, *227*, 431.
25. Emfietzoglou, D.; Garcia-Molina, R.; Kyriakou, I., et al. A dielectric response study of the electronic stopping power of liquid water for energetic protons and a new *I*-value for water. *Phys. Med. Biol.* **2009**, *54*, 3451.
26. Rudd, M. E. Differential cross sections for secondary electron production by proton impact. *Phys. Rev. A* **1988**, *38*, 6129.
27. Stopping powers and ranges for protons and alpha particles, Tech. Rep. 49, ICRU, Bethesda, MD, 1993.
28. Fano, U. Penetration of protons, alpha particles, and mesons. *Annu. Rev. Nucl. Sci.* **1963**, *13*(1), 1–66.
29. Hayashi, H.; Watanabe, N.; Udagawa, Y., et al. The complete optical spectrum of liquid water measured by inelastic X-ray scattering. *Proc. Natl. Acad. Sci. USA* **2000**, *97*, 6264.
30. Dingfelder, M.; Hantke, D.; Inokuti, M. Electron inelastic scattering cross sections in liquid water. *Radiat. Phys. Chem.* **1998**, *53*, 1.
31. Heller, J. M.; Hamm, R. N.; Birchoff, R. D., et al. Collective oscillation in liquid water. *J. Chem. Phys.* **1976**, *60*, 3483.
32. Emfietzoglou, D.; Moscovitch, M. Inelastic collision characteristics of electrons in liquid water. *Nucl. Instrum. Methods Phys. Res., Sect. B* **2002**, *193*, 71.
33. <http://www.nist.gov/physlab/data/ffast/index.cfm>.
34. Fainstein, P. D.; Ponce, V. H.; Rivarola, R. D. Two-centre effects in ionization by ion impact. *J. Phys. B: At. Mol. Opt. Phys.* **1991**, *24*, 3091.
35. Olivera, G. H.; Rivarola, R. D.; Fainstein, P. D. Ionization of the excited states of hydrogen by proton impact. *Phys. Rev. A* **1995**, *51*, 847.
36. Belkić, Dž. Electron detachment from the negative hydrogen ion by proton impact. *J. Phys. B: At. Mol. Opt. Phys.* **1997**, *30*, 1731.
37. Fainstein, P. D.; Olivera, G. H.; Rivarola, R. D. Theoretical calculations of the stopping power for protons traversing H, He and simple molecular targets. *Nucl. Instrum. Methods Phys. Res., Sect. B* **1996**, *107*, 19.
38. Schutten, J.; DeHeer, F. J.; Moustafa, H. R., et al. Cross and partial ionization cross sections for electrons on water vapor in the energy range 0.1–20 keV. *J. Chem. Phys.* **1966**, *44*, 3924.

39. Stopping of ions heavier than Helium, Tech. Rep. 73, ICRU, Bethesda, MD, 2005.
40. Dal Cappello, C.; Champion, C.; Boudrioua, O., et al. Theoretical and experimental investigations of electron emission in $C^{6+} - H_2O$ collisions. *Nucl. Instrum. Methods Phys. Res., Sect. B* **2009**, *267*, 781.
41. Emfietzoglou, D.; Nikjoo, H.; Pathak, A. Electronic cross sections for proton transport in liquid water based on optical-data models. *Nucl. Instrum. Methods Phys. Res., Sect. B* **2006**, *249*, 26.
42. Gobet, F.; Farizon, B.; Farizon, M., et al. Total, partial, and electron-capture cross sections for ionization of water vapor by 20–150 keV protons. *Phys. Rev. Lett.* **2001**, *86*, 3751.
43. Belkić, Dž. Quantum-mechanical methods in loss-excitation and loss-ionization in fast ion–atom collisions. *Adv. Quantum Chem.* **2009**, *56*, 251.
44. Belkić, Dž.; Mančev, I.; Hanssen, J. Four-body methods for high-energy ion–atom collisions. *Rev. Mod. Phys.* **2008**, *80*, 249.
45. Kaneda, M.; Shimizu, M.; Hayakawa, T., et al. Mass spectrometric study of collision interactions of fast charged particles with water and NaCl solutions. *Nucl. Instrum. Methods Phys. Res., Sect. B* **2009**, *267*, 908.
46. Akkerman, A.; Breskin, A.; Chechik, R., et al. Calculation of proton stopping power in the region of its maximum value for several organic materials and water. *Rad. Phys. Chem.* **2001**, *61*, 333.
47. Xu, Y. J.; Khandelwal, G. S.; Wilson, J. W. Proton stopping cross sections of liquid water. *Phys. Rev. A* **1985**, *32*, 629.
48. Bauer, P.; Kaferbock, W.; Necas, V. Investigation of the electronic energy loss of hydrogen ions in H_2O: influence of the state of aggregation. *Nucl. Instrum. Methods Phys. Res., Sect. B* **1994**, *93*, 132.
49. Wenzel, W. A.; Whaling, W. Cross section and angular distribution of the D(D, p)T reaction. *Phys. Rev.* **1952**, *88*, 1149.

CHAPTER NINE

Computation of Distorted Wave Cross Sections for High-Energy Inelastic Collisions of Heavy Ions with Water Molecules

Roberto D. Rivarola[a], **Mariel E. Galassi**[a], **Pablo D. Fainstein**[b] **and Christophe Champion**[c]
[a]Instituto de Física Rosario (CONICET-UNR) and Facultad de Ciencias Exactas, Ingeniería y Agrimensura, Universidad Nacional de Rosario, Avenida Pellegrini 250, 2000 Rosario, Argentina
[b]Centro Atómico Bariloche, Comisión Nacional de Energía Atómica, Avda E. Bustillo 9500, 8400 Bariloche, Argentina
[c]Université Bordeaux 1, CNRS/IN2P3, Centre d' Etudes Nucléaires de Bordeaux-Gradignan, CENBG, Gradignan, France

Contents

Abstract

Irradiation of water and other molecules of biological interest by heavy ion beams is studied. Distorted wave models are employed to investigate the corresponding inelastic collisions. Cross sections for electronic capture, ionization, and excitation processes are determined as well as equilibrium charge-states and electronic stopping power. The influence of multiple ionization in liquid water radiolysis is analyzed.

Advances in Quantum Chemistry, Volume 65
ISSN 0065-3276, http://dx.doi.org/10.1016/B978-0-12-396455-7.00009-1

1. INTRODUCTION

The interaction of charged particles with matter has been a subject of study since the pioneering works of Bethe.[1] In these seminal works Bethe applied the first-Born approximation to calculate the total cross section for single ionization and excitation of H by swift electron and ion impact. Using a multipole expansion of the perturbation, and keeping only the dipole term, he was able to obtain closed formulas of the total cross sections and stopping power. The comparison with experimental results showed good agreement at high impact energy, where these reactions dominate, and that it largely overestimated the cross sections at intermediate and small impact energies. This showed that such a first-order theory could not give a complete representation of the processes. However, the simplicity of the calculation, the compact form of the result, the requirements from different applications for a large quantity of data, and the difficulty to develop higher order methods lead to the addition of semi-empirical corrections to the Bethe formula. This produced what is now called the Bethe–Bloch theory[2] which is the relativistic version of Bethe's theory including the Barkas, shell and polarization corrections.[3] Results with this theory for atomic and molecular targets, the later obtained employing Bragg's rule, are readily available for electron and proton impact in a large range of impact energies.

The corrections included in the Bethe–Bloch theory are mainly related to the dependence of the total cross sections (or stopping power) on the properties of the target. They depend therefore on the number of electrons (shells) or the polarizability of the electron gas. It is well known that in first-order theories the total cross section and stopping power scale with the square of the projectile charge Z_P. Experiments performed by Brandt and coworkers[4] employing He^{2+} and Li^{3+} projectile ions impinging on heavy targets, showed for the first time large discrepancies as deviations from the Z_P^2-scaling law. These discrepancies were explained introducing the binding and polarization effects. The binding effect, which is important from intermediate to low impact energy, arises from the increasing binding of the active electron due to the combined projectile and target potential. This effect lowers the total cross section since the increased binding results in a lower emission probability. The polarization effect, which is important at intermediate to high energies, arises from the distortion of the initial state by the projectile potential. The experiments showed that this effect was responsible for an increase of the total cross section with respect to the prediction of the Bethe–Bloch theory. The projectile potential attracts the electronic cloud, therefore increasing the effective impact parameter and thus increasing the transition probability. Basbas and coworkers developed the perturbed-stationary-state (PSS) theory where all these effects were taken into account as higher order corrections to the first-Born approximation and found very good agreement with the experimental data.[5] In this approach the total cross section results in an expansion in powers of the ratio between the projectile and target nuclear charge. The first-term, proportional to Z_P^2 corresponds to the first-Born approximation. The appearance of even and odd powers indicated that there are not only higher order contributions but also that they differ on the sign of the projectile charge. In this way Brandt and Basbas[6] explained the difference in the total cross sections and stopping power between particle and antiparticle which had already been found experimentally by Barkas and coworkers.[7]

The PSS model has been found to yield good agreement with experiments for asymmetric systems, when the projectile charge Z_P is much smaller than the target nuclear charge Z_T. It is clear that when the projectile charge increases, the parameter Z_P/Z_T will be large and unreasonable for a perturbative development. Therefore a different kind of theoretical approach is required to represent the total cross sections and stopping powers for all values of Z_P and Z_T.

A theoretical method which is well suited for this problem is the distorted wave theory. Since all the particles involved are charged, the interactions are governed by the long-range Coulomb forces. It is well known that the Coulomb potential acts even at infinite long distances. The interaction between two charged particles at long distances might be small but never zero. As a consequence the wavefunction representing this situation cannot be written as a product of free-particle (plane-waves) wavefunctions. The long-range nature of the potential results in the appearance of a Coulomb phase or distortion. In distorted wave theory, the initial and final state wavefunctions are chosen in such a way as to represent the physical problem and the correct asymptotic conditions at very large distances. These wavefunctions can be chosen in different ways leading to different distorted wave models. The Continuum Distorted Wave (CDW) model was first proposed by Cheshire[8] to investigate electron capture and afterwards extended by Belkić[9] for electron ionization. One of the most successful theoretical descriptions is the Continuum Distorted Wave-Eikonal Initial State (CDW-EIS) model introduced by Crothers and McCann[10] to study electron ionization of monoelectronic targets and latter extended by Fainstein et al.[11] for multielectronic targets. The CDW-EIS model was subsequently formulated to investigate the electron capture reaction.[12] The CDW-EIS model was applied with great success in more symmetric systems by Fainstein et al.[13] for single ionization of He by H^+, He^{2+}, and Li^{3+} impact. A very good agreement was obtained with the experimental data available in whole energy range from a few keV/amu to a few MeV/amu. Moreover the calculations explained the large difference between results for proton and antiproton impact which had been found experimentally at CERN by Andersen et al.[14] All these results could be interpreted in terms of the binding and polarization mechanisms of Brandt and coworkers.

For symmetric systems however, another kind of effect, not included in the Bethe and PSS models, must be considered. As the impact energy decreases the cross sections for electron capture increase and become even larger that the corresponding ones for ionization and excitation. As a result, a fraction of the particles in the projectile beam will suffer a change in charge-state. For example, a fraction of a proton beam will be neutralized and even, at very low impact energy, become negatively charged (H^-). In equilibrium at a given impact energy there will be several charge-states and their contribution must be considered to calculate accurately the stopping power. The difficulty in this approach is that a huge number of cross sections are required for all the open channels. Such an approach has been considered up to now with two different models. Schiwietz and coworkers[15,16] calculated the cross sections employing the coupled-channel method using atomic orbitals while Fainstein et al.[17] and Olivera et al.[18] employed the distorted-wave (DW) method. Both methods showed very good agreement with the experiments available for proton impact on H and He targets. Furthermore, the DW method was also successfully applied to stopping power calculations for simple molecular targets.[19]

2. THE DISTORTED WAVE MODEL FOR INELASTIC COLLISIONS

When a fast bare ion beam impacts on atoms or molecules, three main electronic reactions are produced: electron ionization or excitation of the target and electron capture of target electrons by the projectile. This last reaction dominates at low-intermediate collision energies, corresponding to impact velocities $v \lesssim v_e$, where v_e is the velocity of the transferred electron in the initial unperturbed target orbital. As the energy increases electron ionization becomes the dominant channel whereas electron excitation gives larger contributions than electron capture.

In order to describe these one-electron processes in the penetration of light ion beams in a gaseous target a distorted wave model was formulated.[17] In such theoretical description the CDW-EIS model was employed for electron capture[12] and electron ionization[10, 11] while target excitation was included employing the Symmetric Eikonal (SE) one.[20] These models were applied with success to study numerous collision systems (see Ref. 21 and references therein) not only for processes involving one active electron. However, for e.g. two-electron capture from helium by alpha particles, the four-body version of the CDW-EIS model gives total cross sections that are smaller than the experimental data by a factor varying from 1000 to 10 at impact energies 0.1-3 MeV (see review[22a] and references therein). These theoretical approximations introduce the effect of the distortion produced on the promoted electron by the presence of coulombic perturbative potentials in the entry and exit channels, paying particular attention to the asymptotic conditions corresponding to their long-range character.

2.1 The theoretical description for charged projectiles

For simplicity we will consider a three-body system composed by a bare projectile, an active electron, and a one-center residual target. Moreover, it is considered that the passive electrons (those ones that are not promoted) remain in their orbitals during the collision. This assumption is valid at high enough impact velocities for which the collision time is smaller than the one corresponding to relaxation of the passive electrons. For molecular targets it will correspond also to collision times smaller than the vibrational and rotational ones. In the following, the notation is that usually employed for distorted wave models and atomic units will be used except where otherwise stated.

The straight line version of the impact parameter approximations is used, for which:

$$\vec{R} = \vec{\rho} + \vec{v}\,t, \tag{1}$$

where $\vec{R}$ is the internuclear vector, $\vec{\rho}$ the impact parameter, $\vec{v}$ the collision velocity, and t the time evolution. The system is described from a reference frame fixed on the target nucleus.

In the α-entry channel, the initial one-active electron distorted wavefunction is chosen as:

$$\begin{aligned}\chi_\alpha^+ &= \varphi_\alpha(\vec{x}) \exp\left(-i\varepsilon_\alpha t\right) \exp\left[-i\nu \ln\left(vs + \vec{v}\cdot\vec{s}\right)\right] \exp\left[i\frac{Z_P Z_T}{v} \ln\left(vR - v^2 t\right)\right] \\ &= \psi_\alpha \exp\left[i\frac{Z_P Z_T}{v} \ln\left(vR - v^2 t\right)\right],\end{aligned} \tag{2}$$

where the super-index (+) indicates that it preserves correct outgoing boundary conditions. In Eq. (2), $\varphi_\alpha(\vec{x})$ represents the non-perturbed initial electron bound orbital and ε_α the corresponding orbital energy, $\vec{x}$ and $\vec{s}$ are the electron position vectors with respect to the target and projectile nucleus, Z_P and Z_T are the projectile and target nuclear charges and $\nu = Z_\mathrm{P}/v$ (also called the Sommerfeld parameter). The eikonal phase included in the entrance channel depending of the $\vec{s}$ coordinate, takes account of the fact that the electron bound to the target is simultaneously traveling in a continuum state of the projectile field. In fact, the electron is moving in a combined field of the residual target and of the projectile. In this sense χ_α^+ is a two-center wavefunction which contains the information on the long-range coulomb interaction between the projectile and the electron. The other eikonal phase depending on the internuclear distance corresponds to the Coulomb interaction between the nuclei present in the reaction.

The choice of the final distorting wavefunction in the β-exit channel depends on the process investigated. Thus, for electron capture this wavefunction is chosen as

$$\begin{aligned}\chi_\beta^{-(c)} &= \varphi_\beta(\vec{s}) \exp\left(-i\varepsilon_\beta t + i\vec{v}\cdot\vec{x} - i\frac{v^2}{2}t\right)\\ &\quad\times N^*(\varsigma)\,{}_1F_1(-i\varsigma; 1; -ivx - i\vec{v}\cdot\vec{x}) \exp\left[-i\frac{Z_\mathrm{P}Z_\mathrm{T}}{v}\ln\left(vR + v^2 t\right)\right]\\ &= \psi_\beta^{(c)} \exp\left[-i\frac{Z_\mathrm{P}Z_\mathrm{T}}{v}\ln\left(vR + v^2 t\right)\right]. \end{aligned} \tag{3}$$

Now, the super-index (−) indicates that correct ingoing conditions are satisfied, $\varphi_\beta(\vec{s})$ represents the non-perturbed electron bound wavefunction in the exit channel with ε_β the corresponding orbital energy. The other terms in the first phase factor are due to the Galilean transformation of the electron wavefunction from the projectile frame to the target nucleus one. Also in expression (3), ${}_1F_1(-i\varsigma; 1; -ivx - i\vec{v}\cdot\vec{x})$ is a continuum factor of the electron–residual target interaction, $\varsigma = Z_\mathrm{T}^*/v$, with Z_T^* the *effective* target nuclear charge. Thus, the final distorted wavefunction presents again a two-center character associated with the fact that the electron evolves in the combined field of the projectile and residual target ones. The function $N(a) = \exp(\pi a/2)\Gamma(1 - ia)$ gives the normalization of the continuum factor and the eikonal phase depending on the internuclear distance represents again the interaction between the nuclei. According to the prescription of Belkić et al.[22b] the effective charge Z_T^* is chosen as $Z_\mathrm{T}^* = \sqrt{-2n_\alpha^2\varepsilon_\alpha}$, where n_α is the principal quantum number. This choice corresponds to consider an effective Coulomb potential to represent the interaction of the electron with the residual target in the exit channel, even in the case of multielectron targets.

To describe the electron ionization process the final distorted wavefunction is taken as:

$$\begin{aligned}\chi_\beta^{-(i)} &= (2\pi)^{-3/2}\exp\left(i\vec{k}\cdot\vec{x} - i\frac{k^2}{2}t\right)N^*(\xi)\,{}_1F_1\left(-i\xi;1;-ikx-i\vec{k}\cdot\vec{x}\right)\\ &\quad\times N^*(\zeta)\,{}_1F_1\left(-i\zeta;1;-ips-i\vec{p}\cdot\vec{s}\right)\exp\left[-i\frac{Z_\mathrm{P}Z_\mathrm{T}}{v}\ln\left(vR+v^2t\right)\right]\\ &= \psi_\beta^{(i)}\exp\left[-i\frac{Z_\mathrm{P}Z_\mathrm{T}}{v}\ln\left(vR+v^2t\right)\right],\end{aligned} \tag{4}$$

where $\vec{k}$ and $\vec{p}=\vec{k}-\vec{v}$ are the linear momenta of the electron with respect to the target and projectile nucleus, respectively, $\xi = Z_\mathrm{T}^*/k$ and $\zeta = Z_\mathrm{P}/p$. The first part of Eq. (4), depending on the coordinate $\vec{x}$, is a wavefunction describing the electron in a continuum state of the residual target whereas the continuum factor depending on the coordinate $\vec{s}$ corresponds to the electron–projectile interaction. Thus, the final distorted wavefunction indicates that the electron is traveling in a continuum state of the projectile and residual target fields, and their actions on the emitted electron are considered on equal footing.

Finally, for the electron excitation reaction the final distorted wavefunction is chosen as:

$$\begin{aligned}\chi_\beta^{-(e)} &= \varphi_\beta(\vec{x})\exp\left(-i\varepsilon_\beta t\right)\exp\left[i\nu\ln\left(vs-\vec{v}\cdot\vec{s}\right)\right]\exp\left[-i\frac{Z_\mathrm{P}Z_\mathrm{T}}{v}\ln\left(vR+v^2t\right)\right]\\ &= \psi_\beta^{(e)}\exp\left[-i\frac{Z_\mathrm{P}Z_\mathrm{T}}{v}\ln\left(vR+v^2t\right)\right]\end{aligned} \tag{5}$$

with $\varphi_\beta(\vec{x})$ representing an excited state of the target with orbital energy ε_β and the eikonal phase depending on the coordinate $\vec{s}$ describes the electron in a continuum state of the projectile. The last phase factor takes into account the internuclear interaction.

The first-order scattering amplitude for any of the cases mentioned above (the elastic scattering channel is not considered) can be written as:

$$\mathcal{A}_{\alpha\beta}^{+}(\vec{\rho}) = -i\int_{-\infty}^{+\infty}\mathrm{d}t\left\langle\chi_\beta^-\left|\left(H_\mathrm{el}-i\frac{\partial}{\partial t}\right)^\dagger\right|\chi_\alpha^+\right\rangle = (\rho v)^{2iZ_\mathrm{P}Z_\mathrm{T}/v}a_{\alpha\beta}^{+}(\vec{\rho}) \tag{6}$$

and

$$\mathcal{A}_{\alpha\beta}^{-}(\vec{\rho}) = -i\int_{-\infty}^{+\infty}\mathrm{d}t\left\langle\chi_\beta^-\left|\left(H_\mathrm{el}-i\frac{\partial}{\partial t}\right)\right|\chi_\alpha^+\right\rangle = (\rho v)^{2iZ_\mathrm{P}Z_\mathrm{T}/v}a_{\alpha\beta}^{-}(\vec{\rho}) \tag{7}$$

in its post- and prior-versions, respectively, with H_{el} the electronic Hamiltonian which results from solving the full time-dependent Schrödinger equation in the eikonal approximation. In Eqs. (6) and (7), the final distorted wavefunction must be replaced by the corresponding ones defined in Eqs. 3–5 if electron capture, electron ionization or electron excitation are considered, respectively. Also,

$$a^{+}_{\alpha\beta}(\vec{\rho}) = -i\int_{-\infty}^{+\infty} \mathrm{d}t \left\langle \psi_\beta \left| \left(\widetilde{H}_{\mathrm{el}} - i\frac{\partial}{\partial t}\right)^{\dagger} \right| \psi_\alpha \right\rangle \tag{8}$$

and

$$a^{-}_{\alpha\beta}(\vec{\rho}) = -i\int_{-\infty}^{+\infty} \mathrm{d}t \left\langle \psi_\beta \left| \left(\widetilde{H}_{\mathrm{el}} - i\frac{\partial}{\partial t}\right) \right| \psi_\alpha \right\rangle \tag{9}$$

are scattering amplitudes where the internuclear potential is excluded. This interaction is completely contained in the phase factors $(\rho v)^{2iZ_{\mathrm{P}}Z_{\mathrm{T}}/v}$ and not included in the electronic Hamiltonian $\widetilde{H}_{\mathrm{el}}$. These scattering amplitudes (in the prior- or post-versions) can be related to the transition matrix element:

$$T_{\alpha\beta}(\vec{K}) = i\frac{4\pi^2}{v}R_{\alpha\beta}(\vec{\eta}) \tag{10}$$

by using the Fourier transform:

$$a_{\alpha\beta}(\vec{\rho}) = \frac{1}{2\pi}\int \mathrm{d}\vec{\eta}\, e^{-i\vec{\rho}\cdot\vec{\eta}} R_{\alpha\beta}(\vec{\eta}), \tag{11}$$

where $\vec{K}$ is the total momentum transfer and $\vec{\eta}$ its transverse component defined in a direction perpendicular to the incident velocity vector. It is interesting to note that the associated matrix elements $R_{\alpha\beta}(\vec{\eta})$ can be obtained in analytical forms for any of the single electron reactions considered. Thus, for example, a general analytical expression has been obtained by Martínez et al.[23] for electron capture from any target orbital to any final projectile state. Then, for single electron capture and single electron excitation of atomic targets the total cross sections can be obtained from:

$$\sigma_{\alpha\beta} = \int \mathrm{d}\vec{\rho}\, \left|a_{\alpha\beta}(\vec{\rho})\right|^2 = \int \mathrm{d}\vec{\eta}\, \left|R_{\alpha\beta}(\vec{\eta})\right|^2, \tag{12}$$

where the Parseval identity has been employed. In a similar way, for electron ionization doubly differential cross sections as a function of the final electron energy E_k and the solid angle Ω_k subtended by the emitted electron can be found from:[10, 24]

$$\frac{\mathrm{d}^2\sigma_{\alpha k}}{\mathrm{d}E_k\mathrm{d}\Omega_k} = k\int \mathrm{d}\vec{\rho}\,\left|a_{\alpha\beta}(\vec{\rho})\right|^2 = k\int \mathrm{d}\vec{\eta}\,\left|R_{\alpha\beta}(\vec{\eta})\right|^2. \tag{13}$$

Single differential cross sections $\mathrm{d}\sigma_{\alpha k}/\mathrm{d}E_k$ and $\mathrm{d}\sigma_{\alpha k}/\mathrm{d}\Omega_k$ can be obtained by integrating Eq. (13) on Ω_k and E_k, respectively. Total cross sections $\sigma_{\alpha k}$ can then be calculated by integration of $\mathrm{d}\sigma_{\alpha k}/\mathrm{d}E_k$ on the final electron energy E_k or by integration of $\mathrm{d}\sigma_{\alpha k}/\mathrm{d}\Omega_k$ on the solid angle Ω_k.

2.2 The theoretical description for neutral projectiles

For neutral projectiles the incoming nucleus is screened by its bound electrons. The perturbation between the dressed projectile and the target electrons is of short-range, having thus a different character than for the case of charged projectiles. It has been shown[25] that the DW model reduces to the first-Born approximation for neutral aggregates. We will restrict our analysis to the impact of hydrogen atom beams, neglecting the possibility of the double charge exchange reaction[22c] associated with the formation of H^-. By simplicity we will consider an effective monoelectronic target model.

In the present case several channels are opened because both collisions partners can be excited and/or ionized. The final state of the incoming projectile defines the projectile-elastic and projectile-inelastic channels if it remains in the initial ground state or is excited to a bound or continuum state, respectively. In a similar way, target-elastic and target-inelastic channels can be defined. Two-active electron processes like excitation or ionization of the target with simultaneous excitation or ionization of the projectile must be also considered. Following Bates and Griffing,[26] we will investigate all these reactions by using the first-order Born approximation (B1). Initial and final wavefunctions are given now as:

$$\phi_{\alpha\alpha'} = \varphi_\alpha(\vec{x}_\mathrm{t})\varphi_{\alpha'}(\vec{s}_\mathrm{p})e^{i\vec{v}\cdot\vec{x}_p - iv^2t/2 - i(\varepsilon_\alpha+\varepsilon_{\alpha'})t}, \tag{14}$$

and

$$\phi_{\beta\beta'} = \varphi_\beta(\vec{x}_\mathrm{t})\varphi_{\beta'}(\vec{s}_\mathrm{p})e^{i\vec{v}\cdot\vec{x}_p - iv^2t/2 - i(\varepsilon_\beta+\varepsilon_{\beta'})t}, \tag{15}$$

where $\varphi_\alpha(\vec{x}_\mathrm{t})(\varphi_{\alpha'}(\vec{s}_\mathrm{p}))$ describes the initial state of the target (projectile) electron and $\varphi_\beta(\vec{x}_\mathrm{t})(\varphi_{\beta'}(\vec{s}_\mathrm{p}))$ excitation or continuum states of the target (projectile) electron in the field of the parent nucleus. Also, $\vec{x}_\mathrm{t}(\vec{s}_\mathrm{p})$ is the target (projectile) electron coordinate referred to its parent nucleus. Furthermore, $\varepsilon_\alpha(\varepsilon_{\alpha'})$ and $\varepsilon_\beta(\varepsilon_{\beta'})$ are the initial and final energies of the target (projectile) electron, respectively.

Excluding the elastic scattering between the aggregates of the collision and inserting the wavefunctions $\phi_{\alpha\alpha'}$ instead of χ_α^+ and $\phi_{\beta\beta'}$ instead of χ_β^- in Eqs. (6) and (7), we obtain the B1-scattering amplitude corresponding to its post- and prior-versions. Moreover, it is easy to prove[24] that:

$$\left(H_\mathrm{el} - i\frac{\partial}{\partial t}\right)\phi_{\alpha\alpha'} = V_\mathrm{int}\phi_{\alpha\alpha'} \tag{16}$$

with

$$V_\mathrm{int} = -\frac{Z_\mathrm{T}}{\left|\vec{R}+\vec{s}_\mathrm{p}\right|} - \frac{Z_\mathrm{P}}{\left|\vec{R}-\vec{x}_\mathrm{t}\right|} + \frac{1}{\left|\vec{R}+\vec{s}_\mathrm{p}-\vec{x}_\mathrm{t}\right|}. \tag{17}$$

The first to third terms in expression (17) give, following this order, the interactions between the target nucleus and the projectile electron, between the projectile nucleus and the target electron and, between the projectile and target electrons. Moreover, the first (second) term does not contributes to the scattering amplitude if a change in the target (projectile) state is produced.[27] For projectile (target) elastic scattering (monoelectronic reaction) the electron–electron interaction produces a screening of the projectile (target) charge. However, for dielectronic reactions where projectile and target states change simultaneously, this interaction produces an effect known as antiscreening. In fact, the projectile nucleus and the projectile electron act incoherently on the target electron, so that the target electron feels separately the influence of these particles. [28] This effect is present for large momentum transfer under close encounter collisions.

The combined use of the distorted wave approximations for ion beams and B1 approximation for neutral projectiles is known as the distorted wave model (DW).[17, 18]

3. ELECTRONIC STOPPING POWER

In order to calculate the electronic stopping power for a bare ion beam penetrating a gaseous target we will consider the processes of excitation, ionization, and electron capture involving only one active electron, so that it is given by:

$$S_{\mathrm{e}}^{+} = \sum_{\beta} \left(\Delta E_{\alpha\beta}^{(e)} \, \sigma_{\alpha\beta}^{(e)} + \Delta E_{\alpha\beta}^{(c)} \, \sigma_{\alpha\beta}^{(c)} \right) + \int_{0}^{\infty} \mathrm{d}E_k \Delta E_{\alpha k}^{(i)} \frac{\mathrm{d}\sigma_{\alpha k}^{(i)}}{\mathrm{d}E_k}, \tag{18}$$

where the super-indexes (e), (c), and (i) indicates the excitation, capture and ionization processes with the corresponding energy changes $\Delta E_{\alpha\beta}^{(e)} = \varepsilon_\beta - \varepsilon_\alpha$, $\Delta E_{\alpha\beta}^{(c)} = \varepsilon_\beta + v^2/2 - \varepsilon_\alpha$, and $\Delta E_{\alpha k}^{(i)} = E_k - \varepsilon_\alpha$, respectively.

We illustrate in Figure 9.1 distorted wave (DW) calculations of the electronic stopping power S_{e}^{+} for protons impacting on an atomic hydrogen gas target. The only reactions that will give contributions to the energy loss are single excitation:

$$\mathrm{H}^{+} + \mathrm{H}(1s) \longrightarrow \mathrm{H}^{+} + \mathrm{H}(n_\beta l_\beta m_\beta), \tag{19}$$

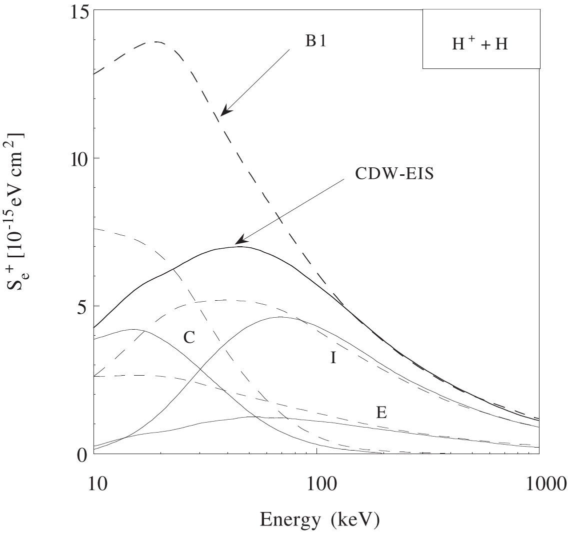

Figure 9.1 Electronic stopping power for proton charge-state S_{e}^{+} on H target. Solid lines, DW from Ref. 17; dashed lines, B1 from Ref. 29.

single ionization:

$$\mathrm{H}^+ + \mathrm{H}(1s) \longrightarrow \mathrm{H}^+ + \mathrm{H}^+ + e^-, \tag{20}$$

and single electron capture:

$$\mathrm{H}^+ + \mathrm{H}(1s) \longrightarrow \mathrm{H}(n_\beta l_\beta m_\beta) + \mathrm{H}^+. \tag{21}$$

The contributions from each of these processes are taken into account (see review 22c and references therein). Electron capture has been considered to final states with principal quantum number $n_\beta \leqslant 2$ and excitation to final states with $n_\beta \leqslant 3$. It is found that electron capture dominates the low energy part of the spectrum whereas ionization gives the main contribution at larger collision velocities. At these velocities, the excitation process contributes to S_e^+ in a percentage of the order of 30% with respect to the ionization reaction. A comparison is given with previous B1 predictions.[29] For energies lower than 100 keV, they overestimate the DW results for the three processes considered. This can be attributed to the limitations of B1 to describe the case of charged beams. However, at high enough velocities results using both models converge to the same values for each one of the processes considered.

In the case of a proton beam, protons can capture electrons and become neutralized. The neutral beams may then be transformed back into protons by electron loss processes and an equilibrium between charge-state components of the beam is consequently attained. At high enough collision energies, the beam consists of a mixture of neutral (H^0) and proton (H^+) charge-states. The fraction at equilibrium of each one of these charge-states is given by the expressions:

$$f(\mathrm{H}^+) = \frac{\sigma_\mathrm{L}}{\sigma_\mathrm{C} + \sigma_\mathrm{L}} \tag{22}$$

and

$$f(\mathrm{H}^0) = \frac{\sigma_\mathrm{C}}{\sigma_\mathrm{C} + \sigma_\mathrm{L}}, \tag{23}$$

where σ_C is the total capture cross section and σ_L is the total loss cross section.

Denoting by S_e^0 the electronic stopping power for the neutral H^0 beam, the total mean stopping power is given by:

$$S_e = f(\mathrm{H}^+)S_e^+ + f(\mathrm{H}^0)S_e^0. \tag{24}$$

To calculate S_e^0 several processes are considered. They are the ones of single excitation:

$$\begin{aligned} H(1s) + H(1s) &\longrightarrow H(1s) + H(n_\beta l_\beta m_\beta) \\ &\longrightarrow H(n_{\beta'} l_{\beta'} m_{\beta'}) + H(1s), \end{aligned} \tag{25}$$

single ionization:

$$\begin{aligned} H(1s) + H(1s) &\longrightarrow H(1s) + H^+ + e^- \\ &\longrightarrow H^+ + e^- + H(1s), \end{aligned} \tag{26}$$

double excitation:

$$H(1s) + H(1s) \longrightarrow H(n_{\beta'} l_{\beta'} m_{\beta'}) + H(n_\beta l_\beta m_\beta) \tag{27}$$

with $n_\beta, n_{\beta'} \neq 1$; double ionization:

$$H(1s) + H(1s) \longrightarrow H^+ + e^- + H^+ + e^- \tag{28}$$

and simultaneous excitation and ionization:

$$\begin{aligned} H(1s) + H(1s) &\longrightarrow H(n_{\beta'} l_{\beta'} m_{\beta'}) + H^+ + e^- \\ &\longrightarrow H^+ + e^- + H(n_\beta l_\beta m_\beta). \end{aligned} \tag{29}$$

The possible formation of H^- ions is neglected in this chapter (for the contribution from the electron capture process $H(1s)+H(1s) \rightarrow H^-(1s^2)+H^+$, see Figures 6.7 and 6.8 in Ref. 22c). Excited states with $n_\beta, n_{\beta'} \leqslant 3$ are considered, assuming that contributions from higher excited states can be neglected.[26, 30] Then, S_e^0 is calculated using the expression:

$$S_e^0 = \sum_{\beta,\beta'} \Delta E^{(e)}_{\alpha\alpha',\beta\beta'} \, \sigma^{(e)}_{\alpha\alpha',\beta\beta'} + \int_0^\infty dE_k \, \Delta E^{(i)}_{\alpha\alpha',k} \, \frac{d\sigma^{(i)}_{\alpha\alpha',k}}{dE_k}, \tag{30}$$

where the first term accounts for target and projectile excitation whereas the second one for ionization from an initial state $\alpha\alpha'$.

Equilibrium charge-state fractions are given in Figure 9.2. DW calculations are in reasonable agreement with experiments, where Bragg's rule has been used to obtain the data for H from measurements for H_2.[31] Results are also in qualitative agreement with B1 calculations.[29] It is shown that the neutral beam fraction is larger than the charged beam fraction at low collision energies while the situation is reversed for energies larger that

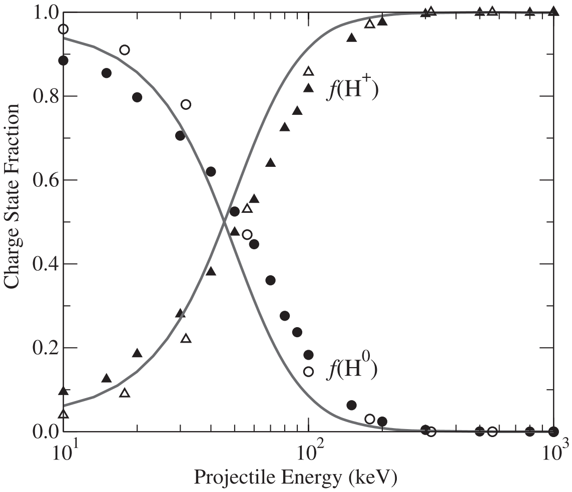

Figure 9.2 Equilibrium charge-state fractions for protons beams traversing H as a function of projectile energy. Solid line, DW calculation; (○), B1 from Ref. 29; (●), experiments for H_2 targets from Ref. 31.

approximately 50 keV. The dominance at low energies can be attributed to the resonant condition of charge exchange.

The total mean electronic stopping power S_e is shown in Figure 9.3 for the case considered above. DW calculations are compared with B1 results[29] and one-center coupled-channel calculations using atomic orbitals (AO)[15, 18] corrected to include double transitions. In fact, AO results are obtained employing S_e^+ computations from Refs. 15, 32 while S_e^0 was obtained with the B1 approximation.[29] Experimental charge-state fractions for $H_2$from Ref. 31 were then used to determine the mean stopping power. We have tested that DW results are not essentially modified if experimental charge fractions are used instead of the theoretical ones. Also included in Figure 9.3 are S_e recommended values from Andersen and Ziegler[33] and various measurements. All calculations give a very good description of experimental data at energies larger than the ones corresponding to the S_e maximum. However, while DW and AO give a good estimation of the corresponding peak, B1 largely overestimates it. In principle, at energies lower than this peak, the best agreement with experiments is given by the AO calculations whereas DW results underestimate them. In order to explain this difference and considering that for the H + H collisional system target and projectile are identical,

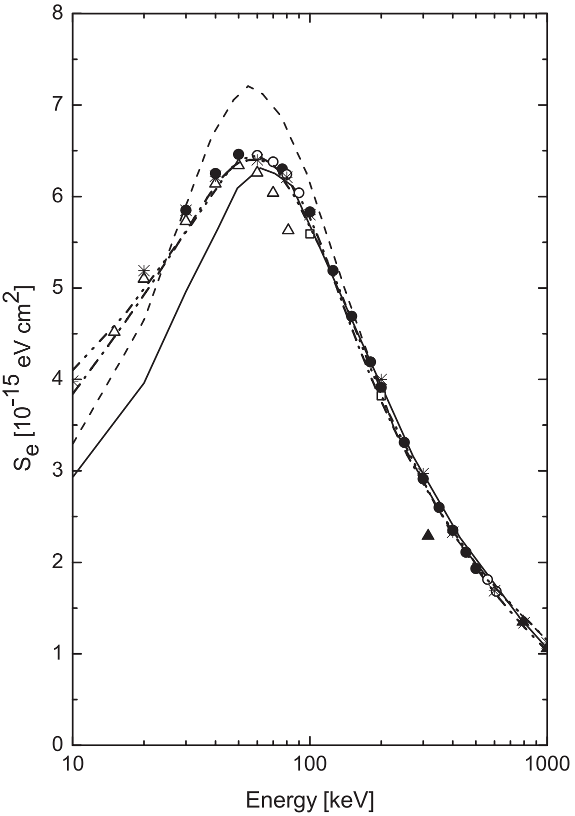

Figure 9.3 Total mean electronic stopping power of proton beams on H targets as a function of projectile energy. Theory: solid line, DW calculations; dashed line, B1 results from Ref. 29; dash-dot line, one-center AO results from Ref. 15 corrected for double transitions; dash-dot-dot line, DW including exchange. Experiments for H_2 targets: see Ref. 17. Stars, tabulated values from Ref. 33.

we included in DW the corresponding exchange contributions. The agreement now is very good.

4. THE CASE OF WATER MOLECULES

In the case of water molecules we must deal with the molecular orbitals of the target. Different possibilities are to use simply Bragg's rule, where the molecule is treated as the ensemble of its separated atomic compounds, or to treat it within a molecular representation. The first method only requires the atomic cross sections or stopping power values. The second case is much more difficult and for that purpose we have chosen to describe the molecular orbitals using a method named Complete Neglect of Differential Overlap (CNDO). In this method the molecular orbitals are expanded in terms of atomic orbitals and both the weights of the expansion and the molecular energies are consequently determined.[34] This method was first proposed by Senger and Rechenmann[35] who employed the B1 approximation considering that the molecular cross section for each molecular orbital can be given by the addition of the atomic cross sections weighted with the corresponding parentage coefficients.

4.1 Differential and total cross sections

Double differential cross sections (DDCS) for single electron ionization from water vapor produced by 0.3 MeV-protons and 2 MeV-alpha particles are shown in Figure 9.4. CDW-EIS results are obtained using the CNDO representation of the initial orbitals and effective Coulomb continuum electron–residual target factors with corresponding effective charges given by $Z_T^* = \sqrt{-2n^2\varepsilon_\alpha}$, where now ε_α is the orbital energy and n the principal

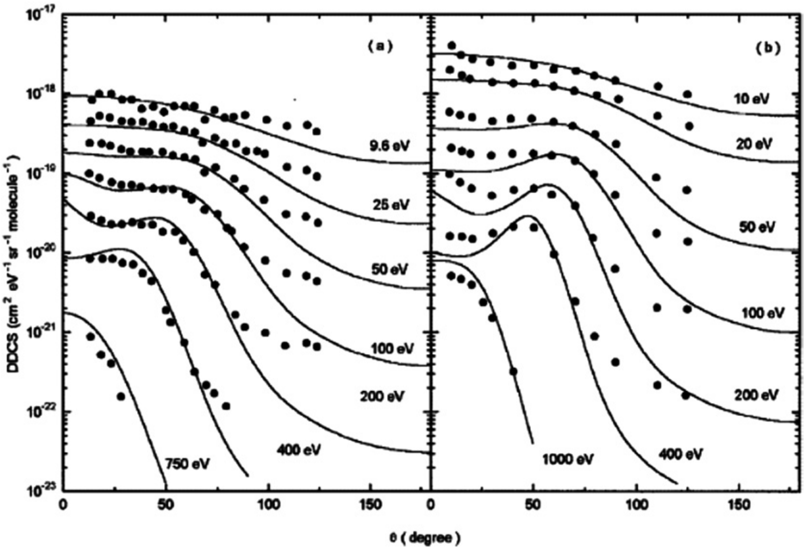

Figure 9.4 Doubly differential cross section for ionization of water vapor: (a) 0.3 MeV H^+ and (b) 2 MeV He^{2+} ions. Theory: solid line, CDW-EIS; experiments: (●), extracted from Senger and Rechenmann.[35]

quantum number corresponding to each one of the atomic components that constitutes the molecular orbital considered. To describe the oxygen orbitals Roothaan–Hartree–Fock wavefunctions were used.[36] A good agreement with experimental data is obtained for fixed ejection energies as a function of the emission angle except in the backward direction where the theoretical results underestimate the experimental data. In a previous work,[37] where hydrogenic wavefunctions have been used to describe the initial orbitals within the CDW-EIS formalism, some differences with experimental data were found, showing the importance of considering the molecular character of the target.

Single differential cross sections (SDCS) for single ionization as a function of the electron ejection energy are shown in Figure 9.5. CDW-EIS

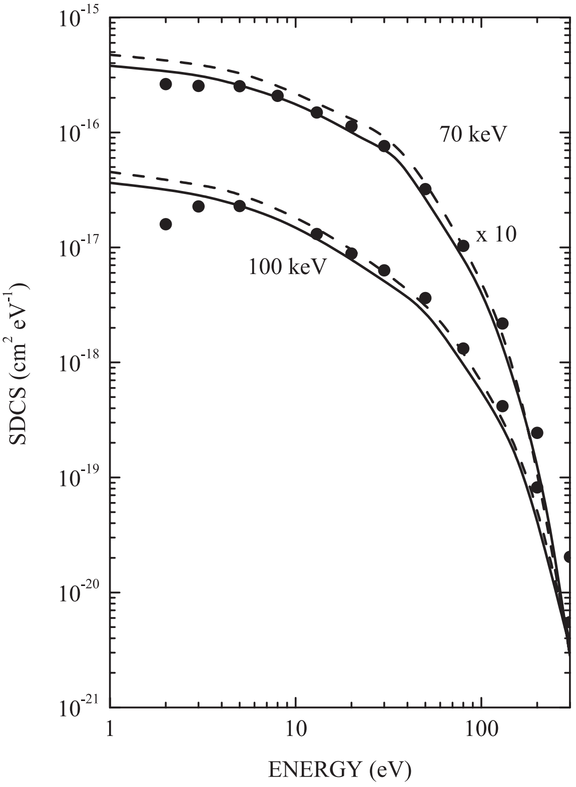

Figure 9.5 Single differential cross section for single ionization of water vapor by 70 keV and 100 keV proton impact as a function of the electron energy. Theory: solid line, CDW-EIS molecular method; dashed line, CDW-EIS Bragg's rule. Experimental data: (●), from Ref. 38.

calculations are performed employing Bragg's rule and the molecular method with CNDO orbital wavefunctions. Proton beams with 70 keV and 100 keV energies are considered, obtaining a good agreement with existing measurements,[38] except at energies lower than 4 keV, for which the perturbative models are not adequate. Differences between theoretical singly differential cross sections calculated using the two different molecular methods are relatively small over all the energy domain considered.

Total cross sections (TCS) for the $H^+ + H_2O$ collision system are presented in Figure 9.6. The one corresponding to single ionization is obtained by integrating the SDCS (calculated using the molecular CDW-EIS model) on the electron ejection energy. Bragg's rule has been employed to compute the TCS for electron capture. For both reactions CDW-EIS calculations give a very good description of experiments[39, 40] for collision energies larger than 30 keV.

In Figure 9.7, ionization TCS for H^+ projectiles at energies larger that 100 keV show a very good agreement with experimental data.[41, 42] TCS for impact of He^{2+} and C^{6+} ion beams are also presented. For He^{2+} the agreement between theory and experiments is also very good. For C^{6+} it is difficult to give any conclusion due to the fact that only one value exists for comparison. This value has been obtained by numerical integration of the corresponding experimental single differential cross section.[43] Experimental results for Cl^{6+} from Ref. 44 are also included

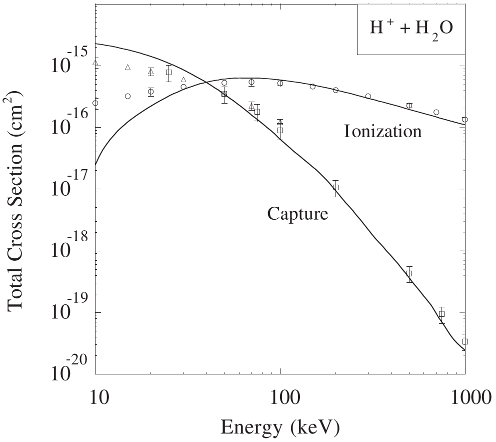

Figure 9.6 Total cross sections for electron capture and single ionization of water vapor by proton impact. Solid lines, CDW-EIS calculations. Experiments: open squares, from Ref. 39; open circles and open triangles, from Ref. 40.

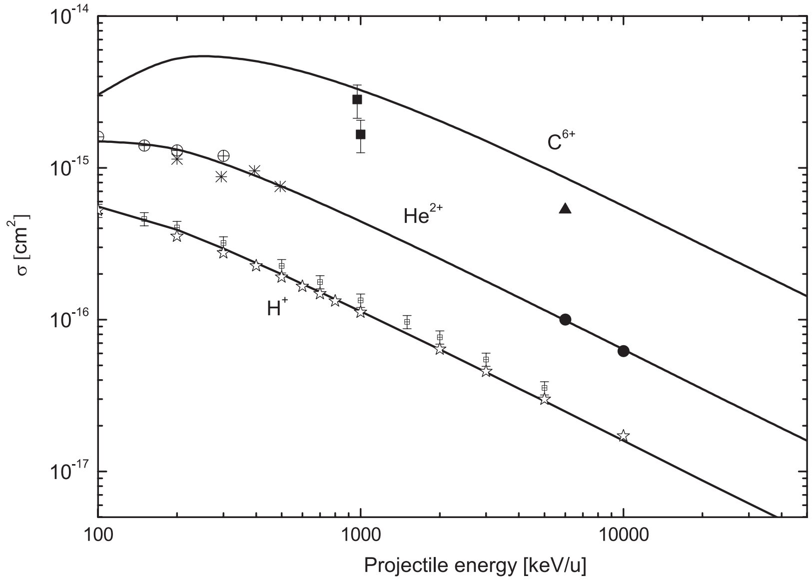

Figure 9.7 Total cross section for single ionization of water vapor by H$^+$, He^{2+}, and C^{6+} ions. Theory: solid lines, CDW-EIS. Experiments: open squares and open circles from Refs. 40 and 41; close circles from Ref. 45; close triangles from Ref. 43; open stars from Ref. 42; close squares from Ref. 44; stars from Ref. 46.

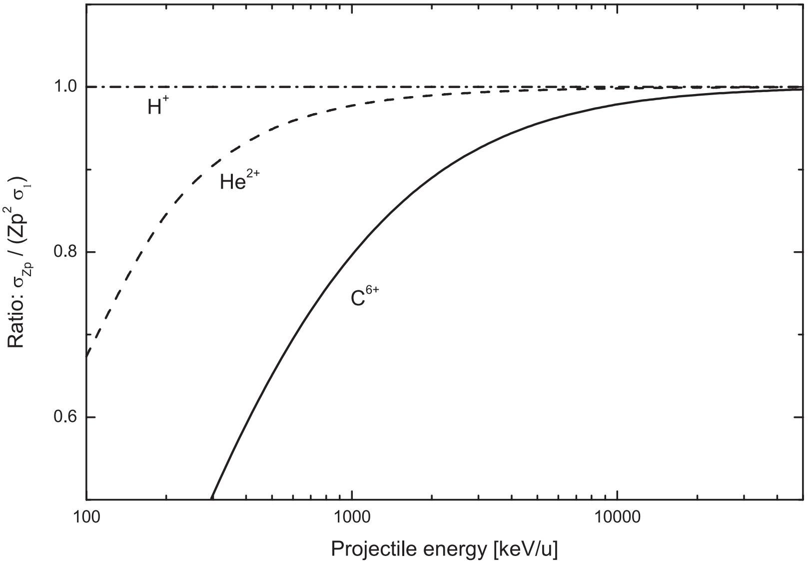

Figure 9.8 Cross section ratios. Theory: Solid line, C^{6+}; dashed line, He^{2+}; dot dashed line, H$^+$.

in Figure 9.7. It is interesting also to analyze the cross section ratio $\sigma_{\alpha\beta}(Z_P)/[Z_P^2\sigma_{\alpha\beta}(Z_P = 1)]$ (with $\sigma_{\alpha\beta}(Z_P)$ the ionization cross section for a projectile of charge Z_P) to determine deviations from the Z_P^2-scaling law of B1. The results presented in Figure 9.8 show a strong deviation from B1, which increases with Z_P. This behavior can be attributed to the binding effect, which arises at low enough impact velocities. The electron moves in the combined fields of the attractive projectile and the attractive residual target. Thus, the electron feels a noticeable increasing of the binding energy and its emission to continuum states is strongly reduced.[13]

4.2 Electronic stopping power

When Bragg's rule is employed, the DW mean electronic stopping power of atomic hydrogen and atomic oxygen are simply added, so that the stopping power for H_2O is given by:

$$S_e(H_2O) = 2S_e(H) + S_e(O), \tag{31}$$

where for H the channels considered are the ones indicated in expression 19–21 and 25–29. In the case of atomic oxygen the reaction processes taken into account are:

$$H^+ + O \longrightarrow H^+ + O^+ + e^-, \tag{32}$$

$$H^+ + O \longrightarrow H + O^+, \tag{33}$$

$$H^+ + O \longrightarrow H^* + O^+, \tag{34}$$

$$H + O \longrightarrow H + O^+ + e^-, \tag{35}$$

$$H + O \longrightarrow H^* + O, \tag{36}$$

$$H + O \longrightarrow H^+ + e^- + O^+ + e^- \tag{37}$$

indicating with asterisk projectile excitation and ionization channels. Oxygen excitation channels are not included, but their influence on the determination of $S_e(H_2O)$ can be estimated using first-Born calculations for excitation produced by electron impact.[47]

Golser and Semrad[48] proved that for a mixture of hydrogen and atomic gases, the electron stopping power deviates from Bragg's rule. This has been attributed to the fact that the corresponding equilibrium charge-state fractions for the mixture differ from the ones predicted by the additivity rule. Thus, a molecular Bragg's rule is considered so that the electronic stopping power for the neutral and charged beams is taken as:

$$S_{\mathrm{e}}^{0}(\mathrm{H_2O}) = 2S_{\mathrm{e}}^{0}(\mathrm{H}) + S_{\mathrm{e}}^{0}(\mathrm{O}), \tag{38}$$

$$S_{\mathrm{e}}^{+}(\mathrm{H_2O}) = 2S_{\mathrm{e}}^{+}(\mathrm{H}) + S_{\mathrm{e}}^{+}(\mathrm{O}). \tag{39}$$

The corresponding equilibrium charge-state fractions can be written as:

$$f_{\mathrm{H_2O}}(\mathrm{H^+}) = \frac{\sigma_{\mathrm{L}}(\mathrm{H_2O})}{\sigma_{\mathrm{C}}(\mathrm{H_2O}) + \sigma_{\mathrm{L}}(\mathrm{H_2O})} \tag{40}$$

and

$$f_{\mathrm{H_2O}}(\mathrm{H^0}) = \frac{\sigma_{\mathrm{C}}(\mathrm{H_2O})}{\sigma_{\mathrm{C}}(\mathrm{H_2O}) + \sigma_{\mathrm{L}}(\mathrm{H_2O})} \tag{41}$$

with

$$\sigma_{\mathrm{C}}(\mathrm{H_2O}) = 2\sigma_{\mathrm{C}}(\mathrm{H}) + \sigma_{\mathrm{C}}(\mathrm{O}) \tag{42}$$

and

$$\sigma_{\mathrm{L}}(\mathrm{H_2O}) = 2\sigma_{\mathrm{L}}(\mathrm{H}) + \sigma_{\mathrm{L}}(\mathrm{O}), \tag{43}$$

where $\sigma_{\mathrm{C}}(\mathrm{J})$ with $\mathrm{J} = \mathrm{H_2O}, \mathrm{H}, \mathrm{O}$ indicates electron capture cross sections from water, atomic hydrogen, and atomic oxygen, respectively. In a similar way $\sigma_{\mathrm{L}}(\mathrm{J})$ indicates the electron loss cross sections for hydrogen beams impacting on the corresponding targets. Thus, the total mean electronic stopping power can be obtained applying the expression:

$$S_{\mathrm{e}}(\mathrm{H_2O}) = f_{\mathrm{H_2O}}(\mathrm{H^+})S_{\mathrm{e}}^{+}(\mathrm{H_2O}) + f_{\mathrm{H_2O}}(\mathrm{H})S_{\mathrm{e}}^{0}(\mathrm{H_2O}). \tag{44}$$

Dissociative processes are not included in the calculations. In particular, the CNDO approximation of the molecular orbitals is applied only to describe the ionization channel:

$$\mathrm{H^+} + \mathrm{H_2O} \longrightarrow \mathrm{H^+} + (\mathrm{H_2O})^+ + e^-. \tag{45}$$

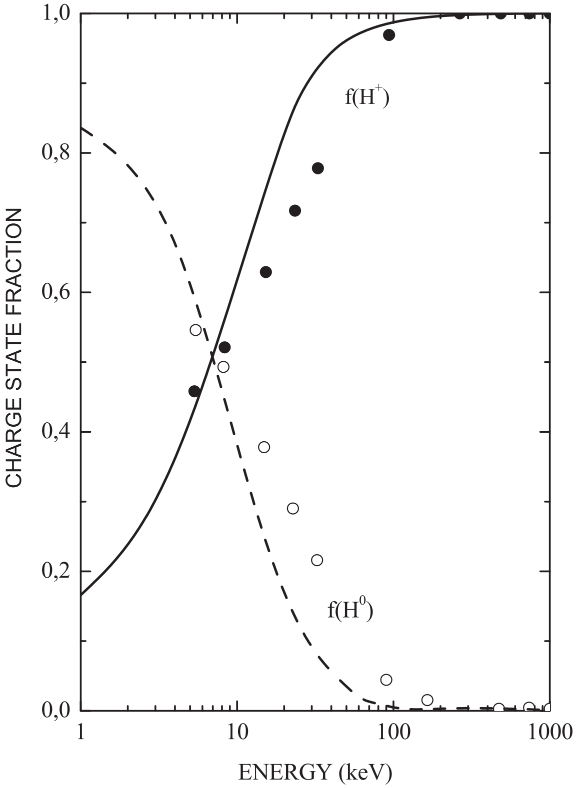

Figure 9.9 Equilibrium charge-state fractions of hydrogen beams in water vapor as a function of the impact energy. Theory: solid line, H^+ charge-state fraction; dashed line, H^0 charge-state fraction; both DW calculations. Experimental data: (•) and (○), from Ref. 39.

Expression (39) must be accordingly modified to incorporate this molecular description of the target ionization reaction.

Equilibrium charge-state fractions for impact of hydrogen beams on water vapor are displayed in Figure 9.9. DW calculations are found to be in qualitative agreement with existing experiments.[39] Total mean electronic stopping power is compared in Figure 9.10 with tabulated[49] and experimental data. At the maximum of the stopping power and at larger energies molecular DW calculations give a good description of experiments and recommended values, except at the peak region when they are compared with the tabulated values from Ref. 49. At energies lower than around 50 keV, molecular DW underestimates the measured and recommended values.

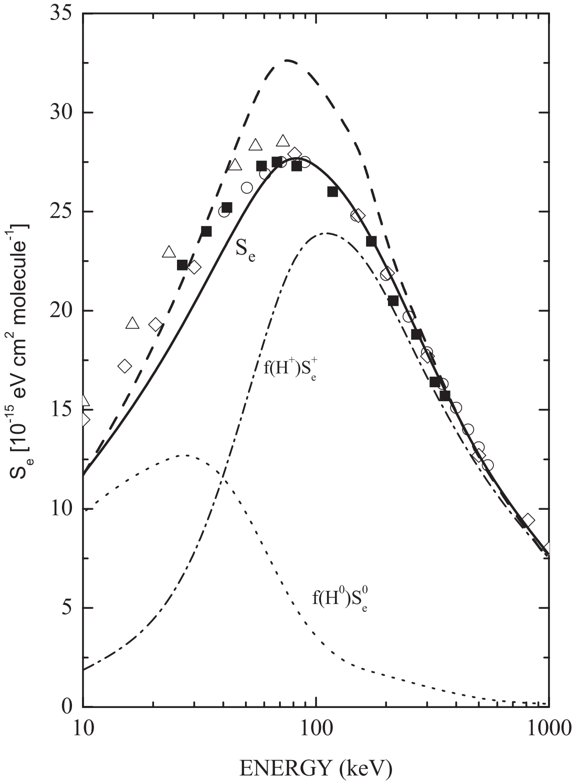

Figure 9.10 Electronic stopping power of water vapor as a function of the impact energy (molecular approximation). Theory: solid line, DW mean stopping power; dash dotted line, contribution of the charged fraction to the mean stopping power; dotted line, contribution of the neutral fraction to the mean stopping power; dashed line, atomic DW Bragg's rule. Tabulations: open diamonds, from ICRU.[49] Experiments data obtained from Ref. 19.

Contributions to the mean stopping power from the charged and neutral beams are discriminated, showing that protons dominates at large energies while neutral hydrogen plays the principal role at lower energies. Also in the figure DW calculations employing Bragg's rule are included. They largely overestimate the stopping power peak region.

5. MULTIPLE IONIZATION OF WATER MOLECULES

The independent electron model has been used to study theoretically multiple transitions. In this picture each electron evolves independently in a mean field created by the projectile and the other electrons. Then, the calculation of cross sections for multiple processes is done by employing a binomial distribution where the computation of single-particle probabilities as a function of the impact parameter is required.[50] The probability P_m to remove m electrons from one particular shell that contains N-equivalent electrons can be expressed as:

$$P_m(\rho) = C_N^m \, p(\rho)^m \left(1 - p(\rho)\right)^{N-m}, \tag{46}$$

where $m = 0, 1, 2, \ldots, N$ and $p(\rho)$ is the probability per electron of single ionization of the shell. In this expression,

$$C_N^m = \frac{N!}{m!(N-m)!} \tag{47}$$

is a binomial coefficient. The cross section corresponding to this multielectronic transition is given by:

$$\sigma_m^{(N)} = 2\pi \int_0^{+\infty} \mathrm{d}\rho \, \rho P_m(\rho) = 2\pi \, C_N^m \int_0^{+\infty} \mathrm{d}\rho \, \rho p(\rho)^m \left(1 - p(\rho)\right)^{N-m}. \tag{48}$$

This approximated expression for $\sigma_m^{(N)}$ contains information both on the dynamics of one-single electron collision and on the statistics of several equivalent electrons in the target. The collision dynamics is included by the choice of a particular $p(\rho)$, which depends on the single-electron potential used, and on the binomial statistics employed.[51] Usually, $\sigma_m^{(N)}$ is named *exclusive cross section*. If we do not explicit the final states of the remaining $N - m$ electrons, we obtain the *inclusive cross sections*, expressed as:

$$s_m^{(N)} = 2\pi \, C_N^m \int_0^{+\infty} \mathrm{d}\rho \, \rho p(\rho)^m \tag{49}$$

with $m = 0, 1, 2, \ldots, N$. The exclusion of the term $\left(1 - p(\rho)\right)^{N-m}$ is associated with the electrons that have a "passive" role in the collision. It must be noted that nowadays, due to the improvements in experimental techniques involving many particle detection in coincidence, the exclusive measured cross sections can be determined.

Exclusive cross sections can be related to the inclusive cross sections and vice versa using the binomial inverse pair relations:[52]

$$\sigma_m^{(N)} = \sum_{j=m}^{N} (-1)^{j-m} C_j^m s_j^{(N)} \tag{50}$$

and

$$s_m^{(N)} = \sum_{j=m}^{N} C_j^m \sigma_j^{(N)}. \tag{51}$$

In the $m = 1$ case, $C_j^m = j$, this equation reduces to:

$$s_1^{(N)} = \sum_{j=1}^{N} j\sigma_j^{(N)} = 2\pi N \int_0^{+\infty} \mathrm{d}\rho\, \rho p(\rho). \tag{52}$$

It provides an example of an inclusive cross section that can be directly measured.[50,53] The sum $\sum_{j=1}^{N} j\sigma_j^{(N)}$ is a quantity directly obtained from experiments where the total current produced by all different ionization events is measured, without the knowledge of any particular $\sigma_j^{(N)}$. This inclusive cross section is also called net ionization cross section or simply total ionization cross section.[54]

We focus here the interest in the calculation of exclusive cross sections for multiple ionization of the water molecule, which as it is well known presents five i-molecular orbitals with an occupancy number $N_i = 2$ for each one of them. After some algebra, exclusive probabilities P_q, for q-fold ionization are given by the expression:

$$P_q(\rho) = \sum_{q_1,\ldots,q_5=0;\, q_1+\cdots+q_5=q}^{N_1,\ldots,N_5} \prod_{i=1}^{5} C_{N_i}^{q_i} \left[p_i(\rho)\right]^{q_i} \left[1 - p_i(\rho)\right]^{N_i - q_i}, \tag{53}$$

where $p_i(\rho)$ is the probability to ionize one electron of the orbital $i$and q_i its corresponding ionization degree. Then, the q-fold ionization cross section σ_q is given by:

$$\sigma_q = 2\pi \int_0^{+\infty} \mathrm{d}\rho\, \rho P_q(\rho). \tag{54}$$

Following the previous definition of the total or net ionization cross section, we obtain:

$$\sigma_{\mathrm{T}} = \sum_{i=1}^{5} 2\pi N_i \int_0^{+\infty} \mathrm{d}\rho\, \rho p_i(\rho) = 2\pi \int_0^{+\infty} \mathrm{d}\rho\, \rho \left(\sum_{q=1}^{10} q P_q(\rho) \right) \tag{55}$$

As in the case of single ionization, the different probabilities that appear in the previous equations are calculated employing the CDW-EIS approximation. We must mention that CDW-EIS has been used with success in the calculation of double ionization of He by heavy ion impact[55] and direct multiple ionization of atoms and molecules by proton and multiply charged ion impact.[54, 56–58] To describe the different molecular orbitals of

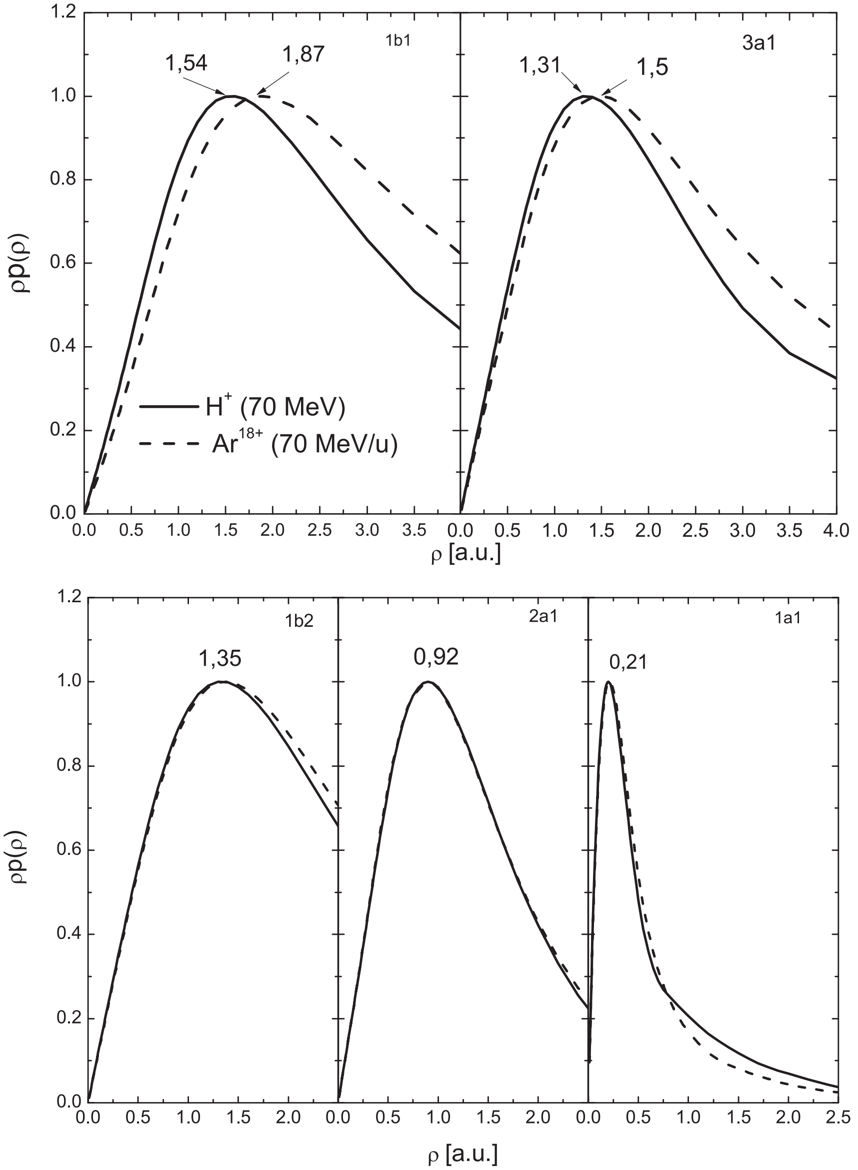

Figure 9.11 Charge effects in the single particle probabilities corresponding to each molecular orbital.

liquid water the CNDO approximation previously employed for water vapor has been used[59] together with RHF initial atomic bound states wavefunctions. In this case, experimental orbital binding energies for liquid water were considered.[60] As the biological tissue is mainly composed by liquid water we focuss our following analysis on this phase of the target. Probabilities $p_i(\rho)$ are obtained using the method given in Galassi et al.[61]

Single ionization reduced probabilities $\rho p_i(\rho)$ are presented in Figure 9.11 for the case of 70 MeV/u-proton and Ar^{18+} impact on liquid water. Ionization from different orbitals are discriminated, being the reduced probabilities normalized to unity at their maxima. For the $1b1$ and $3a1$ external orbitals, with binding energies of -0.32 and -0.44 a.u., respectively, some shift toward larger impact parameter is shown to appear for Ar^{18+} with respect to the H^+ case. However, in this perturbation regime (the Sommerfeld parameter being $\nu \simeq 0.34$ for Ar^{18+} and $\nu = 0.019$ for H^+) this shift almost disappears for the inner shells $1b2, 2a1$, and $1a1$, with binding energies of -0.62, -1.19, and -19.84 a.u., respectively. Thus, the impact parameter at which the reduced probability presents its maximum is not very sensitive to the projectile charge. Moreover, we have tested that

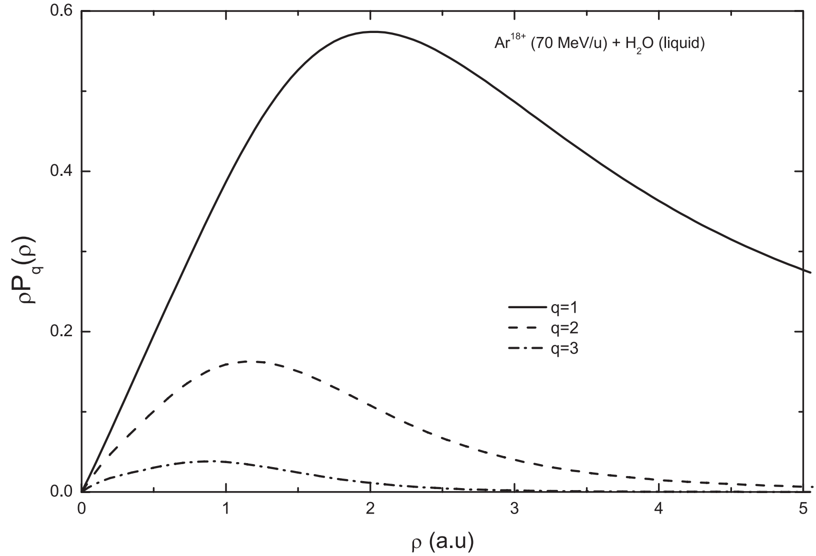

Figure 9.12 Reduced multiple ionization probabilities as a function of the impact parameter for 70 MeV/u–Ar^{18+} ions impact on liquid water.

the impact parameter position corresponding to the maxima above discussed has a weak dependence with the projectile velocity.[56]

In Figure 9.12 we observe how the ionization degree affects the reduced probabilities $\rho P_q(\rho)$. The case of 70 MeV/u-Ar^{18+} is analyzed showing that, as expected, as the q-degree increases $\rho P_q(\rho)$ decreases. Moreover, smaller impact parameters (closer collisions) give the main contribution to the reaction as the ionization degree increases. Thus, postcollisional interorbital Auger and/or intraorbital Coster–Kronig ionization processes may dominate direct ionization (we understand by this the ionization produced by the interaction of the ejected electron with the projectile during the collision time) at high enough energies as q increases. As an example and just to show this effect, in Figure 9.13 we present q-ionization total cross sections for impact of protons on a Ne gas (which presents an isoelectronic character with water). The cases of $q=1$, 2, and 3 are shown[56] and compared with existing experimental data.[62, 63] The direct interaction of the projectile produces the ionization of the target, generating thus holes in the orbitals that are filled through Auger

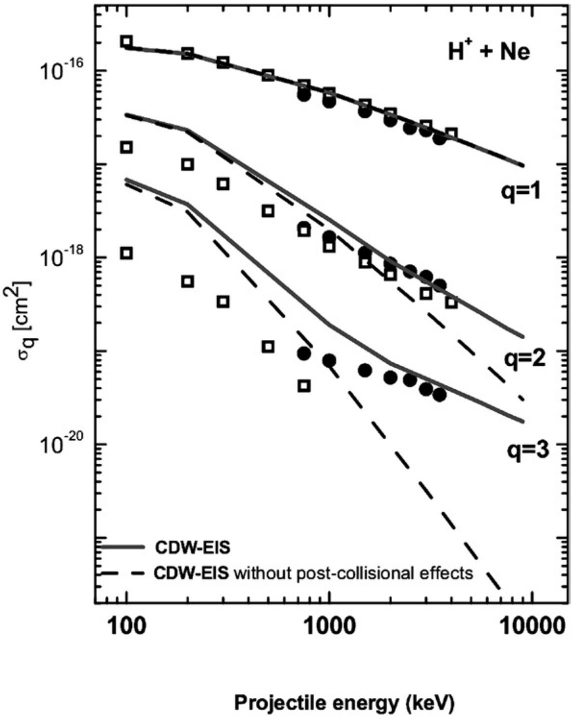

Figure 9.13 Single and multiple ionization cross sections of Ne by proton impact as a function of the projectile energy.

and Coster–Kronig transitions. In order to estimate the influence of these mechanisms, experimental photoionization probabilities were used.[64] To do that, it is assumed that the postcollisional ionization reaction is independent of the nature of the primary vacancy production.[65] This effect was also shown to appear for impact of protons on O_2, N_2, and CO molecular targets (see Ref. 57). Moreover, it has been proven for double ionization that when these molecules collide with multicharged ions, postcollisional mechanisms dominate the direct one for values $\nu = \frac{Z_P}{v} \lesssim 0.3$ of the Sommerfeld parameter with a small shift to larger parameters ν as q increases.[58] So, as the projectile charge increases, the effect appears at larger impact velocities. This behavior can be understood from the fact that as Z_P increases direct single ionization probabilities p_i present a Z_P^2 dependence at high enough energies. As a consequence, the production of q_i electrons by direct ionization increases whereas the postcollisional emission gives the same contribution for any value of the projectile charge, independently of the collision velocity. Thus, for Ar^{18+} the dominance of postcollisional effects should happen for collision energies larger than approximately 90 MeV/u.

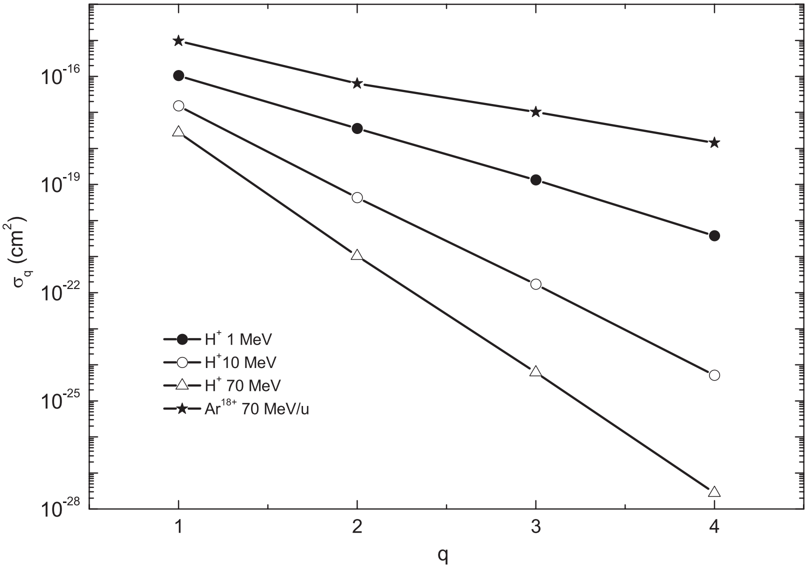

Figure 9.14 Multiple ionization cross sections as a function of the ionization degree for proton and argon ions at different impact energies.

In Figure 9.14 exclusive σ_q-direct ionization cross sections are presented for q-degrees going from 1 to 4. The evolution of the cross section as the collision energy of proton beams increases is shown. The slope of the curves that can be drawn interpolating σ_q for the different q-values is more pronounced for larger impact velocities, proving that multiple ionization plays a weaker role as the velocity increases. For 70 MeV/u-Ar^{18+} ions, exclusive cross sections take the values $\sigma_1 = 9.597 \times 10^{-16}$ cm^2, $\sigma_2 = 0.635 \times 10^{-16}$ cm^2, $\sigma_3 = 0.103 \times 10^{-16}$ cm^2, and $\sigma_4 = 0.014 \times 10^{-16}$ cm^2. However, multiple ionization contributes at least by 14.56% to the total ionization cross section for this system. We will show in the following that multiple ionization may play a determinant role in the formation of free radicals with oxygen excess in water radiolysis. It must be also noted that for the case considered, K-shell ionization followed by Auger emission has been estimated to contribute with a value approximately equal to 0.06×10^{-16} cm^2 (Ref. 66).

5.1 Linear energy transfer

While mean stopping power refers to the energy lost by the particle beam traversing the surrounding media, linear energy transfer (LET) refers to the energy absorbed by the media per unit of distance travelled by the ionizing radiation. LET or restricted stopping power is defined as the ratio:

$$L_{\Delta\varepsilon} = \frac{\mathrm{d}E_{\Delta\varepsilon}}{\mathrm{d}l}, \tag{56}$$

where $\mathrm{d}E_{\Delta\varepsilon}$ is the local mean energy absorbed by the media by means of collisions involving transfer energies lower than a specific value $\Delta\varepsilon$ (cut value) and $\mathrm{d}l$ is the distance traversed by the projectile. We understand by "local" the consideration of absorbed energies limited up by the maximum value $\Delta\varepsilon$. Thus, $L_{\Delta\varepsilon}$ is related to the part of the mean stopping power involving transfer energies smaller than the cut value $\Delta\varepsilon$. It can also be related to the maximum distance reached (range) by electrons from the projectile track.

Different cut levels are usually selected to separate delta rays as they are appropriate for different reactions. L_∞ is defined as the energy absorbed by the media per unit of distance traversed by the projectile when all possible energy transfers are considered. This quantity coincides numerically with the stopping power.

5.2 Free radicals formation in water radiolysis

The ionization of water molecules during the irradiation of biological matter with fast heavy ions produces the formation of free radicals. This process is known as water radiolysis. Three different consecutive stages can be distinguished in water radiolysis:

1. the physical stage where the interaction of the projectile with the water molecules and the subsequent electronic cascade is produced during the first femtoseconds,
2. the physico-chemical stage which deals with the fast dissociation processes that results from molecular excitation and ionization and that ends at the picosecond time scale,
3. the chemical stage that accounts for the evolution of the radicals and molecular species during their diffusion through liquid, which ends at the microsecond scale.

Usually Monte Carlo simulations have been developed to analyze the time evolution of water radiolysis. In the physical stage the cross sections for all interaction processes of the projectile and of the electrons with the medium are calculated and used as input in the Monte Carlo codes.[67–69]

Water radiolysis is characterized by the radiolytical yields G. This is the number of species created per unit of deposited energy. A large amount of experimental work has been performed to measure the yields for solvated electrons, OH, H_2O_2, H, and H_2, which are the main radicals produced by low-LET radiations. Monte Carlo simulations gave an adequate quantitative description of the experimental results, explaining also the different mechanisms involved in the process.[70] The situation is not the same for high LET, where the formation of HO_2 radicals has been experimentally observed.[71, 72] Moreover, recent experiments based on direct optical measurements of HO_2/O_2^- produced in deaerated water for 70 MeV/u Ar (LET $=280\,\text{keV}/\mu\text{m}$) and 77 MeV/u S (LET $=250\,\text{keV}/\mu\text{m}$) ions were measured.[73] However, they are lower than the ones expected by extrapolation of previous experiments for similar LET.[72] It was suggested[74,75] that multiple ionization of water could be responsible for this effect. The main idea is that multiple ionization generates the production of O atoms, which reacts with OH radicals to form HO_2 ones. Moreover, the reaction of HO_2 with hydroxyl radical will produce molecular oxygen. The complete process has been recently investigated by Gervais and coworkers[68,69] considering water irradiation by carbon ions. To consider multiple ionization

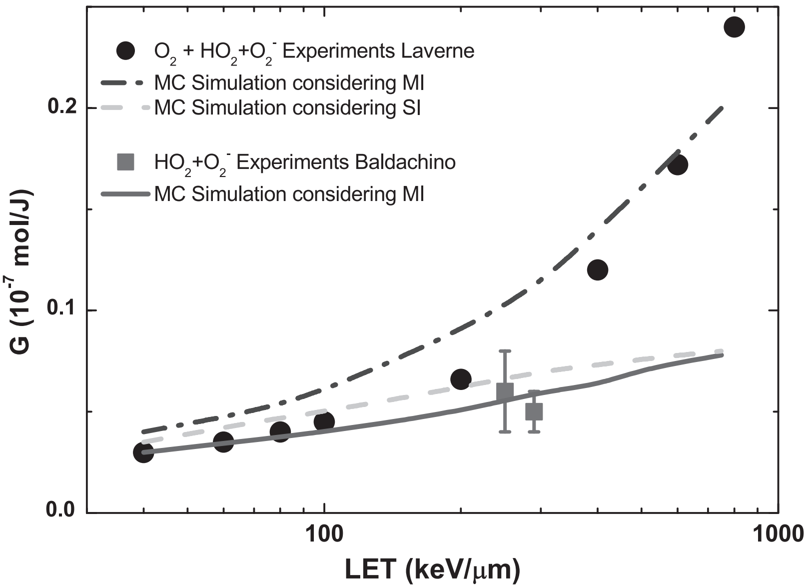

Figure 9.15 Monte Carlo simulation of HO_2 and $HO_2 + O_2$ yields at 1 μs as a function of LET. Lines are square fit to simulation results. For C^{6+} ions: dot dashed line, MC simulation considering multiple ionization (MI) channels; dashed line, MC simulation considering only single ionization (SI); closed circles, experiments from.[72] For Ar^{18+} ions: solid line, MC simulation considering MI; squares, experiments from Ref. 73.

the independent electron model described in the previous section was used. Their results are summarized in Figure 9.15. The inclusion of multiple ionization of liquid water in the physical stage of water radiolysis plays a main role to explain experiments where yields of $HO_2 + O_2^-$ and $O_2 + HO_2 + O_2^-$ formation were measured. This can be concluded by comparison with the case where only single ionization of water is included in the Monte Carlo simulation. Resulting $O_2 + HO_2 + O_2^-$ yields considering single and multiple ionization are included in the figure, showing the increasing influence of multiple ionization as the linear energy transfer is larger. If only single ionization is taken into account, negligible contributions to the $HO_2 + O_2^-$ formation are obtained in comparison to the yields obtained with the inclusion of multiple ionization.

6. CONCLUDING REMARKS

A detailed description of the distorted wave model has been revisited to study the different electronic channels resulting from charged or neutral heavy particles on atomic and molecular targets. This model includes the Continuum Distorted Wave-Eikonal Initial State approximation to describe both single electron ionization and single electron capture reactions for the case of impact of charged particle beams. This approximation takes account properly of the large range of Coulomb interactions present in the different electronic processes. For this type of beams the Symmetric Eikonal approximation is proposed to determine single excitation cross sections. However, in the cases where they were evaluated for molecular targets, estimations have been given from electron impact predictions. The case of impact of neutral charged beams is analyzed using the first-order of the Born approximation. Multiple electron processes that involve electronic reactions of both the projectile and target aggregates are also studied employing this last theoretical description. So, the combination of all these different approximations constitutes the distorted wave model.

The adequacy of this model is tested by comparison of its theoretical predictions with existing experimental differential and total cross sections not only for hydrogen atomic targets but also for water vapor molecules. The completeness of the model allows to extend this analysis to the obtention of equilibrium charge fractions and the consequent calculation of mean electronic stopping power.

Multiple electron ionization of liquid water is investigated employing the Continuum Distorted Wave-Eikonal Initial State approximation within an independent particle model. The influence of postcollisional Auger-type and Coster–Kronig-type emissions on total cross sections is also estimated. The main role played by multiple ionization of water during the physical stage of radiolysis (until a time of the order of one picosecond) on the formation of free radicals with oxygen excess (after a few microseconds) is also revisited.

REFERENCES

1. Bethe H. Zur theorie des durchgangs schneller korpuskularstrahlen durch materie. *Ann. Phys. (Leipzig)* **1930**, *5*, 325.
2. Bloch F. Zur bremsung rasch bewegter teilchen beim durchgang durch materie. *Ann. Phys.* **1933**, *16*, 285.
3. Ziegler J. F. Stopping of energetic light ions in elemental matter. *J. Appl. Phys.* **1999**, *85*, 1249.

4. Ashley J. C.; Ritchie R. H.; Brandt W. Z_1^3-Dependent stopping power and range contributions. *Phys. Rev. A* **1973**, *8*, 2402.
5. Basbas G.; Brandt W.; Laubert R. Universal cross sections for K-shell ionization by heavy charged particles. II. Intermediate particle velocities. *Phys. Rev. A* **1978**, *17*, 1655.
6. Brandt W.; Basbas G. Antiparticle excitation of atomic inner shells. *Phys. Rev. A* **1983**, *27*, 578.
7. Barkas W. H.; Dyer N. J.; Heckmann H. H. Resolution of the Σ^--mass anomaly. *Phys. Rev. Lett.* **1963**, *11*, 26.
8. Cheshire I. M. Continuum distorted wave approximation; resonant charge transfer by fast protons in atomic hydrogen. *Proc. Phys. Soc.* **1964**, *84*, 89.
9. Belkić, Dž. A quantum theory of ionisation in fast collisions between ions and atomic systems. *J. Phys. B* **1978**, *11*, 3529.
10. Crothers D. S. F.; McCann J. F. Ionisation of atoms by ion impact. *J. Phys. B* **1983**, *16*, 3229.
11. Fainstein P. D.; Ponce V. H.; Rivarola R. D. A theoretical model for ionisation in ion–atom collisions. Application for the impact of multicharged projectiles on helium. *J. Phys. B* **1988**, *21*, 287.
12. Martínez A. E.; Deco G. R.; Rivarola R. D.; Fainstein P. D. K-Shell vacancy production in asymmetric collisions. *Nucl. Instrum. Methods B* **1988**, *34*, 32.
13. Fainstein P. D.; Ponce V. H.; Rivarola R. D. Z_P^3 effects in the ionization of helium by ion impact. *Phys. Rev. A* **1987**, *36*, 3639.
14. Andersen L. H.; Hvelplund P.; Knudsen H.; Møller S. P.; Elsener K.; Rensfelt K. G.; Uggerhøj E. Single and double ionization of helium by fast antiproton and proton impact. *Phys. Rev. Lett.* **1986**, *57*, 2147.
15. Schiwietz G. Coupled-channel calculation of stopping powers for intermediate-energy light ions penetrating atomic H and He targets. *Phys. Rev. A* **1990**, *42*, 296.
16. Grande P. L.; Schiwietz G. Nonperturbative stopping-power calculation for bare and neutral hydrogen incident on He. *Phys. Rev. A* **1993**, *47*, 1119.
17. Fainstein P. D.; Ponce V. H.; Martínez A. E. Distorted-wave calculation of stopping powers for light ions traversing H targets. *Phys. Rev. A* **1993**, *47*, 3055.
18. Olivera G. H.; Martínez A. E.; Rivarola R. D.; Fainstein P. D. Electron-capture contribution to the stopping power of low-energy hydrogen beams passing through helium. *Phys. Rev. A* **1994**, *49*, 603.
19. Olivera G. H.; Martínez A. E.; Rivarola R. D.; Fainstein P. D. Theoretical calculation of electronic stopping power of water vapor by proton impact. *Rad. Res.* **1995**, *144*, 241.
20. Deco G. R.; Fainstein P. D.; Rivarola R. D. Symmetric eikonal approximation for electron excitation in ion–atom collisions. *J. Phys. B* **1986**, *19*, 213.
21. Rivarola R. D.; Fainstein P. D. Electron emission in collisions of highly charged ions with atoms and diatomic molecules. *Nucl. Instrum. Methods B* **2005**, *205*, 448.
22. (a)Belkić, Dž. Review of theories on double electron capture in fast ion-atom collisions. *J. Math. Chem.* **2010**, *47*, 1420.(b)Belkić, Dž; Gayet, R.; Salin, A. Electron capture in high-energy ion-atom collisions. *Phys. Rep.* **1979**, *56*, 279.(c)Belkić, Dž. Quantum-mechanical methods for loss excitation and loss-ionization in fast ion-atom collisions. *Adv. Quantum Chem.* **2009**, *56*, 251.
23. Martínez A. E.; Bullrich J. A.; Maidagan J. M.; Rivarola R. D. The continuum distorted wave-eikonal initial state model for single electron capture in ion–atom collisions. *J. Phys. B* **1992**, *25*, 1883.
24. Stolterfoht N.; DuBois R. D.; Rivarola R. D. *Electron Emission in Heavy Ion–Atom Collisions*; Springer-Verlag: Berlin, 1997.
25. Ramírez C. A.; Rivarola R. D. Electron excitation of hydrogenic targets in collisions with ions or atoms. *J. Phys. B* **1993**, *26*, 3835.

26. Bates D. R.; Griffing G. Inelastic collisions between heavy particles. I: Excitation and ionization of hydrogen atoms in fast encounters with protons and with other hydrogen atoms. *Proc. Phys. Soc. London Sect. A* **1953**, *66*, 961.
27. Montenegro E. C.; Meyerhof W. E.; McGuire J. H. Role of two-center electron–electron interaction in projectile electron excitation and loss. *Adv. Atom. Mol. Opt. Phys.* **1994**, *34*, 249.
28. Manson S.T.; Dubois R. D. Multielectron transitions resulting from interactions between target and projectile electrons in ionizing collisions. *Phys. Rev. A* **1992**, *46*, R6773.
29. Dalgarno A.; Griffing G.W. Energy loss of protons passing through hydrogen. *Proc. Phys. Soc. London Sect. A* **1955**, *232*, 423.
30. Hill J.; Geddes J.; Gilbody H. B. Electron capture, loss and collisional destruction of 5–26 keV metastable and ground-state hydrogen atoms in collisions with atomic and molecular hydrogen. *J. Phys. B* **1979**, *12*, 3341.
31. Allison S. K. Experimental results on charge-changing collisions of hydrogen and helium atoms and ions at kinetic energies above 0.2 keV. *Rev. Mod. Phys.* **1958**, *30*, 1137.
32. Grande P.; Schiwietz G. Impact-parameter dependence of electronic energy loss and straggling of incident bare ions on H and He atoms by using the coupled-channel method. *Phys. Rev. A* **1991**, *44*, 2984.
33. Andersen H.; Ziegler J. F. *The Stopping and Ranges of Ions in Matter*; Pergamon
34. Siegbahn K.; Nordling C.; Johansson J.; Hedman J.; Hedén P. F.; Hamrin K.; Gelius U.; Bergmark T.; Werme L. O.; Manne R.; Baer Y. *ESCA Applied to Free Molecules*; North Holland
35. Senger B.; Rechenmann R.V. Angular and energy distributions of δ-rays ejected from low-Z molecular targets by incident protons and α particles. *Nucl. Instrum. Methods B* **1984**, *2*, 204.
36. Clementi E.; Roetti C. Roothaan–Hartree–Fock atomic wavefunctions: basis functions and their coefficients for ground and certain excited states of neutral and ionized atoms, $Z \leqslant 54$. *At. Data Nucl. Data Tables* **1974**, *14*, 177.
37. Bernal M. A.; Liendo J. A. Inelastic-collision cross sections for the interactions of totally stripped H, He and C ions with liquid water. *Nucl. Instrum. Methods B* **2007**, *262*, 1.
38. Bolorizadeh M. A.; Rudd M. E. Angular and energy dependence of cross sections for ejection of electrons from water vapor. II. 15150-keV proton impact. *Phys. Rev. A* **1986**, *33*, 888.
39. Barnett C. F.; Ray J. A.; Ricci E.; Wilker M. I.; McDaniel E. W.; Thomas E. W. *Atomic Data for Controlled Fusion*; Oak Ridge National Laboratory
40. Rudd M. E.; Goffe T.V.; DuBois R. D.; Toburen L. H. Cross sections for ionization of water vapor by 74000-keV protons. *Phys. Rev. A* **1985**, *31*, 492.
41. Rudd M. E.; Kim Y.-K.; Madison, D. H.; Gallagher, J.W. Electron production in proton collisions: total cross sections. *Rev. Mod. Phys.* **1985**, *57*, 965.
42. Wilson W. E.; Miller, J. H.; Toburen L. H.; Manson, S. T. Differential cross sections for ionization of methane, ammonia, and water vapor by high velocity ions. *J. Chem. Phys.* **1984**, *80*, 5631.
43. Dal Capello C.; Champion C.; Boudrioua O.; Lekadir H.; Sato, Y.; Ohsawa D. Theoretical and experimental investigations of electron emission in $C^{6+} + H_2O$ collisions. *Nucl. Instrum. Methods B* **2009**, *267*, 781.
44. Cocke, C. L. Production of highly charged low-velocity recoil ions by heavy-ion bombardment of rare-gas targets. *Phys. Rev. A* **1979**, *20*, 749.
45. Ohsawa, D.; Kawauchi H.; Hirebayashi M.; Okada, Y.; Homma T.; Higashi, A.; Amano S.; Hashimoto Y.; Soga, F.; Sato Y. An apparatus for measuring the energy and angular distribution of secondary electrons emitted from water vapor by fast heavy-ion impact. *Nucl. Instrum. Methods B* **2005**, *227*, 431.

46. Toburen, L. H.; Wilson, W. E.; Popovich, R. J. Secondary electron emission from ionization of water vapor by 0.3- to 2.0-MeV He^+ and He^{2+} ions. *Radiat. Res.* **1980**, *82*, 27.
47. Kazaks, P. A.; Canas, P. S.; Green, A. E. S. Electron-impact excitation and ionization of atomic oxygen. *Phys. Rev. A* **1972**, *6*, 2169.
48. Golser, R.; Semrad, D. Failure of Braggs rule for a mixture of nonreacting gases. *Phys. Rev. A* **1992**, *45*, R4222.
49. Stopping powers of protons and alpha particles, Report 49, International Commission on Units and Measurements, Bethesda, MD, 1992.
50. Lüdde, H. J.; Dreizler, R. Comment on inclusive cross sections. *J. Phys. B* **1985**, *18*, 107.
51. Sant'Anna, M. M.; Montenegro, E. C.; McGuire, J. H. Inversion relations for exclusive and inclusive cross sections within the independent electron approximation. *Phys. Rev. A* **1998**, *58*, 2148.
52. Roberts F. S. Applied Combinatorics; Prentice-Hall: Englewood Cliffs, 1984.
53. Ford, A. L.; Reading, J. F.. In *Atomic, Molecular and Optical Physics Handbook*, ; Drake, G. W. F., Ed.; *Atomic, Molecular and Optical Physics Handbook*; AIP: New York, 1996., pp 571–577.
54. Kirchner T.; Gulyás L.; Moshammer R.; Schulz, M.; Ullrich, J. Doubly differential electron-emission spectra in single and multiple ionization of noble-gas atoms by fast highly-charged-ion impact. *Phys. Rev. A* **2002**, *65*, 042727.
55. Fainstein P. D.; Gulyás, L.; Dubois, A. Single and double ionization of helium by highly charged ions in the independent electron model. *J. Phys. B* **1998**, *31*, L171.
56. Galassi, M. E.; Fainstein, P. D.; Rivarola, R. D. Multiple electron emission from noble gases colliding with proton beams, including postcollisional effects. *Phys. Rev. A* **2007**, *75*, 052708.
57. Tachino C. A.; Galassi M. E.; Rivarola R. D. Postcollisional effects in multiple ionization of diatomic molecules by ion impact. *Phys. Rev. A* **2008**, 77, 032714.
58. Tachino, C. A.; Galassi, M. E.; Rivarola, R. D. Role of Auger-type emission from diatomic molecular targets interacting with fast multicharged ions. *Phys. Rev. A* **2009**, *80*, 014701.
59. Pople, J. A.; Segal, G. A. Approximate selfconsistent molecular orbital theory. II. Calculations with complete neglect of differential overlap. *J. Chem. Phys.* **1965**, *43*, S136.
60. Dingfelder, M.; Hantke, D.; Inokuti, M.; Paretzke, H. G. Electron inelastic-scattering cross sections in liquid water. *Radiat. Phys. Chem.* **1998**, *53*, 1.
61. Galassi, M. E.; Abufager, P. N.; Martínez, A. E.; Rivarola, R. D.; Fainstein, P. D. The continuum distorted wave eikonal initial state model for transfer ionization in $H^+, He^{2+} + He$ collisions. *J. Phys. B* **2002**, *35*, 1727.
62. DuBois, R.; Toburen, L. H.; Rudd, M. E. Multiple ionization of rare gases by H^+ and He^+ impact. *Phys. Rev. A* **1984**, *29*, 70.
63. Cavalcanti, E. G.; Sigaud, G. M.; Montenegro, E. C.; Sant'Anna, M. M.; Schmidt-Böcking, H. Post-collisional effects in multiple ionization of neon by protons. *J. Phys. B* **2002**, *35*, 3937.
64. Carlson, T. A.; Hunt, W. E.; Krause, M. O. Relative abundances of ions formed as the result of inner-shell vacancies in atoms. *Phys. Rev.* **1966**, *151*, 41.
65. Stolterfoht, N. High resolution Auger spectroscopy in energetic ion atom collisions. *Phys. Rep.* **1987**, *146*, 315.
66. Gaigeot, M. P.; Vuilleumier, R.; Stia, C.; Galassi, M. E.; Rivarola, R.; Gervais, B.; Politis, M. F. A multi-scale ab initio theoretical study of the production of free radicals in swift ion tracks in liquid water. *J. Phys. B* **2007**, *40*, 1.
67. Champion, C.; L'Hoir, A.; Politis, M. F.; Fainstein, P. D.; Rivarola, R. D.; Chetioui, A. A Monte Carlo code for the simulation of heavy-ion tracks in water. *Radiat. Res.* **2005**, *163*, 222.

68. Gervais, B.; Beuve, M.; Olivera, G. H.; Galassi, M. E.; Rivarola, R. D. Production of HO_2 and O_2 by multiple ionization in water radiolysis by swift carbon ions. *Chem. Phys. Lett.* **2005**, *410*, 330.
69. Gervais, B.; Beuve, M.; Olivera, G. H.; Galassi, M. E. Numerical simulation of multiple ionization and high LET effects in liquid water radiolysis. *Radiat. Phys. Chem.* **2006**, *75*, 493.
70. Frongillo, Y.; Goulet, T.; Fraser, M. J.; Cobut, V.; Patau, J. P.; Jay-Gérin, J.-P. Monte Carlo simulation of fast electron and proton tracks in liquid water – ii. Nonhomogeneous chemistry. *Radiat. Phys. Chem.* **1998**, *51*, 245.
71. Burns, W. G.; Sims, H. E. Effect of radiation type in water radiolysis. *J. Chem. Soc. Faraday Trans.* **1981**, 77, 2803.
72. LaVerne, J. A.; Schuler, R. H. Track effects in the radiolysis of water: HO_2 production by 200–800 MeV carbon ions. *J. Phys. Chem.* **1992**, *96*, 7376.
73. Baldacchino, G.; Bouffard, S.; Balanzat, E.; Gardès-Albert, M.; Abedinzadeh, Z.; Jore, D.; Deycardand, S.; Hickel, B. Direct time-resolved measurement of radical species formed in water by heavy ions irradiation. *Nucl. Instrum. Methods B* **1998**, *146*, 528.
74. Ferradini, C.; Jay-Gérin, J.-P. Does multiple ionisation intervene for the production of HO_2 radicals in high-let liquid water radiolysis. *Radiat. Phys. Chem.* **1998**, *51*, 263.
75. Meesungnoen, J.; Filali-Mouhim, A.; Snitwongse Na Ayudhya, N.; Mankhetkorn, S.; Jay-Gérin, J.-P. Multiple ionisation effects on the yields of HO_2/O_2^- and H_2O_2 produced in the radiolysis of liquid water with high-let $^{12}C^{6+}$ ions: a Monte-Carlo simulation study. *Chem. Phys. Lett.* **2003**, *377*, 419.

CHAPTER TEN

The First Born Approximation for Ionization and Charge Transfer in Energetic Collisions of Multiply Charged Ions with Water

Christophe Champion[a], **Jocelyn Hanssen**[b] **and Roberto D. Rivarola**[c]
[a]Université Bordeaux 1, CNRS/IN2P3, Centre d'Etudes Nucléaires de Bordeaux–Gradignan, CENBG, Gradignan, France
[b]Laboratoire de Physique Moléculaire et des Collisions, UMR CNRS 7565, Université de Lorraine, Metz, France
[c]Instituto de Física Rosario, CONICET and Universidad Nacional de Rosario, Rosario, Argentina

Contents

Advances in Quantum Chemistry, Volume 65
ISSN 0065-3276, http://dx.doi.org/10.1016/B978-0-12-396455-7.00010-8

Abstract

With the more and more regular use of ionizing radiations in medicine and more particularly in hadrontherapy, it is today necessary to describe—with the highest degree of accuracy—the biological consequences of irradiations. To model the track-structure of charged particles in biological matter and then to quantify the full spectra of radio-induced cellular damages, Monte Carlo simulations are the preferential methods. The latter consist in modelling the history of the ionizing particles by means of a large set of input data, namely, the differential and total interaction cross sections in order to finely describe the complete kinematics of the ion-induced collisions. In these conditions, we clearly understand the necessity for the radiobiologists and the radiotherapists to access to accurate cross sections—in particular for collisions with water target—the latter being commonly used as surrogate of the cellular medium.

We here report a review of the existing 1st Born predictions for describing the ionization and the charge transfer processes in the high-impact energy-regime particularly investigated in hadrontherapy.

1. INTRODUCTION

Interactions of light ions ($Z \leq 10$) with water are of great interest in radiotherapy where protons (and carbon ions in rare cases) are today commonly used in cancer treatments.[1] In fact, compared to photons, ion beams have much more favourable dose-depth distributions, the concentration of the energy deposits at the end of their range giving access to a better ballistic precision. However, the different treatments must be also compared in terms of preservation of the healthy tissues and organs at risk in the tumor vicinity. Indeed, to improve the dose-tumor control, it is essential to conform the delivered dose to the tumor: in this way, hadrontherapy—which uses hadrons i.e., collimated beams of compound particles made of quarks (like neutrons, protons, pions, and heavier ions)—was suggested to treat radio-resistant tumours.[2] Thus, protons, neutrons, and carbon ions have been independently investigated for their dose-depth distribution particularity, namely, the significant increase of the dose profile at the end of the particle range: the so-called Bragg peak.

Nowadays, neutron therapies have been progressively stopped in the most countries, essentially due to their poor depth-dose distribution what implies high effective dose in the tumor as well as in the surrounding healthy tissues.[3] On the other hand, protons—which have been first used in treatments in 1954 at Berkeley[4]—are today clinically used in a large number of centres (with more than 40000 patients irradiated by January 2005) as reported by Amaldi and Kraft[1] who predict that protontherapy will continue to spread with in particular an increasing number of treated patients reaching the value of about 1000–2000 for every 10 million inhabitants. Carbon ion beams have been till now less used in tumor treatments and we only report in 2005 two centres, namely, the GSI Laboratory at Darmstadt (with more than 250 patients treated at the end of 2004) and the Japanese centre HIMAC (for Heavy Ion Medical Accelerator Centre) with more than 2000 treated patients. In fact, despite the disadvantage to have dose deposition after the Bragg peak due to the projectile fragmentation, carbon ions present numerous advantages compared to protons in radiotherapy like, for example, minor lateral and longitudinal straggling of about three times smaller than for protons and a relative biological efficiency (RBE) which increases at the end of the particle range. Thus, as it has been the case for the evolution of the synchrotron radiation sources, hadron therapy is today part of the medical business landscape and numerous centres are actually under construction (or in a planning stage) like for example in Europe (HIT at Heidelberg in Germany, CNAO at Pavia in Italy and ETOILE at Lyon in France).

Protons and carbon ions are advantageous in Intensity Modulated Hadron Therapy (IMHT) essentially for three physical properties: (i) the existence of a maximum energy deposit in a well localized near-Bragg peak region, (ii) a low diffusion during their penetration in matter, and (iii) the possibility to be formed as narrow focused and scanned pencil beams of variable penetration depth permitting an accurate and rapid irradiation of the tumours. In these conditions, a beam of protons or light ions allows highly conformal treatment of deep-seated tumours with millimetre accuracy, giving minimal doses to the surrounding tissues. Furthermore, note that to reach depths of more than 25 cm in soft tissues, proton, and carbon ion beams must have an initial energy greater than 200 MeV and 4500 MeV (i.e., 375 MeV/u), respectively.

Several dose calculation algorithms have been then proposed for treatment planning in hadron therapy (especially for proton therapy), generally based on the pencil beam algorithm method, which consists in dividing the therapeutic beam into narrow pencil beams. Dose from the pencil beam is then usually calculated by using depth-dose distributions combined to the finest description of the beam profile in terms of lateral widening (due to the multiple scattering effects).

In this context, many dedicated Monte Carlo (MC) codes have been proposed since the pioneer works of Berger:[5] see for example the recently published approaches developed in the framework of the SHIELD-HIT, PHITS, and GEANT4 or FLUKA codes (for more details we refer the reader to our recent work[6] and references therein). Indeed, in the field of hadron therapy, MC track structure simulations play an important rôle in particular for understanding the spatial pattern of energy depositions as well as the relative biological effectiveness of radiation qualities. However, MC simulations essentially rely on the accuracy of the cross sections used for describing the ion-induced interactions in matter and more particularly in water, this target being commonly used for modelling the living medium because of its abundance in biological cells (up to 70–80% in mass). In this context, total and multi differential cross sections for ionization and charge transfer in water appear as input data of prime importance, these two processes bringing both the dominant contributions to the slowing-down of charged particles in matter.

The present chapter deals with the existing theoretical models—here limited to the perturbative treatments—as well as the available experimental measurements for ionization and electronic capture induced by heavy charged particles in water. Besides, let us add that more sophisticated models going beyond the perturbative framework may be found in the literature and for more details we refer the interested reader to the recent review of Belkić.[7]

2. ION-INDUCED IONIZATION AND CHARGE TRANSFER CROSS SECTIONS IN WATER: *A REVIEW OF THE EXISTING DATA*

In spite of the broad range of interest, cross section measurements on ion-induced collisions in water are scarce and a number of details have not yet been investigated up to now. Indeed, most of the existing studies so far have been restricted to electron impact ionization while cross sections of water ionization by ion impact remain extremely rare (see for example Refs. 8, 9 for a review on the ionization process by proton and α-particle impact, respectively). Besides, the charge transfer process has been even more rarely investigated and despite the numerous studies on total capture cross sections for incident protons in various gases, there are today only few results on partial electron capture cross sections. With regard to the theory, only few theoretical works—quantum as well as classical—have been developed for describing the ionization and charge transfer processes in water. The existing approaches are essentially based on semi-empirical models which use—for a major part—analytical formulae fitted on experimental measurements. These are reported in the following and compared in terms of differential as well as total cross sections with the 1st Born theoretical models hereafter reported.

2.1 Experimental background

Considering the ionization process, the first extensive work was given by Toburen and Wilson[10] who measured doubly differential cross sections (DDCS) for 300–1500 keV protons and more recently for 300 to 2000 keV He^+ and He^{2+} ions.[11] Later on, Rudd and co-workers performed experiments on the ionization of water vapour by protons and He^+ ion impact[12] and reported total direct cross sections (without capture). More recently, Bolorizadeh and Rudd have extended these pioneer works to the DDCS measurements for the ejection of electrons during the ionization process of water vapour by 15–150 keV protons.[13] Later on, Gibson and Reid[14] reported energy and angular distributions of secondary electrons ejected from various gases including water vapour by 50 keV protons. Finally, multiple ionization and fragmentation of water have been recently studied by Werner et al.[15] for fast protons and He^+ ions by using a position- and time-sensitive multi-particle detector: a good agreement was also observed with the previous measurements of Rudd and co-workers[12] for the total cross sections (TCS). Furthermore, Gobet et al.[16] have determined a complete set of cross sections for the ionization of water molecule by proton impact in the energy range 20–150 keV including total and partial cross sections for H^+ and H_2O^+ fragment production. They also found TCS in good agreement with the measurements of Rudd et al. and those of Werner et al. Recently, Gobet et al.[16] have also presented a full set of absolute partial cross sections corresponding to H^+, H_2O^+, OH^+, O^+, and O^{2+} which allows a detailed comparison between their cross sections for direct ionization of water by proton impact and the electron impact ionization data of Straub et al.[17] Concerning helium ions, the literature remains very poor. We can nevertheless cite the pioneer work of Rudolph and Melton[18] on 2.2 MeV He^{2+} ions, the extensive graphical representation given by Toburen et al.[11] in terms of secondary electron yields, differential in ejected electron energy and emission angle for 0.075 to 0.5 MeV/u helium ions, both singly and doubly charged and finally, the very recent differential cross sections reported by Ohsawa et al. for the energy and angular distributions of secondary electrons produced in collisions of 6- and 10-MeV/u He^{2+} ions in water vapour and more recently for 15-MeV/u α-particles (He^{2+} ions).[19] In the latter, DDCS were presented and compared in the low-energy region to the Toburen's data by means of Fano plots and very good consistency was found. Singly differential cross sections (SDCS) were finally deduced and compared to the semi-empirical model introduced by Rudd.[20] Considering carbon ions, the literature is much poorer since to our knowledge only few experimental measurements have been reported. Let us cite the group of Montenegro and co-workers[21] who have published a study of great interest for the field of hadron therapy on the water molecule fragmentation by carbon ions at the distal region of the Bragg peak. In this work, measurements of the positive ion fragments resulting from the water fragmentation after ionization and electron capture have been reported, allowing for the first time a quantitative determination of the energy lost by carbon ions at the end of the particle range. Finally, note that Dal Cappello et al.[22] have recently reported an extensive set of experimental doubly and singly differential cross sections for 6 MeV/u C^{6+} ions provided by Ohsawa and co-workers.

Considering the capture process, many experimental measurements have been reported since the pioneer works on protons in 1970s. Let us cite the work of Rudd and co-workers on electron capture induced by 5–150 keV protons in many gases like H_2 and O_2 and later on the studies of Rudd et al.[12] on the determination of electron and positive ion production cross sections from which electron capture cross sections for protons in water vapour were extracted. More recently, Lindsay et al.[23] reported measurements of absolute differential cross sections for charge transfer scattering of 0.5-, 1.5-, and 5-keV protons by H_2O at laboratory scattering angles between 0.01° and 2.60°. In their recent letter, Gobet et al.[16] have also reported total and partial electron-capture cross sections for 20–150 keV protons in water vapour. Finally, high-energy protons (15–3500 keV) have been also recently investigated by Luna et al.[24] who studied the water molecule dissociation by proton and hydrogen impact. Concerning helium ions, only few measurements have been reported. Thus, Rudd and co-workers[12] reported absolute total cross sections for 5–450 keV He^+ ions and for 5–150 keV/u α-particles whereas the low-energy regime was only very recently investigated. Let us cite for example the study given by Abu-Haija et al.[25] where total cross sections for 0.1–1 keV He^{2+} ions on triatomic molecules like H_2O were reported, that of Greenwood et al.[26] where single and double capture processes were studied in the energy range 0.05–5 keV/u and finally that of Seredyuk et al.[27] where experimental one-electron capture cross sections have been carried out in the range 0.025–12 keV/u. Heavy ions have been up to now only rarely studied. We can nevertheless mention the very recent study of Mawhorter et al.[28] who reported absolute single, double, and triple charge exchange cross sections for highly charged ions among which C^{q+} ions ($q=5,6$) colliding with molecular species like CO, CO_2, and H_2O. However, this study remains limited to low impact energies (7.0 $q$keV), its aim being the interpretation of the x-ray emissions from comets as they interact with the solar wind. Similarly, Bodewits and Hoekstra[29] have reported absolute total cross sections for 0.1–7.5 keV/u collisions of O^{6+} ions on H_2O molecules.

2.2 Theoretical background

2.2.1 Semi-empirical approaches for describing the ionization process

On the theoretical side, we essentially find semi-empirical models which are limited, for the major part, to the calculation of singly differential and total ionization cross sections. Among them we can first cite the Rudd's model—initially developed for protons—which offers a parameterization of secondary electron spectra after ion impact. This model may be used over the entire range of primary and secondary energies and is in the form of an analytic equation with parameters determined from experimental data. It is based on a simple version of the binary-encounter approximation (BEA) equation modified to yield the correct high-energy asymptotic dependence on energy in agreement with the Bethe equation prediction. It has been further modified by the use of the promotion model at low energies.[20] In brief, the approximation made consists in treating the collision—between a projectile and a single target electron—as a classical one. The nucleus and the remaining target electrons play no rôle except that of providing a binding energy for the ejected electron, the energy transfer E and the kinetic energy E_e being related by $E=E_e+I$, where I denotes the binding energy of the ionized subshell of the target. The justification for using a classical model lies in the fact that doubly differential cross sections for Coulomb scattering between two particles are the same when calculated using either classical physics or quantum mechanics. Thus, the singly differential cross sections are simply expressed as (in atomic units)

$$\frac{d\sigma_{\mathrm{Rudd}}}{\mathrm{d}E_{\mathrm{e}}} = \frac{S/I}{2R} \frac{F_1 + F_2 w}{(1+w)^3[1+\exp(\alpha(w-w_{\mathrm{c}})\tilde{v})]}, \tag{1}$$

where I refers to the binding energy (expressed in atomic units) whereas R denotes the Rydberg energy.

The reduced quantities w and $\tilde{v}$ are given by

$$w = E_{\mathrm{e}}/I, \tilde{v} = \sqrt{E_{\mathrm{i}}/I}, \tag{2}$$

where E_i denotes the incident projectile energy and with

$$w_c = 4\tilde{v}^2 - 2\tilde{v} - 1/8I, \quad S = \pi N/I^2, \tag{3}$$

N being the number of electrons of the ionized molecular subshell whereas F_1, F_2, and α are seen as adjustable fitting parameters. Thus, we have

$$F_1(\tilde{v}) = L_1 + H_1, \begin{cases} L_1 = C_1 \tilde{v}^{D_1} / \left[1 + E_1 \tilde{v}^{(D_1+4)}\right] \\ H_1 = A_1 \ln(1 + \tilde{v}^2)/(\tilde{v}^2 + B_1/\tilde{v}^2) \end{cases} \tag{4}$$

and

$$F_2(\tilde{v}) = L_2 H_2/(L_2 + H_2), \begin{cases} L_2 = C_2 \tilde{v}^{D_2} \\ H_2 = A_2/\tilde{v}^2 + B_2/\tilde{v}^4. \end{cases} \tag{5}$$

The different needed parameters are reported hereafter (see Table 10.1).

Total ionization cross sections were then simply deduced by numerical integration of Eq. (1) over the kinetic energy transfers E_e, the latter ranging from a minimum value equal to 0 to a maximum value $(E_e)_{\max}$ defined as $(E_e)_{\max} = \frac{4m_0 M_P}{(M_P + m_0)^2} E_i \cong \frac{4m_0}{M_P} E_i$ where m_0 and M_P refer to the electron and projectile mass, respectively. Relatively good agreements were then observed for singly differential cross sections, in particular for ion energies lower than 300 keV/u whereas large discrepancies were recently reported by Uehara and Nikjoo[30] for greater energies (up to about 30% at 2 MeV), what led the authors to propose a polynomial fit of existing experimental measurements for expressing the total ionization cross sections in their numerical track-structure code—called LEAHIST—recently developed for modelling the transport of α-particles in water.

The second semi-empirical and well-documented model—called HKS model developed by Hansen, Kocbach, and Stolterfoht[31]—consists in describing the ionization process in the impact parameter 1st Born approximation. In this approach, the initial and the final electron states are described by means of a hydrogenic function and a plane wave, respectively, i.e., without taking into account the electron momentum in its bound state. However, due to singularities observed when the ejected electron energy

Table 10.1 List of the semi-empirical parameters used in the Rudd's model for fitting the singly differential cross sections of proton-induced ionization of isolated water molecules

A_1	B_1	C_1	D_1	E_1	A_2	B_2	C_2	D_2	α
0.97	82.0	0.40	-0.30	0.38	1.04	17.3	0.76	0.04	0.64

tends to zero, further empirical fittings were employed—simultaneously to other semi-empirical terms[32, 33]—to finally provide the well-known HKS model, which can be consequently regarded as an impact parameter-plane wave Born approximation (IP-PWBA).

In this approach, the authors have described the electron emission by heavy ions of charge Z_{ion} in terms of impact parameter dependent probabilities $P(b,\theta_e,E_e)$ where b refers to the impact parameter whereas θ_e and E_e denote the ejection angle and the kinetic energy transfer, respectively. The DDCS (per target electron) were then obtained by means of analytical integrations of the corresponding probabilities over the impact parameter, yielding a simple expression recently reported in Ref. 33 as

$$\frac{d^2\sigma_{\text{HKS}}}{d\Omega_e dE_e} = \left(\frac{Z_{\text{ion}}}{v_i}\right)^2 \frac{32}{3\pi\alpha k_c^3}\left[\frac{\alpha_c^2}{\alpha_c^2 + (\widehat{K}_m - \hat{k}_t\cos\theta_e)^2}\right]^3, \tag{6}$$

where the function in the square brackets describes the binary-encounter maximum that resembles a Lorentzian whose width is governed by

$$\alpha_c = \alpha\left(1.0 + 0.7\frac{v_i^2}{v_i^2 + k_e^2}\right), \tag{7}$$

where $\alpha = \sqrt{2I}$ corresponds to the mean initial momentum parameter, I being the binding energy of the corresponding ionized molecular subshell.

In Eqs.(6) and (7), v_i denotes the projectile velocity while $\widehat{K}_m = \frac{K_m}{\alpha_c}$ represents the normalized minimum momentum transfer with $K_m = (\alpha^2 + k_e^2)/2v_i$.

Similarly, the authors defined the quantities k_t (with $\hat{k}_t = k_t/\alpha_c$) and k_c as small modifications of the momentum of the outgoing electron k_e, respectively given by

$$k_t = \sqrt{k_e^2 + 0.2\alpha^2\sqrt{v_i/\alpha}}\ ,\ k_c = \sqrt{k_e^2 + 2\alpha^2/\ln(2v_i^2/\alpha^2)}. \tag{8}$$

Let us note that the original equations proposed by Hansen and Kocbach[31] imply $k_c = k_e$ due to the fact that in the peaking approximation one neglects the mean momentum of the bound electrons in comparison to that of the outgoing electron. However, as clearly emphasized by Stolterfoht et al.[32] this approximation produces a singularity in the low-electron energy regime, which can be simply removed by adjusting the value of k_c to fit the model results to those of the Born approximation.

To do that, numerous expressions have been proposed like that reported in Eq. (8). We can also mention that reported in Ref. 32, namely,

$$k_c = \sqrt{k_e^2 + \frac{3\alpha^2/2}{[\ln(2v_i^2/\alpha^2)]^{2/3}}}. \tag{9}$$

In the same state of mind, Bernal and Liendo[34] have recently slightly modified the original version of the HKS model, essentially to avoid the "non-physical" descending jump appearing for each electron binding energy in the SDCS due, in major part, to the use of the arctangent term (see Eq. (11)). To do that, the authors proposed a modified expression for the DDCS, denoted in the following $\left[\frac{d^2\sigma_{HKS}}{d\Omega_e dE_e}\right]_{B-L}$ and expressed as

$$\left[\frac{d^2\sigma_{HKS}}{d\Omega_e dE_e}\right]_{B-L} = \left(\frac{Z_{ion}}{v_i}\right)^2 \frac{32}{3\pi\alpha k_c^3}\left[\frac{1}{1+(\widehat{K}_m+\hat{k}_t\cos\theta_e)^2}\right]^3. \tag{10}$$

However, as underlined by Uehara and Nikjoo[30] and more recently by Bernal and Liendo,[34] the DDCS also obtained give only a limited agreement with the experimental data, especially in the backward and forward angle regions what could be relied to the use, in this model, of hydrogenic wave functions instead of realistic bound electron wave functions to describe the target electron initial state.

Furthermore, the semi-empirical SDCS provided by the different existing HKS approaches, namely, the original version $\frac{d\sigma_{HKS}}{dE_e}$ and the recently modified version $\left[\frac{d\sigma_{HKS}}{dE_e}\right]_{B-L}$ may be respectively recast as

$$\begin{aligned}\frac{d\sigma_{HKS}}{dE_e} = \left(\frac{Z_{ion}}{v_i}\right)^2 \frac{16N}{3\alpha k_c^3\hat{k}_t}&\left[\arctan\left(\frac{2\hat{k}_t}{1+\widehat{K}_m^2-\hat{k}_t^2}\right)\right.\\&\left.+\frac{5(\widehat{K}_m+\hat{k}_t)+3(\widehat{K}_m+\hat{k}_t)^3}{2[1+(\widehat{K}_m+\hat{k}_t)^2]^2}-\frac{5(\widehat{K}_m-\hat{k}_t)+3(\widehat{K}_m-\hat{k}_t)^3}{2[1+(\widehat{K}_m-\hat{k}_t)^2]^2}\right]\end{aligned} \tag{11}$$

and

$$\begin{aligned}\left[\frac{d\sigma_{HKS}}{dE_e}\right]_{B-L} = \left(\frac{Z_{ion}}{v_i}\right)^2 \frac{8N}{\alpha k_c^3\hat{k}_t}&\left[\frac{5(\widehat{K}_m+\hat{k}_t)+3(\widehat{K}_m+\hat{k}_t)^3}{3[1+(\widehat{K}_m+\hat{k}_t)^2]^2}\right.\\&-\frac{5(\widehat{K}_m-\hat{k}_t)+3(\widehat{K}_m-\hat{k}_t)^3}{3[1+(\widehat{K}_m-\hat{k}_t)^2]^2}\\&\left.+\arctan(\widehat{K}_m+\hat{k}_t)-\arctan(\widehat{K}_m-\hat{k}_t)\right],\end{aligned} \tag{12}$$

where the factor N corresponds to the number of target electrons per molecular subshell.

Finally, note that for both the original HKS model and its more recent version, the total ionization cross sections are—like for the Rudd's model—numerically obtained by integration of Eq. (11) or Eq. (12), respectively.

2.2.2 Semi-empirical approaches for describing the charge transfer process

When the energy of the charged particles becomes sufficiently low ($E_{\mathrm{i}} \leq 100\,\mathrm{keV/u}$), the ionization probability diminishes rapidly, and the capture process becomes the predominant energy-loss pathway. However, only rare experimental measurements have been up to now reported for vapour water. To overcome this lack, many semi-empirical simulations have been proposed for modelling the electron capture process.

The first one refers to the approach proposed by Rudd et al.[12] which consists in expressing the charge transfer cross section σ as $\sigma = \sigma_+ - \sigma_-$ by means of adjustable parameters for fitting the measured cross sections of positive (ion) and negative (electron) charge production (σ_+ and σ_-, respectively). Thus, Rudd et al propose to write the (ionization + capture) cross section σ_+ and the pure ionization cross section σ_- as

$$\sigma_{\pm} = \frac{1}{\frac{1}{(\sigma_{\mathrm{low}})_{\pm}} + \frac{1}{\sigma_{\mathrm{high}}}}, \tag{13}$$

where the low- and high-energy components σ_{low} and σ_{high} (expressed in atomic units) were fitted as

$$\begin{aligned} (\sigma_{\mathrm{low}})_- &= 4\pi C k_{\mathrm{i}}^{2D}, \\ (\sigma_{\mathrm{low}})_+ &= 4\pi [C k_{\mathrm{i}}^{2D} + F], \\ \sigma_{\mathrm{high}} &= 4\pi [A \ln(1 + k_{\mathrm{i}}^2) + B]/k_{\mathrm{i}}^2, \end{aligned} \tag{14}$$

where k_{i} refers to the incident momentum. The used parameters are reported below (see Table 10.2).

The resulting cross sections agree well with the experimental data for proton energies of 1-100 keV but nevertheless exhibit large discrepancies

Table 10.2 List of the semi-empirical parameters used in the Rudd's model for fitting the experimental cross sections of positive and negative charge production in proton on water molecule collisions

A	**B**	**C**	**D**	**F**
2.98	4.42	1.48	0.75	4.80

with the experimental measurements of Toburen et al.[35] for energies above 100 keV. Moreover, they tend to a constant value for energies below 1 keV what is in complete contradiction with most of the existing experimental values which increase with decreasing proton energies.

The second model was more recently suggested by Dingfelder et al.[36] who expressed the charge transfer cross sections by analytical formula (straight lines for low and high proton energies on a doubly logarithmic scale, both connected by a power law) where the parameters were chosen by considering the experimental data of Lindsay et al.[23] and of Dagnac et al.[37] for low and medium energies, and those of Toburen et al.[35] for higher energies. In detail, the charge transfer cross section is expressed by

$$\sigma = 10^{Y(X)} \tag{15}$$

where $X = \log(\tau)$ (with τ in eV) and

$$\begin{aligned} Y(X) = {} & [a_0 X + b_0 - c_0 (X - x_0)^{d_0} \Theta(X - x_0)]\, \Theta(x_1 - X) \\ & + (a_1 X + b_1)\, \Theta(X - x_1), \end{aligned} \tag{16}$$

where $\Theta(x)$ represents the Heaviside step function. The parameters a_0, b_0, a_1, and b_1 determine the low-energy straight line and the high-energy one, respectively, whereas c_0 and d_0 refer to the power law in between, connected to the low-energy straight line at x_0. The connection point x_1 to the high-energy line and the parameter b_1 are calculated as

$$\begin{cases} x_1 = \left(\frac{a_0 - a_1}{c_0 d_0}\right)^{1/(d_0-1)} + x_0 \\ b_1 = (a_0 - a_1) x_1 + b_0 - c_0 (x_1 - x_0)^{d_0} \end{cases} \tag{17}$$

by using the first derivative. The used parameters are reported below (see Table 10.3).

Finally, let us mention a third model based on the analytical functions developed by Green and co-workers[38] and fitted to the experimental data of Toburen et al.[35] and Dagnac et al.[37] The obtained formula is nowadays

Table 10.3 List of the semi-empirical parameters used in the Dingfelder's model for fitting the total charge transfer cross sections for protons in water

a_0	b_0	c_0	d_0	a_1	b_1	x_0	x_1
-0.180	-18.22	0.215	3.550	-3.600	-1.997	3.450	5.251

Table 10.4 List of the fitting parameters used in the semi-empirical expression of total electron capture cross sections for protons in water[39]

	λ	*J* (keV)	α (keV)	Ω	Λ	*C* (keV)
H_2	2.0	1.215	4084.0	0.271	4.80	75.8
O_2	2.0	0.057	1038.0	0.258	3.50	125.0

commonly used in many track structure codes and is presented as follows (with E_i in keV)

$$\sigma = \sigma_0 \frac{(Z\alpha)^{\Omega}(E_i - I)^{\lambda}}{J^{(\Omega+\lambda)} + E_i^{(\Omega+\lambda)} + (Z\alpha)^{\Omega} E_i^{\lambda} (E_i/C)^{\Lambda}}, \tag{18}$$

where α, λ, *J, Ω, Λ* et *C* are different fitting parameters (see Table 10.4), *I* being the ionization threshold (in keV) of the impacted target and $\sigma_0 = 10^{-16}\,\text{cm}^2$.

For heavier charged particles like He^+ ions, the electron capture cross sections were also fitted to experimental data, namely, those of Rudd et al. [12] for impact energies between 1 and 100 keV/u and those of Sataka et al.[40] for impact energies between 75 keV/u and 500 keV/u. For He^{2+} ions, Rudd et al.[12] have proposed—in the energy range 5 to 150 keV/u—least-squares fitted total cross sections whereas for energies below 5 keV/u and above 150 keV/u, these functions were extrapolated assuming a smooth transition at the boundaries.[30]

Finally, let us note that in this last model the total cross sections for water target were simply obtained by means of the additivity rule from the relationship $\sigma_{H_2O} = \sigma_{H_2} + 0.5\sigma_{O_2}$, what remains still today one of the most common approach for describing the ionizing processes (capture as well as ionization) in complex target molecules like water. However, this technique completely conceals the molecular structure of the target whose influence may become primordial especially at the multi differential scale as it will be discussed hereafter.

3. MOLECULAR DESCRIPTION OF THE WATER TARGET

Describing the molecular ionization by a quantum-mechanical approach remains a difficult task essentially due to the multi-centred nature of the target. To overcome this difficulty, many attempts were made in particular by representing the molecular cross sections as a weighted sum of the cross sections of the different components of the molecule, namely, the well-known Bragg's additivity rule whose applications to vapour water ionization were first proposed by Olivera et al.[41] for proton beams. A second technique, called complete neglect of differential overlap (CNDO) consists in writing the molecular orbitals in terms of atomic orbitals of the atomic constituents, namely, the orbitals H_{1s}, O_{1s}, O_{2s}, and O_{2p} (see Ref. 42). Note that this description was also used in the binary-encounter-dipole model developed by Kim and Rudd[43] for providing singly and total ionization cross sections for a large set of molecules impacted by electrons. However, in both these models the calculated doubly differential cross sections exhibit some discrepancies with the experimental data at small angle regions. The authors linked these discrepancies to the fact that the electronic populations were not correctly reproduced in these two descriptions, especially for the calculations within the Bragg's rule framework. Finally, a third method consists in describing the populations of the target by means of molecular orbitals constructed from a linear combination of atomic orbitals in a self-consistent field approximation (MO-LCAO-SCF). In the past, Champion and co-workers have successfully applied this description for treating the ionization of simple molecules like CH_4, NH_3, and H_2O by electrons[44] as well as by light-ion impact, namely, H^+, He^{2+}, and C^{6+} ions.[8, 9, 22] In these works, the authors have used the simple molecular description provided by Moccia who reported one-centre ground state wave functions for molecules of the type HX_n (see Ref. 45). The molecular orbitals were then expressed in terms of Slater-like functions all centred at a common origin coinciding, in this case, with the X nucleus. In fact, for these molecules, the electronic density is mainly governed by the central atom. Thus, providing suitable analytical wave functions is quite similar to the atomic case, in which the basis set consists of functions all referred to a common origin centred at the one nucleus.

Finally, note that the problem of evaluation of the above-cited multicentre integrals depends on the type of basis functions used. Indeed, whereas it appears that there are no convenient and practical ways to evaluate such integrals for more than two non-aligned centres when Slater-type functions are used, it is worth noting that the use of Gaussian functions for the radial part decreases the difficulties even if it is clear that the Gaussian basis set needs probably 40% more such functions to achieve comparable results. Under these conditions, the ten bound electrons of the water molecule are distributed among five one centre molecular wave functions corresponding to the five molecular orbitals denoted 1b1, 3a1, 1b2, 2a1, and 1a1, respectively, and whose respective ionization potentials (or binding energies)—denoted Ij in the following (with j varying from 1 to 5, *respectively*)—are equal to 0.4954 a.u., 0.5561 a.u., 0.6814 a.u., 1.3261 a.u., and 20.5249 a.u. (see Ref. 44 for more details). Let us note that these molecular wave functions refer to the calculated equilibrium configurations, i.e., to the geometrical configurations which, among many others considered, give the minimum of the total energy, and agree with the experimental data in terms of HOH angle, bound O–H length, 1st ionization potential IP, and electric dipole moment μ (see Ref. 45).

4. BORN APPROXIMATIONS

In the framework of quantum mechanics, the treatment of atomic (or molecular) ionization by charged particles may be divided into different classes according to the intensity of the interaction between the target electron and the incoming and outgoing charged particle. Thus, Rudd et al.[46] distinguished in their review three categories, namely, (i) a first one in which the electron-target is a strong interaction whereas the electron-projectile is weak, (ii) a second one which treats the electron-target interaction as strong whereas the electron-projectile interaction is strong with the incoming particle and weak with the outgoing one, and finally (iii) a third class where the electron-target and the electron-projectile are both strong interactions.

In this scheme, it clearly appears the necessity to treat the ionization process by means of different approaches according to the investigated kinematical conditions. Among them, we distinguish the perturbative approaches—called Born approximations—from the continuum distorted wave methods whose main characteristic is that all two-particle Coulomb interactions are explicitly contained in the initial and final state wave functions. This last approach has been successfully employed for treating ionization as well as charge transfer in many atomic and molecular target systems including water and will be the subject of the next chapter of the present review.

In the perturbative regime, which corresponds to the major part of the cases investigated in the field of hadron therapy, the interaction between the electron and the projectile is ignored in the formation of the electron wave function and, as a result, appears only in the transition matrix element. Furthermore, it is assumed that the projectile may be expressed as a plane wave: this well-known approximation is referred as the plane wave

Born approximation and is commonly denoted PWBA. As reported by Rudd et al.,[46] this approximation will certainly be invalid if the projectile is deflected through a large angle (>1°) and is therefore usually called the standard straight-line trajectory semi-classical approximation. The distinction between the different calculations of this type then lies in the treatment of the ejected electron. Thus, we speak of typical PW when the latter is described by a plane wave whereas the distorted wave (DW) refers to a description of the ejected electron by means of a wave function calculated as the eigenfunction of the potential used for representing the residual target ion (see in the following). Therefore, when letter B is appended to PW and DW, the resulting acronyms PWB and DWB will refer to the plane wave Born and the distorted wave Born approximation, respectively. Finally, if a pure Coulomb potential is preferred to a numerical potential obtained from Hartree–Fock wave functions for the target in question, we speak of the Coulomb Born wave function denoted by CW. In the present work, where we are interested in the impact of bare ions, we consider initial wave functions that include separately the long range Coulomb interactions of the projectile with the electron to be ionized and of the projectile with the rest of the target. Thus these wave functions verify correct boundary conditions *only* in the initial channel, that's why we will use for them the acronym CB1 to distinguish with the case of B1, where asymptotic conditions are not satisfied. Thus, throughout we will talk about CB1-PWB, CB1-CWB, and CB1-DWB models. To avoid confusion with the existing literature on ion-atom collisions,[47] we re-emphasize that the term CB1, presently used in the hybrid models such as CB1-PWB, CB1-CWB, and CB1-DWB, will refer to the correct boundary condition satisfied only in the entrance channel. However, when the letters CB1 are employed, as a stand-alone acronym, they would refer to the first Born approximation with the correct boundary conditions fulfilled in both the initial and final states. We will then observe in the sequel that the differences between the CB1-CWB and the CB1-DWB models are more pronounced for DDCS than for SDCS and more particularly at large ejected angles where the CB1-DWB results generally underestimate the predictions given by the CB1-CWB model. Moreover, note that the CB1-DWB-type calculations can be performed by using different distortion potentials for the final states. In the following, we will essentially speak about the numerical potential issued from the above-cited wave functions taken from Moccia[45] but the procedure here followed could be easily generalized to any potential. In brief, the final state of the active electron—described by means of wave function distorted by the initial-state ion—is simply deduced from the initial self-consistent field one-centre-expanded molecular wave functions taken from Moccia [45] by removing the active electron orbital without any modification of the remaining orbitals: this is the well-known frozen-core approximation. A spherically averaged local radial potential is then deduced from the charge distribution of the target ion represented by the remaining orbitals. The final state distorted wave for the ionized electron is then numerically calculated as an eigenfunction of this radial potential and expressed as distorted waves, not necessarily orthogonal to the initial bound state wave functions. Note that an orthogonalization procedure could be nevertheless used by using, for example, the Schmidt-type procedure.

Finally, it is important to note that the three 1st Born approximations type here reported, namely, the CB1-PWB, the CB1-CWB, and the CB1-DWB, remain valid as far as the projectile velocity is fast in comparison to the orbital velocity of the active electron. In these conditions, plane waves are appropriate for describing the projectile whereas their use is no more valid in large angle scattering conditions. In addition, the present choice for the final state wave function of the active ejected electron should be satisfactory as long as the interaction between the scattered projectile and the ejected electron is weak and the ionization takes place fast enough so that the inactive electron orbitals do not relax before the active electron leaves the target, what corresponds to the major part of the cases encountered in the radiotherapy field. On the contrary, when the ejected electron is leaving the target in the forward direction with a speed comparable to that of the projectile, the interaction between the ejected electron and the projectile can be not necessarily weak. Thus, the ejected electron angular distributions (DDCS) exhibit a big rise at low ejected angles i.e., in the forward direction. This process is called continuum electron capture to the continuum (ECC) or charge transfer to the continuum. Using theoretical models that do not include this effect becomes then inappropriate and results in a substantial underestimation of the doubly differential ionization cross sections (see in the following). Indeed, describing this effect requires taking into account of second order terms of perturbative theory, what is beyond the scope of the present chapter. However, Salin has proposed in Ref. 48 a multiplicative correction factor—called Salin factor in the following—to account for the electron capture to the continuum. Under these conditions, the DDCS clearly present the ECC peak and improves the agreement with the experimental observations at small ejected angles: see for example the 1st Born calculations provided by Madison[49] for He targets impacted by

100 keV and 200 keV protons. Let us note nevertheless that the agreement becomes less satisfactory at large angles as reported in Ref. 49 and shown below for water target.

Furthermore, in view of the centre picture concept introduced by Stolterfoht et al.[50]—which consists in describing the electron production mechanism in terms of Coulomb centres associated to the different nuclei partners involved in the final state of the collision—we distinguish the free-electron Born approximation (or fully plane-wave Born approximation, PWBA) in which a plane wave is used for describing the outgoing electron whose interaction with the nuclei is completely neglected from the 1st Born approximation (B1-CW) which includes the full target interaction in the final state. Then, the free-electron Born approximation which contains neither a projectile nor a target centre is usually referred to a zero-centre case whereas the B1-CW is associated with the target-centre case. Finally, note that if the interaction of the outgoing electron with the target nucleus is neglected (as in the PWBA framework), the ionization process is referred to as a binary-encounter electron emission, which may be described by a classical theory. In this approach, the target electron is assumed to be free and then interacts with the incident projectile independent of the target. Theoretical DDCS were then successfully compared to experimental data for 100 keV and 300 keV protons on He especially in the region of the binary-encounter peak as k_e increases whereas large discrepancies were reported at small k_e for small and large electron scattering angles (see Rudd et al.[51]).

Considering now the charge transfer process, let us first mention that most of the existing theories in fast ion-atom collisions fall naturally in one of the two following categories: (i) plane wave theories where the exact initial and the final states are described by means of products of bound states and plane waves describing the relative motion of the colliding partners and (ii) distorted wave theories, which represent the exact initial and final states by products of bound states, plane waves, and distortion factors.[52]

In this context, Oppenheimer and then Brinkman and Kramers[53] were the first authors to propose a theoretical model for calculating the total cross section in the 1st Born approximation framework via the well-known OBK model. In this later, such as in many other theories, the calculations are simplified by approximating the many-electron collisional system by a one-active electron system. Thus, the remaining electrons screen the target nuclear charge seen by the projectile and the active electron and then provide an effective potential where the active electron evolves, while the "non-captured" electrons are considered as being passive: this is the frozen core approximation previously reported for describing the ionization process. A few years later that the OBK model was proposed, Jackson and Schiff [54] pointed out a strong disagreement between the experimental observations for protons in hydrogen gas and the theoretical OBK predictions, these latter being approximately four times greater than the experimental results at 100 keV and even higher at lower energies. The authors attributed this failure to the description of the perturbation Hamiltonian. Indeed, this latter consists in two terms, namely, the Coulomb interaction between the target active electron and the incident particle and the Coulomb interaction between the target nucleus and the incident projectile. However, as underlined by Jackson and Schiff, the OBK approach only considers the first component of the Hamiltonian neglecting the second one, whose contribution was assumed to be of the order of m_0/M_P (i.e., negligible) by G. C. Wick (see added note in proof in Ref. 54). Thus, the agreement between theory and experiment for protons in hydrogen became better for all energies above 25 keV, even though the Born approximation was still used. Similarly, Omidvar et al.[55] investigated the rôle played by the internuclear interaction in the behaviour of the cross sections in the 1st Born approximation for protons on helium and argon. Comparisons were then reported between different options of calculation, namely, by using different perturbative potentials, including: (i) only the projectile-electron interaction, (ii) the projectile-electron and internuclear interactions, and (iii) the projectile-electron interaction added to an effective internuclear potential where the target nuclear charge was chosen equal to one. Strong discrepancies were then observed exhibiting in particular that the inclusion of the perturbative potential (iii) gave the best fit of the experimental observations for helium and argon targets.

Later on, many authors among which Dollard,[56] Mapleton,[57] Carpenter and Tuan[58] have pointed out divergences in the Born series. More recently Dewangan and Eichler[59] showed that singularities appear in the transition matrix calculated within the Born series. These divergences come from the contribution of the intermediate elastic channel. Higher-order theories, like the impulse approximation (IA)[60] and the strong potential Born approximation (SPB)[61] were also developed providing an improvement of the agreement with experiments, essentially due to the non negligible contribution of the high-order terms to the forward scattering. However, divergences from elastic contributions were shown to appear in the SPB model.[59, 62] To correct the above reported divergences a proper treatment of the Coulomb boundary conditions was proposed. Moreover, it was shown that the IA violates correct asymptotic conditions. A detailed description of the adequate treatment of boundary conditions was given by Belkić and co-workers[63] who have shown that the effective internuclear additional term in the perturbative potential corresponds in fact to the correction of the coulombic tail of the projectile-electron interaction. The long-range Coulomb potentials are, in general, present even when the scattering particles are at infinite separation from each other, what causes distortion of unperturbated channel states which, in turn, yields modifications of the perturbation potentials. Numerous investigations were proposed to include into both the initial- and the final-state wave functions the correct asymptotic behaviour at infinite internuclear separation, confirming that a first Born approximation satisfying Coulomb boundary conditions (referred in the literature as the CB1 model) was quite accurate in reproducing the experimental data at no so high energies, where two-step collisions (Thomas mechanism[64]) give an important contribution to differential cross sections. In the last case a second order of the Born series with correct boundary conditions is necessary. In particular, Belkić reported in Ref. 65 that the sole introduction of the Coulomb phase into the exit channel within the Jackson–Schiff matrix element for H^+-Ar charge exchange reduced the calculated total cross sections by about 200 times, leading to a better agreement with the experiment. In brief, these corrections refer to: (i) the Coulomb distortion of the unperturbated channel states and (ii) the perturbating potentials. Furthermore, it is worth noting that the CB1 transition amplitude coincides fortuitously with the Jackson–Schiff one for proton–hydrogen collisions, i.e., when the projectile charge equals the target charge.

Finally, let us note that such considerations support the development of first order continuum distorted wave (CDW) and continuum distorted wave-eikonal initial state (CDW-EIS) approximations, the last one being extensively detailed in chapter 9 of the present book.

4.1 Theoretical description of the ionization process within the 1st Born approximation

4.1.1 Basic formalisms

Let us here consider the direct ionization process schematized by

$$X + H_2O \rightarrow X + H_2O^+ + e^-, \tag{19}$$

where the initial state of the system is characterized by an incident projectile X (of charge Z_P and of mass μ) with an initial momentum $\vec{k}_i$, which ionizes a stationary water molecule whereas the final state of the system is characterized by a scattered projectile of momentum $\vec{k}_s$ and an ejected electron of momentum $\vec{k}_e$.

In these conditions, the four-fold differential cross sections corresponding to this process, namely, differential in the energy of the ejected electron $k_e^2/2$, differential in the direction of the ejected electron $d\Omega_e$, differential in the energy of the scattered electron $k_s^2/2\mu$, and differential in the direction of the scattered particle $d\Omega_s$ are simply given by

$$\frac{d^4\sigma}{k_s^2 dk_s d\Omega_s k_e^2 dk_e d\Omega_e} = \frac{\mu^2}{4\pi^2 k_i} |T_{fi}|^2 \delta\left(\frac{k_i^2}{2\mu} - |I| - \frac{k_s^2}{2\mu} - \frac{k_e^2}{2\mu} - \frac{(\vec{K} - \vec{k}_e)^2}{2M_{ion}}\right), \tag{20}$$

where I denotes the ionization energy i.e., the binding energy of the molecular subshell ionized. The transferred momentum—from the incident projectile to the water target—is here denoted $\vec{K} = \vec{k}_i - \vec{k}_s$, whereas M_{ion} refers to the mass of the residual water ion.

Furthermore, the energy and the solid angle of the scattered projectile being not measured in the common experiments, we usually define the doubly differential cross sections (DDCS) as

$$\frac{d^2\sigma}{d\Omega_e dE_e} = \frac{\mu^2}{4\pi^2} \frac{k_e}{k_i} \int |T_{fi}|^2 \delta\left(\frac{k_i^2}{2\mu} - |I| - \frac{k_s^2}{2\mu} - \frac{k_e^2}{2\mu} - \frac{(\vec{K} - \vec{k}_e)^2}{2M_{ion}}\right) d\Omega_s. \tag{21}$$

Moreover, let us note also that since the amplitude T_{fi} decreases fast when the momentum transfer K increases only small values of K will contribute to the integration over $d\Omega_s$ in Eq.(21). Thus, we can neglect the term $\frac{(\vec{K}-\vec{k}_e)^2}{2M_{ion}}$ in the delta function of Eq. (21) and then recast the DDCS as

$$\frac{d^2\sigma}{d\Omega_e dE_e} = \frac{\mu^2}{4\pi^2} \frac{k_e}{k_i} \int |T_{fi}|^2 \delta\left(\frac{k_i^2}{2\mu} - |I| - \frac{k_s^2}{2\mu} - \frac{k_e^2}{2\mu}\right) d\Omega_s. \tag{22}$$

In this expression, the scattering matrix $T_{fi} \equiv T_{fi}(\vec{K})$ is given by

$$T_{fi}(\vec{K}) = \left\langle \Psi_f^- \right| V_i \left|\psi_i\right\rangle , \tag{23}$$

where Ψ_f^- and ψ_i are the exact final scattering wave function with correct incoming boundary conditions and the initial wave function, respectively, which both contain the information on the dynamics of all the particles involved in the total collisional system.

In Eq. (23), the perturbative potential V_i depends on the choice of ψ_i. Thus, extending the formulation given by Corchs et al.[66] for single electron capture from molecules to the single ionization one (where all interactions between the projectile and the target nuclei are treated into the eikonal approximation, the target nuclei being supposed to remain in their initial positions during the collision) and after a tedious algebra, the transition amplitude as a function of the impact parameter $\vec{b}$ may be written as

$$A_{fi}(\vec{b}) = \prod_{c=1}^{n} b_c^{2iZ_P Z_c/v_i} a_{fi}(\vec{b}), \tag{24}$$

where the straight line version of the impact parameter approximation $\vec{b} = \vec{r}_0 + \vec{v}_i t$ has been used with v_i for the incident projectile velocity and where $\vec{r}_0$ indicates the projectile position (see Figure 10.1).

In Eq. (24), b_c defines the impact parameter with respect to the nucleus c of the target (composed in total by n nuclei) whereas Z_c designates the corresponding nuclear charge. The transition amplitude a_{fi} $(\vec{b})$ is a purely electronic one which accounts the interaction of all target electrons with the projectile.

Moreover, considering that all passive electrons, namely, the target electrons which are not ionized, all remain as frozen during the collision, Fainstein et al. demonstrated in Ref. 67 that the transition amplitude A_{fi} $(\vec{b})$ reported in Eq. (24) could be recast as

$$A_{fi}(\vec{b}) = \exp\left[-\frac{i}{v_i}\int_{-\infty}^{\infty} \mathrm{d}t V_s(\vec{r}_0)\right] \prod_{c=1}^{n} b_c^{2iZ_P Z_c/v_i} \tilde{a}_{fi}(\vec{b}). \tag{25}$$

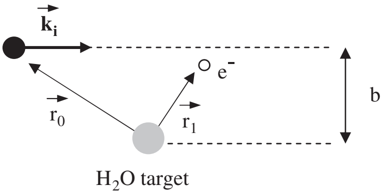

Figure 10.1 Schematic representation of the water ionization process.

In this expression, the static potential $V_{\rm s}(\vec{r}_0)$ contains the information on the interaction between the projectile and the passive electrons and is given by

$$V_{\rm s}(\vec{r}_0) = \langle \zeta_{\rm i}(\{\vec{r}_{\rm k}\})| - \sum_{k=2}^{N} \frac{Z_{\rm P}}{|\vec{r}_{\rm k} - \vec{r}_0|} |\zeta_{\rm i}(\{\vec{r}_{\rm k}\})\rangle \,, \tag{26}$$

where $\zeta_{\rm i}(\{\vec{r}_{\rm k}\})$ refers to the wave function describing the (N-1) passive electrons whose positions are represented by the vectors $\vec{r}_{\rm k}$, the ejected (active) electron position being denoted $\vec{r}_1$.

In these conditions, $\tilde{a}_{fi}(\vec{b})$ appears as a *one-active electron* transition amplitude, where all the interactions between the considered (active) electron and the passive ones are accounted. Furthermore, it is important to note that the interactions of the projectile with the passive electrons and with the target nuclei are here (i.e., in Eq. (25)) considered at all orders and *not only* at the first one, what is valid for any model used to describe the studied reaction. Note that it remains valid for any electronic transition such as ionization, electron capture, or excitation.

Finally, the scattering matrix element is obtained using the well-known Fourier transform

$$T_{fi}(\vec{K}) = i v_{\rm i} \int {\rm d}\vec{b} \exp(i\vec{K}.\vec{b}) A_{fi}(\vec{b}). \tag{27}$$

It is evident from Eq. (25) that the electronic transition is provoked by the interaction of the projectile with the active electron while the interactions of the projectile with the target nuclei and with the passive electrons will only affect the projectile trajectory. Thus, in the case where integration over all projectile scattering angles is considered in order to calculate the corresponding DDCS, only the interaction of the projectile with the active electron must be taken into account. In the following we will focus the study on this case.

The electronic capture process being investigated in the next session let us first consider the single ionization reaction. The asymptotic behavior of the Coulomb projectile-active electron interaction must be included into the initial and final wave functions in order to avoid the presence of disconnected diagrams provoking divergences in the transition amplitudes (and then in the scattering matrix elements) coming from the contribution of intermediate elastic channels.[59, 62] Thus, if multiplicative asymptotic eikonal phases depending on $\vec{r}_0$ are included into the initial asymptotic and final exact wave functions, the one active-electron transition amplitude $\tilde{a}_{fi}(\vec{b})$ can be written under the form

$$\tilde{a}_{fi}(\vec{b}) = b^{-2iZ_{\mathrm{P}}/v_{\mathrm{i}}}\hat{a}_{fi}(\vec{b}). \tag{28}$$

The corresponding projectile-active electron perturbative potential appearing in $\hat{a}_{fi}(\vec{b})$ will be reduced to its short range part. The long range part can be thus also neglected from the calculations if the cross sections of interest do not depend on the projectile scattering angle. Accordingly with this, we can calculate the corresponding scattering matrix element using Eq. (27).

In a first-order approximation, we can consider in Eq. (23) $\Psi_f^- \cong \psi_{\mathrm{f}}$ where ψ_{f} is a specific asymptotic final wave function, so that

$$T_{fi}(\vec{K}) \cong T_{fi}^{(1)}(\vec{K}) = \langle\psi_{\mathrm{f}}|\, V_{\mathrm{i}}\, |\psi_{\mathrm{i}}\rangle\,. \tag{29}$$

Thus, following our analysis given above, this first-order matrix element can be reduced to the one-active electron expression

$$\widehat{T}_{fi}^{(1)}(\vec{K}) \cong \left\langle \phi(\vec{k}_{\mathrm{s}},\vec{r}_0)\zeta_f(\vec{r}_1)\right|\, \widetilde{V}_{\mathrm{i}}\, \left|\phi(\vec{k}_{\mathrm{i}},\vec{r}_0)u(\vec{r}_1)\right\rangle, \tag{30}$$

where $u(\vec{r}_1)$ describes the one-active electron orbital wave function of the molecular target and $\phi(\vec{k}_d,\vec{r}_0)$ (with $d = i,s$) a projectile plane wave (for the incident and the scattered projectile, respectively) whereas $\zeta_f(\vec{r}_1)$ refers to the ejected electron wave function. The perturbative potential $\widetilde{V}_{\mathrm{i}}$ here reported corresponds to the above-mentioned short range part of the projectile-active electron interaction and is given by

$$\widetilde{V}_{\mathrm{i}} = \frac{Z_{\mathrm{P}}}{r_{01}} - \frac{Z_{\mathrm{P}}}{r_0}, \tag{31}$$

with $\vec{r}_{01} = \vec{r}_0 - \vec{r}_1$.

4.1.2 Final state description

In the context of water ionization, several models have been recently tested by Champion and co-workers[8, 9] for describing the final state of the collision in order to go beyond the pure simple CB1-CWB approximation: a first one—referred as CB1-DWB in the following—where the ejected electron is described via a distorted wave function instead of a pure Coulomb wave function whereas the scattered projectile remains described by means of a plane wave, and a second model where the scattered projectile as well as the ejected electron are both described by Coulomb waves (CB1-2CW). Let us add that in these two models, the effective charges seen by the escaping electron and ion—defined as the effective ionic charges—were chosen equal to 1 by Boudrioua et al.[8] whereas some authors defined them as $Z_T = \sqrt{-2n^2\varepsilon_\mathrm{i}}$ (with $\varepsilon_\mathrm{i} = -I_\mathrm{i}$) where n denotes the principal quantum number of each atomic subshell that constitutes the initial bound state of the active electron in the molecule. However, it has been demonstrated that this discrepancy essentially affects the inner subshells of the target for which the cross sections have minor contribution into the ionization process. Finally, Champion and co-workers have tested a third approach which consists in exhibiting a correct asymptotical Coulomb three-body wave function by describing the final state by the product of three Coulomb waves taking into account the interaction between the scattered ion and the nucleus, the interaction between the ejected electron and the nucleus, and the scattered ion-ejected electron interaction. Note that for this model (hereafter denoted CB1–3CW for three-body first Born with correct boundary conditions) we have the well-known asymptotically correct Coulomb three-body wave function for the ejected electron and the scattered proton in the field of the residual ion.

Furthermore, it is important to note that the bound wave functions used in the present water molecular description correspond to a given orientation of the target molecule, commonly expressed via the Euler angles (α, β, γ). Thus, the above-cited multi-differential cross sections refer to the ionization of a single oriented water molecule and need then to be averaged over the Euler solid angle $\mathrm{d}\Omega_\mathrm{Euler} = \sin\beta\,\mathrm{d}\alpha\,\mathrm{d}\beta\,\mathrm{d}\gamma$ to be comparable to those experimentally measured, what may be analytically easily carried out thanks to the property of the rotation matrix.[44] Note that this procedure is obviously performed for each of the $N=5$ orbitals of the water molecule and the multiple differential cross sections presented in the sequel correspond to "global" differential cross sections i.e., obtained by summing up all the sub-shell contributions labelled j and then weighted by the number N_elec of electrons per orbital, i.e., $N_\mathrm{elec}=2$. Thus, we write

$$\frac{\mathrm{d}^2\sigma}{\mathrm{d}\Omega_\mathrm{e}\mathrm{d}E_\mathrm{e}} = \sum_{j=1}^{N=5} N_\mathrm{elec}\left[\frac{\mathrm{d}^2\sigma}{\mathrm{d}\Omega_\mathrm{e}\mathrm{d}E_\mathrm{e}}\right]_j. \tag{32}$$

In further steps, singly-differential and total cross sections (SDCS and TCS, respectively) are obtained by numerical integrations of the DDCS over the ejected direction $\mathrm{d}\Omega_\mathrm{e}$ and the kinetic energy transfer E_e, respectively.

4.1.3 Angular distributions of the secondary ejected electrons

Figure 10.2 shows a comparison between the experimental DDCS taken from Toburen and Wilson[10] and the results provided by Boudrioua et al.[8] within the two above-cited 1st Born models, namely, the CB1-CWB and the CB1-DWB approaches for a proton incident energy of 0.5 MeV and for ejected energies E_e ranging from 12 eV to 750 eV. Except for small angles and at some fixed ejected electron energies, namely, 100 eV, 250 eV, and 750 eV, the CB1-CWB model (solid line) reproduces with a good agreement the experimental observations. This disagreement may be explained by the fact that in the present CB1-CWB calculations, the authors didn't take into account the above-cited ECC process which causes an increase of the doubly differential cross sections at low ejected angles. This process is all the more conspicuous that the velocity of the ejected electron is close to that of the scattered proton and may be seen as a classical capture of a bound

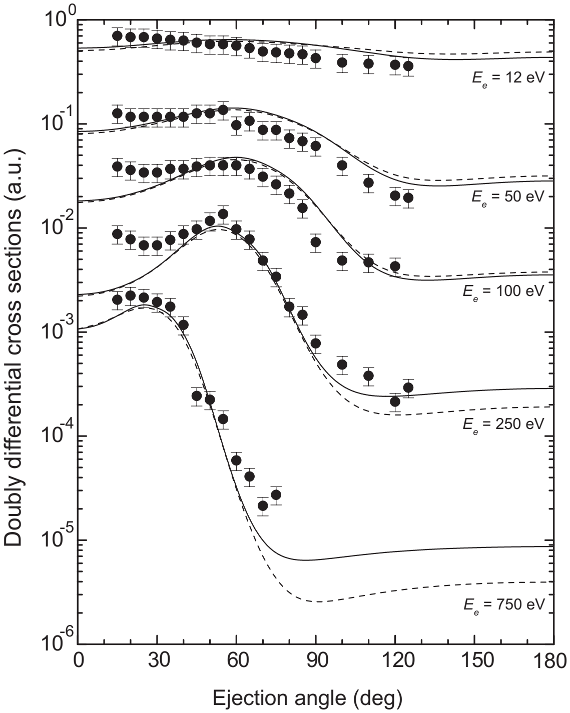

Figure 10.2 Doubly differential cross sections for single ionization of water vapour by 0.5 MeV protons for different ejected electron energies as a function of the ejection angle. Theory: CB1-CWB model (solid line), CB1-DWB model (dashed line). Experiments: circles from Toburen and Wilson.[10]

electron from the target molecule into a continuum state of the proton. The "captured" electron is then emitted in the moving frame of the proton.

Furthermore and as already reported by Rudd et al.,[46] Boudrioua et al.,[8] clearly underline the fact that the CB1-DWB and CB1-CWB methods yield nearly identical cross sections except at large angles where the difference between the two approaches is more pronounced. The authors also report that the two approaches begin to differ from each other by a small amount especially with increasing ejection angles and energies at fixed incident energy.

To improve the agreement between the experimental and the theoretical DDCS for protons, Boudrioua et al. have recently proposed to describe the water ionization process within the CB1-2CW approach i.e., in describing the scattered projectile by means of a Coulomb wave function.[8] However, as shown in Figure 10.3 for incident proton energy of 0.5 MeV

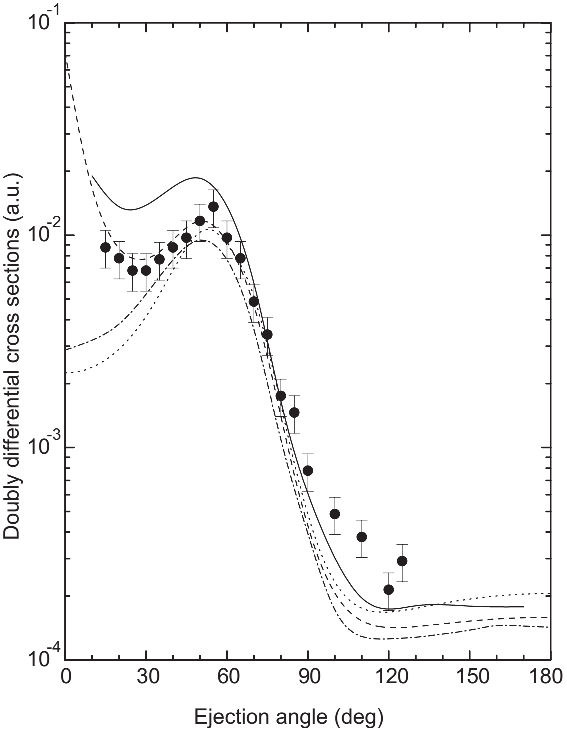

Figure 10.3 Doubly differential cross sections for single ionization of water vapour by 0.5 MeV protons impact with the ejection of a 250 eV electron as a function of the ejection angle θ_e. The lines correspond to the present different models used: CB1-3CW model (solid line), CB1-CWB model (dotted line), CB1-CWB model with the Salin factor (dashed line), CB1-2CW model (dash and dotted line) whereas the experiments of Toburen and Wilson[10] are represented by circles.

and an ejected electron of 250 eV, it appears that both the CB1-CWB and CB1-2CW models are unable to explain the large enhancement of the DDCS for small angles because none of these models treats the interaction between the scattered proton and the ejected electron.

In a second step, Boudrioua et al.[8] have also introduced a first-order correction factor S, namely, the well-known Salin factor[68] into the CB1-CWB model, which consists in introducing the mechanism of electron transfer to the continuum as a multiplicative factor given by

$$S = \frac{2\pi\gamma}{1 - e^{-2\pi\gamma}}, \tag{33}$$

with $\gamma = Z/p$ where Z denotes the *dynamical effective charge* defined as $Z = 1 - p/v_i$ where $\vec{p} = \vec{k}_e - \vec{v}_i$ is the final electron velocity measured from a reference frame fixed at the projectile.

Thus, when the electron moves with a velocity close to that of the projectile ($p \cong 0$), it travels in a continuum state of the projectile which lies just above the threshold of the corresponding continuum spectrum, whereas for an electron ejected in a soft collision ($k_e << k_i$), $Z \cong 0$ what indicates that the ejected electron moves only in the field of the target. An excellent agreement with the experimental data was then observed in particular at small ejection angles whereas a less satisfactory accord was reported for larger angles as already observed by Madison[49] for helium targets impacted by 100 keV and 200 keV protons.

In addition, in their study, Boudrioua et al.[8] have studied the water ionization process in the CB1-3CW framework and reported a better agreement in the large ejected angle region. However, it was noted that the obtained DDCS largely overestimated the experimental observations at small angles. As a matter of fact, the CB1-3CW model exhibits a correct asymptotic Coulomb three-body wave function for the scattered proton and the ejected electron in the residual ion field. Finally, let us note that the Salin factor depends on a *dynamical effective charge* whereas in the CB1-3CW model the projectile nuclear charge is considered.

Similar observations were reported in Figure 10.4 for α-particles impinging on water molecules.

Very good agreement was then observed between the experimental and the theoretical CB1-CWB results in all cases, except for the lower ejection energy reported i.e., for $E_e = 19.2$ eV for which they obtained DDCS overestimate the experimental data essentially at small angles ($\theta_e < 60°$ and $\theta_e > 120°$). For $\theta_e > 60°$, the observed agreement becomes better for each

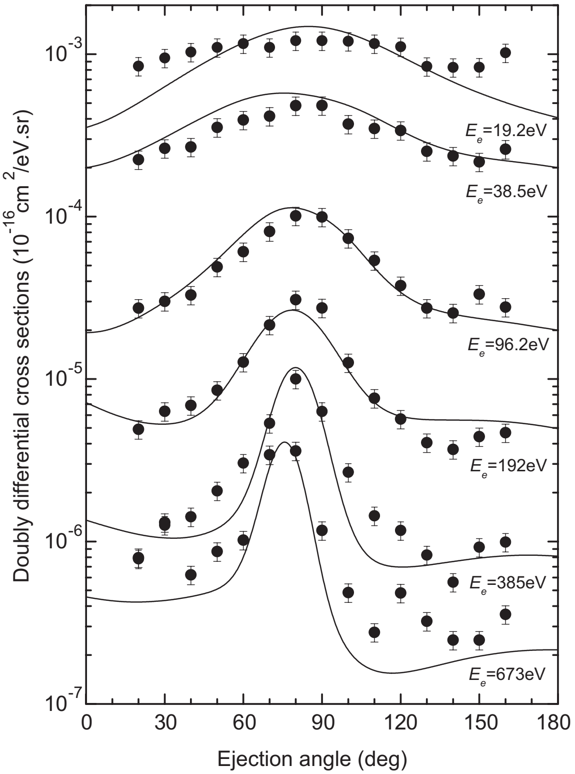

Figure 10.4 Doubly differential cross sections for water ionization by α-particles of 6.0 MeV/u. The experimental data (solid circles) of Ohsawa et al.[19] are compared to the theoretical results (CB1-CWB model) for 6 different ejected electron energies, namely, $E_e = 19.2$ eV, 38.5 eV, 96.2 eV, 192 eV, 385 eV, and 673 eV.

ejected energy here considered exhibiting in particular the existence of the well-known binary-encounter peak whose localisation is here well reproduced, namely, from about 85–90 at $E_e = 19.2$ eV to about 79–80° at $E_e = 673$ eV.

Finally, Figure 10.5 compares the CB1-CWB DDCS (solid line) reported by Dal Cappello et al.[22] to recent experimental measurements for 6 MeV/u C^{6+} ions ejecting electrons of different energies ranging from 9.6 eV to 384 eV. A good agreement is generally reported over the whole range of ejected electron energies with nevertheless slight discrepancies for $\theta_e \cong 70°–80°$. However, as previously, we observe that the position of the binary-encounter peak is well reproduced. Furthermore, we have reported in Figure 10.5, a comparison between the CB1-CWB DDCS of

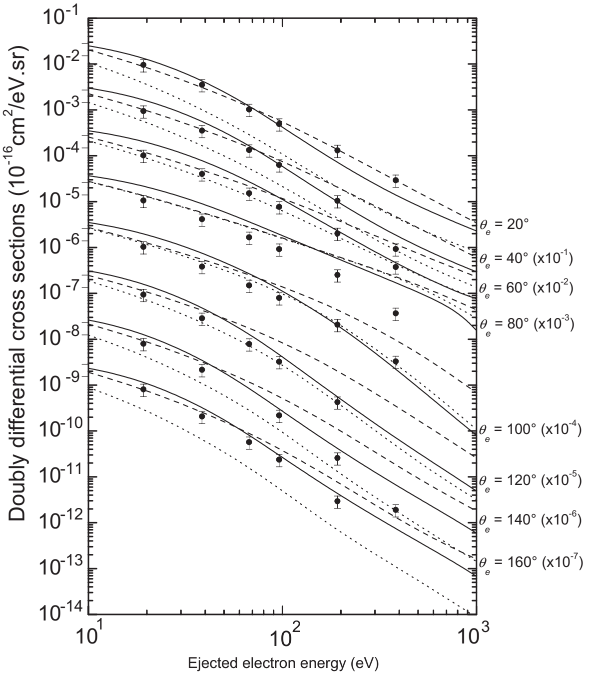

Figure 10.5 Doubly differential cross sections for single ionization of water vapour by 6.0 MeV/u C^{6+} ions for different ejection angles ($20° < \theta_e < 160°$) as a function of the ejected electron energy. The theoretical CB1-CWB results are reported by a solid line whereas the semi-empirical HKS results are represented by a dashed line for the original HKS model[31] and by a dotted line for the expression given by Bernal and Liendo.[34] The experimental measurements are represented by solid circles. Multiplicative factors are used for a better clarity in the plot.

Dal Cappello et al. and those obtained by the two HKS models discussed above, namely, the original version from Hansen and Kocbach[31] (see Eq. (6)) and that slightly modified and proposed by Bernal and Liendo[34] (see Eq. (10)). Minor discrepancies may be observed with in particular a better agreement exhibited by the original HKS model version (dashed line) with nevertheless an overestimation for the large ejection angles, which is all the more important that the energy increases ($E_e > 200$ eV). In comparison, the modified HKS model underestimates the experimental results at backward angles, what is mainly due to the use of hydrogenic wave functions to describe the bound electron initial state instead of an accurate molecular wave function as it is the case for the Dal Cappello calculations. Indeed, the agreement reported by the authors seems better even if we note a slight overestimation in particular for the high energies ($E_e > 200$ eV) when the ejection angle tends towards the binary-encounter peak ($\theta_e \cong 70°–80°$).

4.1.4 Energy spectra of the secondary ejected electrons

By integration of the DDCS with respect to emission angle θ_e, the singly differential cross sections may be obtained. Figure 10.6 shows a comparison between the available experimental data[10, 13] and the theoretical results performed by Boudrioua et al.[8] in the CB1-CWB model for protons in water. A reasonably good agreement between the experiments and the present 1st Born results may be observed especially for ejected electron energies greater than 10 eV, the Auger electron peak being obviously not reproduced

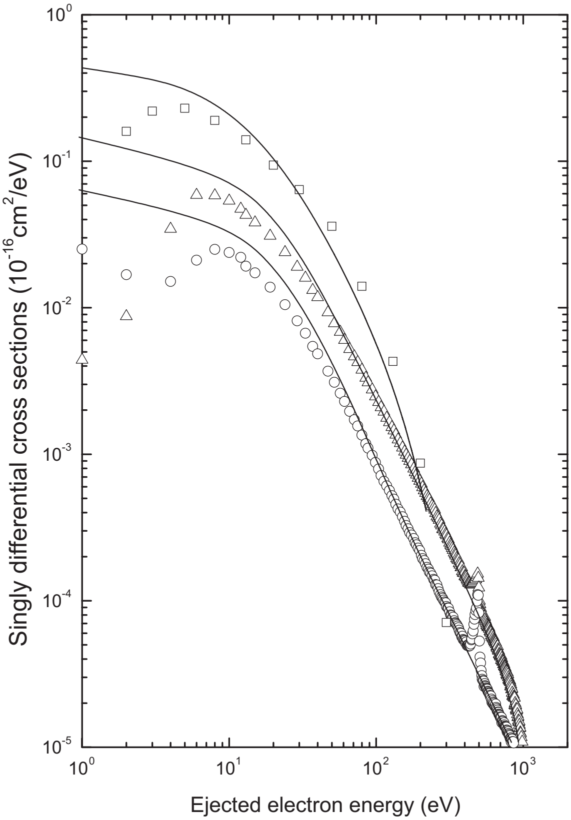

Figure 10.6 Singly differential cross sections for ejection of electrons by protons in water vapour as a function of ejected electron energy. Experimental data taken from Toburen and Wilson[10] (open triangles for 0.5 MeV and open circles for 1.5 MeV) and from Bolorizadeh and Rudd[13] (open squares for 100 keV).

since not included in the present used model. For lower ejected energies ($E_e < 10$ eV), the agreement is obviously less satisfactory, the kinematics being far from the domain of applicability of the 1st Born approximation.

Similarly, Figure 10.7 shows a comparison between the experimental SDCS measurements for C^{6+} ions reported in Dal Cappello et al.[22] and the CB1-CWB calculations as well as the existing semi-empirical (Rudd and HKS) predictions.

A good agreement is generally observed for both the results with in particular a regular underestimation in the low-energy regime and a constant overestimation for high energies ($E_e > 200$ eV). However, we notice that the best agreement is still obtained with the original HKS model in

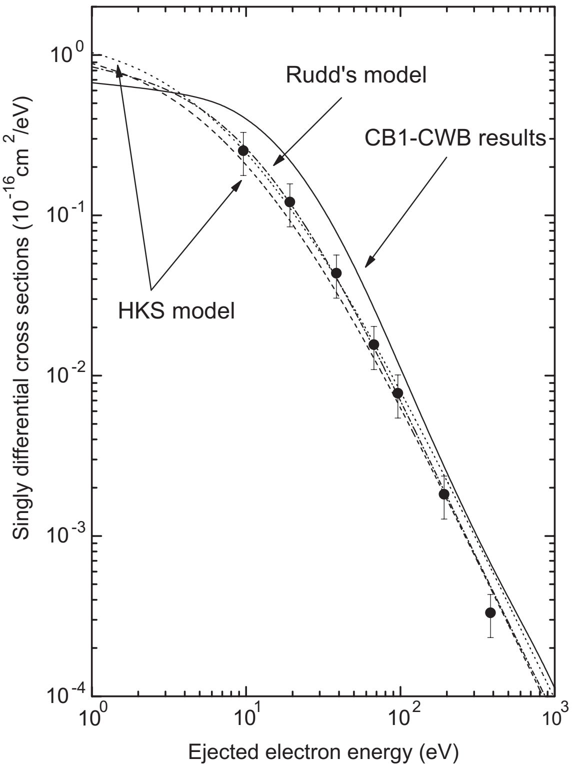

Figure 10.7 Singly differential cross sections for ejection of electrons by 6.0 MeV/u C^{6+} ions in water vapour as a function of the ejected electron energy. The theoretical CB1-CWB results are reported by a solid line whereas the semi-empirical HKS results are represented by a dashed line for the original HKS model[31] and by a dotted line for the expression given by Bernal and Liendo.[34] The experimental measurements are represented by solid circles. Additionally, the Rudd's results are represented by a dash-and-dotted line.

the whole ejected electron energy range. Furthermore, we clearly observe that the CB1-CWB theoretical results generally tend to overestimate the experimental measurements, especially at low-energies ($E_e < 200$ eV). In addition, we note that the results provided by the Rudd model (dash-dot-dotted line) are in remarkably good agreement with the present experimental measurements in the whole ejected electron energy range.

4.1.5 Total ionization cross sections

Figure 10.8 depicts an extensive comparison between the theoretical CB1-CWB TCS (solid line) for protons, α-particles, and carbon ions and the available experimental measurements. Additionally, we have reported the semi-empirical Rudd's and HKS predictions (dashed line and dotted

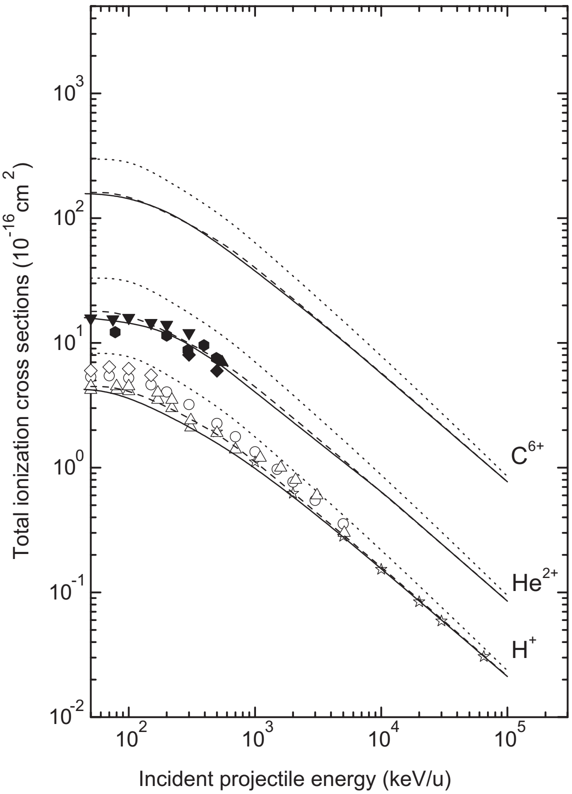

Figure 10.8 Total cross section as a function of the incident energy (keV/u). The theoretical CB1-CWB results are reported by a solid line whereas the semi-empirical HKS and Rudd's results are represented by a dotted and a dashed line, respectively. The experimental measurements taken from various sources are represented by symbols (for more details we refer the reader to Refs. 8, 9, 22).

line, respectively). We clearly observe a very good agreement between the free-parameter calculations of Champion and co-workers[8, 9, 22] and the semi-empirical predictions of the Rudd's model (initially developed for protons) over the whole incident energy range investigated in the present work (50 keV/u–100 MeV/u). On the contrary, the HKS model exhibits large discrepancies with the theoretical results as well as the experimental measurements.

4.1.6 From vapour to liquid water

Water ionization by charged particle impact (electrons as well as heavy charged particles) has been a matter of active research since the 1970s particularly in the field of radiobiology for modelling the radio-induced damages, the biological matter being commonly simulated by water. Numerical track-structure Monte Carlo simulations were then successfully developed for describing the charged particle transport in biological medium and then providing a detailed (macroscopic or microscopic) description of the three-dimensional energetic deposit cartography. To that end, the modelling of the ion-induced ionizing processes in water and more particularly of ionization is of prime importance. However, due to the scarcity of experimental measurements in its liquid phase, water was essentially studied in its vapour phase by assuming that describing the particle track-structure in liquid matter could be done, in a first step, either by applying the well-known "gas-phase approximation" i.e., via a simple linear extrapolation to unit density environment of the liquid or by converting the highly excited Rydberg states occurring in gaseous water into ionizations (see for example Turner et al.[69]). Besides, note that some authors[36] have also used the above-cited Rudd's model by adjusting the fitting parameters to the liquid case in particular the binding energies whose values differ from gaseous to liquid water by about 2–4 eV essentially for the three outermost subshells.[36]

Comparatively, the treatment of liquid water ionization by heavy charged particles was less studied and presents still today a challenge for radiobiologists who are interested by knowing the degree to which non-scaling effects are important in simulating ion transport in biological matter. In this context, various semi-empirical models were developed since the pioneer works of the Oak Ridge group.[70] In this framework, DDCS and SDCS were calculated within the 1st Born approximation by taking advantage that in this framework the doubly differential ionization cross sections were related to the energy-loss function $\eta(E, K) = \mathrm{Im}[\frac{-1}{\varepsilon(E,K)}]$ where ε (E,K) denotes the dielectric-response function with E for the energy transfer and *K* for the magnitude of the momentum transfer on a single collision. Thus, similarly to their previous study on electron impact ionization in liquid water, Dingfelder et al.[36] proposed an extension of their empirical model based on optical measurements, namely, reflectance measurements for describing the liquid water ionization by fast protons ($E_i > 100\,\text{keV/u}$). In brief, the imaginary part of the dielectric-response function is modelled in the optical limit, i.e., at momentum transfer *K* by a superposition of Drude-like functions while the real part is analytically calculated by using the Kramers–Kronig relation. For more details we refer the reader to Dingfelder et al.[36] Furthermore, the model uses experimental data as well as theoretical constraints like sum rule and asymptotic behaviour and the momentum-transfer dependence for the continuum is introduced by an impulse approximation, in which a target electron is seen as nearly free at the moment of energy and momentum transfer whereas its binding through is taken equal to the instantaneous momentum of a stuck electron. Total cross sections were then reported for proton energies in the range from 500 keV to 10 MeV. Finally, to complete their study and then to investigate the low-energy regime ($E_i < 500\,\text{keV/u}$), the authors proposed to use the Rudd's model by adjusting the fitting parameters in order to reproduce the recommended ICRU stopping cross sections[71] for liquid water, which is the only relevant experimental information on the liquid phase. The authors also suggested taking into account a realistic partitioning into the molecular sub-shells, by adjusting in particular the sub-shell contributions of the dielectric model to those provided by the Rudd's model. The obtained values are reported below (see Table 10.5).

They also obtained total ionization cross sections are reported in Figure 10.9. It clearly appears that the vapour and liquid ionization cross sections differ essentially in the region below 100–200 keV, namely, precisely where the semi-empirical model of Rudd is used. On the contrary, when the dielectric-model is used, namely, for $E_i > 500\,\text{keV/u}$, only minor discrepancies are observed.

Table 10.5 Parameters for the proton ionization cross sections in liquid water[36]

A_1	B_1	C_1	D_1	E_1	A_2	B_2	C_2	D_2	α
1.02	82.0	0.45	−0.80	0.38	1.07	14.6	0.60	0.04	0.64

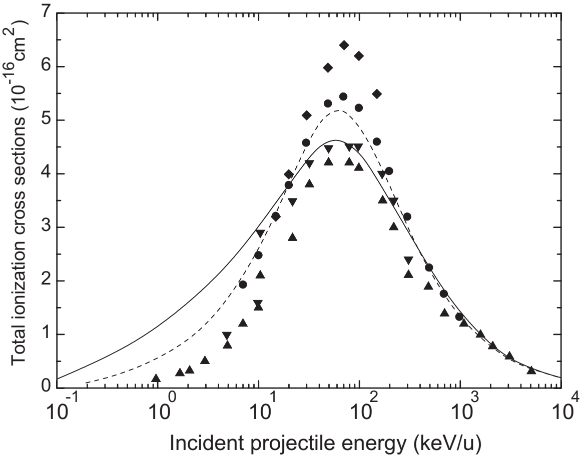

Figure 10.9 Total ionization cross sections as a function of the incident particle energies. Shown are the proton ionization cross sections for liquid and gaseous water (solid and dashed line, respectively) taken from Ref. 36 whereas the experimental data are similar to those reported above for total ionization cross sections of protons in water vapour.

4.1.7 Influence of the target description on the ionization cross sections

Describing the molecular ionization process at the multi-differential level undoubtedly needs an accurate description of the target in terms of electronic distribution. However, to overcome the difficult task of such multi-centre problems, like here for studying the water molecule ionization, we have seen that many authors used an atomic approach among which we find the above-cited Bragg additivity rule—which consists in writing the water cross sections as a mixture of H_2 and O_2 ones—and the complete neglected differential overlap (CNDO) approach. In this context, Olivera and co-workers[41] have already pointed out huge differences in terms of singly differential ionization cross sections for 70 keV protons in water vapour by comparing these two descriptive approaches within the CDW-EIS framework. A good agreement with experimental results taken from Bolorizadeh and Rudd[13] was then reported by the authors when the molecular description was used—except at very low ejected electron energies—whereas the Bragg's additivity addition of atomic singly differential cross sections clearly overestimated the experimental measurements at small electron energies. Note that similar observations were also reported by Senger and co-workers[42] who have calculated—within the 1st Born approximation—angular and energy distributions of δ-rays ejected from low-z molecular targets (including water vapour) impacted by protons and α-particles.

Very recently, Champion et al.[72] have also pointed out strong discrepancies between a CNDO approach and a full-molecular (LCAO-SCF) description. To do that, the authors have successively compared doubly and singly differential ionization cross sections calculated by using both the molecular wave function taken from Moccia[45] and a CNDO approach already used by many authors for describing the ionization process of simple molecules. The selected description was that proposed by Senger and co-workers[42] in which the isolated water molecule was modelled by means of oxygen and hydrogen orbitals, namely, O(1*s*), O(2*s*), O(2*p*), and H(1*s*). Furthermore, it must be noted that to avoid any changes in the theoretical results due to the variations in the molecular orbital binding energies, the authors have taken the same values for both calculations, namely, those provided by Moccia.[45]

The CB1-CWB DDCS also calculated for 500 keV protons are reported in Figure 10.10 (left panel). Evident discrepancies—within a factor 2—may be observed between the two water target descriptions, especially in the low ejection energy regime ($E_e < 100\,\text{eV}$) whereas the cross sections seem to be less sensitive to the molecular description for higher ejected energies. Similar conclusions may be drawn when singly differential cross sections are compared (see right panel of Figure 10.10). Surprisingly, the CB1-CWB SDCS seem to be in better agreement with measurements when the CNDO-initial state representation is used.

4.2 Theoretical description of the charge transfer process within the 1st Born approximation

4.2.1 Basic formalisms

In this section, we investigate the electron capture process induced by fast charged particles impinging on water target which still remains rarely approached in the literature. In fact, except the work of Olivera et al.[41] and that of Fainstein et al.[73] on the CDW-EIS method for single ionizing processes (capture as well as ionization) induced by protons in gaseous water, the quantum mechanical approaches are, to the best of our knowledge, represented only by the recent 1st Born predictions given by Houamer and co-workers[74] for proton projectiles. The theoretical framework used by the authors refers to the above-described CB1 model whose theoretical background is briefly reported in the sequel.

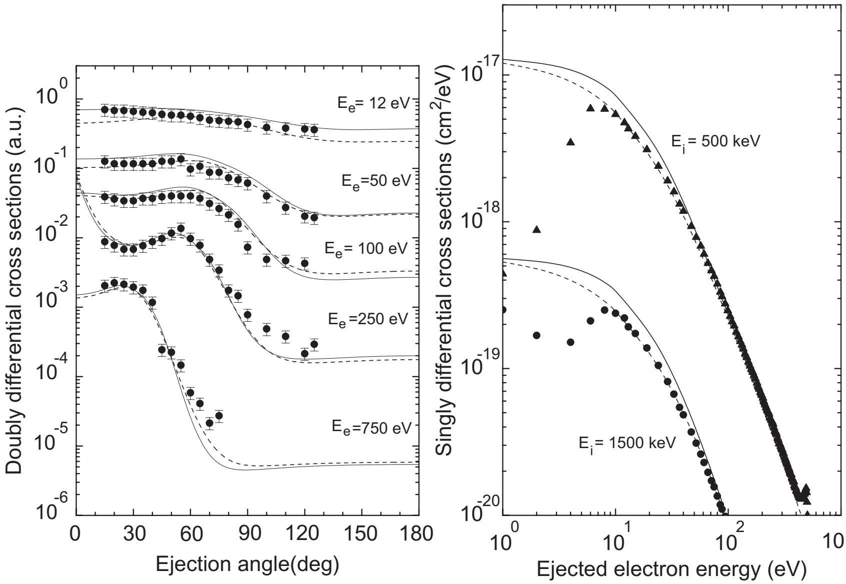

Figure 10.10 Left panel: doubly differential cross sections for single ionization of water vapour by 500 keV protons with different ejected electron energies as a function of the ejection angle θ_e. The calculations were performed within the 1st Born approximation (in the above-described CB1-CWB model) by including the Salin factor. The experimental results are taken from Bolorizadeh and Rudd.[13] Right panel: singly differential cross sections for water ionization by protons of different incident energies (500 keV and 1500 keV). The experimental results are taken from Toburen and Wilson.[10] In both cases, the theoretical results are obtained within the CB1-CWB model by using—for describing the water target—the molecular wave function taken from Moccia[45] and the CNDO approach (solid and dashed line, respectively).

Thus, similarly to the previously referred CB1-CWB approach for describing the ionization process, the multielectron collisional system can—for the single electron capture process—also be reduced to a one-active electron treatment. Indeed, if the long range part of the projectile-active electron interaction is preserved into the wave functions, the scattering matrix element may be rewritten as

$$\widetilde{T}_{fi}^{(1)} \cong \left\langle \chi_f^- \left| -\frac{Z_P}{r_{01}} + \frac{Z_P}{r_0} \right| \chi_i^+ \right\rangle, \tag{34}$$

with

$$\chi_i^+ \cong \phi(\vec{k}_i, \vec{r}_0)\, u(\vec{r}_1) \exp[-i(Z_P/v_i) \ln(v_i r_0 - \tilde{v}_i . \vec{r}_0)], \tag{35}$$

and

$$\chi_{\mathrm{f}}^{-} = \phi(\vec{k}_{\mathrm{s}}, \vec{r}_0)\xi_f(\vec{r}_{01}) \exp[-i(Z_{\mathrm{c}}/v_i)\ln(v_i r_0 - \vec{v}_i.\vec{r}_0)], \tag{36}$$

where $\xi_{\mathrm{f}}(\vec{r}_{01})$ here represents a projectile bound state and Z_{c} the charge of the residual core. Thus, Eq. (34) can be written as

$$\begin{aligned}\widetilde{T}_{fi}^{(1)} = (b v_{\mathrm{i}})^{-2iZ_{\mathrm{c}}/v_{\mathrm{i}}} \int \mathrm{d}\vec{r}_0 \mathrm{d}\vec{r}_1 [\phi(\vec{k}_{\mathrm{s}}, \vec{r}_0)\xi_f(\vec{r}_{01})]^* \left(-\frac{Z_{\mathrm{P}}}{r_{01}} + \frac{Z_{\mathrm{P}}}{r_0}\right)\phi(\vec{k}_{\mathrm{i}}, \vec{r}_0)u(\vec{r}_1) \\ \times \exp[i(Z_{\mathrm{c}} - Z_{\mathrm{P}})/v_{\mathrm{i}}]\ln(v_{\mathrm{i}} r_0 - \vec{v}_{\mathrm{i}}.\vec{r}_0)].\end{aligned} \tag{37}$$

Note that if $\mathrm{Z_c} = \mathrm{Z_P}$, Eq. (37) can be reduced to

$$\widehat{T}_{fi}^{(1)} = \left\langle \phi(\vec{k}_{\mathrm{s}}, \vec{r}_0)\xi_{\mathrm{f}}(\vec{r}_{01}) \right| - \frac{Z_{\mathrm{P}}}{r_{01}} + \frac{Z_{\mathrm{P}}}{r_0} \left| \phi(\vec{k}_{\mathrm{i}}, \vec{r}_0)u(\vec{r}_1) \right\rangle, \tag{38}$$

where $\xi_{\mathrm{f}}(\vec{r}_{01})$ refers to an hydrogenic wave function, what coincides with the expression provided by Jackson and Schiff [54] for the case of proton beam impact on atomic hydrogen.

Furthermore, it is interesting to quote that the scattering matrix element also obtained is in agreement with that reported for ionization in Eq. (30).

In order to calculate the singly differential cross sections as a function of the projectile angular dispersion, we obviously need to take into account all the particles of the collisional system and then consider the scattering matrix element $T_{fi}(\vec{K})$. However, it is possible to show that this latter is simply related to the matrix element $\widehat{T}_{fi}(\vec{K})$ through the expression

$$\begin{aligned}T_{fi}(\vec{K}) = \frac{1}{4\pi^2}\int \mathrm{d}\vec{b}\mathrm{d}\vec{\eta} \exp[i(\vec{\eta} - \vec{\eta}').\vec{b}] \exp[\frac{i}{v_{\mathrm{i}}}\int_{-\infty}^{\infty} \mathrm{d}t V_{\mathrm{s}}(\vec{r}_0)] b^{-2iZ_{\mathrm{c}}/v_{\mathrm{i}}} \\ \times \prod_{c=1}^{N} b_c^{2iZ_{\mathrm{P}}Z_{\mathrm{c}}/v_{\mathrm{i}}} \widehat{T}_{fi}(\vec{K}),\end{aligned} \tag{39}$$

which is the Fourier transform of the Fourier antitransform of $\widehat{T}_{fi}(\vec{K})$ (see Eqs. (27) and (37) and where $\vec{\eta}$ refers to the component of $\vec{K}$ perpendicular to the impact velocity $\vec{v}_{\mathrm{i}}$.

Then, similarly to the ionization case, the singly differential cross sections per molecular subshell $\frac{\mathrm{d}\sigma}{\mathrm{d}\theta_s}$ (where θ_{s} represents the scattering projectile angle) are finally averaged over all the target orientations and then written as

$$\frac{\mathrm{d}\sigma}{\mathrm{d}\theta_{\mathrm{s}}} = (2\pi \sin\theta_{\mathrm{s}})\frac{\mathrm{d}\sigma}{\mathrm{d}\Omega_{\mathrm{s}}} \equiv (2\pi \sin\theta_{\mathrm{s}})\frac{M_{\mathrm{P}}^2}{4\pi^2}(\frac{1}{8\pi^2})\int |T_{fi}|^2 \mathrm{d}\Omega_{\mathrm{Euler}} \tag{40}$$

where M_{P} refers to the incident proton mass.

Thus, for low scattering angles ($\theta_s << 1$), the SDCS take the simple form

$$\frac{d\sigma}{d\theta_s} \cong (2\pi \sin\theta_s) \frac{M_P^2 . \theta_s}{16\pi^3} \int |T_{fi}|^2 d\Omega_{\text{Euler}}. \tag{41}$$

Finally, note that the scattering matrix element T_{fi} being dependent on the impacted molecular subshell, the procedure here described is obviously performed for each of the $N = 5$ orbitals of the water molecule. Thus, similarly to the ionization case, the "global" singly differential cross sections are here also obtained by summing up all the j sub-shell contributions $[\frac{d\sigma}{d\theta_s}]_j$ and then weighted by the number Nelec (=2) of electrons per orbital. Thus, we write

$$\frac{d\sigma}{d\theta_s} = \sum_{j=1}^{N=5} N_{\text{elec}} \left[\frac{d\sigma}{d\theta_s}\right]_j . \tag{42}$$

The total charge transfer cross section is finally obtained by writing that

$$\sigma = \int d\vec{b} \left|A_{fi}(\vec{b})\right|^2 \equiv \int d\vec{b} \left|\hat{a}_{fi}(\vec{b})\right|^2 \equiv \frac{1}{(2\pi\, v_i)^2} \int d\vec{\eta} \left|\widehat{T}_{fi}(\vec{K})\right|^2, \tag{43}$$

where the Parseval identity has been employed.

In conclusion, it clearly appears from Eqs. (41) and (43) that when cross sections differential in the projectile scattering angle are calculated, we cannot ignore the interaction of the projectile with the target nuclei and the passive electrons, whose influence may be not neglected. However, when TCS are calculated, these latter play no rôle since the transition is simply produced by the interaction of the projectile with the active electron.

4.2.2 Total cross sections

We report in Figure 10.11 the total cross sections provided by the CB1 treatment developed by Houamer and co-workers.[74] A good agreement may be observed with the experimental available data in particular for impact energies greater than 100 keV/u. In comparison, the predictions given by the above-cited semi-empirical models are—for the major part and in the overall energy range—in good agreement with the 1st Born predictions, except those provided by the Rudd's model which largely overestimate both the experimental data and the other semi-empirical predictions.

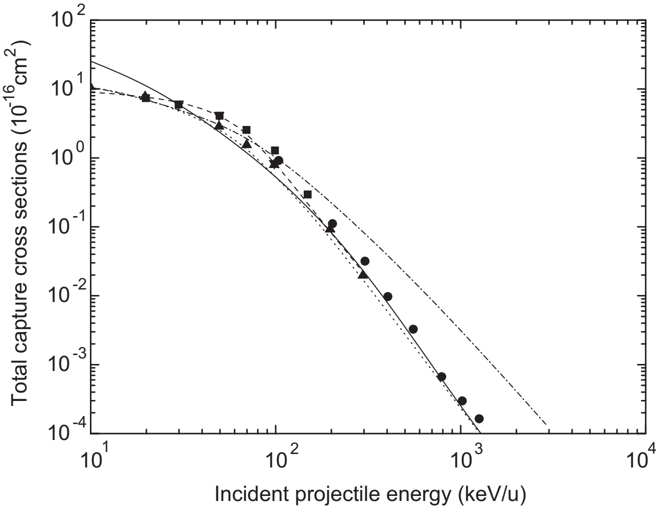

Figure 10.11 Total cross sections for charge transfer induced by protons in water. Comparison between the CB1 predictions from Houamer et al.[74] (solid line) and the results provided by the semi-empirical model of Endo et al [39] (dashed line), Dingfelder et al.[36] (dotted line) and Rudd et al.[12] (dash-and-dotted line). The experimental measurements are taken from Dagnac et al.[37] (solid down triangles), Gobet et al.[16] (solid squares), Date et al.[75] (solid up triangles), Toburen [76] (solid circles).

5. CONCLUSIONS

Single electron ionization and single electron capture of water molecules impacted by charged heavy particles—processes which are of interest for medical applications—have been here theoretically studied within the 1st Born approximation framework.

From multiple differential to total cross sections, the present work reports a detailed description of the ion-induced ionization process in pointing out in particular the rôle played by the target representation in the theoretical modeling. The cross sections also provided have been then compared to a large set of experimental measurements as well as existing semi-empirical predictions in order to clearly identify the pre-requested kinematical conditions of the present perturbative treatment of water ionization. Besides, the influence of the thermodynamical phase of water has been also studied in order to assess its potential impact in numerical simulations dealing with charged particle transport in biological matter.

Finally, proton-induced electron capture has been investigated and then emphasized an overall good agreement in terms of total cross sections between the present 1st Born predictions and the rare existing experimental data.

REFERENCES

1. Amaldi, U.; Kraft, G. Radiotherapy with beams of carbon ions. *Rep. Prog. Phys.* **2005**, *68*, 1861.
2. Wilson, R. R. Radiological use of fast protons. *Radiology* **1946**, *47*, 487.
3. Stone, R. S.; Lawrence, J. H.; Aebersold, P. C. A preliminary report on the use of fast neutrons in the treatment of malignant disease. *Radiology* **1940**, *35*, 322.
4. Lawrence, J. H.; Tobias, C. A.; Linfoot, J. A., et al. Heavy-particle therapy in acromegaly and Cushing disease. *JAMA* **1976**, *235*, 2307.
5. Berger, M. J. Penetration of proton beams through water I. Depth-dose distribution, spectra and LET distribution; National Institute of Standards and Technology: Gaithersburg, MD, 1993; NISTIR Publication 5226.
6. Incerti, S.; Ivanchenko, A.; Karamitros, M., et al. Comparison of GEANT4 very low energy cross section models with experimental data in water. *Med. Phys.* **2010**, *37*, 4692.
7. Belkić, Dž. Reviews of theories on ionization in fast ion-impact collisions with prospects for applications to hadrontherapy. *J. Math. Chem.* **2010**, *47*, 1366.
8. Boudrioua, O.; Champion, C.; Dal Cappello, C., et al. Ab-initio calculation of differential and total cross sections for the ionization of water vapour by protons. *Phys. Rev. A* **2007**, *75*, 022720.
9. Champion, C.; Boudrioua, O.; Dal Cappello, C., et al. Theoretical and experimental investigations of electron emission in He^{2+}+H_20 collision. *Phys. Rev. A* **2007**, *75*, 032724.
10. Toburen, L. H.; Wilson, W. E. Energy and angular distributions of electrons ejected from water vapour by 0.3–1.5 MeV protons. *J. Chem. Phys.* **1977**, *66*, 5202.
11. Toburen, L. H.; Wilson, W. E.; Popowich, R. J. Secondary electron emission from ionization of water vapour by 0.3- to 2.0-MeV He^+ and He^{2+} Ions. *Radiat. Res.* **1980**, *82*, 27.
12. Rudd, M. E.; DuBois, R. D.; Toburen, L. H., et al. Cross sections for ionization of gases by 5–4000-keV protons and for electron capture by 5–150-keV protons. *Phys. Rev. A* **1983**, *28*, 3244.Rudd, M. E.; Goffe, T.V.; DuBois, R. D., et al. Cross sections for ionization of water vapour by 7–4000-keV protons. *Phys. Rev. A* **1985**, *31*, 492.Rudd, M. E.; Goffe, T. V.; Itoh, A. Ionization cross sections for 10–300-keV/u and electron-capture cross sections for 5–150-keV/u He^{2+} ions in gases. *Phys Rev A* **1985**, *32*, 2128.Rudd, M. E.; Itoh, A.; Goffe, T.V. Cross sections for ionization, capture, and loss for 5–450-keV He+ on water vapour. *Phys. Rev. A* **1985**, *32*, 2499.
13. Bolorizadeh, M. A.; Rudd, M. E. Angular and energy dependence of cross sections for ejection of electrons from water vapour. *Phys. Rev. A* **1986**, *33*, 888.
14. Gibson, D. K.; Reid, I. D. Energy and angular distributions of electrons ejected from various gases by 50 keV protons. *Radiat. Res.* **1987**, *112*, 418.
15. Werner, U.; Beckord, K.; Becker, J., et al. 3D imaging of the collision-induced coulomb fragmentation of water molecules. *Phys. Rev. Lett.* **1995**, *74*, 1962.
16. Gobet, F.; Farizon, B.; Farizon, M., et al. Total, partial, and electron-capture cross sections for ionization of water vapour by 20–150 keV protons. *Phys. Rev. Lett.* **2001**, *86*, 3751.
17. Straub, H. C.; Lindsay, B. G.; Smith, K. A., et al. Absolute partial cross sections for electron-impact ionization of H_2O and D_2O from threshold to 100 eV. *J. Chem. Phys.* **1998**, *108*, 109.
18. Rudolph, P. S.; Melton, C. E. Experimental and theoretical considerations for ionization of simple Hydrocarbons, H_2, D_2, O_2, H_2O, and the rare gases by 2.2-MeV α particles and by electrons in a mass spectrometer. *J. Chem. Phys.* **1966**, *45*, 2227.
19. Ohsawa, D.; Sato, Y.; Okada, Y., et al. 6.0–10.0-MeV/u He^{2+}-ion-induced electron emission from water vapour. *Phys. Rev. A* **2005**, *72*, 062710.
20. Rudd, M. E. User-friendly model for the energy distribution of electrons from proton or electron collisions. *Nucl. Tracks Radiat. Meas.* **1989**, *16*, 213.

21. Montenegro, E. C.; Shah, M. B.; Luna, H., et al. Water fragmentation and energy loss by carbon ions at the distal region of the Bragg peak. *Phys. Rev. Lett.* **2007**, *99*, 213201.
22. Dal Cappello, C.; Champion, C.; Boudrioua, O., et al. Theoretical and experimental investigations of electron emission in C^{6+}+H_2O collisions. *Nucl. Instrum. Methods Phys. Res., Sect. B* **2009**, *267*, 781.
23. Lindsay, B. G.; Sieglaff, D. R.; Smith, K. A., et al. Charge transfer of 0.5-, 1.5-, and 5-keV protons with H_2O: absolute differential and integral cross sections. *Phys. Rev. A* **1997**, *55*, 3945.
24. Luna, H.; de Barros, A. L. F.; Wyer, J. A., et al. Water-molecule dissociation by proton and hydrogen impact. *Phys. Rev. A* **2007**, *75*, 042711.
25. Abu-Haija, O.; Kamber, E.Y.; Ferguson, S. M. Single-electron capture by He^{2+} ions from triatomic molecules. *Nucl. Instrum. Methods Phys. Res., Sect. B* **2003**, *205*, 634.
26. Greenwood, B.; Mawhorter, R. J.; Čadež, I., et al. The contribution of charge exchange to extreme ultra-violet and X-ray astronomy. *Phys. Scr.* **2004**, *T110*, 358.
27. Seredyuk, B.; McCullough, R. W.; Tawara, H., et al. Charge exchange and dissociative processes in collisions of slow He^{2+} ions with H_2O. *Phys. Rev. A* **2005**, *71*, 022705.
28. Mawhorter, J.; Chutjian, A.; Cravens, T. E., et al. Absolute single and multiple charge exchange cross sections for highly charged C, O, and Ne ions on H_2O, CO, and CO_2. *Phys. Rev. A* **2007**, *75*, 032704.
29. Bodewits, D.; Hoekstra, R. Electron capture in collisions between O^{6+} ions and H_2O molecules. *Phys. Rev. A* **2007**, *76*, 032703.
30. Uehara, S.; Nikjoo, H. Monte Carlo track structure code for low-energy alpha-particles in water. *J. Phys. Chem.* **2002**, *106*, 11051.
31. Hansen, J. P.; Kocbach, L. Ejection angles of fast delta electrons from K-shell ionization induced by energetic ions. *J. Phys. B* **1989**, *22*, L71.
32. Stolterfoht, N.; DuBois, R.; Rivarola, R. D. *In electron emission in heavy ion-atom collisions*; Springer: Berlin, 1997.
33. Rudd, M. E.; Kim, Y.-K.; Märk, T. D. et al, Technical Report 55, International Commissions on Radiation Units and Measurements, Bethesda, MD, 1996.
34. Bernal, M. A.; Liendo, J. A. The HKS model for electron production in liquid water by light ions. *Nucl. Instrum. Methods Phys. Res., Sect. B* **2006**, *251*, 171 Bernal, M.A.; Liendo, J.A. Inelastic-collision cross sections for the interactions of totally stripped H, He and C ions with liquid water, *Nucl. Instrum. Methods Phys. Res., B,***2007**, *262*, 1.
35. Toburen, L. H.; Nakai, M. Y.; Langley, R. A. Measurement of high-energy charge-transfer cross sections for incident protons and atomic hydrogen in various gases. *Phys. Rev.* **1968**, *171*, 114.
36. Dingfelder, M.; Inokuti, M.; Paretzke, H. G. Inelastic-collision cross sections of liquid water for interactions of energetic protons. *Radiat. Phys. Chem.* **2000**, *59*, 255.
37. Dagnac, R.; Blanc, D.; Molina, D. A study on the collision of hydrogen ions H_1^+, H_2^+ and H_3^+ with a water-vapour target. *J. Phys. B* **1970**, *3*, 1239.
38. Green, A. E. S.; McNeal, R. J. Analytic cross sections for inelastic collisions of protons and hydrogen atoms with atomic and molecular gases. *J. Geophys. Res.* **1971**, *76*, 133.Miller, J. H.; Green, A. E. S. Proton energy degradation in water vapour. *Radiat. Res.* **1973**, *54*, 343.
39. Endo, S.; Yoshida, E.; Nikjoo, H., et al. A Monte Carlo track structure code for low energy protons. *Nucl. Instrum. Methods Phys. Res., Sect. B* **2002**, *194*, 123.
40. Sataka, M.; Yagishita, A.; Nakai, Y. Measurement of charge-changing cross sections in collisions of He and He^+ with H_2, O_2, CH_4, CO and CO_2. *J. Phys. B* **1990**, *23*, 1225.
41. Olivera, G. H.; Martinez, A. E.; Rivarola, R. D., et al. Theoretical calculation of electronic stopping power of water vapour by proton impact. *Radiat. Res.* **1995**, *144*, 241.Olivera, G. H.; Fainstein, P. D.; Rivarola, R. D. Contribution from the inner shell

of water vapour to dose profiles under proton and alpha particle irradiation. *Phys. Med. Biol.* **1996**, *41*, 1633.

42. Senger, B.; Rechenmann, R.V. Angular and energy distributions of Δ-rays ejected from low-z molecular targets by incident protons and α particles. *Nucl. Instrum. Methods Phys. Res., Sect. B* **1984**, *2*, 204.Senger, B. Calculated molecular double-differential cross-sections for ionization under proton impact. *Z. Phys. D* **1988**, *9*, 79.
43. Kim, Y.-K.; Rudd, M. E. Binary-encounter-dipole model for electron-impact ionization. *Phys. Rev. A* **1994**, *50*, 3954.
44. Champion, C.; Hanssen, J.; Hervieux, P.-A. Differential and total (e,2e) cross sections of simple polyatomic molecules. *J. Chem. Phys.* **2004**, *121*, 9423.
45. Moccia, R. One-center basis set SCF MO's. III. H_2O, H_2S, and HCl. *J. Chem. Phys.* **1964**, *40*, 2186.
46. Rudd, M. E.; Kim, Y.-K.; Madison, D. H., et al. Electron production in proton collisions with atoms and molecules: energy distributions. *Rev. Mod. Phys.* **1992**, *64*, 441.
47. Belkić, Dž.; Mančev, I.; Hanssen, J. Four-body methods for high-energy ion-atom collisions. *Rev. Mod. Phys.* **2008**, *80*, 249.
48. Salin, A. Ionization of helium by proton impact. *J. Phys. B* **1972**, *5*, 979.
49. Madison, D. H. Angular distributions of electrons ejected from helium by proton impact. *Phys. Rev. A* **1973**, *8*, 2449.
50. Stolterfoht, N.; Schneider, D.; Tanis, J., et al. Evidence for two-centre effects in the electron emission from 25 MeV/u Mo^{40+}+He collisions: theory and experiment. *Eur. Phys. Lett.* **1987**, *4*, 899.
51. Rudd, M. E.; Sautter, C. A.; Bailey, C. L. Energy and angular distributions of electrons ejected from hydrogen and helium by 100- to 300-keV protons. *Phys. Rev.* **1966**, *151*, 20.
52. Cheshire, I. M. Continuum distorted wave approximation; resonant charge transfer by fast protons in atomic hydrogen. *Proc. Phy. Soc.* **1964**, *84*, 89.
53. Oppenheimer, J. R. On the quantum theory of the capture of electrons. *Phys. Rev.* **1928**, *31*, 349.Brinkman, H. C.; Kramers, H. A. *Proc. Acad. Sci. Amsterdam* **1930**, *33*, 973.
54. Jackson, J. D.; Schiff, H. Electron capture by protons passing through hydrogen. *Phys. Rev.* **1953**, *89*, 359.
55. Omidvar, K.; Golden, J. E.; McGuire, J. H. Single-electron Born approximations for charge transfer from multielectron atoms to protons. *Phys. Rev. A* **1976**, *13*, 500.
56. Dollard, M. D. Ph.D. Thesis, University of Michigan, 1963.Dollard, J. D. Asymptotic convergence and the coulomb interaction. *J. Math. Phys.* **1964**, *5*, 729.
57. Mapleton, R. A. Asymptotic form of the electron capture cross section in the second Born approximation. *Proc. Phys. Soc.* **1967**, *91*, 868.
58. Carpenter, C. P.; Tuan, T. F. On the application of Faddeev equations and the Coulomb t matrix to asymptotic electron capture in hydrogen. *Phys. Rev. A* **1970**, *2*, 1811.
59. Dewangan, D. P.; Eichler, J. Boundary conditions and the strong potential Born approximation for electron capture. *J. Phys. B* **1985**, *18*, L65.
60. Pradhan, T. Electron capture by protons passing through hydrogen. *Phys. Rev.* **1957**, *105*, 1250.
61. Macek, J.; Shakeshaft, R. Second Born approximation with the Coulomb Green's function: electron capture from a hydrogenlike ion by a bare ion. *Phys. Rev. A* **1980**, *22*, 1441.Macek, J.; Taulbjerg, K. Correction to Z_P/Z_T expansions for electron capture. *Phys. Rev. Lett.* **1981**, *46*, 170.Taulbjerg, K.; Barrachina, R.; Macek, J. H. Perturbation theory for strongly interacting atomic systems. *Phys. Rev. A* **1990**, *41*, 207.
62. Rivarola, R. D.; Maidagan, J. M.; Hanssen, J. Coulombic potentials in atomic collisions. *Nucl. Instrum. Methods Phys. Res., Sect. B* **1987**, *27*, 565.
63. Belkić, Dž; Gayet, R.; Salin, A. Electron capture in high-energy ion-atom collisions. *Phys. Rep. A* **1979**, *56*, 279.Belkić, Dž; Taylor, H. S. First-order theory for charge

exchange with correct boundary conditions: General results for hydrogenlike and multielectron target atoms. *Phys. Rev. A* **1987**, *35*, 1991.Belkić, Dž. Reformulated impulse approximation (RIA) for charge exchange in fast ion-atom collisions. *Phys. Scripta* **1996**, *53*, 414.

64. Thomas, L. H. On the capture of electrons by swiftly moving electrified particles. *Proc. R. Soc. Lond. A* **1927**, *114*, 561.
65. Belkić, Dž. Electron capture by fast protons from helium, nitrogen, and oxygen: The corrected first Born approximation. *Phys. Rev. A* **1988**, *37*, 55.
66. Corchs, S. E.; Rivarola, R. D.; McGuire, J. H. Impact-parameter formulation for electron capture from molecular targets. *Phys. Rev. A* **1993**, *47*, 3937.
67. Fainstein, P. D.; Ponce, V. H.; Rivarola, R. D. A theoretical model for ionization in ion-atom collisions. Application for the impact of multicharged projectiles on helium. *J. Phys. B* **1988**, *21*, 287.
68. Salin, A. Ionization of atomic hydrogen by proton impact. *J. Phys. B* **1969**, *2*, 631.
69. Turner, J. E.; Paretzke, H. G.; Hamm, R. N., et al. Comparative study of electron energy deposition and yields in water in the liquid and vapour phases. *Radiat. Res.* **1982**, *92*, 47.
70. Ritchie, R. H.; Hamm, R. N.; Turner, J. E., et al. In *Sixth Symposium on Microdosimetry*, Brussels, Belgium; Booz, J.; Ebert, H. G., Eds.; London: Harwood Academic Publishers, 1978; p 345.
71. International Commission on Radiation Units and Measurements, Bethesda, Maryland, 1993.
72. Champion, C.; Galassi, M. E.; Weck, P. F. et al. Quantum-mechanical contributions to numerical simulations of charged particle transport at the DNA scale. In: *Radiation Damage in Biomolecular Systems, Biological and Medical Physics, Biomedical Engineering*; Gómez-Tejedor, G. G.; Fuss, M. C. Eds.; Springer Science, 2012; p 263.
73. Fainstein, P. D.; Gulyás, L.; Martin, F., et al. Angular asymmetry of low-energy electron emission in ion-atom collisions. *Phys. Rev. A* **1996**, *53*, 3243.
74. Houamer, S.; Popov, Yu. V.; Dal Cappello, C., et al. Charge transfer in collisions of protons with water molecule at high projectile energies and small scattering angles. *Nucl. Instrum. Methods Phys. Res., Sect. B* **2009**, *267*, 802.Houamer, S.; Popov, Yu. V.; Dal Cappello, C. Total cross sections for charge transfer reactions of protons with atomic and molecular targets at high projectile energies: the role of inner orbitals. *Phys. Lett. A* **2009**, *373*, 4447.
75. Date, H.; Sutherland, K. L.; Hayashi, T., et al. Inelastic collision processes of low-energy protons in liquid water. *Radiat. Phys. Chem.* **2006**, *75*, 179.
76. Toburen, L. H. Ionization and charge-transfer: basic data for track structure calculations. *Radiat. Env. Biophys.* **1998**, *37*, 221.

CHAPTER ELEVEN

Ion Collisions with Water Molecules: A Time-Dependent Density Functional Theory Approach

Tom Kirchner[a], **Mitsuko Murakami**[a], **Marko Horbatsch**[a] and
Hans Jürgen Lüdde[b]
[a]Department of Physics and Astronomy, York University, Toronto, Ontario, Canada M3J 1P3
[b]Institut für Theoretische Physik, Goethe-Universität, D-60438 Frankfurt, Germany

Contents

Abstract

Collisions of simple ions from water molecules in the energy range of 10–5000 keV/amu are considered within an independent electron model. The basis generator method applied in the past successfully to ion–atom collisions is adapted to deal with molecular targets. Cross sections for single- and multiple-electron processes (capture and transfer to the continuum) are obtained directly from solving time-dependent Kohn–Sham-type orbital equations and using a Slater determinant based analysis. Fragmentation yields are predicted on the basis of a semi-phenomenological model which uses the calculated cross sections as input. Comparison with experiment is made for proton and He^+ impact collisions.

Advances in Quantum Chemistry, Volume 65
ISSN 0065-3276, http://dx.doi.org/10.1016/B978-0-12-396455-7.00011-X

1. INTRODUCTION

Electron removal from water molecules is one of the most frequent processes taking place when biological tissue is irradiated by protons or heavy ions. In hadron therapy,[1] it contributes to the desired destruction of a tumor and to the undesired damage of the surrounding tissue in at least two ways: (i) the produced free electrons attack DNA molecules in ionizing collisions or via formation of transient molecular resonance states;[2] (ii) the H_2O^{q+} ions left behind are often instable and thus prone to fragmentation, especially if $q \geqslant 1$, i.e., if multiple-electron removal occured. In a liquid environment, fragment ions may recombine to highly reactive oxygen species such as HO_2, which can damage the DNA in chemical reactions (see, e.g., Ref. 3 and references therein).

It is thus important to understand ion-impact induced ionization and the subsequent fragmentation dynamics of water molecules in detail. Early experimental studies determined (total) cross sections for ionization and electron transfer processes,[4, 5] while more recent works were concerned with measuring the yields of charged fragments, sometimes in coincidence with an ionized electron or the projectile charge state.[6–10] Theoretical efforts have focused on calculating cross sections for electron removal processes at impact energies above 20 keV, for which relatively simple self-consistent field descriptions of the water molecule are deemed suitable. They include a molecular orbital based coupled-channel calculation,[11] Born- and continuum distorted-wave-type models[12–14] and classical trajectory Monte Carlo (CTMC) calculations based on one-center[15, 16] and three-center[17] model potentials. Fragmentation cross sections have been deduced from some of the results using (semi-)empirical models to relate electron removal to the production of the different fragment ions.[14, 15, 17]

Our own work in this area is built on an extension of a quantum-mechanical approach developed and tested for ion–atom collisions (see, e.g., Refs. 18–20 and the review article: Ref. 21). The approach is based on density functional theory (DFT) and uses the basis generator method (BGM) to propagate effective single-particle (Kohn–Sham-type) orbitals. The extension to molecular targets was accomplished by a spectral representation of the target Hamiltonian and a single-center expansion of its eigenstates.[22] This enables to separate the ion-molecule multi-center problem into a set of two-center problems and to apply the BGM with only modest modifications.

The approach has been rather successful in describing experimental cross sections for various electron transfer and ionization processes in proton– and He^+–H_2O collisions over wide ranges of impact energies.[22, 23] Recently, we have coupled it with a semi-phenomenological model for water fragmentation after single and multiple electron removal, and have obtained results which agree favorably with experimental cross sections for the production of charged fragments.[24, 25]

In this chapter, we provide a somewhat condensed description of this ion-molecule approach and the results obtained from it. We start with a brief outline of the general framework of the theory and the DFT-perspective on atomic collisions in Section 2.1. This is followed by summaries of the ion-molecule BGM in Section 2.2 and the method used to extract measurable information from the BGM solutions in Section 2.3. Some computational aspects are discussed in Section 2.4, but for a more detailed description the reader is referred to Ref. 24. We present results for electron removal in proton– and He^+–H_2O collisions in Section 3.1 and for fragmentation of H_2O after proton impact in Section 3.2. The chapter ends with a summary and an outline of directions of future work in Section 4. Atomic units ($\hbar = m_e = e = 4\pi\epsilon_0 = 1$) are used throughout, unless specified otherwise.

2. THEORY

Ion-molecule collisions are complex many-body problems. At present, a full theoretical description of their dynamics in terms of a consistent quantum theory for all degrees of freedom is not feasible. Fortunately, it is not necessary either—at least not in the range of impact energies from about 10 keV/amu up to a few MeV/amu in which we are interested. In this range, the different time scales of the electron and nuclear dynamics allow for a separation of the many-body state and a simplified treatment of the different processes at play. The projectile ion is fast enough to assume that it travels on a classical straight-line trajectory. Its interaction time with the target molecule is short, so that the latter neither rotates nor vibrates appreciably while electrons are being transferred or ejected to the continuum. Thus, the Franck–Condon approximation, which assumes that the molecule is frozen to its equilibrium geometry when the electronic transitions occur, can be used. Such a calculation can make (possibly state-specific) predictions for the formation of H_2O^{q+} ions, which may break up subsequently. Fragmentation cross sections can be derived semi-phenomenologically by associating single-and multiple-electron removal processes with probabilities for specific break-up channels using experimental branching ratios as input.

This is the framework we have adopted in our studies of ion-H_2O collisions.[22-25] The main theoretical task is the solution of a time-dependent Schrödinger equation (TDSE) for the electrons, which experience time-dependent and stationary Coulomb forces due to the moving projectile and the non-moving target nuclei, respectively, in addition to their mutual repulsion. In the next subsection, we outline how this complicated many-electron problem can be formulated within time-dependent density functional theory (TDDFT). This is followed by a discussion of our specific approach to solving the ensuing set of single-particle Schrödinger-type equations and a brief description of the methods used to extract measurable information from the solutions.

2.1 The density-functional theory approach to heavy-particle collisions

The problem at hand can be stated as follows: the electronic state vector fulfills the TDSE

$$i\partial_t|\Psi(t)\rangle = \widehat{H}(t)|\Psi(t)\rangle \tag{1}$$

for the initial condition

$$|\Psi(t_0)\rangle = |\Psi_0\rangle \tag{2}$$

and the Hamiltonian

$$\widehat{H}(t) = \widehat{T} + \widehat{W}_{\text{int}} + \widehat{V}_{\text{ext}}(t), \tag{3}$$

which consists of the kinetic energy

$$\widehat{T} = \sum_{j=1}^{N}\left(-\frac{1}{2}\nabla_j^2\right), \tag{4}$$

the *internal* electron–electron interaction

$$\widehat{W}_{\text{int}} = \sum_{i<j}^{N}\frac{1}{|\mathbf{r}_i - \mathbf{r}_j|} \tag{5}$$

with the electron position vectors $\mathbf{r}_i$ being measured from a laboratory (i.e., a non-moving) reference frame, and the *external* Coulomb interaction with the heavy particles. For a target molecule described within the Born–Oppenheimer and Franck–Condon approximations we have

$$\widehat{V}_{\text{ext}}(t) = -\sum_{j=1}^{N}\left(\sum_{\alpha=1}^{M}\frac{Z_\alpha}{r_{\alpha j}} + \frac{Z_{\text{P}}}{|\mathbf{r}_j - \mathbf{R}(t)|}\right), \tag{6}$$

where M denotes the number of target nuclei with charges Z_α ($M = 3$ and $Z_1 = Z_2 = 1, Z_3 = 8$ for H_2O), and $r_{\alpha j}$ is the distance of the αth nucleus to the jth electron. Z_{P} is the charge of the (bare) projectile ion, which moves along the straight-line trajectory $\mathbf{R}(t) = (b, 0, v_0 t)$ characterized by the impact parameter b and the constant projectile speed v_0.

The backbone of TDDFT is the Runge–Gross theorem.[26] It states that the electronic state vector $|\Psi(t)\rangle$ that solves the TDSE (1) is (up to a global time-dependent phase) a unique functional of the time-dependent one-particle density n, if the initial state $|\Psi_0\rangle$ is the (nondegenerate) ground state of the system. The density at time t can be calculated without knowledge of $|\Psi(t)\rangle$ from a set of single-particle Schrödinger-type, so-called time-dependent Kohn–Sham (TDKS), equations

$$i\partial_t \psi_i(\mathbf{r}, t) = \left(-\frac{1}{2}\nabla^2 + v_{\text{TDKS}}[n](\mathbf{r}, t)\right)\psi_i(\mathbf{r}, t), \quad i = 1, \ldots, N \tag{7}$$

according to

$$n(\mathbf{r}, t) = \sum_{i=1}^{N} |\psi_i(\mathbf{r}, t)|^2. \tag{8}$$

The potential v_{TDKS} in (7) is also a unique functional of n. This is another consequence of the Runge–Gross theorem and suggests the following route to solving the time-dependent many-electron problem: (i) determine $v_{\text{TDKS}}[n](\mathbf{r}, t)$; (ii) propagate the TDKS orbitals from initial conditions, that combine to the ground-state density according to (8), up to a final time t_f; (iii) extract all observables of interest from the asymptotic solutions using the fact that $|\Psi(t_f)\rangle$ is uniquely determined by n.

In practice, these steps can only be taken after approximations have been introduced, since the exact functional dependences of v_{TDKS} and $|\Psi\rangle$ on n are not known. Nevertheless, the idea to circumvent the actual solution of the many-electron TDSE (1) is appealing. It provides a firm basis of the independent particle model (IPM) and some clues of how to interpret and improve it.

2.2 The basis generator method adapted for ion-molecule collisions

In our previous works on proton–H_2O collisions[22, 24, 25] we have used a simplified TDKS Hamiltonian, in which the effective electron–electron interaction potential is frozen to its (approximate) form in the initial state:

$$v_{\mathrm{TDKS}}[n](\mathbf{r},t) \approx V^{\mathrm{T}}_{\alpha\beta\gamma}(\mathbf{r}) + V^{\mathrm{P}}(\mathbf{r},t), \tag{9}$$

$$V^{\mathrm{P}}(\mathbf{r},t) = -\frac{Z_{\mathrm{P}}}{|\mathbf{r}-\mathbf{R}(t)|}. \tag{10}$$

$V^{\mathrm{T}}_{\alpha\beta\gamma}$ is a molecular ground-state potential on the Hartree–Fock (HF) level and α, β, γ are the standard Euler angles, which we use to specifiy the orientation of the water molecule with respect to the ion beam axis. The occupied eigenstates of

$$\widehat{H}^{\mathrm{T}}_{\alpha\beta\gamma} = -\frac{1}{2}\nabla^2 + V^{\mathrm{T}}_{\alpha\beta\gamma} \tag{11}$$

form the ground-state density and are the initial conditions for the TDKS-type equations

$$i\partial_t|\psi^{\Gamma}_{\alpha\beta\gamma}(t)\rangle = \left[\widehat{H}^{\mathrm{T}}_{\alpha\beta\gamma} + V^{\mathrm{P}}(t)\right]|\psi^{\Gamma}_{\alpha\beta\gamma}(t)\rangle, \tag{12}$$

$$|\psi^{\Gamma}_{\alpha\beta\gamma}(t_i)\rangle = |\Gamma_{\alpha\beta\gamma}\rangle. \tag{13}$$

The capital Greek letters label the occupied MOs whose time evolution we study, i.e., $\Gamma_{\alpha\beta\gamma} \in \{1b_1, 3a_1, 1b_2, 2a_1\}_{\alpha\beta\gamma}$. The innermost orbital is excluded, since the $1a_1$ electrons are too tightly bound to undergo appreciable transitions in the studied systems.

The no-response approximation (9) can be expected to work well if the projectile is fast (and of low charge), whereas dynamical response may play a role at lower impact energies, at which the electrons have more time to react to changes in the effective potential. This tendency has been confirmed in numerous studies of ion–*atom* collision systems by comparing no-response and response cross sections,[18, 20] and we also see some evidence for it in the results presented further below.

The main difficulty with solving (12) is the structure of $V^{\mathrm{T}}_{\alpha\beta\gamma}$. If one expands the orbitals $|\psi^{\Gamma}_{\alpha\beta\gamma}(t)\rangle$ in a basis, one encounters multi-center integrals, which have plagued molecular structure calculations for many years.[27]

Our approach circumvents the explicit calculation of multi-center integrals by going into an energy representation of the target Hamiltonian

$$\widehat{H}^{\mathrm{T}}_{\alpha\beta\gamma} = \sum_{\Lambda} \epsilon_{\Lambda} |\Lambda_{\alpha\beta\gamma}\rangle\langle\Lambda_{\alpha\beta\gamma}|, \tag{14}$$

in which ϵ_Λ denotes the energy eigenvalue of the MO labeled by quantum number(s) Λ. We use two different basis sets to proceed: an orthonormal single-center basis $\{|s\rangle\}$ for representing the MOs

$$|\Lambda_{\alpha\beta\gamma}\rangle = \sum_{s} d^{\Lambda}_{s,\alpha\beta\gamma} |s\rangle \tag{15}$$

and a nonorthogonal, dynamical two-center basis $\{|\chi^J_j(t)\rangle\}$ for propagating (12):

$$|\psi^{\Gamma}_{\alpha\beta\gamma}(t)\rangle = \sum_{jJ} a^{\Gamma}_{jJ,\alpha\beta\gamma}(t) |\chi^J_j(t)\rangle. \tag{16}$$

Both basis sets will be specified further below. The benefit of using these expansions is that the multi-center molecular matrix elements break up into combinations of energy eigenvalues, (real) expansion coefficients, and simpler overlap matrix elements:

$$\begin{aligned} M^{KJ}_{kj}(\alpha,\beta,\gamma,t) &= \langle\chi^K_k(t)|\widehat{H}^{\mathrm{T}}_{\alpha\beta\gamma}|\chi^J_j(t)\rangle \\ &= \sum\nolimits_{\Lambda} \sum_{su} \epsilon_\Lambda \langle\chi^K_k(t)|s\rangle d^{\Lambda}_{s,\alpha\beta\gamma} d^{\Lambda}_{u,\alpha\beta\gamma} \langle u|\chi^J_j(t)\rangle. \end{aligned} \tag{17}$$

Instead of propagating the initial-state MOs we exploit the linearity of the single-particle equations (12) and use the single-center basis states $|s\rangle$ as initial conditions to obtain

$$|\psi^{s}_{\alpha\beta\gamma}(t)\rangle = \sum_{jJ} a^{s}_{jJ,\alpha\beta\gamma}(t) |\chi^J_j(t)\rangle \tag{18}$$

from solving a set of coupled-channel equations which are very similar to those of a two-center ion–*atom* collision problem. The molecular solutions (16) can be reconstructed

$$|\psi^{\Gamma}_{\alpha\beta\gamma}(t)\rangle = \sum_{s} d^{\Gamma}_{s,\alpha\beta\gamma} |\psi^{s}_{\alpha\beta\gamma}(t)\rangle = \sum_{sjJ} d^{\Gamma}_{s,\alpha\beta\gamma} a^{s}_{jJ,\alpha\beta\gamma}(t) |\chi^J_j(t)\rangle \tag{19}$$

to calculate the density $n(\mathbf{r},t)$ of the system. In principle, this is the starting point for the calculation of observable quantities in the TDDFT framework.

In practice, however, the density is of limited use due to the unknown dependence of the many-electron state on it. A more fruitful, though approximate basis for the final-state analysis is the one-particle density matrix constructed from single-determinantal wave functions.

Before we discuss this method, we have to comment on how we deal with collisions of water molecules with He^+ ions, which involve an additional electron on the projectile. If one were to solve the many-electron TDSE (1), this electron would have to be treated on the same footing as the initial target electrons; in particular, the state vector $|\Psi(t)\rangle$ would depend on the coordinates of *all* electrons and be antisymmetric under interchange of any pair of them. A pragmatic way to account for the projectile electron in an effective single-particle framework is to add an appropriate screening potential to the Hamiltonian and solve the TDKS-type Eqs. (12) for all initially populated orbitals—the target MOs *and* a (moving) atomic orbital (AO) on the projectile center. The pros and cons of this approach as well as more sophisticated alternatives were discussed in Refs. 23, 28. Briefly, the main shortcoming of using a common Hamiltonian with effective target and projectile potentials $V^{\mathrm{T}}_{\alpha\beta\gamma}$ and V^{P} is that either the initial target electrons or the initial projectile electron(s) experience an incorrect asymptotic potential.

Our choice for He^+–water-molecule collisions consists in leaving $V^{\mathrm{T}}_{\alpha\beta\gamma}$ in Eq. (9) unchanged, but replacing the bare projectile potential (10) by

$$V^{\mathrm{P}}(r_P) = -\frac{2}{r_P} + \int \frac{|\varphi^{\mathrm{He}}_{1s}(r')|^2}{|\mathbf{r}' - \mathbf{r}_P|} \mathrm{d}^3 r', \tag{20}$$

where $\varphi^{\mathrm{He}}_{1s}$ is the (normalized) ground-state HF AO of (neutral) helium and $\mathbf{r}_P = \mathbf{r} - \mathbf{R}(t)$. The potential (20) decays like $-1/r_P$ asymptotically, which is correct from the viewpoint of the initial target electrons, but incorrect for the projectile electron, which in reality experiences an unscreened Coulomb potential for the charge number $Z_{\mathrm{P}} = 2$.

One can argue that this choice of a common potential $V^{\mathrm{T}}_{\alpha\beta\gamma} + V^{\mathrm{P}}$ for all electrons is reasonable for situations in which electron transfer from the target to the continuum and to the projectile dominate, while projectile electron loss is relatively unimportant. If one were to choose a different Hamiltonian without the screening term in (20), one would improve the description of the electron loss process, but at the expense of the capture and target ionization channels.

One may be inclined to circumvent these problems by using different potentials in the single-particle equations for the initial target and projectile electrons. This is certainly a possibility, but it comes with a price, too: the propagated orbitals lose their initial orthogonality during the time propagation, which renders the final-state analysis cumbersome.[28, 29] In fact, our main motivation for choosing a simple, common potential for all active electrons was to preserve orthogonality at all times. This makes it straightforward to construct the one-particle density matrix of the system at the final time and to extract observable information from it. Not only is this elegant, it is also crucial for the correct description of channels, for which Pauli blocking effects are important. This will be further discussed in the next subsection and along with the results in Section 3.

2.3 Extraction of measurable cross sections

The first step in the density-matrix analysis of the solutions is the calculation of single-particle state-to-state transition amplitudes

$$A_{if}(t_f) = \langle f | \psi_i(t_f) \rangle \tag{21}$$

at the final time t_f. The propagated states $|\psi_i(t_f)\rangle$ in (21) are those of Eq. (19) plus the propagated projectile-electron orbital in the case of He$^+$ impact. As final states $|f\rangle$ we consider bound projectile and bound target states. All amplitudes are fed into the one-particle density matrix

$$\langle f | \hat{\gamma}^1(t_f) | f' \rangle = \sum_{i=1}^{N} A_{if}(t_f) A^*_{if'}(t_f), \tag{22}$$

whose nondiagonal structure reflects the antisymmetry of the N-electron state, i.e., the Pauli principle. So-called *inclusive* probabilities are obtained as determinants of submatrices of (22),[30] and all many-electron transition probabilities of interest can be written and calculated as appropriate combinations of those inclusive probabilities.

In this work, we are concerned with cross sections which correspond to probabilities $P_{k,l}$ for finding k electrons at the projectile in coincidence with l electrons in the continuum and with sums thereof. Details about how these probabilities are calculated from the inclusive probabilities for occupying bound target and bound projectile states have been provided in Refs. 24, 29 and will not be repeated here.

Let us close this section with a few conceptual comments. The inclusive-probability formalism is derived from the assumption that both the propagated many-electron state and the final states of interest are single Slater determinants.[30] This implies that the TDKS-type orbitals, which combine to the density according to Eq. (8), are assumed to carry the physical information about the active electrons as in HF theory. In other words, such an analysis corresponds to the IPM level and is a (further) departure from a perfect TDDFT, in which only the density is associated with a physical interpretation, while the TDKS orbitals are viewed as auxiliary functions without direct physical significance. The limitations of the IPM are well known, and some of them will be discussed further below in Section 3. Nevertheless, the IPM has been popular, since it can be interpreted relatively easily and, more importantly, since there is no first-principles alternative available that goes beyond it. This is, in fact, one of the main shortcomings of current TDDFT applications to ion-impact or laser-field induced many-electron dynamics.

2.4 Computational aspects

It was mentioned in Section 2.2 that two basis expansions are involved in our method: a single-center basis is used to represent the ground-state MOs [cf. Eq. (15)] and a two-center basis to propagate the TDKS-type orbitals [cf. Eq. (16)]. The latter is obtained from the two-center (TC) extension of the BGM method, which was developed as a general means to describe time-dependent quantum systems in a finite basis.[31] The main idea of the BGM is to construct a subspace of Hilbert space $\mathcal{H}$ that is tailored to representing only the propagated states rather than representing $\mathcal{H}$ completely, which is illusory in any case. It was shown in Ref. 31 how this can be accomplished in terms of a hierarchy of dynamical subspaces of $\mathcal{H}$ starting from one that includes the states which form the initial conditions of the time-dependent problem.

In practice, a TC-BGM basis consists of sets of AOs placed on the projectile center and the target center, which for water molecules we choose to coincide with the position of the oxygen nucleus. Both sets are endowed with electron translation factors to ensure Galilean invariance. In addition, time-dependent pseudo states constructed by the repeated application of a regularized projectile potential on the set of target AOs

$$|\chi_j^J(t)\rangle = \left[\frac{1}{r_P}\left(1 - \mathrm{e}^{-r_P}\right)\right]^J |\varphi_j^{\mathrm{T}}\rangle \tag{23}$$

are included to represent the continuum and quasimolecular effects at low collision energy.

The same set of target AOs is also used to represent the ground-state MOs of the water molecule—taken from the minimal-basis-set HF calculation of Ref. 32—according to Eq. (15), i.e., $\{|\varphi_j^T\rangle\} \equiv \{|s\rangle\}$. It is then consistent to limit the spectral representation of the Hamiltonian (14) to these initially occupied MOs as given in the single-center expansion (15). This might sound drastic, but test calculations that go beyond this model by using a closure approximation have lent credence to its reliability for medium to high impact-energy collisions. Details about the basis sets used are given in Ref. 24.

The measurements we wish to compare with did not record the orientation of the water molecule with respect to the ion beam axis. Hence, we have to perform calculations for a set of orientations characterized by Euler angles α, β, γ and average them in an appropriate way. One may expect a considerable orientation dependence of the electronic transitions at low impact energies, and, in fact, there is ample evidence for that.[11] However, we found that considering just two orientations[†] is sufficient for the purpose of obtaining net and charge-state correlated cross sections for electron removal in the impact energy range from about 20 to 5000 keV/amu. All results discussed in the next section have been obtained in this way.

3. RESULTS

The present model has been used to calculate data for comparison with experiments at various levels. For bare-ion impact one first investigates net processes, such as total electron yield in the continuum σ_-, total positive charged ion yield σ_+, and total net charge transfer σ_{cap} for which extensive experimental data were provided by Rudd and coworkers.[4] For the case of He^+ projectiles σ_- includes contributions from the projectile electron, and one can look at the total electron loss from the projectile, as well. For neutral projectiles these electron loss processes become important, particularly if one is concerned with the problem of energy deposition.

In principle, the net (or gross) cross sections should be the most reliable quantities provided in a density-functional theory framework, as in essence they depend on how the electron density splits into three contributions:

[†] Namely those shown in Figure 1 of Ref. 24.

parts associated with the target after the collision, parts associated with the projectile, and the remainder representing continuum electrons. In practice, however, one should worry about the independent-electron approximation, since it may enhance multiple-electron transitions. Even in the case of bare projectiles one deals with the added difficulty that an *N*-electron density distribution that originated at the target is spread over the three regions, and that in low-energy collisions it is possible to transfer more electrons to the projectile than is physically allowed. In a perfect TDDFT this should be prevented by an appropriate response potential. In practice, however, this can become an issue. Our philosophy will be to treat the net transfer probabilities seriously even when no response is included in the calculations.

While the process of electron removal from the target leads to the total positive ion yield σ_+, more detailed information is obtained from *q*-fold electron removal cross sections σ_q with

$$\sigma_+ = \sum_{q=1}^{N} q\sigma_q. \tag{24}$$

For the projectile space the corresponding detail is given by *k*-fold capture cross sections which sum to net capture according to

$$\sigma_{\text{cap}} = \sum_{k=1}^{N} k\sigma_k^{\text{cap}}. \tag{25}$$

From this expression it becomes clear that for a highly charge-asymmetric system (a low-charge projectile scattering from a multi-electron target) there is the problem that more electrons can be transferred independently from the target to the projectile than what is allowed physically.

The cross sections to find *n* electrons in the continuum σ_n^{ion} add up to the net continuum cross section according to

$$\sigma_- = \sum_{n=1}^{N} n\sigma_n^{\text{ion}}. \tag{26}$$

The next level of sophistication is given by charge-state correlated cross sections. These are obtained in experiment by a coincidence counting technique: by determining the charge states of projectile and target after the collision for each event one has also determined the number of electrons transferred to the continuum. In a purely statistical treatment of the density operator these charge-state correlated processes are related by trinomial statistics. In a treatment based on the one-particle density matrix Pauli correlations are included, as well. Examples of charge-state correlated processes are pure (direct) ionization of the target, pure capture (no simultaneous transfer of electrons to the continuum), or transfer ionization—a process in which both capture and transfer of target electrons to the continuum occurs.

All these cross sections can be obtained from microscopic calculations, i.e., from the independent-electron approach to the *N*-electron TDSE. A substantial body of data has been explained at this level in ion–atom collisions. The practical goal of an IPM is not to describe all of the multi-electron processes, but to concentrate on the dominant channels. How many of these channels can be described successfully depends on the strength of the projectile interaction: for a given projectile charge Z_P it was found that independent-electron dynamics works for more of the *N* target electrons in proportion to Z_P (see Ref. 19).

Compared to atomic targets, molecules present an additional challenge. The production of recoils such as H_2O^{q+} results in fragmentation even for charge states as low as $q = 1$. The fragmentation occurs on time scales longer than the collision itself, and therefore needs to be modelled as a post-collision phenomenon. At high collision energies, i.e., when single-electron removal ($q = 1$) dominates completely, it is possible to deduce branching fractions for H_2O^+ survival vs. production of OH^+, H^+, O^+ (and in principle also H_2^+). The main ionic channels can be linked to exclusive single-vacancy production in one of the MOs. At intermediate and low energies where multiple electron removal from the target plays an increasingly bigger role fragmentation patterns can be modelled by supplementing the $q = 1$ rule with branching rules for $q = 2$ and higher. There is some support for such (semi-)phenomenological assignments from coincidence measurements of water molecule fragments following proton impact at intermediate energies.[6] It led to the first description of a large body of experimental data.[24]

We provide a series of comparisons of our data with experiments for proton–water molecule collisions at collision energies above 20 keV and also discuss some selected results for He^+-impact. Where applicable we compare our results with three-center classical trajectory calculations. For proton impact, we progress through the sequence laid out above: net (gross) cross sections, then *q*-fold electron processes (recoils, transfer to the projectile, transfer to the continuum), and finally, fragmentation. The latter can be observed also specifically for electron removal by capture, or by transfer to the continuum.

3.1 Net cross section results

In Figure 11.1 we show the net capture cross sections in $p - H_2O$ collisions in comparison with experiment and with the three-center CTMC calculations of Illescas et al.[17] The results from the BGM-IPM follow the experimental data very well in the low-to-intermediate energy regime. They overestimate the data at energies above 200 keV displaying a systematic deviation by about a factor of two. The CTMC calculations show a somewhat different energy dependence and lie above our calculations at both low and very high energies. We cannot offer any explanations for the discrepancy between the data and our results at high energies.

In Figure 11.2 a similar comparison is given for transfer of electrons to the continuum. Note that in contrast to Figure 11.1 the vertical axis is linear. The experimental data display visible statistical errors on this scale, and possibly a systematic discrepancy. Our calculations agree with the data at the 30% level. The CTMC calculation is in better agreement with the data over the entire energy range. The classical calculation employs a more complete three-center geometry for the collision calculation, which is likely to be the main reason for the more favorable comparison. In the limit of very high energies it should not yield the correct energy dependence,

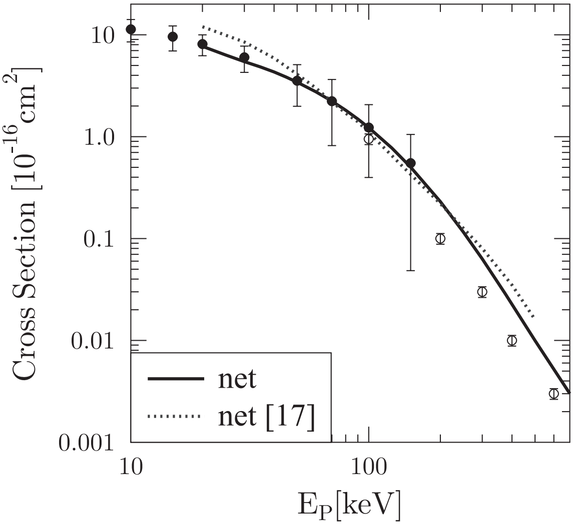

Figure 11.1 Net capture σ_{cap} in $p - H_2O$ collisions vs. projectile energy. Experiments: solid circles—Rudd et al. (1985);[4] open circles: Toburen et al. (1968).[33] Solid line: present theory; dotted line: three-center CTMC calculation of Ref. 17.

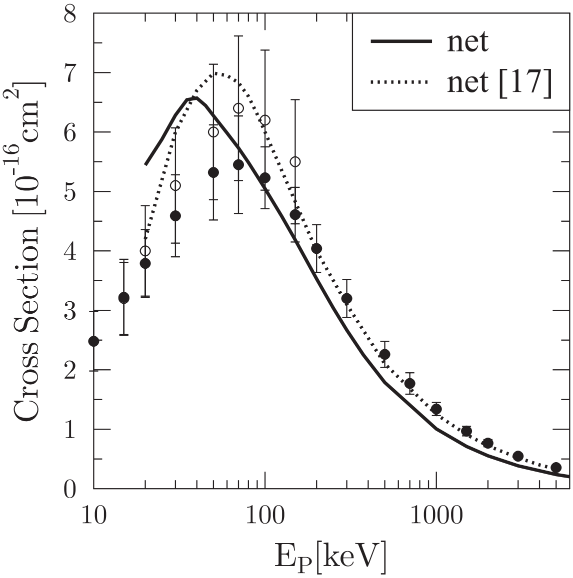

Figure 11.2 Net ionization σ_- in $p - H_2O$ collisions vs. projectile energy. Experiments: solid circles—Rudd et al. (1985);[4] open circles: Bolorizadeh and Rudd (1986).[34] Solid line: present theory; dotted line: three-center CTMC calculation of Ref. 17.

however, since a classical-trajectory calculation based upon a microcanonical distribution does not agree with the Bethe–Born limit.

The net recoil production cross section σ_+ is equal to the sum of net capture and net transfer to the continuum. We present it in Figure 11.3 to demonstrate the fall-off of the net ionization cross section at high energies. The figure also shows how more recent measurements of the individual recoil yields ($H_2O^+, OH^+, H^+, O^+, O^{2+}$) from three different experiments add up to σ_+. They mostly agree with the original data of Rudd et al.,[4] but also show that there is a small uncertainty about the absolute height at the highest energies. The three-center CTMC calculation does well at high energies, but appears to overestimate the experimental data below 50 keV.

The figure also displays how within the BGM-IPM the net recoil production is dominated at high energies by single-electron removal ($q = 1$), but that multiple electron processes become important at intermediate and low energies.

Figure 11.4 shows neutral He production in He^+–H_2O collisions. In the case where projectiles carry active electrons into the collision one cannot define a net capture cross section in a simple way. As shown in

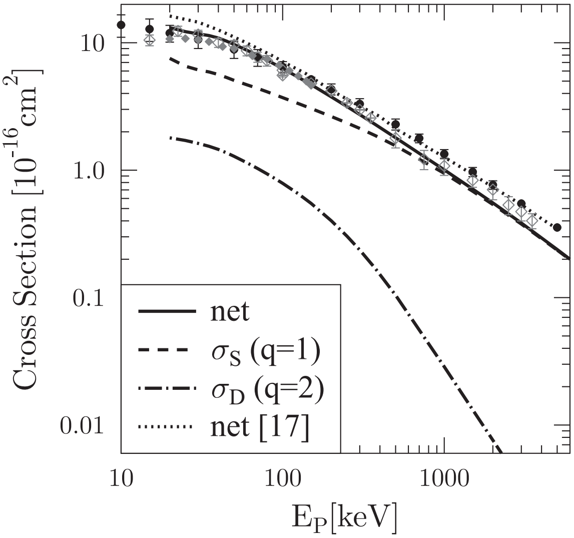

Figure 11.3 Total recoil ion production σ_+ in $p - H_2O$ collisions vs. projectile energy. Experiments: solid circles—Rudd et al. (1985);[4] other symbols: sum of fragment yields for Refs. 6, 8, 9 respectively. Solid line: present results; dotted line: three-center CTMC calculation of Ref. 18. Dashed and dash-dotted lines: present results for σ_q with $q = 1, 2$.

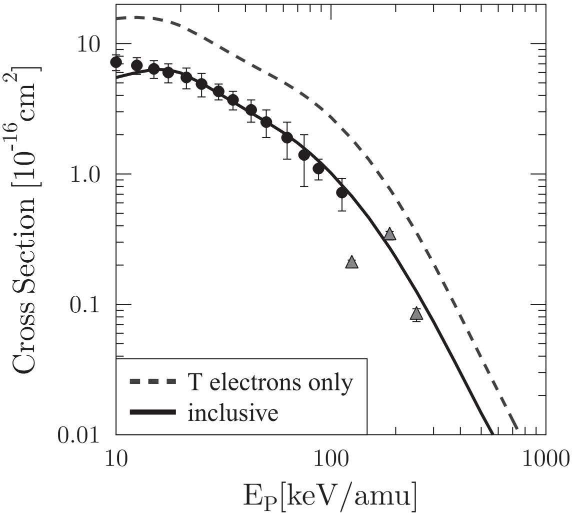

Figure 11.4 Neutral He production in $He^+ - H_2O$ collisions vs. projectile energy. Experiments: solid circles—Rudd et al. (1985);[5] triangles—Garcia et al. (2008).[10] Solid line: all electrons, including the projectile electron are used in the Slater determinant analysis; dashed line: net capture based on target electrons only.

Ref. 23 the net recoil production cross section σ_+ can be reduced considerably when projectile electron transfer to the target is allowed. In lieu of the net capture cross section (25) it is necessary to define a cross section for neutral helium production, which takes into account both projectile electron loss, as well as single and double electron transfer to the projectile from the target. In addition, one has to consider Pauli blocking, since in collision events where the projectile electron is not lost He formation (in the ground state) requires a spin-singlet as the final state. This is taken care of in the inclusive analysis.

We demonstrate the effect in Figure 11.4 to show that the experimental data are described very well by the inclusive analysis. A calculation that ignores projectile electrons overestimates neutral He production by approximately a factor of two, consistently over the entire energy range. The fact that it does not run perfectly parallel to the full analysis can be associated with the fact that electron loss from the projectile varies with impact energy. Note that the theoretical results shown are inclusive in electron transfer to the continuum, i.e., they do not represent pure capture, but include simultaneous target ionization events.

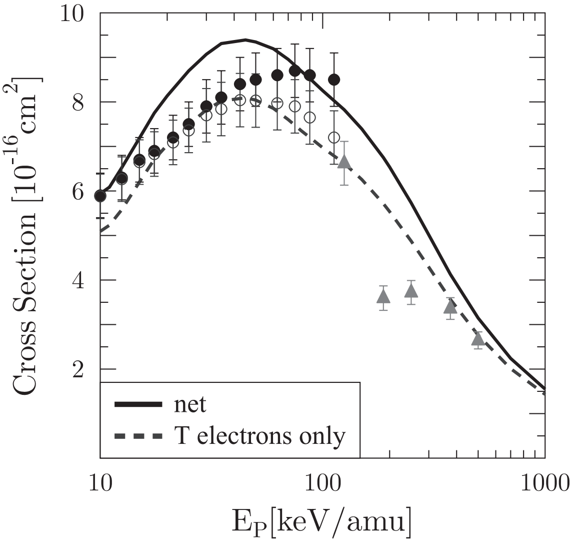

Figure 11.5 Net free-electron production in $He^+ - H_2O$ collisions vs. projectile energy. Experiments: solid circles—Rudd et al. (1985);[5] open circles—σ_- minus projectile electron loss cross section; triangles—Garcia et al. (2008).[10] Solid line: σ_- calculation including projectile electron; dashed line: based on propagation of target electrons only.

Figure 11.5 displays σ_-, as well as $\sigma_- - \sigma_{\text{loss}}$ (where σ_{loss} is the projectile electron loss cross section) in order to highlight the role of the projectile electron. From the experimental data of Rudd et al. one concludes that projectile electron removal becomes an appreciable contributor to σ_- at energies above 40 keV/amu. Note that σ_- is large to begin with, since the water molecule is easily ionized. A theoretical calculation that ignores projectile electron contributions to σ_- is seen to follow the experimental $\sigma_-\sigma_{\text{loss}}$ quite well; it displays a broader maximum than in the related $\mathrm{p} - \mathrm{H_2O}$ case shown in Figure 11.2 (this calculation is very close to the $\mathrm{p} - \mathrm{H_2O}$ case for large impact parameters, but different for close collisions). The full calculation for $\mathrm{He^+}$–$\mathrm{H_2O}$ collisions agrees well with σ_- at high energies, but overestimates the data below $E_{\mathrm{P}} = 70$ keV/amu. The projectile electron is bound too loosely in the present model, it experiences a long-range Coulomb potential from the water molecule even on the incoming part of the trajectory, and therefore is removed too easily at lower energies.

3.2 Fragmentation cross sections

In Figure 11.6 we compare our calculated recoil production cross sections $\sigma_q;\ q = 1\ldots3$ for proton–water collisions with experimental data of Werner et al. For the $q = 3$ case it is safe to assume that the measured coincidences for $\mathrm{H^+ + H^+ + O^+}$ provide the dominant contribution. For $q = 1, 2$ a model-dependent reconstruction was performed on the basis of measured fragment yields. It can be seen that the BGM-IPM calculations agree very well for $q = 1, 2$ and overestimate for $q = 3$ by about a factor of two. It was then argued[25] that fragment yields can be obtained from the cross sections for single ($q = 1$), double ($q = 2$), and triple ($q = 3$) electron removal $\sigma_{\mathrm{S,D,T}}$ according to:

$$\sigma_{\mathrm{H_2O^+}} = 0.68\sigma_{\mathrm{S}}, \tag{27}$$

$$\sigma_{\mathrm{OH^+}} = 0.16\sigma_{\mathrm{S}} + 0.6\sigma_{\mathrm{D}}, \tag{28}$$

$$\sigma_{\mathrm{H^+}} = 0.13\sigma_{\mathrm{S}} + 1.2\sigma_{\mathrm{D}} + 1.0\sigma_{\mathrm{T}}, \tag{29}$$

$$\sigma_{\mathrm{O^+}} = 0.03\sigma_{\mathrm{S}} + 0.2\sigma_{\mathrm{D}} + 0.5\sigma_{\mathrm{T}}. \tag{30}$$

This model as motivated by collision data at 100–350 keV energies takes into account known branching ratios for the $q = 1$ case (high-energy

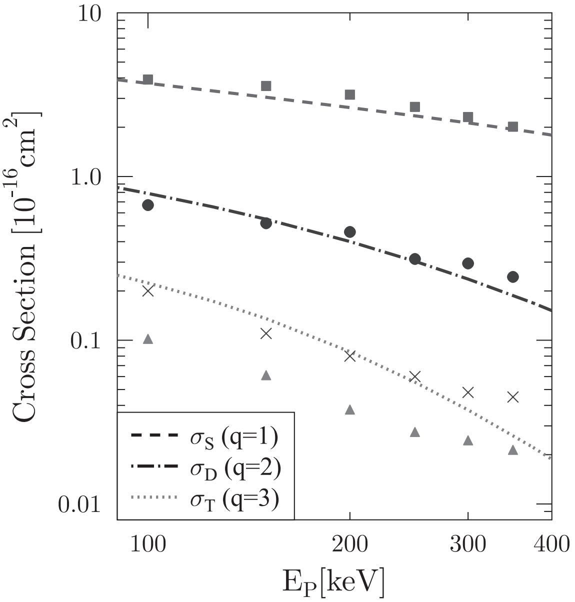

Figure 11.6 Recoil ion production σ_q in $p - H_2O$ collisions vs. projectile energy. Experiments: $q = 1$: squares (model-dependent reconstruction from the data of Werner et al. (1995);[6] $q = 2$: circles. Present theory: $q = 1$ – dashed; $q = 2$ dash-dotted; $q = 3$ dotted. Also shown: coincidence measurements from Ref. 6: triangles: $H^+ + H^+ + O^+ (q = 3)$; crosses: $H^+ + H^+ + O^{0,-}$.

proton collision, electron collisions, photoionization), and blends them with an assumption about which fragments are created when more electrons are removed. At lower energies these multiple electron removal events are due to processes such as transfer ionization and pure multiple ionization.

In Figure 11.7 it is shown that the microscopic BGM-IPM calculations when supplemented with the post-collision fragmentation model are quite capable of describing the details of the fragmentation pattern over a wide range of energies. The effect of multiple-electron removal is to produce a reversal in strength of the H^+ versus OH^+ yields, and a dramatic increase of O^+ yields at low energies. The H_2O^+ channel (which is exclusive to $q = 1$) is seen to be predicted too low by the theory below 100 keV impact energy.

There are more detailed experimental data at low energies, namely fragmentation following electron capture vs. pure ionization. An analysis can be found in Ref. 25.

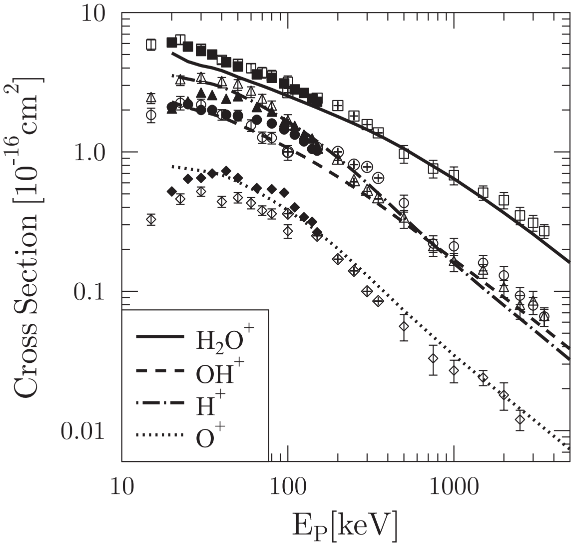

Figure 11.7 Fragmentation cross sections in $p - H_2O$ collisions vs. projectile energy. Experiments: Squares: H_2O^+; triangles: H^+, circles OH^+; diamonds: O^+. Symbols with crosses: Werner et al.;[6] solid symbols: Gobet et al.;[8] open symbols: Luna et al.[9] Present theory: H_2O^+—solid line; H^+—dash-dotted; OH^+—dashed; O^+—dotted.

4. SUMMARY AND OUTLOOK

In the past 15 years the density functional theory based calculations using the basis generator method as a means to propagate Kohn–Sham-type orbitals have explained a wealth of data in ion–atom collisions. While much emphasis was placed on neon and argon target atoms, successful applications to an open-shell system such as atomic oxygen were also developed. In recent years we extended this work to simple molecules and applied the formalism to the case of H_2O targets. In the regime of fast collisions (above 10 keV/amu) we can safely ignore molecular rotational and vibrational degrees of freedom due to their longer time scales. Fragmentation of the ionized molecule happens also on much longer time scales than the collision itself, and is therefore not treated as part of the time-dependent dynamics.

Nevertheless, the extension of the TDDFT approach to molecular targets faces the following challenges: (i) in principle, multi-center matrix elements of the electrostatic interactions are necessary; (ii) an orientation average has to be carried out when total cross sections are calculated. In the present work multi-center matrix elements are avoided by working in an energy representation of the target Hamiltonian. The calculations are carried out very efficiently by representing the molecular orbitals (from a restricted HF calculation) in terms of an atomic oxygen basis. A short coming of this representation may be that the orbital densities are not accurate as far as electric multipole moments are concerned. On the other hand, it may actually help by requiring a reduced effort in the orientation averaging procedure. For most of the results shown this does not appear to be a significant weakness. Some work in the future should be dedicated, however, to test these assumptions in more detail.

The independent particle model (using a determinantal analysis) does respect the Pauli principle. This becomes important even for basic total cross sections when the projectile carries electrons into the collision. Some open questions remain in this subfield, and should be addressed by using a more sophisticated effective potential which is common to both target and projectile electrons, but which does not suffer from incorrect asymptotic behavior.

The dynamical TDDFT calculations (which so far are carried out only at the no-response level) are then supplemented with a semi-phenomenological fragmentation model. This model takes into account multi-electron processes as predicted by the independent particle model. Fragmentation patterns change as one goes from the high-energy limit towards lower energies. Their main features have been explained by the present work for the first time.

Future work should concentrate on some improvements. In particular, we can imagine that dynamic response will play a role at energies below 100 keV/amu—it ought to suppress some of the multi-electron processes. More realistic molecular orbital representation is also on our wish list. A short-term goal, however, should be the application of the methodology to other small molecules.

ACKNOWLEDGMENTS

This work was supported by NSERC Canada and by SHARCNET.

REFERENCES

1. Belkić, Dž. Review of theories on ionization in fast ion–atom collisions with prospects for applications to hadron therapy. *J. Math. Chem.* **2010**, *47*, 1366.
2. Boudaïffa, B.; Cloutier, P.; Hunting, D.; Huels, M. A.; Sanche, L. Resonant formation of DNA strand breaks by low-energy (3 to 20 eV) electrons. *Science* **2000**, *287*, 1658.
3. Tavernelli, I.; Gaigeot, M.-P.; Vuilleumier, R.; Stia, C.; Hervé du Penhoat, M.-A.; Politis, M.-F. Time-dependent density functional theory molecular dynamics simulations of liquid water radiolysis. *Chem.Phys.Chem.* **2008**, *9*, 2099.
4. Rudd, M. E.; Goffe, T.V.; DuBois, R. D.; Toburen, L. H. Cross sections for ionization of water vapor by 7–4000 keV protons. *Phys. Rev. A* **1985**, *31*, 492.

5. Rudd, M. E.; Itoh, A.; Goffe, T. V. Cross sections for ionization, capture, and loss for 5–450 keV He^+ on water vapor. *Phys. Rev. A* **1985**, *32*, 2499.
6. Werner, U.; Beckord, K.; Becker, J.; Lutz, H. O. 3D imaging of the collision-induced Coulomb fragmentation of water molecules. *Phys. Rev. Lett.* **1995**, *74*, 1962.
7. Gobet, F.; Farizon, B.; Farizon, M.; Gaillard, M. J.; Carré, M.; Lezius, M.; Scheier, P.; Märk, T. D. Total, partial and electron-capture cross sections for ionization of water vapor by 20–150 keV protons. *Phys. Rev. Lett.* **2001**, *86*, 3751.
8. Gobet, F.; Eden, S.; Coupier, B.; Tabet, J.; Farizon, B.; Farizon, M.; Gaillard, M. J.; Carré, M.; Ouaskit, S.; Märk, T. D.; Scheier, P. Ionization of water by (20–150) keV protons: separation of direct-ionization and electron-capture process. *Phys. Rev. A* **2004**, *70*, 062716.
9. Luna, H.; de Barros, A. L. F.; Wyer, J. A.; Scully, S. W. J.; Lecointre, J.; Garcia, P. M. Y.; Sigaud, G. M.; Santos, A. C. F.; Senthil, V.; Shah, M. B.; Latimer, C. J.; Montenegro, E. C. Water-molecule dissociation by proton and hydrogen impact. *Phys. Rev. A* **2007**, *75*, 042711.
10. Garcia, P. M. Y.; Sigaud, G. M.; Luna, H.; Santos, A. C. F.; Montenegro, E. C.; Shah, M. B. Water-molecule dissociation by impact of He^+ ions. *Phys. Rev. A* **2008**, 77, 052708.
11. Gabás, P. M. M.; Errea, L. F.; Méndez, L.; Rabadán, I. Ab initio treatment of charge transfer in ion-molecule collisions based on one-electron wave functions. *Phys. Rev. A* **2012**, *85*, 012702.
12. Boudrioua, O.; Champion, C.; Dal Cappello, C.; Popov, Y. V. Ab initio calculation of differential and total cross sections for the ionization of water vapor by protons. *Phys. Rev. A* **2007**, *75*, 022720.
13. Dubois, A.; Carniato, S.; Fainstein, P. D.; Hansen, J. P. Ionization of water molecules by fast charged projectiles. *Phys. Rev. A* **2011**, *84*, 012708.
14. Gervais, B.; Beuve, M.; Olivera, G. H.; Galassi, M. E. Numerical simulation of multiple ionization and high LET effects in liquid water radiolysis. *Radiat. Phys. Chem.* **2007**, *75*, 493.
15. Errea, L. F.; Illescas, Clara; Méndez, L.; Pons, B.; Rabadán, I.; Riera, A. Classical calculation of ionization and electron-capture total cross sections in $H^+ - H_2O$ collisions. *Phys. Rev. A* **2007**, *76*, 040701R.
16. Abbas, I.; Champion, C.; Zarour, B.; Lasri, B.; Hanssen, J. Single and multiple cross sections for ionizing processes of biological molecules by protons and ß-particle impact: a classical Monte Carlo approach. *Phys. Med. Biol.* **2008**, *53*, N41.
17. Illescas, Clara; Errea, L. F.; Méndez, L.; Pons, B.; Rabadán, I.; Riera, A. Classical treatment of ion-H_2O collisions with a three-center model potential. *Phys. Rev. A* **2011**, *83*, 052704.
18. Kirchner, T.; Horbatsch, M.; Lüdde, H. J.; Dreizler, R. M. Time-dependent screening effects in ion–atom collisions with many active electrons. *Phys. Rev. A* **2000**, *62*, 042704.
19. Kirchner, T.; Horbatsch, M.; Lüdde, H. J. Nonperturbative calculation of charge-changing processes in C^{4+} scattering from neon atoms. *Phys. Rev. A* **2001**, *64*, 012711.
20. Kirchner, T.; Horbatsch, M.; Lüdde, H. J. Time-dependent independent-particle model calculation of multiple capture and ionization processes in p–Ar, $\bar{p}$–Ar, and He^{2+}–Ar collisions. *Phys. Rev. A* **2002**, *66*, 052719.
21. Kirchner, T.; Lüdde, H. J.; Horbatsch, M. A time-dependent quantal approach to electronic transitions in atomic collisions. *Recent Res. Dev. Phys.* **2004**, *5*, 433.
22. Lüdde, H. J.; Spranger, T.; Horbatsch, M.; Kirchner, T. Nonperturbative, quantum-mechanical approach to ion collisions from molecular targets. *Phys. Rev. A* **2009**, *80*, 060702R.
23. Kirchner, T.; Murakami, M.; Horbatsch, M.; Lüdde, H. J. Calculations for charge transfer and ionization in heavy-particle collisions from water molecules. *J. Phys.: Conf. Ser.*, **2012**,

388, 012038 (Part 1); Murakami, M.; Kirchner, T.; Horbatsch, M.; Lüdde, H.J. Quantum -mechanical calculation of multiple electron removal and fragmentation cross sections in $\mathrm{He}^+ - \mathrm{H_2O}$ collisions. *Phys. Rev. A* 2012, *86*, 022719.

24. Murakami, M.; Kirchner, T.; Horbatsch, M.; Lüdde, H. J. Single and multiple electron removal processes in proton–water-molecule collisions. *Phys. Rev. A* **2012**, *85*, 052704.
25. Murakami, M.; Kirchner, T.; Horbatsch, M.; Lüdde, H. J. Fragmentation of water molecules by proton impact: the role of multiple electron processes. *Phys. Rev. A* **2012**, *85*, 052713.
26. Runge, E.; Gross, E. K. U. Density-functional theory for time-dependent systems. *Phys. Rev. Lett.* **1984**, *52*, 997.
27. Pople, J. A. Nobel lecture: quantum chemical models. *Rev. Mod. Phys.* **1999**, *71*, 1267.
28. Kirchner, T.; Horbatsch, M.; Lüdde, H. J. Coupled mean-field description of electron removal processes in $\mathrm{He}^+ + \mathrm{Ne}$ and $\mathrm{He}^+ + \mathrm{Ar}$ collisions. *J. Phys. B* **2004**, *37*, 2379.
29. Kirchner, T.; Santos, A. C. F.; Luna, H.; Sant'Anna, M. M.; Melo, W. S.; Sigaud, G. M.; Montenegro, E. C. Charge-state-correlated cross sections for electron loss, capture, and ionization in C^{3+}–Ne collisions. *Phys. Rev. A* **2005**, *72*, 012707.
30. Lüdde, H. J.; Dreizler, R. M. Comments on inclusive cross sections. *J. Phys. B* **1985**, *18*, 107.
31. Kroneisen, O. J.; Lüdde, H. J.; Kirchner, T.; Dreizler, R. M. The basis generator method: optimized dynamical representation of the solution of time-dependent quantum problems. *J. Phys. A* **1999**, *32*, 2141.
32. Aung, S.; Pitzer, R. M.; Chan, S. I. Approximate Hartree–Fock wavefunctions, one-electron properties, and electronic structure of the water molecule. *J. Chem. Phys.* **1968**, *49*, 2071.
33. Toburen, L. H.; Nakai, M. Y.; Langley, R. A. Measurement of high-energy charge-transfer cross sections for incident protons and atomic hydrogen in various gases. *Phys. Rev.* **1968**, *171*, 171.
34. Bolorizadeh, M. A.; Rudd, M. E. Angular and energy dependence of cross sections for ejection of electrons from water vapor. II. 15–150 keV proton impact. *Phys. Rev. A* **1986**, *33*, 888.

CHAPTER TWELVE

Four-Body Theories for Transfer Ionization in Fast Ion-Atom Collisions

Dževad Belkić[a], **Ivan Mančev**[b] **and Nenad Milojević**[b]
[a]Nobel Medical Institute, Karolinska Institute, Stockholm, Sweden
[b]Department of Physics, Faculty of Sciences and Mathematics, University of Niš, Niš, Serbia

Contents

Abstract

Total cross sections for high-energy transfer ionization in collisions between bare projectiles with helium are investigated using several three- and four-body methods in the semi-classical impact-parameter and quantum-mechanical formalisms. The results are compared with experimental data for transfer ionization in the H^+ — He, He^{2+} — He, and Li^{3+}—He collisions. It is found that the cross sections from the four-body continuum distorted wave and the four-body Born distorted wave methods compare favorably with the available measured findings, especially at higher impact energies that are within the expected region of validity of these theories.

1. INTRODUCTION

Two-electron transitions in four-body fast ion-atom collisions have been extensively studied in the last two decades both theoretically and experimentally. This includes transfer ionization (TI) as a collision between a nucleus as a projectile and a two-electron target from which one electron is captured and the other ionized. Transfer ionization, which is the subject

Advances in Quantum Chemistry, Volume 65
ISSN 0065-3276, http://dx.doi.org/10.1016/B978-0-12-396455-7.00012-1

of the present study, remains one of the most challenging collisional processes with two active electrons, even in the simplest case which involves helium-like targets. This collisional phenomenon has opened interesting and fruitful discussions about different scattering mechanisms within the first- and second-order theories, including the role of static as well as dynamic electron correlations.

The majority of the theoretical investigations[1–5] that have considered TI collisions employed the independent particle model (IPM) and the independent event (IEV) model. The IPM and IEV models ignore the inter-electron correlations from the outset and compute the probability for TI as a product of the individual probabilities for capture of one electron and independent ionization of the other electron. The basic feature of these previous investigations within the IPM and its variants is the preservation of a pure three-body formalism, despite the fact that the studied four-body problems include two active electrons. The IPM has been applied to TI within the continuum distorted wave (CDW-IPM) and the continuum distorted wave eikonal initial state (CDW-EIS-IPM) approximations. Although the IPM or IEV versions of other competitive models were outperformed by the CDW-IPM and CDW-EIS-IPM approximations, these two latter methods still gave cross sections that were larger than the experimental values, especially for the case of the H^+ impact. Such drawbacks can be partially overcome by employing the four-body formalism of scattering theory within e.g., the continuum distorted wave (CDW-4B)[6, 7] and Born distorted wave (BDW-4B)[8] approximations that are capable of yielding satisfactory agreement with the existing experimental data. This will be demonstrated in the present review.

2. THE INDEPENDENT PARTICLE/EVENT MODELS

The simplest way to carry out a theoretical examination of TI in fast ion-atom (two- or multi-electron) collisions is the IPM, in which the interaction between the electrons is considered primarily in the so-called mean field approximation. In this picture each electron evolves independently in an effective potential created by the other electrons. For evaluations of cross sections for multiple processes, this method requires the computation of single-particle probabilities as a function of the impact parameter.

In general, the IPM has been frequently used for describing collisions of multiply-charged nuclei with helium-like targets, but many computations have shown that the IPM model fails to reproduce experimental data in a systematic manner, thus casting doubt about its practical usefulness. Therefore, it can be anticipated that multiple processes induced by impact of light bare ions should require a theoretical description that goes beyond the IPM when single-particle probabilities are obtained from the existing perturbation models. One method that achieves this purpose, without actually solving the fully correlated problem, is the IEV model of Dunseath and Crothers,[1] who studied the TI process using the three-body CDW method for computations of single-particle probabilities. In the IEV model the TI process is a result of different steps (events) involving one active electron. The net probability is computed as the product of individual probabilities for each event. The main feature is that the second electron makes a transition to the final state, not from its initial unperturbed state, but from an intermediate state where it was left after the first electron made the transition to its final state. The case where the electrons follow different reaction channels is taken into account in the IEV model through different sequences of events. It is clear that a full description of the processes depends on the time sequence in which the events are produced. The IEV model gives a reasonable framework to deal with multiple-electron processes. Computations of total cross sections for TI in $He^{2+} + He$ collisions by Dunseath and Crothers,[1] using the CDW model to obtain the single-particle probabilities, show an improvement with respect to the IPM in comparison with the available experimental data.

The three-body CDW method for single ionization was formulated by Belkić.[9] In this method, the distortions due to electronic continuum intermediate states are properly included in the entrance and exit channels. Nevertheless, the corresponding full Coulomb wave function within the initial scattering state was found in applications to lead to overestimation of experimentally measured total cross sections near and below the Massey peak. Typically, all total cross sections computed by the CDW method keep on rising as the impact energy decreases, whereas the corresponding experimental data generally decline in the same region exhibiting the Massey peak. This bending of the curve for the total cross sections can be obtained within the CDW methodologies, if the full Coulomb wave function for the distortion of the initial state in the entrance channel is approximated by its long-range asymptotic eikonal form through the well-known logarithmic factor. The product of this latter factor and the unperturbed initial state in the entrance channel represents the eikonal initial state (EIS). The resulting simplification of the CDW method is abbreviated as CDW-EIS.[10] In this way, the Massey peak is systematically reproduced by the CDW-EIS method, leading to quantitative agreement with measurements. The CDW and CDW-EIS methods are computationally attractive, since the fully analytical expressions are available for the transition amplitudes for ionizing collisions involving one active electron. Recently Belkić[12] reviewed theories on ionization in fast ion-atom collisions with prospects for applications to hadron therapy for patients with deep-seated cancer for which high-energy ions ($\sim$400 MeV/amu) are employed.

We shall first present the CDW-EIS approximation for TI within the IPM (CDW-EIS-IPM) and IEV (CDW-EIS-EIV) models. The CDW-EIS approach has been introduced by Crothers and McCann[10] for single ionization of hydrogen-like targets and later extended by Fainstein et al.[11] to multi-electronic targets with a remarkable success in many applications. In the CDW-EIS-IPM and CDW-EIS-EIV both probabilities for electron capture and ionization are computed by means of the CDW-EIS approximation.

Using the straight-line version of the IPM, the initial and final undistorted wave functions are distorted by multiplicative factors. These distorted waves satisfy the asymptotic conditions for the Coulomb potentials in both channels. In the entrance channel the target bound-state wave function is multiplied by an eikonal phase which, at large distances, describes the state of the active electron in the projectile field. In the outgoing channel the distortion scheme varies according to different reactions. For electron capture (or ionization) the projectile bound-state (or target continuum) wave function is multiplied by a Coulomb factor which accounts for the fact that the active electron is simultaneously in the residual target (or projectile) continuum. Importantly, such a modeling acknowledges the following two features. First, in the final state the emitted or captured electron evolves in a two-center potential. Second, the perturbation represents the residual potential obtained from the application of the full Hamiltonian to the ansatz for the initial or final distorted waves. The differences between the CDW and CDW-EIS methods are in the initial bound-state distortion and the residual potential. Several possibilities are available for the construction of the target wave functions. Thus, for example, Galassi et al.[2] followed Fainstein et al.[11] and used analytical wave-functions that permit obtaining the transition amplitude in a closed form. This is very useful since the computations of the single-particle impact-parameter-dependent probabilities could be very time consuming.

For computations of the total cross sections for a TI process, we will employ the IPM and IEV. To this end, it is necessary to obtain the transition amplitude as a function of the impact parameter ρ. The differential cross section for the TI process is given by:

$$\frac{\mathrm{d}Q}{\mathrm{d}\vec{\kappa}} = 2\pi \int_0^\infty \mathrm{d}\rho\rho P_{\mathrm{TI}}(\rho,\vec{\kappa}). \tag{1}$$

The quantity $P_{\mathrm{TI}}(\rho,\vec{\kappa})$ in the case of IPM is expressed by:

$$P_{\mathrm{TI}}^{(\mathrm{IPM})}(\rho,\vec{\kappa}) = 2P_{\mathrm{I}}(\rho,\vec{\kappa})P_{\mathrm{C}}(\rho). \tag{2}$$

Here, $P_{\mathrm{I}}(\rho,\vec{\kappa})$ is the ionization probability per electron as a function of impact parameter ρ and the emitted electron momentum $\vec{\kappa}$ in the final state. Further, $P_{\mathrm{C}}(\rho)$ is the impact-parameter-dependent single-particle probability for electron capture which is computed using the three-body CDW-EIS model, as in the work of Busnengo et al.[13]

In the IEV model the collisional process involving helium can occur by following two different pathways. One electron can become ionized first, and then the other electron may be captured (ionization-capture). Or, capture of one electron occurs first, and then the other electron is emitted (capture-ionization). If we label the two electrons of helium as 1 (the first active electron) and 2 (the second active electron) the probability for TI can be written as:

$$P_{\mathrm{TI}}^{(\mathrm{IEV})}(\rho,\vec{\kappa}) = P_{\mathrm{I1}}(\rho,\vec{\kappa})P_{\mathrm{C2}}(\rho) + P_{\mathrm{I2}}(\rho,\vec{\kappa})P_{\mathrm{C1}}(\rho). \tag{3}$$

Quantity $P_{\mathrm{I1}}(\text{or}\, P_{\mathrm{I2}})$ is the probability that electron 1 (or 2) is emitted, whereas $P_{\mathrm{C1}}(\text{or}\, P_{\mathrm{C2}})$ is the probability that electron 1 (or 2) is captured. In the IPM model, we have $P_{\mathrm{I1}} = P_{\mathrm{I2}}$ and $P_{\mathrm{C1}} = P_{\mathrm{C2}}$. Therefore, taking these features into account within Eq. (3), one can retrieve Eq. (2). In contrast, in the IEV model these probabilities are different and they are computed as follows. If the electron 1 is ionized, then P_{I1} corresponds to single ionization of helium, as computed using e.g., the CDW-EIS model according to the study by Fainstein et al.[11] Further, P_{C2} is the probability for one-electron capture from $\mathrm{He}^+(1s)$ which may also be computed using the CDW-EIS model, as done by Martínez et al.[14] In the second pathway, the first electron is captured from helium and P_{C1} is computed using the CDW-EIS model with the Roothaan–Hartree–Fock wave functions of Clementi and Roetti[15] to describe the initial active electron orbital. In the computation from Ref. 2, capture is included to the ground state as well as to the excited states with the principal quantum numbers $n = 2$ and 3. The non-captured electron is supposed to remain frozen during this first step. The second step corresponds to ionization of $He^+(1s)$ with the probability P_{I2}. In the case of the H^+ impact, P_{I2} corresponds to ionization of $He^+(1s)$ by a neutral hydrogen atom and is computed considering that the projectile electron remains frozen during this second step. Thus, we take into account a screening effect due to the projectile electron, but neglect the anti-screening effects (excitation of the projectile electron). In the experiment of Bernardi et al.[16] the emitted electron is recorded in coincidence with the neutral projectile and, therefore, a process of simultaneous emission from the projectile and target cannot occur. If the first step corresponds to capture to the projectile ground state, two-center effects will be of minor importance for the H(1*s*) impact and thus P_{I2} can be computed using e.g., the first Born approximation of Bates and Griffing.[17, 18] In the case of capture to the excited states H(*nlm*) (with $n \geqslant 2$), we consider that capture has been produced at small impact parameters, so that TI is dominated by this region.

Since the excited projectile electron remains, on the average, outside the interaction region, it is assumed that it does not contribute to the ionization reaction. In this way, the process is considered to be produced by the projectile nucleus and, therefore, the CDW-EIS model can be employed. The same assumptions are used to study the He^+ impact case. The only difference with the hydrogen atom impact is in the fact that a Coulomb asymptotic perturbation potential of the effective charge +1 appears for He^+. Thus, for the $He^+(1s)$ impact, the CDW-EIS computation is performed corresponding to an effective projectile Coulomb potential with the net charge +1, whereas for the $He^+(nlm)$ ($n \geqslant 2$), the CDW-EIS is applied using the effective projectile Coulomb potential of charge +2. Hence, the IEV model requires not only the single capture and ionization probabilities for a neutral helium atom, but also for the He^+ ion.

Although multiple differential cross sections provide detailed information about collision processes, the total cross sections also yield good insights into global trends. Therefore, in the present review, we shall focus on total cross sections. Total cross sections for TI are obtained from differential cross sections after integration over the emitted

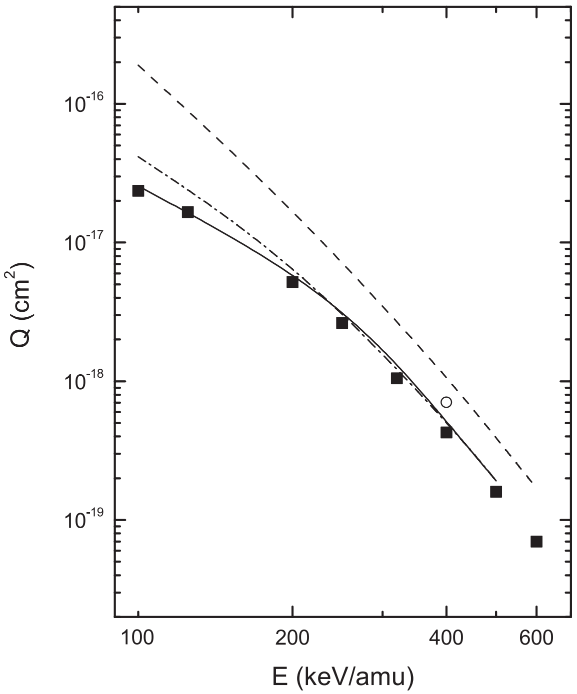

Figure 12.1 Total cross sections $Q(\mathrm{cm}^2)$ as a function of the laboratory incident energy E(keV/amu) for transfer ionization: $\mathrm{He}^{2+} + \mathrm{He} \longrightarrow \mathrm{He}^{+} + \mathrm{He}^{2+} + \mathrm{e}$. The full curve: CDW-EIS-IEV model;[2] the dot-dashed curve: CDW-EIS-IPM model;[2] the dashed curve: CDW-IEV model;[1] the symbol ○ represents the theoretical result of the CDW-Born-IPM.[3] Experimental data: ■ Shah and Gilbody.[20]

electron momenta $(\vec{\kappa})$. The results of total cross sections for TI in the $\mathrm{He}^{2+} + \mathrm{He}$ and $\mathrm{H}^{+} + \mathrm{He}$ collisions are plotted in Figures 12.1 and 12.2, respectively. It is seen that with the CDW-EIS-EIV model,[2] there is an improvement with respect to the findings from the CDW-IEV approach of Dunseath and Crothers,[1] most notably at the intermediate impact energies. This could be a confirmation of the conjecture of these authors that the normalization of the CDW wave function might be the reason for which the CDW method overestimates the experimental data for TI. The computations in the CDW-EIS-IPM[2] are in good qualitative agreement with the experimental data. Nevertheless, with the CDW-EIS, the IEV model yields better results than the IPM. This supports the picture of a process in two successive steps. Notice that the difference between these two models is larger at intermediate impact energies and

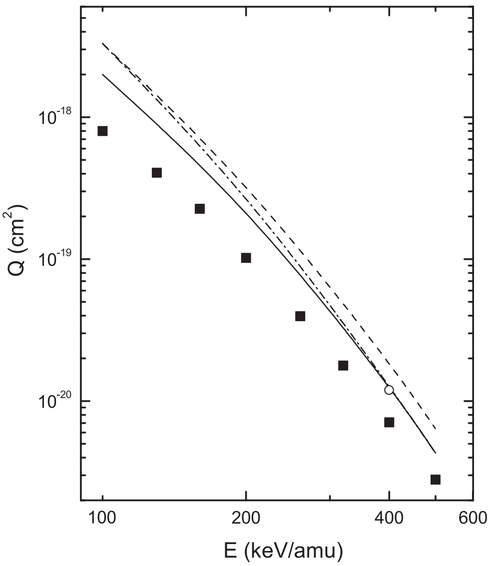

Figure 12.2 Total cross sections $Q(\mathrm{cm}^2)$ as a function of the laboratory incident energy E(keV/amu) for transfer ionization: $\mathrm{H}^+ + \mathrm{He} \longrightarrow \mathrm{H} + \mathrm{He}^{2+} + \mathrm{e}$. The full curve: CDW-EIS-IEV model;[2] the dot-dashed curve: CDW-EIS-IPM model;[2] the dashed curve: CDW-IEV model;[1] the symbol ○ represents the theoretical result of the CDW-Born-IPM.[3] Experimental data: ■ Shah and Gilbody.[20]

that they converge to each other at high energies. At high energies the ionization-capture channel dominates, but capture-ionization still gives a significant contribution of the order of 20%. Therefore, confluence of the IEV and IPM at high energies can be attributed to a subtle addition from different channels and not necessarily to the dominance of one of the channels.

Gayet and Salin[3] used the IPM and the Hartree–Fock wave function for the initial two-electron bound state of helium and assumed that the second electron is not affected when the first electron is ionized or captured. In their computations,[3] the capture amplitude was evaluated within the CDW-3B approximation by including a contribution from capture into low-lying excited states of the projectile. The ionization amplitude was computed using the first Born approximation. The authors from Ref. 3 carried out their computations only at a single energy (400 keV/amu) and the results of such a CDW-Born model are displayed by the open circle in Figures 12.1 and 12.2.

We can conclude that the total cross sections in the CDW-EIS-IEV model are in better agreement with the experimental data than those due to the CDW-EIV model. However, the results of the CDW-EIS-IEV are still larger than the experimental values, especially for the case of proton impact. In contrast, the cross sections from the IPM overestimate the experimental data, even if we use the single-particle probabilities from the CDW-EIS approximation. This supports a description of the investigated process as a combination of successive events in different paths. It should be re-emphasized that the IEV and IPM completely ignore the dynamic correlations and compute the net probability for transfer ionization as a product of the individual probabilities for transfer of one electron and independent ionization of the other electron.

Focusing our interest on the case of a bare swift ion impacting on a two-electron atomic target, a four-body theoretical representation appears as necessary in order to include the static and dynamic correlations. Therefore, we propose the formalism of a four-body reaction under study as a pure four-body problem, thus avoiding the said limitations of a three-body representation. The four-body formalism of scattering theory within e.g., the CDW-4B and BDW-4B approximations could be anticipated as being more capable of yielding satisfactory agreement with the existing experimental data.

3. THE FOUR-BODY CONTINUUM DISTORTED WAVE METHOD

The CDW-4B method for TI has been formulated and implemented by Belkić et al.[21] for the $He^{2+} + He$ collisions and good agreement was found with measurements. Later, the CDW-4B method employed by Mančev[22] has also been reported to be in satisfactory agreement with the experimental data for the $Li^{3+} + He$ collisions.

Let $\vec{s}_{1,2}$ and $\vec{x}_{1,2}$ be the position vectors of the electrons $e_{1,2}$ relative to the nuclear charges Z_P and Z_T, respectively. Let electron e_1 be captured and electron e_2 simultaneously ionized. We denote by $\vec{R}$ the position vector of the target nucleus (T) with respect to the projectile nucleus (P). The distance between the two electrons will be denoted by $\vec{r}_{12}$. The transition amplitudes in the "prior" (T_{if}^{-}) and "post" (T_{if}^{+}) forms for TI in the CDW-4B theory can be written as:[21]

$$\begin{aligned}T_{if}^{-} = \mathcal{N}\iiint & \mathrm{d}\vec{R}\,\mathrm{d}\vec{s}_1\,\mathrm{d}\vec{s}_2(\rho v)^{2i\nu}e^{i\vec{\alpha}\cdot\vec{s}_1+i\vec{\beta}\cdot\vec{x}_1-i\vec{\kappa}\cdot\vec{x}_2}\varphi_f^*(\vec{s}_1)\,{}_1F_1(i\nu_{\mathrm{T}},1,ivx_1+i\vec{v}\cdot\vec{x}_1)\\ &\times{}_1F_1(i\zeta,1,ipx_2+i\vec{p}\cdot\vec{x}_2)\,[V_{\mathrm{P}}(R,s_2)\,{}_1F_1(i\nu_{\mathrm{P}},1,ivs_1+i\vec{v}\cdot\vec{s}_1)\varphi_i(\vec{x}_1,\vec{x}_2)\\ &-\vec{\nabla}_{x_1}\varphi_i(\vec{x}_1,\vec{x}_2)\cdot\vec{\nabla}_{s_1}\,{}_1F_1(i\nu_{\mathrm{P}},1,ivs_1+i\vec{v}\cdot\vec{s}_1)\\ &-{}_1F_1(i\nu_{\mathrm{P}},1,ivs_1+i\vec{v}\cdot\vec{s}_1)(E_i-H_{\mathrm{T}})\varphi_i(\vec{x}_1,\vec{x}_2)]\,,\end{aligned}\tag{4}$$

$$\begin{aligned}T_{if}^{+} = \mathcal{N}\iiint & \mathrm{d}\vec{R}\,\mathrm{d}\vec{x}_1\,\mathrm{d}\vec{x}_2(\rho v)^{2i\nu}e^{i\vec{\alpha}\cdot\vec{s}_1+i\vec{\beta}\cdot\vec{x}_1-i\vec{\kappa}\cdot\vec{x}_2}\varphi_i(\vec{x}_1,\vec{x}_2)\\ &\times{}_1F_1(i\nu_{\mathrm{P}},1,ivs_1+i\vec{v}\cdot\vec{s}_1)\,{}_1F_1(i\zeta,1,ipx_2+i\vec{p}\cdot\vec{x}_2)\\ &\times\Big\{[V_{\mathrm{P}}(R,s_2)+V(r_{12},x_1)]\,{}_1F_1(i\nu_{\mathrm{T}},1,ivx_1+i\vec{v}\cdot\vec{x}_1)\varphi_f^*(\vec{s}_1)\\ &-\vec{\nabla}_{s_1}\varphi_f^*(\vec{s}_1)\cdot\vec{\nabla}_{x_1}\,{}_1F_1(i\nu_{\mathrm{T}},1,ivx_1+i\vec{v}\cdot\vec{x}_1)\Big\}\,,\end{aligned}\tag{5}$$

$$V_{\mathrm{P}}(R,s_2)=Z_{\mathrm{P}}\left(\frac{1}{R}-\frac{1}{s_2}\right),\quad V(r_{12},x_1)=\left(\frac{1}{r_{12}}-\frac{1}{x_1}\right),\tag{6}$$

where $\nu = Z_{\mathrm{P}}Z_{\mathrm{T}}/v$, whereas the factor $(\rho v)^{2i\nu}$ originates from internuclear potential $Z_{\mathrm{P}}Z_{\mathrm{T}}/R$ and it disappears from differential $Q_{if}^{\pm}(\vec{\kappa})$ as well as total cross section $Q_{if}^{\pm}$ after integration over $\vec{\eta}$ (see Eqs. (7) and (8)). The symbol ${}_1F_1(a,b,x)$ stands for the usual Kummer hypergeometric function. The momentum vector of the ejected electron e_2 with respect to its parent nucleus T is denoted by $\vec{\kappa}$. The wave function of the initial bound state is labeled by $\varphi_i(\vec{x}_1,\vec{x}_2)$, whereas $\varphi_f(\vec{s}_1)$ is the single electron hydrogen-like wave function of the $(Z_{\mathrm{P}};e_1)$ system in the exit channel. The remaining quantities in transition amplitudes $T_{if}^{\pm}$ are defined as follows:

$$\begin{aligned}&\mathcal{N}=(2\pi)^{-3/2}N^{-*}(\zeta)N',\quad N'=N^{+}(\nu_{\mathrm{P}})N^{-*}(\nu_{\mathrm{T}}),\\ &N^{-}(\zeta)=\Gamma(1+i\zeta)\mathrm{e}^{\pi\zeta/2},\\ &N^{-}(\nu_{\mathrm{T}})=\Gamma(1+i\nu_{\mathrm{T}})\mathrm{e}^{\pi\nu_{\mathrm{T}}/2},N^{+}(\nu_{\mathrm{P}})=\Gamma(1-i\nu_{\mathrm{P}})\mathrm{e}^{\pi\nu_{\mathrm{P}}/2},\\ &\nu_{\mathrm{P}}=\frac{Z_{\mathrm{P}}}{v},\quad\nu_{\mathrm{T}}=\frac{Z_{\mathrm{T}}-1}{v},\quad\zeta=\frac{Z_{\mathrm{T}}}{p},\quad\vec{p}=\vec{v}+\vec{\kappa}.\end{aligned}$$

The momentum transfers $\vec{\alpha}$ and $\vec{\beta}$ are given by:

$$\vec{\alpha}=\vec{\eta}-\left(\frac{v}{2}-\frac{Q}{v}\right)\hat{\vec{v}},\quad\vec{\beta}=-\vec{\eta}-\left(\frac{v}{2}+\frac{Q}{v}\right)\hat{\vec{v}},$$

whereas the vector $\vec{\eta}$ is the transverse momentum transfer: $\vec{\alpha} + \vec{\beta} = -\vec{v}$ and $\vec{\eta} \cdot \vec{v} = 0$, where the impact velocity vector $\vec{v}$ is directed along the Z-axis. The Q factor or the inelasticity factor is defined as: $Q = E_i - (E_f + E_\kappa)$, where E_i and $E_f = -{\rm Z_P}^2/(2n_f^2)$ are the initial and final binding energies, and $E_\kappa = \kappa^2/2$. The "prior" transition amplitude contains the term with the factor $(E_i - H_{\rm T})\varphi_i(\vec{x}_1, \vec{x}_2)$ where $H_{\rm T} = -\nabla_{x_1}^2/(2b) - \nabla_{x_2}^2/(2b) - {\rm Z_T}/x_1 - {\rm Z_T}/x_2 + 1/r_{12}$, with $b = m_{\rm T}/(m_{\rm T} + 1)$, and $m_{\rm T}$ is the mass of the target nucleus. If the bound-state wave function for helium were known exactly, the function $\varphi_i'(\vec{x}_1, \vec{x}_2) \equiv (E_i - H_{\rm T})\varphi_i(\vec{x}_1, \vec{x}_2)$ would vanish identically. Since the helium exact wave function is unavailable, the contribution from $\varphi_i'(\vec{x}_1, \vec{x}_2)$ is not equal to zero. This implies that this term, in principle, should be kept throughout in the "prior" transition amplitude. Such an addendum to the T-matrix element has been suggested by Belkić[23] within the four-body first Born approximation with the correct boundary conditions (CB1-4B) for double electron capture. The numerical computations for double electron capture[23] and for TI[21] in the α–He collisions show that this correction does not give a significant contribution at high impact energies. For this reason, we shall not consider this term as a perturbation in the transition amplitude.

The triple differential cross sections for the TI process is given by:

$$Q_{if}^{\pm}(\vec{\kappa}) \equiv \frac{{\rm d}Q_{if}^{\pm}}{{\rm d}\vec{\kappa}} = \int {\rm d}\vec{\eta} \left| \frac{T_{if}^{\pm}}{2\pi v} \right|^2, \tag{7}$$

whereas the total cross section reads as:

$$Q_{if}^{\pm} = \int {\rm d}\vec{\kappa}\; Q_{if}^{\pm}(\vec{\kappa}). \tag{8}$$

As it has been shown in Ref. 21, after analytical calculations carried out by means of the standard Nordsieck technique,[24] the expressions for the total cross sections for the TI process in the CDW-4B model can be reduced to a seven-dimensional numerical quadrature.

In the "prior" and "post" forms of the transition amplitudes, there is a common perturbation: $V_{\rm P}(R, s_2) = {\rm Z_P}(1/R - 1/s_2)$. Of course, considered outside the T-matrix element, the potential $V_{{\rm P}_2} = -{\rm Z_P}/s_2$ represents the direct Coulomb interaction between e_2 and ${\rm Z_P}$. Its asymptotic value $V_{{\rm P}_2}^{\infty}(R)$ at large distances s_2 is given by $-{\rm Z_P}/R$, since

$s_2 \longrightarrow R$ as $R \longrightarrow \infty$. Hence, the term $V_P(R, s_2)$ is precisely the difference between the finite and asymptotic value of the same overall *short-range* potential $V_P(R, s_2) = V_{P_2}(s_2) - V_{P_2}^{\infty}(R)$, in accordance with the correct boundary condition.[7, 25–27] However, when placed in the T-matrices, the potential V_{P_2} plays the role of a perturbation which can cause capture of electron e_1. This could only occur through some kind of underlying correlations between e_2 and e_1. For example, a part of the energy received by the electron e_2 in its collision with Z_P could be sufficient to facilitate the transfer of e_1 to the projectile.

The "post" form T_{if}^{+} contains an additional term: $V(r_{12}, x_1) = 1/r_{12} - 1/x_1$, which is completely absent from the T_{if}^{-}. Here the dielectronic interaction $1/r_{12}$ appears explicitly and when combined with the initial and final distorted wave functions on both centers Z_P and Z_T, it describes the well-known Thomas P-e-e scattering. Due to the perturbation $V(r_{12}, x_1)$, even the total cross section in the "post" form should be more adequate than its "prior" counterpart. The potential $1/x_1$ in $V(r_{12}, x_1) = 1/r_{12} - 1/x_1$ is the asymptotic tail of the $1/r_{12}$, since $r_{12} \to x_1$ as $x_1 \to \infty$. Hence, the term $V(r_{12}, x_1)$ is the difference between the finite and asymptotic values of the *same* potential. As such, $V(r_{12}, x_1)$ is a short-range interaction, as required by the correct boundary conditions. Using the relation $r_{12} = |\vec{x}_2 - \vec{x}_1|$, we can develop $1/x_1 = 1/|\vec{r}_{12} - \vec{x}_2|$ in a power series around $\vec{x}_2$ according to $1/x_1 = 1/|\vec{r}_{12} - \vec{x}_2| = 1/r_{12} - \vec{r}_{12} \cdot \vec{x}_2/r_{12}^3 + \cdots$, so that $V(r_{12}, x_1) = 1/r_{12} - 1/x_1 = \vec{r}_{12} \cdot \vec{x}_2/r_{12}^3 + \cdots$. This is justified by the small value of the x_2 coordinate (of the order of the Bohr radius a_0), since electron e_2 always remains bound to the projectile. From here we can see that the potential $V(r_{12}, x_1)$ contains information on the dielectronic correlation $e_1 - e_2$. When the potential $V(r_{12}, x_1)$ is placed in the T-matrix element, it plays the role of a perturbation which causes capture of electron e_1.

As an illustration of the validity of the CDW-4B method for the TI process, we shall consider the total cross sections for the following reactions:

$$\mathrm{He}^{2+} + \mathrm{He}(1s^2) \longrightarrow \mathrm{He}^{+}(1s) + \mathrm{He}^{2+} + e, \tag{9}$$

$$\mathrm{Li}^{3+} + \mathrm{He}(1s^2) \longrightarrow \mathrm{Li}^{2+}(1s) + \mathrm{He}^{2+} + e. \tag{10}$$

The total cross sections for process (9) at energies 40–1000 keV/amu are shown in Figures 12.3 and 12.4. In Figure 12.3, a comparison is made

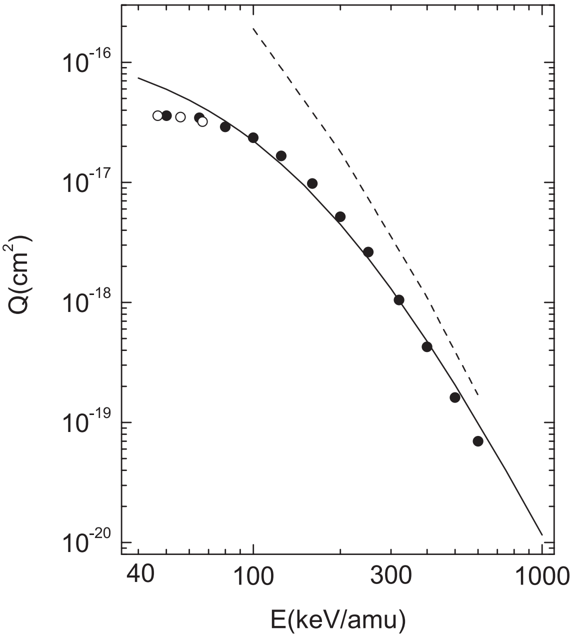

Figure 12.3 Total cross sections $Q(\mathrm{cm}^2)$ as a function of the laboratory incident energy E(keV/amu) for transfer ionization: $\mathrm{He}^{2+} + \mathrm{He}(1s^2) \longrightarrow \mathrm{He}^{+}(1s) + \mathrm{He}^{2+} + e$. The full curve represents the "post" total cross section of the CDW-4B method[21]. The dashed curve represents the corresponding "post" cross sections of the CDW-IEV model.[1] Experimental data: ○, Shah et al.;[19] and ●, Shah and Gilbody.[20]

between the CDW-4B method[21] and the CDW-IEV model.[1] From the numerical point of view, the CDW-IEV model also encounters seven-dimensional scattering integrals when dealing with the total cross sections for a TI process. The main difference between the CDW-IEV and the CDW-4B method is in the electron correlation treatment. Namely, the CDW-IEV model includes the static electron correlation (SEC) in the target by using the bound-state wave function of Pluvinage:[28]

$$\varphi_i(\vec{x}_1, \vec{x}_2) = c(k)\frac{Z_T^3}{\pi}\mathrm{e}^{-Z_\mathrm{T}(x_1+x_2)}e^{-ikr_{12}}{}_1F_1(1-ik', 2, 2ikr_{12}), \qquad (11)$$

where $k' = 1/(2k)$ and $c(k)$ is the normalization constant, with k being a non-linear variational parameter. The corresponding lowest binding energy $E_{i,\mathrm{Pluv}} = -2.878$ for the ground state ^1S of helium is obtained for $k = 0.41$, in which case $c(k) = 0.603366$. The wave function (11)

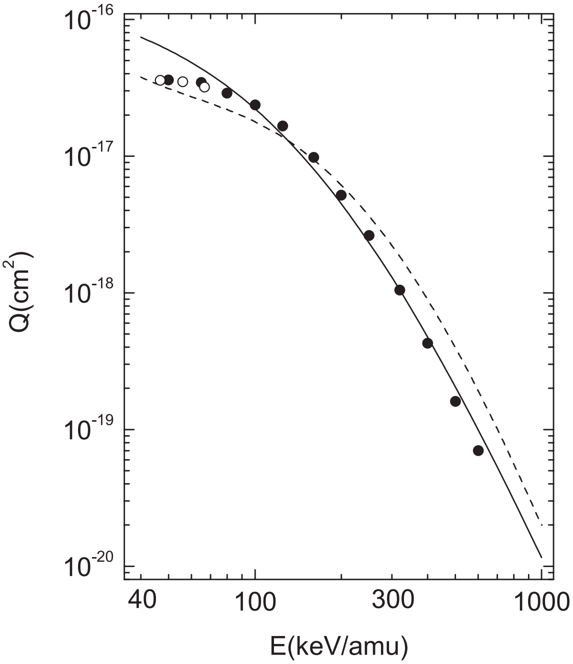

Figure 12.4 Total cross sections $Q(\mathrm{cm}^2)$ as a function of the laboratory incident energy E(keV/amu) for transfer ionization: $\mathrm{He}^{2+} + \mathrm{He}(1s^2) \longrightarrow \mathrm{He}^{+}(1s) + \mathrm{He}^{2+} + e$. The full and the dashed curves correspond, respectively, to the "post" and "prior" cross sections of the CDW-4B method.[21] Experimental data: ○, Shah et al.;[19] and ●, Shah and Gilbody.[20]

contains two entirely uncorrelated hydrogen-like wave functions with the unscreened charge Z_T multiplied with a corrective r_{12}-dependent term of the form $\exp(-ikr_{12})\,_1F_1(1 - ik', 2, 2ikr_{12})$.

In the CDW-IEV model,[1] the dynamic electron correlations (DEC) are completely neglected. In sharp contrast, the CDW-4B method explicitly includes the DEC through the dielectronic interaction $1/r_{12}$ in the transition T-operator. It should be noted that the SEC can also be fully included in the CDW-4B method by using the corresponding wave function, but it is ignored in the present illustrations that provide an unambiguous assessment of the DEC alone. The relative role of the SEC and the DEC is otherwise apparent from the two curves associated with the CDW-IEM and CDW-4B methods, as depicted in Figure 12.3. A comparison of these two theories with the experimental data in Figure 12.3, clearly shows that the CDW-4B method represents a substantial improvement over the CDW-IEV model. It can be concluded that the DEC plays a more important role than the SEC.

Further, we evaluate the "post-prior" discrepancy which arises from the unequal perturbation potentials used in the T-matrices (4) and (5). In Figure 12.4, we give the "prior" (Q_{if}^{-}) and the "post" (Q_{if}^{+}) cross sections of the CDW-4B method.[21] A comparison in Figure 12.4 reveals that the "post-prior" discrepancy is very significant throughout the energy range 40–1000 keV/amu. The "post" cross sections are larger by nearly 50% than the "prior" results at lower energies, with precisely the opposite pattern at higher energies. Such a considerable difference can be attributed to the role of the dielectronic repulsion $1/r_{12}$. We recall that the difference between Q_{if}^{-} and Q_{if}^{+} is due solely to the potential $V(r_{12}, x_1) = 1/r_{12} - 1/x_1$, which is present in the "post" and absent from the 'prior" cross sections. In the same Figure 12.4, the theoretical cross sections are compared with the experimental data for reaction (9). It can be seen from Figure 12.4 that, in contrast to the "prior" variant Q_{if}^{-}, the "post" version Q_{if}^{+} of the CDW-4B method is in good agreement with the measurements at impact energies $E \geqslant 80$ keV/amu. At lower energies, the results for Q_{if}^{+} are larger than the experimental values, as expected, since the CDW-4B method is a high-energy approximation. The superiority of the "post" over the "prior" version can be attributed primarily to the electron–electron interaction $1/r_{12}$ in the perturbation of the former variant.

The "post" and the "prior" total cross sections for TI in reaction (10), derived with the full three-term perturbation are plotted in Figure 12.5, where the experimental findings[20, 32, 33] are also shown. The CDW-4B method is seen to be in good agreement with the experimental data. The "post" cross sections lie below the "prior" ones at impact energies between 100 and 3000 keV/amu, with the reverse behavior above 3000 keV/amu. These computations have been performed for electron transfer to the ground state alone. Agreement between the CDW-4B method and the measurements at lower impact energies could be improved by including a contribution from all the excited states. The theoretical results from Ref. 34 are also depicted in Figure 12.5. These cross sections have been obtained using a relativistically covariant field approach via the second-order Feynman diagrams. As can be observed from Figure 12.5, the results from[34] largely overestimate the experimental data.

As shown by Mančev,[22] the "prior" total cross sections for reaction (10) computed with and without the term $V_P(R, s_2)$ differ from each other by a considerable amount, which can reach 67% at 50–5000 keV/amu.

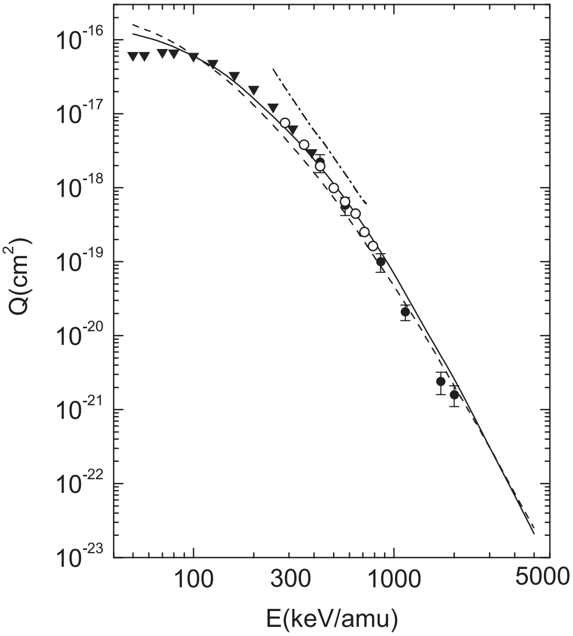

Figure 12.5 Total cross sections $Q(\mathrm{cm}^2)$ as a function of the laboratory incident energy E(keV/amu) for reaction: $\mathrm{Li}^{3+} + \mathrm{He}(1s^2) \longrightarrow \mathrm{Li}^{2+}(1s) + \mathrm{He}^{2+} + e$. The full and the dashed curves represent, respectively, the "prior" Q_{if}^{-} and "post" Q_{if}^{+} cross sections of the CDW-4B method[22] with the complete three-term perturbation potentials. The dot-dashed curve is due to a second-order method[34] from the field theory. Experimental data: ▼ Shah and Gilbody;[20] ●, Woitke et al.;[32] ○ Sant'Anna et al.[33]

The potential $-Z_P/s_2$ from $V_P(R, s_2)$ can cause capture of the electron e_1 through the $e_1 - e_2$ correlation. This points to a possible role of the DEC in the process (10). As we have seen above, the CDW-4B method is in very good accord with the experimental data on TI for the $\mathrm{He}^{2+} + \mathrm{He}$ and the $\mathrm{Li}^{3+} + \mathrm{He}$ collisions. Regarding the total cross sections for TI in the $\mathrm{H}^{+} + \mathrm{He}$ collisions at higher impact energies, the CDW-4B method overestimates some of the measured data,[28–31] whereas at intermediate energies satisfactory agreement is found with the experimental findings from Ref. 20.

4. THE FOUR-BODY BORN DISTORTED WAVE METHOD

The BDW-4B method has been formulated by Belkić and Mančev.[8] This is a fully quantum-mechanical four-body model which explicitly takes into account all the particles and their interactions in the collision, allowing for a systematic study of the correlated dynamics of the process. Further, the BDW-4B method preserves the correct boundary conditions in both scattering channels according to the principles of scattering theory.[25] Moreover, the BDW-4B method takes full account of the Coulomb continuum intermediate states of the captured electron in the exit channel. This makes the BDW-4B method coincide with the CDW-4B[21] method in the exit channel and with the CB1-4B method in the entrance channel.

The transition amplitude in the BDW-4B method can be written as:[8]

$$T_{if}^{+} = \langle \chi_f^{-} | U_f | \Phi_i^{+} \rangle. \tag{12}$$

The initial wave function Φ_i^{+} with asymptotically correct boundary condition is given by:

$$\Phi_i^{+} = \varphi_i(\vec{x}_1, \vec{x}_2) e^{i\vec{k}_i \cdot \vec{r}_i + i\nu_i \ln(vR - \vec{v} \cdot \vec{R})}, \tag{13}$$

where $\vec{r}_i$ is the relative vector of Z_P with respect to the center of mass of $(Z_T; e_1, e_2)_i$. Function $\varphi_i(\vec{x}_1, \vec{x}_2)$ represents the two-electron bound-state wave function of the atomic system $(Z_T; e_1, e_2)_i$, whereas $\vec{k}_i$ is the initial wave-vector, v is the incident velocity, and $\nu_i = Z_P(Z_T - 2)/v$. The initial state is distorted even at infinity, due to the presence of the asymptotic Coulomb repulsive potential, $V_i^{\infty} = Z_P(Z_T - 2)/R$, between the projectile and the screened target nucleus.

In the BDW-4B theory the distorted potential U_f and distorted wave χ_f^{-} are chosen according to:[21]

$$U_f = V_P(R, s_2) + V(r_{12}, x_1) - \vec{\nabla}_{s_1} ln\, \varphi_f \cdot \vec{\nabla}_{x_1}, \tag{14}$$

$$\begin{aligned} \chi_f^{-} &= N^{-}(\zeta) N^{-}(\nu_T) \phi_f \varphi_f(\vec{s}_1) {}_1F_1(-i\zeta, 1, -ipx_2 - i\vec{p} \cdot \vec{x}_2) \\ &\quad \times {}_1F_1(-i\nu_T, 1, -ivx_1 - i\vec{v} \cdot \vec{x}_1) e^{-i\vec{k}_f \cdot \vec{r}_f - i\nu \ln(vR + \vec{v} \cdot \vec{R})}, \end{aligned} \tag{15}$$

where the function ϕ_f is defined by $\phi_f = (2\pi)^{-3/2} e^{-i\vec{k}_f \cdot \vec{r}_f + i\vec{\kappa} \cdot \vec{x}_2}$, whereas $\vec{r}_f$ is the position vector of T with respect to the center of mass of the system $(Z_P, e_1)_f + e_2$ in the exit channel, $\vec{k}_f$ is the final wave-vector, and $\nu = Z_P(Z_T - 1)/v$. The quantities $\varphi_f(\vec{s}_1)$, $N^{-}(\zeta)$, and $N^{-}(\nu_T)$ have the same meaning as in CDW-4B model. The wave function χ_f^{-} obeys the correct boundary conditions.

Using Eqs. (13)–(15), the expression for the transition amplitude T_{if}^{+} in the BDW-4B method becomes:

$$\begin{aligned} T_{if}^{+} = \mathcal{M} \iiint & \mathrm{d}\vec{R}\, \mathrm{d}\vec{x}_1\, \mathrm{d}\vec{x}_2 e^{i\vec{\alpha}\cdot\vec{s}_1 + i\vec{\beta}\cdot\vec{x}_1 - i\vec{\kappa}\cdot\vec{x}_2} \mathcal{L}(R)\varphi_i(\vec{x}_1, \vec{x}_2) \\ & \times {}_1F_1(i\zeta, 1, ipx_2 + i\vec{p}\cdot\vec{x}_2)\, \{[V_{\mathrm{P}}(R, s_2) + V(r_{12}, x_1)] \\ & \times {}_1F_1(i\nu_{\mathrm{T}}, 1, i\upsilon x_1 + i\vec{\upsilon}\cdot\vec{x}_1)\varphi_f^{*}(\vec{s}_1) \\ & - \vec{\nabla}_{s_1}\varphi_f^{*}(\vec{s}_1)\cdot\vec{\nabla}_{x_1}{}_1F_1(i\nu_{\mathrm{T}}, 1, i\upsilon x_1 + i\vec{\upsilon}\cdot\vec{x}_1)\Big\}, \end{aligned} \tag{16}$$

where

$$\mathcal{M} = (2\pi)^{-3/2} N^{-*}(\nu_{\mathrm{T}}) N^{-*}(\zeta).$$

The product of logarithmic Coulomb factors is denoted by the auxiliary function $\mathcal{L}(R)$ which can be reduced to the single term:

$$\mathcal{L}(R) = e^{i\nu_i \ln(\upsilon R - \vec{\upsilon}\cdot\vec{R}) + i\nu \ln(\upsilon R + \vec{\upsilon}\cdot\vec{R})} = (\rho\upsilon)^{2i\nu_i}(\upsilon R + \vec{\upsilon}\cdot\vec{R})^{i\xi}, \tag{17}$$

where $\xi = Z_{\mathrm{P}}/\upsilon$. The multiplying term $(\rho\upsilon)^{2i\nu_i}$ does not contribute to the total cross section and can be dropped from the transition amplitudes.

Hence, such a formulated BDW-4B method is exactly equal to the CDW-4B method[21] in the exit channel and to the CB1-4B method in the entrance channel. Therefore, the BDW-4B method satisfies the correct boundary conditions in both scattering channels.

As an illustration of the validity of the BDW-4B model for the TI process, we shall show the total cross sections for the following reaction:

$$\mathrm{H}^{+} + \mathrm{He} \longrightarrow \mathrm{H}^{+} + \mathrm{He}^{2+} + e. \tag{18}$$

The results of computations of total cross sections at impact energies 300–10000 keV are depicted in Figure 12.6. As can be seen from this figure, the BDW-4B method is found to be in good agreement with the available experimental data.[20, 29, 31] The displayed theoretical results in Figure 12.6 have been obtained by using only the leading term $\vec{\nabla}\cdot\vec{\nabla}$ in Eq. (16). In such computations the total cross section is reduced to a five-dimensional numerical quadrature. The number of integration points is gradually and systematically increased until convergence to two decimal places has been reached. The computations of the total cross sections with all the terms in perturbation potential (14) require a nine-dimensional quadrature which is numerically extensive and shall be pursued in full details in the near future. In the present work, for an illustration, the Table 12.1 reports on the results obtained by means of the Gauss–Legendre quadrature with

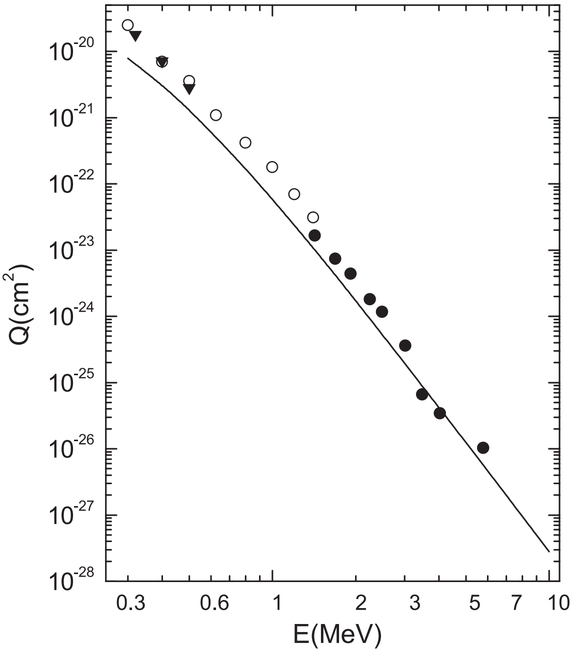

Figure 12.6 Total cross sections (in cm^2) as a function of the laboratory incident energy for reaction $H^+ + He \longrightarrow H + He^{2+} + e$. The full line represents the results of the BDW-4B theory.[8] Experimental data: ●, Schmidt et al.,[31] ▼, Shah and Gilbody[20] and ○ Mergel et al.[29]

Table 12.1 Total cross sections (in cm^2) as a function of incident energy E for electron capture in reaction $H^+ + He \longrightarrow H^+ + He^{2+} + e$. The presented theoretical results are obtained by means of the BDW-4B model using the one-parameter Hylleraas-type wave function for the initial helium bound state. The symbols Q represent the cross sections obtained with the complete perturbation potentials according to Eq. (16), whereas Q_∇ refer to the cross sections obtained without terms $V(r_{12}, x_1)$ and $V_P(R, s_2)$ in Eq. (16). The results are obtained by the Gauss–Legendre quadrature with $N_{GL} = 8, 16$, and 24 points. The numbers in the square brackets denote the powers of 10

***E*(keV)**	***N*GL**	**Q_∇(cm^2)**	**Q(cm^2)**
300	8	7.82[−21]	6.64[−21]
300	16	7.86[−21]	5.94[−21]
300	24	7.87[−21]	5.93[−21]
1000	8	5.92[−23]	5.28[−23]
1000	16	5.88[−23]	6.73[−23]
1000	24	5.89[−23]	5.73[−23]

$N_{\mathrm{GL}} = 8, 16$, and 24 points at 300 and 1000 keV/amu. A comparison is made between the cross section obtained by using only the leading term $\vec{\nabla} \cdot \vec{\nabla}$ (as labeled with Q_{∇} in Table 12.1) and results obtained with all the terms in perturbation potential (as denoted by Q). The latter results Q include the dynamic correlations. Only capture into the ground state is taken into account.

As mentioned, the BDW-4B method describes the four-body nature of the original problem and satisfies the correct boundary conditions in the exit and exit channel. Double charge exchange has already been investigated by means of the BDW-4B method.[7, 35–37] This approximation has also been applied, after the appropriate adaptation, to single electron capture.[38–40] Recently, Monti et al.[41, 42] proposed a four-body distorted wave-eikonal initial state (CDW-EIS-4B) model for single ionization of dielectronic atomic targets by impact of protons. It would be interesting in the future to adapt their model[41, 42] to TI and compare it with the CDW-4B and BDW-4B theories.

5. CONCLUSIONS

We have investigated the problem of transfer ionization in collisions between bare ions and two-electron atomic systems at high impact energies. Our objective is twofold. One is to compare the formalisms of the independent particles/events with the four-body correlated electronic dynamics. The other is to contrast the continuum distorted wave theory, or CDW, with its two hybrid approximations known as the continuum distorted wave eikonal initial state, or CDW-EIS, and the Born distorted wave, or BDW, models. These three methods coincide with each other only in one channel regarding both the total scattering wave function and the associated perturbation potential in the T-matrix element. In the other channel (entrance or exit depending whether the “prior” or “post” form of the transition amplitude is employed), both the total scattering wave functions and the corresponding perturbation interaction potentials are different. The CDW method always uses the full Coulomb wave functions in the entrance and exit channels for the independent as well as the correlated motions of the electrons. These electronic dynamics in the continuum are simplified in the CDW-EIS and BDW models through the replacements of the full Coulomb waves by their asymptotic forms (eikonal logarithmic Coulomb phases) valid at infinitely large inter-particle separations. The two phases differ only in the spatial variable, which is $\vec{s}$ or $\vec{R} = \vec{x} - \vec{s}$ in the CDW-EIS or BDW method, where $\vec{x}$ and $\vec{s}$ are the position vectors of the electron to be captured relative to the projectile and the target nucleus, respectively. This difference yields two different perturbation potentials in the transition amplitudes in the CDW-EIS and BDW methods. Thus, any difference in the performance of these two latter formalisms can be traced back to the fact that the dynamic variables $\vec{s}$ and $\vec{x}$ are coupled through $\vec{R}$ in the eikonal Coulomb state from the BDW method, whereas only the decoupled position vector $\vec{s}$ appears in the eikonal logarithmic distorting phase in the CDW-EIS approximation.

First, we compared the IPM and IEV models with the CDW and CDW-EIS approximations. We made use of the IEV model to simulate the successive events of ionization-capture and capture-ionization. The single-particle probabilities as a function of impact parameters were computed using the three-body CDW and CDW-EIS approximations. It was found that the total cross sections obtained by means of the CDW-EIS-IEV model are in slightly better agreement with the experimental data than the results from the CDW-IEV model. However, the results from the CDW-EIS-IEV model are still significantly larger than the corresponding experimental values, especially for the case of proton impact. This points to a failure of the CDW-EIS method within the independent particle formalism for transfer ionization. Such a finding adds to a much more pronounced breakdown of the corresponding correlated version in the CDW-EIS-4B model, by some formidable 2–3 orders of magnitudes for double charge exchange in fast collisions between alpha particles and helium.

Second, the four-body theories, such as the CDW-4B and BDW-4B methods are presently applied to transfer ionization in the $\mathrm{H}^{+} + \mathrm{He}$, $\mathrm{He}^{2+} + \mathrm{He}$ and, $\mathrm{Li}^{3+} + \mathrm{He}$ collisions at intermediate and high impact energies. Agreement of the measurements with the theoretical total cross sections obtained by means of these two methods is favorable, especially at sufficiently higher impact energies.

Overall, similarly to the situation of double charge exchange, it can be concluded that at high energies, the CDW-4B and BDW-4B methods for transfer ionization are capable of reproducing the available experimental data. This represents an extrapolation of the well-known success of the CDW method for three-body collisions. Such a stable performance builds confidence into this theory when passing from simpler to complicated collisional problems with more than one active electron. This is in sharp contrast with the CDW-EIS approximation, which is utterly inadequate for double charge exchange and also fails for transfer ionization for which, however, the CDW and BDW methods are successful. The same situation is likely to be encountered with molecular targets, such as water, which is the main tissue-like medium. Two or more electrons are expected to play a larger role in making transitions between ions and water molecules in the close vicinity of the Bragg peak. This is because at the end of their path through the traversed medium, the initially energetic ions abruptly slow down, thus enhancing the probability for single and multiple electron capture, as well as for simultaneous capture and ionization/excitation. At the last couple of centimeters before they eventually stop, partially or fully neutralized ions readily lose one or all their electrons only to quickly capture them again. Such direct and inverse processes occur literally thousands of times for each ion near the Bragg peak prior to the establishment of a kind of equilibrium. These higher order collisional phenomena are anticipated to make noticeable contributions to the overall stopping power, calling for the corresponding improvements of the existing data bases for energy losses of ions in the traversed matter. Thus far, these data bases have exclusively been restricted to single electron transitions consisting mainly of the ionization or excitation scattering channels, and ignoring simultaneous transitions of two or more electrons.

ACKNOWLEDGMENTS

Dž. Belkić appreciates research funds from the Karolinska Institute, the Karolinska University Hospital's Radiumhemmet and the Swedish Cancer Society (Cancerfonden). I. Mančev and N. Milojević thank the Ministry of Science of the Republic of Serbia (Project No. 171020) for support.

REFERENCES

1. Dunseath, K. M.; Crothers, D. S. F. Transfer and ionization processes during the collision of fast H^+, He^{2+} nuclei with helium. *J. Phys. B: At. Mol. Opt. Phys.* **1991**, *24*, 5003.
2. Galassi, M. E.; Abufager, P. N.; Martinez, A. E.; Rivarola, R. D.; Fainstein, P. D. The continuum distorted wave eikonal initial state model for transfer ionization in H^+, He^{2+} + He collisions. *J. Phys. B: At. Mol. Opt. Phys.* **2002**, *35*, 1727.
3. Gayet, R.; Salin, A. Simultaneous capture and ionisation by fast ion impact on helium. *J. Phys. B: At. Mol. Phys.* **1987**, *20*, L571.
4. Sidorovich, V. A.; Nikolaev, V. S.; McGuire, J. H. Calculation of charge-changing cross sections in collisions of H^+, He^{2+}, and Li^{3+} with He atoms. *Phys. Rev. A* **1985**, *31*, 2193.
5. Shingal, R.; Lin, C. D. Calculations of two-electron transition cross sections between fully stripped ions and helium atoms. *J. Phys. B: At. Mol. Opt. Phys.* **1991**, *24*, 251.
6. Belkić, Dž.; Mančev, I.; Hanssen, J. Four-body methods for high-energy ion-atom collisions. *Rev. Mod. Phys.* **2008**, *80*, 249.

7. Belkić, Dž. *Quantum Theory of High-Energy Ion-Atom Collisions*; Taylor & Francis: London, 2009.
8. Belkić, Dž.; Mančev, I. Transfer ionization in fast ion-atom collisions: four-body Born distorted-wave theory. *Phys. Rev. A* **2011**, *83*, 012703.
9. Belkić, Dž. A quantum theory of ionisation in fast collisions between ions and atomic systems. *J. Phys. B: At. Mol. Phys.* **1978**, *11*, 3529.
10. Crothers, D. S. F.; McCann, J. F. Ionisation of atoms by ion impact. *J. Phys. B: At. Mol. Phys.* **1983**, *16*, 3229.
11. Fainstein, P. D.; Ponce, V. H.; Rivarola, R. D. A theoretical model for ionisation in ion-atom collisions. Application for the impact of multicharged projectiles on helium. *J. Phys. B: At. Mol. Opt. Phys.* **1988**, *21*, 287.
12. Belkić, Dž. Review of theories on ionization in fast ion-atom collisions with prospects for applications to hadron therapy. *J. Math. Chem.* **2010**, *47*, 1366.
13. Busnengo, H. F.; Martínez, A. E.; Rivarola, R. D.; Dubé, J. L. Distorted-wave models for electron capture in asymmetric collisions. II. Differential cross sections and the double scattering region. *J. Phys. B: At. Mol. Opt. Phys.* **1995**, *28*, 3283.
14. Martínez, A. E.; Deco, G. R.; Rivarola, R. D.; Fainstein, P. D. K-Shell vacancy production in asymmetric collisions. *Nucl. Instrum. Methods Phys. Res., Sect. B* **1988**, *34*, 32.
15. Clementi, E. C.; Roetti, C. Roothaan–Hartree–Fock atomic wavefunctions. *At. Data Nucl. Data Tables* **1974**, *14*, 177.
16. Bernardi, G.; Focke, P.; González, A. D.; Suarez, S.; Fregenal, D. Electron emission for transfer ionization in 70 keV H^+ on He. *J. Phys. B: At. Mol. Opt. Phys.* **1999**, *32*, L451.
17. Bates, D. R.; Griffing, G. W. Inelastic collisions between heavy particles I: excitation and ionization of hydrogen atoms in fast encounters with protons and with other hydrogen atoms. *Proc. R. Soc. A* **1953**, *66*, 961.
18. Bates, D. R.; Griffing, G. W. Inelastic collisions between heavy particles IV: contribution of double transitions to certain cross sections including that associated with the ionization of hydrogen atoms in fast encounters with other hydrogen atoms. *Proc. R. Soc. A* **1955**, *68*, 90.
19. Shah, M. B.; McCallion, P.; Gilbody, H. B. Electron capture and ionisation in collisions of slow H^+ and He^{2+} ions with helium. *J. Phys. B: At. Mol. Phys.* **1989**, *22*, 3037.
20. Shah, M. B.; Gilbody, H. B. Single and double ionisation of helium by H^+, He^{2+} and Li^{3+} ions. *J. Phys. B: At. Mol. Phys.* **1985**, *18*, 899.
21. Belkić, Dž.; Mančev, I.; Mergel, V. Four-body model for transfer ionization in fast ion-atom collisions. *Phys. Rev. A* **1997**, *55*, 378.
22. Mančev, I. Single-electron capture and transfer ionization in collisions of Li^{3+} ions with helium. *Phys. Rev. A* **2001**, *64*, 012708.
23. Belkić, Dž. Symmetric double charge exchange in fast collisions of bare nuclei with heliumlike atomic systems. *Phys. Rev. A* **1993**, *47*, 189.
24. Nordsieck, A. Reduction of an integral in the theory of Bremsstrahlung. *Phys. Rev.* **1954**, *93*, 785.
25. Belkić, Dž.; *Principles of quantum scattering theory*, Institute of Physics, Bristol, 2004.
26. Belkić, Dž.; Gayet, R.; Salin, A. Electron capture in high-energy ion-atom collisions. *Phys. Rep.* **1979**, *56*, 279.
27. Dollard, J. D. Asymptotic convergence and the Coulomb interaction. *J. Math. Phys.* **1964**, *5*, 729.
28. Pluvinage, P. Fonction d'onde approchée a un parametre pour l'état fondamental de l'hélium. *Ann. Phys. (NY)* **1950**, *5*, 145.
29. Mergel, V.; Dörner, R.; Achler, M.; Khayyat, Kh.; Lencinas, S.; Euler, J.; Jagutzki, O.; Nüttgens, S.; Unverzagt, M.; Spielberger, L.; Wu, W.; Ali, R.; Ullrich, J.; Cederquist, H.; Salin, A.; Wood, C.; Olson, R.; Belkić, Dž.; Cocke, C.; Schmidt-Böcking, H. Intra-atomic

electron-electron scattering in p-He collisions (Thomas process) investigated by Cold Target Recoil Ion Momentum Spectroscopy. *Phys. Rev. Lett.* **1997**, *79*, 387.

30. Schmidt, H.T.; Fardi, A.; Schuch, R.; Schwartz, S.; Zettergren, H.; Cederquist, H.; Bagge, L.; Danared, H.; Källberg, A.; Jensen, J.; Rensfelt, K.; Mergel, V.; Schmidt, L.; Schmidt-Böcking, H. Double-to-single target ionization ratio for electron capture in fast p-He collisions. *Phys. Rev. Lett.* **2002**, *89*, 163201.
31. Schmidt, H. T.; Jensen, J.; Reinhed, P.; Schuch, R.; Støchkel, K.; Zettergren, H.; Cederquist, H.; Bagge, L.; Danared, H.; Källberg, A.; Schmidt-Böcking, H.; Cocke, L. Recoil-ion momentum distributions for transfer ionization in fast proton-He collisions. *Phys. Rev. A* **2005**, *72*, 012713.
32. Woitke, O.; Závodszky, P. A.; Ferguson, S. M.; Houck, J. H.; Tanis, J. A. Target ionization and projectile charge changing in 0.5 – 8 MeV/q Li^{q+}+He(q=1, 2, 3) collisions. *Phys. Rev. A* **1998**, *57*, 2692.
33. Sant'Anna, M. M.; Santos, A. C.; Coelho, L. F.; Jalbert, G.; de Castro Faria, N.V.; Zappa, F.; Focke, P.; Belkić, Dž. Double-electron-capture cross sections for Li^{3+} collisions with He at intermediate-to-high velocities. *Phys. Rev. A* **2009**, *80*, 042707.
34. Bhattacharyya, S.; Rinn, K.; Salzborn, E.; Chatterjee, L. High-energy electron capture by fully stripped ions from He atoms—a QED approach. *J. Phys. B: At. Mol. Opt. Phys.* **1988**, *21*, 111.
35. Belkić, Dž. Double charge exchange at high impact energies. *Nucl. Instrum. Methods Phys. Res., Sect. B* **1994**, *86*, 62.
36. Belkić, Dž.; Mančev, I.; Mudrinić, M. Two-electron capture from helium by fast α particles. *Phys. Rev. A* **1994**, *49*, 3646.
37. Belkić, Dž. Review of theories on double electron capture in fast ion-atom collisions. *J. Math. Chem.* **2010**, *47*, 1420.
38. Mančev, I. Single charge exchange in fast collisions of alpha particles with helium. *J. Phys. B: At. Mol. Opt. Phys.* **2003**, *36*, 93.
39. Mančev, I. Single-electron capture from helium-like atomic systems by bare projectiles. *Euro. Phys. Lett.* **2005**, *69*, 200.
40. Mančev, I. Continuum distorted wave—Born initial state (CDW-BIS) model for single charge exchange. *J. Comput. Methods Sci. Eng.* **2005**, *5*, 73.
41. Monti, M.; Fojón, O. A.; Hanssen, J.; Rivarola, R. D. Ionization of helium targets by proton impact: a four-body distorted wave-eikonal initial state model and electron dynamic correlation. *J. Phys. B: At. Mol. Opt. Phys.* **2009**, *42*, 195201.
42. Monti, M.; Fojón, O. A.; Hanssen, J.; Rivarola, R. D. A four-body fully distorted wave—eikonal initial state model for ionization of He targets by ion impact. *J. Phys.: Conf. Ser.* **2009**, *163*, 012068.

CHAPTER THIRTEEN

Distorted Wave Theories for One- and Two-Electron Capture in Fast Atomic Collisions

Volodymyr Yu. Lazur and Mykhaylo V. Khoma
Theoretical Physics, Uzhgorod National University, Uzhgorod, Ukraine

Contents

Abstract

On the basis of the Dodd–Greider integral equations with Coulomb interactions, we have reviewed the theory of one-electron capture in collisions of hydrogen-like atoms and positively charged ions with account taken for electron re-scattering effects. This theory can be applied to study the influence of Coulomb interactions in the final state on angular and energy distributions of the products of a charge-transfer reactions at intermediate collision energies.

Using the four-body Dodd–Greider integral equations, we have reviewed a four-particle formalism of the continuum distorted wave (CDW) method, applicable for describing a two-electron capture reaction in energetic ion-atomic collisions. An attractive feature of the CDW method is consistent and accurate consideration of asymptotic wave functions, which take into account the long-range nature of Coulomb interactions in both the entrance and exit reaction channels. In the past, this method been applied to double electron transfer in energetic H^++ He and He^{2+} + He collisions, yielding good agreement with measurements.

Advances in Quantum Chemistry, Volume 65
ISSN 0065-3276, http://dx.doi.org/10.1016/B978-0-12-396455-7.00013-3

1. INTRODUCTION

The one-electron charge-transfer process:

$$A^{Z_\alpha +} + B \rightarrow A^{(Z_\alpha -1)+} + B^{+} \tag{1}$$

for swift ion-atomic collisions has attracted steady attention both from theoretical and experimental groups for many decades.[1] The necessary information about process (1) is not limited to the integral characteristics (total cross section, reaction constant), but also includes details about the energy and angular distributions of the reaction products. This places high demands both for completeness and precision of the theoretical calculation. In the context of this work, swift collisions signify that the relative velocity of the colliding particles is greater than the effective orbital velocity υ_0 of the captured electron.

The theoretical analysis of experimental data on the processes of type (1) may be summarized as follows. At collision velocities $\upsilon \sim \upsilon_0 Z_\alpha^{1/2}$ the cross sections of charge exchange and ionization are of the same order of magnitude. In the range $\upsilon > \upsilon_0 Z_\alpha^{1/2}$, the probability of charge transfer decreases, such that ionization and excitation of atoms by energetic projectiles become the dominant processes. However, the latter is not always the case. A high probability of target excitation (or ionization) initiates new mechanisms of electron transfer that are the main subject of the present study. It is commonly accepted that in the range of intermediate and high collision velocities, the dominant processes are a one-step mechanism of electron transfer (1) and a two-step Thomas mechanism of electron capture through the intermediate discrete or continuum state. The latter becomes especially important with increasing collision energy.

Charge exchange in low- and intermediate-energy ion-atomic collisions is commonly described by close coupling methods (see for instance Ref. 2, and references therein), whereas energetic collisions are usually treated by analytical perturbative approaches. The latter include different variations of the distorted wave method[3] which are used for both symmetrical and asymmetrical collisions. The main drawback of the mentioned approaches is the assumptions about the short-range character of the considered interaction potential. It was pointed out, however (see Refs. 4–6) that such assumptions are not justified for applications to atomic collisions. As an illustration, we refer to Ref. 4 where it was demonstrated that the Strong Potential Born (SPB) approximation[7] cannot serve as a basis for constructing adequate charge-exchange theories, since the scattering amplitude includes a contribution from the divergent terms. The reason for this drawback is the inaccurate account taken for the Coulomb effects in the initial and final states.[4–6, 8–10] This circumstance confirms the general result of Merkuriev[11] as well as of Merkuriev and Faddeev,[12] who demonstrated how theories elaborated for short-range potentials could be adapted to long-range potentials.

In approximations of a single collision, the mentioned theoretical approaches reproduce the standard formulae of the Oppenheimer Brinkman Kramer (OBK) approximation.[3, 13] However, one should keep in mind that the OBK-approximation is not, strictly speaking, a first order perturbation theory. The numerical calculations[3] show that, compared to the experiment, the OBK-approximation systematically overestimates the cross sections and gives the wrong position of the maximum. The first order perturbation theory (the first Born approximation) uses perturbation as the "full" interaction (i.e., the interaction of the electron with the projectile and the internuclear repulsion), which gives rise to the well known result of Jackson and Schiff (JS).[14] Generally speaking, the validity of the Born approximation (and perturbation theory in general) for describing charge-exchange reactions is not at all obvious.[3] In the case of excitation or ionization, it is possible, physically and mathematically, to determine the conditions for applicability of the perturbation theory. However, such conditions are not as clear in the case of charge-exchange reactions. In Refs. 15, 16 it was shown that at high collision velocities the second Born cross section for electron capture from a hydrogen-like atom with charge Z_β by a bare ion of charge Z_α increases rapidly as Z_β increases. These results indicate that second- and higher-order Born terms must be considered in calculating the cross section for electron capture. The question of the asymptotic behavior of charge-exchange amplitudes has also been investigated in Ref. 17 on the basis of Faddeev equations.[18]

Apart from the general problem of the Born approximation convergence, there is also the long-standing difficulty regarding the choice of the perturbing potential. Due to the non-orthogonality of the initial and final states, different forms of the perturbing potential yield different results for the cross sections. The formal derivation (based on general scattering theory) of the first Born scattering amplitude for charge exchange gives rise to interaction potentials that include the internuclear potential. The simplest of these in the one-electron model reads:

$$U_\alpha^{\mathrm{JS}} = -\frac{Z_\alpha}{s} + \frac{Z_\alpha Z_\beta}{R}, \tag{2}$$

where $\vec{s}$ is the radius-vector of the electron relative to the center of ion $A^{Z_\alpha +}$ and R is the internuclear separation. The first term in (2) describes the interaction of the active electron with ion $A^{Z_\alpha +}$. The second term describes the internuclear interaction in the entrance channel. Due to the orthogonality of the initial and final wave functions, the second term of (2) makes no contribution to the amplitude of the direct ionization. However, this term gives a non-zero contribution to the amplitude of the charge-exchange reaction. Potential (2) has been used in Refs. 14, 19 for calculating the Born cross sections of charge exchange of hydrogen atom by proton. This reaction does not contain the Coulomb interaction in the entrance and exit channels at large interatomic separations, and hence good agreement with experiment has been obtained. However, application of potential (2) for calculating the cross sections of electron capture by nucleus H^+ and He^{2+} from the inner shell of multi-electron atoms (carbon, neon, and argon) gives rise to non-physical results that differ from the experiment by several orders of magnitude.[20, 21]

By investigating the non-orthogonality problem, Bates[22] has shown that orthogonalization of the wave functions of the initial and final states leads to a modification of the perturbing potential. More precisely, this orthogonalization makes the contribution from the internuclear potential in (2) vanish. Instead, a new term appears which is similar to the internuclear interaction.[23] At large interatomic separations, this new term has the asymptotic form Z_α/R. The resulting perturbing potential which now approximately accounts for orthogonalization of the wave functions reads:

$$U_\alpha = -\frac{Z_\alpha}{s} + \frac{Z_\alpha}{R}. \tag{3}$$

The authors Omidvar et al.[24] and Halpern[25] explained the usage of potential (3) by full electron shielding of the nuclei of atom B. Despite the criticism of this argumentation[23, 26] (especially for electron capture from inner shells), the results of cross section calculations within the Born approximation with potential (3) are in good agreement with experiment, even for electron capture from K-shell of the multi-electron atom.[24]

In this connection, it is important to be accurate and systematic in choosing the perturbing potential. At the very least, one should realize that the results of the obtained cross sections will differ according to the selection of U_α. One such approach is considered in the present work and consists of using few-body problem integral equations that are properly modified for Coulomb interaction.

On the basis of these introductory considerations, it is clear that the correct account of the Coulomb interaction in the charge-exchange reaction channels has not had a compelling solution based upon Refs. 20, 21, 23–25. On the other hand, the existing methods from few-body physics allow us to take account of Coulomb effects and to test these effects in the framework of the widely used continuum distorted wave (CDW) approximation.[3]

In the present work on the basis of modified Coulomb interaction three-body Dodd–Greider integral equations,[27, 28] the method of one-electron capture cross section calculation is presented. The amplitude of reaction (1) is obtained as the first term of the iteration expansion of the solution of the corresponding Dodd–Greider equations for the three-body scattering operator. This is the boundary-corrected continuum intermediate state (BCIS)[5] method. It is shown that without accounting for the effects of the Coulomb re-scattering of the captured electron, it is not possible to reproduce the Thomas peak in the angular distribution of the reaction products. In the approximation of the "single-step" collision, the BCIS method reduces to the version of the boundary-corrected first Born (CB1) method,[8–10] where the asymptotic behavior of the particles in the entrance and exit channels of the reactions is described by the two-body Coulomb wave functions. The short-range interaction due to incomplete screening of the nucleus by atomic electrons is taken into account in the perturbing potential.

2. BASIC KINEMATICS AND DYNAMICS

The complex problem of an ion-atomic collision reaction (1) considered here is an idealized problem of nonrelativistic interaction of three spinless particles α (projectile A^{+Z_α}), γ (active electron e^-), and β (target ion B^+) with masses $m_\alpha, m_\gamma, m_\beta$, respectively. The center of mass motion is assumed to be separated. Corresponding to possible separation of the three-body problem on fragments $(\beta,\gamma)+\alpha; (\alpha,\gamma)+\beta; (\alpha+\beta)+\gamma$, we introduce, together with the full Hamiltonian $H = H_0 + V$, the arrangement channel Hamiltonians $H_j = H_0 + V_j$ $(j=\alpha,\beta,\gamma)$, where H_0 is the three-body kinetic energy operator in the center of the mass system of coordinates and $V=\sum_{\alpha,\beta,\gamma} V_j$ is the full interaction. The subscript index j in V_j defines the missing particle in this interaction (i.e., the V_α is the operator of β and γ interaction). Finally, $\upsilon_j = V - V_j$ is the arrangement channel interaction. Let us introduce the Jacobi-type coordinates:

$$\vec{s} = (a/m_\gamma)\vec{x} - \vec{r}_\alpha, \quad \vec{x} = (b/m_\gamma)\vec{s} - \vec{r}_\beta, \quad \vec{R} = \vec{x} - \vec{s}, \tag{4}$$

where $a = m_\gamma m_\beta/(m_\gamma + m_\beta)$ and $b = m_\gamma m_\alpha/(m_\gamma + m_\alpha)$ are the reduced masses. Here $\vec{x}$ is the radius-vector of the electron relative to the center of the residual target ion B$^+$ in reaction (1). In terms of these coordinates, the operator H_0 can be represented in two equivalent forms:

$$H_0 = -\frac{1}{2\mu_\alpha}\Delta_{\vec{r}_\alpha} - \frac{1}{2a}\vec{\nabla}_{\vec{x}} = -\frac{1}{2\mu_\beta}\Delta_{\vec{r}_\beta} - \frac{1}{2\beta}\vec{\nabla}_{\vec{s}}, \tag{5}$$

where the standard definition for the Laplace operator is used, and:

$$\mu_\alpha = \frac{m_\alpha(m_\beta + m_\gamma)}{m_\alpha + m_\beta + m_\gamma}, \quad \mu_\beta = \frac{m_\beta(m_\alpha + m_\gamma)}{m_\alpha + m_\beta + m_\gamma}. \tag{6}$$

We shall split the potentials υ_j, $j = 1, 2$ into two parts:

$$\upsilon_j = V - V_j = U_j + W_j, \tag{7}$$

where W_j defines the so-called "disturbing" potential which represents the weak long-range Coulomb forces partly responsible for the asymptotic behavior of the wave functions and U_j is the pure short-range perturbation responsible for electronic transitions.

From the definition of the Hamiltonian H_α, (H_β) immediately follows its eigenfunctions $|\Phi_i^\alpha\rangle$ $(|\Phi_f^\beta\rangle)$:

$$|\Phi_i^\alpha\rangle = |\varphi_i(\vec{x})\rangle \exp(i\vec{k}_\alpha \cdot \vec{r}_\alpha), \quad |\Phi_f^\beta\rangle = |\varphi_f(\vec{s})\rangle \exp(i\vec{k}_\beta \cdot \vec{r}_\beta), \tag{8}$$

where φ_i (φ_f) is the wave function of the bound state of the pair (β, γ) $((\alpha, \gamma))$ and $\exp(i\vec{k}_\alpha \cdot \vec{r}_\alpha)$ $(\exp(i\vec{k}_\beta \cdot \vec{r}_\beta))$ is the plane wave, describing the relative motion of the free particles α (β) and (β, γ) $((\alpha, \gamma))$ in the initial (final) state with momentum $\vec{k}_\alpha$ $(\vec{k}_\beta)$. Rigorously speaking, in the case of charged particles, the wave functions in (8) should be distorted by a phase factor which logarithmically depends on the distance between the particles.[9] This is because the asymptotic motion of the particles in the Coulomb potential is not free, due to its long-range character.

Hence, following Ref. 3 we introduce modified arrangement channel asymptotic states $|\Phi_i^{\alpha+}\rangle$ $(|\Phi_f^{\beta-}\rangle)$ which, compared to $|\Phi_i^\alpha\rangle$ $(|\Phi_f^\beta\rangle)$ correctly describe the effects of the long-range Coulomb fields on the course of the collision process. Let $\xi_\alpha = r_\alpha - \hat{\vec{k}}_\alpha \cdot \vec{r}_\alpha$ $(\xi_\beta = r_\beta - \hat{\vec{k}}_\beta \cdot \vec{r}_\beta)$ be the parabolic coordinates of the α (β) particles before (after) the collision, then $\hat{\vec{k}}_j$ $(j = \alpha, \beta)$ are the identity vectors: $\hat{\vec{k}}_j = \vec{k}_j/k_j$. The functions $\Phi_i^{\alpha+}(\Phi_f^{\beta-})$ are represented by the product of the bound state wave function of the pair $(\beta,\gamma)\,((\alpha,\gamma))$ and distorted plane wave f_α^+ (f_β^-) with the unity amplitude:

$$\Phi_i^{\alpha+} = \varphi_i(\vec{x})f_\alpha^+(\vec{r}_\alpha) \equiv \varphi_i(\vec{x})\exp(i\vec{k}_\alpha\cdot\vec{r}_\alpha + i\sigma_\alpha), \tag{9}$$

$$\Phi_f^{\beta-} = \varphi_f(\vec{s})f_\beta^-(\vec{r}_\beta) \equiv \varphi_f(\vec{s})\exp(i\vec{k}_\beta\cdot\vec{r}_\beta - i\sigma_\beta), \tag{10}$$

with Coulomb phases σ_α and σ_β given by:

$$\begin{aligned}\sigma_\alpha &= \nu_\alpha \ln(k_\alpha\sigma_\alpha), \quad \nu_\alpha = n_\alpha/\upsilon, \quad \vec{\upsilon} = \vec{k}_\alpha/\mu_\alpha,\\ \sigma_\beta &= \nu_\beta \ln(k_\beta\sigma_\beta), \quad \nu_\beta = n_\beta/\upsilon', \quad \vec{\upsilon}' = \vec{k}_\beta/\mu_\beta,\end{aligned} \tag{11}$$

where $n_\alpha = Z_\alpha(Z_\beta + Z_\gamma), n_\beta = Z_\beta(Z_\alpha + Z_\gamma)$, and Z_j is the charge of the jth particle ($j = \alpha,\beta,\gamma$); $Z_\gamma = -1$.

We shall split the perturbing potential W_α and W_β into two parts:

$$W_\alpha = w_\alpha + W_{\alpha d}, \quad W_\beta = w_\beta + W_{\beta d}, \tag{12}$$

where w_α and w_β are the arbitrary short-range potentials that depend only on the relative coordinates $\vec{r}_\alpha$ and $\vec{r}_\beta$, respectively. The distorting potentials $W_{\alpha d}$ and $W_{\beta d}$ in the asymptotic limits have a pure Coulomb behavior:

$$W_{\alpha d} \underset{r_\alpha\to\infty}{\longrightarrow} \frac{n_\alpha}{r_\alpha}, \quad W_{\beta d} \underset{r_\beta\to\infty}{\longrightarrow} \frac{n_\beta}{r_\beta}. \tag{13}$$

We shall introduce the arrangement channel Hamiltonian $H_{\alpha d}$ ($H_{\beta d}$):

$$H_{\alpha d} = H_\alpha + W_{\alpha d}, \quad H_{\beta d} = H_\beta + W_{\beta d}, \tag{14}$$

and construct potentials $W_{\alpha d}$ and $W_{\beta d}$ in such a way that the Schrödinger equations:[3]

$$(H_{\alpha d} - E)\Phi_i^{\alpha+} = 0, \quad E = E_i + k_\alpha^2/2\mu_\alpha, \tag{15}$$

$$(H_{\beta d} - E)\Phi_f^{\beta-} = 0, \quad E = E_f + k_\beta^2/2\mu_\beta, \tag{16}$$

shall be satisfied. Here E_i (E_f) is the energy of the bound state of the pair (β,γ) $((\alpha,\gamma))$ and E is the total energy of the three-body system.

The use of the arrangement channel Hamiltonian $H_{\alpha d}$ ($H_{\beta d}$) in the form of Eq. (14) has a clear physical motivation. Since electrons are influenced by the Coulomb field in any point of configurational space, the perturbations $W_{\alpha d}$ and $W_{\beta d}$ (which approximate the potential of the distant Coulomb center) shall be included in the arrangement channel (i.e., zero-order) Hamiltonian.

Let us obtain $W_{\alpha d}$ in an explicit form. From definition (14), $W_{\alpha d} = H_{\alpha d} - H_{\alpha}$. Acting with operator $(H_{\alpha d} - H_{\alpha})$ on the state $|\Phi_i^{\alpha +}\rangle$ and taking into account relations (5), (9), and (15), one obtains:

$$\begin{aligned} W_{\alpha d}|\Phi_i^{\alpha +}\rangle &= \varphi_i(\vec{x})(k_\alpha^2/2\mu_\alpha + \Delta_{\vec{r}_\alpha}/2\mu_\alpha)|f_\alpha^{+}(\vec{r}_\alpha)\rangle \\ &= (n_\alpha/r_\alpha)[1-(\nu_\alpha/(k_\alpha\xi_\alpha))]|\Phi_i^{\alpha +}\rangle. \end{aligned} \tag{17}$$

Using a similar technique, one obtains:

$$W_{\beta d}|\Phi_f^{\beta +}\rangle = (n_\beta/r_\beta)[1-(\nu_\beta/(k_\beta\xi_\beta))]|\Phi_f^{\beta -}\rangle. \tag{18}$$

Let us note that representations (9) and (10) are not valid along the so-called *forward scattering direction* $(\hat{\vec{r}}_\alpha = \hat{\vec{k}}_\alpha, \xi_\alpha = 0)$ $((\hat{\vec{r}}_\beta = \hat{\vec{k}}_\beta, \xi_\alpha = 0))$, where the phases σ_α (σ_β) become infinite. On this special direction, the asymptotic of the functions $\Phi_i^{\alpha +}$ and $\Phi_f^{\beta -}$ can be described in terms of special functions.[12]

Consider the full Green's function (resolvent) for the system of three particles:

$$G^{\pm}(E) = (E - H \pm i\varepsilon)^{-1}, \tag{19}$$

where ε is an infinitely small positive number. Let us define $G_{\alpha d}^{+}$ and $G_{\beta d}^{-}$ as the Green's functions of the model arrangement channel Hamiltonian $H_{\alpha d}$ and $H_{\beta d}$, respectively:

$$G_{\alpha d}^{+} = (E - H_{\alpha d} + i\varepsilon)^{-1}, \quad G_{\beta d}^{-} = (E - H_{\beta d} - i\varepsilon)^{-1}. \tag{20}$$

Let us introduce the Møller wave operators ω_α^{+} (ω_β^{-}):

$$\omega_\alpha^{+} = 1 + g_{\alpha d}^{+} w_\alpha \equiv 1 + (E - H_{\alpha d} - w_\alpha + i\varepsilon)^{-1} w_\alpha, \tag{21}$$

$$\omega_\beta^{-} = 1 + g_{\beta d}^{-} w_\beta \equiv 1 + (E - H_{\beta d} - w_\beta - i\varepsilon)^{-1} w_\beta, \tag{22}$$

that transform the eigenfunction $\Phi_i^{\alpha+}$ ($\Phi_f^{\beta-}$) into the distorted wave $\chi_i^{\alpha+}$ ($\chi_f^{\beta-}$) in the entrance (exit) channel of reaction (1):

$$|\chi_i^{\alpha+}\rangle = \omega_\alpha^+ |\Phi_i^{\alpha+}\rangle, \tag{23}$$

$$|\chi_f^{\beta-}\rangle = \omega_\beta^- |\Phi_f^{\beta-}\rangle. \tag{24}$$

We shall define now operators $U_{\alpha\beta}^\pm$ as in Refs. 27, 28:

$$U_{\alpha\beta}^+ = \omega_\beta^{-\dagger}(\upsilon_\beta - W_\beta)[1 + G^+(\upsilon_\alpha - W_\alpha)]\omega_\alpha^+, \tag{25}$$

$$U_{\alpha\beta}^- = \omega_\beta^{-\dagger}[1 + (\upsilon_\beta - W_\beta)G^+](\upsilon_\alpha - W_\alpha)\omega_\alpha^+, \tag{26}$$

where the symbol † denotes Hermitian conjugation. The matrix elements of the operators $U_{\alpha\beta}^\pm$ between the Coulomb asymptotic states $|\Phi_i^{\alpha+}\rangle$ and $|\Phi_f^{\beta-}\rangle$ are the transition amplitudes $T_{\alpha\beta}^\pm$ from channel α to channel β correspondingly in the *post*- and *prior*-formalisms:

$$T_{\alpha\beta}^\pm = \langle\Phi_f^{\beta-}|U_{\alpha\beta}^\pm|\Phi_i^{\alpha+}\rangle. \tag{27}$$

The integral equations for transition operators $U_{\alpha\beta}^\pm$, obtained by Greider and Dodd,[27] read (for illustration consider the operator $U_{\alpha\beta}^-$ only):

$$U_{\alpha\beta}^- = \omega_\beta^{-\dagger}(\upsilon_\alpha - W_\alpha)\omega_\alpha^+ + \omega_\beta^-(\upsilon_\beta - W_\beta)G_{\beta d}^- U_{\alpha\beta}^-. \tag{28}$$

In the *prior* formalism of the considered theory, potential W_β is arbitrary and potential W_α should not lead to rearrangement in the channel β, i.e.,

$$\lim_{\varepsilon\to 0} i\varepsilon\langle\Phi_f^{\beta-}|\omega_\alpha^+|\Phi_i^{\alpha+}\rangle = 0.$$

The first term on the right hand of Eq. (28) leads to the following transition amplitude in the Born approximation with distorted waves:

$$T_{\alpha\beta}^-(\text{DWB}) = \langle\Phi_f^{\beta-}|\omega_\beta^{-\dagger}(\upsilon_\alpha - W_\alpha)\omega_\alpha^+|\Phi_i^{\alpha+}\rangle \equiv \langle\chi_f^{\beta-}|\upsilon_\alpha - W_\alpha|\chi_i^{\alpha+}\rangle. \tag{29}$$

Although Eq. (28) is formally exact, its solution cannot be obtained within the standard integral equations methods. The reasoning is the following. The kernel of integral equation (28) contains disconnected diagrams responsible for processes where one particle does not interact with the other two. As a consequence, integral equation (28) contains singularities due to the presence of delta-functions representing the momentum conservation for the particles that do not interact with the selected pair of other particles. These arguments (for detailed discussion see Ref. 27) raise questions about the convergence of the Born series within the distorted waves method, i.e., the iteration expansion of Eq. (28). One should note that the arguments used in Ref. 27, although applicable in the case of the iteration series for transition operator $U^{+}_{\alpha\beta}$ in *post*-formalism, lead to a conclusion about its divergence. Essentially, these findings generalize the results of Ref. 29, concerning the divergence of the Born iteration series within the plane wave representation of the three-body rearrangement scattering problem.

All these circumstances dictate the need for some restructuring (or rearrangement) of Eq. (28) similar to that carried out for the multiple scattering theory[30] and Faddeev equations.[18] Such restructuring must be done with the condition that the kernel of the integral equation (28) contains no disconnected diagrams. The details of such a cumbersome restructuring can be found in Ref. 28 and are omitted here. We shall present only the final result. With this aim, we shall introduce the auxiliary potential υ_x, that corresponds to the virtual intermediate channel "x" and the Green's operator $g^{+}_{x} = (E - H + \upsilon_x + i\varepsilon)^{-1}$ corresponding to this potential. In these designations the modified (with account for the long-range nature of Coulomb interaction) Dodd–Greider equation for quantum mechanical operator $U^{-}_{\alpha\beta}$ of the three-particle rearrangement scattering has the final form:

$$U^{-}_{\alpha\beta} = I + KU^{-}_{\alpha\beta}, \tag{30}$$

where

$$\begin{aligned} I &= \omega^{-\dagger}_{\beta}[1 + (\upsilon_\beta - W_\beta)g^{+}_{x}](\upsilon_\alpha - W_\alpha)\omega^{+}_{\alpha}, \\ K &= \omega^{-\dagger}_{\beta}(\upsilon_\beta - W_\beta)g^{+}_{x}\upsilon_x G^{+}_{\beta d}. \end{aligned} \tag{31}$$

The main advantage of (30) compared to (28) is that different choices of υ_x and W_β can be made, all satisfying the prescribed condition of eliminating disconnected diagrams. Thus, in the case when the mass of one particle is much less (or much greater) than the mass of the other two, the auxiliary potentials υ_x and W_β can be chosen in such a way that kernel K of the rearranged integral equation (30) is continuous in a suitable Banach space, i.e., it does not include disconnected diagrams and all the Green's functions in this equation are the solutions of equations with separable variables, and hence, can be evaluated in the explicit form. Inhomogeneous term I in Eq. (30) differs from the inhomogeneous term of Eq. (28) and represents a 1st order approximation for convergent iteration series of the solution of Eq. (30). Now, using (30), the amplitude $T^{-}_{\alpha\beta}$ from Eq. (27) reads:

$$T^{-}_{\alpha\beta} = \langle \Phi_f^{\beta-} | I | \Phi_i^{\alpha+} \rangle + \langle \Phi_f^{\beta-} | K U^{-}_{\alpha\beta} | \Phi_i^{\alpha+} \rangle = \langle \Phi_f^{\beta-} | I | \Phi_i^{\alpha+} \rangle + \mathrm{RS}, \quad (32)$$

where RS designate all the terms that take into account multiple re-scattering, where the rest $\langle \Phi_f^{\beta-} | K U^{-}_{\alpha\beta} | \Phi_i^{\alpha+} \rangle$, according to (31), contains the terms with at least three sequential re-scatterings. If we assume that the processes with multiple re-scatterings do not significantly affect the shape of angular distribution, the second term of (32) can be omitted. Hence, the amplitude of reaction (1) in the *prior*-formalism reads:

$$T^{-}_{\alpha\beta} = T^{-}_{\alpha\beta}(\mathrm{DWB}) + \langle \Phi_f^{\beta-} | \omega_\beta^{-\dagger} [g_x^{+}(\upsilon_\beta - W_\beta)](\upsilon_\alpha - W_\alpha)\omega_\alpha^{+} | \Phi_i^{\alpha+} \rangle. \quad (33)$$

Comparison of (29) and (33) demonstrates that the first term $T^{-}_{\alpha\beta}(\mathrm{DWB})$ of (33) allocates the amplitude of the direct one-step mechanism for charge transfer within the distorted wave Born approximation method. The second term of (33) describes the two-step mechanism of electron capture through the intermediate discrete or continuous state. A similar result holds for the transition amplitude $T^{+}_{\alpha\beta}$ in the *post*-formalism:

$$T^{+}_{\alpha\beta} = \langle \Phi_f^{\beta-} | \omega_\beta^{-\dagger} (\upsilon_\beta - W_\beta)[1 + g_x^{+}(\upsilon_\alpha - W_\alpha)]\omega_\alpha^{+} | \Phi_i^{\alpha+} \rangle. \quad (34)$$

To conclude this section we should discuss once more the fundamental property of Eq. (30). From a formal point of view, it is as complicated for a direct solution as the Faddeev-type equations.[18] However, there is no need for an exact solution of Eq. (30). The essence of the method considered here consists of the following. It is enough to make only the iterative approximation for the operator that describes the rearrangement of the system.

Transformation of Eq. (28) into Eq. (30) in the framework of distorted wave method allows one to obtain the iteration series (the so-called Coulomb boundary-corrected Born series) for the transition operator which, as shown by many calculations (see Refs. 3, 31, 32) rapidly converges.

3. THE FIRST BORN METHOD WITH CORRECT BOUNDARY CONDITIONS

Let us calculate the contribution of the direct one-step mechanism to the cross section of reaction (1) in the framework of the first Born approximation with distorted waves, when the amplitude of the process is given by:

$$T^{-}_{\alpha\beta} = \langle \Phi^{\beta-}_{f} | \omega^{-\dagger}_{\beta} (\upsilon_\alpha - W_\alpha) \omega^{+}_{\alpha} | \Phi^{\alpha+}_{i} \rangle = \langle \chi^{\beta-}_{f} | U_\alpha | \chi^{\alpha+}_{i} \rangle, \tag{35}$$

$$T^{+}_{\alpha\beta} = \langle \Phi^{\beta-}_{f} | \omega^{-\dagger}_{\beta} (\upsilon_\beta - W_\beta) \omega^{+}_{\alpha} | \Phi^{\alpha+}_{i} \rangle = \langle \chi^{\beta-}_{f} | U_\beta | \chi^{\alpha+}_{i} \rangle. \tag{36}$$

By acting with operators $(E - H_\alpha - W_\alpha + i\varepsilon)$ and $(E - H_\beta - W_\beta + i\varepsilon)$ on both parts of Eqs. (23) and (24), respectively, and taking the limit $\varepsilon \to 0$ with account of Eqs. (15) and (16), we come to the following equations:

$$(E - H_0 - V_\alpha - W_\alpha) | \chi^{\alpha+}_{i} \rangle = 0, \tag{37}$$

$$(E - H_0 - V_\beta - W_\beta) | \chi^{\beta+}_{f} \rangle = 0. \tag{38}$$

The boundary conditions have the forms:

$$\chi^{\alpha+}_{i} \xrightarrow[r_\alpha \to \infty]{} \Phi^{\alpha+}_{i}, \quad \chi^{\beta-}_{f} \xrightarrow[r_\alpha \to \infty]{} \Phi^{\beta-}_{f}, \tag{39}$$

where the Coulomb asymptotic waves are defined by relations (9) and (10). Let us define the explicit form of the potentials of arrangement channel interactions υ_α and υ_β:

$$\upsilon_\alpha = V_\beta + V_\gamma = -\frac{Z_\alpha}{s} + \frac{Z_\alpha Z_\beta}{R}, \quad \upsilon_\beta = V_\alpha + V_\gamma = -\frac{Z_\beta}{x} + \frac{Z_\alpha Z_\beta}{R}. \tag{40}$$

Here for $R \to \infty$, it follows: $\upsilon_\alpha \approx Z_\alpha (Z_\beta - 1)/R \equiv W^{c}_{\alpha d}$ and $\upsilon_\beta \approx Z_\beta (Z_\alpha - 1)/R \equiv W^{c}_{\beta d}$. The specific form of the short-range potentials w_α and w_β will be chosen in the symmetric form:

$$w_\alpha = W^{c}_{\alpha d} - W_{\alpha d}, \quad w_\beta = W^{c}_{\beta d} - W_{\beta d}, \tag{41}$$

which ensures the identical interpretation of the distortion in the entrance and exit channels. Using the above formulae for w_α and w_β, we rewrite partitioning (7) for channel interactions $\upsilon_\alpha, \upsilon_\beta$ in the following form:

$$W_\alpha = \frac{Z_\alpha(Z_\beta - 1)}{R}, \quad U_\alpha = \upsilon_\alpha - W_\alpha = \frac{Z_\alpha}{R} - \frac{Z_\alpha}{s}, \tag{42}$$

$$W_\beta = \frac{Z_\beta(Z_\alpha - 1)}{R}, \quad U_\beta = \upsilon_\beta - W_\beta = \frac{Z_\beta}{R} - \frac{Z_\beta}{x}. \tag{43}$$

With these partitioning Eqs. (37) and (38) read:

$$\left(E + \frac{\Delta_{\vec{r}_\alpha}}{2\mu_\alpha} + \frac{\Delta_{\vec{x}}}{2a} + \frac{Z_\beta}{x} - \frac{n_\alpha}{R}\right)\chi_i^{\alpha+} = 0, \tag{44}$$

$$\left(E + \frac{\Delta_{\vec{r}_\beta}}{2\mu_\beta} + \frac{\Delta_{\vec{s}}}{2b} + \frac{Z_\alpha}{s} - \frac{n_\beta}{R}\right)\chi_f^{\beta-} = 0. \tag{45}$$

The main technical problems with solving Eqs. (44) and (45) occur when distortion potential W_α (W_β) and Laplace operator $\Delta_{\vec{r}_\alpha}$ ($\Delta_{\vec{r}_\beta}$) depend on different relative variables. The connection between those variables follows from Eq. (4) as:

$$\vec{r}_\alpha = \vec{R} - (a/m_\beta)\vec{x}, \quad \vec{r}_\beta = \vec{R} + (b/m_\alpha)\vec{s}. \tag{46}$$

Since the electronic mass is much smaller than the mass of the particles α and β, one can simplify Eqs. (44) and (45). Neglecting the terms proportional to a/m_β and b/m_α, one obtains for the coordinates: $\vec{r}_\alpha \simeq \vec{r}_\beta \simeq \vec{R}$. Hence, the variables in Eqs. (44) and (45) can be separated and the wave functions $\chi_i^{\alpha+}, \chi_f^{\beta-}$ can be represented in the factorized forms:

$$\chi_i^{\alpha+} = \varphi_i(\vec{x})F_\alpha^+(\vec{r}_\alpha), \quad \chi_f^{\beta-} = \varphi_f(\vec{s})F_\beta^-(\vec{r}_\beta), \tag{47}$$

where F_α^+ (F_β^-) is the continuum Coulomb wave function which describes the motion of the particle α (β) relative to the center of mass of the pair (β, γ) $((\alpha, \gamma))$ in the initial (final) state with the relative kinetic energy $k_\alpha^2/2\mu_\alpha(k_\beta^2/2\mu_\beta)$:

$$F_\alpha^+(\vec{r}_\alpha) = N^{(+)}(\nu_\alpha)\exp(i\vec{k}_\alpha \cdot \vec{r}_\alpha)\,{}_1F_1(-i\nu_\alpha, 1, ik_\alpha\xi_\alpha), \tag{48}$$

$$F_\beta^-(\vec{r}_\beta) = N^{(-)}(\nu_\beta)\exp(i\vec{k}_\beta \cdot \vec{r}_\beta)\,{}_1F_1(i\nu_\beta, 1, -ik_\beta\xi_\beta), \tag{49}$$

$$N^{(\pm)}(\nu_j) = \Gamma(1 \pm i\nu_j)\exp(-\pi\nu_j/2), \quad j = \alpha, \beta. \tag{50}$$

Here ${}_1F_1(a, b, x)$ is the confluent Kummer hypergeometric function. By substitution of the explicit expressions for $\chi_i^{\alpha+}$, $\chi_f^{\beta-}$ and $U_{\alpha,\beta}$ into (35) and (36), one obtains:

$$T^-_{\alpha\beta} = \int\int \mathrm{d}\vec{r}_\alpha\, \mathrm{d}\vec{x}\, \varphi_f^*(\vec{s}) \left(\frac{Z_\alpha}{R} - \frac{Z_\alpha}{s}\right) \varphi_i(\vec{x}) e^{i\vec{k}_\alpha\cdot\vec{r}_\alpha - i\vec{k}_\beta\cdot\vec{r}_\beta} L(\vec{r}_\alpha, \vec{r}_\beta), \tag{51}$$

$$T^+_{\alpha\beta} = \int\int \mathrm{d}\vec{r}_\beta\, \mathrm{d}\vec{s}\, \varphi_f^*(\vec{s}) \left(\frac{Z_\beta}{R} - \frac{Z_\beta}{x}\right) \varphi_i(\vec{x}) e^{i\vec{k}_\alpha\cdot\vec{r}_\alpha - i\vec{k}_\beta\cdot\vec{r}_\beta} L(\vec{r}_\alpha, \vec{r}_\beta), \tag{52}$$

where

$$L(\vec{r}_\alpha, \vec{r}_\beta) = N^{(+)}N^{(-)}F(-i\nu_\alpha, 1, ik_\alpha\xi_\alpha)\,{}_1F_1(i\nu_\beta, 1, -ik_\beta\xi_\beta). \tag{53}$$

Taking into account that $m_\gamma \ll m_\alpha \sim m_\beta$, the following kinematic relations are straightforward:

$$\vec{k}_\alpha \cdot \vec{r}_\alpha - \vec{k}_\beta \cdot \vec{r}_\beta = -a\vec{\upsilon} \cdot \vec{x} - \vec{\alpha} \cdot \vec{R} = \vec{\beta} \cdot \vec{x} + \vec{\alpha} \cdot \vec{s}, \tag{54}$$

where we use the following definitions:

$$\vec{\alpha} = (b/m_\gamma)\vec{k}_\beta - \vec{k}_\alpha = \alpha_z\hat{\vec{\upsilon}} + \vec{\eta}, \quad \alpha_z = -m_\gamma\upsilon/2 - \Delta E/\upsilon, \tag{55}$$

$$\vec{\beta} = (a/m_\gamma)\vec{k}_\alpha - \vec{k}_\beta = \beta_z\hat{\vec{\upsilon}} - \vec{\eta}, \quad \beta_z = -m_\gamma\upsilon/2 + \Delta E/\upsilon, \tag{56}$$

$$\vec{\alpha} + \vec{\beta} + \vec{\upsilon} = 0, \quad \Delta E = E_f - E_i, \quad \vec{\upsilon}' \simeq \vec{\upsilon}, \tag{57}$$

$$\vec{\eta} = (\eta\cos\Phi_{\vec{\eta}}, \eta\sin\Phi_{\vec{\eta}}, 0), \quad \eta^2 = 4\mu_\alpha\mu_\beta\upsilon^2\sin^2(\theta/2), \tag{58}$$

and $\vec{\eta}$ is the orthogonal (relative to vector $\vec{\upsilon}$) component of the transmitted momentum ($\vec{\eta} \cdot \vec{\upsilon} = 0$) and θ is the scattering angle (the angle between the vectors $\vec{k}_\alpha$ and $\vec{k}_\beta$). Now, taking into account assumption $\vec{r}_\alpha \approx \vec{r}_\beta \approx \vec{R}$, the reaction amplitude $T^\pm_{\alpha\beta}$ reads:

$$T^{+}_{\alpha\beta} = N_1 Z_\beta \int \mathrm{d}\vec{R} \int \mathrm{d}\vec{x} \left(\frac{1}{R} - \frac{1}{x} \right) \varphi^*_f(\vec{s}) \varphi_i(\vec{x}) e^{-ia\vec{v}\cdot\vec{x} - i\vec{\alpha}\cdot\vec{R}} \widetilde{F}(\vec{R}), \tag{59}$$

where

$$T^{-}_{\alpha\beta} = N_1 Z_\alpha \int \mathrm{d}\vec{R} \int \mathrm{d}\vec{s} \left(\frac{1}{R} - \frac{1}{s} \right) \varphi^*_f(\vec{s}) \varphi_i(\vec{x}) e^{ib\vec{v}\cdot\vec{s} + i\vec{\beta}\cdot\vec{R}} \widetilde{F}(\vec{R}), \tag{60}$$

$$\widetilde{F}(\vec{R}) = {}_1F_1(-i\nu_\alpha, 1, ik_\alpha R - i\vec{k}_\alpha \cdot \vec{R})\, {}_1F_1(-i\nu_\beta, 1, ik_\beta R + i\vec{k}_\beta \cdot \vec{R}),$$
$$N_1 = N^{(+)} N^{(-)} = \Gamma(1 + i\nu_\alpha)\Gamma(1 + i\nu_\beta) \exp\left(-\frac{\pi(\nu_\alpha + \nu_\beta)}{2} \right).$$

In further calculations we assume that the atoms in the entrance and exit channels have zero orbital momentum, hence the wave functions read:

$$\varphi_i(\vec{x}) = Z_\beta^{3/2} \pi^{-1/2} e^{-Z_\beta x}, \quad \varphi_f(\vec{s}) = Z_\alpha^{3/2} \pi^{-1/2} e^{-Z_\alpha s}, \tag{61}$$

and the energies are defined as $E_{i,f} = -Z^2_{\alpha,\beta}/2$. We shall demonstrate the calculation of the scattering amplitude on example of $T^{-}_{\alpha\beta}$. Consider the integral:

$$K^{(-)}(Z_\alpha, Z_\beta) = \int \mathrm{d}\vec{R}\, R^{-1} \exp(i\vec{\beta} \cdot \vec{R}) \widetilde{F}(\vec{R}) I^{-}_{\alpha\beta}(\vec{R}), \tag{62}$$

where

$$I^{-}_{\alpha\beta}(\vec{R}) = \int \mathrm{d}\vec{s} (xs)^{-1} \exp(-Z_\alpha s - Z_\beta x - ib\vec{v} \cdot \vec{s}). \tag{63}$$

Using the integral Fourier representation for $\exp(-Z_\beta x)/x$:

$$\frac{\exp(-Z_\beta x)}{x} = \frac{1}{2\pi^2} \int \frac{\exp(i\vec{q} \cdot \vec{x})}{q^2 + Z_\beta^2} \mathrm{d}\vec{q}, \tag{64}$$

where $\vec{x} = \vec{s} + \vec{R}$, and equality:

$$\frac{1}{uv} = \int_0^1 \mathrm{d}t (ut + (1 - t)v)^{-2}, \tag{65}$$

the integration in (63) over $\vec{s}$ leads to expression:

$$I^{-}_{\alpha\beta}(\vec{R}) = \frac{2}{\pi b^2}\int_0^1 \mathrm{d}t \int \frac{\mathrm{d}\vec{q}\,\exp(-i\vec{q}\cdot\vec{R})}{\left[|\vec{q}-\vec{Q}|^2+\Delta_-^2\right]^2}. \tag{66}$$

Here, the following definitions have been used:

$$\vec{Q} = (t-1)\vec{\upsilon}, \quad \Delta_-^2 = \upsilon^2 t(1-t) + tZ_\beta^2 + (1-t)(Z_\alpha/b)^2. \tag{67}$$

Computing the integral in (66) by employing the theorem residues, one obtains:

$$I^{-}_{\alpha\beta}(\vec{R}) = 2\pi b^{-2}\int_0^1 \mathrm{d}t[\Delta_-]^{-1}\exp(-i\vec{Q}\cdot\vec{R} - R\Delta_-). \tag{68}$$

Calculation of the integral in (62) can be made in the framework of the method proposed by Nordsieck.[33] We shall omit the algebra and give here only the final result for reaction amplitude $T^{-}_{\alpha\beta}$ in the form of a one-dimensional integral:

$$T^{-}_{\alpha\beta} = N_1 N_2^{(-)} Z_\alpha \int_0^1 \mathrm{d}t \frac{\partial}{\partial Z_\beta}\left(-\frac{1}{\Delta_-}\frac{\partial}{\Delta_-} + \frac{\partial}{\partial Z_\alpha}\frac{1}{\Delta_-}\right)\Xi^{(-)}(\Delta_-), \tag{69}$$

$$\Xi^{(-)}(\Delta_-) = \frac{4\pi}{\omega_-^2}\left[1-\frac{2\mu_\alpha \upsilon\sigma_+}{\omega_-^2}\right]^{i\nu_\alpha}\left[1-\frac{2\mu_\beta \upsilon\sigma_-}{\omega_-^2}\right]^{i\nu_\beta} {}_2F_1(-i\nu_\beta, -i\nu_\alpha, 1, \tau_-), \tag{70}$$

where, ${}_2F_1(a, b, c, x)$ is the Gauss hypergeometric function, and

$$N_2^{(-)} = (2/b^2)(Z_\alpha Z_\beta)^{3/2}, \quad \omega_-^2 = p^2 + \Delta_-^2, \tag{71}$$

$$\tau_- = \frac{4\mu_\alpha\mu_\beta p_\perp^2 \upsilon^2}{(\omega_-^2 - 2\mu_\alpha \upsilon\sigma_+)(\omega_-^2 - 2\mu_\beta \upsilon\sigma_-)}, \quad \sigma_\pm = i\Delta_- \pm p_z. \tag{72}$$

Here, vector $\vec{p} = \vec{\beta} - \vec{Q}$ is decomposed into the parallel p_z and perpendicular $p_\perp$ components relative to the vector $\vec{\upsilon}$:

$$\vec{p} = (p_z, p_\perp), \quad p_z = \vec{p}\cdot\hat{\vec{\upsilon}} = \upsilon\left(\frac{1}{2} - t\right) + \frac{\Delta E}{\upsilon}, \quad \vec{p}_\perp = \vec{\eta}. \tag{73}$$

In order to compute the integral (69), one should first differentiate over the Z_α, Z_β, and Δ_- variables and, at the final stage, make the following substitutions:

$$\nu_\alpha \to Z_\alpha(Z_\beta - 1)/\upsilon, \quad \nu_\beta \to Z_\beta(Z_\alpha - 1)/\upsilon.$$

Using the same approach, one can compute the reaction amplitude $T^+_{\alpha\beta}$ in the *post*-formalism. Omitting the algebra, we represent here only the final result:

$$T^+_{\alpha\beta} = Z_\beta N_1 N_2^{(+)} \int_0^1 \mathrm{d}t \frac{\partial}{\partial Z_\alpha} \left(-\frac{1}{\Delta_+}\frac{\partial}{\Delta_+} + \frac{\partial}{\partial Z_\beta}\frac{1}{\Delta_+} \right) \Xi^{(+)}(\Delta_+), \quad (74)$$

$$\Xi^{(+)}(\Delta_+) = \frac{4\pi}{\omega_+^2}\left[1 - \frac{2\mu_\alpha \upsilon \sigma_-}{\omega_+^2}\right]^{i\nu_\alpha}\left[1 - \frac{2\mu_\beta \upsilon \sigma_+}{\omega_+^2}\right]^{i\nu_\beta} {}_2F_1(-i\nu_\beta, -i\nu_\alpha, 1, \tau_+), \quad (75)$$

$$N_2^{(+)} = (2/a^2)(Z_\alpha Z_\beta)^{3/2}, \quad \tau_+ = \frac{4\mu_\alpha \mu_\beta q_\perp^2 \upsilon^2}{(\omega_+^2 - 2\mu_\alpha \upsilon \sigma_-)(\omega_+^2 - 2\mu_\beta \upsilon \sigma_+)}, \quad (76)$$

and the following designations have been used:

$$\vec{q} = (q_z, \vec{q}_\perp), \quad \vec{q}_\perp \cdot \vec{\upsilon} = 0, \quad q_z = (t - 1/2)\upsilon + \Delta E \upsilon^{-1}, \quad \vec{q}_\perp = -\vec{\eta}.$$

Employing the same differentiation technique over the charges Z_α and Z_β, one can take into account the polynomial structure of the wave functions of the excited states of hydrogen-like atom or ion.

Let us compare the described method for calculating charge-transfer amplitude with the traditional approximations of the first order perturbation theory. First, we discuss the asymptotic properties of the perturbing potentials U_α and U_β as a function of R. Using (4), we shall represent vector $\vec{s}(\vec{x})$ in terms of $\vec{R}$ and $\vec{x}(\vec{s})$ and expand the Coulomb potential $V_\beta = -Z_\alpha/s$ ($V_\alpha = -Z_\beta/x$) into the series over the small parameter x/R (s/R). As a result, we come to the following asymptotic (at $R \to \infty$) representations:

$$V_\beta \simeq -\frac{Z_\alpha}{R} - \frac{Z_\alpha(\hat{\vec{R}} \cdot \vec{x})}{R^2} + \cdots, \quad V_\alpha \simeq -\frac{Z_\beta}{R} - \frac{Z_\beta(\hat{\vec{R}} \cdot \vec{s})}{R^2} + \cdots \quad (77)$$

which implies that when R tends to infinity, the potential U_α (U_β) tends to zero as R^{-2}:

$$U_\alpha = -\frac{Z_\alpha}{R} - \frac{Z_\alpha}{s} \to -Z_\alpha O(R^{-2}), \quad U_\beta = -\frac{Z_\beta}{R} - \frac{Z_\beta}{x} \to -Z_\beta O(R^{-2}). \quad (78)$$

This gives us grounds to assume that potentials U_α (U_β) are short-range. Hence, one can observe a correlation between the behavior of the perturbing potentials U_α (U_β) at large distances R and the asymptotic properties of distorted waves $\chi_i^{\alpha+}$ and $\chi_f^{\beta-}$. This correlation leads to the short-range character of the perturbation U_α (U_β) at the correct behavior (39) of the $\chi_i^{\alpha+}$ $(\chi_f^{\beta-})$ functions at infinity. Substitution in Eq. (51) of the plane waves $\exp(i\vec{k}_{\alpha,\beta} \cdot \vec{r}_{\alpha,\beta})$ instead of functions $F^{\pm}_{\alpha,\beta}$ and the channel interaction υ_α instead of the transition operator U_α leads to the final result for transition amplitude:

$$T^{(\mathrm{B1})}_{\alpha\beta}(\vec{\eta}) = \int\int \mathrm{d}\vec{r}_\alpha\, \mathrm{d}\vec{x}\, \varphi_f^*(\vec{s}) \left[\frac{Z_\alpha Z_\beta}{R} - \frac{Z_\alpha}{s}\right] \varphi_i(\vec{x}) e^{i\vec{k}_\alpha \cdot \vec{r}_\alpha - i\vec{k}_\beta \cdot \vec{r}_\beta}. \quad (79)$$

This determines the direct one-step mechanism of reaction (1) in the framework of the standard first Born (B1) approximation (the so-called Jackson–Schiff approximation[14]). In the case of resonant charge transfer of atomic hydrogen on the proton ($Z_\alpha = Z_\beta = 1$), the Coulomb wave functions $F^{\pm}_{\alpha,\beta}$ reduce to the plane waves and formulae (51) and (79) coincide. The discrepancy of these formulae for $Z_{\alpha,\beta} \neq 1$ is due to the fact that in the standard Born approximation, the Coulomb interaction in the entrance and exit channels are not taken into account. Hence, the channel wave function does not satisfy the Coulomb boundary conditions of the scattering problem. Thus, expression (51) may be considered as a correct generalization of the Born approximation which accounts for Coulomb distortion of the asymptotic behavior of the wave functions in both the entrance and exit channels of the charge-exchange reaction (1). This generalization, which is the boundary-corrected first Born approximation, or CB1, will be used in the next sections of this work. When the collision energies of the projectiles are sufficiently high, the Coulomb wave functions do not differ substantially from the plane waves, and hence the CB1 and the usual first Born approximations almost coincide.[24, 25] However, already at intermediate collision energies, it is necessary to take into account the long-range Coulomb effects that substantially influence the behavior of the charge-exchange cross sections.

We now reemphasize that when using the CB1 approximation, we neglect the re-scattering effects, i.e., possible multiple-step reaction mechanisms. The role of two-step transitions through the intermediate (bound or continuum) state increases with increasing projectile energy.[32] The quantitative description of such transitions becomes possible only with inclusion of the post-collision interaction into the final state wave function. That is equivalent to accounting for the effects of multiple-step re-scattering of the electron on the rest of the target ion. In the next section, on the basis of the first iteration of the Dodd–Greider equations (30) we shall disuss the one- and two-step electron capture mechanisms and clarify their connection with the angular distribution of the reaction products. Alternatively, re-scattering effects can be described by the boundary-corrected second Born (CB2) approximation.[32]

4. THE CONTINUUM-INTERMEDIATE STATE METHOD WITH THE CORRECT BOUNDARY CONDITIONS

Let us transform the expression for the reaction amplitude $T^{-}_{\alpha\beta}$ in the following way. We introduce the scattering vector $|\Psi_f^{\beta-}\rangle$ by definition:

$$|\Psi_f^{\beta-}\rangle = [1 + g_x^{+\dagger}(\upsilon_\beta - W_\beta)]\chi_f^{\beta-}\rangle. \tag{80}$$

Substitution of (23) and (80) into (33) leads to the following representation of the reaction amplitude $T^{-}_{\alpha\beta}$, which takes into account both the direct and the two-step mechanisms:

$$T^{-}_{\alpha\beta} = \langle\Psi_f^{\beta-}|\upsilon_\alpha - W_\alpha|\chi_i^{\alpha+}\rangle. \tag{81}$$

In order to obtain the differential equation for the wave function $\Psi_f^{\beta-}$, we shall multiply both parts of Eq. (80) with $(E - H + \upsilon_x^{\dagger} - i\varepsilon)$ from the left and compute the limit $\varepsilon \to 0^+$ taking into account Eq. (38). As a result we obtain:

$$(E - H + \upsilon_x^{\dagger})|\Psi_f^{\beta-}\rangle = \upsilon_x^{\dagger}|\chi_f^{\beta-}\rangle. \tag{82}$$

Since the solution of Eq. (82) with realistic local potential υ_x involves considerable mathematical difficulties, one should attempt to replace potential υ_x with an operator, which should be chosen so the condition:

$$\upsilon_x^{\dagger}|\chi_f^{\beta-}\rangle = 0, \tag{83}$$

is satisfied. Also, the solution of the corresponding homogeneous equation should be represented as:

$$|\Psi_f^{\beta-}\rangle = |\varphi_f(\vec{s})h_\beta^-\rangle \tag{84}$$

with the following boundary conditions:

$$\Psi_f^{\beta-} \underset{r_\beta\to\infty}{\longrightarrow} \Phi_f^{\beta-} = \varphi_f(\vec{s}) \exp[i\vec{k}_\beta \cdot \vec{r}_\beta - i\nu_\beta \ln(k_\beta \xi_\beta)]. \tag{85}$$

By substituting Eq. (85) into (82) and taking into account (83), we come to the following equation relative to the h_β^-:

$$\varphi_f(\vec{s})(E - E_f - H_0 - \upsilon_\beta)h_\beta^- + \frac{1}{b}\vec{\nabla}_{\vec{s}}\varphi_f(\vec{s})\cdot\vec{\nabla}_{\vec{s}}h_\beta^- + \upsilon_x^\dagger(\varphi_f(\vec{s})h_\beta^-) = 0. \tag{86}$$

We now return to the question concerning the choice of operator υ_x. Closely related to this choice is the need to improve the convergence of the iteration series of integral equation (30) for operator $U_{\alpha\beta}^-$. As described in the previous section, the proper choice of the operator υ_x eliminates the disconnected diagrams from its kernel (31). Indeed, by definition, (43) of the perturbation $U_\beta = \upsilon_\beta - W_\beta$ as a part of (31), contains terms that depend solely on the relative vectorial variables $\vec{x}$ and $\vec{R}$. Hence, in order to eliminate the disconnected diagrams from the K operator, υ_x should only act over the variable $\vec{s}$, which is related to pair (α, γ). Such an operator can be constructed by the following definition:

$$\upsilon_x\Psi = -\frac{1}{b}\vec{\nabla}_{\vec{s}}\varphi_f(\vec{s})\cdot\vec{\nabla}_{\vec{s}}\left(\Psi/\varphi_f(\vec{s})\right), \tag{87}$$

on the set of elements $\Psi \in \mathcal{H}$, where $\mathcal{H}$ is the subspace of continuum states of the Hamiltonian H. The domain of differential operator υ_x includes only those elements $\Psi \in \mathcal{H}$ whose image Ψ' obtained by the action υ_x belongs to the same Hilbert space $\mathcal{H}$ (i.e., $\upsilon_x\Psi = \Psi'$ under the condition $\Psi, \Psi' \in \mathcal{H}$). The latter is equivalent to the requirement that elements Ψ admit a representation similar to (84). As a consequence, although the operator contains singularities at the points of configurational space where function $\varphi_f(\vec{s})$ is equal to zero, the result of action $\upsilon_x\Psi$ has no such singularities. That the operator υ_x satisfies condition (83) is easily seen by using the obvious relation $\vec{\nabla}_{\vec{s}}(\chi_f^{\beta-}/\varphi_f(\vec{s})) = \vec{\nabla}_{\vec{s}}F_\beta^-(\vec{r}_\beta) = 0$.

Thus, when choosing the operator υ_x in a form (87), the kernel K of the integral equation (30) is defined only by those variables which completely correspond to the connected diagrams. This means that the iteration series of Eq. (30) should, in principle, converge faster and in a wider energetic range than the original Born series of the three-body problem.

Taking into account the explicit form (87) of operator υ_x and using expression (5) for kinetic energy operator H_0, Eq. (86) becomes:

$$\left(E - E_f + \frac{1}{2\mu_\alpha}\Delta_{\vec{r}_\alpha} + \frac{1}{2a}\Delta_{\vec{x}} + \frac{Z_\beta}{x} - \frac{Z_\alpha Z_\beta}{R}\right) h_\beta^- = 0. \tag{88}$$

According to Eqs. (84) and (85), the asymptotic limit of a function h_β^- at $r_\beta \to \infty$ has the form of a distorted plane wave with a unit amplitude:

$$h_\beta^- \xrightarrow[r_\beta \to \infty]{} f_\beta^-(\vec{r}_\beta) = \exp\left[i\vec{k}_\beta \cdot \vec{r}_\beta - \frac{iZ_\beta(Z_\alpha - 1)}{\upsilon'}\ln(k_\beta t_\beta + \vec{k}_\beta \cdot \vec{r}_\beta)\right]. \tag{89}$$

With the approximation $R \approx r_\alpha$, the variables in Eq. (88) are separable and the corresponding wave functions become explicitly representable in the following form:

$$h_\beta^- = C^{(-)}\mathcal{F}^{(-)}(\vec{x})\Im^{(-)}(\vec{r}_\alpha). \tag{90}$$

The two-body scattering Coulomb wave functions $\mathcal{F}^{(-)}(\vec{x})$ and $\Im^{(-)}(\vec{r}_\alpha)$ are defined through the confluent hypergeometric function as follows:[3]

$$\mathcal{F}^{(-)}(\vec{x}) = \Gamma\left(1 + \frac{iaZ_\beta}{q}\right)\exp\left(\frac{\pi a Z_\beta}{2q} + i\vec{q}\cdot\vec{x}\right){}_1F_1\left(-\frac{iaZ_\beta}{q}, 1, iqx - i\vec{q}\cdot\vec{x}\right), \tag{91}$$

$$\begin{aligned}\Im^{(-)}(\vec{r}_\alpha) = \Gamma\left(1 - \frac{i\mu_\alpha Z_\alpha Z_\beta}{q_\alpha}\right)\exp\left(-\frac{\pi\mu_\alpha Z_\alpha Z_\beta}{2q} + i\vec{q}_\alpha\cdot\vec{r}_\alpha\right)\\ \times{}_1F_1(-i\mu_\alpha Z_\alpha Z_\beta/q, 1, iq_\alpha r_\alpha - i\vec{q}_\alpha\cdot\vec{r}_\alpha).\end{aligned} \tag{92}$$

The coefficient $C^{(-)}$ and vectors $\vec{q}, \vec{q}_\alpha$, that appear due to variable separation, can be defined by matching h_β^- with the eikonal asymptotic limit (89) at $r_\beta \to \infty$. Using the asymptotic form of the confluent hypergeometric function $F(a, b, t)$ at $t \to \infty$, we find from the matching conditions that:

$$\vec{q} = a\vec{\upsilon}' \simeq \vec{\upsilon}', \quad \vec{q}_\alpha = (b/m_\gamma)\vec{k}_\beta \simeq \vec{k}_\beta, \quad C^{(-)} = \mu_\beta^{iZ_\beta/\upsilon'}. \tag{93}$$

Summing up, let us represent the wave function of the final state $\Psi_f^{\beta-}$, which describes the scattering of the charged particle β on the hydrogen-like system (α, γ) as:

$$\Psi_f^{\beta-} = \mu_\beta^{i\nu'_{\mathrm{t}}} \varphi_f(\vec{s}) \exp(i\vec{k}_\beta \cdot \vec{r}_\beta) \mathcal{F}^{(-)}(\vec{x}) \Im^{(-)}(\vec{r}_\alpha), \tag{94}$$

where

$$\mathcal{F}^{(-)}(\vec{x}) = N^{(+)} F(-i\nu'_{\mathrm{t}}, 1, -i\upsilon' x - i\vec{\upsilon}' \cdot \vec{x}), \quad \nu'_{\mathrm{t}} = Z_\beta/\upsilon', \quad \vec{\upsilon}' = \vec{k}_\beta/\mu_\beta, \tag{95}$$

$$\Im^{(-)}(\vec{r}_\alpha) = N^{(-)}{}_1F_1(i\nu', 1, -ik_\beta r_\alpha - \vec{k}_\beta \cdot \vec{r}_\alpha), \quad \nu' = Z_\alpha Z_\beta/\upsilon', \tag{96}$$

$$N^{(+)} = \Gamma(1 + i\nu'_{\mathrm{t}}) \exp(\pi \nu'_{\mathrm{t}}/2), \quad N^{(-)} = \Gamma(1 - i\nu') \exp(-\pi \nu'/2). \tag{97}$$

From the form of the function $\Psi_f^{\beta-}$ one can readily appreciate its convenience for studying the influence of the post-collision interaction on differential cross sections of charge transfer, because it equally takes into account the interaction of bound electron γ with the residual target ion β and the interaction of heavy particles α and β. Recall that the initial wave function $\chi_i^{\alpha+}$ is defined by expressions (47) and (48).

Using now the expressions for the wave functions (94), (47), and (48), the transition operator (42), and relation (81), we come to the following charge-transfer reaction amplitude with account for Coulomb interaction in the final state:

$$\begin{aligned} T_{\alpha\beta}^{-}(BCIS) = N(\upsilon, \nu_\alpha) \int\!\!\int \mathrm{d}\vec{r}_\alpha\, \mathrm{d}\vec{x}\, e^{i\vec{k}_\alpha \cdot \vec{r}_\alpha - i\vec{k}_\beta \cdot \vec{r}_\beta} \varphi_f^*(\vec{s}) \left(\frac{Z_\alpha}{r_\alpha} - \frac{Z_\alpha}{s} \right) \varphi_i(\vec{x}) \\ \times {}_1F_1(i\nu'_{\mathrm{t}}, 1, i\upsilon' x + i\vec{\upsilon}' \cdot \vec{x}) {}_1F_1(-i\nu_\alpha, 1, ik_\alpha r_\alpha - i\vec{k}_\alpha \cdot \vec{r}_\alpha) {}_1F_1(-i\nu', 1, ik_\beta r_\alpha + i\vec{k}_\beta \cdot \vec{r}_\alpha), \end{aligned} \tag{98}$$

where

$$N(\upsilon, \nu_\alpha) = \mu_\beta^{-i\nu'_{\mathrm{t}}} \Gamma(1 + i\nu_\alpha) \Gamma(1 - i\nu'_{\mathrm{t}}) \Gamma(1 + i\nu') \exp\left(\frac{\pi}{2} \left[\nu_\alpha + \nu' - \nu'_{\mathrm{t}} \right] \right). \tag{99}$$

This is the boundary-corrected conntinuum intermediate state approximation,[5] or BCIS. Without the eikonalization of the $\vec{r}_\alpha$- and $\vec{r}_\beta$-dependent Coulomb waves, the calculation of amplitude (98) in the general case when $Z_\beta \neq 1$ is complicated by the presence of three confluent hypergeometric functions under the integral sign. However, there is one important case, when integration in (98) can be reduced to a one-dimensional numerical integration. This is the case of charge exchange of a proton (or other charged particle) with atomic hydrogen ($Z_\beta = 1$). In this case the Coulomb parameter $\nu_\alpha = 0$ and the hypergeometric function ${}_1F_1(-i\nu_\alpha, 1, ik_\alpha r_\alpha - i\vec{k}_\alpha \cdot \vec{r}_\alpha)$ in formula (98) is equal to 1.

For further calculations we shall use expression (61) for bound state wave functions and integral representation for confluent hypergeometric function:

$$ {}_1F_1(a, c, z) = \frac{1}{B(a, c-a)} \int_0^1 t^{a-1}(1-t)^{c-a-1}\exp(zt)\mathrm{d}t, \tag{100} $$

where $B(a, c-a)$ is the Euler beta-function. By changing the order of integration for integrals in expression (98), we come to the following representation for $T^-_{\alpha\beta}$:

$$ \begin{aligned} T^-_{\alpha\beta} &= N(v, 0)N_2[B(i\nu'_{\mathrm{t}}, 1 - i\nu'_{\mathrm{t}})B(-i\nu', 1 + i\nu')]^{-1} \\ &\quad \times \int_0^1 t_1^{i\nu'_{\mathrm{t}}-1}(1-t_1)^{-i\nu'_{\mathrm{t}}}\mathrm{d}t_1 \int_0^1 t_2^{-i\nu'-1}(1-t_2)^{i\nu'} I(t_1, t_2)\mathrm{d}t_2, \end{aligned} \tag{101} $$

$$ I(t_1, t_2) = \lim_{\varepsilon \to 0} Z_\alpha \left(\frac{\partial^2}{\partial\lambda_\alpha \partial\lambda_\beta} - \frac{\partial^2}{\partial\lambda_\beta \partial\varepsilon} \right) J, \quad N_2 = (Z_\alpha Z_\beta)^{3/2}\pi^{-1}. \tag{102} $$

Here J is defined by the expression:

$$ J = \int\int \mathrm{d}\vec{r}_\alpha \, \mathrm{d}\vec{x} \, e^{-i\vec{k}_\beta \cdot \vec{r}_\beta} \frac{e^{-\lambda_\alpha s}}{s} e^{i(\vec{k}_\alpha + \vec{k}_\beta t_2)\cdot \vec{r}_\alpha} \frac{e^{-\delta_1 r_\alpha}}{r_\alpha} \frac{e^{-\delta_2 x}}{x} e^{it_1 \vec{v}' \cdot \vec{x}}, \tag{103} $$

where

$$ \delta_1 = \varepsilon - ik_\beta t_2, \quad \delta_2 = \lambda_\beta - iv't_1, \quad \lambda_\alpha = Z_\alpha, \quad \lambda_\beta = Z_\beta. $$

Using the Fourier transformation:

$$ \frac{\exp(-\lambda_a s)}{s} = \frac{1}{2\pi^2} \int \exp(i\vec{k} \cdot \vec{s})(k^2 + \lambda_\alpha^2)^{-1}\mathrm{d}\vec{k}, \tag{104} $$

and the following relations:

$$ \vec{r}_\beta = (b/m_\gamma)\vec{r}_\alpha + (a/\mu_\beta)\vec{x}, \quad \vec{s} = (a/m_\gamma)\vec{x} - \vec{r}_\alpha, $$

one can perform integration in (103) over the $\vec{x}$ and $\vec{r}_\alpha$ variables. As a result one obtains the following expression for the matrix element J:

$$J = \frac{8m_\gamma^2}{a^2} \int \frac{d\vec{k}}{(k^2 + \lambda_\alpha^2)\left(|\vec{k} - \vec{q}_1|^2 + \rho_1^2\right)\left(|\vec{k} - \vec{q}_2|^2 + \rho_2^2\right)}, \quad (105)$$

where

$$\vec{q}_1 = \frac{m_\gamma}{\mu_\beta}\vec{k}_\beta + \frac{m_\gamma}{a}\vec{v}' t_1, \quad \vec{q}_2 = \left(\vec{k}_\alpha - \frac{b}{m_\gamma}\vec{k}_\beta\right) + \vec{k}_\beta t_2,$$

and $\rho_1 = \delta_2 m_\gamma / a$, $\rho_2 = \delta_1$. Using the results obtained in Ref. 34 for a rearrangement of the expression for J, and omitting the lengthy derivation, we give the final result for charge-transfer amplitude $T^-_{\alpha\beta}$:

$$T^-_{\alpha\beta} = \frac{16\pi^2}{a^2} N(v, 0) N_2 Z_\alpha \lim_{\varepsilon \to 0} \left(\frac{\partial^2}{\partial\lambda_\alpha\,\partial\lambda_\beta} - \frac{\partial^2}{\partial\lambda_\beta\,\partial\varepsilon} \right) \int_0^\infty \mathcal{K}(x)\,dx, \quad (106)$$

where

$$\begin{aligned}\mathcal{K}(x) = {} & [B(i\nu'_t, 1 - i\nu'_t) B(-i\nu', 1 + i\nu')]^{-1} \int_0^1 t_1^{i\nu'_t - 1}(1 - t_1)^{-i\nu'_t} dt_1 \\ & \times \int_0^1 t_2^{-i\nu' - 1}(1 - t_2)^{i\nu'}(A + Bt_1 + Dt_2 + Ct_1 t_2)^{-1} dt_2.\end{aligned} \quad (107)$$

The expressions for coefficients A, B, C, and D are quite involved and we do not show them here. The integrals over t_1 and t_2 can be evaluated by the formula from Ref. 33. The final result for $\mathcal{K}(x)$ reads:

$$\begin{aligned}\mathcal{K}(x) = {} & A^{-1}(1 + D/A)^{i\nu'}(1 + B/A)^{-i\nu'_t} \\ & \times {}_2F_1\left(i\nu'_t, -i\nu, 1; (BD - AC)(A + D)^{-1}(A + B)^{-1}\right).\end{aligned} \quad (108)$$

The one-dimensional integral over x in expression (106) should be computed numerically.

Let us compare the proposed approach for investigating the charge-exchange reactions with the traditional continuum distorted wave approximation,[3] or CDW. The transition amplitude of the CDW approximation in the *prior*-formalism is given by formulae:

$$T^{-}_{\alpha\beta}(\mathrm{CDW}) = N_{\mathrm{CDW}} \int\!\!\int d\vec{r}_\alpha \, d\vec{x} \, \exp(i\vec{k}_\alpha \cdot \vec{r}_\alpha - i\vec{k}_\beta \cdot \vec{r}_\beta)\mathcal{Z}^{-}_{\alpha\beta} J(\vec{r}_\alpha, \vec{r}_\beta), \quad (109)$$

where

$$\begin{aligned} J(\vec{r}_\alpha, \vec{r}_\beta) &= N^{(+)} N^{(-)}{}_1F_1(-i\nu, 1, ik_\alpha \xi_\alpha){}_1F_1(i\nu, 1, -ik_\beta \xi_\beta), \\ \mathcal{Z}^{-}_{\alpha\beta} &= \varphi_f^*(\vec{s}){}_1F_1(i\nu_{\mathrm{t}}', 1, i\upsilon' x + i\vec{\upsilon}' \cdot \vec{x}')\vec{\nabla}_{\vec{x}} \cdot \varphi_i(\vec{x}) \cdot \vec{\nabla}_{\vec{s}}{}_1F_1(i\nu_{\mathrm{p}}, 1, i\upsilon s + i\vec{\upsilon} \cdot \vec{s}), \end{aligned} \quad (110)$$

$$N_{\mathrm{CDW}} = \Gamma(1 - i\nu_{\mathrm{t}}')\Gamma(1 - i\nu_{\mathrm{p}}) \exp(\pi(\nu_{\mathrm{t}}' + \nu_{\mathrm{p}})/2), \quad (111)$$

with $\nu = Z_\alpha Z_\beta/\upsilon$, $\nu_{\mathrm{p}} = Z_\alpha/\upsilon$, $\nu_{\mathrm{t}}' = Z_\beta/\upsilon'$. The CDW approximation was first used by Cheshire[35] for calculation of the cross section of resonant charge transfer of fast protons on atomic hydrogen. Subsequently, Gayet[36] showed that amplitude (109) in the *prior*-formalism can be obtained as a first term of the Dodd–Greider perturbation series[28] for operators of three-body rearrangement scattering. Note that due to small scattering angles of heavy projectiles, the eikonal approximation can be used with the replacement of all the $\vec{r}_\alpha$ - and $\vec{r}_\beta$ -dependent Kummer functions ${}_1F_1(a_1, b_1, \xi_\alpha)$ and ${}_1F_1(a_1, b_2, \xi_\beta)$ in the CB1, BCIS and CDW methods from Eqs. (53), (98) and (110), respectively, by their logarithmic Coulomb phase factors.[3] This significantly simplifies the calculations.[3, 8–10, 46]

5. ANGULAR AND ENERGY DEPENDENCIES OF CHARGE-TRANSFER CROSS SECTIONS

As seen from the previous section, the quantum scattering theory equations for a few-body system can serve as a universal mathematical background for constructing various approximations for charge-transfer. The iterations of such equations represent scattering amplitudes in the form of series (32). The number of terms taken into account defines the order of re-scattering. The obtained representations (33)–(36) for scattering amplitude are based only on accounting for the first terms of the iteration series of the Dodd–Greider equations. Therefore, such an approach is applicable if the specific collision energy conditions are satisfied. These energies must significantly exceed the binding energies of the compound particles in the initial and final channels. However, they should not be extremely high, because with increasing collision energy the role of multiple scattering of electrons is also augmented. The influence of the higher terms of the iteration series for three-body rearrangement scattering operator has been studied in Refs. 15–17, 32. The qualitative estimates of the contribution of such mechanisms in the nonrelativistic collision energy range showed that this contribution is small compared to the cross sections of one- and two-step mechanisms.

The first applications of the reviewed formalism were for studying the charge-transfer collisions:[3, 35]

$$H^{+} + H(1s) \rightarrow H(1s) + H^{+}. \tag{112}$$

This reaction is of interest for many applications and also plays an important role in testing a variety of theoretical approaches for rearrangement processes. Before proceeding to analysis of reaction (112), we notice the following. For process (1) the scattering amplitude $T^{-}_{\alpha\beta}$ has a sharp maximum in the region of small angles:[3, 37]

$$\theta \leqslant m_{\gamma}/\mu \ll 1, \quad \mu = m_{\alpha} m_{\beta}/(m_{\alpha} + m_{\beta}).$$

In the case of reaction (112), when particles α and β are the protons, the exchange part of scattering amplitude is negligible.[38] Exhaustive comparisons of the CB1 and CDW approximations with all the experimental data for process (112) and for other similar charge-transfer collision, have systematically shown good agreement at intermediate and high energies ($\gtrsim$80 keV/amu).[3, 9]

The need for improvements in the theoretical approaches as well as the development of ion-atomic collision physics led to a shift of emphasis from studies of the integral characteristics toward the differential nature of collision processes. The latter includes more detailed information concerning the role of various reaction mechanisms and are a much more stringent test of theoretical approaches.

The question concerning charge-transfer mechanisms at intermediate and high velocities has remained open for a long time. The lack of reliable experimental data on differential cross sections hampered the choice among various theoretical calculations. For instance, the first Born approximation[14] gives a forward scattering peak in the cross sections, corresponding to a direct one-step mechanism of electron capture with a minimum at angle $\theta_{\rm LS} \sim \sqrt{3}/2m_{\rm p}$ ($m_{\rm p}$ is the ratio of proton mass to the electronic mass, $\theta_{\rm LS}$ is the scattering angle of the formed hydrogen in the laboratory system of coordinates). However, the more precise asymptotic analysis of the scattering amplitude[17] indicated that the maximum at angle $\theta_{\rm LS} \sim \sqrt{3}/2m_{\rm p}$ is related to a classical Thomas mechanism of electron capture.[39] The quantum counterpart of the classical Thomas mechanism is the electronic transition through the continuum spectra from the target into the states bound to the fast projectile. In the BCIS method, the effects of multiple Coulomb re-scattering of the captured electron are taken into account by approximate summation in the distortion factor $\mathcal{F}^{(-)}(\vec{x})$ from (95).

In the differential cross sections of charge transfer a two-step mechanism of electron capture is reflected by a maximum (Thomas peak) at special scattering angle θ_T. For the first time, the Thomas peak was observed in p + He and p+H collisions at energies of a few MeV at scattering angle 0.47 mrad.[40, 41]

In Refs 1, 3 the results of the calculations of the differential cross section for electron capture in the p+H collisions using amplitudes (69) and (109) are compared with experimental data.[41] Similar comparisons have also been carried out between the CB2 method[32] and the measurement of angular distributions[41, 42] for the same process (112). These comparisons have shown that the CB2 method is in good agreement with experiments. The most interesting from a methodological point of view is the comparison of calculations of angular distribution with amplitude (69) of a one-step mechanism and calculations by formula (109), which also takes into account the two-step (Thomas) mechanism of electron capture. Here, one can observe that account of the two-step effects gives rise to a maximum (Thomas peak) at the site of the dip in the JS method, obtained in a simple one-step mechanism. At large scattering angles the interaction of heavy particles is taken into account in the BCIS and CDW methods through the factors $\Im^{(-)}(\vec{r}_\alpha)$ and $J(\vec{r}_\alpha, \vec{r}_\beta)$ in Eqs. (96) and (100), respectively.

Regarding the discussed theoretical investigations on the Thomas peak in differential cross sections, the most significant influence on the shape of angular distributions is from Coulomb re-scattering of the electron on the remaining target ion in the final state. In contradistinction, by neglecting the Coulomb interaction in the final state or by calculations using the single-step collision approximation, the Thomas peak is not reproduced. The obtained agreement between the theoretical and experimental data on differential and total cross sections in a wide range of collision energies demonstrates the reliability of the described approach based on the first iteration of the Dodd–Greider equations.

The main restriction of the method described herein is related to the nature of the three-body problem which assumes only one-electronic degree of freedom. This means that the theory is applicable, rigourously speaking, only to one-electronic systems. However, in some cases multi-electronic systems can be considered as a quasi three-body system with a corresponding non-local or effective local interaction potential between the active electron and the electronic core.

The multi-electronic atom is described by a one-electronic approximation, i.e., it is assumed that the active electron is moving in the frozen atomic core. In that case, all the arguments presented in this section remain valid, except that instead of hydrogen-like wave functions $\varphi_i(\vec{x})$ and $\varphi_f(\vec{s})$ from Eq. (61) one should use the eigenfunctions of the Hamiltonians H_α, H_β with effective one-center potentials V_α^{eff} and V_β^{eff}. For calculation of the charge-transfer amplitude, the CB1-approximation (see Section 3) can be used. The electron capture amplitude $T_{\alpha\beta}^{+}$ from (74) with the perturbing post-collision potential U_β from (43) is correct for $Z_\alpha > Z_\beta$ (Ref. 3). In the case of electron capture by protons from multi-electron atoms for $Z_\alpha < Z_\beta$, one should use the transition amplitude $T_{\alpha\beta}^{-}$ from (69) with the pre-collision perturbation U_α from (42).

When describing the electronic bound states in multi-electronic target atom, the simple model for one-particle wave functions is usually employed in the Roothaan–Hartree–Fock (RHF)[43] model with the effective charge $Z_\beta^{\text{RHF}} = (-2E_{\text{RHF}})^{-1/2}$ for the initial wave function. For testing the sensitivity of the results of the chosen model on the wave functions, also utilized is the hydrogen-like (HL) model with the effective charge Z_β^{RHF}. The values of the cross sections computed within the CB1, CDW and BCIS approximations by means of the RHF and HL models are in good agreement with experimental data.[3, 8, 10, 44]

6. THE DODD–GREIDER INTEGRAL EQUATION IN THE THEORY OF TWO-ELECTRON PROCESSES

This section is devoted to a theoretical description of two-electron capture:[45–51]

$$A^{Z_\alpha +} + B \to A^{(Z_\alpha - 2)+} + B^{2+}, \tag{113}$$

which will be reviewed following Refs. 6, 48 at intermediate and large velocities of colliding particles. The cross sections of a two-electron process (113) are quite large ($\sim 10^{-18} - 10^{-16}$ cm^2) and for certain collisions their contribution to charge transfer could reach the same order of magnitude as one-electron processes.

The success of the CDW theory regarding one-electron processes stimulated the development of the reviewed distorted wave approach for describing two-electron processes.[48] This latter formalism is similar to the CDW method[3] for one-electron capture, but more complicated. The amplitude of reaction (113) can be calculated by approximating the mechanism of simultaneous capture of two electrons. The application of the general theory has been demonstrated in the past by the example of two-electron capture in collisions of helium atoms with nuclei.[48–5]

In the framework of nonrelativistic quantum mechanics, we shall consider collisions in the system of four particles $\alpha, \beta, \gamma_1, \gamma_2$ in which three particles are bound (i.e., they form a "compound" particle) both in the initial and in the final reaction channel:

$$\alpha + (\beta; \gamma_1, \gamma_2) \to (\alpha; \gamma_1, \gamma_2) + \beta, \tag{114}$$

where symbol $(\lambda; \gamma_1, \gamma_2)$ designates the corresponding compound particle ($\lambda = \alpha, \beta$ are the atomic nuclei, and γ_1, γ_2 are the electrons). We did not take into account the spin of particles (the Coulomb effects studied here do not depend on spin). Consider the full Hamiltonian of the system $H_0 + V$, where H_0 is the kinetic energy operator of the four-particle system in the center of mass system. The full interaction potential V is given by expression:

$$V = \sum_{k=1}^{2} (V_{\alpha,\gamma_k} + V_{\beta,\gamma_k}) + V_{\gamma_1,\gamma_2} + V_{\alpha,\beta}, \tag{115}$$

where V_{α,γ_1} is the operator of the pair interaction of α and γ_1, etc. We shall denote by V_α (V_β) the effective interaction potential which forms the compound particle in the initial (final) channel of reaction (114); $H_\alpha = H_0 + V_\alpha$ ($H_\beta = H_0 + V_\beta$) the Hamiltonian of initial (final) channel of reaction (114); $G(W) = [W - H]^{-1}$ is the Greens' function of the Hamiltonian H. Let us also define operator $\upsilon_\lambda = V - V_\lambda$ ($\lambda = \alpha, \beta$).
In the *prior*-formalism the transition amplitude $T^-_{\alpha\beta}$ from channel "α" to channel "β" is given by the standard form:

$$T^-_{\alpha\beta} = \lim_{W \to E + i0} \langle \Phi_\beta | \upsilon_\alpha + \upsilon_\beta G(W) \upsilon_\alpha | \Phi_\alpha \rangle \equiv \langle \Phi_\beta | U^-_{\alpha\beta} | \Phi_\alpha \rangle. \tag{116}$$

Here, $U^-_{\alpha\beta}$ is an operator responsible for the $\alpha \to \beta$ transition; $|\Phi_\alpha\rangle$ and $\langle \Phi_\beta|$ are the initial and final asymptotic states of the system that are the eigenfunctions of the operators H_α, H_β with eigenvalues $\widetilde{E}_\alpha, \widetilde{E}_\beta$; E is the total energy of the four-particle system.

In order to write the Dodd–Greider integral equation for a system of four particles, we shall represent the channel interaction $\upsilon_\lambda(\lambda = \alpha, \beta)$ as the following sum $\upsilon_\lambda = (\upsilon_\lambda - \omega_\lambda) + \omega_\lambda$. Here, $\omega_\alpha, \omega_\beta$ are the disturbing potentials in the initial and final channels of reaction (114). Corresponding to these potentials, we shall introduce the Møller wave operators:

$$\omega_\alpha^+ = 1 + (E - H_\alpha - w_\alpha + i\varepsilon)^{-1} w_\alpha = 1 + g_\alpha^+ w_\alpha, \tag{117}$$

$$\omega_\alpha^- = 1 + (E - H_\beta - w_\beta - i\varepsilon)^{-1} w_\beta = 1 + g_\beta^- w_\beta, \tag{118}$$

where ε is an infinitely small positive number. By analogy with the three-particle case, we introduce the auxiliary potential υ_x, which corresponds to an intermediate virtual channel "x" and the Greens operator $g_x^+ = (E - H + \upsilon_x + i\varepsilon)^{-1}$. Using these definitions the operator $U_{\alpha\beta}^-$ reads:

$$U_{\alpha\beta}^- = \omega_\beta^{-\dagger} \left\{ [1 + (\upsilon_\beta - w_\beta) g_x^+](\upsilon_\alpha - w_\alpha)\omega_\alpha^+ + (\upsilon_\beta - w_\beta) g_x^+ \upsilon_x G_\beta^+ U_{\alpha\beta}^- \right\}. \tag{119}$$

Up to now, Eq. (119) has been exact. Consider the approximation for the transition operator $U_{\alpha\beta}^-$, namely on the right-hand side of (119), we shall keep only the first iteration. As a result, we come to the following representation of transition amplitude $T_{\alpha\beta}^-$:

$$\begin{aligned} T_{\alpha\beta}^- &= \langle \Phi_\beta | \omega_\beta^{-\dagger} [1 + g_x^+ (\upsilon_\beta - w_\beta)](\upsilon_\alpha - w_\alpha)\omega_\alpha^+ | \Phi_\alpha \rangle \\ &= T_{\alpha\beta}^-(\mathrm{DWB}) + \langle \Phi_\beta | \omega_\beta^{-\dagger} [g_x^+ (\upsilon_\beta - w_\beta)](\upsilon_\alpha - w_\alpha)\omega_\alpha^+ | \Phi_\alpha \rangle, \end{aligned} \tag{120}$$

where $T_{\alpha\beta}^-(\mathrm{DWB}) = \langle \Phi_\beta | \omega_\beta^{-\dagger} (\upsilon_\alpha - w_\alpha)\omega_\alpha^+ | \Phi_\alpha \rangle$ is the amplitude of reaction (114) in the distorted wave Born approximation (DWB). The first term on the right-hand side of (120) corresponds to the direct electronic transition without any re-scattering, whereas the second term describes the two-step mechanism of electron capture.

Consider the system which consists of four particles with coordinates $\vec{r}_i$ and masses m_i $(i = 1, 2, 3, 4)$. The numbers $1, 2, 3, 4$ denote the particles γ_1, γ_2, α, β, correspondingly. We shall introduce two sets of coordinates $\vec{r}_\alpha, \vec{x}_k'$ and $\vec{r}_\beta, \vec{s}_k'$ $(k = 1,\ 2)$ defined by equations:

$$\vec{r}_\alpha = \vec{r}_3 - \frac{\vec{r}_1 + \vec{r}_2 + m_\beta \vec{r}_4}{m_\beta + 2}, \quad \vec{x}_k' = \vec{r}_k - \frac{m_\beta \vec{r}_4 + \sum_{i=1}^{k-1} \vec{r}_i}{m_\beta + k - 1}, \tag{121}$$

$$\vec{r}_\beta = \vec{r}_4 - \frac{\vec{r}_1 + \vec{r}_2 + m_\alpha \vec{r}_3}{m_\alpha + 2}, \quad \vec{s}_k' = \vec{r}_k - \frac{m_\alpha \vec{r}_3 + \sum_{i=1}^{k-1} \vec{r}_i}{m_\alpha + k - 1}, \tag{122}$$

where $m_{\alpha,\beta} = m_{3,4}/m$ and $m_1 = m_2 = m$. Introducing the radius-vectors $\vec{x}_k$ and $\vec{s}_k$ which determine the position of the kth electron (γ_k) relative to the nuclei β and α, respectively, the difference $\vec{x}_k - \vec{s}_k = \vec{R}$ is the distance between the nuclei α and β. In these designations the channel interactions υ_α and υ_β read:

$$\upsilon_\alpha = -\frac{Z_\alpha}{s_1} + \frac{Z_\alpha Z_\beta}{R} - \frac{Z_\alpha}{s_2}, \quad \upsilon_\beta = -\frac{Z_\beta}{x_1} + \frac{Z_\alpha Z_\beta}{R} - \frac{Z_\beta}{x_2}, \tag{123}$$

where Z_α and Z_β are the charges of nuclei α and β, respectively.

The eigenstates $|\Phi_\alpha\rangle$ $(|\Phi_\beta\rangle)$ of the Hamiltonian H_α (H_β) are the product of a wave function $\varphi_\alpha(\vec{x}_1', \vec{x}_2')$ $(\varphi_\beta(\vec{s}_1', \vec{s}_2'))$ of the bound state of system $(\beta; \gamma_1, \gamma_2)$ $((\alpha; \gamma_1, \gamma_2))$ and a plane wave of the relative motion of particles in the initial (final) state:

$$\Phi_\alpha = \varphi_\alpha(\vec{x}_1', \vec{x}_2') \exp(i\vec{k}_\alpha \cdot \vec{r}_\alpha), \quad \Phi_\beta = \varphi_\beta(\vec{s}_1', \vec{s}_2') \exp(-i\vec{k}_\beta \cdot \vec{r}_\beta), \tag{124}$$

where $\vec{k}_\alpha$ $(\vec{k}_\beta)$ are the momentum of the incident (scattered) particle in the system of a center of masses before (after) the collision.

From the formal point of view, the operator ω_α^+ (ω_α^-) may be considered as a transition operator from the initial (final) asymptotic state $|\Phi_\alpha\rangle$ $(|\Phi_\beta\rangle)$ into the distorted wave $|\chi_\alpha^+\rangle$ $(|\chi_\beta^-\rangle)$ in entrance (exit) reaction channel:

$$|\chi_\alpha^+\rangle = \omega_\alpha^+ |\Phi_\alpha\rangle, \tag{125}$$

$$|\chi_\beta^-\rangle = \omega_\beta^- |\Phi_\beta\rangle. \tag{126}$$

Note that one can consider $U_\alpha = \upsilon_\alpha - w_\alpha$ as the operator responsible for the transition from state (α) into state (β).

We introduce the state vector $|\Psi_\beta^-\rangle$ by the definition:

$$|\Psi_\beta^-\rangle = \left[1 + g_x^{+\dagger}(\upsilon_\beta - w_\beta)\right] |\chi_\beta^- . \tag{127}$$

In designations (125)-(127), transition amplitude (120) can be represented as follows:

$$T_{\alpha\beta}^- = \langle \Psi_\beta^- | U_\alpha | \chi_\alpha^+ \rangle. \tag{128}$$

In order to obtain the explicit differential equations for calculation of the distortion in the initial and final channels, we shall apply operator

$(E - H_\alpha - w_\alpha)$ to both parts of Eq. (125). Taking the limit $\varepsilon \to 0^+$, we come to the following expression for the distorted wave in the exit channel:

$$(E - H_\alpha - w_\alpha)|\chi_\alpha^+\rangle = (E - H_\alpha)|\Phi_\alpha\rangle = 0, \quad E = E_\alpha + k_\alpha^2/2\mu_\alpha. \tag{129}$$

On the basis of Eq. (126), one obtains a similar expression for the distorted wave in the exit channel:

$$(E - H_\beta - w_\beta)|\chi_\beta^-\rangle = (E - H_\beta)|\Phi_\beta\rangle = 0, \quad E = E_\beta + k_\beta^2/2\mu_\beta. \tag{130}$$

Here, E_α and E_β are the bound energies of compound particles $(\beta; \gamma_1, \gamma_2)$ and $(\alpha; \gamma_1, \gamma_2)$, where $\mu_\alpha = m_\alpha(2 + m_\beta)/M$ and $\mu_\beta = m_\beta(2 + m_\alpha)/M$ are the reduced masses of the corresponding compound and $M = m_\alpha + m_\beta + 2$ is the total mass of the system.

Further calculations are based on the special requirements concerning the choice of function χ_β^- which, essentially, make the problem considered here explicitly solvable. Assume that solution χ_β^- is represented in the following factorized form:

$$|\chi_\beta^-\rangle = |\varphi_\beta(\vec{s}_1', \vec{s}_2') f(\vec{r}_\beta)\rangle, \tag{131}$$

where $f(\vec{r}_\beta)$ is the function which describes the asymptotic motion of a compound $(\alpha; \gamma_1, \gamma_2)$ in a Coulomb field of particle β. We note that assumption (131) is only applicable if the relative motion of heavy particles is larger than the effective orbital velocity of a bound electron.

The differential equation (130) must be supplemented with the boundary condition, which in this case has the following form:

$$\chi_\beta^- \xrightarrow[r_\beta \to \infty]{} \varphi_\beta(\vec{s}_1', \vec{s}_2') \exp\left\{-i\vec{k}_\beta \cdot \vec{r}_\beta - \frac{iZ_\beta(Z_\alpha - 2)}{\upsilon'} \ln(k_\beta r_\beta - \vec{k}_\beta \cdot \vec{r}_\beta)\right\}, \tag{132}$$

where $\vec{\upsilon}' = \vec{k}_\beta/k_\beta$. The fulfilment of the condition on the function χ_β^- can be achieved by the corresponding choice of distortion potential w_β in Eq. (130). For instance, w_β may be defined as $w_\beta = Z_\beta(Z_\alpha - 2)/r_\beta$, and then the function $f(\vec{r}_\beta)$ can be represented through the confluent hypergeometric function. However, we omit explicit representation of $f(\vec{r}_\beta)$ since it is not necessary for our purpose.

Let us now construct the differential form of Eq. (127). Applying the operator $(E - H + \upsilon_x^\dagger)$ to both sides of (127) and taking into account (130) we obtain (in the limit $\varepsilon \to 0^+$):

$$(E - H + \upsilon_x^\dagger)|\Psi_\beta^-\rangle = \upsilon_x^\dagger|\chi_\beta^-\rangle. \tag{133}$$

The solution of Eq. (133) for realistic potential υ_x is an extremely complicated task. Hence, it is reasonable to substitute this potential by an operator chosen in such a way that the following condition is satisfied:

$$\upsilon_x^\dagger|\chi_\beta^-\rangle = 0. \tag{134}$$

Similarly to expression (131)) the solution to (133) is represented as:

$$|\Psi_\beta^-\rangle = |\varphi_\beta(\vec{s}_1', \vec{s}_2')\mathcal{Y}^-\rangle, \tag{135}$$

where the unknown function $\mathcal{Y}^-$ describes the distortion of the wave function $\varphi_\beta(\vec{s}_1', \vec{s}_2')$ of the bound state of system $(\alpha; \gamma_1, \gamma_2)$ induced by the interaction with nucleus β in the exit channel.

By virtue of condition (134), Eq. (133) reduces to a homogeneous one:

$$\left[E - H_0 + \sum_{k=1}^{2}\left(\frac{Z_\beta}{x_k} + \frac{Z_\alpha}{s_k}\right) - \frac{Z_\alpha Z_\beta}{R} - \frac{1}{|\vec{s}_1 - \vec{s}_2|} + \upsilon_x^\dagger\right]|\Psi_\beta^-\rangle = 0. \tag{136}$$

Using the above-defined two sets of relative variables, one can represent the Hamiltonian H_0 in two equivalent forms:

$$H_0 = -\frac{\triangle_{\vec{r}_\alpha}}{2\mu_\alpha} - \sum_{k=1}^{2}\frac{\triangle_{\vec{x}_k'}}{2\mu_{\beta k}} = -\frac{\triangle_{\vec{r}_\beta}}{2\mu_\beta} - \sum_{k=1}^{2}\frac{\triangle_{\vec{s}_k'}}{2\mu_{\alpha k}}, \tag{137}$$

where

$$\mu_{\beta k} = (m_\beta + k - 1)/(m_\beta + k), \quad \mu_{\alpha k} = (m_\alpha + k - 1)/(m_\alpha + k).$$

The interaction potentials in H_0 depend on different combinations of relative variables. This circumstance leads to severe complications when solving Eq. (136). In order to avoid this difficulty, consider the approximate variable separation in Eq. (136) based on the natural approximation that the masses of particles γ_1, γ_2 (electrons) are much smaller than the masses of the two other particles α and β (atomic nuclei), i.e., $m_1 = m_2 \ll m_{3,4}$. Therefore, one can neglect the terms that contain the ratio $m_k/m_{3,4}$

($k = 1,\ 2$) in expressions (121) and (122). As a result we come to the following approximate relations:

$$\vec{x}'_k \simeq \vec{x}_k, \quad \vec{s}'_k \simeq \vec{s}_k, \quad \vec{r}_\alpha \simeq \vec{R}, \quad \vec{r}_\beta \simeq -\vec{R}. \tag{138}$$

By substituting expression (135) for the wave function $|\Psi_\beta^-\rangle$ into Eq. (136) and taking into account (130) and (138), one obtains the equation for $\mathcal{Y}^-$:

$$\varphi_\beta(E - E_\beta - H_0 - \upsilon_\beta)\mathcal{Y}^- + \sum_{k=1,2} \mu_{\alpha k}^{-1} \vec{\nabla}_{\vec{s}'_k}\varphi_\beta \cdot \vec{\nabla}_{\vec{s}'_k}\mathcal{Y}^- + \upsilon_x^\dagger(\varphi_\beta \mathcal{Y}^-) = 0. \tag{139}$$

As an operator υ_x we chose a potential whose action on the arbitrary function $\Psi(\vec{r}_\beta, \vec{s}'_1, \vec{s}'_2)$ is defined as follows:

$$\upsilon_x \Psi = -\sum_{k=1,2} \mu_{\alpha k}^{-1} \vec{\nabla}_{\vec{s}'_k}\varphi_\beta \cdot \vec{\nabla}_{\vec{s}'_k}(\Psi/\varphi_\beta). \tag{140}$$

By substituting (140) into Eq. (139) and taking into account (138), we obtain the equation for $\mathcal{Y}^-$:

$$\left[E - E_\beta + \frac{\triangle_{\vec{r}_\alpha}}{2\mu_\alpha} + \sum_{k=1,2}\left(\frac{\triangle_{\vec{x}'_k}}{2\mu_{\beta k}} + \frac{Z_\beta}{x'_k}\right) - \frac{Z_\alpha Z_\beta}{r_\alpha}\right]\mathcal{Y}^- = 0. \tag{141}$$

The solution to Eq. (141) should behave at infinity as a distorted plane wave:

$$\mathcal{Y}^- \xrightarrow[r_\beta \to \infty]{} f(\vec{r}_\beta) \xrightarrow[r_\beta \to \infty]{} \exp\left\{-i\vec{k}_\beta \cdot \vec{r}_\beta - \frac{iZ_\beta(Z_\alpha - 2)}{\upsilon'}\ln(k_\beta r_\beta - \vec{k}_\beta \cdot \vec{r}_\beta)\right\}. \tag{142}$$

Solving Eq. (141) by the method of variable separations, we obtain the following solution, as in Ref. 48:

$$\mathcal{Y}^- = C^{(-)}\mathcal{F}^{(-)}(\vec{r}_\alpha)\prod_{k=1}^{2}\mathcal{F}_k^{(-)}(\vec{x}'_k), \quad C^{(-)} = \text{const}, \tag{143}$$

where the two-particle Coulomb distorting functions and $\mathcal{F}_k^{(-)}(\vec{x}'_k)$ ($\mathcal{F}^{(-)}(\vec{r}_\alpha)$) are given by:

$$\mathcal{F}_k^{(-)}(\vec{x}'_k) = N^{(+)}(\nu'_{\beta k})\exp(i\vec{q}_k \cdot \vec{x}'_k)\,{}_1F_1(-i\nu'_{\beta k}, 1, -iq_k\xi_k), \tag{144}$$

$$\mathcal{F}^{(-)}(\vec{r}_\alpha) = N^{(-)}(\nu'_\alpha)\exp(i\vec{q}_\alpha\cdot\vec{r}_\alpha)\,{}_1F_1(i\nu'_\alpha, 1, -iq_\alpha\xi_\alpha), \tag{145}$$

where $N^{(\pm)}(\nu) = \Gamma(1 \pm i\nu)\exp(\pm\pi\nu/2)$ are the normalization coefficients, $\xi_k = x'_k + \hat{\vec{q}}_k\cdot\vec{x}'_k$, $\xi_\alpha = r_\alpha + \hat{\vec{q}}_\alpha\cdot\vec{r}_\alpha$ are the two-particle parabolic variables, $\hat{\vec{q}}_k$ and $\hat{\vec{q}}_\alpha$ are the unit vectors directed along the vectors $\vec{q}_k$ and $\vec{q}_\alpha$, $\nu'_{\beta k} = Z_\beta\mu_{\beta k}/q_k$ and $\nu'_\alpha = Z_\alpha Z_\beta\mu_\alpha/q_\alpha$ are the Sommerfeld parameters. Energy conservation implies the following relation between $\vec{q}_\alpha$ and $\vec{q}_k$:

$$E - E_\beta = \frac{k_\beta^2}{2\mu_\beta} = \frac{q_\alpha^2}{2\mu_\alpha} + \sum_{k=1,2}\frac{q_k^2}{2\mu_{\beta k}}. \tag{146}$$

Matching the asymptotic forms of function (143) and their eikonal expressions (142) leads to:

$$\sum_{k=1,2}\vec{q}_k\cdot\vec{x}'_k + \vec{q}_\alpha\cdot\vec{r}_\alpha = -\vec{k}_\beta\cdot\vec{r}_\beta. \tag{147}$$

The coordinates $\vec{r}_\alpha, \vec{r}_\beta, \vec{x}'_1$, and $\vec{x}'_2$ are related by:

$$\vec{r}_\beta = -a_2\vec{r}_\alpha - \sum_{k=1,2}\mu_\beta^{-1}b_k\vec{x}'_k, \quad a_k = \frac{m_\alpha}{(m_\alpha + k)}, \quad b_k = \frac{m_\beta}{(m_\beta + k)}. \tag{148}$$

Substituting now (148) into the right-hand side of (147) and taking into account the asymptotic limits:

$$\vec{q}_\alpha = a_2\vec{k}_\beta \xrightarrow[m_\alpha\to\infty]{} \vec{k}_\beta, \quad \vec{q}_k = b_k\mu_\beta^{-1}\vec{k}_\beta \xrightarrow[m_\beta\to\infty]{} \vec{v}' \qquad (k = 1, 2), \tag{149}$$

$$-\frac{iZ_\beta}{v'}\ln\left(\frac{k_\beta r_\beta - \vec{k}_\beta\cdot\vec{r}_\beta}{v'x'_k + \vec{v}'\cdot\vec{x}'_k}\right) \xrightarrow[r_\beta\to\infty]{} \ln\left(\mu_\beta^{-iZ_\beta/v'}\right) \qquad (k = 1, 2), \tag{150}$$

one obtains that $C^{(-)} = \mu_\beta^{-2iZ_\beta/v'}$. From Eqs. (143)–(145) and (149), the distorted wave distortion function $\mathcal{Y}^{(-)}$ in the exit channel can be represented as:[48]

$$\begin{aligned}\mathcal{Y}^- = {} & \mu_\beta^{2i\nu'_\beta}N^{(-)}(\nu')[N^{(+)}(\nu'_\beta)]^2\exp(-i\vec{k}_\beta\cdot\vec{r}_\beta) \\ & \times {}_1F_1(i\nu', 1, -ik_\beta r_\alpha - i\vec{k}_\beta\cdot\vec{r}_\alpha)\prod_{k=1}^{2}{}_1F_1(-i\nu'_\beta, 1, -iv'x'_k - i\vec{v}'\cdot\vec{x}'_k),\end{aligned} \tag{151}$$

where $\nu'_\beta = Z_\beta/\upsilon', \nu' = Z_\alpha Z_\beta/\upsilon'$. Hence, we constructed the wave function Ψ^-_β (defined by Eqs. (135) and (151)) that describes the scattering of charged particle β on a bound compound of three particles $\alpha, \gamma_1, \gamma_2$.

The wave function of the initial state χ^+_α can be constructed in a similar manner:

$$\chi^+_\alpha = \varphi_\alpha(\vec{x}'_1, \vec{x}'_2)\mathcal{Y}^+, \tag{152}$$

where $\mathcal{Y}^+$ satisfies the following differential equation:

$$\left[E - E_\alpha + \frac{\triangle_{\vec{r}_\beta}}{2\mu_\beta} + \sum_{k=1,2}\left(\frac{\triangle_{\vec{s}'_k}}{2\mu_{\alpha k}} + \frac{Z_\alpha}{s'_k}\right) - \frac{Z_\alpha Z_\beta}{r_\beta}\right]\mathcal{Y}^+ = 0. \tag{153}$$

The solution of Eq. (153) can be constructed by comparison of its asymptotic with the corresponding eikonal approximation. We omit the cumbersome derivation (which was explained for the $\mathcal{Y}^-$ construction) and represent only the final result (in the limit $m_{3,4} \gg m_1 = m_2$):

$$\begin{aligned}\mathcal{Y}^+ = {} & \mu_\alpha^{-2i\nu_\alpha} N^{(-)*}(\nu)[N^{(+)*}(\nu_\alpha)]^2 \exp(i\vec{k}_\alpha \cdot \vec{r}_\alpha) \\ & \times {}_1F_1(-i\nu, 1, ik_\alpha r_\beta + i\vec{k}_\alpha \cdot \vec{r}_\beta) \prod_{k=1}^{2} {}_1F_1(i\nu_\alpha, 1, i\upsilon s'_k + i\vec{\upsilon} \cdot \vec{s}'_k),\end{aligned} \tag{154}$$

where $\nu_{\alpha,\beta} = Z_{\alpha,\beta}/\upsilon, \nu = Z_\alpha Z_\beta/\upsilon$.

Substituting now expressions (135), (151), (152), and (154) into (128), one can obtain the reaction amplitude $T^-_{\alpha\beta}$ which describes the simultaneous capture of two electrons by fast ions in collisions with atoms:[48]

$$\begin{aligned}T^-_{\alpha\beta} = {} & -\left[N^{(+)*}(\nu_\alpha)N^{(+)*}(\nu'_\beta)\right]^2 \iiint d\vec{x}'_1\, d\vec{x}'_2\, d\vec{r}_\alpha \exp(i\vec{k}_\alpha \cdot \vec{r}_\alpha + i\vec{k}_\beta \cdot \vec{r}_\beta) \\ & \times \mathcal{Z}(\vec{r}_\alpha, \vec{r}_\beta)\varphi^*_\beta(\vec{s}'_1, \vec{s}'_2) \prod_{j=1}^{2} {}_1F_1(i\nu'_\beta, 1, i\upsilon' x'_j + i\vec{\upsilon}' \cdot \vec{x}'_j) \sum_{k=1,2} \vec{\nabla}_{\vec{x}'_k}\varphi_\alpha(\vec{x}'_1, \vec{x}'_2) \\ & \cdot \vec{\nabla}_{\vec{s}'_k}[{}_1F_1(i\nu_\alpha, 1, i\upsilon s'_1 + i\vec{\upsilon} \cdot \vec{s}'_1)\, {}_1F_1(i\nu_\alpha, 1, i\upsilon s'_2 + i\vec{\upsilon} \cdot \vec{s}'_2)],\end{aligned} \tag{155}$$

where

$$\begin{aligned}\mathcal{Z}(\vec{r}_\alpha, \vec{r}_\beta) = {} & \mu_\alpha^{-2i\nu_\alpha} \mu_\beta^{-2i\nu_\beta} N^{(-)*}(\nu) N^{(-)*}(\nu') \\ & \times {}_1F_1(-i\nu, 1, ik_\alpha r_\beta + i\vec{k}_\alpha \cdot \vec{r}_\beta)\, {}_1F_1(-i\nu', 1, ik_\beta r_\alpha + i\vec{k}_\beta \cdot \vec{r}_\alpha).\end{aligned} \tag{156}$$

In the case of fast collisions ($k_\alpha^2/2\mu_\alpha > |E_\beta - E_\alpha|$) when forward scattering is dominant, the expression (156) can be simplified. At small scattering angles (i.e., $\hat{\vec{k}}_\alpha \simeq \hat{\vec{k}}_\beta$) we can assume that nuclear motion occurs with a constant velocity and the trajectories are close to linear. Hence, the vector $\vec{R}$ is represented as the orthogonal sum $\vec{R} = \vec{\rho} + \vec{z}, \vec{\rho} \cdot \vec{z} = 0$. Taking into account that $\vec{\upsilon}\,' \simeq \vec{\upsilon}$ and $m_1 = m_2 = m \ll m_3 \sim m_4$, one obtains immediately:

$$\vec{k}_\alpha \cdot \vec{r}_\alpha + \vec{k}_\beta \cdot \vec{r}_\beta \simeq \vec{p} \cdot (\vec{x}_1 + \vec{x}_2) + \vec{q} \cdot (\vec{s}_1 + \vec{s}_2), \tag{157}$$

where

$$-2\vec{p} = \vec{\upsilon} + \left(\upsilon - \frac{E_\beta - E_\alpha}{\upsilon}\right)\hat{\vec{\upsilon}}, \quad 2\vec{q} = \vec{\upsilon} - \left(\upsilon - \frac{E_\beta - E_\alpha}{\upsilon}\right)\hat{\vec{\upsilon}}, \quad \hat{\vec{\upsilon}} = \frac{\vec{\upsilon}}{\upsilon}, \tag{158}$$

where $\vec{\eta}$ is orthogonal to the $\vec{\upsilon}$ component of the transmitted momentum ($\vec{\eta}\cdot\vec{\upsilon} = \vec{\eta}\cdot\vec{z} = \vec{\rho}\cdot\vec{z} = 0$). Using the asymptotic form[3] for the function $\mathcal{Z}(\vec{r}_\alpha, \vec{r}_\beta)$, the amplitude $T_{\alpha\beta}^{-}$ for scattering at small angles reads:

$$T_{\alpha\beta}^{-} = -[N^{(+)*}(\nu_\alpha)N^{(+)*}(\nu_\beta)]^2 \sum_{k=1,2} I_{\alpha\beta}^{(k)}, \tag{159}$$

where $T_{\alpha\beta}^{-}$ is given by the following expression[48]:

$$\begin{aligned} T_{\alpha\beta}^{-} = \iiint & \mathrm{d}\vec{x}_1\, \mathrm{d}\vec{x}_2\, \mathrm{d}\vec{s}_1 \exp\left[i\vec{p} \cdot (\vec{x}_1 + \vec{x}_2) + i\vec{q} \cdot (\vec{s}_1 + \vec{s}_2)\right] \varphi_\beta^{(*)}(\vec{s}_1, \vec{s}_2) \\ & \times \prod_{j=1}^{2} {}_1F_1(i\nu_\beta, 1, i\upsilon x_j + i\vec{\upsilon} \cdot \vec{x}_j)\vec{\nabla}_{\vec{x}_k}\varphi_\alpha(\vec{x}_1, \vec{x}_2) \\ & \cdot \vec{\nabla}_{\vec{s}_k}[{}_1F_1(i\nu_\alpha, 1, i\upsilon s_1 + i\vec{\upsilon} \cdot \vec{s}_1)\,{}_1\mathrm{F}_1(i\nu_\alpha, 1, i\upsilon s_2 + i\vec{\upsilon} \cdot \vec{s}_2)]. \end{aligned} \tag{160}$$

As an example, consider charge transfer in collision of helium atom with nuclei. The initial and final states are the s^2-states:

$$\varphi_\alpha(\vec{x}_1, \vec{x}_2) = \varphi_\alpha(\vec{x}_1)\varphi_\alpha(\vec{x}_2), \quad \varphi_\beta(\vec{s}_1, \vec{s}_2) = \varphi_\beta(\vec{s}_1)\varphi_\beta(\vec{s}_2), \tag{161}$$

where $\varphi_\alpha(\vec{x}_k)$ and $\varphi_\beta(\vec{s}_k)$ are the hydrogen-like wave functions with effective charges Z_α and Z_β:

$$\varphi_\alpha(\vec{x}_k) = (\alpha^3/\pi)^{1/2} \exp(-\alpha x_k), \quad \varphi_\beta(\vec{s}_k) = (\beta^3/\pi)^{1/2} \exp(-\beta s_k).$$

We shall proceed to calculation of a matrix element (160). Consider the first term $I^{(1)}_{\alpha\beta}$ which we shall write in the momentum representation:

$$I^{(1)}_{\alpha\beta} = (2\pi)^{-3}\int d\vec{\tau}\,\vec{R}^{(1)}_{\beta}(\vec{q}-\vec{\tau})\vec{R}^{(1)}_{\alpha}(\vec{p}+\vec{\tau})R^{(2)}_{\beta}(\vec{q}+\vec{\tau})R^{(2)}_{\alpha}(\vec{p}-\vec{\tau}), \tag{162}$$

where the following designations are introduced:

$$\vec{R}^{(j)}_{\beta}(\vec{k}) = \int d\vec{s}_j \exp(i\vec{k}\cdot\vec{s}_j)\varphi^{*}_{\beta}(\vec{s}_j)\vec{\nabla}_{\vec{s}_j}\,{}_1F_1(i\nu_\alpha, 1, i\upsilon s_j + i\vec{\upsilon}\cdot\vec{s}_j), \tag{163}$$

$$\vec{R}^{(j)}_{\alpha}(\vec{k}) = \int d\vec{x}_j \exp(i\vec{k}\cdot\vec{x}_j)\,{}_1F_1(i\nu_\beta, 1, i\upsilon x_j + i\vec{\upsilon}\cdot\vec{x}_j)\left[\vec{\nabla}_{\vec{x}_j}\varphi_\alpha(\vec{x}_j)\right], \tag{164}$$

$$R^{(j)}_{\beta}(\vec{k}) = \int d\vec{s}_j \exp(i\vec{k}\cdot\vec{s}_j)\varphi^{*}_{\beta}(\vec{s}_j)\,{}_1F_1(i\nu_\alpha, 1, i\upsilon s_j + i\vec{\upsilon}\cdot\vec{s}_j), \tag{165}$$

$$R^{(j)}_{\alpha}(\vec{k}) = \int d\vec{x}_j \exp(i\vec{k}\cdot\vec{x}_j)\,{}_1F_1(i\nu_\beta, 1, i\upsilon x_j + i\vec{\upsilon}\cdot\vec{x}_j). \tag{166}$$

The exact numerical integration over $\vec{\tau}$ in $I^{(k)}_{\alpha\beta}\,(k = 1, 2)$ needed in (159) has been carried out in Refs. 5, 6, 48–51. For a rough estimate at high energies, a peaking approximation of the quadrature from (162) might be made as follows. The expression under the integral (162) is localized in the following four regions of momentum $\vec{\tau}$ subspace:

$$|\vec{q}-\vec{\tau}| \leqslant 1/a, \quad |\vec{p}+\vec{\tau}| \leqslant 1/a, \quad |\vec{q}+\vec{\tau}| \leqslant 1/a, \quad |\vec{p}-\vec{\tau}| \leqslant 1/a, \tag{167}$$

where a is the effective radius of a pairwise interaction. Since $\vec{R}^{(1)}_{\alpha}(\vec{\tau})$ and $\vec{R}^{(1)}_{\beta}(\vec{\tau})$ decrease faster than $\vec{R}^{(2)}_{\alpha}(\vec{\tau})$ and $\vec{R}^{(2)}_{\beta}(\vec{\tau})$, the contribution to the integral (162) from the third and fourth region from (167) is negligible. In addition, the slowly varying function $\vec{R}^{(1)}_{\beta}(\vec{q}-\vec{\tau})\vec{R}^{(1)}_{\alpha}(\vec{p}+\vec{\tau}) \equiv R_{\alpha\beta}(\vec{\tau})$ can be taken outside the integral sign in (162). Applying the convolution theorem and using the Nordsieck integral technique[33], we obtain:

$$I^{(1)}_{\alpha\beta} = -N_\alpha N_\beta(1/2)\left[\vec{R}^{(1)}_{\beta}(\vec{q}-\vec{p})\vec{R}^{(1)}_{\alpha}(2\vec{p}) + \vec{R}^{(1)}_{\beta}(2\vec{q})\vec{R}^{(1)}_{\alpha}(\vec{p}-\vec{q})\right]$$
$$\times\frac{\partial}{\partial\alpha}J(\alpha+\beta, \vec{p}+\vec{q}, \nu_\alpha, \nu_\beta, \vec{\upsilon}, \vec{\upsilon}), \tag{168}$$

where the following designations have been used:

$$\begin{aligned} J(\lambda,\vec{k},\nu_1,\nu_2,\vec{v}_1,\vec{v}_2) &= \int \mathrm{d}\vec{x}\, x^{-1} e^{-\lambda x+i\vec{k}\cdot\vec{x}}\,{}_1F_1(i\nu_1,1,iv_1x+i\vec{v}_1\cdot\vec{x}) \\ &\times {}_1F_1(i\nu_2,1,iv_2x+i\vec{v}_2\cdot\vec{x}) = \frac{4\pi}{(k^2+\lambda^2)}\left[1+\frac{2(\vec{k}\cdot\vec{v}_1-i\lambda v_1)}{(k^2+\lambda^2)}\right]^{-i\nu_1} \\ &\times[1+2(\vec{k}\cdot\vec{v}_2-i\lambda v_2)/(k^2+\lambda^2)]^{-i\nu_2}\,{}_2F_1(i\nu_1,i\nu_2;1,\omega), \end{aligned} \tag{169}$$

$$\omega = \frac{4(\vec{k}\cdot\vec{v}_1-i\lambda v_1)(\vec{k}\cdot\vec{v}_2-i\lambda v_2)-2(k^2+\lambda^2)(\vec{v}_1\cdot\vec{v}_2-v_1v_2)}{[k^2+\lambda^2+2(\vec{k}\cdot\vec{v}_1-i\lambda v_1)][k^2+\lambda^2+2(\vec{k}\cdot\vec{v}_2-i\lambda v_2)]},$$

with $N_\gamma = (\gamma^3/\pi)^{1/2}$ and $\gamma = \alpha,\beta$. The interpretation of Eqs. (168) and (169) is as follows. The matrix element $R_\alpha^{(1)}$ and $R_\beta^{(1)}$ describe the two-step (Thomas) mechanism of capture of electron r_1 through the continuum from target atom $(\beta;\gamma_1,\gamma_2)$ in the states bounded with the projectile (α). The factor $\partial J/\partial\alpha$, which corresponds to the integration in $I_{\alpha\beta}^{(1)}$ over the coordinates of second electron (γ_2), is reduced to the overlap integral. In a similar way one can construct the expression for $I_{\alpha\beta}^{(2)}$ which is omitted here for the sake of brevity.

In detailed applications to double electron capture[5, 6, 48-51] in collisions of fast ions (protons, alpha particles, lithium nuclei) with helium, the CDW method was found to be in good agreement with measurements. Reasonably successful description of double charge exchange has also been accomplished by the CB1,[45] BCIS[46] and BDW (Born distorted wave)[47] approximations, albeit in certain restricted intervals of impact energies.

In the present exposition only one mechanism of reaction (113) for the simultaneous capture of two electrons is taken into account. The other mechanisms, such as sequential one-electron capture may also contribute to the cross section of (113). The electronic correlation has been neglected in the present formalism. Obviously, simultaneous account of different mechanisms and effects should improve the theoretical picture of this rather complicated process of two-electron capture in atomic collisions.

7. CONCLUSION

In the present work, the three-body Dodd–Greider integral equations have been reviewed by focusing on the correct Coulomb asymptotic forms of the wave functions for the problem of rearrangement scattering. Specifically, distorted wave theories for one-electron capture reactions in energetic collisions of hydrogen-like atoms with positive ions are recapitulated.

In particular, a reaction amplitude is highlighted as a first iteration term of the solution of the Dodd–Greider equations for the three-body scattering operator. It is emphasized that to reproduce the Thomas peak in the angular distribution of the reaction products, it is necessary to account for the effects of Coulomb re-scattering of the captured electron. In approximation of the "single-step" collision, this method reduces to the version of the well-known boundary-corrected first Born approximation, where the asymptotic behavior of the particles in the entrance and exit reaction channels is described by two-body Coulomb wave functions. The short-range interaction due to incomplete screening of the nucleus by atomic electrons is taken into account in the perturbing potential.

On the basis of the Dodd–Greider integral equations for a quantum mechanical operator of a four-particle rearrangement scattering, we have reviewed a version of the continuum distorted wave method to describe two-electron capture in energetic ion-atomic collisions. An important feature of this method is a consistent preservation of the proper asymptotic limits of the wave functions of a colliding system in the entrance and exit reaction channels that takes into account the long-range nature of the Coulomb interactions. The reaction amplitude can be calculated in approximation of simultaneous two-electron transitions. The corresponding results from the literature have been discussed for two-electron capture in energetic $\mathrm{H}^+ + \mathrm{He}$ and $\mathrm{He}^{2+} + \mathrm{He}$ collisions. The related theoretical cross sections are in good agreement with the experimental data in the region of high impact energies. Further development of this method is foreseen by accounting for sequential mechanisms of two-electron transitions and including electronic correlations in the wave functions of the initial and final states. Such corrections are expected to improve the agreement between theory and experiment at lower collision energies.

REFERENCES

1. Belkić, Dž. *Principles of Quantum Scattering Theory*; Taylor & Francis: London, 2003.
2. Fritsch, W.; Lin, C. D. The semiclassical close-coupling description of atomic collisions: Recent developments and results. *Phys. Rep.* **1991**, *202*, 1.
3. Belkić, Dž.; Gayet, R.; Salin, A. Electron capture in high-energy ion-atom collisions. *Phys. Rep.* **1979**, *56*, 279.Belkić, Dž. Leading distorted wave theories and computational methods for fast ion-atom collisions. *J. Comput. Meth. Sci. Eng.* **2001**, *1*, 1.
4. Salin, A. Comments on 'Strong potential Born expansions for ion-atom collisions'. *Comments At. Mol. Phys.* **1991**, *26*, 1.Salin, A. Some remarks on theory of high energy electron capture in ion-atom collision. *J. Phys. B* **1992**, *25*, L137.Mapleton, R. Asymptotic form of the electron capture cross section in the second Born approximation. *Proc. Phys. Soc.* **1968**, *91*, 868.Dewangan, D. P.; Eichler, J. Boundary conditions and the strong potential Born approximation for electron capture. *J. Phys. B*

1985, *91*, L65.Macek, J. H. Treatment of divergent terms in the strong potential Born approximation. *J. Phys. B* **1985**, *18*, L71.McGuire, J. H. Non-orthogonality in the strong potential Born approximation. *J. Phys. B* **1985**, *18*, L75.

5. Belkič, Dž. *Quantum Theory of High-Energy Ion-Atom Collisions*; Taylor & Francis: London, 2008.
6. Belkić, Dž.; Mančev, I.; Hanssen, J. Four-body methods for high-energy ion-atom collisions. *Rev. Mod. Phys.* **2008**, *80*, 249.
7. Macek, J.; Alston, S. Theory of electron capture from a hydrogenlike ion by a bare ion. *Phys. Rev. A* **1982**, *26*, 250.
8. Belkić, Dž.; Saini, S.; Taylor, H. S. Electron capture by protons from the K-shell of H and Ar. *Z. Phys. D* **1986**, *3*, 59.
9. Belkić, Dž.; Saini, S.; Taylor, H. S. A critical test of first-order theories for electron transfer in collisions between multi-charged ions and atomic hydrogen. *Phys. Rev. A* **1987**, *36*, 1601.
10. Belkić, Dž.; Taylor, H. S. First-order theory for charge exchange with correct boundary conditions: general results for hydrogen-like and multi-electron targets. *Phys. Rev. A* **1987**, *35*, 1991.Belkić, Dž. Electron capture by fast protons from helium, nitrogen and oxygen: the corrected first Born approximation. *Phys. Rev. A* **1988**, *37*, 55.
11. Merkuriev, S. P. On the three-body Coulomb scattering problem. *Ann. Phys.* **1980**, *130*, 395.
12. Mekuriev, S. P.; Faddeev, L. D. *Quantum Scattering Theory for Several Particle Problems*; Kluwer Academic Publishing: Dortrecht, 1993.
13. Oppenheimer, J. R. On the quantum theory of the capture of electrons. *Phys. Rev.* **1928**, *31*, 349.Brinkman, H. C.; Kramers, H. A. Zur Theorie der Eifangung von Elektronen durch α–Teilchen. *Proc. Acad. Sci. Amsterdam* **1930**, *33*, 973.
14. Jackson, J. D.; Schiff, H. Electron capture by protons passing through hydrogen. *Phys. Rev.* **1953**, *89*, 359.Schiff, H. Electron capture cross sections. *Canad. J. Phys.* **1954**, *32*, 393.Jackson, J. D. On the use of the complete interaction Hamiltonian in atomic rearrangement collisions. *Proc. Phys. Soc. A* **1957**, *70*, 26.
15. Macek, J. H.; Shakeshaft, R. Second Born approximation with the Coulomb Green's function: electron capture from hydrogen-like ion by a bare ion. *Phys. Rev. A* **1980**, *22*, 1441.
16. Shakeshaft, R. Inner shell electron capture by a swift bare ion: second Born effects. *Phys. Rev. Lett.* **1980**, *44*, 442.
17. Brodskii, A. M.; Potapov, V. S.; Tolmachev, V. V. Asymptotic behaviour of the cross section for charge exchange. *Sov. Phys. JETP* **1970**, *31*, 144. [*Zh. Eksper. Teor. Fiz.* **1970,** *58 264*].
18. Faddeev, L. D. Scattering theory for a system of three particles. *Sov. Phys. JETP* **1961**, *12*, 1011 [*Eh. Eksper. Teor. Fiz.* **1960**, *39* 1459]; Faddeev, L. D. *Mathematical Aspects of the Three-Body Problem in the Quantum Scattering Theory*; Israel Program of Scientific Translations: Jerusalem, 1965.
19. Bates, D. R.; Dalgarno, A. Electron capture – I: resonance capture from hydrogen atoms by fast protons. *Proc. Phys. Soc. A* **1952**, *65*, 919.Bates, D. R.; Dalgarno, A. Electron capture – III: capture into excited states in encounters between hydrogen atoms and fast protons. *Proc. Phys. Soc. A* **1953**, *66*, 972.
20. Band, Y. Differential cross sections for electron capture in high energy proton-atom collisions. *Phys. Rev. Lett.* **1976**, *37*, 634.
21. Halpern, A.; Low, J. Full first Born approximation for inner-shell pickup in heavy-ion collisions. *Phys. Rev. A* **1975**, *12*, 776.
22. Bates, D. Electron capture in fast collisions. *Proc. Roy. Soc. A* **1958**, *274*, 294.
23. Lin, L.; Soong, S.; Tunnel, L. Two-state atomic expansion methods for electron capture from multielectron atoms by fast protons. *Phys. Rev. A* **1978**, *17*, 1616.

24. Omidvar, K.; Golden, J.; McGuire, J.; Weaver, L. Single-electron Born approximation for charge transfer from multielectron atom to protons. *Phys. Rev. A* **1976**, *13*, 500 [*Erratum: Phys. Rev A* **1976**, *13*, 1604].
25. Halpern, A. Inner-shell charge transfer in a distorted-wave eikonal approximation using the asymptotic interaction. *Phys. Rev. A* **1977**, *15*, 619.
26. Lin, C.; Soong, S. Differential cross section for electron capture in fast proton–multielectron atom collisions. *Phys. Rev. A* **1978**, *17*, 499.
27. Greider, K. R.; Dodd, L. R. Divergence of the distorted-wave Born series for rearrangement scattering. *Phys. Rev.* **1966**, *146*, 671.
28. Dodd, L. R.; Greider, K. R. Rigorous solution of three-body scattering process in the distorted-waves formalism. *Phys. Rev.* **1966**, *146*, 675.
29. Aaron, R.; Amado, R. D.; Lee, B. W. Divergency of the Green's function series for rearrangements collisions. *Phys. Rev.* **1961**, *121*, 319.
30. Goldberger, M. L.; Watson, K. M. *Collision Theory*; John Wiley & Sons: New York, 1964.
31. Lendyel, V. I.; Lazur, V. Yu.; Karbovanets, M. I.; Janev, R. K. *Introduction to Atomic Collision Theory*; Lviv University, 1989 (in Russian).
32. Belkić, Dž. Second Born approximation for charge exchange with correct boundary conditions. *Europhys. Lett.* **1988**, 7, 323.Toshima, N.; Igarashi, A. Second Born approxi mation differential cross sections for p+H and p+He charge-exchange collisions. *Phys. Rev. A* **1992**, *45*, 6313.Toshima, N. Convergence of the perturbation series for high-energy electron capture. *J. Phys. B* **1993**, *26*, L281.Shakeshaft, R.; Spruch, L. Mechanisms for charge transfer (or capture any of any light particle) at asymptotically high impact velocities. *Rev. Mod. Phys.* **1979**, *51*, 369.
33. Nordsieck, A. Reduction of an integral in the theory of bremsstrahlung. *Phys. Rev.* **1954**, *93*, 785.
34. Lewis, R. R. Potential scattering of high-energy electrons in second Born approximation. *Phys. Rev.* **1956**, *102*, 537.
35. Cheshire, I. M. Continuum distorted wave approximation; resonant charge transfer by fast protons in atomic hydrogen. *Proc. Phys. Soc.* **1964**, *84*, 89.
36. Gayet, R. Charge exchange scattering amplitude to first order of a three body expansion. *J. Phys. B* **1972**, *5*, 483.
37. Belkić, Dž.; Salin, A. Differential cross section for charge exchange at high energies. *J. Phys. B* **1978**, *11*, 3905.Ho, T. S.; Eichler, J.; Lieber, M.; Chan, F. T. Calculation of the differential cross section for electron capture in fast ion-atom collisions. *Phys. Rev. A* **1982**, *25*, 1456.
38. Karnakov, B. M. Asymptotic behavior of charge-transfer cross sections. *Sov. Phys. JETP* **1982**, *55*, 816 [*Zh. Eksper. Teor. Fiz.* **1982**, *82* 1407].
39. Thomas, L. H. On the capture of electrons by swiftly moving electrified particles. *Proc. Roy. Soc. A* **1927**, *114*, 561.
40. Horsdal-Pedersen, E.; Cocke, C. L.; Stockli, M. Experimental observation of the Thomas peak in high-velocity electron capture by protons from He. *Phys. Rev. Lett.* **1983**, *50*, 1910.
41. Vogt, H.; Schuch, R.; Justiniano, E.; Schulz, M.; Schwab, W. Experimental test of higher-order electron-capture processes in collisions of fast protons with atomic hydrogen. *Phys. Rev. Lett.* **1986**, *57*, 2256.
42. Martin, P. J.; Blankenship, D. M.; Kvale, T. J.; Redd, E.; Peacher, J. L.; Park, J. T. Electron capture at very small scattering angles from atomic hydrogen by 25-125-keV protons. *Phys. Rev. A* **1981**, *23*, 3357.
43. Clementi, E.; Roetti, C. Roothaan–Hartree–Fock atomic wave functions. *Atom. Data Nucl. Data Tables* **1974**, *14*, 177.
44. Ghosh, M.; Mandal, C. R.; Mukherjee, S. C. Charge-transfer cross sections for asymmetric collisions of protons with carbon, nitrogen, oxygen, neon and argon. *Phys. Rev. A*

1987, *35*, 2815.Mandal, C. R.; Mandal, M.; Mukherjee, S. C. K-shell capture by He^{2+} and Li^{3+} on carbon and neon. *Phys. Rev. A* **1990**, *42*, 1803.

45. Belkić, Dž. Symmetric double charge exchange in fast collisions of bare nuclei with heliumlike atomic systems. *Phys. Rev. A* **1993**, *47*, 189.Belkić, Dž. Two-electron capture from helium-like atomic systems by completely stripped projectiles. *J. Phys. B* **1993**, *26*, 497.
46. Belkić, Dž. Importance of intermediate ionization continua for double charge exchange at high energies. *Phys. Rev. A.* **1993**, *47*, 3824.
47. Belkić, Dž. Double charge exchange at high impact energies. *Nucl. Inst. Meth. Phys. Res. B* **1994**, *86*, 62.Belkić, Dž.; Manćev, I.; Mudrinić, M. Two-electron capture from helium by fast alpha particles. *Phys. Rev. A* **1994**, *49*, 3646.
48. Belkić, Dž.; Mančev, I. Formation of H^- by double charge exchange in fast proton-helium collisions. *Phys. Scr.* **1992**, *45*, 35.Belkić, Dž.; Mančev, I. Four-body CDW approximation: dependence of prior and post total cross sections for double charge exchange upon bound-state wave-functions. *Phys. Scr.* **1993**, *46*, 18.
49. Gayet, R.; Hanssen, J.; Martínez, A.; Rivarola, R. Double electron capture in ion-atom collisions at high impact velocities. *Nucl. Instr. Meth. Phys. Res. B* **1994**, *86*, 158.Gayet, R.; Hanssen, J.; Jacqui, L.; Martínez, A.; Rivarola, R. Double electron capture by fast bare ions in helium atoms: production of singly and doubly excited states. *Phys. Scr.* **1996**, *53*, 549.
50. Sant'Anna, M. M.; Santos, A. C. F.; Coelho, L. F. S.; Jalbert, G.; de Castro Faria, N. V.; Zappa, F.; Focke, P.; Belkić, Dž. Double-electron capture cross sections for Li^{3+} collisions with He at intermediate-to-high velocities. *Phys. Rev. A* **2009**, *80*, 042707.
51. Belkić, Dž. Review of theories on double-electron capture in high-energy ion-atom collisions. *J. Math. Chem.* **2010**, *47*, 1420.

CHAPTER FOURTEEN

Mechanistic Repair-Based Padé Linear-Quadratic Model for Cell Response to Radiation Damage

Dževad Belkić, and Karen Belkić
Nobel Medical Institute, Karolinska Institute, P.O. Box 260, S-171 76 Stockholm, Sweden

Contents

Abstract

This work is on a novel radiobiologal theory of cell survival after radiation of unspecified modality or quality. The analyzed biophysical model, the Padé linear-quadratic model, for cell surviving fractions and the related observable of clinical usefulness is equally applicable to photon beams, as well as to light (electrons) and heavy (atomic nuclei) charged particles of low, intermediate, or high energies. The presented formalism is valid for both the single cell and entire cell populations. The analyzed description can

Advances in Quantum Chemistry, Volume 65
ISSN 0065-3276,http://dx.doi.org/10.1016/B978-0-12-396455-7.00014-5

be incorporated into any type of radiation delivery, including all fractionated treatments ranging from the conventional (2 Gy per fraction, one fraction per day), through hyperfractionation (more than one smaller fraction per day) to hypofractionation (larger doses with shorter overall exposure time, as in stereotactic radiosurgery). The major clinical application of the proposed theory is envisaged to be in providing a better input to dose planning systems for radiotherapy, as expected from the clear biological meaning of the derived parameters. The main strength of the Padé linear-quadratic model is in its foundation on the mechanistic description of radiation damage through enzymatic repair systems governed by the Michaelis–Menten catalysis. It is from this latter origin, which passed the test of time in mainstream biochemistry, that the present theory derives its biomedical adequacy. This, in turn, yields a powerful outperformance of the standard linear-quadratic model, the current workhorse of radiobiological modeling for the purpose of radiotherapy, as amply illustrated in the present study.

1. INTRODUCTION

Radiotherapy is multifaceted, since it relies upon interdisciplinary research in order to meet with success, which is the patient's cure. Different radiation qualities or modalities (photons, charged particles, etc.), deposit their energies in the traversed tissue according to different depth-dose profiles. A typical Bragg peak is a remarkable example of such profiles for heavy ions with most energy delivered to the encountered targets, mainly near the very end the beam's traversal. Electrons and photons deposit most of their energy close to the entrance to the tissue. This makes these radiations unsuitable for treating deep-seated tumors. In sharp contrast, high-energy heavy ions can be optimally conformed to the target location deep inside the patient's body. Such a key feature is associated with negligibly small multiple scattering effects of heavy ions due to large masses of atomic nuclei relative to light electrons.

Nevertheless, irrespective of the existence of diametrically opposite dose-depth profiles, all these different radiation modalities produce cell survival curves of a similar kind, characterized by typical sigmoid shapes, as a function of the absorbed dose. Ionization density and linear energy transfer are larger for heavy ions than for X-rays. This is expected to be biologically expressed by the targeted cell in two distinct ways. Indeed, the so-called relative biological effectiveness is typically 2–3 times larger for heavy ions than that of X-rays. Yet, there are some other aspects of a less appreciable variation for different radiation qualities. For example, the numbers of double strand breaks of deoxyribo-nucleic acid (DNA) molecules could be close to each other for heavy ions and X-rays under the comparable irradiation conditions.

It is of great importance for radiotherapy to have reliable predictions on tumor control and healthy tissue complications. This is where radiobiological modeling comes into its full function to assist tailoring dose planning systems for individual treatments of patients in a manner which is as comprehensive as possible.[1, 2] Biophysical models can, in principle, design dose distributions for each treated patient by taking into account different biological factors ranging from anatomical to physiological. As to the patient, the ultimate goal is to enhance survival and diminish toxicity to the normal tissues. This aim could be attained through several strategies. One of them is an improved understanding of the radiation-tissue interactions on molecular, cellular, and tissue levels. Among other things, this would yield the ever needed amendments of the current dose planning systems. Another strategy is a better comprehension of the individual patient feedback from the administered dose, given that the same amount of the identical irradiation could have markedly different outcomes for different patients with the same type of cancer. These two strategies among others should be considered in concert to achieve the best outcome.

There are two major variabilities in radiation-tissue interactions. One is variability of dose in the irradiated volume. The other is variability of cell response. Both variabilities are multifaceted, ranging from some self-evident to more intricate, hidden aspects. Dose varies through the irradiated tissue due to the stochastic nature of collisions between the beam species and the targeted particles. This does not imply that dose variation is completely random. Certain non-stochastic factors can also influence dose variability, e.g., organ motion, some external settings, etc. Radiation imparts damage to both normal and tumorous cells. Tumor topology is highly complex due to intertwining of healthy with diseased tissue. Critical to the variability of cell responses is the key difference in the way normal and tumor cells cope with the same radiation insult. This variability implies the existence of different interaction mechanisms of radiation with these two kinds of cells. Radically different proliferation rates represent the main cause of unequal mechanisms for healthy and tumor cells. The former have a controllable cell cycle, whereas the latter proliferate uncontrollably with time changing rates.

A key to the overall success of radiotherapy is cell repair of the imparted damage. Therefore, it is of critical importance to investigate various repair mechanisms within the context of the mentioned variabilities of interactions between the applied radiation and the targeted tissue. This problem is addressed in the present chapter by reference to some of the existing radiobiological models, such as the linear-quadratic (LQ) model[3] as well as from the viewpoint of a recently introduced Padé linear-quadratic model (PLQ).[4–6]

The most salient feature of the three constant parameters $\{\alpha, \beta, \gamma\}$ from the PLQ model is their clear biological interpretation based upon chemical kinetics of the Michaelis–Menten[7] mechanism for cell repair through enzyme-lesion catalysis. This automatically provides a cell surviving fraction $S_{\rm F}(D)$ of universal validity at all absorbed doses D. Moreover, this biophysical model possesses the built-in correct asymptotic exponential inactivation modes at low and high doses, separated by a shoulder. Further, the passage from the intermediate shoulder region to both small and large doses occurs in a smooth manner through a typical rectangular hyperbola for the dose-modifying factor—the relative effectiveness $\mathrm{RE}(D) = \{1 + (\beta/\alpha)D\}/(1 + \gamma D)$. The main significance of this is to indicate that Barendsen's concept[8] of biologically effective dose (BED) of radiation is not connected to the total absorbed dose D by a simple relation $\mathrm{BED} = \lambda D$, with λ being a proportionality dimensionless constant (dose-independent). Rather, the cell response, mediated by the enzymatic repair of radiation damage, profoundly alters the physical dose D deposited to the tissue through a modifying factor $M(D)$, in the name of the relative effectiveness $M(D) = \mathrm{RE}(D)$. This changes the said simple proportionality relation to a more structured function $\mathrm{BED}(D) = D \cdot \mathrm{M}(D)$, which becomes linear in D at both low and high doses, as indeed is typical for most mammalian cells. Comparison with several representative sets of experimental data for cell surviving fractions is presented to assess the relative performance of the PLQ model and to challenge the LQ model, which is currently the workhorse of radiobiological modeling in radiotherapy.

2. DOSE–EFFECT CURVE (RESPONSE CURVE OR CELL SURVIVING CURVE)

2.1 Poisson distribution of radiation events, mean lethal dose

Belonging to statistical phenomena, the distribution of events involving cell-radiation interactions fluctuates following the Poisson probability. This can be understood from the arguments which run as follows. On the one hand, particle tracks traversing a tissue are certain to cross at least some of the cell structures. On the other hand, randomness of radiation-cell interactions implies that they are intrinsically uncertain, i.e., probabilistic. For example, single and double strand breaks (SSB, DSB) or any other type of lesions from interactions between the cell and radiation, can take place only with some probability. It is precisely this lack of certainty, which classifies such events as non-deterministic. Upon irradiation, the cell finds itself in a kind of "all-or-nothing" state, as being either alive or dead with respect to its clonogenic ability for proliferation. This naturally leads to the Bernoulli statistics of binary (dichotomous) events. When the number of these events is large, the Bernoulli distribution takes the form of the Poisson distribution. A particular case of this passage from the Bernoulli to the Poisson distribution is interesting to illustrate. In order to highlight this aspect, let us consider some m independent hits that are delivered to the same target. We could inquire about the probability $\pi(m)$ that this target receives no hit. Being independent, each hit has the same probability $1/m$ to arrive at the same target. Conversely, the probability of missing this target is $1 - 1/m$. Furthermore, the probability that all the m hits will miss the target is $(1 - 1/m)^m$. This is precisely the sought probability $\pi(m)$:

$$\pi(m) = \left(1 - \frac{1}{m}\right)^m. \tag{1}$$

In the limit of large values of m, it follows:

$$\lim_{m\to\infty} \pi(m) = \lim_{m\to\infty} \left(1 - \frac{1}{m}\right)^m = \frac{1}{e} \equiv P(0). \tag{2}$$

This is a special case $P(0) = e^{-1}$ of the more general Poisson law for the distribution of a large number m of specific events[†]:

$$P(m) = \frac{x^m}{m!} e^{-x}. \tag{3}$$

Here, x is the *average* number of specific events. For $m = 0$ and $x = 1$, this expression is reduced to:

$$\begin{gathered} P(0) = \frac{1}{e} \approx 0.367879, \quad \text{or,} \\ P(0) \text{ reduced by } 36.7879\% \quad (e \approx 2.71828). \end{gathered} \tag{4}$$

[†] The word specific is used to refer to a particular kind of the cell-radiation interaction, e.g., single or double ionization, excitation, etc.

The classical hit-target model for cell-radiation interaction assumes the Poisson distribution of m events, such as creation of lesions whose average number x is supposed to be directly proportional to the absorbed dose D:

$$x = \frac{D}{D_0}, \tag{5}$$

and therefore,

$$P(m) = \frac{1}{m!}\left(\frac{D}{D_0}\right)^m e^{-D/D_0}. \tag{6}$$

In this model, the number of hits is equal to the number of events, m, and moreover each hit is assumed to lead to a cell inactivation by producing a lethal lesion (cell death). Thus, the probability of survival of a cell as a target is the chance $P(0)$ of not being hit, i.e., when no hit takes place at all, $m = 0$. In the latter case, by setting $x = 1$:

$$x = 1 = \frac{D}{D_0}, \tag{7}$$

it is possible to give the definition of the proportionality constant D_0 in (5) by reference to (3). Namely, since $x = 1$ corresponds to $D = D_0$, as per (7),

$$P(0) = \left\{e^{-D/D_0}\right\}_{x=1, D=D_0} = e^{-1}, \tag{8}$$

we can say that D_0 is a particular dose D, which yields, on the average, one lethal event per target ($x = 1$). Due to this circumstance, D_0 is usually termed *the mean lethal dose*. Moreover, according to (4) and (8), quantity D_0 is the dose at which the surviving fraction is reduced by $1/e \approx 0.367879$, or equivalently, by 36.7879% ≈ 37%. Due to this circumstance, D_0 is often called the "37% dose" and accordingly denoted by $D_{37} (= D_0)$. Reciprocal $1/D_0 \equiv k_0$ is the measure of cell sensitivity to radiation and it is called either the inactivation constant or the radiosensitivity constant (or radiosensitivity, for short). By reference to the special name for dose D_0, it is convenient to refer to k_0 as the mean lethal radiosensitivity, because it is also associated with the $1/e$ reduction of the cell surviving fraction. Mathematically, $1/D_0$ is the final slope of the terminal (exponential) part of the cell survival curve at high doses, e^{-D/D_0}. Note that formally the same decay law or cell surviving fraction applies to a single cell and to a cell population consisting initially of some N_0 cells. Here, the surviving fraction $S_{\rm F}(D)$ would be defined by N/N_0, with the specification $N/N_0 = e^{-D/D_0}$, where N is the number of the surviving cells after irradiation by dose D. In this case, D_0 would represent the dose needed to deliver an average of one lethal event per cell in a total population of N_0 cells.

The curve for the cell surviving fraction $S_{\rm F}(D)$ plotted as a function of dose D is called the dose–effect curve or response curve. The latter name is used to indicate that $S_{\rm F}(D)$ describes the response of the cell to irradiation. This response is the information about the number of cells that survived by absorbing a dose D. Such curves have different characteristics at low, intermediate, and high doses. They seem to decay exponentially at both low and high doses. However, their initial and final slopes are different for these two asymptotes when $D \to 0$ and $D \to \infty$, respectively. At relatively lower doses there is a so-called shoulder. There are three other quantifying characteristics of the dose–effect curves. These are the mean lethal dose D_0, quasi-threshold dose $D_{\rm q}$ and the extrapolation number n.

2.2 Extrapolation number and quasi-threshold dose

A shoulder in the response curve $S_{\rm F}(D)$ is situated in the low-dose region, where cell inactivation per unit dose is noticeably smaller than that at high doses. The passage from these two regions of low and high doses is anything but abrupt. Therefore, a transition dose for delineation of the precise extent of the shoulder cannot be sharply determined. Nevertheless, an approximate procedure could still be designed to obtain a reasonable estimate of a dose located near the transition point (threshold) between the terminal part of the dose–effect curve and the shoulder region. For this reason, such a dose is called a threshold dose, or more appropriately, a quasi-threshold dose because of the said uncertainty. An alternative name for the same dose is the shoulder width or the quasi-width. Both names are associated with the symbol $D_{\rm q}$. In order to determine $D_{\rm q}$, we introduce the high-dose exponential tail or asymptote $S_{\rm F}^{\infty}(D)$ of $S_{\rm F}(D)$ as:

$$S_{\rm F}^{\infty}(D) \equiv e^{\lambda - D/D_0}, \tag{9}$$

or equivalently,

$$S_{\rm F}^{\infty}(D) \equiv n e^{-D/D_0}, \tag{10}$$

where λ is a positive constant connected to the extrapolation number n by the relation:

$$\lambda = \ln n > 0, \quad n > 1. \tag{11}$$

When this definition is linked to a cell survival curve versus dose, the value D_{q} is seen as the dose located at a point at which the tangent to $S_{\mathrm{F}}^{\infty}(D)$ crosses the horizontal line parallel to the abscissa D at the height of the ordinate reaching the maximal cell survival, $S_{\mathrm{F}}(0) = 1$:

$$\begin{aligned}&\big\{\text{Maximal surviving fraction}\big\}_{D=0}\\&\quad = \big\{\text{High dose asymptote of surviving fraction}\big\}_{D=D_{\mathrm{q}}}.\end{aligned} \tag{12}$$

In other words, D_{q} is the dose to which the terminating exponential region of $S_{\mathrm{F}}(D)$ is back-extrapolated to the 100% survival level. Relation (12) represents the condition for isosurvival at which the same value of the cell surviving fraction is obtained for two different doses $D = 0$ and $D = D_{\mathrm{q}}$:

$$\left.\begin{array}{rl} & 1 = e^{\lambda - D_{\mathrm{q}}/D_0} \\ \text{or} & 1 = ne^{-D_{\mathrm{q}}/D_0}\end{array}\right\} \quad \text{(Isosurviving fractions).} \tag{13}$$

In this case, isosurvival, as the identical surviving fraction at both $D = 0$ and $D = D_{\mathrm{q}}$ is obtained if $\lambda - D_{\mathrm{q}}/D_0 = 0$, so that $e^{\lambda - D_{\mathrm{q}}/D_0} = 1$. Here, 1 (unity) is the maximal survival at $D = 0$, signifying the 100% survival, as it ought to be for any form of $S_{\mathrm{F}}(D)$. Therefore, the isosurvival condition $\lambda - D_{\mathrm{q}}/D_0 = 0$ from (13), or equivalently:

$$\left.\begin{array}{l}\ln 1 = 0 = \lambda - \frac{D_{\mathrm{q}}}{D_0}\\ \ln 1 = 0 = \ln n - \frac{D_{\mathrm{q}}}{D_0}\end{array}\right\}, \tag{14}$$

gives the shoulder quasi-width, or the quasi-threshold dose, D_{q} as:

$$D_{\mathrm{q}} = D_0 \ln n. \tag{15}$$

If a shoulder is viewed as an indication of the existence of accumulation of sublethal damage, then, e.g., a wide shoulder width D_{q} would mean that the amount of repaired sublethal damage is large. The name extrapolation number stems from "extrapolating" the terminal, high-dose asymptote ne^{-D/D_0} of the survival curve $S_{\mathrm{F}}(D)$ back to the zero dose ($D = 0$). The intercept of the asymptote ne^{-D/D_0} and the ordinate gives the extrapolation number, $\{ne^{-D/D_0}\}_{D=0} = n$.

3. THE LINEAR-QUADRATIC MODEL

3.1 Biological effect, relative effectiveness, and biologically effective dose

The cell surviving fraction in the linear-quadratic model (LQ) is introduced by:

$$S_{\mathrm{F}}^{(\mathrm{LQ})}(D) = e^{-\alpha D - \beta D^2}, \tag{16}$$

or equivalently,

$$S_{\mathrm{F}}^{(\mathrm{LQ})}(D) = e^{-\mathrm{E}_{\mathrm{B}}^{(\mathrm{LQ})}(D)}, \tag{17}$$

where $\mathrm{E}_{\mathrm{B}}^{(\mathrm{LQ})}$ is the biological effect (BE):

$$\mathrm{E}_{\mathrm{B}}^{(\mathrm{LQ})} \equiv -\ln S_{\mathrm{F}}^{(\mathrm{LQ})}(D) = \alpha D + \beta D^2. \tag{18}$$

This expression can be written in the following two alternative forms:

$$\mathrm{E}_{\mathrm{B}}^{(\mathrm{LQ})} = \alpha \mathrm{BED}^{(\mathrm{LQ})}, \tag{19}$$

$$\mathrm{E}_{\mathrm{B}}^{(\mathrm{LQ})} = \xi \mathrm{RE}^{(\mathrm{LQ})}, \tag{20}$$

where ξ is the approximate expected number of lethal lesions:

$$\xi \equiv \alpha D \quad \text{(Expected number of lethal lesions)}. \tag{21}$$

The quantity $\mathrm{BED}^{(\mathrm{LQ})}$ is the LQ-based biologically effective dose:

$$\mathrm{BED}^{(\mathrm{LQ})} = D + \frac{\beta}{\alpha} D^2, \tag{22}$$

whereas the quantity $\mathrm{RE}^{(\mathrm{LQ})}$ is the relative effectiveness (RE) from the LQ model:

$$\mathrm{RE}^{(\mathrm{LQ})} \equiv 1 + \frac{\beta}{\alpha} D. \tag{23}$$

The $\mathrm{BED}^{(\mathrm{LQ})}$ and $\mathrm{RE}^{(\mathrm{LQ})}$ are interconnected through the relationship:

$$\mathrm{BED}^{(\mathrm{LQ})} = D \cdot \mathrm{RE}^{(\mathrm{LQ})}. \tag{24}$$

Thus, the effect $E_B^{(LQ)}$ can also be understood as being given by the product of the expected number of lesions αD and the relative effectiveness $RE^{(LQ)}$.

3.2 The Barendsen formula

The simple form (22) of $BED^{(LQ)}$ is attractive especially in fractionated radiotherapy, because only the ratio β/α is employed, but the separate values of α and β are not required. Based upon the LQ model, the ratios α/β are estimated to be about 3 Gy and 10 Gy for healthy and tumorous tissues, respectively. The specific numerical values for α/β can be fully meaningful only if they are provided by a mechanistically-based radiobiological model which is universally valid at all doses of interest. However, the LQ model is a low-dose approximation. As a consequence, in order to cover all the needed doses, one might be required to perform several (say J) separate fits to the given experimental data resulting in different sets of values $\{\alpha_j/\beta_j\}(j \leqslant J)$ for the selected J dose intervals. This has the drawback of yielding a dose-range dependence of the $BED^{(LQ)}$, which severely limits inter-comparisons of different patterns of radiation delivery in fractionated radiotherapy. Therefore, it would be desirable to have a model which would give the biologically effective dose applicable to all doses for the same quantifying parameters estimated by using *all* the available experimental data points. Such a feature would enable the extraction of the biologically effective dose from the reconstructed parameters that do not change when passing from one to another dose range. The occurrence that the mentioned ratios α/β are so different for tumorous and normal tissue is an indication of the existence of substantially different mechanisms by which these two types of tissues respond to irradiation. As stated in the Introduction, the main reason for this difference is in the cell proliferation which is uncontrolled (chaotic) in tumor, and well regulated by the cell cycle growth in normal tissue.

What made the LQ model clinically useful was precisely Barendsen's[8] idea about linking the radiation dose with the ensuing biological effect. In general, irrespective of any particular model, this concept states that the biologically effective dose is equal to the product of the total dose D and a dose-modifying factor, which is the relative effectiveness:

$$\text{Biologically effective dose} = \{\text{Total dose}\} \cdot \Big\{\text{Modifying factor}\Big\}, \tag{25}$$

$$\text{BED} = D \cdot \text{RE}. \tag{26}$$

It is through the modifying factor, the RE, that a particular pattern of radiation delivery can be taken into account. This is especially important for fractionated radiotherapy, where the RE can help improve the effectiveness of the specific dose-time schedule by means of which the total dose is administered. In searching for some plausible ways that could make the LQ model clinically applicable, Barendsen[8] entered only the ratio β/α into the dose-dependent relative effectiveness $\mathrm{RE}^{(\mathrm{LQ})}$, but not the individual parameters α and β. Because the quotients of the form β/α are tissue-specific parameters, quantity $\mathrm{RE}^{(\mathrm{LQ})} = 1 + (\beta/\alpha)D$ from (23) can express the differences in radiation effects for various tissues. In other words, $\mathrm{RE}^{(\mathrm{LQ})}$ can be employed to investigate the differences in biological effectiveness among various tissues as a consequence of alterations in the dose delivery patterns. Thus, since different tissue effects are associated with different values of the quotient β/α, it is possible to use Eq. (26) to evaluate alterations in the therapeutic ratio due to changes in fractionation. The therapeutic ratio can be improved by e.g., reducing dose per fraction, in which case there should be proportionally more sparing of the healthy (late reacting) than tumorous (early reacting) tissues. These considerations indicate that the LQ model can be used as a predictive model, when considering certain alternative radiation treatments aimed at maximizing tumorous cell kill effects, while simultaneously minimizing some of the adverse healthy-tissue effects (e.g., normal tissue complication rates). The Barendsen relation (26) is general, as it is not limited to fractionated radiotherapy. Rather, it can be used for an arbitrary kind of radiation treatment. Note that Barendsen[8] originally coined a term "extrapolated response dose" (ERD) in (26). This was subsequently renamed by Fowler[9] to the "biologically effective dose," or the BED, as a better terminology for Barendsen's idea.

3.3 Low- and high-dose asymptotes of biological effect and surviving fraction

The effect (18) in the LQ model has the following asymptotic behavior at infinitesimally small and infinitely large values of D:

$$\mathrm{E}_{\mathrm{B}}^{(\mathrm{LQ})} \underset{D\to 0}{\longrightarrow} \alpha D, \tag{27}$$

$$\mathrm{E}_{\mathrm{B}}^{(\mathrm{LQ})} \underset{D\to \infty}{\longrightarrow} \beta D^2, \tag{28}$$

respectively. This gives the corresponding asymptotes for $\mathrm{BED}^{(\mathrm{LQ})}$ as:

$$\mathrm{BED}^{(\mathrm{LQ})} \underset{D\to 0}{\longrightarrow} D, \tag{29}$$

$$\mathrm{BED}^{(\mathrm{LQ})} \underset{D\to \infty}{\longrightarrow} \frac{\beta}{\alpha} D^2. \tag{30}$$

Using the asymptotes (29) and (30) for $\mathrm{E}_{\mathrm{B}}^{(\mathrm{LQ})}$, it follows that the survival curve given by $S_{\mathrm{F}}^{(\mathrm{LQ})}(D)$ from (16) is mainly exponential and Gaussian at small and large values of D:

$$S_{\mathrm{F}}^{(\mathrm{LQ})}(D) \underset{D\to 0}{\longrightarrow} e^{-\alpha D}, \tag{31}$$

$$S_{\mathrm{F}}^{(\mathrm{LQ})}(D) \underset{D\to \infty}{\longrightarrow} e^{-\beta D^2}, \tag{32}$$

respectively. A stronger repair, with a significant ratio β/α, is seen in the plot of cell surviving fraction as a more pronounced shoulder due to the Gaussian with its quadratic term βD^2, which yields a more curved function $S_{\mathrm{F}}^{(\mathrm{LQ})}(D)$. For small β/α, cell kill prevails and $S_{\mathrm{F}}^{(\mathrm{LQ})}(D)$ is less curvy because of the dominance of the purely exponential function. As such, the ratio β/α appears as a measure of the curvature of $S_{\mathrm{F}}^{(\mathrm{LQ})}(D)$ and this influences the cell response to radiation. Moreover, the smaller β/α implies that the dose-response relationship will be less sensitive to fractionation when fractionated radiotherapy is applied. Conversely, the larger β/α means that radiation damage was accumulated to a sufficient level to produce various lesions in DNA molecules. In such a case of an elevated β/α, the repairing molecules are triggered more proactively, so that repair of repairable lesions can become a key factor in determining the overall biological response of the cell to radiation.

The number of lesions could be assumed to be proportional to D as indicated in (21). Therefore, the LQ-based effect $\mathrm{E}_{\mathrm{B}}^{(\mathrm{LQ})} = (\alpha D)(1 + \beta D/\alpha)$ from Eq. (18), interpreted as the yield of elementary lesions, is proportional to the product of the average number of primary lesions ($\sim D$) and the average energy deposited around the lesions ($\sim \{1 + \beta D/\alpha\}$). This can also be written as:

$$\mathrm{E}_{\mathrm{B}}^{(\mathrm{LQ})} = \beta D(\zeta + D) = \beta D\left(z_{\mathrm{D}} + D\right), \tag{33}$$

where,

$$\zeta \equiv z_{\mathrm{D}} = \frac{\alpha}{\beta}. \tag{34}$$

Parameter ζ (or $z_{\mathrm{D}} \equiv \bar{z}_{\mathrm{D}}$) is a microdosimetric quantity called the "dose-averaged" specific energy, which is given in terms of a sequence of increments of the specific energy z associated with single events:

$$z_{\mathrm{D}} \equiv \zeta = \frac{1}{z_{\mathrm{F}}} \int_0^{\infty} \mathrm{d}z\, z^2 f_1(z), \quad z_{\mathrm{F}} = \int_0^{\infty} \mathrm{d}z\, z f_1(z), \tag{35}$$

where $\bar{z}_{\mathrm{F}} \equiv z_{\mathrm{F}}$ is the "frequency-averaged" specific energy.[‡] The term "frequency" refers to the frequency of occurrence of single events in a given volume. Quantity $f_1(z)\mathrm{d}z$ is the probability distribution in z, where the subscript "1" refers to single events alone. Event distributions appear in the analysis because ionizing collisions are random and, therefore, the energy deposited in the tissue by such collisions represents a stochastic quantity or variable. In the microdosimetric formalism, the average number of events $\bar{N}$ at a fixed dose D is given by $\bar{N} = \lceil D/z_{\mathrm{F}} \rceil$, where $\lceil r \rceil$ is the ceiling symbol which denotes the largest integer obtained by rounding up the number r, which can be a rational or any other real number or a real value of any function.

4. THE PADÉ LINEAR-QUADRATIC MODEL

4.1 Differentiation between physical and biological doses

As mentioned, the two most salient aspects of the cell surviving fraction, $S_{\mathrm{F}}(D)$, are the direct cell kill and cell repair. They can be simultaneously taken into account by introducing a biological dose D_{B} to be determined for the given physical, single radiation dose D. The sought dose D_{B} can be found from the Poisson statistics. In the context of radiation damage, the targeted cell is certain to survive if it receives no dose when the dose D_{B} is expected to be absorbed. The chance for such an event to occur is given by the Poisson probability:

$$P(0) = e^{-\mu D_{\mathrm{B}}}, \tag{36}$$

[‡] In microdosimetry, a single absorbed dose D is defined as the expected value of the so-called specific energy z. On the other hand, specific energy z is the energy per unit mass per unit volume deposited per event per cell nucleus.

where μ is the repair constant in units of Gy^{-1}. The constant $\mu \geqslant 0$ is connected to the repair time τ during which the cell becomes effectively insensitive to any two consecutive hits (events, particle or ray traversals through the treated tissue) whenever they follow each other within the time interval Δt, which is smaller than the recovery time ($\Delta t < \tau$). When the repair mechanism is activated, the delivered physical dose D is reduced and becomes only an apparent dose D_{appar}. On the other hand, the true dose D_{true}, which is actually received by the cell, represents the biological dose D_{B}. In other words, repair effectively diminishes the values of D and transforms it to D_{B}. The difference between D and D_{B} is that the latter accounts for a correction due to the missed/wasted hits during the time lag $\Delta t < \tau$ whenever $\tau > 0$. Such a discrepancy between D and D_{B} can be modeled by the said Poisson probability $P(0)$. This settles the issue of the *definition* of $D_{\text{B}} = D_{\text{B}}(D)$ for a fixed D as:

$$D_{\text{B}}P(0) = D, \tag{37}$$

or explicitly,

$$D_{\text{B}}e^{-\mu D_{\text{B}}} = D, \tag{38}$$

where,

$$D \leqslant D_{\text{B}}. \tag{39}$$

Employing the alternative notation:

$$D_{\text{appar}} \equiv D, \quad D_{\text{true}} \equiv D_{\text{B}}, \tag{40}$$

we can rewrite (38) as:

$$D_{\text{true}}e^{-\mu D_{\text{true}}} = D_{\text{appar}}, \tag{41}$$

$$D_{\text{appar}} \leqslant D_{\text{true}}. \tag{42}$$

It will also prove useful to introduce a repair degree by the following quotient of doses:

$$\nu \equiv \frac{D_{\text{appar}}}{D_{\text{true}}} = \frac{D}{D_{\text{B}}}, \quad 0 \leqslant \nu \leqslant 1 \quad \text{(Cell repair measure or degree).} \tag{43}$$

The mechanism driving the pattern (38), or equivalently (41), which describes the cell recovery during the repair time τ consists of the following twofold pattern:

(a) What is usually considered to be a single absorbed dose D is modified by repair to become merely an apparent dose D_{appar}, which is smaller than the true dose D_{true}, which is expected to be deposited to the sensitive part of the cell.

(b) A measure or degree of the cell repair is the quotient ν of D_{appar} and D_{true} from (43) as given by the Poisson probability (38) that the cell receives no dose when the dose $D_{\text{true}} = D_{\text{B}}$ is anticipated. This degree varies from 0 to 1 due to its coincidence with the Poisson probability (36) via $\nu = P(0) = e^{-\mu D_{\text{true}}} = e^{-\mu D_{\text{B}}}$.

The inequality in (39) is evident from e.g., (41) where D_{true} has to be exponentially damped via $D_{\text{true}} e^{-\mu D_{\text{true}}}$ to become equal to D_{appar} as $D_{\text{true}} e^{-\mu D_{\text{true}}} = D_{\text{appar}}$. Stated equivalently, the apparent dose $D_{\text{appar}} = D$ is smaller than its true counterpart $D_{\text{true}} = D_{\text{B}}$ because D ought to be enhanced by a positive factor $1/P(0) = e^{\mu D_{\text{B}}}$ in order to match the value D_{B} through:

$$De^{\mu D_{\text{B}}} = D_{\text{B}}. \tag{44}$$

Parameter μ could be related to the microdosimetric dose-averaged specific energy $z_{\text{D}} = \zeta$ from (34). In microdosimetric formalism, the probability of receiving no dose when the dose D_{B} is expected is given by $P(0) = e^{-D_{\text{B}}/z_{\text{D}}}$. This is the same Poisson formula which is in the formalism of this Section denoted by $P(0) = e^{-\mu D_{\text{B}}}$ in (36). Therefore, the parameter μ from (36) or (38) could have a microdosimetric meaning, in which case it would represent the reciprocal of the dose average specific energy:

$$\mu = \frac{1}{z_{\text{D}}} \equiv \frac{1}{\zeta}. \tag{45}$$

With this relation, a link to the parameters α and β from the LQ model can readily be made. Parameter z_{D}, which appears in the second moment of the dose-averaged specific energy has already been identified in dosimetry as $z_{\text{D}} = \alpha/\beta$ and, therefore:

$$\mu = \frac{\beta}{\alpha}. \tag{46}$$

It is important to formulate the following inverse dose problem for radiobiological modeling:

$$\left.\begin{array}{l}\text{Given the physical dose } D \text{ applied to the treated tissue,}\\ \text{what would be the biological dose } D_{\text{B}} \text{ received by}\\ \text{the irradiated cells when the cell repair system is active?}\end{array}\right\}. \tag{47}$$

Within the Poisson statistics (36), one of the possible answers to this question is given by the exact real-valued solution $D_{\rm B}$ of the transcendental equation (38).

If $D_{\rm B}$ were known, the dose which was applied to the tissue could be retrieved by a direct computation of the so-called Ricker function, $D_{\rm B}e^{-\mu D_{\rm B}}$. Then the inverse Ricker function would give D. In reality, however, the biological dose $D_{\rm B}$ is unknown, but could nevertheless be determined by finding the inverse Ricker function. Although the exact inverse Ricker function is known and can be used through the Lambert function,[4, 10] in the present work we shall deal with a simpler and more instructive exposition. To this end, we shall derive an approximate solution for $D_{\rm B}$ from the non-linear, transcendental equation (38) through the process of linearization, by using only the known simplest elementary functions. With this goal, we start from (44) where we use the series for the exponential $e^{\mu D_{\rm B}}$ as:

$$e^{\mu D_{\rm B}} = 1 + \frac{\mu D_{\rm B}}{1!} + \frac{(\mu D_{\rm B})^2}{2!} + \cdots , \tag{48}$$

where the rhs converges for every value of $\mu D_{\rm B}$. A further simplification of the rhs of Eq. (45) can be deduced by assuming that the recovery time is short ($\tau \ll 1$ or $\mu \ll 1$) and that the dose D permits the relation $\mu D_{\rm B} \ll 1$. In such a case, it is justified to retain e.g., only the first 2 terms of the series from (48), so that (44) becomes:

$$D_{\rm B} = De^{\mu D_{\rm B}} \approx D(1 + \mu D_{\rm B}) \quad (\mu D_{\rm B}\ \text{small}). \tag{49}$$

This implicit, linearized version of the non-linear Eq. (38) can be written more explicitly by collecting the unknown $D_{\rm B}$ on the same side of the equation to yield:

$$D_{\rm B} \approx \frac{D}{1 - \mu D} \quad (\mu D_{\rm B}\ \text{small}). \tag{50}$$

The expression $D/(1 - \mu D)$ from (50) is the diagonal Padé approximant (PA)[11] to $D_{\rm B}(D)$, as a quotient of two polynomials of the same first degree in variable D. This PA possesses an equivalent representation obtained by employing the binomial series:

$$D_{\rm B} \approx \frac{D}{1 - \mu D} = D\{(1 + \mu D) + (\mu D)^2 + \cdots\}, \tag{51}$$

which converges for $\mu D < 1$. If we keep only the first two terms within the square brackets from the rhs of Eq. (51), we will finally arrive at:

$$D_{\mathrm{B}} \approx D(1 + \mu D) \quad (\mu D \text{ small}), \tag{52}$$

or equivalently, by reference to (39):

$$D_{\mathrm{true}} = D_{\mathrm{appar}}(1 + \mu D_{\mathrm{appar}}) \quad (\mu D_{\mathrm{appar}} \text{ small}). \tag{53}$$

As discussed for the exact relation (38), we see that the corresponding approximation (52) also obeys the inequality $D \leqslant D_{\mathrm{B}}$ from (39), since a non-negative term ($\mu D^2 \geqslant 0$) must be added to $D \geqslant 0$ to obtain an approximate D_{B}. Division of (52) by D or (53) by D_{appar} yields:

$$\frac{D_{\mathrm{B}}}{D} \approx 1 + \mu D, \tag{54}$$

so that,

$$\nu = \frac{1}{1 + \mu D}. \tag{55}$$

Using (46), the rhs of Eq. (54) can be identified as the relative effectiveness $\mathrm{RE}^{(\mathrm{LQ})}$ from Eq. (23). Thus, the quantity $\mathrm{RE}^{(\mathrm{LQ})}$ can equivalently be conceived as the quotient D_{B}/D of an approximate expression for the biological dose D_{true} (or D_{B}) and the apparent dose D_{appar} (or D):

$$\mathrm{RE}^{(\mathrm{LQ})} = \frac{D_{\mathrm{B}}}{D}. \tag{56}$$

The approximate formula for the effect E_{B} related to (52) is now given by:

$$\mathrm{E}_{\mathrm{B}} \approx \alpha D_{\mathrm{B}} \approx \alpha D + \beta D^2. \tag{57}$$

Therefore, the definition (46) permits a connection of Eqs. (52) and (57) with the LQ model via:

$$D_{\mathrm{B}} \approx D_{\mathrm{B}}^{(\mathrm{LQ})}, \quad \mathrm{E}_{\mathrm{B}} \approx \mathrm{E}_{\mathrm{B}}^{(\mathrm{LQ})}, \tag{58}$$

where $\mathrm{E}_{\mathrm{B}}^{(\mathrm{LQ})}$ is defined in (18), and:

$$D_{\mathrm{B}}^{(\mathrm{LQ})} = D\left(1 + \frac{\beta}{\alpha} D\right). \tag{59}$$

The binomial series (51) for $D_{\rm B}$ can alternatively be obtained by solving the implicit, linearized equation (49) through iterations. The first iterate is generated via the replacement of $D_{\rm B}$ from the rhs of Eq. (49) by $D(1+\mu D_{\rm B})$ so that $D_{\rm B} \approx D\{1+\mu\,[D(1+\mu D_{\rm B})]\}$. If in the rhs of the latter equation, $D_{\rm B}$ is written as $D(1+\mu D_{\rm B})$, the second iterate follows, $D_{\rm B} \approx D(1+\mu D+\mu^2D^2+\mu^3 D_{\rm B})$. The higher iterates within this procedure of self-substitutions shall yield the binomial series, which sums up to closed expression $D_{\rm B} \approx D/(1-\mu D)$ for $\mu D < 1$ in agreement with Eq. (51).

The approximate solution (52) for $D_{\rm B}$ is the sum of the linear ($\sim D$) and quadratic ($\sim D^2$) terms. Without repair, all the impinging radiation quanta are absorbed by the targeted cell, so that:

$$D_{\rm B} = D, \quad \mu = 0 \ (\tau = 0\!: \ \text{no repair}), \tag{60}$$

and this goes for both (38) and (59). However, with repair ($\tau > 0, \mu > 0$), there would be some wasted radiation quanta, as if they were removed from the beam or annihilated in the traversed tissue and this gives the quadratic term $\sim D^2$. Our derivation shows that the quadratic term $\sim D^2$ is directly rooted in the cell repair mechanism and brought about by reconstruction of the unknown biological dose $D_{\rm B} \approx D_{\rm B}^{\rm (LQ)}$ from the given physical dose D. This gives the approximate answer (52) to the stated inverse dose problem (47). By reference to (59), it follows that the quantity $\text{BED}^{\rm (LQ)}$ coincides with $D_{\rm B}^{\rm (LQ)}$:

$$\text{BED}^{\rm (LQ)} = D_{\rm B}^{\rm (LQ)}. \tag{61}$$

In the present formulation of the LQ model, parameters α and β are associated in a distinct manner with the cell kill and cell repair per ${\rm Gy}^{-1}$ and ${\rm Gy}^{-2}$, respectively. However, in the present derivation of the approximate effect $\text{E}_{\rm B}^{\rm (LQ)}$ from (18), these two parameters are correlated through the relationship (46). Thus, if μ were known, only α would be a free parameter when reconstructing $\text{E}_{\rm B}^{\rm (LQ)}$ from e.g., its least-square adjustment to the corresponding experimental data. Parameter $\mu = \beta/\alpha$ is the measure of the deviation of the parabola $\alpha D + \beta D^2$ from the straight line αD plotted versus D as the abscissa. The higher the μ, the more parabolic the effect $\text{E}_{\rm B}^{\rm (LQ)}$ and the more significant the repair βD^2. Conversely, the lower the μ, the more straight line behavior of $\text{E}_{\rm B}^{\rm (LQ)}$ and the more pronounced the cell kill αD.

This derivation clearly demonstrates that the LQ model represents a low-dose approximation of a more general model,[4] which solves the transcendental equation (38) exactly, rather than using the approximate solution (54), which is valid for small μD. More specifically, we employed the convergence radius $\mu D < 1$ in the result $D_{\mathrm{B}}/D \approx 1 + \mu D$ from (54). This latter low-dose restriction is due to the use of the binomial series for $1/(1-\mu D)$, which is meaningful only for $\mu D < 1$. Retaining the first two terms in this series via $1/(1-\mu D) \approx 1 + \mu D$ leads straight to the LQ model. The binomial $1/(1-\mu D)$ itself is the Padé approximant as a ratio of the simplest two polynomials of degree 0 and 1 in the numerator and denominator, respectively, according to $1/(1-\mu D) = P_0(D)/Q_1(D)$, where $P_0(D) = 1$ and $Q_1(D) = 1 - \mu D$.

4.2 Repair-mediated non-linear damping of linear direct cell kill mechanism

At larger values of D, experimental data for $S_{\mathrm{F}}(D)$ usually exhibit an exponential fall-off, $S_{\mathrm{F}}(D) \sim e^{-D/D_0} = P(0)$, where D_0 is the dose at which the surviving fraction is reduced by $1/e \approx 0.367879$ or by 36.7879%, as per (4). In other words, the final slope of most measured curves for cell surviving fractions is given by $1/D_0$. This is opposed to the LQ-type high-dose dominance of the Gaussian $S_{\mathrm{F}}^{(\mathrm{LQ})}(D) \sim e^{-\beta D^2}$ from (32), which continues to bend and thus has no final slope. In the LQ model, the initial slope, determined by the low-dose asymptote $S_{\mathrm{F}}^{(\mathrm{LQ})}(D) \sim e^{-\alpha D}$ from (31), is given by α which is associated with single radiation events (single hits) to a sensitive part of the cell. Even in the low-dose limit, the LQ model was seen to deviate from experimental data[12] thus pointing to unreliable numerical values of the parameters α and β in the LQ-based cell surviving fraction $S_{\mathrm{F}}^{(\mathrm{LQ})}(D)$. According to the above derivation, α is also present in β. The said drawbacks of the LQ model at both low- and high-dose asymptotic regions could partially be attributed to the assumption that the linear part $\xi = \alpha D$ is associated exclusively with lethal events as in the classical hit-target model. We shall relax this limitation and modify the term αD so as to allow for cell repair. In other words, as opposed to the hit-target model, where the direct hits ($\sim\alpha D$) describe irreparable lesions that cause cell death, we shall permit that even direct hits could be repaired. As discussed, this can be done by damping αD when the dose is progressively augmented. To this end, we shall modify the LQ model by introducing the repairable lesion ξ_{B} in lieu of ξ as:

$$\xi_{\mathrm{B}} e^{\omega \xi_{\mathrm{B}}} \equiv \xi \quad \therefore\ \xi_{\mathrm{B}} \leqslant \xi, \tag{62}$$

where $\omega \geqslant 0$ is a dimensionless repair-related constant. Here,

$$\left.\begin{array}{l}\xi_{\rm B} = \text{Expected number of repairable lesions from direct hits} \\ \xi \ = \text{Expected number of irreparable lesions from direct hits}\end{array}\right\}, \tag{63}$$

The inequality $\xi_{\rm B} \leqslant \xi$ from (62) is evident from the defining relation $\xi_{\rm B} e^{\omega \xi_{\rm B}} = \xi$, since $\xi_{\rm B}$ needs to be multiplied by a non-negative number $e^{\omega \xi_{\rm B}} \geqslant 0$ to be equalized to ξ. Moreover, biologically, the plus sign of $\xi_{\rm B}$ in the argument of the exponential in $\xi_{\rm B} e^{\omega \xi_{\rm B}}$ from the lhs of Eq. (62) coheres with the fact that repair diminishes the number of expected lethal lesions from direct hits (single interaction of radiation with the cell). At this point of the analysis, it suffices to find an approximate solution of the transcendental equation (62). This can be done if in Eq. (62), rewritten as $\xi_{\rm B} = \xi e^{-\omega \xi_B}$, we replace the exponential $e^{-\omega \xi_{\rm B}}$ by its first-order diagonal Padé approximant[11] in variable $\omega \xi_{\rm B}/2$ as:

$$e^{-\omega \xi_{\rm B}} \approx \frac{1 - \omega \xi_{\rm B}/2}{1 + \omega \xi_{\rm B}/2} \quad \text{(Padé approximant for exponential).} \tag{64}$$

This transforms the transcendental equation (62) into a quadratic equation for the unknown $\xi_{\rm B}$:

$$\frac{1}{2}\omega \xi_{\rm B}^2 + Q\xi_{\rm B} - \xi = 0, \tag{65}$$

where,

$$Q = 1 + \frac{1}{2}\omega \xi = 1 + \gamma D, \tag{66}$$

$$\gamma = \frac{1}{2}\omega \alpha. \tag{67}$$

The roots of the quadratic equation (66) are:

$$\xi_{\rm B}^{\pm} = \frac{Q}{\omega}\left(-1 \pm \sqrt{1 + \frac{2\omega \xi}{Q^2}}\right), \tag{68}$$

where $\xi_{\rm B}^{+} > 0$ (physical) and $\xi_{\rm B}^{-} < 0$ (unphysical). We retain only the positive-definite root $\xi_{\rm B}^{+}$, which is re-labeled as $\xi_{\rm B}^{(\rm P)}$:

$$\xi_{\rm B}^{+} \equiv \xi_{\rm B}^{(\rm P)}. \tag{69}$$

Next, the term $(1 + 2\omega\xi/Q^2)^{1/2}$ is expanded in a series with powers of $2\omega\xi/Q^2$:

$$\left(1 + \frac{2\omega\xi}{Q^2}\right)^{1/2} = \left\{1 + \frac{\omega\xi}{Q^2}\right\} + \frac{3}{8}\frac{(\omega\xi)^2}{Q^4} + \cdots . \tag{70}$$

By keeping solely the first two terms, i.e., the terms from the curly brackets, and using (66), it follows:

$$\left(1 + \frac{2\omega\xi}{Q^2}\right)^{1/2} \approx 1 + \frac{\omega\xi}{Q^2}. \tag{71}$$

In this way, Eqs. (68) and (69) yield the final result $\xi_{\mathrm{B}} \approx \xi_{\mathrm{B}}^{(\mathrm{P})} \approx \xi/Q$ or:

$$\xi_{\mathrm{B}} \approx \xi_{\mathrm{B}}^{(\mathrm{P})} \approx \frac{\xi}{1 + \gamma D} = \frac{\alpha D}{1 + \gamma D}. \tag{72}$$

The replacement of the term ξ by its Padé-equivalent $\xi_{\mathrm{B}}^{(\mathrm{P})}$ yields the Padé Linear-Quadratic model, as denoted by PLQ, for the biological effect of radiation:

$$\mathrm{E}_{\mathrm{B}}^{(\mathrm{PLQ})} \equiv \xi_{\mathrm{B}}^{(\mathrm{P})}(1 + \mu D), \tag{73}$$

or equivalently,

$$\mathrm{E}_{\mathrm{B}}^{(\mathrm{PLQ})} = \frac{\alpha D}{1 + \gamma D}(1 + \mu D). \tag{74}$$

The corresponding cell surviving fraction in the PLQ model reads as:

$$S_{\mathrm{F}}^{(\mathrm{PLQ})}(D) \equiv e^{-\mathrm{E}_{\mathrm{B}}^{(\mathrm{PLQ})}}. \tag{75}$$

If parameter μ is chosen according to (46), we can cast Eqs. (74) and (75) into the forms:

$$\mathrm{E}_{\mathrm{B}}^{(\mathrm{PLQ})} = \frac{\alpha D + \beta D^2}{1 + \gamma D}, \tag{76}$$

$$S_{\mathrm{F}}^{(\mathrm{PLQ})}(D) = e^{-\frac{\alpha D + \beta D^2}{1 + \gamma D}}. \tag{77}$$

The numerator of the quotient from the rhs of Eq. (76) represents the effect in the LQ model, so that we can also write:

$$\mathrm{E}_{\mathrm{B}}^{(\mathrm{PLQ})} = \frac{\mathrm{E}_{\mathrm{B}}^{(\mathrm{LQ})}}{1+\gamma D}. \tag{78}$$

As per derivation of the PLQ model, there are two "repair ratios" $\Gamma_{\beta\alpha}$ and $\Gamma_{\gamma\alpha}$ that can be introduced by:

$$\Gamma_{\beta\alpha} = \frac{\beta}{\alpha}, \quad \Gamma_{\gamma\alpha} = \frac{\gamma}{\alpha}, \tag{79}$$

in terms of which, the biological effect (76) can be rewritten as:

$$\mathrm{E}_{\mathrm{B}}^{(\mathrm{PLQ})} = \frac{D+\Gamma_{\beta\alpha}D^2}{\delta+\Gamma_{\gamma\alpha}D}, \quad \delta = \frac{1}{\alpha}. \tag{80}$$

Quotient $\Gamma_{\beta\alpha}$ is a repair degree β/α, which gives the relative importance of the linear (D) and quadratic (D^2), as also encountered in the LQ model, according to (59) and (61). The additional repair ratio $\Gamma_{\gamma\alpha}$ in the PLQ model is a repair measure γ/α of the strength of some higher-order mechanisms appearing through all the powers of dose D that are implicitly present in (80) and could be made explicit by expanding the binomial $1/(\delta+\Gamma_{\gamma\alpha}D)$ into its Macularin series. The quotient of $\Gamma_{\beta\alpha}$ and $\Gamma_{\gamma\alpha}$ is useful, since it gives the degree of the departure of the PLQ from the LQ model:

$$\Gamma_{\beta\gamma} = \frac{\Gamma_{\beta\alpha}}{\Gamma_{\gamma\alpha}} = \frac{\beta}{\gamma}. \tag{81}$$

This quantity is also the final slope of the dose–effect curve $S_{\mathrm{F}}^{(\mathrm{PLQ})}(D)$, as will be discussed later on. The expression (73) for the effect $\mathrm{E}_{\mathrm{B}}^{(\mathrm{PLQ})}$ in the PLQ model was obtained in the two main steps: (i) derivation of the approximate biological dose $D_{\mathrm{B}} = D(1+\mu D)$ from (52), which by way of the definition $\mu = \beta/\alpha$ from (46) coincides with the biologically effective dose $\mathrm{BED}^{(\mathrm{LQ})}$ in the LQ model, $D_{\mathrm{B}} = \mathrm{BED}^{(\mathrm{LQ})}$, as per (61), and (ii) replacement of the lethal (irreparable) lesions $\xi = \alpha D$ in the effect $\mathrm{E}_{\mathrm{B}} \equiv \alpha D_{\mathrm{B}} = \xi(1+\mu D)$ from (61) by the sublethal (repairable) lesion $\xi_{\mathrm{B}}^{(\mathrm{P})}$ via $\xi \Longrightarrow \xi_{\mathrm{B}}^{(\mathrm{P})} = \xi/(1+\gamma D) = (\alpha D)/(1+\gamma D)$. The net result of the steps (i) and (ii), through the product of $\xi_{\mathrm{B}}^{(\mathrm{P})}$ and the relative effectiveness $1+\mu D$ as $\xi_{\mathrm{B}}^{(\mathrm{P})}(1+\mu D)$ represents the effect $\mathrm{E}_{\mathrm{B}}^{(\mathrm{PLQ})} = (\alpha D+\beta D^2)/(1+\gamma D)$

from (73) in the PLQ model. This recapitulation through the said two steps (i) and (ii) illustrates the origin of the name "Padé + Linear-Quadratic" and the associated acronym PLQ for this new radio-biological model which has originally been introduced in our recent works.[4–6]

4.3 Initial slope, final slope, and extrapolation number

For the choice $\mu = \beta/\alpha$ from (46), the low- and high-dose asymptotes of $\mathrm{E}_{\mathrm{B}}^{(\mathrm{PLQ})}$ read as:

$$\mathrm{E}_{\mathrm{B}}^{(\mathrm{PLQ})} \underset{D\to 0}{\longrightarrow} \alpha D, \tag{82}$$

$$\mathrm{E}_{\mathrm{B}}^{(\mathrm{PLQ})} \underset{D\to\infty}{\longrightarrow} \frac{\beta}{\gamma} D, \tag{83}$$

respectively. For brevity, the high-dose asymptote (83) is written to exhibit only the leading term ($\sim D$), whereas the constant ($\sim D^0$) is ignored. As it stands, Eq. (76) is the para-diagonal Padé approximant with the numerator and denominator polynomial of the second- and first-degree, respectively in variable D.

The expression for $\mathrm{E}_{\mathrm{B}}^{(\mathrm{PLQ})}$ from (76) leads to the corresponding biologically effective dose $\mathrm{BED}^{(\mathrm{PLQ})}$ in the PLQ model:

$$\mathrm{BED}^{(\mathrm{PLQ})} \equiv \frac{\mathrm{E}_{\mathrm{B}}^{(\mathrm{PLQ})}}{\alpha} = \frac{D + \beta D^2/\alpha}{1 + \gamma D}. \tag{84}$$

This can also be written in analogy with (24) as:

$$\mathrm{BED}^{(\mathrm{PLQ})} = D \cdot \mathrm{RE}^{(\mathrm{PLQ})}, \tag{85}$$

where $\mathrm{RE}^{(\mathrm{PLQ})}$ is the relative effectiveness in the PLQ model:

$$\mathrm{RE}^{(\mathrm{PLQ})} = \frac{1 + (\beta/\alpha)D}{1 + \gamma D} = \frac{\mathrm{RE}^{(\mathrm{LQ})}}{1 + \gamma D}. \tag{86}$$

Insertion of the asymptotes (82) and (83) for $\mathrm{E}_{\mathrm{B}}^{(\mathrm{PLQ})}$ into Eq. (84) yields:

$$\mathrm{BED}^{(\mathrm{PLQ})} \underset{D\to 0}{\longrightarrow} D, \tag{87}$$

$$\mathrm{BED}^{(\mathrm{PLQ})} \underset{D\to\infty}{\longrightarrow} \frac{\beta}{\alpha\gamma} D. \tag{88}$$

As expected, the PLQ and LQ models exhibit the same low-dose behaviors in (29) and (87), but differ substantially at high doses according to (30) and (88).

The behaviors (82) and (83) of $\mathrm{E}_{\mathrm{B}}^{(\mathrm{PLQ})}$ yield the following two asymptotes of $S_{\mathrm{F}}^{(\mathrm{PLQ})}(D)$ at small and large values of D:

$$S_{\mathrm{F}}^{(\mathrm{PLQ})}(D) \underset{D\to 0}{\longrightarrow} e^{-\alpha D}, \tag{89}$$

$$S_{\mathrm{F}}^{(\mathrm{PLQ})}(D) \underset{D\to\infty}{\longrightarrow} e^{-\beta D/\gamma}, \tag{90}$$

respectively. This gives the initial and final slopes s_{i} and s_{f}, respectively, in the dose–effect curve from the PLQ model as:

$$\text{PLQ}: \quad \text{Initial slope}: \; s_{\mathrm{i}} = \alpha, \quad \text{Final slope}: \; s_{\mathrm{f}} = \frac{\beta}{\gamma}. \tag{91}$$

In the high-dose asymptotes (90), only the leading term βD^2 is retained in the numerator of the biological effect $E_{\mathrm{B}}^{(\mathrm{PLQ})} = (\alpha D + \beta D^2)/(1 + \gamma D)$. However, it is also useful to extrapolate the high-dose limit of the cell surviving curve back to the ordinate axis ($D = 0$). This would give the so-called extrapolation number n. Thus, alongside the same high-dose approximation for the denominator $1 + \gamma D \approx \gamma D$, which has already been made in (90), we shall now retain the full numerator $\alpha D + \beta D^2$ in $(\alpha D + \beta D^2)/(1 + \gamma D)$ to arrive at:

$$\begin{aligned}
-\ln S_{\mathrm{F}}^{(\mathrm{PLQ})}(D) &\underset{D\to\infty}{\longrightarrow} \left\{ \frac{\alpha D + \beta D^2}{1 + \gamma D} - \frac{\beta}{\gamma} \right\} + \frac{\beta}{\gamma} D \\
&= \left\{ \frac{(\alpha\gamma - \beta) D}{\gamma(1 + \gamma D)} \right\} + \frac{\beta}{\gamma} D \\
&\underset{D\to\infty}{\longrightarrow} \left\{ \frac{(\alpha\gamma - \beta) D}{\gamma^2 D} \right\} + \frac{\beta}{\gamma} D \\
&= \left\{ \frac{\alpha\gamma - \beta}{\gamma^2} \right\} + \frac{\beta}{\gamma} D
\end{aligned}$$

so that,

$$S_{\mathrm{F}}^{(\mathrm{PLQ})}(D) \underset{D\to\infty}{\longrightarrow} e^{\frac{\beta - \alpha\gamma}{\gamma^2} - \frac{\beta}{\gamma} D}. \tag{92}$$

This can conveniently be rewritten as:

$$\left.\begin{array}{l} S_{\mathrm{F}}^{(\mathrm{PLQ})}(D) \underset{D\to\infty}{\longrightarrow} ne^{-\frac{\beta}{\gamma}D} \\ \ln S_{\mathrm{F}}^{(\mathrm{PLQ})}(D) \underset{D\to\infty}{\longrightarrow} \ln n - \frac{\beta}{\gamma}D \end{array}\right\}, \tag{93}$$

where the extrapolation number n is given by:

$$\begin{aligned} ln\, n &= \frac{\beta - \alpha\gamma}{\gamma^2} \\ &= \frac{\Delta s_{\mathrm{fi}}}{\gamma}, \quad \Delta s_{\mathrm{fi}} = s_{\mathrm{f}} - s_{\mathrm{i}}. \end{aligned} \tag{94}$$

Thus, the extrapolation number is proportional to the difference Δs_{fi} between the final and initial slopes, $ln\, n \sim s_{\mathrm{f}} - s_{\mathrm{i}} = \Delta s_{\mathrm{fi}}$. The extrapolation number n must be positive and this imposes the following condition:

$$ln\, n > 0 \quad \text{if} \quad \beta > \alpha\gamma. \tag{95}$$

At high doses, it might be useful to constrain the free parameter γ to the relationship:

$$\gamma = \beta D_0, \tag{96}$$

in which case (90) can alternatively be written as:

$$S_{\mathrm{B}}^{(\mathrm{PLQ})}(D) \underset{D\to\infty}{\longrightarrow} e^{-D/D_0} \quad \text{at} \quad \gamma = \beta D_0. \tag{97}$$

With the selection (96), the extrapolation number n from (94) becomes:

$$ln\, n = \frac{1 - \alpha D_0}{\beta D_0^2} \quad \text{at} \quad \gamma = \beta D_0, \tag{98}$$

where the restriction condition (95) is now specified as:

$$ln\, n > 0 \quad \text{if } \alpha < \frac{1}{D_0} \quad \text{at} \quad \gamma = \beta D_0. \tag{99}$$

This positivity requirement (99) for the extrapolation number $n > 0$ reflects the proper relationship between the initial (α) and final $(1/D_0)$ slopes when the third parameter γ in the PLQ model is not adjustable, but rather fixed via $\gamma = \beta D_0$:

$$\text{Initial slope } (\alpha) < \text{Final slope } (1/D_0) \quad \text{at} \quad \gamma = \beta D_0. \tag{100}$$

We re-emphasize that when γ is constrained to the relation $\gamma = \beta D_0$, the high-dose limit of the PLQ model becomes $S_{\rm F}^{\rm (PLQ)}(D) \sim e^{-D/D_0}$, as required by the experimental data. Of course, any constraint imposed on one parameter inevitably introduces a bias into the estimates of the remaining parameters. However, irrespective of whether γ is pre-assigned to be of the form $\gamma = \beta D_0$ or kept free, the other two parameters α and β are always mutually dependent, since by definition $\beta = \mu\alpha$. Moreover, in view of (67) instead of γ, we could use $\omega\alpha/2$, where ω takes the role of an adjustable parameter. This shows that in the general case without resorting to (96), the third parameter $\omega\alpha/2$ in the PLQ model is connected to the direct cell kill component α. Overall, the unconstrained version of the PLQ model is negligibly more involved than the LQ model from the computational viewpoint due to the presence of merely one additional parameter γ or equivalently, $\omega\alpha/2$. The constrained variant of the PLQ model, with γ fixed by the prescription $\gamma = \beta D_0$, has only two parameters α and β, since D_0 can be considered as the input data to be read off from the final slope of the experimentally measured cell surviving fraction at larger values of D. In either case, the advantage of the PLQ over the LQ model is at least twofold:

- (A) a richer mathematical function with the underlying mechanisms and,
- (B) a smooth switch from the incorrect quadratic (Gaussian) to the correct (exponential) asymptote at high doses, as required by the measurements.

4.4 The Padé linear-quadratic model and the Michaelis–Menten kinetics

Inserting (18) for $\mathrm{E}_{\rm B}^{\rm (LQ)}$ into the numerator of $\mathrm{E}_{\rm B}^{\rm (PLQ)}$ from the Padé quotient (78), we can alternatively write the biological effect in the PLQ model as:

$$\mathrm{E}_{\rm B}^{\rm (PLQ)} = v_0(\zeta + D) = v_0(z_{\rm D} + D), \tag{101}$$

where,

$$v_0 = \frac{\beta D}{1 + \gamma D}. \tag{102}$$

In (101), use is made of the quantity ζ, or equivalently, z_{D} from (34), where z_{D} is the dose-averaged specific energy from microdosimetry. The quantity v_0 is velocity or rate, which is equivalent to the initial reaction velocity from the enzyme kinetics of Michaelis–Menten (MM)[7] for the following irreversible chemical reaction (enzyme catalysis) with formation and destruction of the enzyme-lesion complex:

$$[\mathrm{E}] + [\mathrm{L}] \xrightarrow[k_1]{} [\mathrm{EL}] \xrightarrow[k_2]{} [\mathrm{E}] + [\mathrm{R}]. \tag{103}$$

Here [E], [L], [EL], and [R] are the concentrations of the free enzyme molecules, lesions (primarily DNA), enzyme-lesion complex and repaired lesions, respectively. Quantities k_1 and k_2 are the rate coefficients for formation and destruction/dissociation of the intermediate complex molecule [EL]. In this chemical reaction, the free enzyme molecule [E] binds the radiation damaged DNA molecule (a lesion [L]) into an intermediate and temporarily living unstable complex molecule [EL]. This compound facilitates the enzymatic synthesis of DNA. After completion of this intermediate stage of the reaction, the complex [EL] decays, thus producing the repaired lesions [R] and enzymes [E] that are again free for further bindings with other lesions. As mentioned earlier in (21), the number of lesions is usually assumed to be proportional to dose D:

$$[\mathrm{L}] \sim D = \kappa D \equiv D, \tag{104}$$

where κ could be taken as $\kappa = k_0 \equiv 1/\mathrm{D}_0$ or as a constant of unit absolute value ($\kappa \equiv 1$). When writing $[\mathrm{L}] = D$ in (104) and afterwards, it is understood that $[\mathrm{L}] = D \equiv 1 \cdot D$, where "1" takes care of the proper units in the passage from a dose to a molar concentration. This convention is done to avoid introducing a superfluous parameter only for the purpose of conversion of the units. In this way, Eq. (102) can equivalently be written as:

$$v_0 = \frac{\beta[\mathrm{L}]}{1 + \gamma[\mathrm{L}]}. \tag{105}$$

Using Eq. (104) and the definition:

$$K_{\mathrm{M}} \equiv \frac{1}{\gamma}, \tag{106}$$

we can cast expression (105) into its form used in the MM kinetics:

$$v_0 = \frac{v_{\max}[\mathrm{L}]}{K_{\mathrm{M}} + [\mathrm{L}]}, \tag{107}$$

where $\upsilon_{\max}$ is the maximal velocity given by:

$$\upsilon_{\max} \equiv \frac{\beta}{\gamma}. \tag{108}$$

Velocities υ_0, and consequently, $\upsilon_{\max}$ are given in units Gy^{-1}. On the other hand, in the original Michaelis–Menten velocity for irreversible reaction (103), we have:

$$K_\mathrm{M} = \frac{k_2}{k_1}, \tag{109}$$

$$\upsilon_{\max} = k_2[\mathrm{E}]_0, \tag{110}$$

where $[\mathrm{E}]_0$ is the initial concentration of enzymes (the number of enzymes at the onset of the reaction), which is assumed to be constant throughout and, therefore, equal to the total enzyme concentration $[\mathrm{E}] \equiv [\mathrm{E}]_\mathrm{tot}$ at any subsequent time. Quantity K_M is the Michaelis–Menten[7] constant with the dimension of concentration. More specifically, this constant for irreversible variant (103) of the general MM enzyme catalysis, represents the concentration of lesions ($[\mathrm{L}] \approx K_\mathrm{M}$) at which velocity υ_0 attains one half of $\upsilon_{\max}$, as follows $\{\upsilon_0\}_{[\mathrm{L}]\approx K_\mathrm{M}} \approx \upsilon_{\max}[\mathrm{L}]/([\mathrm{L}] + [\mathrm{L}]) = \upsilon_{\max}/2$:

$$\upsilon_0 \approx \frac{\upsilon_{\max}}{2} \quad \text{at} \quad [\mathrm{L}] \approx K_\mathrm{M}. \tag{111}$$

In the same approximation, the biological effect $\mathrm{E}_\mathrm{B}^{(\mathrm{PLQ})}$ becomes:

$$\mathrm{E}_\mathrm{B}^{(\mathrm{PLQ})} \approx \frac{\upsilon_{\max} + \alpha}{2} K_\mathrm{M} \quad \text{at} \quad [\mathrm{L}] \approx K_\mathrm{M}. \tag{112}$$

At small concentration of lesions, the reaction velocity υ_0 is reduced to:

$$\upsilon_0 = \frac{\upsilon_{\max}[\mathrm{L}]}{K_\mathrm{M}\,(1 + [\mathrm{L}]/K_\mathrm{M})} \underset{[\mathrm{L}]/K_\mathrm{M} \ll 1}{\approx} \upsilon_{\min}, \tag{113}$$

where,

$$\upsilon_{\min} = \frac{\upsilon_{\max}[\mathrm{L}]}{K_\mathrm{M}}. \tag{114}$$

The use of Eqs. 106 and (108)–(110) permits connecting e.g., the final slope (β/γ) in the PLQ model with the enzyme kinetic parameters as:

$$\text{Final slope}: \quad \Gamma_{\beta\gamma} = \frac{\beta}{\gamma} = \upsilon_{\max} = k_2[\mathrm{E}]_0. \tag{115}$$

A similar connection can also be deduced for the extrapolation number using Eq.(94) as follows: $\ln n = (\beta - \alpha\gamma)/\gamma^2 = (\beta/\gamma - \alpha)/\gamma = (\upsilon_{\max} - \alpha)K_{\mathrm{M}}$, so that:

$$\text{Logarithm of the extrapolation number:} \quad \ln n = (\upsilon_{\max} - \alpha)K_{\mathrm{M}}. \tag{116}$$

Hence, the larger (the smaller) the product of the enzyme concentration $[\mathrm{E}]_0$ and the dissociation rate constant k_2, the steeper (the shallower) the final slope of the dose–effect curve. This is correct, since more significant values of $k_2[\mathrm{E}]_0$ would enhance the chance for a greater enzymatic activity with the ensuing larger concentration [R] of repaired lesions. Such an outcome should mitigate the influence of the direct cell kill mechanism (αD) and, therefore, would increase cell survival, as manifested by a departure from the pure exponential bending $\mathrm{e}^{-\alpha D}$ in the dose–effect curve. Consequently, a shouldered cell surviving curve appears, as a signature of the enzymatic repair of radiation-induced lesions. This is also reflected in the repair ratio $\Gamma_{\beta\alpha} = \beta/\alpha$ from (79), which can be rewritten in the form:

$$\Gamma_{\beta\alpha} = \frac{\beta}{\alpha} = \Gamma_{\gamma\alpha}\{k_2[\mathrm{E}]_0\}, \tag{117}$$

where the second repair ratio $\Gamma_{\gamma\alpha}$ is equal to γ/α, according to (79). The larger values of β/α imply a more noticeable influence of repair. Expression (117) confirms this expectation through a direct proportionality between the quotient β/α and the enzyme concentration $[\mathrm{E}]_0$ available for repair. Moreover, the same ratio β/α is also directly proportional to the catalysis rate k_2 and, thus, to the efficiency of the enzymatic repair system in converting the radiation damage [L] to the repaired lesions [R] in the final reaction path $[\mathrm{EL}] \xrightarrow[k_2]{} [\mathrm{E}] + [\mathrm{R}]$, so that:

$$\Gamma_{\beta\alpha} \sim k_2[\mathrm{E}]_0. \tag{118}$$

In the equivalence relation (118), the proportionality constant is $\Gamma_{\gamma\alpha}$, where $\Gamma_{\gamma\alpha} = \gamma/\alpha$ from (117). This constant is associated with linear and nonlinear contributions from all the powers that are inherent in the binomial $(\delta + \Gamma_{\gamma\alpha}D)^{-1}$, as mentioned earlier.

Rewriting (104) as $\mathrm{E}_{\mathrm{B}}^{(\mathrm{PLQ})} = (\alpha D + \beta D^2)/(1 + \gamma D) = (\beta/\gamma)(\alpha/\beta + D) \times (1/\gamma + D)$ and using (106) and (108) for $1/\gamma = K_{\mathrm{M}}$ and $\beta/\gamma = \upsilon_{\max}$, respectively, we can equivalently express the biological effect (76) and the cell surviving fraction (77) in the Michaelis–Menten representation as:

$$\begin{aligned} \mathrm{E}_{\mathrm{B}}^{(\mathrm{PLQ})} &= v_0\,(z_{\mathrm{D}} + [\mathrm{L}]) \\ &= \left(\frac{v_{\max}[\mathrm{L}]}{K_{\mathrm{M}} + [\mathrm{L}]}\right)(z_{\mathrm{D}} + [\mathrm{L}])\,, \end{aligned} \tag{119}$$

and,

$$\begin{aligned} S_{\mathrm{F}}^{(\mathrm{PLQ})}(D) &= e^{-v_0(z_{\mathrm{D}}+[\mathrm{L}])} \\ &= e^{-\left(\frac{v_{\max}[\mathrm{L}]}{K_{\mathrm{M}}+[\mathrm{L}]}\right)(z_{\mathrm{D}}+[\mathrm{L}])}. \end{aligned} \tag{120}$$

The connection among the three parameters $\{\alpha, \beta, \gamma\}$ with the equivalent triple $\{z_{\mathrm{D}}, v_{\max}, K_{\mathrm{M}}\}$ from the PLQ model is summarized as:

$$\left.\begin{array}{ll} z_{\mathrm{D}} = \frac{\alpha}{\beta}; & \text{Direct/Indirect mechanisms , (Cell kill)/(Cell repair)} \\ v_{\max} = \frac{\beta}{\gamma}; & \text{Experimentally measurable maximal enzyme velocity} \\ K_{\mathrm{M}} = \frac{1}{\gamma}; & \text{Experimentally measurable Michaelis–Menten constant} \end{array}\right\}. \tag{121}$$

Overall, the MM rate constant K_{M} and the maximal enzyme velocity $v_{\max}$ can be measured in standard enzyme experiments. Moreover, the initial (α) and final $(v_{\max})$ slopes can be extracted from the experimental data for the given cell surviving curve and so could the extrapolation number n. Also, as soon as the triple $\{\alpha, v_{\max}, K_{\mathrm{M}}\}$ becomes available, the extrapolation number can be obtained from Eq. (116). Thus, the basic elements of the dose–effect curve in the PLQ model are recapitulated via:

$$\left.\begin{array}{ll} \mathrm{s}_i = \alpha; & \text{Initial slope} \\ \mathrm{s}_f = v_{\max}; & \text{Final slope} \\ \ln n = (v_{\max} - \alpha)K_{\mathrm{M}}; & \text{logarithm of the extrapolation number} \end{array}\right\}. \tag{122}$$

When parameter γ is pre-assigned as $\gamma = \beta D_0$, by reference to (96), then according to (100) the final slope β/γ becomes $1/D_0$, so that:

$$D_0 = \frac{1}{v_{\max}} = \frac{1}{k_2[\mathrm{E}]_0} \quad \text{at} \quad \gamma = \beta D_0. \tag{123}$$

This result $(D_0 \sim 1/k_2)$ shows that the mean lethal dose D_0 is proportional to the reciprocal of rate constant k_2 for enzyme-mediated creation of a repaired lesion [R], which is the product substance in reaction (103) for enzyme catalysis.

At high doses, the enzyme-lesion reaction velocity v_0 tends to the constant value $v_{\max}$, which is the fastest rate possible for the given enzyme concentration $[\mathrm{E}]_0$. This means that the rectangular hyperbola $v_0 = \alpha D/(1+\gamma D)$ from (102) as a function of D has reached a plateau at larger doses. Stated equivalently, the curve $v_0 = v_{\max}[\mathrm{L}]/(K_{\mathrm{M}} + [\mathrm{L}])$ from (107), as a function of $[\mathrm{L}]$ is leveled off for higher lesion concentrations, $[\mathrm{L}]$. Such a high-dose or a high concentration of lesions described by the reaction velocity v_0 in terms of the independent variable D or $[\mathrm{L}]$ is due to the limited amount of enzymes (~ 100 enzyme molecules per lesion) that are available for repair of radiation-damaged cells. At high doses, the average number of lesions is sufficiently large to overwhelm and thus inactivate the enzyme repair system, after which point every radiation damage is essentially lethal. This saturation of enzymes by lesions is the signature for a switch from the cell repair to the cell kill mechanism corresponding to the passage from the second- to the first-order Michaelis–Menten kinetics.

Expressions (119) and (120) are written in a way which separates the two parts of the PLQ model, by exhibiting the contributions from: the enzyme velocity $v_0 = v_{\max}[\mathrm{L}]/(K_{\mathrm{M}} + [\mathrm{L}])$ and the precipitation of the dose-averaged specific energy around the lesion $z_{\mathrm{D}} + [\mathrm{L}]$. This is merely a formal separation, since the dose-averaged specific energy z_{D} is not a quantity which is independent of the enzymatic repair. Quite the contrary, combining the definition $z_{\mathrm{D}} = \beta/\alpha$ with $\beta = v_{\max}/K_{\mathrm{M}}$, we have:

$$z_{\mathrm{D}} = \alpha \left\{ \frac{v_{\max}}{K_{\mathrm{M}}} \right\}. \tag{124}$$

Thus, the enzyme repair system effectively modifies the cell radiosensitivity α by the multiplying factor $v_{\max}/K_{\mathrm{M}}$ due to the Michaelis–Menten chemical kinetics. Because of this inter-connection between z_{D} and $\{v_{\max}, K_{\mathrm{M}}\}$, the product $v_0(z_{\mathrm{D}}) + [\mathrm{L}]$, or equivalently, $v_0(z_{\mathrm{D}} + D)$ appearing in the effect $\mathrm{E}_{\mathrm{B}}^{(\mathrm{PLQ})}$ from the PLQ model should not be taken too literally to mean a true separation of the two independent mechanisms, the one being enzymatic repair (v_0) and the other being of microdosimetric origin ($z_{\mathrm{D}} + D$). It is merely for the reason of drawing an analogy rather than making a one-to-one correspondence that we used the notation z_{D} from microdosimetry for the defining quotient α/β of the two parameters in the PLQ model for the cell kill (α) and cell repair (β) mechanisms of the cell response to radiation. The microdosimetric parameter z_{D} was also employed earlier in Eq. (33)

for the effect $\mathrm{E}_{\mathrm{B}}^{(\mathrm{LQ})}$ in the LQ model. There, following Kellerer and Rossi,[13] we expressed the defining relation $\mathrm{E}_{\mathrm{B}}^{(\mathrm{LQ})} = \alpha D + \beta D^2 = \beta D(\alpha/\beta + D)$ as $\mathrm{E}_{\mathrm{B}}^{(\mathrm{LQ})} = \beta D(z_{\mathrm{D}} + D)$, where $z_{\mathrm{D}} = \alpha/\beta$. Using the assumed direct proportionality between the lesion number (concentration) [L] and dose D, via $[\mathrm{L}] = \kappa D \equiv D$, as per (106) and (108), we can further write:

$$\begin{aligned} \mathrm{E}_{\mathrm{B}}^{(\mathrm{LQ})} &= \beta D\,(z_{\mathrm{D}} + D) \\ &= \{\beta[\mathrm{L}]\}\,(z_{\mathrm{D}} + [\mathrm{L}]) \\ &\equiv v_0^{(\mathrm{LQ})}\,(z_{\mathrm{D}} + [\mathrm{L}])\,, \end{aligned}$$

where,

$$\begin{aligned} v_0^{(\mathrm{LQ})} &= \beta[\mathrm{L}] \\ &= \frac{v_{\max}[\mathrm{L}]}{K_{\mathrm{M}}}. \end{aligned} \tag{125}$$

In this way, the effect (33) and the surviving fraction (16) from the LQ model can be cast in the following form of the Michaelis–Menten terminology:

$$\begin{aligned} \mathrm{E}_{\mathrm{B}}^{(\mathrm{LQ})} &= v_0^{(\mathrm{LQ})}\,(z_{\mathrm{D}} + [\mathrm{L}]) \\ &= \left(\frac{v_{\max}[\mathrm{L}]}{K_{\mathrm{M}}}\right)(z_{\mathrm{D}} + [\mathrm{L}])\,, \end{aligned} \tag{126}$$

and,

$$\begin{aligned} S_{\mathrm{F}}^{(\mathrm{LQ})}(D) &= e^{-v_0^{(\mathrm{LQ})}(z_{\mathrm{D}} + [\mathrm{L}])} \\ &= e^{-\left(\frac{v_{\max}[\mathrm{L}]}{K_{\mathrm{M}}}\right)(z_{\mathrm{D}} + [\mathrm{L}])}. \end{aligned} \tag{127}$$

Notice that both surviving fractions (120) and (127) in the PLQ and LQ models, respectively, are expressed through *three* parameters $\{z_{\mathrm{D}}, v_{\max}, K_{\mathrm{M}}\}$. However, there is a special circumstance within $v_0^{(\mathrm{LQ})}$ in the LQ model permitting a reduction from this apparent three to only two degrees of freedom. This is possible because the two parameters $v_{\max}$ and K_{M} do not appear individually in $S_{\mathrm{F}}^{(\mathrm{LQ})}(D)$ at different places, but rather they enter Eq. (127) through $v_0^{(\mathrm{LQ})}$ exclusively as the ratio $v_{\max}/K_{\mathrm{M}}$. This leads to a reduction from $\{z_{\mathrm{D}}, v_{\max}, K_{\mathrm{M}}\}$ to $\{z_{\mathrm{D}}, \beta\}$, where $\beta = v_{\max}/K_{\mathrm{M}}$ and $z_{\mathrm{D}} = \alpha/\beta$.

As such, the apparent three parameter set $\{z_{\rm D}, v_{\rm max}, K_{\rm M}\}$ is, in fact, a collection of the usual two parameters α and β from the LQ model. In the general version of the PLQ model[§], none of the three parameters could be eliminated so as to have only two remaining degrees of freedom. The reason is that, instead of the velocity $v_0^{\rm (LQ)} = v_{\rm max}/K_{\rm M}$ from the effect $\mathrm{E}_{\rm B}^{\rm (LQ)} = v_0^{\rm (LQ)}(z_{\rm D} + [\mathrm{L}])$ in the LQ model, the initial enzyme velocity $v_0 = v_{\rm max}[\mathrm{L}]/(K_{\rm M} + [\mathrm{L}])$ appears in the corresponding effect in the LQ model via:

$$\begin{aligned}\mathrm{E}_{\rm B}^{\rm (PLQ)} &= v_0\,(z_{\rm D} + [\mathrm{L}]) = \left\{\frac{v_{\rm max}[\mathrm{L}]}{K_{\rm M} + [\mathrm{L}]}\right\}(z_{\rm D} + [\mathrm{L}]) \\ &= \left\{\frac{v_{\rm max}[\mathrm{L}]}{K_{\rm M}}\,(z_{\rm D} + [\mathrm{L}])\right\}\left(1 + \frac{[\mathrm{L}]}{K_{\rm M}}\right)^{-1} \\ &= \mathrm{E}_{\rm B}^{\rm (LQ)}\left(1 + \frac{[\mathrm{L}]}{K_{\rm M}}\right)^{-1},\end{aligned}$$

so that,

$$\mathrm{E}_{\rm B}^{\rm (PLQ)} = \frac{\mathrm{E}_{\rm B}^{\rm (LQ)}}{1 + [\mathrm{L}]/K_{\rm M}}, \tag{128}$$

as in (78). Thus, the general PLQ model possesses three parameters because any attempt to express $\mathrm{E}_{\rm B}^{\rm (PLQ)}$ through the two parameters $\{\alpha, \beta\}$ in $\mathrm{E}_{\rm B}^{\rm (LQ)}$ invariably leads to the emergence of the third parameter via the isolated term $1/K_{\rm M} = \gamma$. The above juxtaposition of enzyme velocities $v_0^{\rm (LQ)}$ and v_0 from the LQ and PLQ models, respectively, is instructive, since it facilitates one of the mechanistic levels of comparison between these two formalisms. This is best seen by observing that:

$$v_0^{\rm (LQ)} = v_{\rm min}, \tag{129}$$

where $v_{\rm min}$ is the asymptote of the reaction velocity v_0 at small concentration of lesions, as per (113). Hence, the PLQ model with its Michaelis–Menten chemical kinetics of enzyme catalysis for lesion repair can help

---

[§] The general PLQ model is the one which excludes the special case in which the final slope $v_{\rm max}$ is constrained to satisfy the relation $v_{\rm max} = 1/D_0$ from (123), provided that the mean lethal dose D_0 is viewed as known by e.g., reading off the ending, exponential part of the curve for the cell surviving fraction.

understand one of the limitations of the LQ model, such as the restriction to (129). A small concentration of lesions is associated with low-dose exposure of cells to radiation. Therefore, restriction of $v_0^{(\mathrm{LQ})}$ to only small repair velocity $v_{\min}$ of enzyme molecules means that the validity of the LQ model is limited to low doses. This conclusion from the Michaelis–Menten formalism is in accordance with the well-known fact that the LQ model is a low-dose approximation to cell surviving fraction.

5. RESULTS: COMPARISON OF RADIOBIOLOGICAL MODELS WITH MEASUREMENTS

The relative performance of the PLQ and LQ models is illustrated by their comparisons with experimental data. This is done on the level of cell surviving fractions $S_{\mathrm{F}}(D)$ and also by plotting the so-named full effect graph.[4] Such twofold comparisons are deemed necessary for the reasons that run as follows.

At low-to-intermediates doses, quite different radiobiological models can still be in reasonably close agreement with experimental data when plotted as cell surviving fractions $S_{\mathrm{F}}(D)$ versus D. This is also evident from each panel (i) on Figures 14.1–14.3 when comparing the PLQ and LQ models with measurements. Of course, it is also clear from the same panel (i) on these figures that this type of relatively good agreement between these two formalisms ceases to exist at larger doses because of the prevailing Gaussian and exponential shapes of cell surviving fractions in the LQ and PLQ model, respectively. The displayed experimental data for the corresponding cell surviving fractions favor the predictions by the PLQ model at all doses. This confirms the theoretical expectation that the PLQ model is universally valid at any dose D. By contrast, at high doses the LQ model is seen to break down, as it largely underestimates the surviving fractions from the measurements.

Overall, at small and intermediate doses, survival curves do not appear to be the most suitable for differentiating among various models while evaluating their clinical usefulness in radiotherapy. Moreover, dose–effect functions $S_{\mathrm{F}}(D)$ are rarely of direct use in dose planning systems that, instead, most frequently employ the biological effect $\mathrm{E}_{\mathrm{B}}(D)$ and the biologically effective dose $\mathrm{BED}(D)$. There is yet another useful relationship, which offers the possibility for a more stringent assessment of clinical adequacy of different biophysical models. This is the so-called full-effect plot, or Fe-plot,[4] which is associated with the ratio of the biological effect and the absorbed dose,

$\mathrm{Fe}(D) = (1/D)\mathrm{E_B}(D)$, or equivalently, $\mathrm{Fe}(D) = -(1/D)\ln S_\mathrm{F}(D)$. This quantity is also known by the alternative name "reactivity"[13] and denoted by $R(D)$, which is also used in panel (ii) on Figures 14.1–14.3:

$$\begin{aligned}\mathrm{Fe}(D) &\equiv R(D)\\ &= \frac{1}{D}\mathrm{E_B}(D)\\ &= -\frac{1}{D}\ln S_\mathrm{F}(D).\end{aligned} \tag{130}$$

Such a biological effect per unit dose represents the full effectiveness of radiation on cell survival for each given level of dose exposure. It is this Fe-plot, depicting $\mathrm{Fe}(D)$ versus D, or equivalently, $R(D)$ as a function of dose, which can distinguish one model from another in the most dramatic way, as is clear from panel (ii) on Figures 14.1–14.3. In the Fe-plot, the LQ model yields a linear radiation response, as displayed by a straight line of a slope β and the intercept α on the ordinate:

$$\mathrm{Fe}^{(\mathrm{LQ})}(D) = R^{(\mathrm{LQ})}(D) = \alpha + \beta D. \tag{131}$$

This means that the effectiveness of radiation at every dose level would have no bound, as it would be indefinitely increased with augmentation of D. Such a pattern is at variance with most experimental data $\mathrm{Fe}^{(\mathrm{exp})}(D)$ that are seen on plot (ii) of Figures 14.1–14.3 to saturate to some constant values at high doses. This behavior is also predicted by the PLQ model whose Fe-plot levels off to the constant final slope β/γ, as D becomes very large:

$$\mathrm{Fe}^{(\mathrm{PLQ})}(D) = R^{(\mathrm{PLQ})}(D) = \frac{\alpha + \beta D}{1 + \gamma D} \underset{D\to\infty}{\longrightarrow} \frac{\beta}{\gamma}. \tag{132}$$

Here, the rectangular hyperbola $(\alpha + \beta D)/(1 + \gamma D)$ from the PLQ model implies the existence of repair of radiation damage to the cell through a mechanism of the Michaelis–Menten type for enzyme-lesion catalysis. As such, panel (ii) on Figures 14.1–14.3 for the Fe-plot shows excellent agreement of the PLQ model with the corresponding experimental data.

Overall, we can conclude that the universal applicability of the PLQ model to all doses is demonstrated in both panels (i) and (ii) of Figures 14.1–14.3 for cell surviving fractions and the Fe-plot. Simultaneously, these comparisons prove the marked superiority of the PLQ over the LQ model. This outperformance of the latter by the former radiobiological model testifies to the adequacy of the mechanistic underpinning of the

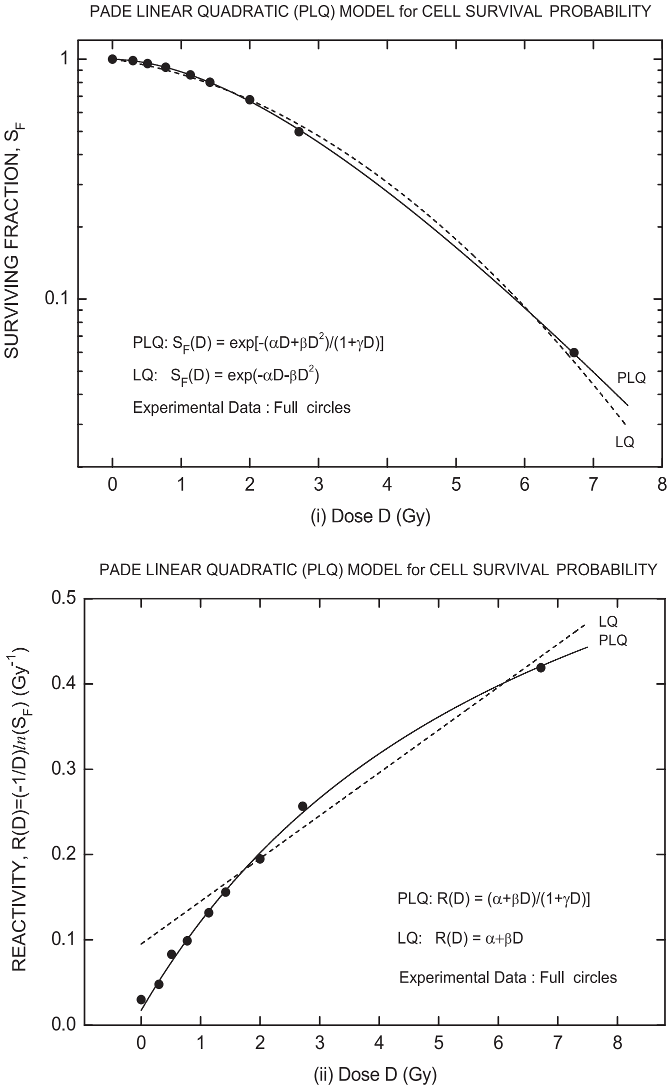

Figure 14.1 Cell surviving fractions $S_F(D)$ as a function of radiation dose D in Gy (top panel (i)). Bottom panel (ii), as the Fe-plot, shows the so-called reactivity $R(D)$ given by the product of the reciprocal dose D^{-1} and the negative natural logarithm of $S_F(D)$, as the ordinate versus D as the abscissa. Any departure of experimental data from a straight line indicates inadequacy of the LQ model for the Fe-plot. Experimental data (full circles):[30] the mean clonogenic surviving fractions $S_F(D)$ (panel(i)) and $R(D) \equiv -(1/D)\ln(S_F)$ (panel (ii)) for the human small cell lung cancer line (U1690) irradiated by 190 kVp X-rays. Theories: solid curve for the PLQ (Padé linear-quadratic) model and dashed curve for the LQ (linear-quadratic) model (the straight line $\alpha + \beta D$ on panel (ii)).

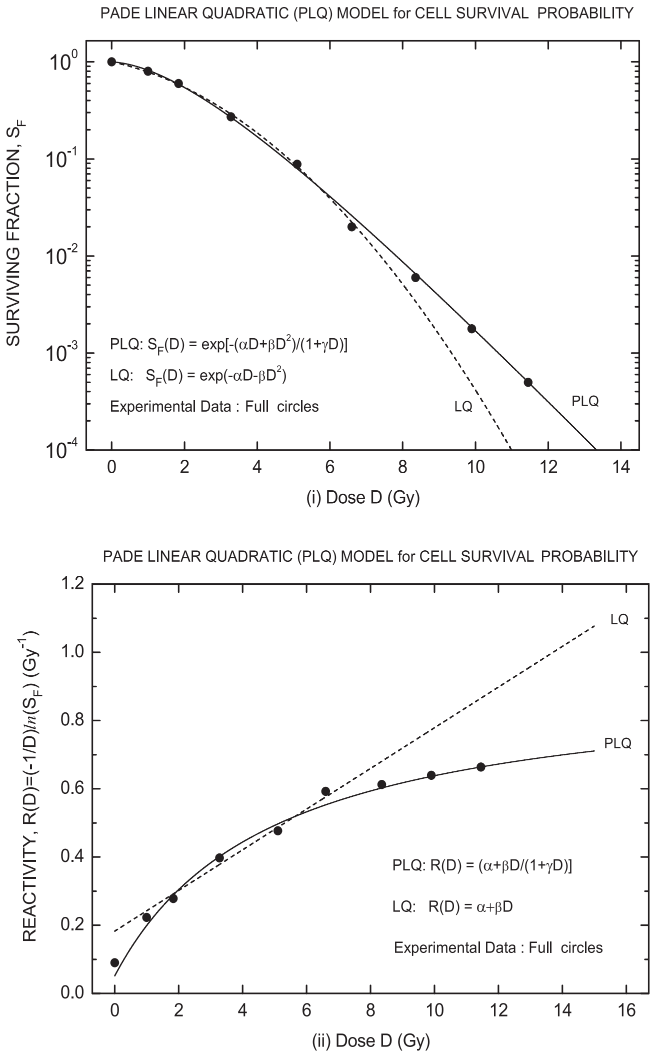

Figure 14.2 Cell surviving fractions $S_F(D)$ as a function of radiation dose D in Gy (top panel (i)). Bottom panel (ii), as the Fe-plot, shows the so-called reactivity $R(D)$ given by the product of the reciprocal dose D^{-1} and the negative natural logarithm of $S_{\mathrm{F}}(D)$, as the ordinate versus D as the abscissa. Any departure of experimental data from a straight line indicates inadequacy of the LQ model for the Fe-plot. Experimental data (full circles):[17] the mean clonogenic surviving fractions $S_{\mathrm{F}}(D)$ (panel(i)) and $R(D) \equiv -(1/D)\ln(S_{\mathrm{F}})$ (panel (ii)) for the Chinese hamster cells grown in culture and irradiated by 50 kVp X-rays. Theories: solid curve for the PLQ (Padé linear-quadratic) model and dashed curve for the LQ (linear-quadratic) model (the straight line $\alpha + \beta D$ on panel (ii)).

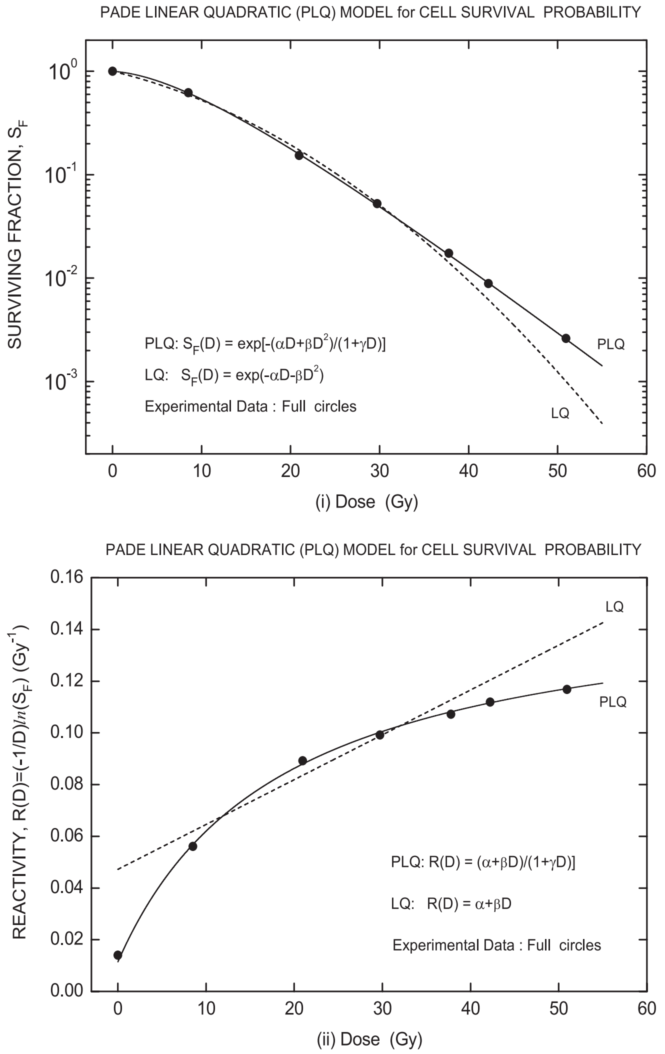

Figure 14.3 Cell surviving fractions $S_F(D)$ as a function of radiation dose D in Gy (top panel (i)). Bottom panel (ii), as the Fe-plot, shows the so-called reactivity $R(D)$ given by the product of the reciprocal dose D^{-1} and the negative natural logarithm of $S_F(D)$, as the ordinate versus D as the abscissa. Any departure of experimental data from a straight line indicates inadequacy of the LQ model for the Fe-plot. Experimental data (full circles):[31] the mean clonogenic surviving fractions $S_F(D)$ (panel(i)) and $R(D) \equiv -(1/D)\ln(S_F)$ (panel (ii)) for the asynchronous V79 Chinese hamster cells irradiated hypoxically by 250 kVp X-rays with a concurrent 30 min exposure to the sulfhydryl-binding agent, N-ethylmaleimide, of low concentration 0.75 μM. Theories: solid curve for the PLQ (Padé linear-quadratic) model and dashed curve for the LQ model (the straight line $\alpha + \beta D$ on panel (ii)).

Padé linear-quadratic formalism, which is rooted in a firm theoretical and practical basis of chemical kinetics for repair of radiation damage by means of enzyme-lesion catalytic reaction.

It should be noted that the concept of the Fe-plot is critically important for both the conventional fractionation and hypofractionation. It impacts one of the most delicate decisions by radiotherapists regarding the question: given that radiation indiscriminately damages both tumorous and healthy cells, how should the total dose vary as a function of the overall irradiation time, as well as the number of fractions, in order to maintain a constant biological end effect and also minimize complications to the normal tissues at risk?

6. DISCUSSION AND CONCLUSION

6.1 Biologically expressed response of the cell to irradiation

It has been argued that the ultimate success of radiotherapy rests upon the possibility to properly understand cell repair after irradiation.[14, 15] The main focus of this chapter is on enzymatic repair mechanisms encountered in radiobiological descriptions of dose–effect relationships. With this goal, we further elaborate the Padé linear-quadratic model, or the PLQ model[4–6] for cell surviving fraction, $S_F^{(PLQ)}(D)$, as a function of a single absorbed dose D. In this novel biophysical model, the biological effect of radiation, $E_B^{(PLQ)}(D) = -\ln S_F^{(PLQ)}(D)$, is given by the Padé approximant, $E_B^{(PLQ)}(D) = (\alpha D + \beta D^2)/(1 + \gamma D)$. By a smooth transition, this rational function becomes automatically linear at both low and high doses, $E_B^{(PLQ)}(D) \underset{D\to 0}{\longrightarrow} \alpha D$ and $E_B^{(PLQ)}(D) \underset{D\to\infty}{\longrightarrow} (\beta/\gamma)D$. Precisely such types of exponentials have been observed by numerous measurements in the said two dose limits. The PLQ model has three parameters $\{\alpha, \beta, \gamma\}$. Here, as usual, radiosensitivity α is a single event inactivation constant in units of Gy^{-1}. However, parameter β, which is in units of Gy^{-2}, is derived from the introduction of a delay time in the cell response to radiation insult. This delay is associated with the existence of a repair or recovery time τ. Any two consecutive radiation events or hits would be wasted, i.e., not registered at all by the cell, if they were separated by a time interval Δt such that $\Delta t < \tau$. The cell becomes effectively insensitive to such consecutive hits. Parameter γ is the reciprocal of the Michaelis–Menten constant, K_M, from the theory of chemical kinetics for enzyme catalysis. This latter quantity is the concentration of lesions at which the enzyme velocity of repair, v_0, attains one half of its maximum,[7] i.e. $v_{\max}$.

6.2 Dose–effect relationships at low, intermediate (shoulder), and high doses

One of the most important advantages of the PLQ model relative to the linear-quadratic model is of particular relevance to radiotherapy by high doses per fraction used especially in stereotactic radiosurgery. For this treatment modality, called hypofractionation, the LQ model is inadequate, since its biological effect, $\mathrm{E}_{\mathrm{B}}^{(\mathrm{LQ})}(D) = \alpha D + \beta D^2$, has a high-dose asymptote $\mathrm{E}_{\mathrm{B}}^{(\mathrm{LQ})}(D) \underset{D\to\infty}{\longrightarrow} \beta D^2$, which is at variance with the corresponding experimental data exhibiting the exponential shape, $\mathrm{E}_{\mathrm{B}}^{(\exp)}(D) \sim D$, as $D \to \infty$. This severely hampers the proper use of one of the key quantities in dose planning systems, the so-named biologically effective dose, which is a scaled biological effect, $\mathrm{BED}(D) = (1/\alpha)\mathrm{E}_{\mathrm{B}}(D)$. Since the LQ model is not universally valid at all doses, the entire set of the given experimental data for $\mathrm{BED}^{(\exp)}(D)$ cannot be used for extracting the biological parameters. Therefore, the usual practice is to carry out a segmentation of the given set of experimental data $\mathrm{BED}^{(\exp)}(D)$ into different dose ranges to estimate the ratio β/α from the postulated relation $\mathrm{BED}^{(\exp)}(D) \approx \mathrm{BED}^{(\mathrm{LQ})}(D)$, where $\mathrm{BED}^{(\mathrm{LQ})}(D) = (1/\alpha)\mathrm{E}_{\mathrm{B}}^{(\mathrm{LQ})}(D) = 1 + (\beta/\alpha)D$. A serious disadvantage of such a procedure is that the quotient β/α and, therefore, $\mathrm{BED}^{(\exp)}(D)$ become dose-range dependent. This introduces complications in employing the BED concept to compare the conventional fractionation (2 Gy per fraction)[16–20] with hypofractionation.[21, 22] Such comparisons are critical for extrapolating the abundant experience with conventional fractionation to hypofractionated treatments. This is vital given that larger doses per fraction have a tendency of causing more severe late side effects relative to the conventional small size fractions. Additionally, the LQ model has difficulties in coping with cell survival curves with broad shoulders.[23, 24] Moreover, on top of continuously bending down as dose D is enlarged, pointing to the non-existence of the final slope and the extrapolation number n, the LQ model can break down at very low doses, as well.[12]

6.3 Beyond the linear-quadratic model of cell inactivation

In order to partially overcome the mentioned drawbacks of the LQ model, Paganetti and Goitein[25] introduced in 2001, within the amorphous track partition (ATP) model, a modification containing a Heaviside step function with a transition dose D_{T}. Their surviving fraction coincides with the linear-quadratic response $\mathrm{e}^{-\alpha D - \beta D^2}$ from the LQ model at $D \leqslant D_{\mathrm{T}}$

and, conversely, becomes a linear function of dose D at $D > D_{\mathrm{T}}$ via $\mathrm{e}^{-\alpha D_{\mathrm{T}}-\beta D_{\mathrm{T}}^2-\gamma(D-D_{\mathrm{T}})}$. Here, γ is either a third independent fitting parameter or the final slope fixed by the continuity constraint of the derivative of the surviving fraction at $D = D_{\mathrm{T}}$, which leads to $\gamma = \alpha + 2\beta D_{\mathrm{T}}$. More recently in 2008, the modified LQ model from Ref. 25 has been renamed as the universal survival curve (USC) model by Park et al.,[26] and the linear-quadratic-linear (LDL) model by Astrahan.[27] However, the common feature of Refs. 25–27 is an *ad hoc* switch from the incorrect D^2 high-dose component in the LQ model to the corresponding term with a linear dose dependence ($\sim D$) in the cell surviving fraction. The transition dose $D = D_{\mathrm{T}}$ at this switch has no justifiable biological significance, as it represents just another free parameter. Typical measurements of surviving fractions for most mammalian cell lines can be trustworthy only down to the 10^{-3} survival level. For this reason, extraction of parameter D_{T} from such experimental data could hardly be reliable. Astrahan[27] tried to attribute a clinical meaning to D_{T} by claiming that it delineates the region of the passage from the shoulder region to the linear component of the LQ model. Evidently, this is merely rewording the mathematical meaning of the mentioned Heaviside step function from Refs. 25–27 and, as such, cannot constitute a clinical nor biological interpretation of the transition dose D_{T}. Moreover, it has been found in applications[27, 28] that D_{T} can be anywhere in a quite wide dose range 15Gy–30 Gy. Such locations of D_{T} are incompatible with Astrahan's[27] interpretation of the transition dose, since shoulders do not typically extend to even the lowest limit (15 Gy) of the mentioned interval.

6.4 Mixed-order chemical kinetics for enzymatic cell repair systems

The mentioned problems with the LQ model have also been addressed within the PLQ model.[4–6] In this mechanistic description, as opposed to an empirical transition dose D_{T}, different passages from intermediate to high doses are governed by natural switches from various orders (zero, first, second) of chemical kinetics that underlies interactions of radiation with the cell. A key role in these different switches from one to another dose dependence of cell surviving fraction is the overall activity of enzyme molecules in the process of repair of radiation damage of the cell. This mixed-order enzyme catalysis, which is at the center of the cell repair system, guarantees the emergence of the correct asymptotes of the biological effect at both small and large doses. It also secures the existence of a shoulder of the proper width at intermediate doses in typical cell surviving fractions. Such a clear mechanism is backed by the accompanying mathematical formalism in the PLQ model through the Padé approximant, which is known to provide optimal interpolations and extrapolations between different regions of a given function.[11] This is achieved smoothly without ever resorting to unnecessary artifices, such as sewing two different regions by a transition dose D_{T} placed at an empirically found point through the Heaviside step function as in Refs. 25–27. Our initial testings,[4–6] as reviewed here, and our more recent thorough comparisons of nine different models with six cell lines[28] resulted in the common conclusion that the PLQ model systematically provides the most satisfactory description of cell survival after irradiation. This is most prominently evidenced at high doses in the reconstructed dose–effect curves as well as in the associated Fe-plots.[29]

ACKNOWLEDGMENTS

This work is supported by research funds from the Karolinska Institute, the Karolinska University Hospital's Radiumehemmet and the Swedish Cancer Society(Cancerfonden).

REFERENCES

1. Dale, R. G. The potential for radiobiological modelling in radiotherapy treatment design. *Radioth. Oncol.* **1990**, *19*, 245.
2. Jones, B.; Dale, R. G. Mathematical models of tumour and normal tissue response. *Acta Oncol.* **1999**, *38*, 883.
3. Sinclair, W. K. Biophysical aspects of radiation quality, Technical Report Series, 58, IAEA, Vienna, Austria, 1966.
4. Belkić, Dž. Parametric analysis of time signals and spectra from perspective of quantum physics and chemistry. *Adv. Quantum Chem.* **2011**, *61*, 145.
5. Belkić, Dž.; Belkić, K. Padé-Froissart exact signal-noise separation in nuclear magnetic resonance spectroscopy. *J. Phys. B: At. Mol. Opt. Phys.* **2011**, *44*, 125003.
6. Belkić, Dž.; Belkić, K. High-resolution signal processing in magnetic resonance spectroscopy for early cancer diagnostics. *Adv. Quantum Chem.* **2011**, *62*, 243.
7. Michaelis, L.; Menten, M. L. Die kinetik der invertinwirkung. *Biochem. Z.* **1913**, *49*, 333.
8. Barendsen, G. W. Dose fractionation, dose rate, and isoeffect relationships for normal tissue response. *Int. J. Radiat. Oncol. Biol. Phys.* **1982**, *8*, 1981.
9. Fowler, J. F. The linear-quadratic formula and progress in fractionated radiotherapy. *Br. J. Radiol.* **1989**, *62*, 679.
10. Corless, R. M.; Gonnet, G. H.; Hare, D. E. G.; Jeffrey, D. J.; Knuth, D. E. On the Lambert W function. *Adv. Comput. Math.* **1996**, *5*, 329.
11. Belkić, Dž. *Quantum-Mechanical Signal Processing and Spectral Analysis*; Taylor & Francis: London, 2005.
12. Thames, H. D.; Ang, K. K.; Stewart, F. A.; van der Schueren, E. Does incomplete repair explain the apparent failure of the basic LQ model to predict spinal cord and kidney responses to low doses per fraction?. *Int. J. Radiat. Biol.* **1988**, *54*, 13.
13. Kellerer, A. M.; Rossi, H. H. RBE and the primary mechanism of radiation action. *Rad. Res.* **1971**, *47*, 15.
14. Steel, G. G.; Duchesne, J. M.; Horwich, G. M.; Kelland, L. R.; Peacock, J. H. The dose-rate effect in human tumour cells. *Radioth. Oncol.* **1987**, *9*, 299.

15. Stephens, T. C.; Eady, J. J.; Peacock, J. H.; Steel, G. G. Split-dose and low-dose rate recovery in four experimental tumour systems. *Int. J. Rad. Biol.* **1987**, *52*, 157.
16. Jacobson, B. Evidence of recovery from X-ray damge in Chlamydominas. *Rad. Res.* **1957**, *1*, 394.
17. Elkind, M. M.; Sutton, H. X-ray damage and recovery in mammilian cells in culture. *Nature* **1959**, *184*, 1293.
18. Elkind, M. M.; Sutton, H. Radiation response to mammilian cell growth in culture: I. Repair of X-ray damage in surviving Chinese Hamster cells. *Rad. Res.* **1960**, *13*, 556.
19. Elkind, M. M.; Sutton-Gilbert, H.; Moses, W. B.; Kamper, C. Sublethal and lethal radiation damage. *Nature* **1967**, *214*, 1088.
20. Fowler, J. F. What next in fractionated radiotherapy. *Br. J. Cancer* **1984**, *49*, 285.
21. Muriel, V. P. Hypofractionation for radiotherapy. *Clin. Transl. Obncol.* **2007**, *9*, 21.
22. Hopewell, J. W.; Millar, W. T.; Ang, K. K. Toward improving the therapeutic ratio in stereotactic radiosurgery: selective modulation of the radiation responses of both normal tissue and tumor. *J. Neurosurg.* **2007**, *107*, 84.
23. Hutchinson, F.; Easter, S. S., Jr; A difference between biological effect of gamma rays and heavy ions. *Science* **1960**, *132*, 1311.
24. Utsumi, H.; Elkind, M. M. Potentially lethal damage versus sublethal damage: Independent repair processes in actively growing Chinese Hamster cells. *Rad. Res.* **1979**, 77, 346.
25. Paganetti, H.; Goitein, M. Biophysical modelling of proton radiation effects based on amorphous track models. *Int. J. Radiat. Biol.* **2001**, 77, 911.
26. Park, C.; Papiez, L.; Zhang, S.; Story, M.; Timmerman, R. D. Universal survival curve and single fraction equivalent dose: Useful tools in understanding potency of ablative radiotherapy. *Int. J. Radiat. Oncol. Biol. Phys.* **2008**, *70*, 847.
27. Astrahan, M. Some implications of linear-quadratic radiation dose-response with regard to hypofractionation. *Med. Phys.* **2008**, *35*, 4161.
28. Abdisheh, B.; Edgren, M.; Belkić, Dž.; Mavroidis, P.; Lind, B.; Brahme, A. A comparative analysis of radio-biological models for cell-surviving fractions at high doses. *Tech. Cancer Res. Treatm.* Ahead of print 2012 (DOI:10.7785/tcrt.2012.500306).
29. Douglas, B. G.; Fowler, J. F. The effect of multiple small doses of X-rays on skin reactions in the mouse and basic interpretation. *Rad. Res.* **1976**, *66*, 401.
30. Persson, L. Cell survival at low and high ionization densities investigated with a new model. PhD Thesis (unpublished), Stockholm University, Stockholm, 2002.
31. Kimmler, B. F.; Sinclair, W. K.; Elkind, M. M. N-Ethylmaleimide sensitization of X-irradiated hypoxic Chinese Hamster cells. *Rad. Res.* **1977**, *71*, 204.

INDEX